PRINCIPLES OF RADIATION SHIELDING

Arthur B. Chilton
J. Kenneth Shultis
Richard E. Faw

PRINCIPLES OF RADIATION SHIELDING

Arthur B. Chilton
Professor of Nuclear and Civil Engineering
University of Illinois at Urbana-Champaign

J. Kenneth Shultis
Professor of Nuclear Engineering
Kansas State University

Richard E. Faw
Professor of Nuclear Engineering
Kansas State University

PRENTICE-HALL, INC., Englewood Cliffs, NJ 07632

Library of Congress Cataloging in Publication Data

Chilton, Arthur B.
Principles of radiation shielding.

Includes bibliographical references and index.
1. Shielding (Radiation) I. Shultis, J. Kenneth.
II. Faw, Richard E. III. Title.
TK9210.C48 1984 621.48 83-3086
ISBN 0-13-709907-X

Editorial/production supervision and
interior design: *Shari Ingerman*
Cover design: *Edsal Enterprises*
Manufacturing buyer: *Tony Caruso*

Printed in the United States of America

10 9 8 7 6 5 4 3 2 1

ISBN 0-13-709907-X

Prentice-Hall International, Inc., *London*
Prentice-Hall of Australia Pty. Limited, *Sydney*
Editora Prentice-Hall do Brasil, Ltda., *Rio de Janeiro*
Prentice-Hall Canada Inc., *Toronto*
Prentice-Hall of India Private Limited, *New Delhi*
Prentice-Hall of Japan, Inc., *Tokyo*
Prentice-Hall of Southeast Asia Pte. Ltd., *Singapore*
Whitehall Books Limited, *Wellington, New Zealand*

contents

preface

This book is intended to fill a need for an adequate beginner's text in the subject of shielding against penetrating ionizing radiation, principally neutrons and photons. The presentation is directed toward the senior undergraduate or graduate student. The treatment in the early chapters is sufficiently fundamental that senior undergraduates could be expected to grasp the material without the benefit of previous extensive exposure to nuclear science and engineering. For the graduate student, the latter part of the text contains more sophisticated material, and references to important topics beyond the scope of the text are provided. Most chapters are provided with problem sets having a wide variation in difficulty, so that an instructor may to some extent adapt the text to the background of the students. Carefully selected data sets are provided and are designed to allow numerical solution of all problem sets as well as many other practical problems in radiation shielding.

For all chapters except Chapter 10, the student's mathematical background need include little beyond calculus and elementary vector concepts. Chapter 10, containing the most advanced material, requires of the student some knowledge in the areas of differential equations, orthogonal functions, mathematical transforms, and statistics. Mathematical functions of special importance in radiation shielding are introduced and discussed in an appendix to the text.

A few words on the underlying ideas behind the organization of textual material are appropriate. It is the conviction of the authors that nuclear radiation shielding contains an integrated body of common principles which do not depend on specific applications of the technology. Most textbooks on shielding have presented the subject within the framework of a single purpose, such as the

shielding of nuclear reactors. In our text, various radiation sources are noted, such as reactors, x-ray machines, radioisotopes, and fallout fields; but protection from these hazards are discussed largely as examples of the use of certain shielding principles or as the bases for homework problems.

Our experience in teaching the subject of radiation shielding has led us to stress in this text what we believe to be two unifying approaches to shielding methodology. The first is based on the recognition that much of the treatment for neutron shielding is essentially the same as that for photon shielding and, with some effort to establish common nomenclature and symbolism, can be presented in a unified manner. Such a unified approach is exemplified by Chapter 6. The second is the emphasis on determining the response of matter to radiation as being the ultimate goal of shielding analysis. Of particular importance in this regard is the concept of a "detector response function" as a means of bringing together many diverse elements of the subject.

The use of the International System of Units (SI) has been followed generally, leavened with the inclusion of other units in common usage, such as the electron-volt and its multiples. Nomenclature, symbols, abbreviations, and definitions have followed the practices prescribed by the International Commission on Radiation Units and Measurements and the American National Standards Institute to the greatest extent practicable, but a few arbitrary decisions have been made between various conflicting choices in order to provide the unity of approach we have emphasized.

We wish to acknowledge and express appreciation for the help and advice received from many friends and colleagues in the process of writing this text. The aid and suggestions of James Stubbins, Jai-Ki Lee, and Jeffrey Ryman are especially appreciated. Finally, we gratefully acknowledge the valuable comments from the many students who have been exposed to earlier drafts of the text and whose reactions have been our guide in trying to achieve clarity in our presentation of the principles of radiation shielding.

A.B.C., J.K.S., and R.E.F.

1 introduction

What is a shield? As used in this text, a *shield* is a physical entity interposed between a source of ionizing radiation and an object to be protected such that the radiation level at the position of that object will be reduced. The physical entity is usually composed of matter, but under some circumstances can be of a noncorporeal nature.[1] The object to be protected is most often a human being, but it can be anything that is sensitive to ionizing radiation.

The term *shielding* can be used to refer to a system of shields assembled for a specific radiation protection purpose. It is also the term for the technical area to which this text is devoted—the study of shields. This study has many aspects: radiation transport within the shield, radiation levels in the vicinity of shields, deposition of heat in shields, radioactivation of materials in the shield and surrounding environment, radiation penetration through holes in shields, radiation scattering around shields, selection of materials for shield use, optimization of shield configuration, and the economics of shield design. It also involves the understanding of related matters, such as radiation source characteristics, radiation protection criteria, radiation reflection properties of media, and the fundamental physics of the interaction of radiation with matter. Diverse areas of physics, mathematics, nuclear technology, radiation protection practice (health physics), and material science all bear on this subject.

The definition of a shield given above makes it clear that this text is concerned with the type of radiation that causes ionization of the media with which

[1] A magnetic field, for example, can deflect a moving charged particle from its original direction of motion. The earth's magnetic field acts to some extent as a shield which protects persons on its surface from bombardment by charged particles from outer space.

it interacts. Such radiations may be energetic particles carrying an electric charge, such as beta particles, alpha particles, protons, and other bare nuclei. These radiations have sometimes been called directly ionizing, since they cause ionization by forcing electrons from atoms of the media through which they pass. Other types of radiation, such as neutrons and x-ray or gamma-ray photons,[2] are not charged and therefore cause ionization through a more complicated mechanism involving the emission of energetic secondary charged particles, which cause most of the ionization. Consequently, photons and neutrons have sometimes been called indirectly ionizing particles [1].

The ionizing ability of these types of radiation is the reason for the importance of the study of shields, since the significant biological effects resulting from exposure to the radiation are intimately related to ionization of atoms in the human body. This text does not undertake an examination of such biological effects. The interested reader can obtain an excellent review of the biological effects of radiation from publications by the International Commission on Radiological Protection (ICRP) [2–4], the United Nations Scientific Committee on the Effects of Atomic Radiation (UNSCEAR) [5], the National Council on Radiation Protection and Measurements [6], and the Advisory Committee on the Biological Effects of Ionizing Radiation of the National Academy of Sciences (NAS-BEIR) [7].

The division of ionizing radiations into two types has important implications in the study of shields. The directly ionizing radiations interact very strongly with shielding media and are therefore easily stopped. Indirectly ionizing radiation may be quite penetrating and the shielding required may be quite massive and expensive. The reader will find that most of the attention in this text is, therefore, paid to the shielding of the two types of indirectly ionizing radiation, neutrons and photons.

A brief comment on the historical developments that have led to the present state of knowledge in shielding against ionizing radiation may be useful. The origins go back to the science of optics, before ionizing radiation was even discovered. The exponential attenuation behavior of light in its transmission through semitransparent media has long been recognized; and the use of the "ray" approach in geometric optics has been carried over and is still useful in dealing with many shielding situations involving photons and neutrons. It is also a matter of history that the attenuating effect of various media was the means whereby many new types of radiation were discovered and analyzed, from Roentgen's original discovery of x rays in 1895 to the present.

The first quarter of the twentieth century was a period in which the hazards from ionizing radiation gradually became known, and the use of heavy materials

[2]Both gamma and x rays (photons) are of shielding interest, but the distinction between them is of little importance here. The former are emissions from atomic nuclei and are generally of higher energy per individual photon. X rays will normally be identified specifically in this text only when there is some special reason to do so, since shielding principles relating to gamma photons are also applicable to x-ray photons.

such as lead in the form of sheets and bricks became commonplace for shielding use against x rays and gamma rays. The uses of such radiation were largely confined to medical applications or to fundamental scientific studies. A body of shielding knowledge of elementary character began to be accumulated, largely summarized in the form of "half-thickness" values or simple exponential factors involving "absorption coefficients."

The second quarter of the twentieth century was marked by a rapid increase in the knowledge of the fundamentals of the interaction between radiation and matter, made possible by the development of quantum mechanics as a theoretical tool. The discovery of the neutron in 1930 began the chain of events which led eventually to the use of intense neutron-emitting sources such as nuclear reactors and nuclear explosives. This new type of particle was soon recognized to be a most significant hazard, protection against which might require massive shielding.

Until recently, most information on shielding was developed on an ad hoc basis, with little concern being felt that the subject might deserve attention as an abstract discipline in its own right. Medical radiologists, supported by radiological physicists, have developed, largely on an experimental basis, shielding data for radiation from x-ray machines and from the more commonly used radioisotopes. These data are expressed either in graphical or tabular form [8]. The advent of nuclear weapons required new programs for radiological defense in the military establishment and its counterpart in the civil defense establishment. As a result of extensive experimental work in nuclear weapons testing during the 1950s, supplemented by some profound theoretical work on gamma radiation transport [9, 10], a technology on weapons radiation shielding evolved. In the early 1960s, particular emphasis was placed on fallout gamma radiation shielding, and a well-developed system of shielding analysis resulted from a combination of theoretical calculations, experimental laboratory work, and extensive engineering methodology development [11–14].

The development of nuclear power reactors introduced new ideas and data on shielding, especially against neutrons. The specific programs that emphasized these shielding advances included the submarine nuclear propulsion program, the nuclear-powered aircraft program, and the development of central-station nuclear power plants. In the 1950s the approach to neutron shielding was largely empirical, involving variants of the old exponential attenuation approach. Since that time, these empirical methods have been supplemented by more accurate and more powerful techniques for solving the basic mathematical equations governing radiation transport.

In the 1960s, manned space vehicle development brought about an increase in knowledge of shielding against the very high energy charged particles encountered in outer space. In the 1970s, the rapid increase in fusion reactor studies brought about an emphasis on such specialized shielding problems as heat deposition, thermoelastic stress analysis, and tritium production within the reaction blanket, which also serves as the shield.

It is important to recognize how important the development of computer technology has been in improving the art of shielding. Although the basic physical principles governing the transport of radiation (the "Boltzmann equation") were known many decades previously, it was only through the use of computers that these principles could be applied to photon and neutron shielding with any hope of high accuracy. Although many of the ideas and techniques still used in shielding do not require direct access to computers, much of the data on which they depend were developed by computerized calculations; and, if reasonably accurate answers in complex situations are needed, it is almost mandatory to use computerized techniques.

The science of shielding is one that is still developing. It is still not possible, with all the theoretical and calculational means at hand, to guarantee reasonable accuracy for the prediction of radiation levels within and beyond a complex shield, especially for neutrons. Some of the difficulty is related to the lack of adequate knowledge of the interaction probabilities for the radiation interacting with the shielding media. Difficulties exist in the development of satisfactory computational methods for analyzing radiation transport. In particular, computerized approaches are hampered by the amount of data that needs to be handled, the computer time requirements, and the difficulties involved in handling complex geometrical shapes. Continued progress in shielding analytical capability is thus strongly linked to advances in the computer-hardware field.

No personal credit has been given up to this point to the many individuals who have contributed to the development of shielding technology. Their names will become known to the student as he or she reads the text, especially the bibliographic information provided as references at the end of each chapter. Significant textbooks and handbooks providing broad coverage on shielding are also listed at the end of this chapter [10, 14–22]. Similarly, many reports, monographs, and journal articles have been published on various particular aspects of nuclear radiation shielding. Particularly significant sources of such information are the following organizations: Radiation Shielding Information Center, Oak Ridge National Laboratory, Oak Ridge, Tennessee; National Council on Radiation Protection and Measurements, Bethesda, Maryland; Radiation Protection and Shielding Division of the American Nuclear Society, LaGrange Park, Illinois; OECD Nuclear Energy Agency Data Bank, Gif-sur-Yvette, France; and the European Shielding Information Service, Ispra, Italy.

One thing is noteworthy about the reference works. To a great extent, they were written within the context of the needs of a single research program—sometimes a single source type. The basic ideas are all present in one or another of these books and reports, but there is a great diversity in what they emphasize, the nomenclature they employ, and the form in which the information is cast. It is the purpose of the present text to emphasize those principles which are common to all shielding applications and thus establish shielding as an integrated

field of knowledge. It is hoped that the student who uses this work will thereby learn the fundamentals of shielding in a way that will permit their application to a wide variety of practical problems.

REFERENCES

1. "Radiation Quantities and Units," ICRU Report 19, International Commission on Radiation Units and Measurements, Washington, D.C., 1971.
2. "The Evaluation of Risks from Radiation, a Report Prepared for Committee 1 of the International Commission on Radiological Protection," ICRP Publication 8, Pergamon, Oxford, 1968.
3. "Radiosensitivity and Spatial Distribution of Dose," ICRP Publication 14, Pergamon, Oxford, 1969.
4. "News from the International Commission on Radiological Protection," *Health Phys.* **24**, 360 (1973).
5. "Ionizing Radiation: Levels and Effects," United Nations Scientific Committee on the Effects of Atomic Radiation, United Nations, New York, 1972.
6. "Basic Radiation Protection Criteria," NCRP Report 39, National Council on Radiation Protection and Measurements, Washington, D.C., 1971.
7. "The Effects on Populations of Exposure to Low Levels of Ionizing Radiation," National Academy of Sciences/National Research Council, Washington, D.C., 1980.
8. "Structural Shielding Design and Evaluation for Medical Use of X Rays and Gamma Rays of Energies up to 10 MeV," NCRP Report 49, National Council on Radiation Protection and Measurements, Washington, D.C., 1976.
9. L. V. Spencer and U. Fano, "Penetration and Diffusion of X-Rays: Calculation of Spatial Distributions by Polynomial Expansion," *J. Res. Natl. Bur. Stand.* **46**, 446 (1951).
10. U. Fano, L. V. Spencer, and M. J. Berger, "Penetration and Diffusion of X-Rays," in *Handbuch der Physik*, Vol. 38/2, S. Flügge (ed.), Springer-Verlag, Berlin, 1959, p. 660.
11. L. V. Spencer, "Structure Shielding against Fallout Radiation from Nuclear Weapons," NBS Monograph 42, U.S. Government Printing Office, Washington, D.C., 1962.
12. "Shelter Design and Analysis, Vol. 1: Fallout Radiation Shielding," Doc. TR-20-(Vol. 1), Office of Civil Defense (July 1967), as amended by Change 1 (July 1969), Change 2 (Jan. 1970), and Change 3 (Nov. 1974).
13. W. R. Kimel (ed.), "Radiation Shielding: Analysis and Design Principles as Applied to Nuclear Defense Planning," OCD/KSU Doc. TR 40, U.S. Government Printing Office, Washington, D.C., 1966.
14. L. V. Spencer, A. B. Chilton, and C. M. Eisenhauer, "Structure Shielding against Fallout Gamma Rays from Nuclear Detonations," NBS Special Publication 570, U.S. Government Printing Office, Washington, D.C., 1980.

15. T. Rockwell III (ed.), *Reactor Shielding Design Manual*, D. Van Nostrand, Princeton, N.J., 1956.
16. B. T. Price, C. C. Horton, and K. T. Spinney, *Radiation Shielding*, Pergamon, Elmsford, N.Y., 1957.
17. H. Goldstein, *Fundamental Aspects of Reactor Shielding*, Addison-Wesley, Reading, Mass., 1959.
18. T. Jaeger, *Grundzuge der Strahlenshutztechnik*, Springer-Verlag, Berlin, 1960; translated by L. Dresner as *Principles of Radiation Protection Engineering*, McGraw-Hill, New York, 1965.
19. E. P. Blizard (ed.), *Reactor Handbook*, Vol. III, Part B: *Shielding*, 2nd ed., Interscience, New York, 1962.
20. N. M. Schaeffer (ed.), *Reactor Shielding for Nuclear Engineers*, TID-25951, National Technical Information Service, Springfield, Va., 1973.
21. R. G. Jaeger (ed.), *Engineering Compendium on Radiation Shielding*, Vol. I: *Shielding Fundamentals and Methods*; Vol. II, *Shielding Materials and Design*; Vol. III, *Shield Design and Engineering*, Springer-Verlag, New York, 1968–1975.
22. A. E. Profio, *Radiation Shielding and Dosimetry*, Wiley, New York, 1979.

2 characterization of radiation fields and sources

2.1 FUNDAMENTAL RADIATION FIELD VARIABLES

Since shielding technology largely involves the study of radiation fields in and near shields, it is always necessary to describe in some manner the physical characteristics of the radiation fields. Conceivably, one could try to use a very detailed description of a radiation field by specifying at every instant of time the position, direction of travel, energy, and internal state of each particle[1] in the radiation field. However, such a detailed microscopic description, even if it were possible, is hardly practical. A shielding analyst would be so overwhelmed by the sheer amount of information about the field that he or she would be unable to use the data in the design of shields. Clearly, radiation fields should be characterized by macroscopic concepts that lend themselves more readily to physical interpretation and applicability. In this section are introduced those field concepts that have been found to be of practical use in shielding calculations.

The evolution of shielding technology has benefited from contributions made in many areas of radiation physics, and consequently, there exist several different nomenclatures and symbolisms for the same radiation field concepts. To the greatest extent possible, standard nomenclature and symbols recognized by the shielding community [1,2] are used throughout this book.

[1]The term "particle" in this text includes the photon.

2.1.1 Fluence, Net Flow, and Associated Rates

One of the more fundamental and important measures of a radiation field is the number of its particles that enter a specified volume, since for the particles to cause damage in a medium they first must enter it. To describe this aspect of a radiation field, the concept of *particle fluence* is used. The particle fluence, or simply *fluence*, at any point in a radiation field may be thought of in terms of the number of particles, ΔN_p, that penetrate a hypothetical sphere of cross-sectional area ΔA centered at the given point [see Fig. 2.1(a)]. The fluence at that point is then defined by

$$\Phi \equiv \lim_{\Delta A \to 0} \frac{\Delta N_p}{\Delta A}. \tag{2.1}$$

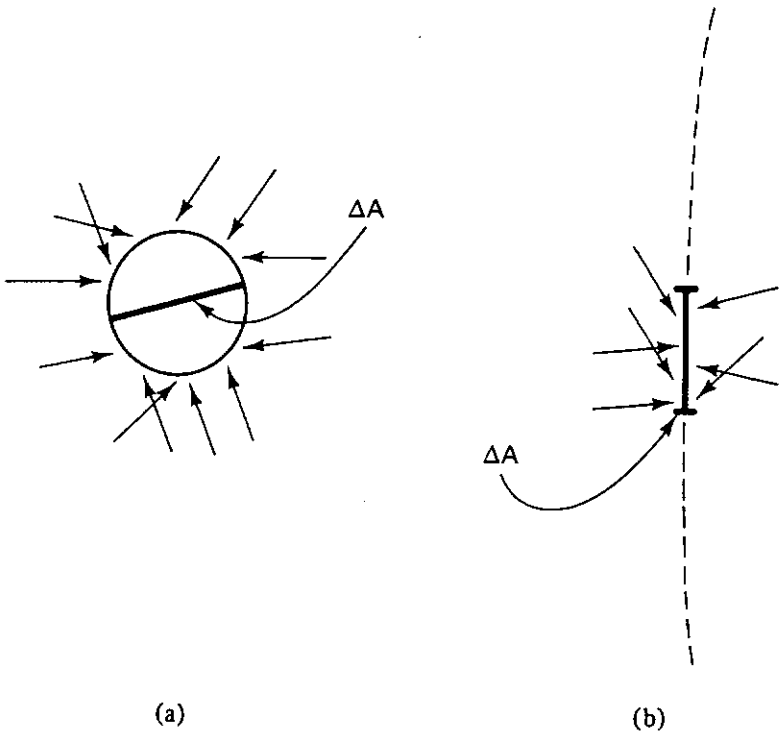

Figure 2.1 Basic detector configurations for definitions of fluence and particle flow concepts.

The limiting process in this definition must be carefully qualified. Any radiation field has a finite particle density; that is, there is a graininess to the radiation field. As ΔA becomes smaller, $\Delta N_p/\Delta A$ will no longer vary smoothly but will begin to exhibit statistical fluctuations (see Fig. 2.2). Fluence is a macroscopic concept, and the required limiting value must be extrapolated from those conceptual values of $\Delta N_p/\Delta A$ for which statistical fluctuations in ΔN_p caused by the graininess of the radiation field are negligible. In effect, this extrapolation averages the stochastic nature of the radiation field. For a situation in which ΔN_p is small (e.g., x rays from a distant star), even when ΔA is large, an accurate extrapolation may be impossible, and the concept of fluence is meaningless in such a case.

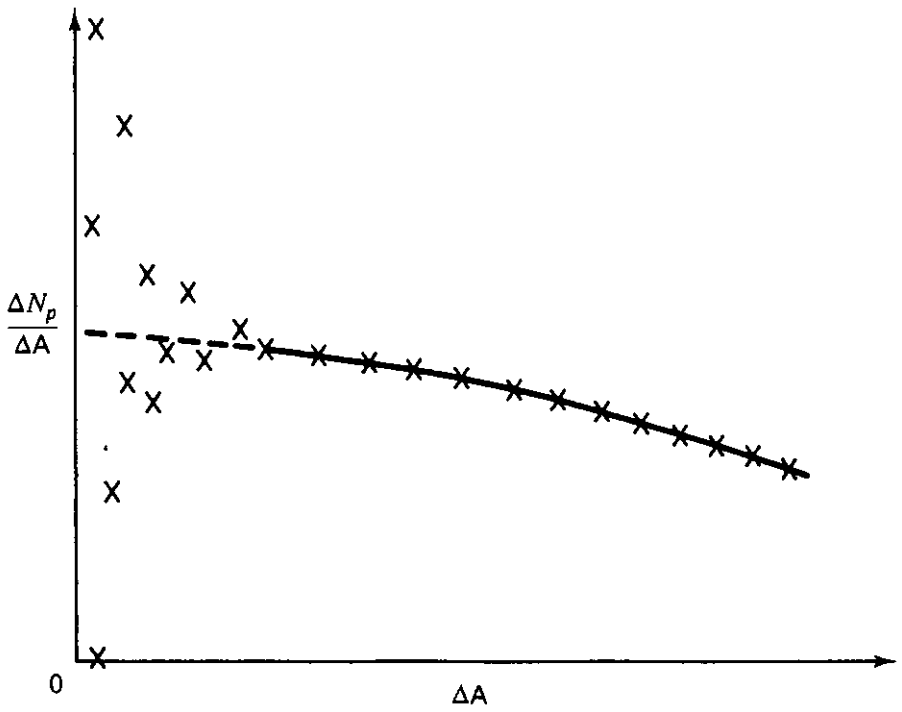

Figure 2.2 Extrapolation of data to zero value of ΔA to obtain a value of fluence.

Another macroscopic measure of a radiation field is the net number of particles crossing a given surface with a well-defined orientation. In this text, the term *net particle flow*, or simply *net flow*, at a point on a surface is the net number of particles in some specified time interval that flow across a surface area at the point, per unit area in the surface, in the direction specified as positive (one of the two sides of the surface). One may thus visualize an incremental area ΔA on some geometric surface, with the specified surface point included in ΔA [see Fig. 2.1(b)]. If the number of particles crossing ΔA from the negative to positive side is ΔM_p^+ and the number from the positive to negative side is ΔM_p^-, the *net* number crossing in the positive direction is $\Delta M_p \equiv \Delta M_p^+ - \Delta M_p^-$. The net flow at the given point, designated as J_n (for reasons to be made clear shortly), is defined by

$$J_n \equiv \lim_{\Delta A \to 0} \frac{\Delta M_p}{\Delta A}, \tag{2.2}$$

where the limiting process is qualified in the same manner as that of Eq. (2.1). The partial flows of particles in the positive and negative directions, J_n^+ and J_n^-, respectively, are defined in terms of ΔM_p^+ and ΔM_p^- in a similar manner. The relation between the net and partial flows is thus

$$J_n = J_n^+ - J_n^-. \tag{2.3}$$

The concepts of fluence and particle flow appear to be very similar, both being defined in terms of a number of particles per unit area. Both have dimensions of inverse square of length and usually are expressed in units of cm^{-2}. However, in the concept of fluence the area presented to the incoming particles is independent of the direction of the particles, whereas for the particle flow concept the area ΔA has a well-defined orientation in space.

Associated with the concepts of fluence and net flow are their rates of change with time. The *fluence rate* is usually called the *flux density*, or quite often just "flux."[2] *Net flow rate* has no officially accepted alternative name, although among some shielding specialists it is often called "current." (However, such usage will be avoided in this book because of possible confusion with other current variables to be defined in Section 2.1.4.)[3] The flux density ϕ is defined in terms of the incremental fluence $\Delta\Phi$ that occurs at a specified position in a time interval Δt by the equation

$$\phi \equiv \lim_{\Delta t \to 0} \frac{\Delta \Phi}{\Delta t}. \tag{2.4}$$

Similarly, the net flow rate j_n can be expressed in terms of the incremental net flow ΔJ_n that occurs in an increment of time Δt at a specified position by

$$j_n \equiv \lim_{\Delta t \to 0} \frac{\Delta J_n}{\Delta t}. \tag{2.5}$$

The limiting process in these definitions must again be visualized as extrapolations from values for sufficiently large Δt intervals so that the stochastic fluctuations in the radiation field are negligible.

For mathematical convenience, except under circumstances in which the statistical approach to radiation behavior is emphasized, one may consider the flux density to be a proper time derivative of the fluence, and the fluence during a period of time to be an integral of the flux density over that time period. Similar statements can be made about net flow rate and net flow.

Fluence and its time rate, flux density, can be defined in ways other than through the spherical detector approach presented above (see Problem 2.1). It can be shown that all these approaches are mutually consistent. One alternative approach is to identify the flux density at a point, for monoenergetic particles, as the product of the particle number density at the point and the speed of the particles. For particles of varied kinetic energies the total flux density is obtained by integrating (or summing) the product of the density and speed of particles of each kinetic energy $\left[\text{i.e., } \int_0^\infty dv\, vn(v)\right]$. Another alternative approach is to base the definitions on some small volume ΔV of arbitrary shape surrounding the point in question. To define fluence, the lengths of the track segments within the volume are summed for the particles that pass through or within the volume increment. The fluence is then defined as

$$\Phi \equiv \lim_{\Delta V \to 0} \frac{\text{sum of the internal track segment lengths}}{\Delta V}, \tag{2.6}$$

[2]The standard glossaries do not recognize "flux" as an approved alternative, in spite of its common use[1,2]. The International Commission on Radiation Units and Measurements suggests that "fluence rate" is preferred over "flux density." However, in order to facilitate reader understanding, and in accordance with widely accepted usage among shielding specialists, this text will continue to employ the term "flux density."

[3]It has also been suggested that this be called the plane (or planar) fluence rate [3].

where the limiting process is on the same stochastic basis used for the original definition of fluence. In this text, the definition of fluence used in a specific instance will depend on which is more convenient.

2.1.2 Differential Energy and Directional Flux Density

The foregoing definitions are useful for the development of a conceptual understanding, but for a detailed mathematical analysis it is best to start from the differential point of view. If one considers, at a point established by the position vector $\mathbf{r}$, the flux density of only those particles having an energy within a certain energy band ΔE about the energy E and moving in directions within a narrow solid angle $\Delta\Omega$ about the direction specified by the unit vector $\mathbf{\Omega}$, there is established a flux density which is a density function of two further variables, energy and solid angle:

$$\phi(\mathbf{r}, E, \mathbf{\Omega}) \equiv \lim_{\substack{\Delta E \to 0 \\ \Delta\Omega \to 0}} \frac{\Delta\phi(\mathbf{r}; E, \Delta E; \mathbf{\Omega}, \Delta\Omega)}{\Delta E\, \Delta\Omega}, \tag{2.7}$$

where the limiting process is of the same stochastic nature as previously explained in the case of the basic definitions of fluence and flux density. The quantity $\phi(\mathbf{r}, E, \mathbf{\Omega})$ is called the *doubly* (perhaps more accurately, "trebly," since it takes two angle variables to specify a direction) *differential energy and directional flux density*, with units of $\text{cm}^{-2}\ \text{MeV}^{-1}\ \text{sr}^{-1}\ \text{s}^{-1}$ (or equivalent units).[4] This quantity may also be called a *joint energy and directional distribution of the flux density*. Clearly,

$$\phi(\mathbf{r}) \equiv \int_0^\infty \int_{4\pi} \phi(\mathbf{r}, E, \mathbf{\Omega})\, dE\, d\Omega, \tag{2.8}$$

where $\phi(\mathbf{r})$, previously designated as the *flux density*, is often called in this context the *total flux density*, to distinguish it from the *doubly differential flux density*.

Similar relationships and terminology exist for the fluence concept.

2.1.3 Angular Flux Density and Flux Density Spectrum

By integrating the doubly differential flux density with respect to energy, one obtains what is alternatively called the *angular distribution of the flux density*, the *angular differential flux density*, or simply the *angular flux density*:

$$\phi(\mathbf{r}, \mathbf{\Omega}) \equiv \int_0^\infty \phi(\mathbf{r}, E, \mathbf{\Omega})\, dE. \tag{2.9}$$

If the angular flux density is independent of direction $\mathbf{\Omega}$, it is called *isotropic*.

By integrating the doubly differential flux density with respect to direction coordinates, one obtains the *energy distribution of the flux density*, or simply the

[4] In the spherical coordinate system, $d\Omega \equiv d\omega\, d\psi$, where ω is the cosine of the polar angle and ψ is the azimuthal angle.

flux density spectrum:

$$\phi(\mathbf{r}, E) \equiv \int_{4\pi} \phi(\mathbf{r}, E, \boldsymbol{\Omega})\, d\Omega \tag{2.10}$$

$$= \int_0^{2\pi} \int_{-1}^{1} \phi(\mathbf{r}, E, \boldsymbol{\Omega})\, d\omega\, d\psi, \tag{2.11}$$

where ψ is the azimuthal angle of the direction vector $\boldsymbol{\Omega}$ with respect to some reference plane in a spherical polar coordinate system and ω is the cosine of the angle between the direction vector and the polar axis. It will be found in Chapter 5 that most idealized types of "dose rates" are derivable from the flux density spectrum.

Obviously, the total flux density can be obtained either by integration of the angular flux density with respect to direction or by integration of the flux density spectrum with respect to energy.

Similar relationships exist for the fluence.

2.1.4 Vector Current Density and Angular Flow Rate

Either the angular flux density or the doubly differential flux density, which refer to particles moving in a well-defined direction, may be multiplied by the unit vector $\boldsymbol{\Omega}$, the product being a vector which one may call the *angular flux density vector* $\phi(\mathbf{r}, \boldsymbol{\Omega})\boldsymbol{\Omega}$ or the *doubly differential flux density vector* $\phi(\mathbf{r}, E, \boldsymbol{\Omega})\boldsymbol{\Omega}$. These quantities both lead to similar concepts of particle flow, and therefore the discussion here will deal only with the simpler one, the angular flux density vector.

The *vector current density*, sometimes called simply the *current density* (although the latter terminology leads to some confusion as to whether the vector, the absolute value of the vector, or the value of a component of the vector is intended), is given by integration of the angular flux density vector over all directions, that is,

$$\mathbf{j}(\mathbf{r}) \equiv \int_{4\pi} \phi(\mathbf{r}, \boldsymbol{\Omega})\boldsymbol{\Omega}\, d\Omega. \tag{2.12}$$

It is of particular interest to establish the relationship of $\mathbf{j}(\mathbf{r})$ to the net flow rate $j_n(\mathbf{r})$ already introduced and defined by Eq. (2.5). Figure 2.3 shows a point on a surface at which a unit normal vector $\hat{\mathbf{n}}$ is established. The orientation of $\hat{\mathbf{n}}$ defines positive directions of particle flow across the surface. The circle shown represents a spherical detector of cross-sectional area ΔA at that location. It is clear from basic definitions [see Eqs. (2.1) to (2.6)] that the angular flow rate per unit solid angle, which can be designated as $j_n(\mathbf{r}, \boldsymbol{\Omega})$, is less than the angular flux density $\phi(\mathbf{r}, \boldsymbol{\Omega})$ by a factor $\cos\alpha$. Since $\cos\alpha = \hat{\mathbf{n}} \cdot \boldsymbol{\Omega}$, this provides a mathematical definition for the *angular flow rate*:

$$j_n(\mathbf{r}, \boldsymbol{\Omega}) \equiv \hat{\mathbf{n}} \cdot \boldsymbol{\Omega}\phi(\mathbf{r}, \boldsymbol{\Omega}); \tag{2.13}$$

consequently,

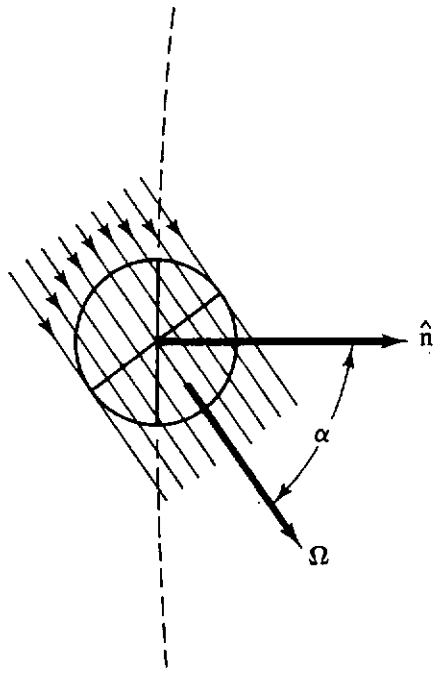

Figure 2.3 Relationship of vector current density to flow rate across a unit area of prescribed orientation. See the text for description.

$$j_n(\mathbf{r}) \equiv \int_{4\pi} j_n(\mathbf{r}, \boldsymbol{\Omega})\, d\Omega \tag{2.14}$$

$$= \hat{\mathbf{n}} \cdot \int_{4\pi} \boldsymbol{\Omega}\phi(\mathbf{r}, \boldsymbol{\Omega})\, d\Omega \tag{2.15}$$

$$= \hat{\mathbf{n}} \cdot \mathbf{j}(\mathbf{r}). \tag{2.16}$$

The net flow rate j_n is thus shown to be a component of the vector current density $\mathbf{j}$ with respect to the normal to the surface through which the flow is occurring.

These concepts have a parallel for the fluence field, so that the net flow across a surface at a given point, designated by J_n, is given by

$$J_n = \hat{\mathbf{n}} \cdot \mathbf{J}, \tag{2.17}$$

where $\mathbf{J}$, called the *vector flow*, is the time integral of the vector current density over an appropriate time interval.

2.1.5 Energy Flux Density and Energy Fluence

It is sometimes more convenient to analyze a radiation field from the standpoint of *energy* flux density and *energy* flow rate rather than in terms of the corresponding *particle* concepts. For any of the foregoing concepts involving only monoenergetic particles of energy E, it is possible to define similar concepts involving energy instead of particles. Thus, one can for monoenergetic particles establish the *energy flux density* $E\phi(\mathbf{r})$, the *net energy flow rate* $Ej_n(\mathbf{r})$, the *angular energy flux density* $E\phi(\mathbf{r}, \boldsymbol{\Omega})$, and even the *doubly differential energy flux density* $E\phi(\mathbf{r}, E, \boldsymbol{\Omega})$. For nonmonoenergetic radiation, the energy flux density is defined as

$$I(\mathbf{r}) \equiv \int_0^\infty E\phi(\mathbf{r}, E)\, dE, \tag{2.18}$$

where I is the symbol for energy flux density. (This symbol arises from the traditional physics usage of the term *intensity* as a synonym for energy flux density.) Similar concepts can be defined for the *energy fluence*.

2.2 DIRECTIONAL PROPERTIES OF THE RADIATION FIELD

The angular flux density has a directional dependence which may be expressed with respect to any set of angular variables by which a direction itself is specified, for example, in direction cosines. It is more convenient mathematically, in most circumstances, to express the directional dependence with respect to orthogonal coordinate angles such as the spherical polar set θ (the polar angle) and ψ (the azimuthal angle). The angular flux density may then be expressed in the most general way in terms of spherical harmonics, with respect to some reference direction taken as the "pole."

Under some circumstances the physical situation for the radiation field is such that one can expect azimuthal symmetry with respect to some preferred direction (i.e., the angular flux density is independent of ψ). In such a case the directional distribution can be expressed as an infinite series based on Legendre polynomials (see Appendix 2):

$$\phi(\mathbf{r}, \boldsymbol{\Omega}) = \phi(\mathbf{r}, \omega) = \frac{\phi(\mathbf{r})}{4\pi} \sum_{l=0}^{\infty} a_l P_l(\omega)(2l + 1), \tag{2.19}$$

where

$$a_l = \frac{2\pi}{\phi(\mathbf{r})} \int_{-1}^{1} \phi(\mathbf{r}, \omega) P_l(\omega)\, d\omega. \tag{2.20}$$

The symbol ω is the cosine of θ, the angle between the direction vector $\boldsymbol{\Omega}$ and the preferred (reference) direction. The angular flux density is still to be considered as having the angular unit "per steradian" even when expressed as a function of ω or of θ. (This is generally true throughout this entire text, although other texts sometimes have different conventions in this respect.) It is easily shown that the coefficients in this expression are normalized so that a_0 equals unity. Furthermore, the values of all the a's should be such that $\phi(\omega)$ is never negative, since a negative value of angular flux density is not physically meaningful.

When all coefficients except a_0 are zero, the distribution is independent of ω as well as ψ and is thus isotropic.

Since the Legendre functions P_l are all polynomials in ω, the series expansion above could be written as

$$\phi(\omega) = \sum_{l=0}^{\infty} b_l \omega^l. \tag{2.21}$$

When b_1 is a positive number and all other coefficients b_n are zero, the distribution is proportional to ω and is called a *cosine distribution*. This is a physically valid description for nonnegative values of ω; but for negative values $\phi(\omega)$ appears

to be negative, which is not physically allowable. One way to avoid this anomaly is to consider that only positive values of ω are meaningful. For example, if one wishes to describe the angular flux density only in outward directions from the surface of a finite body, ϕ^+, only the directional distribution in the outward, or positive, direction is of significance.

Alternatively, the term "cosine distribution" may refer to all directions, involving both positive and negative values of ω, with the distribution symmetric in ω, so that $\phi(\omega) = b|\omega|$. Here, b equals the total flux density divided by 2π, as is easily demonstrated by integration over all values of the solid angle.

The foregoing comments on the flux density ϕ apply equally to the flow rate j_n. It should be noted, however, that if the axis of azimuthal symmetry is the same as the normal to the surface of interest at the point in question, an *isotropic distribution for angular flux density* establishes a *cosine distribution for the angular flow rate.*

This relationship might be amplified by the following tabulations, each one involving a directional distribution—one isotropic with respect to flux density and the other isotropic with respect to flow rate. In both cases, the distributions are assumed to be independent of the azimuthal angle about the normal to the hypothetical surface at the point in question. This is illustrated in Fig. 2.4, in which ω is the cosine of angle measured from $\hat{\mathbf{n}}$.

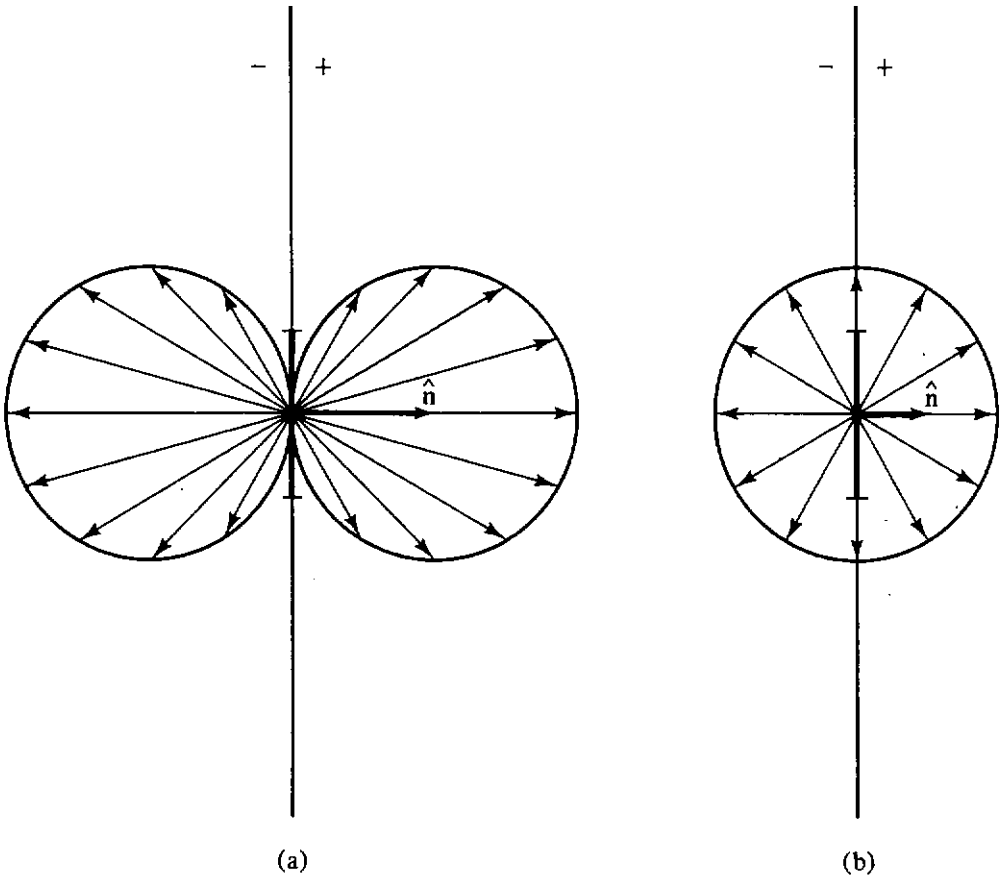

Figure 2.4 Characteristics at a point on a surface for radiation fields involving (a) isotropic flux density and (b) isotropic flow rate. The lengths of the lines are proportional to the equivalent source strengths in the directions indicated.

Isotropic angular flux density distribution. If the total flux density is ϕ:

1. The partial flux density in the positive (forward) hemisphere of directions ϕ^+ is $\phi/2$.
2. The angular flux density $\phi(\Omega)$, or $\phi(\omega)$, is given by $\phi/4\pi$ or $\phi^+/2\pi$.
3. The angular flow rate $j_n(\Omega)$, or $j_n(\omega)$, is given by $\phi\omega/4\pi$ or $\phi^+\omega/2\pi$.
4. The total net flow rate is zero.

Isotropic angular flow rate distribution. If the partial flow rate in the positive (forward) hemisphere of directions is j_n^+:

1. The partial flow rate in the backward direction j_n^- equals j_n^+.
2. The total net flow rate is zero.
3. The angular flow rate $j_n(\Omega)$, or $j_n(\omega)$, is equal to $j_n^+/2\pi$.
4. The angular flux density $\phi(\Omega)$, or $\phi(\omega)$, is given by $j_n^+/(2\pi|\omega|)$ (this is called a "secant distribution").
5. Neither the total flux density nor the partial flux density in the forward direction are finite because of the singularity existing in $\phi(\Omega)$ when ω equals zero.

The first of these two situations can be used as a rough approximation of conditions at the surface of a reactor core. There, an almost isotropic flux density distribution (cosine flow rate distribution) has been shown to be a reasonable approximation [4].

The second situation may seem nonphysical, but actually it can be approached and can exist as an idealization of certain real situations. An example is the angular flux density near the surface of a smooth plane uniformly contaminated with a radiation-emitting source (see Section 6.4.3).

An important reciprocal relationship exists between the angular flux density distribution at a given point and the angular flux density values at various points on a surface[5] (possibly hypothetical) which surrounds the original point under the condition that there is a vacuum (or at least a noninteractive medium) between the given position and the surrounding surface. In the simplest form for this relationship, no sources exist within the surface. Then the radiation field at the given point, where a directional flux density detector may be visualized, is established entirely as a result of the radiation coming through the surface toward the detector position. A simple example would be a directional detector at a given position inside a room providing shelter from a radioactive fallout field outside: the interior faces of the walls form the surrounding surface, and the air in the room may be treated as a vacuum without appreciable error.

[5]For this simple situation, the surface is considered "non-reentrant"; that is, no line from the detector cuts the surface in more than one point.

The explication of this reciprocity relationship is provided in the following paragraphs.

Figure 2.5 represents a spherical flux density detector of differential size located at a point specified by position vector $\mathbf{r}_d$ and, on the surface A_s, a typical point located by $\mathbf{r}_s$. A differential area of the surface, dA_s, with inward normal $\hat{\mathbf{n}}$, surrounds the surface point. The cross-sectional area of the spherical detector is dA_d. At the detector, dA_s subtends a solid angle of $d\Omega_s$ steradians; at the surface point, dA_d subtends a solid angle of $d\Omega_d$. The unit vector $\boldsymbol{\Omega}$ is in the direction from dA_s to dA_d. No medium of a scattering or absorbing nature exists between the surface and the detector, and no particles enter the detector except those which have passed through the surface (i.e., no sources exist within the surface). Steady-state conditions are assumed.

The rate at which particles flow through dA_s in directions within $d\Omega_d$ about

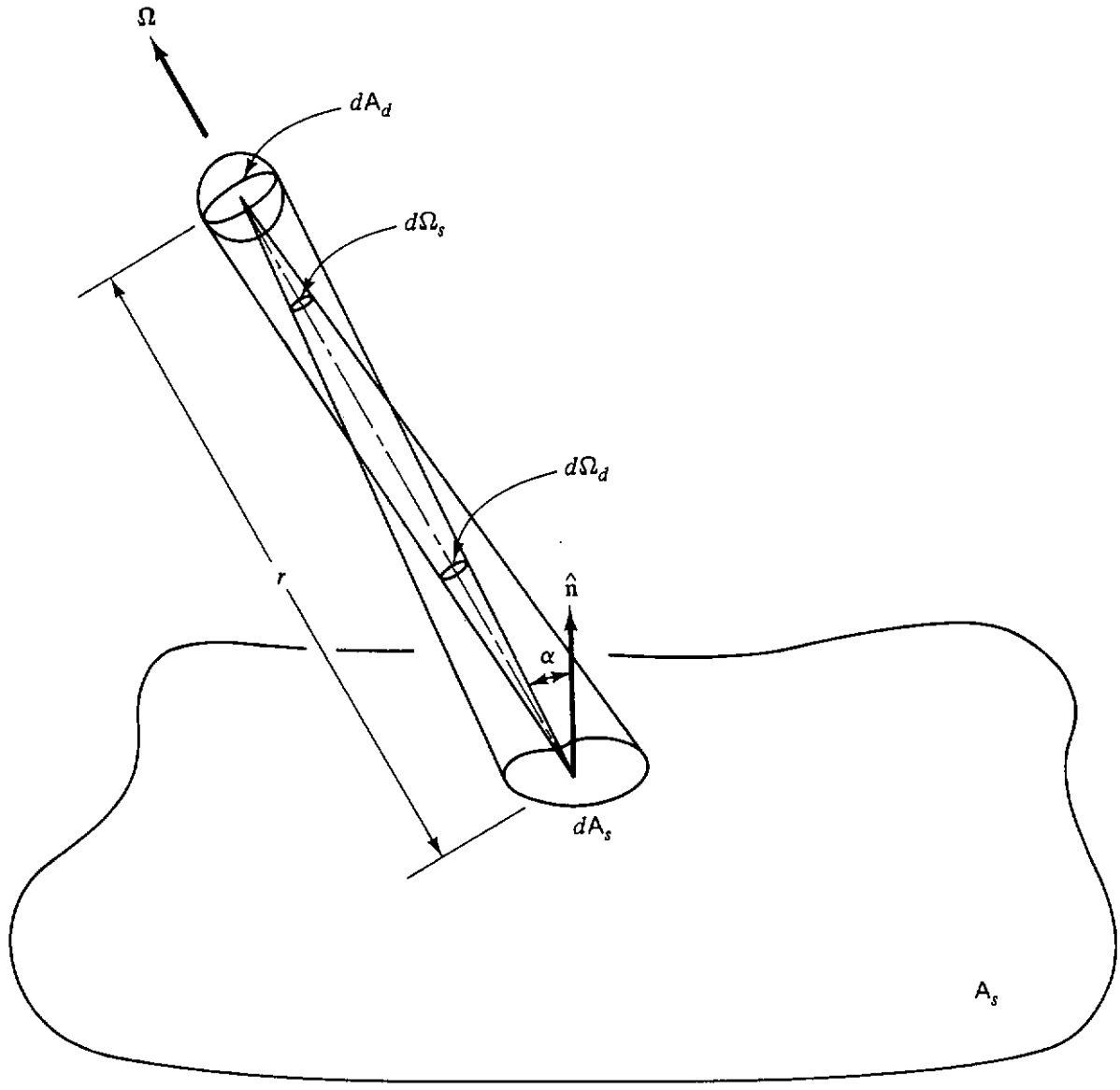

Figure 2.5 Geometric relationships involved in the discussion of the angular flux density reciprocity principle.

$\boldsymbol{\Omega}$ is given by

$$j_n(\mathbf{r}_s, \boldsymbol{\Omega})\, dA_s\, d\Omega_d \equiv \frac{j_n(\mathbf{r}_s, \boldsymbol{\Omega})\, dA_s\, dA_d}{r^2}, \tag{2.22}$$

where $r \equiv |\mathbf{r}_s - \mathbf{r}_d|$. This quantity, divided by dA_d, is the contribution to the flux density at $\mathbf{r}_d$ from dA_s, as one would surmise from Eq. (2.1), and it can be considered the contribution coming from differential solid angle $d\Omega_s$:

$$d\phi(\mathbf{r}_d, \boldsymbol{\Omega}) \equiv \phi(\mathbf{r}_d, \boldsymbol{\Omega})\, d\Omega_s = \frac{j_n(\mathbf{r}_s, \boldsymbol{\Omega})\, dA_s}{r^2}, \tag{2.23}$$

and thus[6]

$$\phi(\mathbf{r}_d) = \int_{A_s} \frac{j_n(\mathbf{r}_s, \boldsymbol{\Omega})}{r^2}\, dA_s, \tag{2.24}$$

in which the integration over the entire surface implies an integration over the directions from which the radiation is *coming* rather than the directions toward which it is *going*, which is more customary.

One may arrive at a more symmetrical expression by substituting $j_n(\mathbf{r}_s, \boldsymbol{\Omega}) \equiv \phi(\mathbf{r}_s, \boldsymbol{\Omega}) \cos\alpha$, where $\cos\alpha \equiv \hat{\mathbf{n}} \cdot \boldsymbol{\Omega}$. Then,

$$d\phi(\mathbf{r}_d, \boldsymbol{\Omega}) = \phi(\mathbf{r}_s, \boldsymbol{\Omega}) \frac{\cos\alpha\, dA_s}{r^2}. \tag{2.25}$$

But $d\Omega_s \equiv \cos\alpha\, dA_s/r^2$, and thus

$$d\phi(\mathbf{r}_d, \boldsymbol{\Omega}) = \phi(\mathbf{r}_s, \boldsymbol{\Omega})\, d\Omega_s \tag{2.26}$$

or

$$\phi(\mathbf{r}_d, \boldsymbol{\Omega})\, d\Omega_s = \phi(\mathbf{r}_s, \boldsymbol{\Omega})\, d\Omega_s, \tag{2.27}$$

leading in turn to the reciprocity relationship valid for $\boldsymbol{\Omega} = (\mathbf{r}_d - \mathbf{r}_s)/r$:

$$\phi(\mathbf{r}_d, \boldsymbol{\Omega}) = \phi(\mathbf{r}_s, \boldsymbol{\Omega}). \tag{2.28}$$

This may be integrated with respect to $d\Omega_s$ to obtain

$$\phi(\mathbf{r}_d) = \int_{4\pi} \phi(\mathbf{r}_s, \boldsymbol{\Omega})\, d\Omega_s, \tag{2.29}$$

where the integration is over the entire solid angle subtended at the detector by the surface (4π steradians in the example of a detector inside a room).

2.3 DOSIMETRIC QUANTITIES OF A PURELY PHYSICAL NATURE

A shielding analysis, if taken to the extreme of completeness, would provide a detailed description of the radiation field at every point in and near the shield and, if time-varying, at every moment when the person or object to be protected is present. Such a description would provide for each point the distribution in

[6]It is interesting to observe that a flow rate at one point can be considered a flux density at another. This matter is particularly significant in albedo studies (see Chapter 9).

direction and energy at each instant. However, the amount of data would be so voluminous as to overwhelm the user. It is therefore desirable to reduce these data to only that information pertinent to the hazard one is trying to protect against or the phenomenon one is trying to quantify.

Use of the particle fluence would be a step toward data compression, involving summation (or integration) over direction and energy variables; yet this quantity is not closely enough related to the radiation hazard to be an adequate measure of it. Energy fluence appears to be a better choice, since the kinetic energy carried by a particle must have some correlation with the damage it may do to biological tissue or some other radiosensitive material. Even this choice is not entirely adequate: one has good reason to believe that the effect of a thermal neutron, for example, must be much greater than one would expect based on its relatively small amount of kinetic energy.

One must examine more deeply the mechanism of the effect of radiation on matter in order to determine what properties of the radiation are best correlated with its hazard. It is apparent that one should be concerned not so much with the passage of particles or energy through a region of the material being subjected to the hazard, but with the creation of certain physical effects in that material. These effects may be the deposition of energy, ionization of the medium, induction of atomic displacements, production of molecular changes, or other phenomena. Historically, since medical radiologists were those first concerned with the effects of radiation on biological material, any such effect is called a "dose" if accumulated over a period of time or a "dose rate" if the effect per unit of time is of interest.

As is seen, a number of different physical phenomena may be involved and these may be quantified in a variety of ways. Thus, "dose" is not a precise term and is best used in a generic sense to relate to any measure (actual or conceptual) of physical phenomena involving the effect of radiation on materials. There are a few particular dosimetric quantities which have been precisely defined and which are found useful in shielding analysis. These are defined below [1]. To understand these definitions, one must appreciate the several-stage process in the passage of energy from its original to its final location and form. In general, these stages are as follows:

1. Neutrons or photons (the "primary" radiation) have interactions with the electrons or the nuclei of atoms of the material through which they are passing.
2. As a result of the interactions, "secondary" charged particles are emitted from the atoms involved, and each of these starts out with kinetic energy related to the energy of the primary particle and the type of interaction.
3. The secondary charged particles lose energy while traversing the material either (a) through ionization and associated processes (atomic and molecular excitation and molecular rearrangement), or (b) through emission of photons called *bremsstrahlung*. The progress of energy degradation need

not be considered further; suffice it to say that the energy removed from the secondary charged particles by the process of ionization and associated mechanisms is distributed along the tracks of the charged particles, for the most part promptly being degraded into thermal energy of the medium.

4. The uncharged primary particles may also produce uncharged particles through scattering or other processes. These uncharged particles also carry off part of the energy of the interaction, but this is not of immediate concern in the definitions which follow.

If a small incremental volume of material ΔV around a given point in space has mass Δm and the energy imparted[7] to it by ionizing radiation is $\Delta\epsilon$, the *absorbed dose* D in the given material at this point is defined by

$$D \equiv \lim_{\Delta V \to 0} \frac{\Delta\epsilon}{\Delta m}, \tag{2.30}$$

in which the limit process, as before, is such as to ignore statistical variability. The standard unit of absorbed dose is the *gray* (abbreviation Gy), with 1 gray being equal to an imparted energy of 1 joule per kilogram.[8] (Sometimes it is desirable, however, to use other units, such as ergs per gram or MeV per gram.) From a macroscopic point of view, absorbed dose is treated as a point function.

The material involved in the hypothetical measurement process just described is usually contained in an incremental volume of the medium actually present, but this is not necessarily so. One may conceive of the incremental volume as being a small inclusion used as the measuring instrument within some other medium. Thus, one may speak of "tissue absorbed dose" at a point in the middle of a concrete shield or for that matter even in a vacuum. For this reason it is always important in speaking of absorbed dose to indicate, if it is not clearly implied, the actual absorbing medium.

The concept of absorbed dose is useful in two aspects of shielding. First, absorbed dose becomes a heat source in problems involving heat flow and temperature distribution within a shield. Second, the energy imparted to biological tissue is very closely correlated with the hazard to living creatures, especially for radiation particles having the same ionization density along their tracks [6]. (See the discussion in Section 2.4 on the effect of LET.)

[7]The "energy imparted" is precisely defined [1] as the sum of the energies (excluding rest mass energies) of all charged and uncharged ionizing particles entering the volume minus the sum of the energies (excluding rest mass energies) of all charged and uncharged ionizing particles leaving the volume, further corrected by subtracting the energy equivalent of any increase in rest mass of the material in the incremental volume. Thus, the energy imparted is that which is involved in the ionization and excitation of atoms within the incremental volume, plus any rearrangement of molecules within that volume. This energy is degraded almost entirely into thermal energy.

[8]Until recently [5], the standard unit of absorbed dose was the *rad*, which was defined as 100 ergs per gram. Thus, 1 gray equals 100 rads.

A closely related quantity, used only in connection with uncharged radiation, is that called *kerma* (an acronym for *k*inetic *e*nergy of *r*adiation produced per unit *ma*ss in matter). It is symbolized by K and defined by

$$K \equiv \lim_{\Delta V \to 0} \frac{\Delta E_k}{\Delta m}, \tag{2.31}$$

where the limit process as usual is such as to ignore the statistical variations, ΔE_k is the energy transferred as kinetic energy of the secondary charged particles released by neutral particle interactions within ΔV, and the other symbols are as previously defined. Kerma has the same units as absorbed dose (gray or rad) and is also considered as a point function.

The use of the kerma requires some knowledge of the material present in the incremental volume, possibly hypothetical, used as the idealized detector, in the same fashion as does the use of the absorbed dose concept. Thus, one may speak conceptually of tissue kerma in a concrete shield or in a vacuum, even though the incremental volume of tissue may not actually be present.

Absorbed dose and kerma are sometimes used interchangeably and, if expressed in the same units, will frequently be almost equal to one another. Kerma is rather more easily calculated, since the accounting of the energy is at the point of primary beam interaction and the transport of the secondary particles can be ignored; however, it is difficult to measure directly. Absorbed dose, on the other hand, can be measured rather more easily (e.g., by calorimetry, since the energy transferred is eventually almost entirely transformed into thermal energy) but is much more difficult to calculate precisely. Kerma is not as directly related in principle to biological effects of radiation nor to the shield heating effects as absorbed dose and is therefore of value to shielding analysts largely by reason of the relative simplicity of its calculation and the hope of approximating the correct absorbed dose by its use. (Chapter 5 gives more details on the degree of validity of this substitution.)

The quantity called *exposure* (abbreviation X) is used traditionally to specify the radiation field of gamma or x-ray photons. It is defined as the absolute value of the ion charge (of one sign) produced anywhere in air by the complete stoppage of all electrons (positrons and negatrons) that are liberated by the interaction of the photon field in an incremental volume of air, per unit mass of air in that volume. The exposure is closely related to air kerma, but differs in an important respect. The phenomenon measured by the interaction of the photons in the incremental volume of air (or an air-like material) is not the kinetic energy of the secondary electrons but the ionization caused by the further interaction of these secondary electrons with air (or an air-like medium).

The basic unit of exposure is the roentgen (abbreviation R) which is defined as 2.58×10^{-4} C of separated charge (either positive or negative) per kilogram of air in the incremental volume where the primary photon interactions occur.

It is possible to convert a calculation of air kerma into exposure by two steps. The first involves the change from kinetic energy to ionization by the

conversion factor W, which fortunately is almost energy independent for any given material. For air, it is estimated to be 33.85 ± 0.15 electron volts of kinetic energy per ion pair [7]. In addition, the result must be reduced somewhat to account for the fact that in general some of the original energy of the secondary electrons may go not into ionization but into bremsstrahlung.

Since exposure is a kerma-like concept, there are difficulties in the measurement process. The measurement must be such as to ensure that all the ionic charge resulting from interaction in air in a small test volume at a certain location is collected for measurement. However, much of the ionization occurs in air (or an air-like medium) outside the test volume. This makes charge collection complicated, especially since ions created by secondary particles from interactions just outside the test volume are present also. The problem can be surmounted, at least for low-energy photons, if in the vicinity of the test volume there is "electronic equilibrium," a concept explained in detail in Chapter 5. Further details concerning the measurement of exposure are beyond the scope of this text but may be found in other specialized works [8,9].

The use of exposure as a measure of the photon field is sometimes criticized but has survived because it correlates reasonably well with the biological hazard from photons. This is due primarily to the fact that air and tissue are roughly similar in their interaction properties with photons on a per-unit-mass basis. Furthermore, air is an easy material to use in the sensitive volume of a detector. On the other hand, absorbed dose in tissue is more closely related to biological effects and its use appears more fundamentally sound. It is possible that the concept of exposure will some day be discarded as obsolete.

The definitions given above have been for *dose* quantities. *Dose rate* quantities follow naturally. These are symbolized in standard fashion by putting dots over the appropriate symbols specified above (i.e., $\dot{D}$, $\dot{K}$, and $\dot{X}$).

2.4 RADIATION QUANTITIES CLOSELY RELATED TO BIOLOGICAL RISK

If the energy deposited by ionizing radiation per unit of tissue were by itself an adequate criterion of biological damage, absorbed dose would be the best dosimetric quantity to use for radiation protection purposes. However, there are also other factors to consider, for example, the linear density of ionization in the tissue cells. (These charged particles may be the primary radiation or they may be the secondary emissions from interactions of uncharged ionizing radiation. Since this text is concerned almost entirely with photon and neutron shielding, the latter circumstance is of particular concern here.)

In dealing with the fundamental behavior of biological material or organisms subjected to radiation, one needs to take into account variations in the sensitivity of the biological material to different types or energies of radiation. For this purpose, radiobiologists define a *relative biological effectiveness* (RBE)

for each type and energy of radiation as the ratio of the absorbed dose of a reference type of radiation (such as x rays from a 250-kVp machine) producing a certain kind and degree of biological effect to the absorbed dose of the radiation under consideration required to produce the same kind and amount of effect. RBE is normally determined experimentally and takes into account all factors relating to biological response to radiation in addition to absorbed dose [2].

RBE depends on many variables: the physical nature of the radiation field, the type of biological material, the particular biological response considered, and even the degree of that response. For this reason, it is too complicated for practical, everyday use. In 1964, therefore, a group of specialists established somewhat arbitrarily a related but much simplified concept called *quality factor* for use in routine protection practice. To understand the definition of this quantity, another concept, called "linear energy transfer," must first be explained.

Linear energy transfer (LET) is the spatial transfer rate of energy from a charged particle to a medium in the locality of the particle track through the medium [2]. Before precise values of the LET can be given, one must indicate just what is meant by "locality" in the preceding sentence. This can be done in either of two ways. It may refer either to a maximum distance from the track or to a maximum value of the discrete energy loss by the charged particle, beyond which losses are no longer considered as local. In either case, the limits chosen should be specified. This is normally done by means of a subscript on L, the symbol for LET. Thus, L_∞, for example, means that all distances or all energies are included; and in this case the LET is equivalent to the "collisional stopping power" (see Section 3.9), differing only in the units normally employed (keV μm^{-1} for LET).

Since linear ionization density is believed to be an important parameter in explaining variation in biological effects of radiations of different type and energies, and since linear ionization density is clearly proportional to LET (see Sec. 5.5), quality factor is defined primarily in terms of LET. In particular, since tissue is largely water and has an average atomic number close to that of water, quality factor is generally made a mathematical function of the linear collisional stopping power, or L_∞, in water.[9]

The relationship between the two concepts, given in Table 2.1, is prescribed by the International Commission on Radiation Protection (ICRP). Values of Q are specified only for certain values of L_∞, and any reasonable interpolation procedure is allowed. ICRP indicates that, for electrons, a Q-value of unity is to be used at all energies, regardless of what Table 2.1 might seem to require.

Quality factors can be ascribed to uncharged ionizing radiation also, through a knowledge of the properties of the secondary charged particles they

[9]Since quality factor plays the same role in normal radiation protection practice as RBE does in radiobiology, some authorities use essentially the same definition for quality factor as RBE [4]; but this practice gives quality factor more scientific objectivity than it deserves.

TABLE 2.1 Values of Quality Factor (Q) as a Function of L_∞ in Water

L_∞ (keV μm^{-1})	Q
3.5 or less	1
7.0	2
23	5
53	10
175	20

Source: *Ref. 6.*

release upon interaction with matter. Since secondary electrons released by gamma- or x-ray photons are always assigned a quality factor of unity, the same quality factor also applies universally to all ionizing photons. The situation for neutrons is not quite so simple, and average values must be determined; however, a value of 10 is usually quite a safe value to use if more detailed analysis cannot be performed or is otherwise undesirable.

The overall risk of radiation is then considered to be closely correlated with a dosimetric quantity called *dose equivalent*, where the dose equivalent at some point in tissue is defined as being equal to the product of the tissue absorbed dose at the point and the average quality factor for the entire fluence of charged particles at the point. The unit of the dose equivalent is the *sievert*[10] (abbreviation Sv) and the symbol prescribed is H [1]. The size of the sievert is such that

$$H \text{ (sieverts)} = D \text{ (grays)} \times \bar{Q}, \tag{2.32}$$

where $\bar{Q}$, the *average* quality factor, is defined as

$$\bar{Q} = \frac{\sum_i D_i Q_i}{\sum_i D_i}, \tag{2.33}$$

in which the index i relates to the variations in the type and energy of the charged particles located in the incremental volume at the point of measurement.

Because dose equivalent is defined in terms of a quality factor, which is based to some extent on human judgment and therefore susceptible to change, the objectively physical nature of the quantity is open to argument. Its direct measurement is not as straightforward as that of absorbed dose; and it is more common to determine it either completely by calculation or by conversion from a more elementary quantity such as absorbed dose.

Since quality factor is defined for use in conventional and routine radiation

[10]Until 1980, the standard unit for the dose equivalent was the *rem* [5], which is $\frac{1}{100}$ of the size of the sievert. Equation (2.32) is still valid when the absorbed dose is in rads and the dose equivalent is in rems.

protection practice, the quantity dose equivalent is, similarly, firmly established only within this context. It is nevertheless not uncommon for "dose" to be measured in sieverts (or rems) in the context of very high exposures that might be sustained in emergency peacetime or wartime conditions. One school of thought is that such practice should be deplored and such exposures should be measured in terms of quantities such as absorbed dose; the opposite school of thought is that the use of dose equivalent units is permitted provided that one employs, not the quality factors provided for conventional purposes, but a more basic relative biological effectiveness suitable to the particular circumstances. For the purpose of this text, we shall continue to use the quality factor in the standard manner.

Dosimetric quantities partly of a biological nature, just as those of a completely physical nature, have time rates associated with them. These are symbolized usually by putting dots over the appropriate symbols already specified. Thus, $\dot{H}$ refers to a dose equivalent rate in units such as Sv h^{-1}.

2.5 GENERAL SOURCE PROPERTIES

An adequate solution of a shielding problem generally requires an understanding of the characteristics of the source(s) from which the radiation emerges. In this section, sources will be discussed from a rather abstract point of view, but the properties noted are those one must identify and quantify in practical cases. Detailed source descriptions are provided in Chapter 4.

The most fundamental type of source is a *point source.* Although this may be impossible to visualize in the precise mathematical sense, any volume of matter sufficiently small which emits radiation may be treated as a point source. The term "sufficiently small" implies that the physical dimensions of the volume are small compared to the other important dimensions of the problem, such as source–detector distance. Furthermore, there should be negligible interaction of the radiation with the matter within the volume concerned. This last requirement can sometimes be relaxed by allowing the volume source to be replaced by a hypothetical point source having possibly modified characteristics, including reduced source strength (resulting from self-absorption), degradation of the source spectrum, and change in directional distribution of emissions.

A discrete point source has a *strength* $S_p(\mathbf{r}, \boldsymbol{\Omega}, E, t)$ which indicates the number of particles emitted per unit time, per unit solid angle about the direction $\boldsymbol{\Omega}$, per unit energy interval about the energy E, at time t, and at the location specified by the position vector $\mathbf{r}$. The time dependence may be very rapid (e.g., the 60-Hz variation from certain x-ray machines); it may be rather slow (e.g., the steady diminution in activity of a radioisotope of appreciable half-life); or it may be nonexistent to all practical purposes (e.g., the radiation from a reactor that has been operating a long time in a steady-state condition). Since most shielding problems assume steady-state conditions, the time dependence

can usually be averaged or neglected. We shall do so, for the most part, henceforth.

One readily defines the source strength directional distribution

$$S_p(\mathbf{r}, \mathbf{\Omega}) = \int_0^\infty S_p(\mathbf{r}, \mathbf{\Omega}, E)\, dE, \tag{2.34}$$

the source strength spectrum

$$S_p(\mathbf{r}, E) = \int_{4\pi} S_p(\mathbf{r}, \mathbf{\Omega}, E)\, d\Omega, \tag{2.35}$$

and the total source strength

$$S_p(\mathbf{r}) = \int_{4\pi} \int_0^\infty S_p(\mathbf{r}, \mathbf{\Omega}, E)\, dE\, d\Omega. \tag{2.36}$$

The concepts above represent rates. Integration over a certain period of time provides a quantity called *emission*. The distributions of this quantity with respect to direction and energy are like those given above for source strength, and only the latter will be discussed in further detail.

Sources are often distributed throughout a volume in space, so that one may identify a volumetric density function $S_V(\mathbf{r}, \mathbf{\Omega}, E)$ which represents the strength per unit volume. Each differential volume element dV may then be considered as a point source of strength $S_V(\mathbf{r}, \mathbf{\Omega}, E)\, dV$. Nuclear reactors are an obvious example in which the source is a volume distribution.

Sources can often be distributed in thin layers at surfaces or as point sources spread on a surface. Such a situation can be considered as a surface, or area, distribution of the source; and it is reasonable to establish a function $S_A(\mathbf{r}, \mathbf{\Omega}, E)$ as the strength per unit area, where $\mathbf{r}$ represents position vectors only for points on the surface. The deposition of fallout particles on the earth's surface is an example where this concept is useful.

The surface considered as a location of an area distributed source, however, need not be an obvious medium boundary but may in certain cases be a mathematically defined surface within some medium. Thus, a source distributed throughout a sphere may also be considered an infinite collection of spherical surface sources, each located at a concentric shell of differential thickness out of which the sphere can be considered to be composed.

There is a similarity of a flow rate to a source which sould be noted here. Assume that, in the situation depicted in Fig. 2.5, a surface source $S_A(\mathbf{r}_s, \mathbf{\Omega})$ is uniformly distributed within the differential area $d\mathrm{A}_s$; and eliminate any other source of radiation causing a flux density at that location. The differential area then behaves as a point angular source of strength $S_A(\mathbf{r}_s, \mathbf{\Omega})\, d\mathrm{A}_s$ particles per unit time per steradian. The flux density $d\phi(\mathbf{r}_d, \mathbf{\Omega})$ resulting from this source at the detector position is given by

$$d\phi(\mathbf{r}_d, \mathbf{\Omega}) = \frac{S_A(\mathbf{r}_s, \mathbf{\Omega})\, d\mathrm{A}_s\, d\Omega_d}{d\mathrm{A}_d}, \tag{2.37}$$

according to Eq. (2.1); and since $d\Omega_d \equiv d\mathrm{A}_d/r^2$,

$$\circledR d\phi(\mathbf{r}_d, \mathbf{\Omega}) \equiv \phi(\mathbf{r}_d, \mathbf{\Omega})\, d\Omega_s = \frac{S_A(\mathbf{r}_s, \mathbf{\Omega})\, dA_s}{r^2}. \tag{2.38}$$

This expression is exactly like Eq. (2.23) except that j_n has been replaced by S_A. One may conclude from this that a flow rate through a surface has the properties of a surface source at that point and may be treated as equivalent. This is illustrated in Fig. 2.4, where the equivalent source relationships are shown for points in an isotropic flux density field and an isotropic flow rate field.

This important result has been demonstrated here only, of course, if there is no interacting medium present. It is possible to show that this is valid even in the case an interacting medium is present, but the proof must be deferred until a more advanced exposition can be provided in Chapter 10.

2.6 CONVERSION FROM DISTRIBUTED TO DISCRETE CONCEPTS, AND VICE VERSA

Much of the analytical methodology in shielding depends on the assumption that a field or source is discrete in some sense or another. For example, we may develop formulas and theories in which a source is assumed to be located at a point, a stream of particles is assumed to be monoenergetic, or a beam is assumed to be parallel, with each particle having the same direction. In order to use these methods for cases that actually involve distributed variables, some sort of conversion is necessary. For example, a distributed source over a small region of space may be assumed to be a point source if the region is sufficiently small, thus:

$$S_p = \int_{\Delta V} S_V(\mathbf{r})\, dV. \tag{2.39}$$

Similarly, a flux density spectrum may be considered a sum of discrete monoenergetic densities by suitable integration over small increments of energy, thus:

$$\phi \equiv \int_0^\infty \phi(E)\, dE = \sum_i \phi_i, \tag{2.40}$$

where

$$\phi_i \equiv \int_{E_i}^{E_i + \Delta E} \phi(E)\, dE. \tag{2.41}$$

Other examples can be found.

On the other hand, much of the analytical theory in shielding has been developed through the use of continuous functions, and it is sometimes desirable to apply this theory to situations in which some of the variables are actually discrete in one or more of the independent variables. The description of discrete variables in a format which permits their mathematical manipulation as continuous variables is provided through the use of the Dirac delta function (DDF) formalism. The properties of the Dirac delta function are listed in Appendix 2. By use of these properties it can be shown that the following descriptions are proper in this formalism.

1. The flux density of a monoenergetic, broad, parallel beam of particles of energy E_0 passing through the plane at x and proceeding in direction $\mathbf{\Omega}_0$:

$$\phi(x, E, \mathbf{\Omega}) \longrightarrow \phi(x)\delta(E - E_0)\delta(\mathbf{\Omega} - \mathbf{\Omega}_0) \tag{2.42}$$

$$\equiv \phi(x)\delta(E - E_0)\delta(\omega - \omega_0)\delta(\psi - \psi_0), \tag{2.43}$$

   where $\phi(x, E, \mathbf{\Omega})$ would typically have units of $cm^{-2}\ s^{-1}\ MeV^{-1}\ sr^{-1}$ and $\phi(x)$ would have corresponding units of $cm^{-2}\ s^{-1}$.

2. A plane, isotropic, monoenergetic source of particles of energy E_0 at a plane $x = 0$:

$$S_A(x, E, \mathbf{\Omega}) \longrightarrow \frac{S_A\delta(x)\delta(E - E_0)}{4\pi}, \tag{2.44}$$

   where $S_A(x, E, \mathbf{\Omega})$ would typically have units of $cm^{-2}\ s^{-1}\ MeV^{-1}\ sr^{-1}$ and S_A would have corresponding units of $cm^{-2}\ s^{-1}$.

In addition, the DDF is sometimes used to permit expressing and formally treating a function of two variables as if the two variables were independent, even when there is an auxiliary expression relating the two variables. The auxiliary relationship, when arranged so as to equal zero, is made the argument of the DDF in this case. Scattering coefficients, as functions of energy and the scattering angle, are examples of this. (See Chapter 3 for specific cases.)

REFERENCES

1. "Radiation Quantities and Units," ICRU Report 33, International Commission on Radiation Units and Measurements, Washington, D.C., 1980.
2. "Glossary of Terms in Nuclear Science and Technology," USAS NI.1-1967, American National Standards Institute, New York, 1967.
3. C. A. Carlsson, "Relationships between Energy Fluence and Energy Incident on, Emitted by, or Imparted to a Body," *Phys. Med. Biol.* **24**, No. 6, 1209–1215 (1979).
4. B. T. Price, C. C. Horton, and K. T. Spinney, *Radiation Shielding*, Pergamon, Elmsford, N.Y., 1957, pp. 192–193.
5. "Radiation Quantities and Units," ICRU Report 19, International Commission on Radiation Units and Measurements, Washington, D.C., 1971. (Superseded by ICRU Report 33; see Ref. 1.)
6. "Radiation Protection: Recommendations of the International Commission on Radiological Protection, Adopted Sept. 17, 1965," ICRP Publication 9, Pergamon, Elmsford, N.Y., 1966, 1969, pp. 3–4.
7. "Average Energy Required to Produce an Ion Pair," ICRU Report 31, International Commission on Radiation Units and Measurements, Washington, D.C., 1979.
8. G. N. Whyte, *Principles of Radiation Dosimetry*, Wiley, New York, 1959.
9. "Physical Aspects of Irradiation: Recommendations of the International Commission on Radiation Units and Measurements," NBS Handbook 85, National Bureau of Standards, Washington, D.C., 1964. Also listed as ICRU Report 10b, 1962.

10. "Radiation Quantities and Units: International Commission on Radiation Units and Measurements (ICRU) Report 10a," NBS Handbook 84, National Bureau of Standards, Washington, D.C., 1964.
11. "Protection against Neutron Radiation," NCRP Report 38, National Council on Radiation Protection and Measurements, Washington, D.C., 1971, para. 7.6.
12. A. B. Chilton, "A Note on the Fluence Concept," *Health Phys.* **34**, 715–716 (1978).
13. A. B. Chilton, "Further Comments on an Alternate Definition on Fluence," *Health Phys.* **36**, 637–638 (1979).

PROBLEMS

2.1. Flux density is defined three ways in Section 2.1.1. Prove that these definitions are equivalent. First prove the results for a monoenergetic, monodirectional beam of particles. The generalization is trivial. You may assume that in any sphere or other volume you set up for discussion, the volume is so small that the interactions within the sphere are negligible. The inquiring student may wish to consult Refs. 12 and 13.

2.2. The direction (unit) vector $\mathbf{\Omega}$ is commonly expressed in terms of the polar angle θ and azimuthal angle ψ as shown in Fig. P2.2. Express $\mathbf{\Omega}$ in terms of the unit vectors, $\hat{\mathbf{i}}$, $\hat{\mathbf{j}}$, and $\hat{\mathbf{k}}$, directed along the x, y, and z axes of a Cartesian coordinate system.

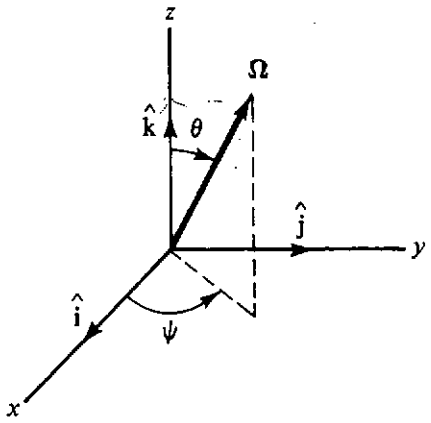

2.3. Show that, if the angular flux density $\phi(\mathbf{r}, \mathbf{\Omega})$ is isotropic, the current density $\mathbf{j}(\mathbf{r})$ is equal to zero.

2.4. Give a physical interpretation of $\nabla \cdot \mathbf{j}(\mathbf{r})$, the divergence of the current density.

2.5. Show that the angular flux density $\phi(\mathbf{r}, \mathbf{\Omega})\, d\Omega$ is the number of particles per unit time, with directions within $d\Omega$ crossing the unit differential area perpendicular to the direction $\mathbf{\Omega}$.

2.6. Consider a broad, uniform, unidirectional beam of particles intersecting a plane surface. All particles travel in the direction $\mathbf{\Omega} = \hat{\mathbf{i}} \sin\theta_0 \cos\psi_0 + \hat{\mathbf{j}} \sin\theta_0 \sin\psi_0 + \hat{\mathbf{k}} \cos\theta_0$. The unit vector $\hat{\mathbf{k}}$ is perpendicular to the plane and $\hat{\mathbf{i}}$, $\hat{\mathbf{j}}$, and $\hat{\mathbf{k}}$ define a Cartesian coordinate system. Show that the angular flux density $\phi(\mathbf{r}, \mathbf{\Omega})$ can be written as $\phi(\mathbf{r}, \mathbf{\Omega}) = \phi(\mathbf{r})\delta(\omega - \omega_0)\delta(\psi - \psi_0)$ in which δ represents the Dirac delta function and $\omega = \cos\theta$. Use Eq. (2.12) to determine $\mathbf{j}(\mathbf{r})$, the current density. Show that the number of particles crossing the surface per unit area per

unit time is $\omega_0\phi(\mathbf{r})$, that is, that the z component of $\mathbf{j}$ is the number of particles per unit time crossing unit area perpendicular to the z axis.

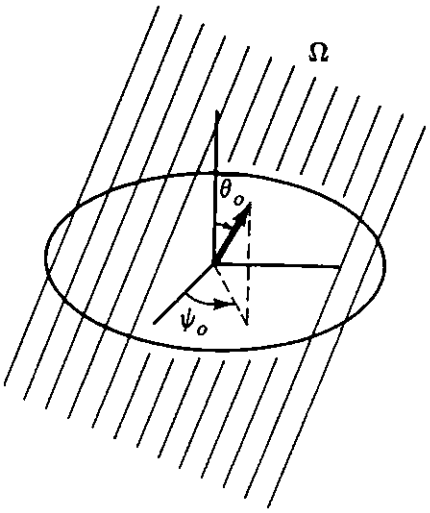

2.7. Show that the solid angle subtended by a disk at a point at distance z from the disk on a line perpendicular to the center of the disk is $2\pi(1 - \cos\theta_0)$, in which θ_0 is defined by Fig. P2.7.

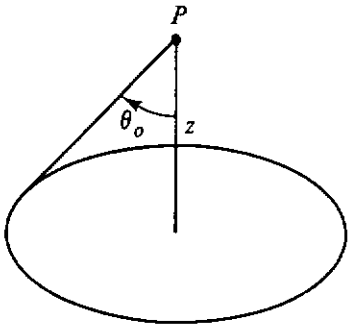

2.8. Show that the solid angle subtended by a rectangular area, $W \times L$, at a point at distance z from the area on a line perpendicular to the center of the area is given by $4\tan^{-1}[(\epsilon/\eta)(1 + \epsilon^2 + \eta^2)^{-1/2}]$, in which $\epsilon = W/L$ and $\eta = 2z/L$.

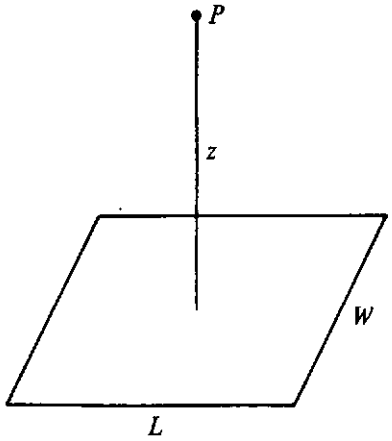

2.9. In Section 2.2, a number of assertions are made about "isotropic angular flux density distributions." Take item 2 as given and verify that the total flux density is ϕ. Verify assertions 1, 3, and 4.

2.10. In Section 2.2, a number of assertions are made about "isotropic angular flow rate distributions." Take item 3 as given and verify that the partial flow rate in

the positive (forward) hemisphere of directions is j_n^+. Verify assertions 1, 2, 4, and 5.

2.11 The outward angular flow rate of particles from a point on a surface is $j_n(\omega) = 10^{13}\omega^2$, where $\theta = \cos^{-1}\omega$ is measured from the normal to the surface. The units of $j_n(\omega)$ are $\text{cm}^{-2}\ \text{s}^{-1}\ \text{sr}^{-1}$. What is the partial flow rate j_n^+? What is the outward angular flux density $\phi(\omega)$? What is the partial flux density ϕ^+?

2.12. If the disk of Problem 2.7 represents an isotropic plane source of strength S_A ($\text{cm}^{-2}\ \text{s}^{-1}$) in a nonattenuating medium, show by using Eq. (2.38) that

$$\phi(P) = \frac{S_A}{2} \ln(\sec\theta_0).$$

2.13. If the rectangular area of Problem 2.8 represents an isotropic plane source of strength S_A in a nonattenuating medium, using Eq. (2.38) derive an expression for $\phi(P)$.

2.14 Disk sources are sometimes used to approximate rectangular sources. One could base the approximation on sources of the same area or on sources subtending the same solid angle at a detector location. Which would be more correct? Justify your assertion.

2.15 Suppose that gamma photons are emitted from the base of a cylindrical reactor shield with an angular flux density proportional to the square of the cosine of the polar angle measured from the normal to the surface. The flux density spectrum is independent of position and direction. If the base is 5 m in radius and the exposure rate at the surface is 100 mr h^{-1}, what is the exposure rate, in air, 5 m from the surface and on the cylinder axis? Neglect air interaction. (For a given flux density spectrum, the exposure rate is proportional to the flux density.)

2.16. For the simplified case of thermal neutrons diffusing in a semi-infinite, noncapturing, and isotropically scattering medium, the emergent flow rate angular distribution from the boundary surface is given by Fermi's approximate formula [4]:

$$j_n(\theta) = k(\cos\theta + 3^{1/2}\cos^2\theta),$$

where θ is the polar angle from the outward normal of the surface. If j_n^+ is given as unity, what is the corresponding value of k? If, on the other hand, ϕ^+ is unity, what is the value of k?

3 interaction of radiation with matter

3.1 INTERACTION COEFFICIENT

The interaction of a given type of radiation with matter may be classified according to the type of interaction and the unit of matter with which the interaction takes place. The interaction may take place with an electron and in many cases the electron behaves as though it were free. Similarly, the interaction may take place with an atomic nucleus which, in many cases, behaves as though it were not bound in a molecule or crystal lattice. However, in some cases, particularly for radiation particles of comparatively low energy, molecular or lattice binding must be taken into account.

The interaction may be scattering of the incident radiation, that is, deflection accompanied by energy change. A scattering interaction may be elastic or inelastic. Consider, for example, the interaction of a photon with an electron in what is called Compton scattering. The scattering interaction of the electron and photon can be well approximated as being purely elastic. However, the interaction of the photon with the atom, within which the electron is bound, must be considered as inelastic since some of the photon energy must compensate for the binding energy of the electron in the atom. The reason that the photon interaction with the electron may be treated as elastic is that electron binding energies are usually orders of magnitude lower than gamma-photon energies of interest. It is important to remember that for scattering there are unique relationships between energy exchanges and the angles of scattering.

Other types of interactions are absorptive in nature. The incident radiation is completely transformed to excitation of the nucleus, the atom, the molecule,

or the crystal lattice. The ultimate result may be the emission of particulate radiation (including photons), stable nuclear transmutation, chemical change, or heat.

The interaction of radiation with matter is always statistical in nature, and therefore must be described in probabilistic terms. Consider a particle traversing a homogeneous material and let P denote the probability that this particle interacts in some specified manner (e.g., absorption or scattering) while traveling a distance Δx. It is found that the quantity $\mu \equiv \lim_{\Delta x \to 0} (P/\Delta x)$ is a property of the material for a given interaction. Here the limit process must be interpreted in the manner described in Section 2.1.1. In the limit of small path lengths, μ is seen to be the probability per unit path length that a particle will undergo a specified interaction. That μ is constant for a given material and for a given type of interaction implies that the probability of interaction per unit path length is independent of the path length traveled prior to the interaction.

The interaction probability per unit path length is fundamental in describing how radiation interacts with matter and is usually called the *linear attenuation coefficient* [1]. It is perhaps more appropriate to use the words *linear interaction coefficient* since many interactions do not "attenuate" the particle in the sense of an absorption interaction. Although this nomenclature is widely used to describe photon interactions, μ is often referred to as the *macroscopic cross section* and given the symbol Σ when describing neutron interactions. In some ways the latter designation is unfortunate since μ does not have dimensions of a cross section. Although it is well established in the shielding community, this alternative designation will, for the most part, be avoided in this text.

The utility of the linear interaction coefficient to describe the interaction of radiation with matter becomes apparent when, as in Eq. (2.6), one interprets the flux density ϕ as the path length traveled by particles per unit volume per unit time. The product $\mu\phi$ is thus seen to be the number of interactions per unit volume per unit time—the volumetric interaction rate. Division by the material density yields $(\mu/\rho)\phi$, the interaction rate per unit mass.

The linear interaction coefficient is a function of the energy of the particle. Depending on the nature of the interaction, it may also be a function of the energy of the particle after scattering, the energy of the recoil atom or electron, the angles of deflection of the scattered radiation and recoil atom or electron and angles of emission of secondary particles, all measured from the initial direction of the incident particle. For example, the scattering interaction coefficient is usually defined in such a way that $\mu(E, E', \theta_s)\, dE'\, d\Omega$ is the probability per unit path length for an interaction in which the incident particle of energy E emerges from the interaction with energy between E' and $E' + dE'$ and with scattering angle θ_s within the differential solid angle $d\Omega$. In this form, μ would have units such as $\text{cm}^{-1}\,\text{MeV}^{-1}\,\text{sr}^{-1}$. Alternatively, the interaction coefficient could be expressed in terms of energies and angles for recoil electrons or atoms, or secondary radiations.

Often it is of interest to deal only with, say, the energy dependence or the

angular distribution of scattered radiation. In this case, one or the other of the following forms of the linear interaction coefficient may be used:

$$\mu(E, E') \equiv \int_{4\pi} d\Omega\, \mu(E, E', \theta_s), \tag{3.1}$$

$$\mu(E, \theta_s) \equiv \int_0^\infty dE'\, \mu(E, E', \theta_s). \tag{3.2}$$

Here $\mu(E, E')\, dE'$ is the probability per unit path length for scattering into dE' at E' without regard to angle and $\mu(E, \theta_s)\, d\Omega$ is the interaction coefficient for scattering into direction range $d\Omega$ without regard to energy. Also of interest is

$$\mu(E) = \int_0^\infty dE'\, \mu(E, E'). \tag{3.3}$$

This is just the total linear interaction coefficient for the scattering of incident radiation of energy E, without regard to energy loss or angle of scattering. Often to indicate a specific type of interaction, the symbol μ will be subscripted (e.g., μ_s for scattering).

3.2 MICROSCOPIC CROSS SECTION

The linear interaction coefficient depends on the type and energy of the particle, the type of interaction, and the composition and density of the interacting medium. One of the more important quantities that determine μ is the density of target atoms or electrons in the material. It seems reasonable to expect that μ should be proportional to the "target" atom or electron density N in the material, that is, $\mu = \sigma N$, where σ is a constant of proportionality independent of N.[1] The quantity σ is called the *microscopic cross section* and is seen to have dimensions of area. It is often interpreted as being the effective cross-sectional area presented by the target atom or electron to the incident particle for a given interaction. Indeed, in many cases σ has dimensions comparable to those expected from the physical size of the nucleus. However, this simplistic interpretation of the microscopic cross section, although conceptually easy to grasp, leads to philosophical difficulties when it is observed that σ generally varies with the energy of the incident particle and, for a crystalline material, the particle direction. The view that σ is the interaction probability per unit path length, normalized to one target atom or electron per unit volume, avoids such conceptual difficulties while emphasizing the statistical description of the interaction process.

When the microscopic cross section is for the electron, the symbol σ is preceded by the subscript e; otherwise, no subscript is used. Cross sections are

[1]This proportionality is not strictly true for coherent interactions in which the incident particle interacts simultaneously with multiple target atoms or electrons (e.g., orbital electrons of a single atom or multiple atoms of a crystal lattice). Even for such cases, though, the microscopic cross section is usually defined in this manner.

usually expressed in units of cm^2. A widely used special unit is the *barn*, having dimensions 10^{-24} cm^2.

Just as the linear interaction coefficients may be differential in nature, so also may be the corresponding microscopic cross sections. In this text, these differential microscopic cross sections will be denoted by $\sigma(E, E', \theta_s)$, $\sigma(E, E')$, and $\sigma(E, \theta_s)$, which are related by integral expressions analogous to those of Eqs. (3.1) to (3.3). The reader should be aware of alternative forms of notation; for example, $\sigma(E, E', \theta_s) \equiv d^2\sigma/dE'd\Omega$, and the latter form is used in some texts. Sometimes, to emphasize the transition from one energy E to another E', or from one direction $\mathbf{\Omega}$ to another $\mathbf{\Omega}'$, the notation $E \rightarrow E'$ or $\mathbf{\Omega} \rightarrow \mathbf{\Omega}'$ is used. The following are samples of identical notations: $\sigma(E \rightarrow E') \equiv \sigma(E, E')$ and $\sigma(E \rightarrow E', \mathbf{\Omega} \rightarrow \mathbf{\Omega}') \equiv \sigma(E, E', \mathbf{\Omega}, \mathbf{\Omega}') \equiv \sigma(E, E', \omega_s)$, where $\omega_s \equiv \mathbf{\Omega} \cdot \mathbf{\Omega}'$. All these alternative forms are used in this text.

In Section 2.2, the Legendre polynomial expansion of the angular flux density was discussed. Similarly, data for cross sections are frequently expressed in terms of Legendre polynomials; for example,

$$\sigma(E, \theta_s) = \frac{\sigma(E)}{4\pi} \sum_{n=0}^{\infty} (2n + 1) f_n(E) P_n(\cos \theta_s). \tag{3.4}$$

Application of the orthogonality property of Legendre polynomials (see Section A2.4) to Eq. (3.4) results in the following expression for the Legendre expansion coefficients f_n:

$$f_n = \frac{2\pi}{\sigma(E)} \int_{-1}^{+1} d(\cos \theta_s) \sigma(E, \theta_s) P_n(\cos \theta_s). \tag{3.5}$$

It should be noted that f_0 is unity, and that f_1 has the physical interpretation of being the average cosine of the scattering angle; that is,

$$\langle \cos \theta_s \rangle = \frac{1}{\sigma(E)} \int_{4\pi} d\Omega \cos \theta_s \sigma(E, \theta_s). \tag{3.6}$$

Data on cross sections and linear interaction coefficients, especially for photons, are frequently expressed as the ratio of μ to the density ρ, called the *mass interaction coefficient*. Since the atomic density N is

$$N = \frac{\rho}{\mathfrak{a}} N_A, \tag{3.7}$$

in which N_A is Avogadro's number (6.022×10^{23} mol^{-1}), and $\mathfrak{a}$ is the atomic weight (g mol^{-1}),

$$\frac{\mu}{\rho} = \frac{N\sigma}{\rho} = \frac{N_A}{\mathfrak{a}} \sigma. \tag{3.8}$$

Thus μ/ρ is an intrinsic property of the interacting medium—independent of density. This method of data presentation is used much more for photons than for neutrons, in part because, for a wide variety of materials and a wide range of photon energies, μ/ρ is only weakly dependent on the nature of the interacting medium.

For compounds or homogeneous mixtures, the linear and mass interaction coefficients are, respectively,

$$\mu = \sum_i \mu_i = \sum_i N_i \sigma_i \tag{3.9}$$

and

$$\frac{\mu}{\rho} = \sum_i w_i \left(\frac{\mu}{\rho}\right)_i, \tag{3.10}$$

in which w_i is the weight fraction of component i. In Eq. (3.9), the atomic density N_i and the linear interaction coefficient μ_i are values for the ith material *after* mixing. Evaluation of average interaction coefficients for materials of inhomogeneous composition is discussed in Section 9.3.

3.3 CROSS SECTIONS FOR PHOTON INTERACTIONS

3.3.1 Classification of Types of Interactions

For details of the mechanisms of photon interactions, the reader is referred to the standard reference works of Heitler [2] and Evans [3]. For most radiation shielding studies, photon energies of 10 keV to 10 MeV are important. For this energy range, the photoelectric effect, pair production, and Compton scattering mechanisms of interaction predominate over all others. Of these three, the photoelectric effect predominates at the lower photon energies. Pair production is important only for higher-energy photons. Compton scattering predominates at intermediate energies. In rare instances the shielding analyst may need to account also for coherent (Rayleigh) scattering and for annihilation and fluorescence radiation.

3.3.2 Compton Scattering

The process of Compton scattering is explained with the help of Fig. 3.1. A photon of energy E interacts with an electron initially at rest. After the interaction, the photon has energy E' and moves at angle θ_s measured from its initial direction. The electron moves with kinetic energy T at angle θ_e measured from the initial direction of the photon. Application of the principles of conservation of (total relativistic) energy and linear momentum leads to the well-

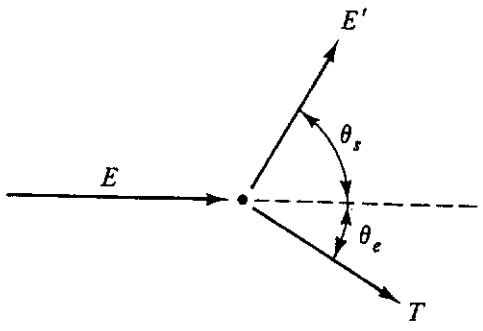

Figure 3.1 Illustration of the Compton scattering process. E and E' are photon energies before and after scattering at angle θ_s. The electron, initially stationary, is deflected by angle θ_e, and receives kinetic energy T.

known Compton formula,

$$E' = \frac{E}{1 + (E/m_e c^2)(1 - \cos\theta_s)}, \tag{3.11}$$

in which $m_e c^2$ is the rest mass energy of the electron, 8.186×10^{-14} J (0.5110 MeV). Photon transport calculations are frequently carried out using wavelength, rather than energy, as an independent variable. Furthermore, to avoid carrying along various constants, the wavelength is usually measured in multiples of a *Compton unit*, the ratio of the wavelength hc/E to the so-called Compton wavelength λ_C $(= hc/m_e c^2 = 2.426 \times 10^{-10}$ cm), where h is Planck's constant, 6.624×10^{-34} J s, and c is the speed of light, 2.998×10^{10} cm s^{-1}. In this unit,

$$\lambda \equiv \frac{m_e c^2}{E} = \frac{0.511}{E(\text{MeV})}. \tag{3.12}$$

With the use of Compton units, the Compton scattering relationship, Eq. (3.11), is quite simple:

$$\lambda' = \lambda + 1 - \cos\theta_s. \tag{3.13}$$

The kinetic energy T of the recoil electron is given by

$$\frac{m_e c^2}{T} = \lambda\left(1 + \frac{\lambda}{1 - \cos\theta_s}\right). \tag{3.14}$$

The scattering angles of the electron and photon are related by the equation

$$\cot\theta_e = (1 + \lambda^{-1}) \tan\left(\frac{\theta_s}{2}\right). \tag{3.15}$$

The maximum transfer of energy from the incident photon to the recoil electron occurs when $\theta_s = \pi$ or $\theta_e = 0$, for which case

$$(\lambda' - \lambda)_{\max} = 2, \tag{3.16}$$

$$\left(\frac{E'}{E}\right)_{\min} = \frac{\lambda}{\lambda + 2}, \tag{3.17}$$

$$\left(\frac{T}{E}\right)_{\max} = \frac{2}{\lambda + 2}. \tag{3.18}$$

The relationships among T, E, θ_s, and θ_e are illustrated in Figs. 3.2 and 3.3.

Thomson cross section. In the limit of zero photon energy, scattering of the photon by a free electron may be treated by the classical theory of radiation. The electron in the electromagnetic field of the incident radiation vibrates with the same frequency as that of the incident radiation, thereby giving rise to the emission of secondary electromagnetic radiation of the same frequency. The total cross section for such scattering, called Thomson scattering, is

$$_e\sigma_T = \tfrac{8}{3}\pi r_e^2, \tag{3.19}$$

in which r_e is the "classical electron radius." The value of r_e is given by

$$r_e = \frac{e^2}{4\pi\epsilon_0 m_e c^2}, \tag{3.20}$$

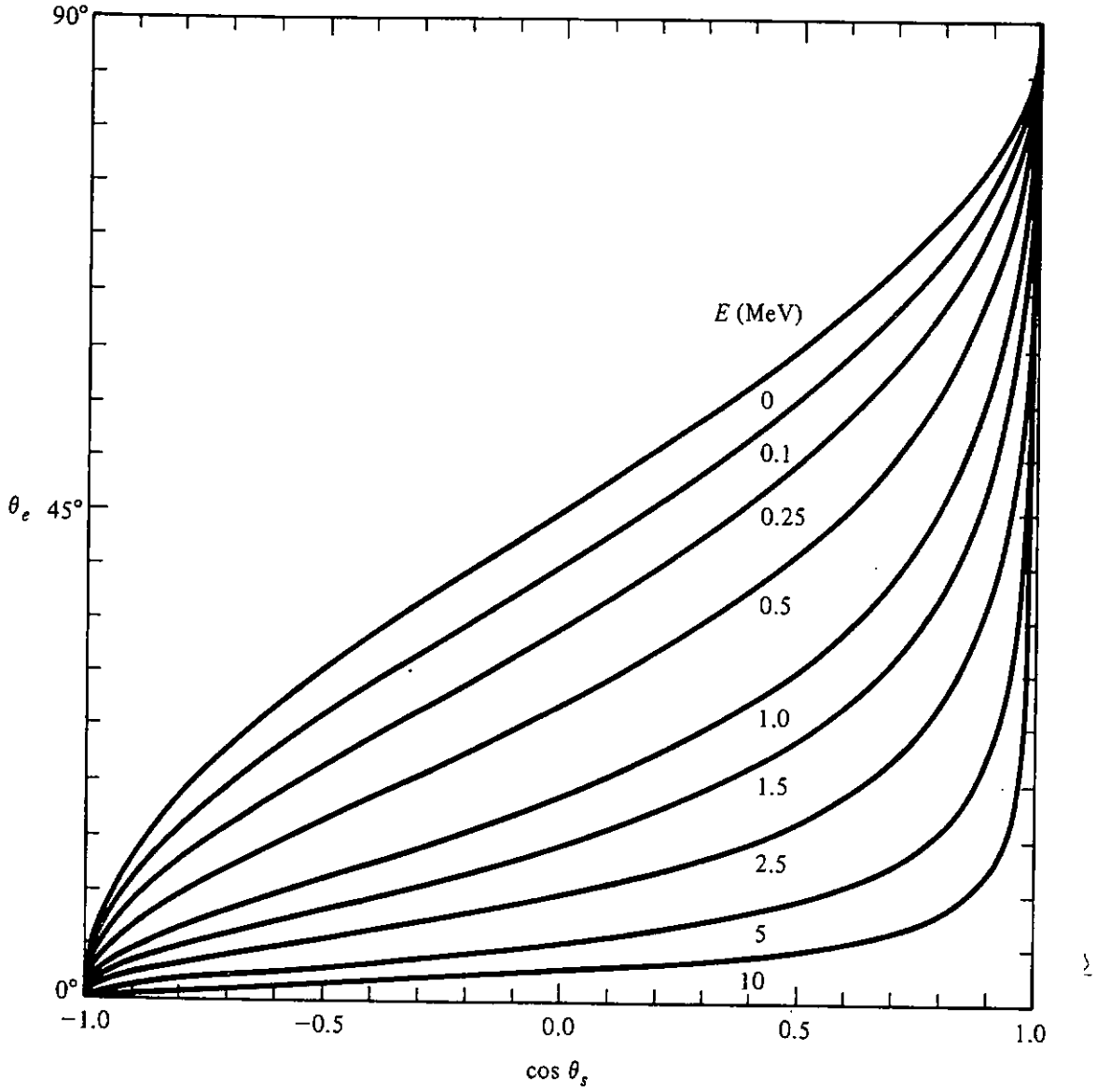

Figure 3.2 Relationship between the angle of electron scattering, θ_e (degrees), and the cosine of the angle of photon scattering in the Compton process.

where e is the electronic charge, 1.602×10^{-19} C, and ϵ_0 is the permittivity of free space, 8.854×10^{-14} F/cm. Thus, $r_e = 2.818 \times 10^{-13}$ cm and ${}_e\sigma_T = 6.653 \times 10^{-25}$ cm^2.

For unpolarized incident radiation, the Thomson cross section per steradian for scattering at angle θ_s is

$$ {}_e\sigma_T(\theta_s) = \tfrac{1}{2} r_e^2 (1 + \cos^2 \theta_s). \tag{3.21}$$

Knowledge of the Thomson cross section is important for two reasons. It is the low-energy limit for the incoherent (Compton) scattering cross section. It is also the basis from which are evaluated coherent (Rayleigh) scattering cross sections for interactions of photons with atomic electrons.

Incoherent (Compton) scattering cross sections. Incoherent scattering refers to the interaction of a photon with an individual electron, as distinguished from the coherent interaction of a photon with all electrons of

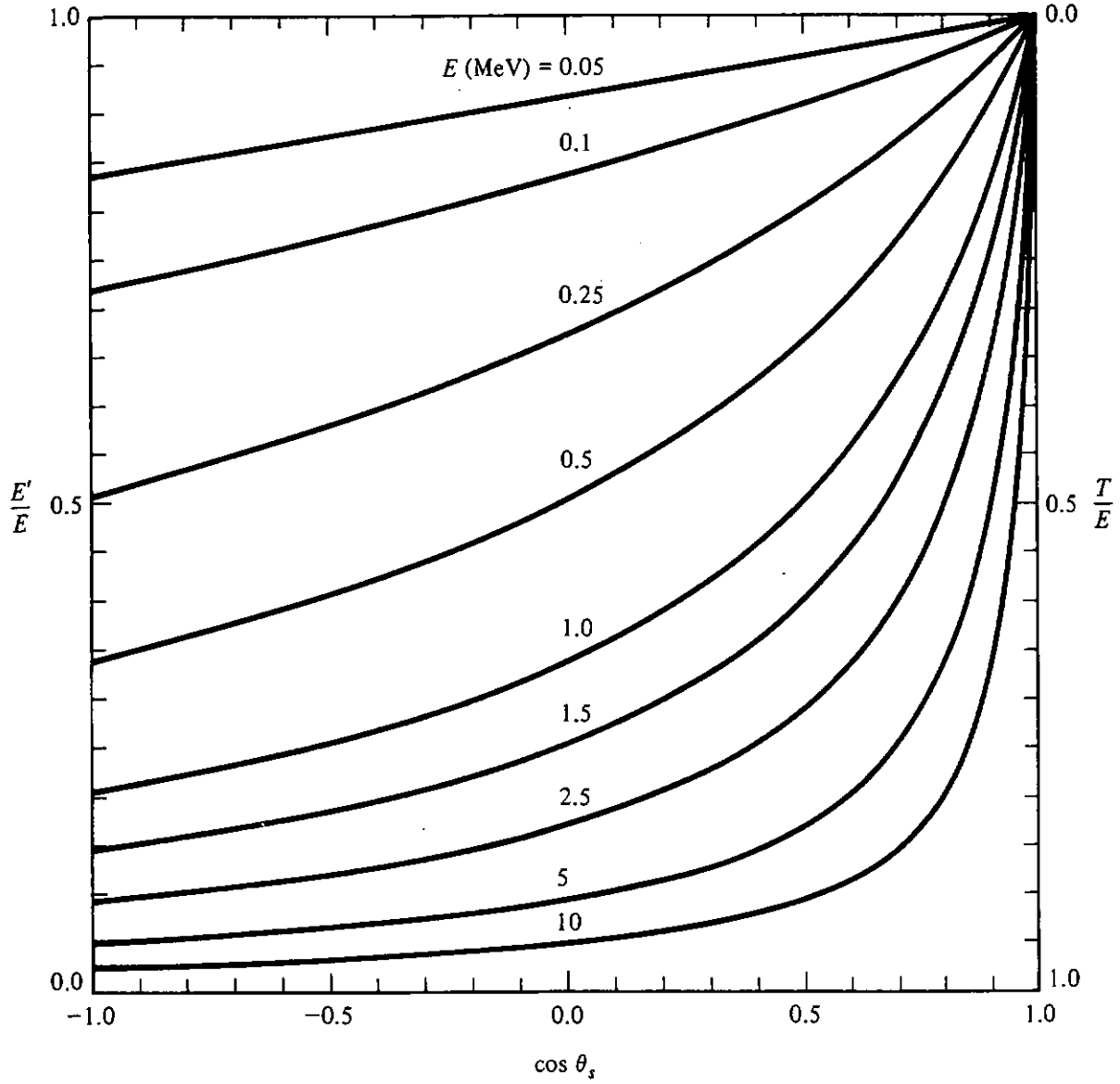

Figure 3.3 Relationship between the energy E' of the scattered photon, the energy T of the scattered electron, and the initial photon energy E as a function of the cosine of the angle of scattering in the Compton process.

an atom. It is assumed in the discussion below that the incident radiation is not polarized.

For free electrons, the incoherent scattering cross section is given by the formula[2]

$$ {}_e\sigma_C(\lambda, \lambda', \theta_s) = \frac{1}{2} r_e^2 \left(\frac{\lambda}{\lambda'}\right)^2 \left[\left(\frac{\lambda}{\lambda'}\right) + \left(\frac{\lambda'}{\lambda}\right) + (\lambda' - \lambda)(\lambda' - \lambda - 2)\right] \times \delta(1 + \lambda - \lambda' - \cos\theta_s). \tag{3.22} $$

In this form, ${}_e\sigma_C(\lambda, \lambda', \theta_s)\, d\lambda'\, d\Omega$ is the cross section per electron for the interaction of a photon of wavelength λ resulting in scattering at angle θ_s within

[2]Here and in all subsequent discussion, the wavelength of the photon is considered to be in Compton units, unless specifically indicated otherwise.

differential solid angle $d\Omega$ and with final wavelength within λ' and $\lambda' + d\lambda'$. The Dirac delta function occurs in Eq. (3.22), so that the scattering angle and wavelength can be considered as independent variables in a formal sense. They are, of course, related by Eq. (3.13) and the argument of the Delta function assures that this fact is taken into account. For further discussion of the Delta function, see Section 2.6 and Appendix 2. Equation (3.22) derives from the work of Klein and Nishina [4], and it is thoroughly developed, for polarized as well as unpolarized incident radiation, by Heitler [2] and Evans [3].

The cross section per steradian is given by the following equation and illustrated in Fig. 3.4:

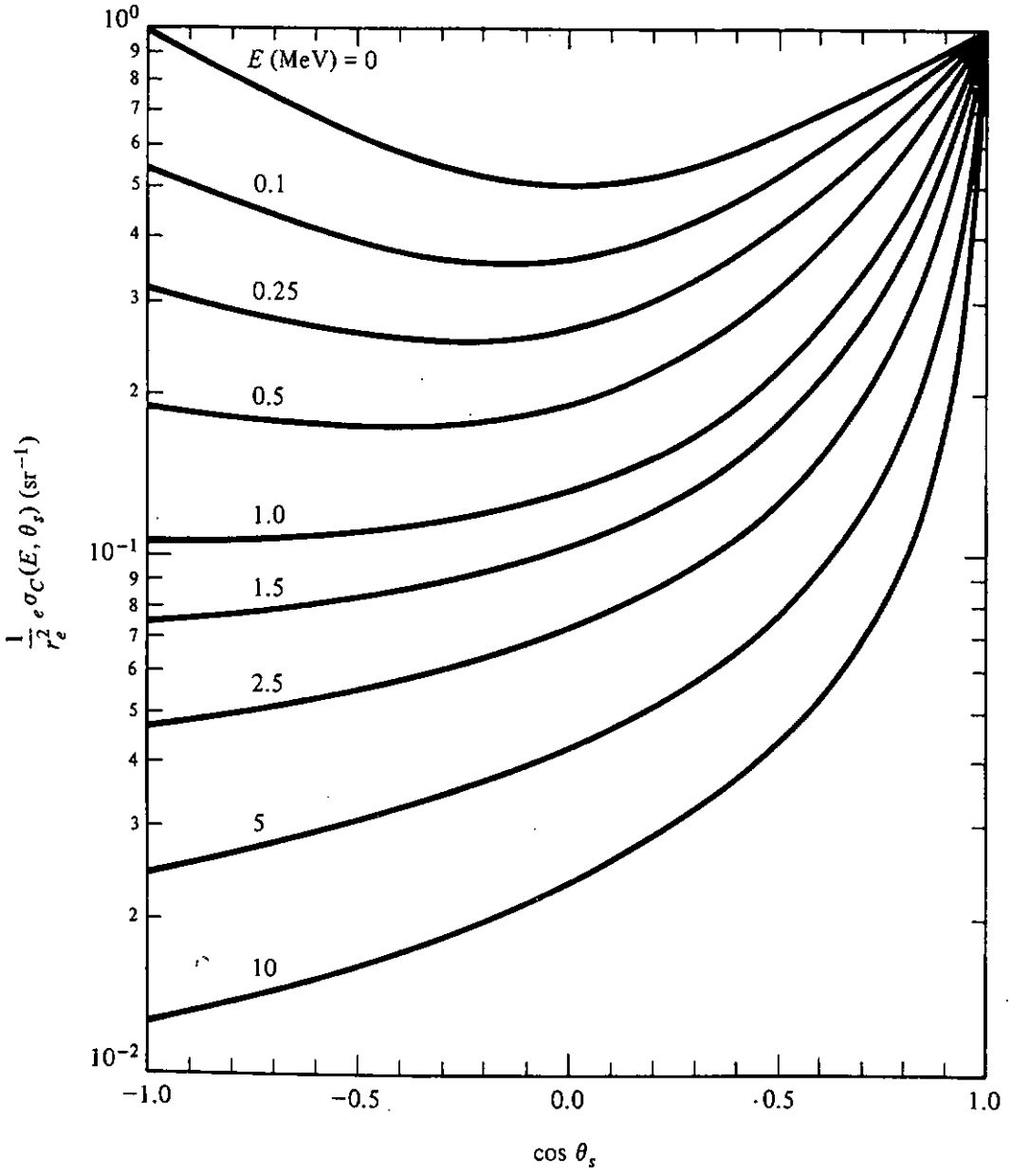

Figure 3.4 Photon incoherent scattering cross section (Compton scattering involving a free electron) as a function of the cosine of the angle of scattering. The factor r_e is the classical radius of the electron.

$$
\begin{aligned}
{}_e\sigma_C(\lambda, \theta_s) &= \int_{\lambda}^{\lambda+2} d\lambda' \, {}_e\sigma_C(\lambda, \lambda', \theta_s) \\
&= \frac{1}{2} r_e^2 \frac{\lambda^2}{(1 + \lambda - \cos\theta_s)^2} \\
&\quad \times \left(\frac{\lambda}{1 + \lambda - \cos\theta_s} + \frac{1 + \lambda - \cos\theta_s}{\lambda} - \sin^2\theta_s \right).
\end{aligned} \tag{3.23}
$$

An alternative form for Eq. (3.23) is

$$
{}_e\sigma_C(E, \theta_s) = \tfrac{1}{2} r_e^2 p[1 + p^2 - p(1 - \cos^2\theta_s)], \tag{3.24}
$$

in which

$$
p \equiv \frac{E'}{E} = \frac{\lambda}{1 + \lambda - \cos\theta_s}. \tag{3.25}
$$

Note that, as λ approaches infinity, or E approaches zero, p approaches unity and Eqs. (3.23) and (3.24) reduce to the Thomson formula, Eq. (3.21). A related quantity is the Klein–Nishina *energy scattering* cross section:

$$
{}_e\sigma_{Ce}(E, \theta_s) \equiv \frac{E'}{E} {}_e\sigma_C(E, \theta_s) = \tfrac{1}{2} r_e^2 p^2[1 + p^2 - p(1 - \cos^2\theta_s)]. \tag{3.26}
$$

The total cross section is obtained from Eq. (3.23) by integration over all directions.

$$
\begin{aligned}
{}_e\sigma_C(\lambda) &= 2\pi \int_{-1}^{1} d(\cos\theta_s) \, {}_e\sigma_C(\lambda, \theta_s) \\
&= \pi r_e^2 \lambda \left[(1 - 2\lambda - 2\lambda^2) \ln\left(1 + \frac{2}{\lambda}\right) + \frac{2(1 + 9\lambda + 8\lambda^2 + 2\lambda^3)}{(\lambda + 2)^2} \right].
\end{aligned} \tag{3.27}
$$

Incoherent scattering cross sections for bound electrons. The equations above break down when the kinetic energy of the recoil electron would be comparable to its binding energy in the atom. Thus, binding effects might be thought to be an important consideration for the attenuation of low-energy photons in media of high atomic number. For example, the binding energy of K-shell electrons in lead is 88 keV. However, under these same circumstances, cross sections for the photoelectric interaction of photons greatly exceed incoherent scattering cross sections. Radiation attenuation in this energy region is dominated by photoelectric interactions and, in most shielding calculations, the neglect of electron binding effects on incoherent scattering causes negligible error. Corrections for electron binding and related data are available in the literature, for example, in Refs. 5 to 7. Figure 3.5 shows the relative importance, in lead, of electron binding effects by comparing incoherent scattering and photoelectric cross sections.

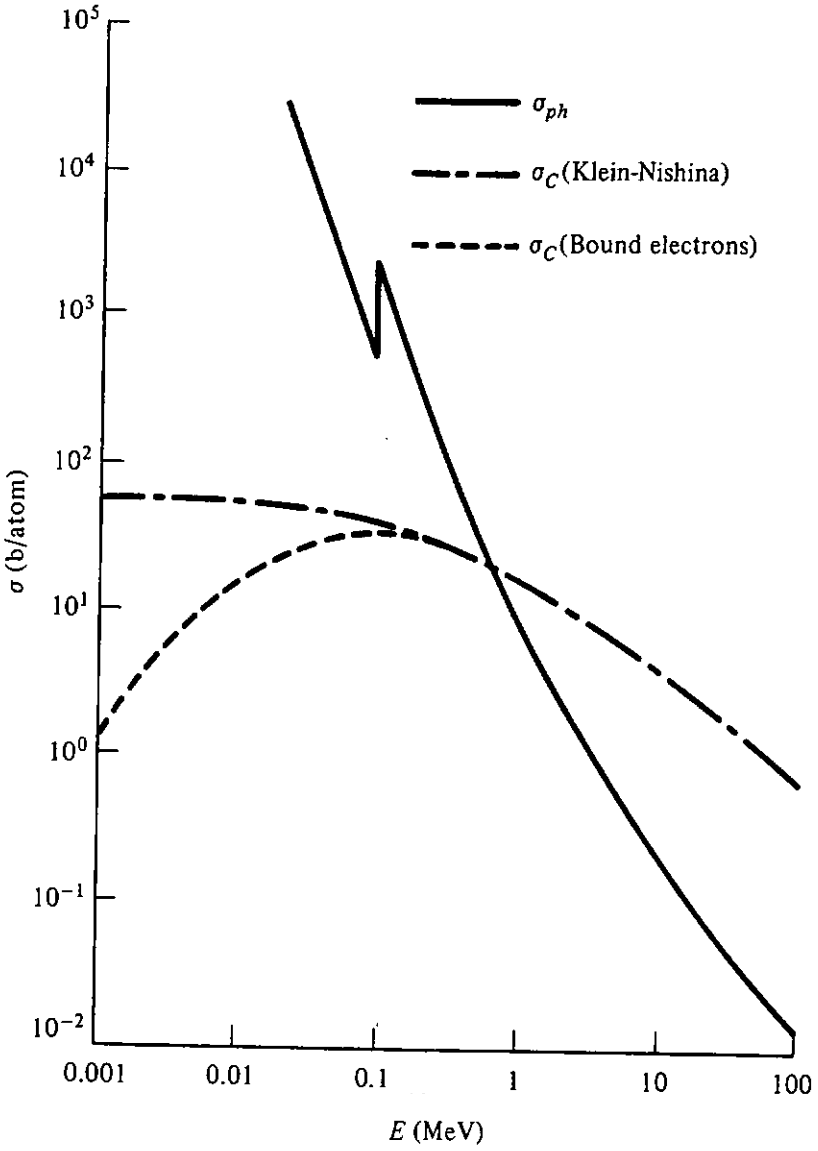

Figure 3.5 Comparison of incoherent-scattering and photoelectric-effect cross sections for photon interactions in lead. Units are barns per atom.

3.3.3 Coherent (Rayleigh) Scattering

In competition with the incoherent scattering of photons by individual electrons is coherent scattering on the electrons of an atom collectively. Since the recoil momentum in the Rayleigh interaction is taken up by the atom as a whole, the energy loss of the gamma photon is slight and the scattering angle small. Coherent scattering cross sections may greatly exceed incoherent scattering cross sections, especially for low-energy photons and high-Z materials. Because of the minimal effect on photon energy or direction, it is common practice to ignore Rayleigh scattering in radiation shielding calculations, especially when the electron binding effect mentioned in the preceding paragraph is ignored.

3.3.4 Photoelectric Effect

In the photoelectric effect, a photon interacts with an entire atom, resulting in the emission of a photoelectron, usually from the K shell of the atom. Momentum is conserved by the recoil of the residual atom. Although the photon

energy in excess of the electron binding energy E_b is distributed between the electron and the recoil atom, virtually all of that energy is carried as kinetic energy of the photoelectron. Thus, $T = E - E_b$.

K-shell binding energies E_k vary from 13.6 eV for hydrogen to 7.11 keV for iron, 88 keV for lead, and 116 keV for uranium. If the photon energy is less than E_k, only the L and higher-shell electrons can take part in the photoelectric interactions.

As the photon energy decreases, the photoelectric cross section increases until $E = E_k$, at which point the cross section drops discontinuously (see Fig. 3.5, which illustrates the K "edge" in lead). As E decreases further, the cross section increases until the first L edge is reached, at which energy it drops again, then rises once more, and so on for the remaining edges. The cross section varies as E^{-n}, where $n \simeq 3$ at low energies ($E \lesssim 150$ keV), and $n \simeq 1$ at higher energies ($E \gtrsim 5$ MeV). The atomic cross section varies as Z^m, where m varies from about 4 at $E = 100$ keV to 4.6 at $E = 3$ MeV. As a very crude approximation

$$\sigma_{\text{ph}}(E) \propto \frac{Z^4}{E^3} \tag{3.28}$$

in the energy region for which the photoelectric effect is relatively paramount. Note that the average cross section per electron is

$$_e\sigma_{\text{ph}}(E) = Z^{-1}\sigma_{\text{ph}}(E) \tag{3.29}$$

As a general rule, about 80% of photoelectric interactions with heavy nuclei result in ejection of a K-shell electron, while for light nuclei, K-shell electrons are responsible for almost all photoelectric interactions. Consequently, the approximation is often made for heavy nuclei that the total photoelectric cross section is the factor 1.25 times the cross section for K-shell electrons.

As the vacancy left by the photoelectron is filled by an electron from an outer shell, either fluorescence x rays or Auger electrons may be emitted. The probability of x-ray emission is given by the fluorescent yield. For the K shell, fluorescent yields vary from 0.005 for $Z = 8$ to 0.965 for $Z = 90$. Although x rays of various energies may be emitted, as a general rule the approximation can be made that only one x ray or Auger electron is emitted, with energy equal to the binding energy of the photoelectron.

3.3.5 Pair Production

In this process, the incident photon is completely absorbed and in its place appears a positron–electron pair. The phenomenon is induced by the strong electric field in the vicinity of the nucleus and has a photon threshold energy of $2m_ec^2$ ($= 1.02$ MeV). It is possible but much less likely that the phenomenon is induced by the electric field of an electron (triplet production), for which case the threshold energy is $4m_ec^2$. The discussion below is limited to the *nuclear* pair production process.

In this process, the nucleus acquires indeterminate momentum but

negligible kinetic energy. Thus,

$$T_+ + T_- = E - 2m_e c^2, \tag{3.30}$$

in which T_+ and T_- are the kinetic energies of the positron and electron, respectively. To a first approximation, the total atomic pair production cross section varies as Z^2. The cross section increases with photon energy, approaching a constant value at high energy. The fate of the positron is annihilation in an interaction with an electron, generally after slowing to practically zero kinetic energy. This process usually results in the creation of two photons moving in opposite directions, each with energy $m_e c^2$ (= 0.511 MeV). The angular distributions of the positron and electron are complicated and generally not important in radiation shielding calculations.

3.4 PHOTON ATTENUATION COEFFICIENTS

The photon linear attenuation coefficient μ is, in the limit of small distance, the probability per unit distance of travel that a gamma photon undergoes any significant interaction. Thus, for a specified medium,

$$\mu(E) = ZN_e\sigma_C(E) + N\sigma_{\text{ph}}(E) + N\sigma_{\text{pp}}(E), \tag{3.31}$$

in which N is the atom density and ZN is the electron density. More common in data presentation is the mass interaction coefficient (see Section 3.2):

$$\frac{\mu}{\rho} = \frac{\mu_C}{\rho} + \frac{\mu_{\text{ph}}}{\rho} + \frac{\mu_{\text{pp}}}{\rho}. \tag{3.32}$$

Note that Rayleigh scattering and other minor effects are specifically excluded from the definition.[3] In Eq. (3.32),

$$\frac{\mu_C}{\rho} = \frac{Z}{\mathfrak{A}} N_A \sigma_C(E), \tag{3.33}$$

$$\frac{\mu_{\text{ph}}}{\rho} = \frac{1}{\mathfrak{A}} N_A \sigma_{\text{ph}}(E), \tag{3.34}$$

$$\frac{\mu_{\text{pp}}}{\rho} = \frac{1}{\mathfrak{A}} N_A \sigma_{\text{pp}}(E), \tag{3.35}$$

in which N_A is Avogadro's number.

3.5 PHOTON ABSORPTION COEFFICIENTS AND RELATED QUANTITIES

3.5.1 Compton Absorption and Scattering Cross Sections

The cross section for scattering of a photon into Compton wavelength range $d\lambda'$ without regard to angle may be determined from Eq. (3.22):

[3]The reader, when referring to data tables in other publications, should be aware that occasionally Rayleigh scattering *is* included.

$$ {}_e\sigma_C(\lambda, \lambda')\, d\lambda' = \int_{4\pi} d\Omega\, {}_e\sigma_C(\lambda, \lambda', \theta_s)\, d\lambda' \tag{3.36} $$

$$ {}_e\sigma_C(\lambda, \lambda') = \pi r_e^2 \left(\frac{\lambda}{\lambda'}\right)^2 \left[\left(\frac{\lambda}{\lambda'}\right) + \left(\frac{\lambda'}{\lambda}\right) + (\lambda' - \lambda)(\lambda' - \lambda - 2)\right]. \tag{3.37} $$

A related quantity is the cross section for creating a recoil electron with energy T in the range dT [i.e., ${}_e\sigma_C(E, T)\, dT$]. Here it is convenient to use the ratio $\tau\ (= T/m_e c^2)$. Since $1/\lambda - 1/\lambda' = \tau$,

$$ \frac{d\lambda'}{d\tau} = \lambda^2(1 - \lambda\tau)^{-2}. \tag{3.38} $$

It follows that

$$ {}_e\sigma_C(\lambda, \tau) = {}_e\sigma_C(\lambda, \lambda')\frac{d\lambda'}{d\tau}, \tag{3.39} $$

or

$$ {}_e\sigma_C(\lambda, \tau) = \pi r_e^2 \lambda^2 \left[(1 - \lambda\tau) + (1 - \lambda\tau)^{-1} + \frac{(\lambda^2\tau)(\lambda^2\tau + 2\lambda\tau - 2)}{(1 - \lambda\tau)^2}\right]. \tag{3.40} $$

The mean fraction of the photon energy transferred to the recoil electron is designated as f_C and the Compton energy absorption cross section[4] per electron is defined as

$$ {}_e\sigma_{Ca}(\lambda) \equiv f_C\, {}_e\sigma_C(\lambda). \tag{3.41} $$

The factor f_C is the weighted average of $T/E\ (\doteq \lambda\tau)$:

$$ f_C = \frac{1}{{}_e\sigma_C(\lambda)} \int_0^{2/\lambda(\lambda+2)} d\tau\, (\lambda\tau)\, {}_e\sigma_C(\lambda, \tau). \tag{3.42} $$

The energy scattering cross section is the product of the total cross section and the mean fraction of the photon energy retained by the scattered photon.

$$ {}_e\sigma_{Ce}(\lambda) = (1 - f_C)\, {}_e\sigma_C(\lambda). \tag{3.43} $$

It is evident from the definition of f_C that the factor $(1 - f_C)$ can be evaluated as the mean value of $E'/E\ (= \lambda/\lambda')$:

$$ 1 - f_C = \frac{1}{{}_e\sigma_C(\lambda)} \int_\lambda^{\lambda+2} d\lambda' \frac{\lambda}{\lambda'}\, {}_e\sigma_C(\lambda, \lambda'). \tag{3.44} $$

Associated with the energy absorption and energy scattering cross sections are the mass energy absorption and energy scattering coefficients:

[4]The Compton energy absorption cross section thus defined is not a true cross section for photon absorption since, in the interaction, a scattered photon always results. Rather, it is an effective energy absorption cross section with respect to the incident photon energy such that the product $E(\mu_{Ca}/\rho)\phi$ is the rate per unit mass at which energy is transferred to kinetic energy of Compton recoil electrons.

$$\frac{\mu_{Ca}}{\rho} = \frac{Z}{\mathfrak{A}} N_A \sigma_{Ca}(E), \tag{3.45}$$

$$\frac{\mu_{Ce}}{\rho} = \frac{Z}{\mathfrak{A}} N_A \sigma_{Ce}(E). \tag{3.46}$$

3.5.2 Photoelectric Absorption Cross Section

The photoelectric absorption cross section σ_{pha} is the product of σ_{ph} and the fraction f_{ph} of the incident photon energy appearing as the initial kinetic energy of the photoelectron and Auger electron. Thus, to a good approximation,

$$\begin{aligned} f_{\text{ph}} &= \frac{1}{E}[(E - E_b) + (1 - \omega)E_b] \\ &= 1 - \frac{\omega E_b}{E} \end{aligned} \tag{3.47}$$

in which E_b is the binding energy of the electron, ω the fluorescent yield, $E - E_b$ the kinetic energy of the photoelectron, and $(1 - \omega)E_b$ the average energy transferred to Auger electrons. In a more precise determination, f_{ph} could be refined to weight the relative importance of the photoelectric effect in the K, L, and M electron shells.

The photoelectric linear and mass energy absorption coefficients are

$$\mu_{\text{pha}} = N\sigma_{\text{pha}}, \tag{3.48}$$

$$\frac{\mu_{\text{pha}}}{\rho} = \frac{1}{\mathfrak{A}} N_A \sigma_{\text{pha}}. \tag{3.49}$$

3.5.3 Absorption Cross Section for Pair Production

In a pair production interaction, the fraction of the incident photon energy appearing as the initial kinetic energies of the positron and electron is

$$f_{\text{pp}} = 1 - \frac{2m_e c^2}{E}. \tag{3.50}$$

The pair production energy absorption cross sections and coefficients are

$$\begin{aligned} \sigma_{\text{ppa}} &= f_{\text{pp}} \sigma_{\text{pp}}, \\ \mu_{\text{ppa}} &= N\sigma_{\text{ppa}}, \\ \frac{\mu_{\text{ppa}}}{\rho} &= \frac{1}{\mathfrak{A}} N_A \sigma_{\text{ppa}}. \end{aligned} \tag{3.51}$$

3.5.4 Radiation Corrections

The absorption cross sections as defined above were based on the transfer of photon energy to initial kinetic energy of electrons and positrons. As these charged particles slow down, most of this kinetic energy is dissipated locally by atomic and molecular excitation and ionization processes. Some of the

kinetic energy, however, is transferred to bremsstrahlung. The fraction radiated may be quite large for charged particles with kinetic energies substantially in excess of their rest-mass energies. Under certain circumstances it is necessary to correct the absorption cross sections to account for radiation losses. The correction factor is $1 - G$, where G is the fraction of the initial kinetic energies of the charged particles, averaged over all types of interactions and all energies, which is lost radiatively. This correction factor may be evaluated for and applied individually to cross sections for Compton scattering, pair production, and the photoelectric effect [see Eq. (5.20)].

The fraction G may be determined from radiation yields which are listed in Table 3.1. The yield $Y(T)$ is defined as the fraction of the initial electron kinetic

TABLE 3.1 Radiation Yields for Electrons

	Electron Radiation Yield, $Y(T)$[a]						
T (MeV)	Air	H_2O	C	Al	Fe	Pb	U
0.1	0.0008	0.0007	0.0064	0.0016	0.0037	0.0167	0.0192
1	0.0055	0.0049	0.0045	0.0107	0.0231	0.0867	0.0975
2	0.0099	0.0089	0.0084	0.0188	0.0394	0.133	0.149
3	0.0141	0.0129	0.0121	0.0262	0.0542	0.170	0.188
4	0.0182	0.0168	0.0159	0.0335	0.0684	0.201	0.222
5	0.0223	0.0208	0.0197	0.0408	0.0820	0.229	0.252
6	0.0264	0.0249	0.0236	0.0481	0.0951	0.254	0.278
8	0.0346	0.0332	0.0315	0.0627	0.120	0.299	0.324
10	0.0428	0.0416	0.0395	0.0772	0.144	0.336	0.362
100	0.299	0.317	0.306	0.444	0.583	0.764	0.780

[a] $Y(T)$ is the fraction of the initial kinetic energy T lost as bremsstrahlung. The yields do not include radiation losses from energetic secondary electrons (delta rays) produced during the deceleration of the primary electron. This is of minor importance.

Source: *Data from Ref. 8.*

energy T which is lost by radiation. For the photoelectric effect involving photons of energy E, the kinetic energy of the photoelectron is fixed at $T = E - E_b$; thus, neglecting radiative losses from Auger electrons, the value of G is uniquely determined as

$$G_{\text{ph}} = Y(T). \tag{3.52}$$

For Compton scattering, on the other hand, there is a spectrum of secondary-electron energies, and the value of G in this case is an average, weighted by the energy and the energy spectrum of secondary electrons, that is,

$$G_C = \frac{\int dT\, TY(T)_e\sigma_C(E, T)}{\int dT\, T_e\sigma_C(E, T)}. \tag{3.53}$$

For pair production, both the positron and the electron must be accounted for in a calculation similar to that of Eq. (3.53).

3.6 CROSS SECTIONS FOR NEUTRON INTERACTIONS

The interaction processes of neutrons with matter are fundamentally different from those for the interactions of photons. Whereas photons interact almost exclusively with the atomic electrons, neutrons interact essentially only with the atomic nucleus. Although neutron–electron interactions do occur, this type of interaction is highly improbable and therefore negligible when compared to the neutron–nucleus interactions. The cross sections that describe the various neutron interactions are also very unlike those for photons. Neutron cross sections not only can vary rapidly with the incident neutron energy, but they vary erratically from one element to another and even between isotopes of the same element. The description of the interaction of a neutron with a nucleus involves complex interactions between all the nucleons in the nucleus and the incident neutron, and consequently fundamental theories which can be used to predict neutron-cross-section variations in any exact way are still lacking. As a result all cross-section data are empirical in nature, with little guidance available for interpolation between different energies or isotopes.

In the past 30 years much effort and money have been expended to measure cross sections for various neutron reactions with many different materials and for wide ranges of neutron energies. Extensive compilations of neutron cross sections have been generated, and the more extensive of these compilations, such as the evaluated nuclear data files (ENDF) [9], contain so much information that digital computers are used almost exclusively to process these cross-section libraries to extract averaged cross sections or data for a particular neutron interaction. Even with the large amount of cross-section information available for neutrons, there are still energy regions and special interactions for which the cross sections are poorly known. For example, cross sections which exhibit sudden decreases in value as the neutron energy changes only slightly or cross sections for interactions which produce energetic secondary photons are of obvious concern to shielding problems and often still are unknown to an accuracy sufficient to perform satisfactory deep-penetration shielding calculations.

3.6.1 Classification of Types of Interactions

There are many possible neutron–nuclear interactions, only some of which are of concern in shielding calculations. Ultra-high-energy interactions can produce a myriad of exotic secondary particles; however, the energies required for such reactions are usually well above the neutron energies encountered in common shielding situations, and consequently these exotic interactions can be neglected. Similarly, for low-energy neutrons many complex neutron interactions are possible—Bragg scattering from crystal planes, phonon excitation in a crystal, coherent scattering from molecules, and so on—none of which are

of particular importance in neutron shielding problems. For shielding applications, only the high-energy scattering interactions (and the various associated angular distributions) and the absorption reactions are of importance, as summarized in Table 3.2.

TABLE 3.2 Principal Nuclear Data Required for Neutron Shielding Calculations

High-energy interactions (1 eV $< E <$ 20 MeV)
Elastic scattering cross sections
Angular distribution of elastically scattered neutrons
Inelastic scattering cross sections
Angular distribution of inelastically scattered neutrons
Gamma-photon yields from inelastic neutron scattering
Resonance absorption cross sections
Low-energy interactions ($<$1 eV)
Thermal-averaged absorption cross sections
Yield of neutron capture gamma photons
Fission cross sections and associated gamma-photon and neutron yields

The total cross section, which is the sum of cross sections for all possible interactions, gives a measure of the probability that a neutron of a certain energy will interact in some manner with the medium. From a shielding point of view, the component of the total cross section for absorption and scattering interactions is of primary concern. Nonetheless, when the total cross section is large the probability of some type of interaction is great and thus the total cross section, which is the most easily measured and the most widely reported, gives the neutron shield designer at least an indication of the neutron energy regions over which he or she must investigate the neutron interactions in greater detail.

The total cross sections, although they vary from nuclide to nuclide and with the incident neutron energy, have certain common features. For the sake of classification, the nuclides are usually divided into three broad categories: light nuclei (mass number $\lesssim$25), intermediate nuclei (mass number between 25 and 150), and heavy nuclei (mass number $\gtrsim$150). Examples of these total cross sections are shown in Figs. 3.6 through 3.8.

For light nuclei and some *magic number* nuclei[5] the cross section at low energies ($<$1 MeV) often varies as

$$\sigma_t = \sigma_1 + \frac{\sigma_2}{\sqrt{E}} \tag{3.54}$$

where E is the neutron energy, σ_1 and σ_2 are constants, and the two terms on the right-hand side represent the elastic scattering contribution and the radiative capture (or absorption) reaction, respectively. At low energies there may be a "Bragg cutoff" representing an energy below which coherent scattering from

[5]A magic number nucleus is one in which the number of neutrons or protons equals 2, 8, 20, 50, 82, or 126. When the nucleus is magic, a particularly stable configuration of the nucleons in the nucleus is achieved analogous to closed electron shells in atomic physics.

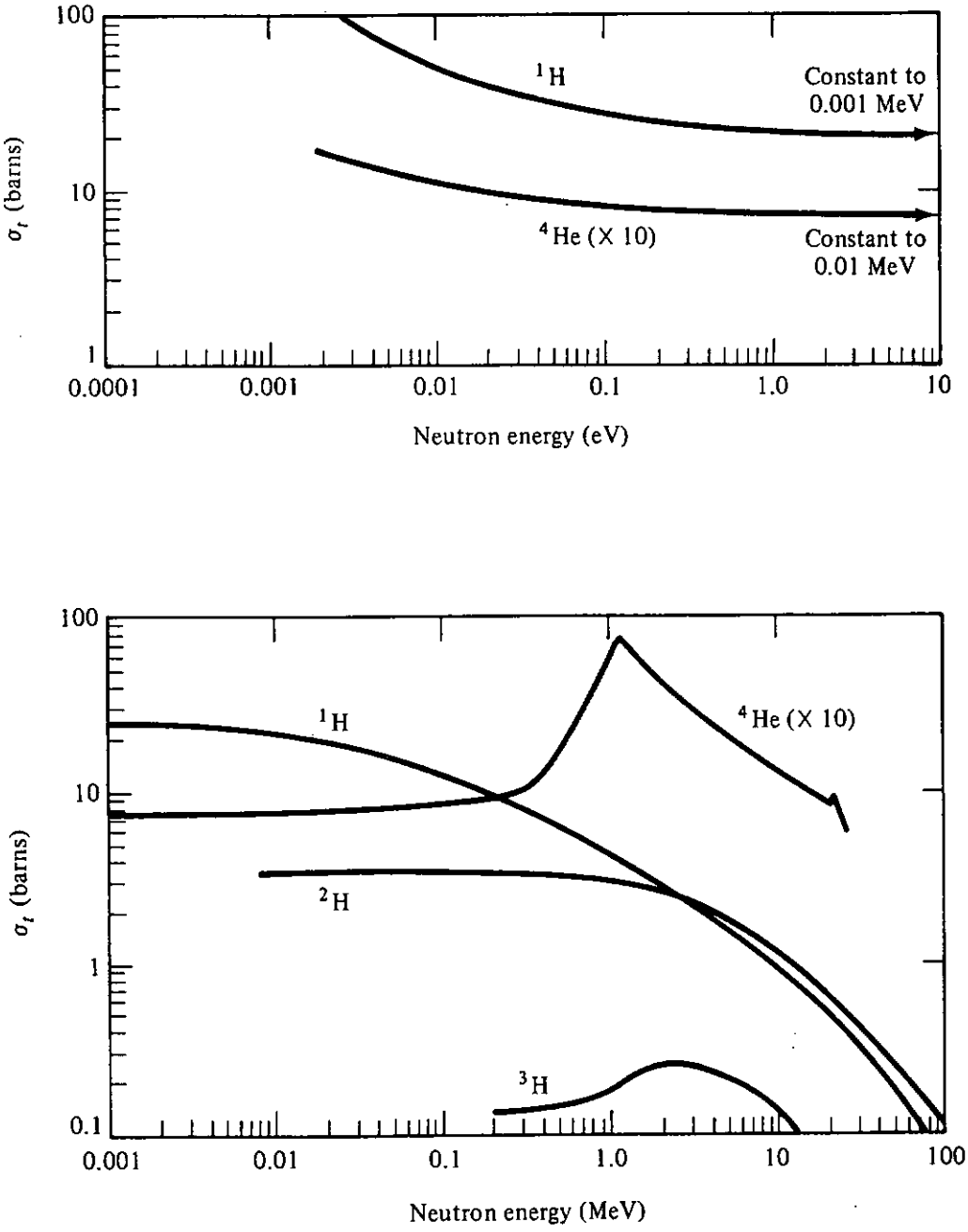

Figure 3.6 Total cross sections for neutron interactions with the lightest nuclei. (Data are from Ref. 10.)

the crystalline planes of the material is no longer possible. Above thermal energies, the cross sections are usually slowly varying and smooth up to the MeV energy range, at which energies fairly wide (keV to MeV) resonances appear.

Of all the elements, only the lightest (hydrogen and its isotope deuterium) exhibit no resonances (see Fig. 3.6). Notice that for hydrogen the cross section is almost constant up to the MeV region, where it begins to decrease. This falling off of the hydrogen cross section will be shown to have an important implication in the shielding of fast neutrons (Chapter 8).

For heavy nuclei (e.g., Fig. 3.8), the total cross section may or may not exhibit a $1/\sqrt{E}$ behavior at low energies and a Bragg cutoff. The resonances

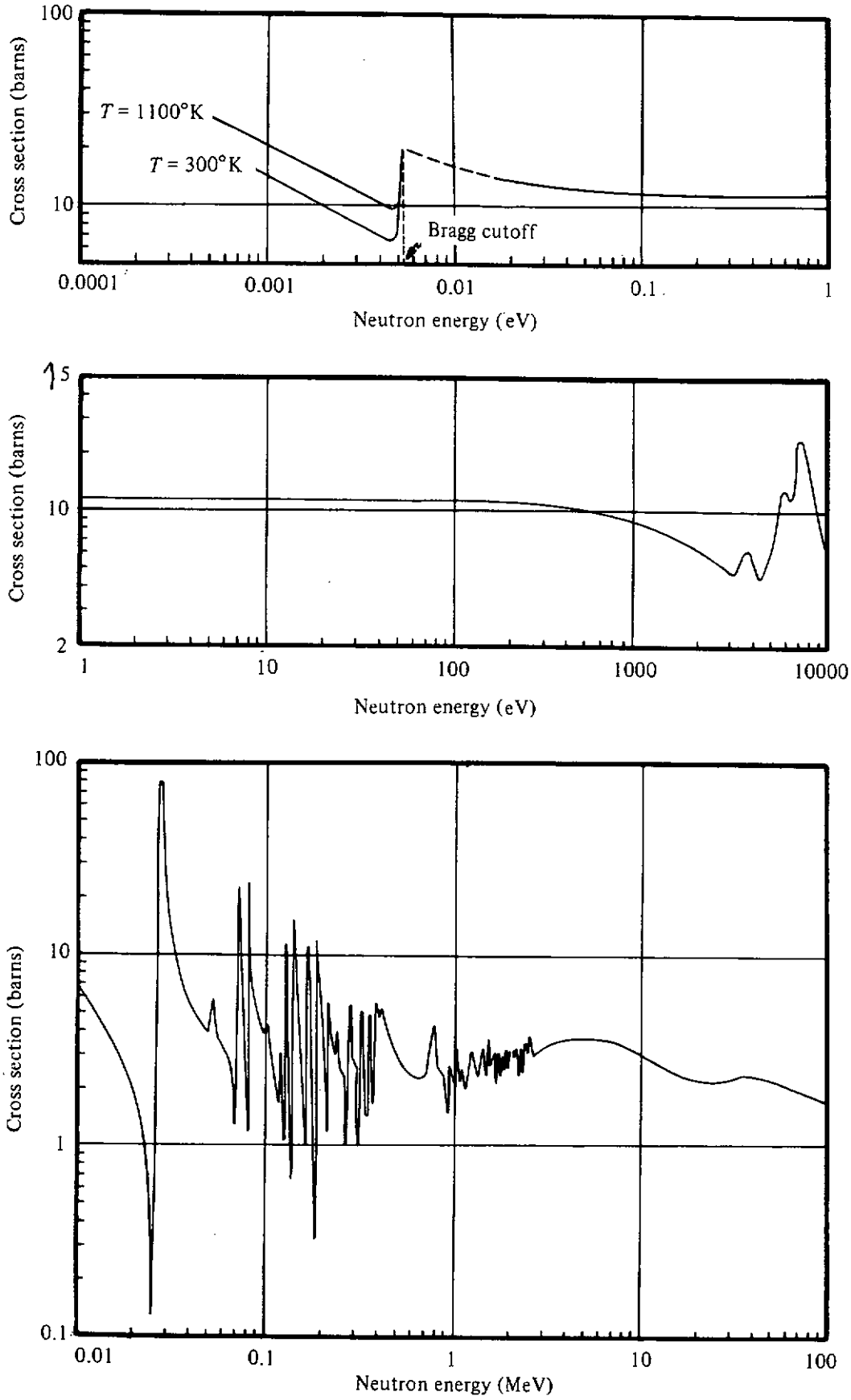

Figure 3.7 Total cross section for neutron interactions with iron. (Data are from Ref. 10.)

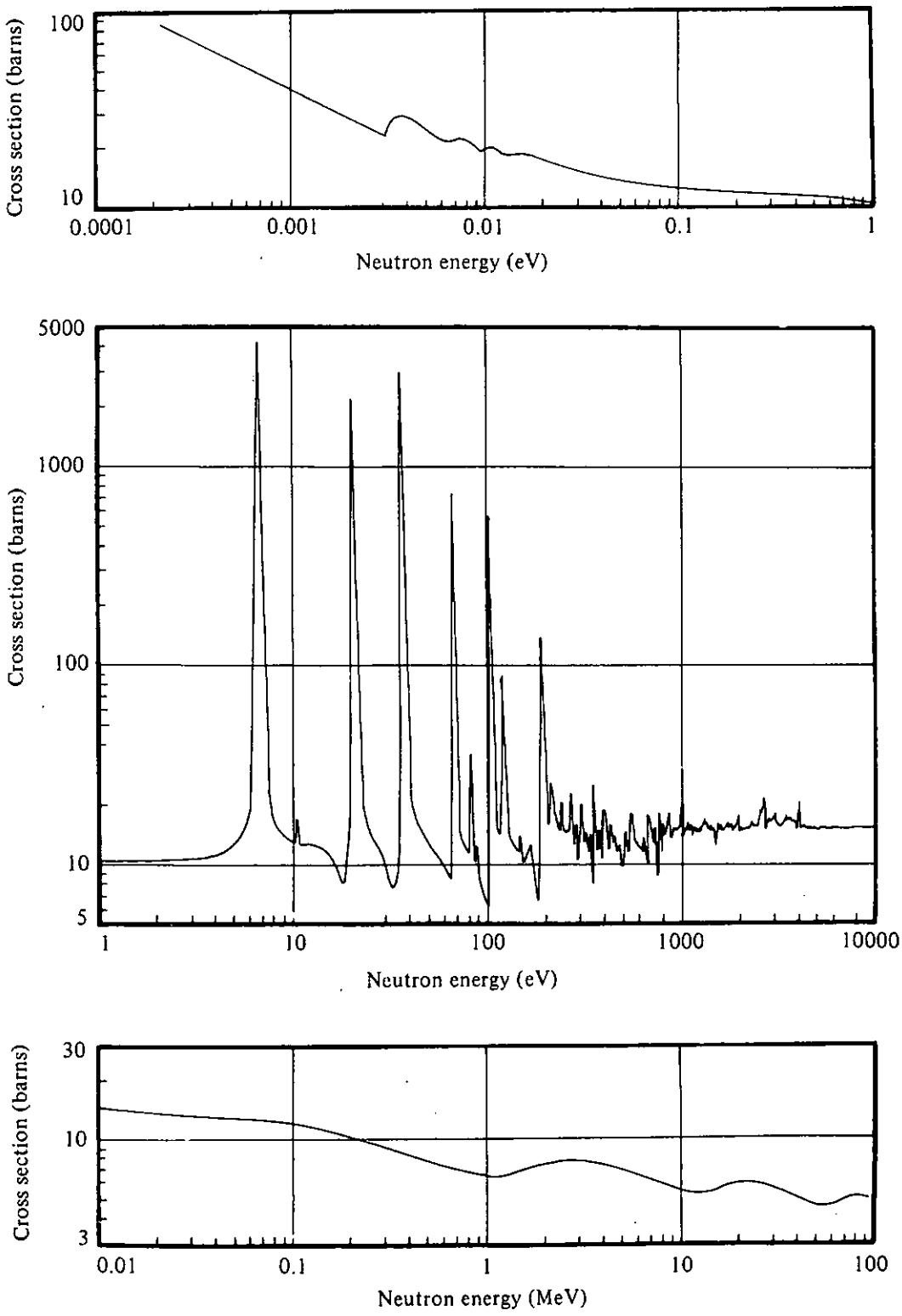

Figure 3.8 Total cross section for neutron interactions with ^{238}U. (Data are from Ref. 10.)

appear at much lower energies than for the light nuclei (usually in the eV region) and have very narrow widths (1 eV or less) with large peak values. Above 1 keV the resonances are so close together and so narrow that they cannot be resolved and the cross sections appear to be smooth except for a few broad resonances. Finally, the intermediate nuclei (Fig. 3.7), as would be expected, are of intermediate character between the light and heavy nuclei with

resonances in the region from 100 eV to several keV. The resonances are not as high or as narrow as for the heavy nuclei.

For neutron shielding purposes, one is usually concerned with fast neutrons (>500 keV). Neutron penetration studies are somewhat simplified in this energy region compared with the lower-energy case since the heavy nuclides have no resolved resonances and the cross sections vary smoothly with the neutron energy. Only for the light elements must the complicating resonances be considered. Further, the absorption cross sections for all nuclides are usually very small compared to those for other reactions at all energies except thermal energies. Over the fission neutron energy spectrum, the (n, γ) reaction cross sections seldom exceed 200 mb for the heavy elements, and for the lighter elements this cross section is considerably smaller. Only for thermal neutrons and a few isolated absorption resonances in the keV region for heavy elements is the (n, γ) reaction important.

In the high-energy region, by far the most important neutron interaction is the scattering process. Generally, elastic scattering is more important, although, when the neutron energy somewhat exceeds the energy level of the first excited state of the scattering nucleus, inelastic scattering becomes possible [see Eq. (3.63)]. At very high levels ($\gtrsim$8 MeV) multiple particle reactions become possible [e.g., $(n, 2n)$ and (n, np)]. In most materials of interest for shielding purposes the thresholds for these reactions are sufficiently high and the cross sections sufficiently small that these neutron-producing reactions may be ignored compared to the inelastic scattering reactions. However, a few rare secondary-neutron-producing reactions should be noted. The threshold for $(n, 2n)$ reactions are particularly low for D and Be (3.3 MeV and 1.84 MeV, respectively) and for these two nuclei there is no inelastic scattering competition. Similarly, for fissionable nuclei the fast neutrons may cause fission events in which multiple secondary fast neutrons are liberated. In most shielding situations these particular secondary-neutron-producing reactions are not encountered.

Finally, charged-particle-producing interactions [(n, p), (n, α), etc.] may be of importance when light elements are involved. In the MeV region the (n, α) reaction cross sections for Be, N, and 0 are appreciable fractions of the total cross sections and may exceed the inelastic scattering contributions. This situation is probably true for most light elements, although only partial data are available. For heavy and intermediate nuclei the charged-particle-emission interactions are at most a few percent of the total inelastic interaction cross section and hence are usually ignored.

3.7 NEUTRON SCATTERING INTERACTIONS

The scattering interaction is by far the most common of the neutron interactions, and is the mechanism on which the shield designer relies to slow fast neutrons to thermal energies, at which they can be absorbed through the (n, γ) reactions.

There are two distinct types of scattering processes, both of importance in fast neutron shielding. In *capture scattering* the incident neutron is absorbed by the scattering nucleus to form a compound nucleus which subsequently decays by the emission of a neutron. If the residual nucleus is left in the ground state, the scattering is called *elastic*. If the residual nucleus is left in an excited state, the scattering is called *inelastic*. The other type of scattering is referred to as *potential scattering*. In this process, which is always elastic, the incident neutron is scattered by the nucleus as a whole—analogous to the diffraction of the incident neutron wave by the entire nuclear potential. Capture-scattering cross sections generally exhibit resonance behavior, whereas the potential scattering cross sections are usually very slowly varying with energy.

3.7.1 Kinematics of Neutron Scattering

In all scattering processes the total energy and momentum must be conserved, and consequently, for any given scattering interaction, there is a unique relationship among the initial and final neutron energies and the scattering angle. Except for thermal neutron scattering, for which the thermal motion of the target atoms may be comparable to the neutron speed, one can successfully neglect the initial kinetic energy of the scattering nucleus in the laboratory coordinate system. If it is further assumed that an amount $-Q$ of kinetic energy[6] is absorbed and retained by the residual nucleus (the excitation energy), then application of the principles of conservation of energy and momentum give, in the laboratory system (see Fig. 3.9),

$$\tfrac{1}{2}mv^2 = \tfrac{1}{2}mv'^2 + \tfrac{1}{2}MV'^2 - Q \tag{3.55}$$

$$m\mathbf{v} = m\mathbf{v}' + M\mathbf{V}', \tag{3.56}$$

where $\mathbf{v}$ and $\mathbf{v}'$ are the velocities of the neutron before and after scattering, respectively, and $\mathbf{V}'$ is the velocity of the recoil nucleus. From the law of cosines, with $\omega_s \equiv \cos\theta_s$,

$$|\mathbf{v}' - \mathbf{v}|^2 = v^2 + v'^2 - 2vv'\omega_s, \tag{3.57}$$

and hence Eq. (3.56) after squaring, becomes

$$V'^2 = \left(\frac{m}{M}\right)^2 (v^2 + v'^2 - 2vv'\omega_s). \tag{3.58}$$

Substitution of V'^2 from Eq. (3.58) into Eq. (3.55) yields

$$mv^2(m - M) + mv'^2(m + M) - 2m^2vv'\omega_s = 2MQ. \tag{3.59}$$

Rearrangement and expression of the speeds v and v' in terms of the initial and

[6]The *Q value* of any nuclear reaction is the excess of the kinetic energy of the product particles over that of the original particles. For inelastic scattering, the kinetic energy of the scattered neutron and the resulting excited scattering nucleus is less than that of the initial kinetic energies, and thus the Q value is always negative for this reaction.

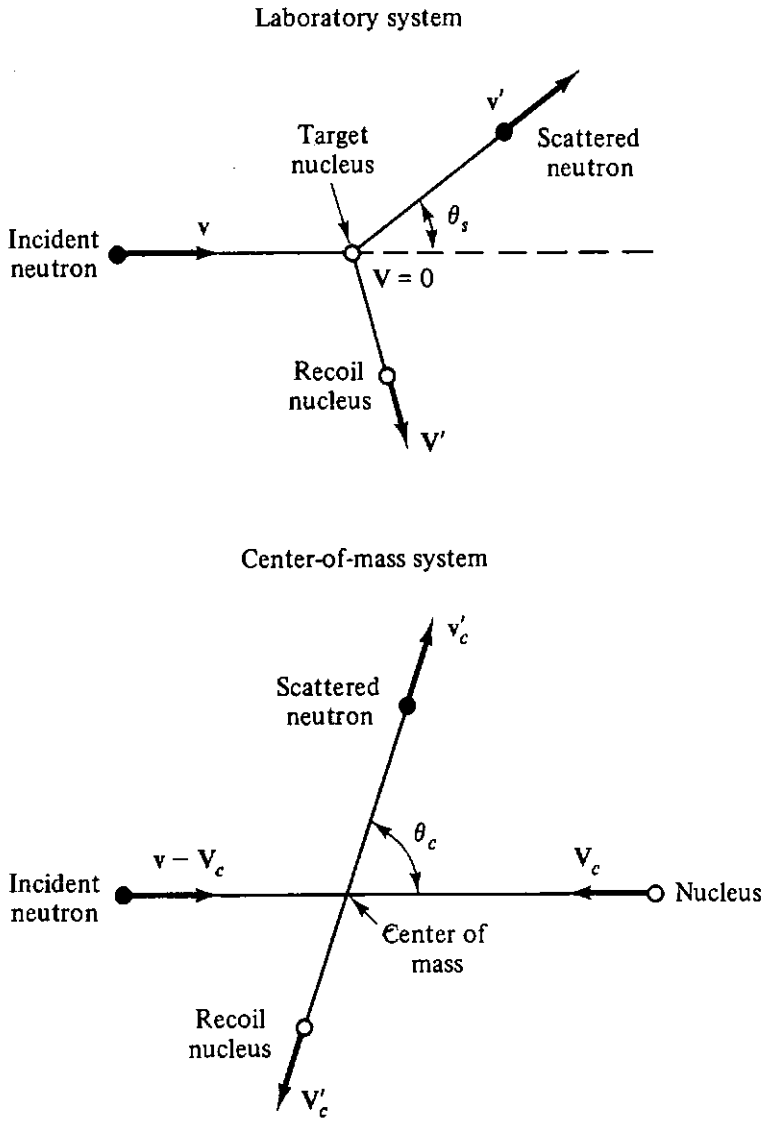

Figure 3.9 Laboratory and center-of-mass systems for the kinematics of neutron scattering. Rather than use the reflection angles θ_s and θ_c in the description of the scattering process, it is often more convenient to use their cosines ω_s and ω_c.

final laboratory system neutron energies, E and E', respectively, yields

$$\omega_s(E, E') = \frac{1}{2}\left[(A+1)\sqrt{\frac{E'}{E}} - (A-1)\sqrt{\frac{E}{E'}} - \frac{QA}{\sqrt{EE'}}\right], \tag{3.60}$$

in which $A = M/m$. This equation gives the relationship among the neutron energies before and after collision and the cosine of the scattering angle in the laboratory coordinate system. For the special case of elastic scattering, Q should be set equal to zero.

Equation (3.60) is a quadratic equation in $\sqrt{E'}$ whose solution yields

$$E'(\omega_s, E) = \frac{1}{(A+1)^2}[\omega_s\sqrt{E} \pm \sqrt{E(\omega_s^2 + A^2 - 1) + A(A+1)Q}]^2. \tag{3.61}$$

On physical grounds E' must be real and positive. If $-Q$ is large enough, Eq. (3.61) implies that E' becomes complex, and hence the reaction is not possible. The threshold energy E_t for inelastic scattering with given ω_s is readily obtained from Eq. (3.61) by recognizing that at the threshold energy the term in the second

square root must vanish, that is,

$$E_t(\omega_s) = -\frac{A(A+1)Q}{\omega_s^2 + A^2 - 1}. \tag{3.62}$$

The minimum threshold energy is observed to occur at $\theta_s = 0$, and

$$E_t(\omega_s = 1) = -\frac{A+1}{A}Q. \tag{3.63}$$

Thus, inelastic scattering is impossible if the energy of the incident neutron is less than $(A + 1)/A$ times the energy level of the first excited state (minimum value of $-Q$) of the scattering nucleus. In Table 3.3 the energy levels of the

TABLE 3.3 Energies of the First and Second Excited States in MeV for Selected Nuclides

Nuclide	First Excited State	Second Excited State	Nuclide	First Excited State	Second Excited State
$^{1}_{1}$H, $^{4}_{2}$He[a]	none	none	$^{54}_{26}$Fe[b]	1.408	2.538
$^{6}_{3}$Li	2.185	3.562	$^{56}_{26}$Fe	0.847	2.085
$^{7}_{3}$Li	0.478	4.63	$^{57}_{26}$Fe	0.014	0.136
$^{10}_{5}$B	0.718	1.740	$^{58}_{26}$Fe	0.811	1.675
$^{11}_{5}$B	2.125	4.445	$^{58}_{28}$Ni[b]	1.454	2.776
$^{12}_{6}$C	4.439	7.654	$^{60}_{28}$Ni[b]	1.332	2.159
$^{13}_{6}$C	3.088	3.684	$^{206}_{82}$Pb[b]	0.803	1.167
$^{14}_{6}$C[b]	6.094	6.590	$^{207}_{82}$Pb[b]	0.570	0.898
$^{16}_{8}$O[a]	6.049	6.130	$^{208}_{82}$Pb[a]	2.615	3.198
$^{17}_{8}$O[b]	0.871	3.055	$^{208}_{83}$Bi	0.063	0.510
$^{18}_{8}$O[b]	1.982	3.555	$^{209}_{83}$Bi[b]	0.897	1.609
$^{39}_{19}$K[b]	2.523	2.814	$^{232}_{90}$Th	0.049	0.162
$^{40}_{19}$K	0.030	0.800	$^{233}_{92}$U	0.040	0.092
$^{40}_{20}$Ca[a]	3.352	3.736	$^{234}_{92}$U	0.043	0.143
$^{41}_{20}$Ca[b]	1.943	2.001	$^{235}_{92}$U	75 eV	0.013
$^{45}_{21}$Sc	0.012	0.376	$^{236}_{92}$U	0.045	0.149
$^{55}_{23}$Mn	0.126	0.984	$^{238}_{92}$U	0.045	0.148

[a]Indicates the numbers both of neutrons and protons are magic.
[b]Indicates a magic number of neutrons or protons.
Source: *Based on data from Ref. 12.*

first two excited states are listed for selected nuclides. There it is seen that the threshold for inelastic scattering tends to decrease as the atomic mass of the scatterer increases. Notice that the level spacings of the light elements and the magic number nuclides are comparatively large and hence inelastic scattering is generally less significant for these nuclides. Moreover the odd–even and even–odd nuclides tend to have smaller thresholds than the even–even nuclides.

From Eq. (3.61) it is seen that two discrete values of the final energy E' are possible when $E > E_t(\omega_s)$, $\omega_s > 0$, and when

$$\omega_s \sqrt{E} - \sqrt{E(\omega_s^2 + A^2 - 1) + A(A+1)Q} \geq 0. \tag{3.64}$$

This condition can be simplified to

$$E \leq -\frac{AQ}{A-1} \equiv E_c,$$

where E_c is the largest value of the incident neutron energy for which two final neutron energies are possible in the laboratory system and is referred to as the *cutoff energy*. Thus, as the source neutron energy is increased above the threshold energy, but kept below the cutoff energy, the secondary neutron can appear in the forward direction ($\omega_s > 0$) with either of two discrete values of kinetic energy E'. This region of E [i.e., $E_t(\omega_s) < E < E_c$] is called the *double-valued region.*

As the kinetic energy of the incident neutron E is increased above E_c, the value of the left-hand side of the inequality (3.64) is negative. Thus, only a single value of E is obtained from Eq. (3.61); that is, only the positive sign in front of the square root term of this equation gives a physically realistic solution. This region of E above E_c is called the *single-valued region.*

For elastic scattering ($Q = 0$), $E_t = E_c = 0$ and no double energy region occurs. The energy of the scattered neutron E' can be obtained from Eq. (3.61) with $Q = 0$ as

$$E' = \frac{E[(A^2 - 1 + \omega_s^2)^{1/2} + \omega_s]^2}{(A+1)^2}. \tag{3.65}$$

3.7.2 Cross Sections for Neutron Scattering

Corresponding to each energy level of a nucleus, there is an associated cross section for neutron scattering which may be zero if the incident neutron has insufficient energy to excite the scattering nucleus to that level. The total scattering cross section for an isotope is simply the sum of scattering cross sections associated with all energy levels for which scattering is energetically possible (the ground state is always included). The total inelastic scattering cross section is then the difference between the total scattering and the elastic (ground state) scattering cross sections. The measurement of the inelastic cross section is quite difficult, and although many data have been obtained during the past 10 years, there are still many elements and energies for which the inelastic cross sections are unknown. A much easier cross section to measure is the total *nonelastic* cross section, which is the difference between the total cross section and the elastic scattering cross section. When fission and other neutron absorbing cross sections are small, the nonelastic cross section is approximately equal to the sum of all the inelastic scattering cross sections. In Fig. 3.10 nonelastic cross sections for several elements are shown for the MeV energy region and compared to the elastic scattering (total) cross section for hydrogen. Most nuclides show a rapid rise in the nonelastic cross section with increasing neutron energy and then fairly constant values in the MeV range. Finally, it should be emphasized that, although much has been said here about the inelastic scattering cross section,

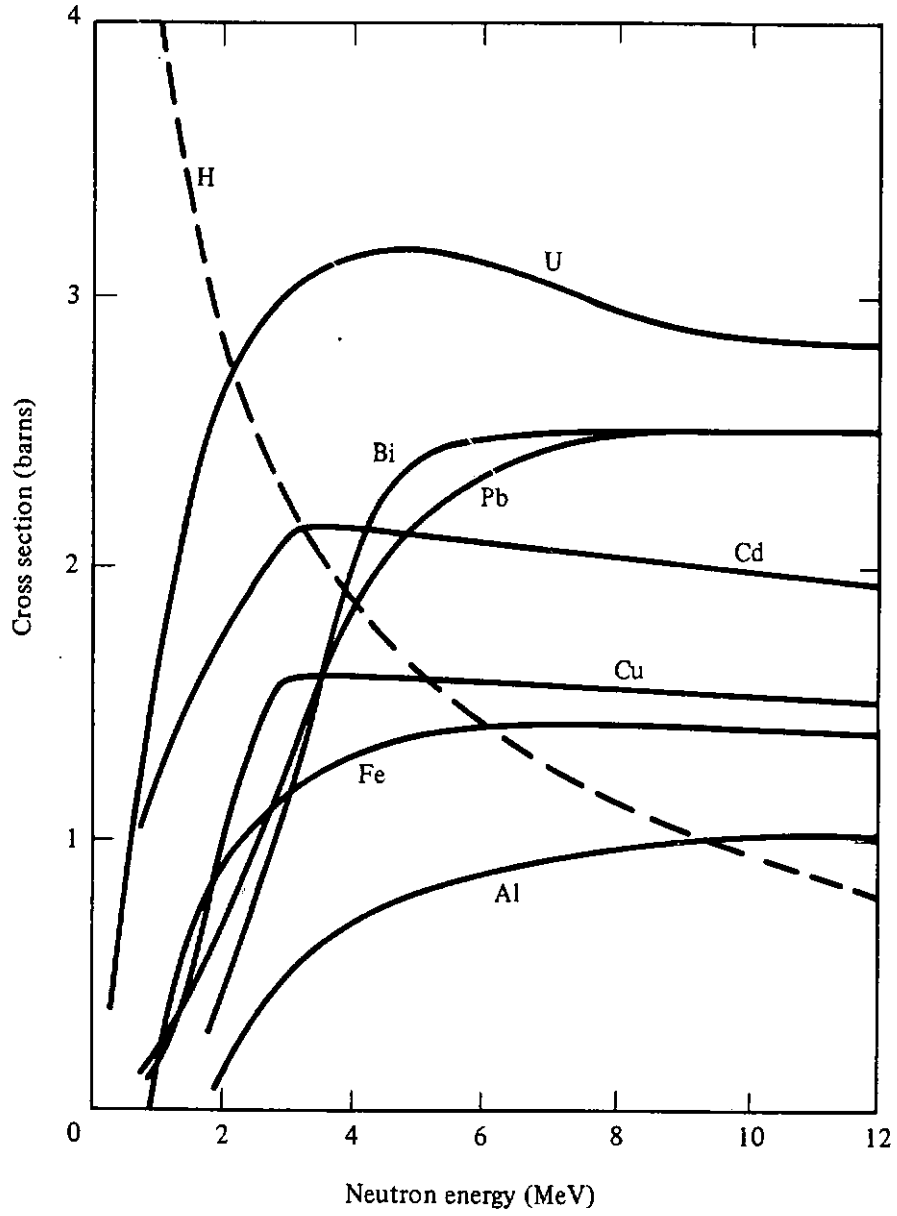

Figure 3.10 Nonelastic cross sections for several elements in the fast-neutron energy range. By contrast, the total hydrogen cross section (dashed line) decreases rapidly as the neutron energy increases in this energy region. (Data are from Ref. 10.)

the elastic scattering cross section is usually greater than any other cross section in the MeV energy region. However, as will be seen, elastic scattering for heavy nuclides does little to degrade the energy of a fast neutron and consequently inelastic scattering, although usually less likely, becomes the dominant mechanism for slowing down of neutrons with energies much greater than E_t.

The differential angular cross section, $\sigma_s(E, \theta)$, is usually reported in cross-section libraries in terms of ω_c, the cosine of the scattering angle in the center-of-mass coordinate system. This is done because, in the center-of-mass system, scattering of low- and intermediate-energy neutrons is nearly isotropic, that is,

$$\sigma_s(E, \omega_c) \simeq \frac{\sigma_s(E)}{4\pi}. \tag{3.66}$$

As a consequence of the near-isotropy of neutron scattering in the center-of-mass system, the differential scattering cross section is usually very well represented by a low-order Legendre polynomial expansion [see Eq. (3.4)] as

$$\sigma_s(E, \omega_c) = \frac{\sigma_s(E)}{4\pi} \sum_{n=0}^{N} (2n + 1) f_n(E) P_n(\omega_c). \tag{3.67}$$

The data for differential scattering cross sections are usually reported in terms of the expansion coefficients, $f_n(E)$. These expansion coefficients generally are rapidly varying functions of energy, characteristic of the resonant behavior for neutron interactions. The order of expansion needed to represent adequately experimental data seldom exceeds $N = 8$, and often only the first few Legendre coefficients are required. In the tabulations of f_n in the literature, one does not find f_0, since f_0 is always equal to unity (see Section 3.2).

To describe the scattering in the laboratory system from data in the center-of-mass system, a relation between the two coordinate systems must be used. The relation between the scattering angle θ_s in the laboratory system and the scattering angle θ_c in the center-of-mass system for scattering with a definite Q value is (Problem 3.12)

$$\omega_s = \frac{\gamma + \omega_c}{(1 + 2\gamma\omega_c + \gamma^2)^{1/2}} \tag{3.68}$$

or

$$\omega_c = -\gamma(1 - \omega_s^2) \pm \omega_s[1 - \gamma^2(1 - \omega_s^2)]^{1/2}, \tag{3.69}$$

where $1/\gamma$ is the ratio of v to the speed of the center of mass, given by

$$\frac{1}{\gamma} = \left(A^2 + \frac{A(A + 1)Q}{E}\right)^{1/2}. \tag{3.70}$$

In terms of the center-of-mass scattering angle, the relation between the initial and final neutron energies in the laboratory system can be obtained by substituting Eq. (3.68) into Eq. (3.60) to give

$$E' = \tfrac{1}{2}E(1 + \alpha) + \tfrac{1}{2}(1 - \alpha)E\sqrt{1 + \Delta}\omega_c + Q\frac{A}{A + 1}, \tag{3.71}$$

where

$$\alpha \equiv \left(\frac{A - 1}{A + 1}\right)^2 \quad \text{and} \quad \Delta \equiv \frac{Q}{E}\frac{A + 1}{A}. \tag{3.72}$$

The relation between the laboratory and center-of-mass scattering angular distributions can be obtained by a formal change of independent variable or by noting that the probability of scattering into corresponding differential solid angles about corresponding angles must be the same,[7] that is,

$$\sigma_s(E, \omega_s)\, d\Omega_s = \sigma_s(E, \omega_c)\, d\Omega_c \tag{3.73}$$

[7]It should be noted that $\sigma_s(E, \omega_s)$ is a different function from $\sigma_s(E, \omega_c)$ even though they are both given the same symbol, σ_s, following standard usage. One refers to the laboratory system distribution, while the other refers to the center-of-mass system distribution, which may be quite different.

or, since $d\Omega = 2\pi \sin\theta \, d\theta$ (the factor of 2π implying that the scattering is azimuthally symmetric about the initial direction of the neutron),

$$\sigma_s(E, \omega_s) = \sigma_s(E, \omega_c) \frac{d\omega_c}{d\omega_s}. \tag{3.74}$$

The derivative $d\omega_c/d\omega_s$ is obtained from Eq. (3.68) or Eq. (3.69), and hence the relation between the differential scattering cross sections in the two coordinate systems becomes

$$\sigma_s(E, \omega_s) = \sigma_s(E, \omega_c) \frac{(1 + 2\gamma\omega_c + \gamma^2)^{3/2}}{1 + \gamma\omega_c} \tag{3.75}$$

or

$$\sigma_s(E, \omega_c) = \sigma_s(E, \omega_s) \frac{[1 - \gamma^2(1 - \omega_s^2)]^{1/2}}{\{\gamma\omega_s \pm [1 - \gamma^2(1 - \omega_s^2)]^{1/2}\}^2}. \tag{3.76}$$

The singly differential scattering cross section $\sigma_s(E \rightarrow E')$ can be obtained in terms of $\sigma_s(E, \omega_c)$ since the probability of scattering into dE' about E' is the same as the probability of scattering into $d\Omega_c = 2\pi \, d\omega_c$ about the corresponding direction θ_c, that is,

$$\sigma_s(E \rightarrow E') \, dE' = \sigma_s(E, \omega_c) 2\pi \, d\omega_c. \tag{3.77}$$

From Eq. (3.71) the quantity $d\omega_c/dE'$ can be calculated, and thus

$$\sigma_s(E \rightarrow E') = \frac{4\pi}{(1 - \alpha)E\sqrt{1 + \Delta}} \sigma_s(E, \omega_c). \tag{3.78}$$

Because of the constraints between the scattering angle and the energy of the scattered neutron imposed by the conservation of energy and momentum in the scattering process, the doubly differential scattering cross section can be expressed in terms of the singly differential scattering cross section, by use of Eq. (3.61), as

$$\sigma_s(E \rightarrow E', \omega_s) = \sigma_s(E, \omega_s) \delta(E' - E'(\omega_s, E)) \tag{3.79}$$

or, equivalently, by use of Eq. (3.60),

$$\sigma_s(E \rightarrow E', \omega_s) = \frac{1}{2\pi} \sigma_s(E \rightarrow E') \delta(\omega_s - \omega_s(E, E')). \tag{3.80}$$

The delta functions in the relations above are required because the final energy E' is uniquely determined by the scattering angle and the initial neutron energy [see Eq. (3.60) or (3.61)]. This doubly differential cross section is often denoted by $\sigma_s(E \rightarrow E', \boldsymbol{\Omega} \rightarrow \boldsymbol{\Omega}')$, and, upon combining Eqs. (3.67), (3.78), and (3.80), may be rewritten as

$$\begin{aligned} \sigma_s(E \rightarrow E', \boldsymbol{\Omega} \rightarrow \boldsymbol{\Omega}') = {} & \frac{\sigma_s(E)}{2\pi(1 - \alpha)E\sqrt{1 + \Delta}} \\ & \times \sum_{n=0}^{N} (2n + 1) f_n(E) P_n(\omega_c) \delta(\boldsymbol{\Omega} \cdot \boldsymbol{\Omega}' - \omega_s(E, E')), \end{aligned} \tag{3.81}$$

where, from Eq. (3.71),

$$\omega_c = \frac{(E'/E)(A+1)^2 - (1+A^2) - A^2\Delta}{2A\sqrt{1+\Delta}}. \tag{3.82}$$

To evaluate Eq. (3.81), one needs the cross-section data $\sigma_s(E)$ and $f_n(E)$, which are the usual quantities reported in cross-section libraries.

The angular distributions of the scattering cross sections, both elastic and inelastic, are never isotropic in the laboratory system. However, at low energies (less than a few hundred keV) many of the elastic scattering cross sections are isotropic in the center-of-mass system. In fact, for hydrogen, the scattering in the center-of-mass system is isotropic up to 30 MeV. Generally, the heavier the nuclide, the lower is the energy above which elastic scattering becomes anisotropic. Few data are available on the angular distribution of inelastically scattering neutrons. When only one or two levels are involved, the scattering may be anisotropic; however, it has generally been found that it is a good approximation to assume that the inelastically scattered neutrons are emitted isotropically in the center-of-mass system. This is particularly true when multiple levels are involved in the inelastic process. Finally, the potential scattering of fast neutrons is never isotropic, but is highly peaked in the forward directions. In fact, the angular distribution can exhibit several maxima as the scattering angle increases from $\theta_c = 0$. The rapidly changing shape of the angular distribution of scattered neutrons is illustrated in Fig. 3.11 for the case of oxygen. Clearly, such erratic behavior can be expected to greatly complicate detailed calculations of the penetration of a neutron beam into such a material.

3.7.3 Average Energy Loss in Neutron Scattering

The probability, $P(E \rightarrow E')\,dE'$, that a neutron with initial energy E will upon scattering have an energy in dE' about E' is simply the ratio of the differential scattering cross section $\sigma_s(E \rightarrow E')$ (multiplied by dE') to the total scattering cross section $\sigma_s(E)$. From Eq. (3.78) one thus obtains

$$P(E \rightarrow E') = 4\pi \frac{\sigma_s(E, \omega_c)}{\sigma_s(E)} \frac{1}{(1-\alpha)E\sqrt{1+\Delta}}, \qquad E'_{\min} < E' < E'_{\max}. \tag{3.83}$$

The minimum and maximum energies of the neutron after scattering, $E'_{\min}$ and $E'_{\max}$, respectively, can be found from Eq. (3.71) to be

$$E'_{\min} = \frac{(1 - A\sqrt{1+\Delta})^2 E}{(1+A)^2}$$

and (3.84)

$$E'_{\max} = \frac{(1 + A\sqrt{1+\Delta})^2 E}{(1+A)^2}.$$

If the final energy E' is outside of the possible energy range allowed by scattering, $P(E \rightarrow E') = 0$. For elastic scattering the final energy range is $\alpha E < E' < E$.

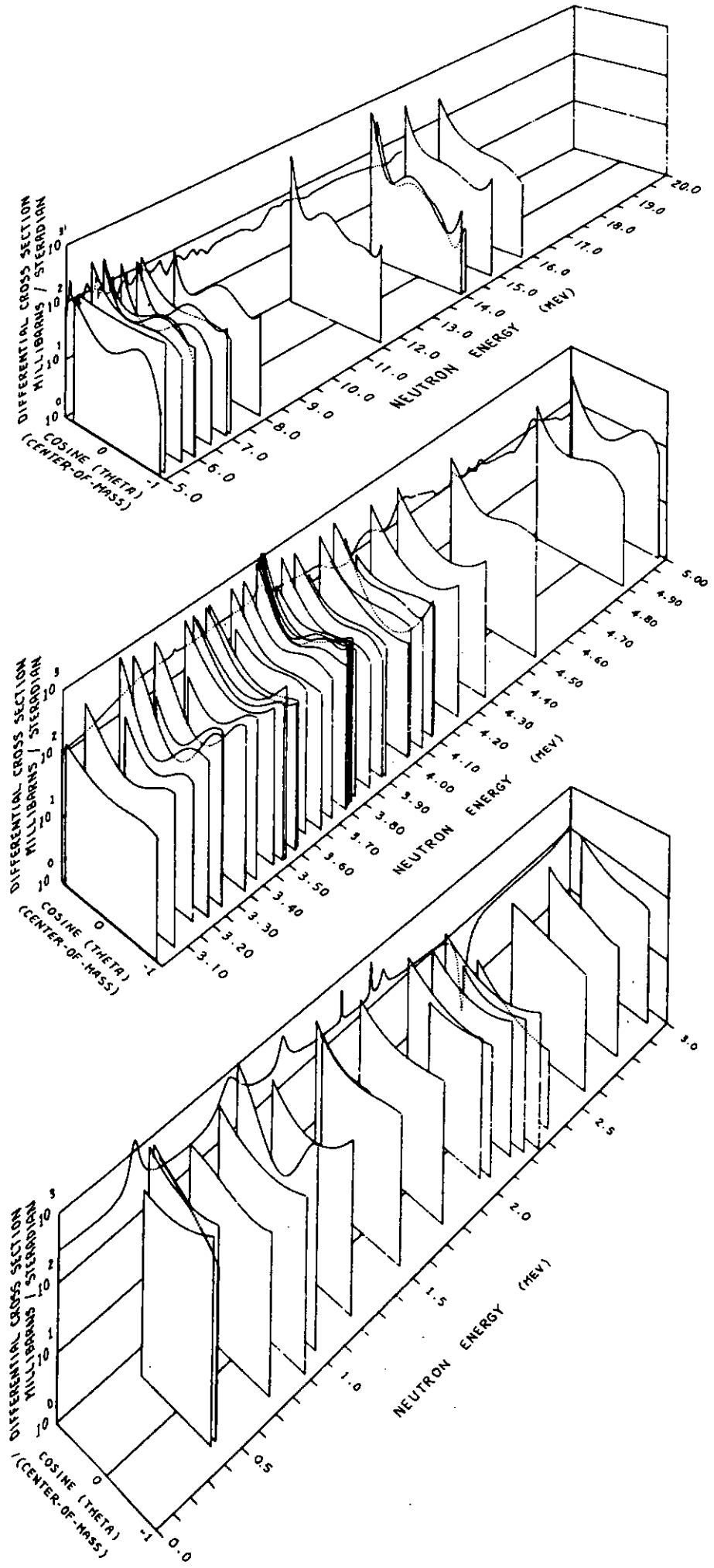

Figure 3.11 Differential elastic scattering cross section of oxygen as a function of neutron energy. (From Ref. 13.)

The average energy loss of the scattered neutron or, equivalently, the average energy of the recoil nucleus is thus given by

$$\overline{E - E'} = \int_{E'_{\min}}^{E'_{\max}} dE' \, (E - E') P(E \rightarrow E'). \tag{3.85}$$

For isotropic inelastic scattering in the center-of-mass system, the integral above is readily evaluated analytically to give

$$\overline{E - E'}_{\text{inel}} = \frac{1}{2}(1 - \alpha)E\left(1 - \frac{Q}{E}\frac{A+1}{2}\right). \tag{3.86}$$

(For anisotropic inelastic scattering, the result is given in Problem 3.16.) For elastic scattering ($Q = 0$) Eq. (3.86) reduces to $\overline{E - E'}_{\text{elas}} = (1 - \alpha)E/2$. Notice that as A becomes large, α approaches unity, and the average energy loss in elastic scattering becomes very small. Only by inelastic scattering can appreciable energy losses be realized. Although for hydrogen the average energy loss is one-half of the initial energy, the total scattering cross section, $\sigma_s(E)$, falls off rapidly in the MeV energy region and hydrogen scattering events become relatively improbable. For this reason inelastic scattering by heavy nuclides plays a crucial role in the slowing down of fast neutrons.

The energy of the recoil nucleus from a scattering event caused by a fast neutron is quickly dissipated in solid materials, and hence for all practical purposes the recoil energy can be assumed to be deposited locally. For example, a 5-MeV proton travels at most 0.5 mm in aluminum. Heavier recoiling nuclei are stopped in much shorter distances. Only for the case of neutron scattering in a gas does one have to be concerned with the travel of the recoil atoms and then only if very detailed calculations are required. The energy distribution of the recoil nuclei is usually of little concern in shielding analysis. However, if one is interested in precise radiation damage studies, in either biological or nonbiological material, it may be necessary to develop such detailed information for the scattering process.

Of much greater concern to the shielding analyst are the secondary gamma photons that are emitted by the recoil nuclei formed in inelastic scattering interactions. Such secondary-photon production is a most difficult aspect of fast-neutron shielding since a shield designed only to slow down a fast-neutron beam is usually not adequate to stop the inelastic scattering photons. Further, the production of the secondary photons in the shield is far from uniform since, as the energy spectrum of the neutron beam changes, so will the number and type of inelastic reactions vary. In Table A3.10 some total cross sections for the production of inelastic gamma photons are listed. The cross sections for producing a photon associated with a given energy level in the scattering nucleus (see Fig. 3.12) are known only for a few nuclides and then only for the low-lying energy levels. Secondary-photon cross-section data for neutron scattering has received much attention in the past 10 years; nevertheless, much information is still lacking and much design work is performed on the basis of theoretical nuclear models for inelastic scattering.

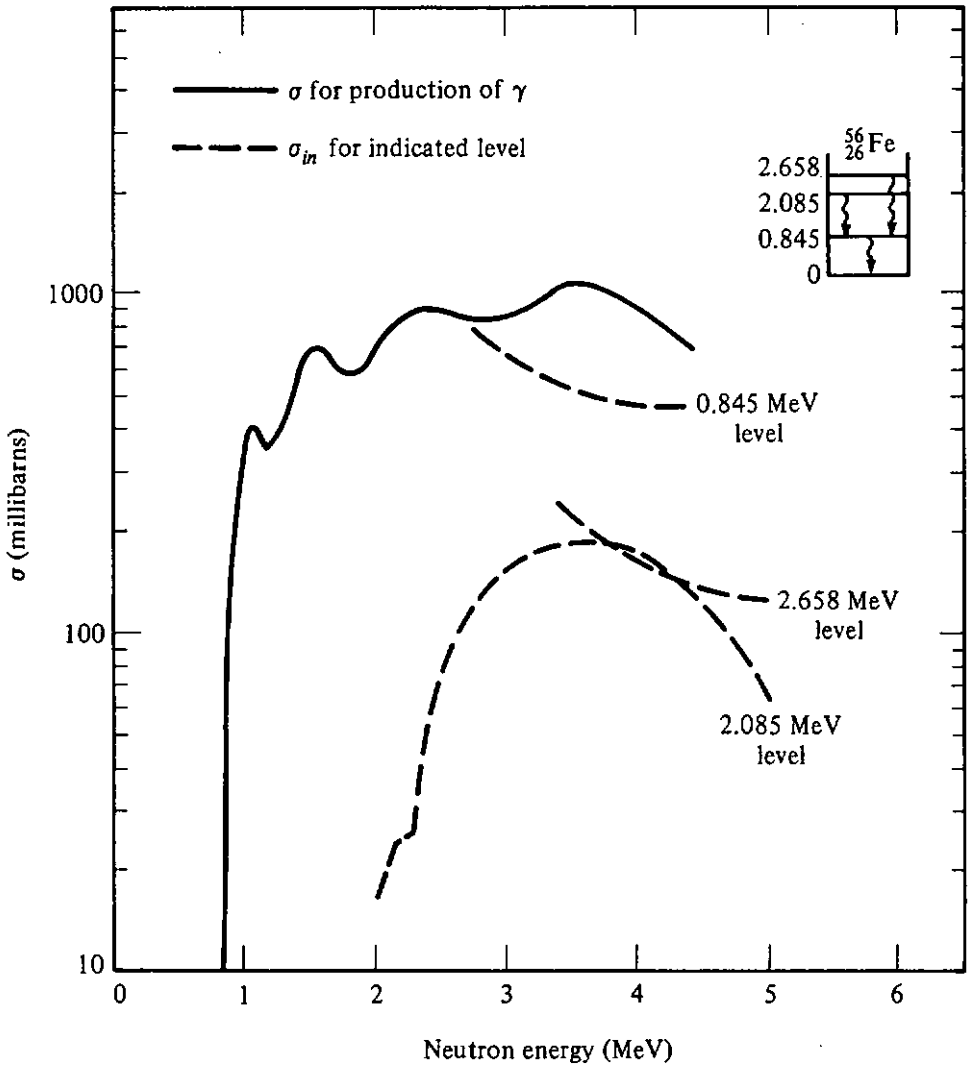

Figure 3.12 Total inelastic scattering cross sections for ^{56}Fe from the first three excited levels (dotted curves). Also shown is the total cross section for the production of the 0.845-MeV photon (solid line). (Data are from Ref. 10.)

3.8 RADIATIVE CAPTURE

Almost every neutron penetrating into a shield will be absorbed in an atom of the shield. Any kinetic energy of the neutron plus its binding energy in the resulting compound nucleus (usually around 7 to 9 MeV) leaves the compound nucleus in a highly excited state. The excited nucleus usually decays within 10^{-12} second of the capture, often through several intermediate states, thereby emitting one or more energetic gamma photons. These "capture gamma photons" from (n, γ) reactions can be an important consideration in neutron shielding analyses since they are often produced deep in a neutron shield near the outer surface and, consequently, the energetic capture photons may have only a small amount of shield to traverse before escaping.

The cross section for radiative capture is very small for high-energy neutrons, typically no more than a few hundred millibarns for neutrons with energies between 20 keV and 10 MeV. For many nuclides the (n, γ) cross section

is poorly known in the keV and MeV energy region. Only for certain important nuclides (e.g., fissionable isotopes) is the cross section known with a good degree of certainty. However, because the cross sections are almost always less than a few percent of the scattering cross sections, (n, γ) reactions are not of particular importance in fast-neutron shielding situations. Of far greater concern are the (n, γ) reactions caused by thermal neutrons which have slowed down by scattering and come into equilibrium with the thermal motion of atoms in the shield. The (n, γ) cross section may be quite large, up to thousands of barns for nuclides which have a capture resonance near the thermal energy region (e.g., cadmium), and for most isotopes it comprises almost the total absorption cross section. In a material at room temperature, the thermal neutrons will have an average energy of 1/40 eV, corresponding to a speed of 2200 m s^{-1}. In Table A3.8, thermal neutron cross sections are given for elements of interest in shielding analyses.

The absorption of neutrons in a shielding material can result in a complex photon energy spectrum characterized by many photons with energies of several MeV. The yields and energies of these capture photons are summarized in Table A3.11. Fortunately, the severity of the capture-gamma-photon problem can be ameliorated somewhat in many shielding situations. To minimize the production of these energetic photons, often a material can be used that has a high cross section for charged-particle reactions with thermal neutrons. For example, ^{6}Li has a large cross section for (n, α) reactions and lithium can be used in a neutron shield to absorb thermal neutrons without secondary photon emission. Usually, less expensive boron is used in neutron shields because ^{10}B also has a large (n, α) cross section for thermal neutrons. Although the product of the reaction, ^{7}Li*, produces a 0.48-MeV photon by isomeric transition, this photon is of less significance than the capture gamma photons because of its relatively low energy.

3.9 PENETRATION OF CHARGED PARTICLES THROUGH MATTER

Although this text for the most part treats shielding of neutrons and photons, knowledge of the ranges of ionizing charged particles and the rates at which energy is dissipated along their paths is important also, for three reasons. First, secondary charged particles resulting from neutron and photon interactions are responsible for the radiation effects of principal concern: biological, chemical, or structural change. Second, detection and measurement of photons or neutrons is almost always effected through interactions of secondary charged particles. Indeed, the roentgen unit of photon exposure (Section 2.3) is defined in terms of ionization produced by secondary electrons. Finally, a knowledge of the ranges of charged particles leads directly to the determination of shield thicknesses necessary to stop them.

Two concepts are important: *range* and *stopping power*. Initially, with kinetic energy T_0, a particle is slowed to kinetic energy $T(s)$ at path length s due to both Coulombic interactions with (atomic) electrons and radiation losses

(bremsstrahlung). During deceleration, the stopping power, $-dT/ds$, generally increases until the energy of the particle is so low that charge neutralization or quantum effects bring about a reduction in stopping power. Only for particles of very low energy do collisions with atomic nuclei of the stopping medium become important. The distance the particle travels before being stopped is called the range Λ. Idealized graphs for the range and stopping power are illustrated in Fig. 3.13, which shows the variation of energy and the rate of change of energy with distance along the path of a charged particle.

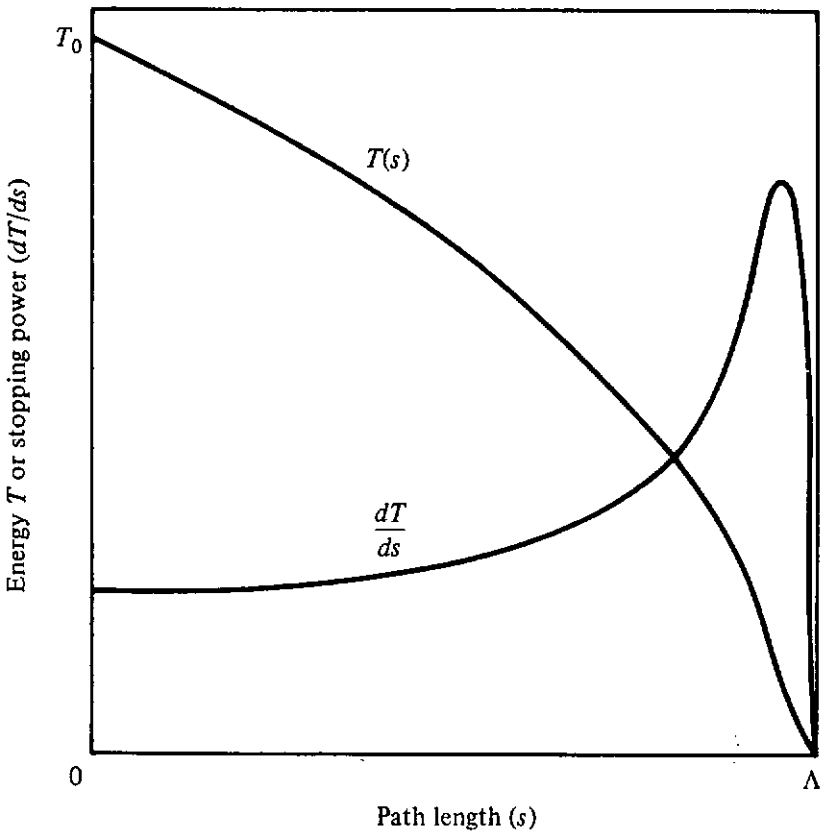

Figure 3.13 Variation of energy and stopping power along the path of a charged particle.

Heavy charged particles (those with masses greater than or equal to the proton mass) slow down almost entirely due to Coulombic interactions. A multitude of such interactions take place—so many that the slowing down is virtually continuous and along a straight-line path. These interactions, taken individually, may range from ionization processes producing energetic recoil electrons (*delta rays*) to weak atomic or molecular excitation which may not result in ionization at all. The stopping power resulting from Coulombic interactions, $(-dT/ds)_{\text{coll}}$, is called the *collisional stopping power*, or the *ionization stopping power*.

Another mechanism, which is important for electrons, is radiative energy loss, characterized by $(-dT/ds)_{\text{rad}}$, the *radiative stopping power*. Careful treatment of electron slowing down requires accounting for the possibility of delta-ray production and the concomitant deflection of the incident electron from its

original direction. In this discussion, electron range will refer to the mean path length rather than the straight-line penetration distance. Information is also available in the literature [14] for electron ranges based on straight-line penetration distance as well as for effective ranges and energy loss rates for beta particles from selected radionuclides.

3.9.1 Collisional Stopping Power

The collisional stopping power depends strongly on the charge number z and speed v of the particle. The speed v is commonly expressed in terms of β, the ratio of v to the speed of light. If M is the mass of the particle and T its kinetic energy, then $\beta = v/c = (T^2 + 2TMc^2)^{1/2}/(T + Mc^2)$. The collisional stopping power also depends on the density ρ of the stopping medium, the ratio $Z/\mathcal{A}$ of the medium atomic number to the atomic mass (atomic mass units), and the effective ionization potential I of the medium. Selected values of I are given in Table 3.4. For Z greater than or equal to 13, I, in units of eV, is given

TABLE 3.4 Selected Values of the Mean Excitation Energy

Material	I (eV)
H	18.7
Be	60.0
C	78.0
Al	163.0
Air	86.8
Water	65.1
—CH_2—	54.6

Source: *Ref. 15.*

by the empirical formula

$$I = 9.76Z + 58.8Z^{-0.19}. \tag{3.87}$$

For mixtures of elements identified by the index i, the average values of $Z/\mathcal{A}$ and I are given by the empirical formulas

$$\frac{Z}{\mathcal{A}} = \sum_i w_i \left(\frac{Z}{\mathcal{A}}\right)_i, \tag{3.88}$$

$$\ln I = \sum_i w_i \left[\frac{(Z/\mathcal{A})_i}{(Z/\mathcal{A})}\right] \ln I_i, \tag{3.89}$$

in which w_i is the weight fraction of the ith constituent.

For *heavy charged particles*, an excellent approximation for the collisional stopping power is given by the following result (valid for protons with energies between about 2 and 10 MeV or other heavy particles with comparable speeds) [3]:

$$\frac{(-dT/ds)_{\text{coll}}}{\rho(Z/\mathcal{A})z^2} = (4\pi N_A r_e^2 m_e c^2)\beta^{-2}\left[\ln \frac{2m_e c^2 \beta^2}{(1-\beta^2)I} - \beta^2\right], \tag{3.90}$$

in which N_A is Avogadro's number, z is the charge number of the particle, and r_e is the classical electron radius. The reader will note that $m_e c^2$ and I must be in the same units. The formula has been arranged to emphasize that the stopping power, divided by $\rho(Z/\mathcal{A})z^2$, is a function only of β (or v) and I. For a nonrelativistic particle, $v = (2T/M)^{1/2}$. Thus, in a given medium, a 1-MeV proton has the same collisional stopping power as a 2-MeV deuteron, and one-fourth that of a 4-MeV alpha particle, and stopping-power data for protons may be used to evaluate stopping powers for other heavy charged particles. Such data, computed from a slightly more refined version of Eq. (3.90), are presented in Fig. 3.14.

For *electrons*, the collisional stopping power may be evaluated approxi-

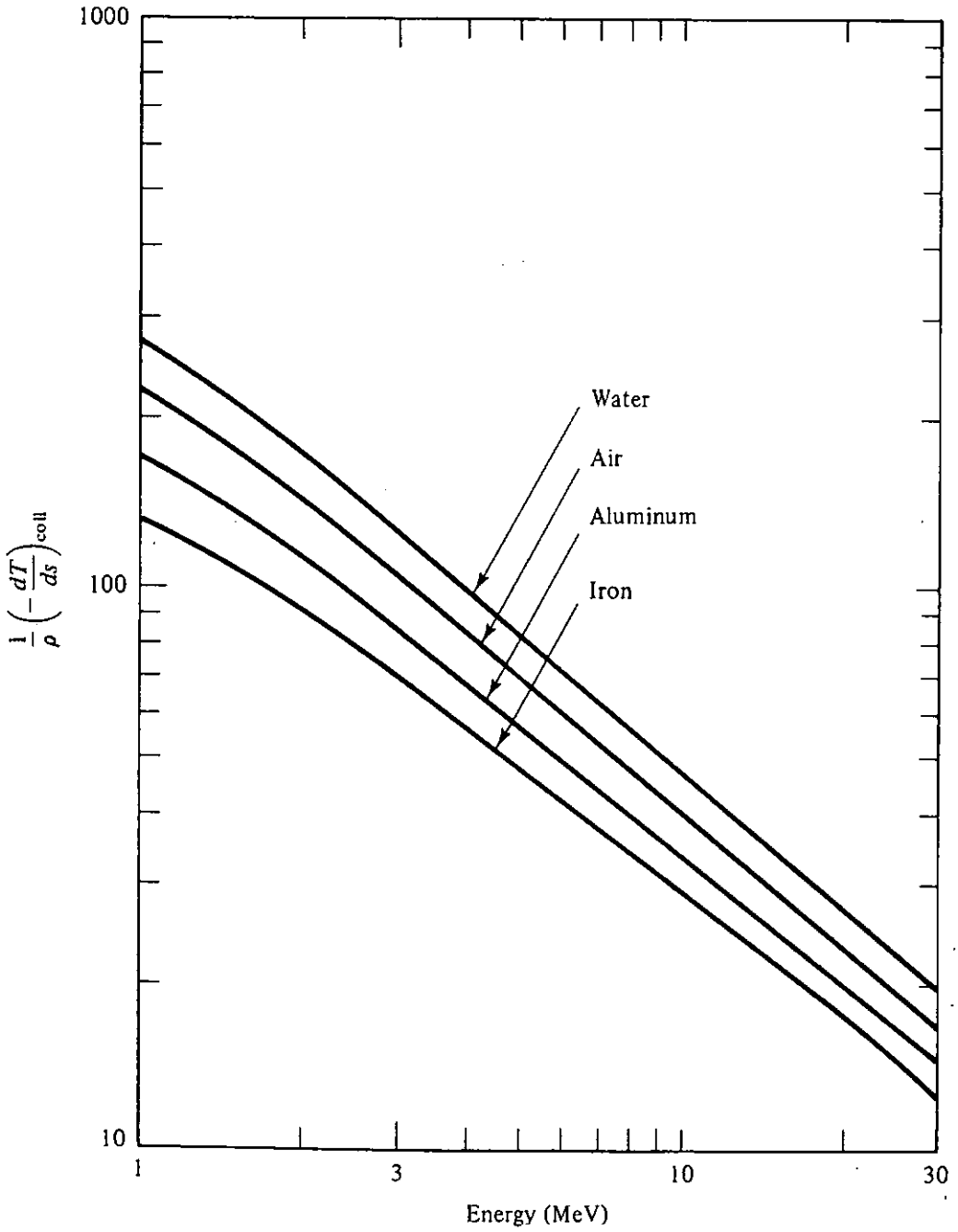

Figure 3.14 Collisional stopping power for protons in air, water, aluminum, and iron. (Data are from Ref. 15.)

mately using the following formula [3], which is accurate within 10% for electrons of energies from 0.01 to 10 MeV and materials ranging from hydrogen through iron:

$$\frac{(-dT/ds)_{\text{coll}}}{\rho(Z/\mathcal{A})} = (2\pi N_A r_e^2 m_e c^2)\beta^{-2} \times \left(\ln\left\{\frac{\beta^2(m_e c^2)^2}{I^2(1-\beta^2)}[(1-\beta^2)^{-1/2}-1]\right\} - \beta^2\right). \tag{3.91}$$

This formula has been arranged to emphasize that the stopping power, divided by $\rho(Z/\mathcal{A})$, is a function only of β and I. The formula applies to positrons as well as electrons. Selected stopping-power data, computed using a slightly more refined version of Eq. (3.91), are presented in Fig. 3.15.

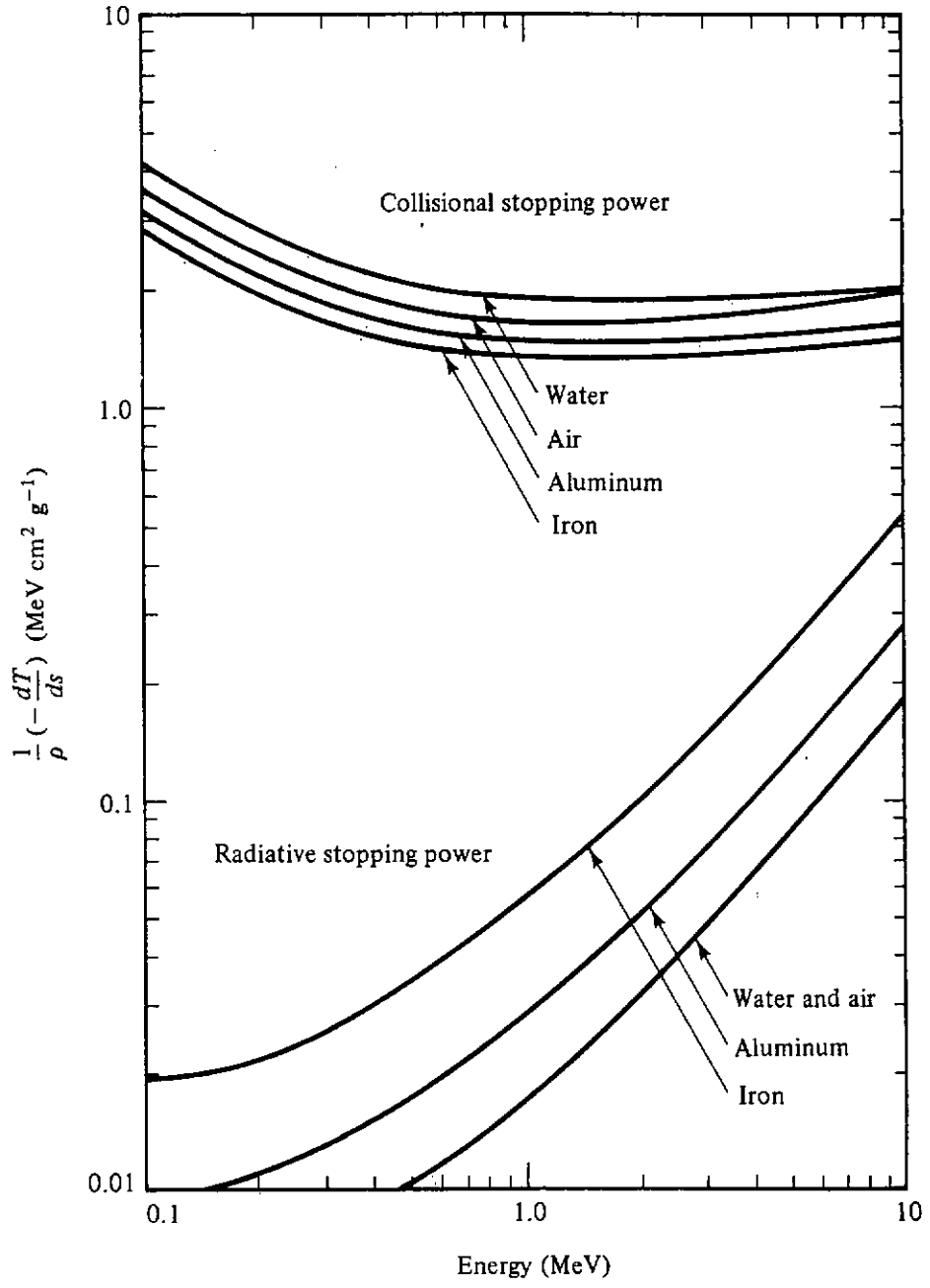

Figure 3.15 Collisional and radiative stopping power for electrons in air, water, aluminum, and iron. (Data are from Ref. 8.)

3.9.2 Radiative Stopping Power for Electrons

No single formula can adequately describe the radiative stopping power over a wide range of electron kinetic energies. It may be said that $(-dT/ds)_{\text{rad}}$ is proportional to $(\rho Z^2/\mathcal{A})(T + m_e c^2)$ multiplied by a function of energy which is constant for $T \ll m_e c^2$, then increases with increasing T, and finally reaches a plateau for $T \gg 137 m_e c^2 Z^{-1/3}$. Selected data for the radiative stopping power are presented in Fig. 3.15.

3.9.3 Charged-Particle Range

The range, here defined as mean path length, of a charged particle of initial speed v_0 may, in principle, be determined by evaluating the integral

$$\Lambda = \int_0^{\Lambda} ds = \int_0^{v_0} \frac{dv}{-dv/ds}, \tag{3.92}$$

in which $dv/ds = (dv/dT) \cdot (dT/ds)$. Evaluation of the integral is complicated by difficulties in formulating both the radiative stopping power and the collisional stopping power for low-velocity particles. Data for heavy-charged-particle range and electron range are presented in Figs. 3.16 and 3.17, respectively.

If radiation losses and charge fluctuation may be neglected, interpolation of range data is facilitated by the following rules which may be deduced from Eq. (3.92):

1. For particles of the *same initial speed* in a given medium, $\rho\Lambda$ is proportional to M/z^2.
2. For particles of the *same initial speed*, in different media, $\rho\Lambda$ is *approximately* proportional to $M/z^2(Z/\mathcal{A})$.

Thus, from rule 1, in a given medium a 4-MeV alpha particle has the same range as a 1-MeV proton.

3.9.4 Approximate Formulas for Range and Stopping Power

Very useful methods are available for making estimates of range and stopping power. Range may be estimated using the formula

$$\rho\Lambda \simeq \delta T^n, \tag{3.93}$$

in which δ and n are empirical constants. Since $(-dT/ds) = (d\Lambda/dT)^{-1}$, it follows that

$$-\frac{dT}{ds} \simeq \frac{\rho T^{1-n}}{n\delta}. \tag{3.94}$$

Values of the constants are given in Table 3.5.

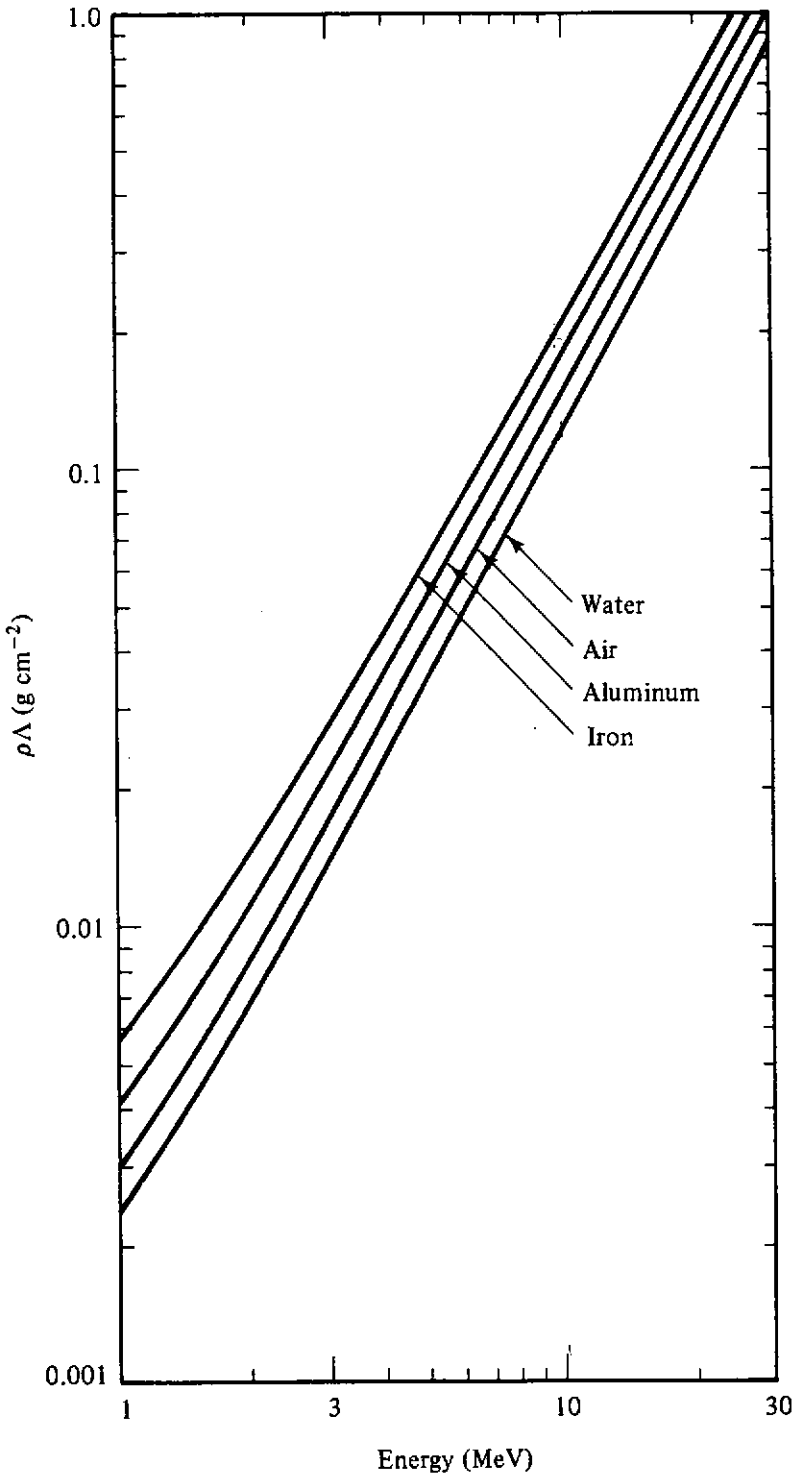

Figure 3.16 Proton range in air, water, aluminum, and iron. (Data are from Ref. 15.)

3.9.5 Charged-Particle Shielding

For the most part, shielding of charged particles is straightforward. Obviously, shield thickness must be greater than the range of the highest-energy incident particles, with some extra allowance for range straggling [3]. Complications arise from the production of bremsstrahlung and this topic is addressed in the chapters of this text devoted to photon shielding. Bremsstrahlung can be

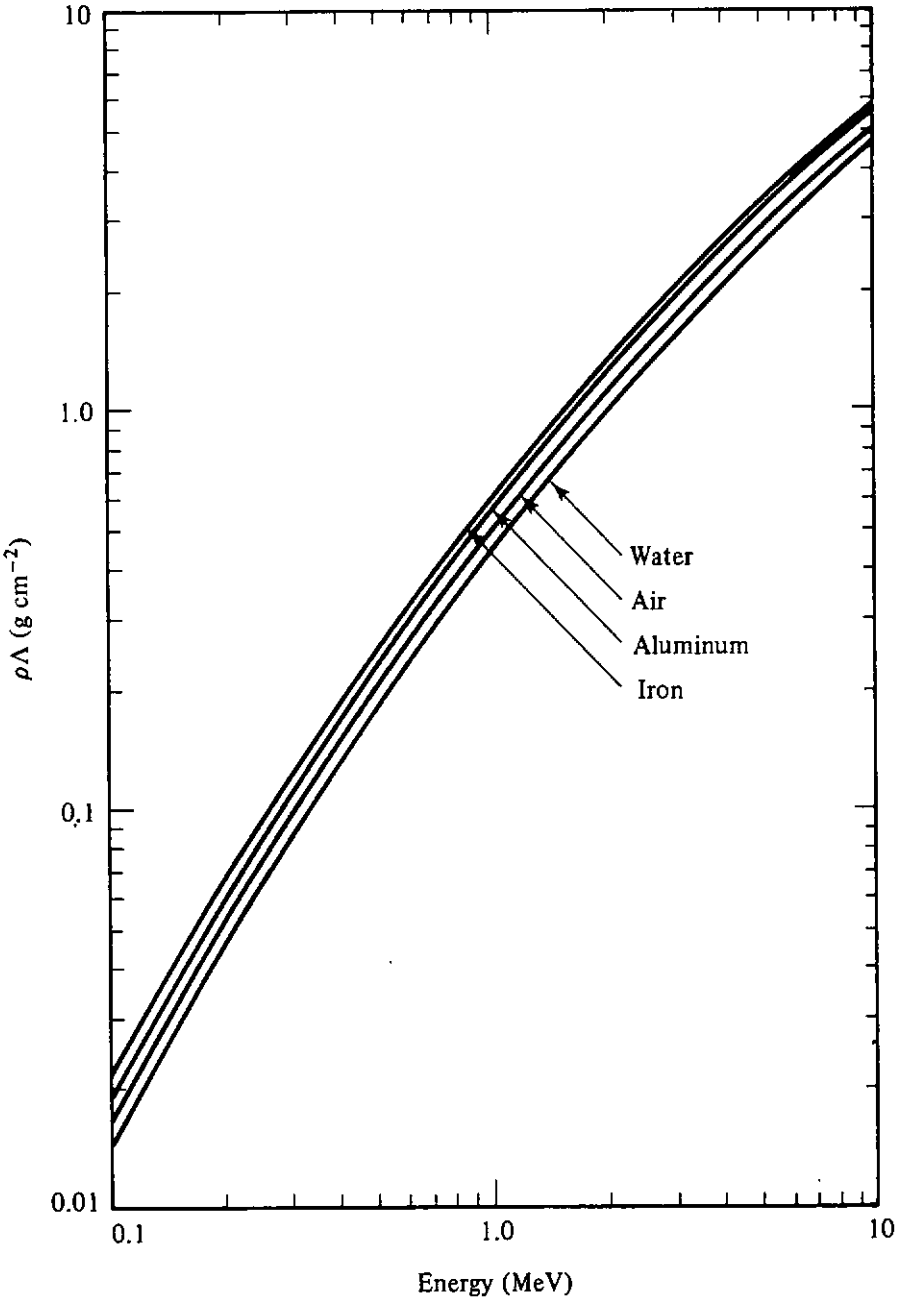

Figure 3.17 Electron range in air, water, aluminum, and iron. (Data are from Ref. 8.)

TABLE 3.5 Constants for the Empirical Energy-Range Formula: $\rho\Lambda\ (\text{g cm}^{-2}) = \delta[T(\text{MeV})]^n$

	Protons		Alpha Particles		Electrons	
Material	n	δ	n	δ	n	δ
Hydrogen	1.817	8.21(−4)[a]	1.817	6.62(−5)	1.32	0.155
Carbon	1.787	2.22(−3)	1.787	1.86(−4)	1.32	0.356
Aluminum	1.730	3.47(−3)	1.730	3.15(−4)	1.32	0.400
Lead	1.680	7.18(−3)	1.680	7.00(−4)	1.32	0.640
Water	1.793	1.95(−3)	1.793	1.62(−4)	1.32	0.356
Tissue	1.783	2.17(−3)	1.783	1.83(−4)	1.32	0.353

[a]Parentheses indicate powers of ten. Read as 8.21×10^{-4}, etc.

Source: *Ref. 16; by permission of author and Academic Press.*

minimized by using shielding materials of low atomic number. Other complications arise if the charged particles have sufficient energy to induce nuclear reactions, thereby leading to production of neutrons, photons, and mesons as well as other charged particles. Such complications are beyond the scope of this text, and the reader is referred to works dealing, for example, with shielding against cosmic rays [14].

One problem in charged-particle shielding is commonly encountered: Given that charged particles of a prescribed energy spectrum are incident on a shield, what is the energy spectrum of those particles penetrating the shield? Suppose that charged particles of one type and with flux density energy spectrum $\phi_i(T)$ are normally incident on a shield of thickness x. Just as the range of a particle is a function of its energy, the energy of a particle can be thought of as a function of its range [i.e., $T(\Lambda)$]. Of the incident particles, none with ranges less than x or with energies less than $T(x)$ will emerge from the shield. Particles that emerge with energy T' must have entered the shield with a range of $\Lambda(T) = \Lambda(T') + x$, and with an energy corresponding to this range [i.e., $T(\Lambda(T') + x)$]. Thus, the flux density energy spectrum of emergent particles, $\phi_e(T')$, is given by

$$\phi_e(T')\,dT' = \phi_i(T(\Lambda(T') + x))\,dT. \tag{3.95}$$

Since $\Lambda(T) = \Lambda(T') + x$,

$$\frac{dT}{dT'} = \frac{d\Lambda(T')/dT'}{d\Lambda(T)/dT}, \tag{3.96}$$

and the emergent flux density energy spectrum is thus

$$\phi_e(T') = \phi_i(T(\Lambda(T') + x))\,\frac{d\Lambda(T')/dT'}{d\Lambda(T)/dT}. \tag{3.97}$$

As an example, suppose that $\phi_i(T) = CT^{-m}$, in which C and m are positive constants. (Such a flux density energy spectrum is characteristic of that for cosmic rays.) From Eq. (3.93) and the result above, it follows that

$$\phi_e(T') = C(T')^{n-1}\left[(T')^n + \frac{\rho x}{\delta}\right]^{(1-n-m)/n} \tag{3.98}$$

If two conditions are satisfied, it is a straightforward matter to evaluate the absorbed dose rate (Section 2.3) given the flux density energy spectrum of charged particles. One condition is a requirement of negligible nuclear reactions. This condition holds except for extremely high-energy charged particles. The second condition is a requirement for electronic equilibrium. This topic is taken up in detail in Section 5.2. Suffice it to say here that lack of electronic equilibrium would be of concern only when the radiative stopping power is a significant factor in charged-particle attenuation, and radiative losses are ignored in the discussion to follow. The path length traveled per unit volume per unit time by charged particles with energies between T and $T + dT$ is given by $\phi(T)\,dT$. The rate of energy transfer per unit path length to the stopping medium from a charged particle of energy T is $(-dT/ds)_{\text{coll}} \equiv L_\infty(T)$. Thus, $[L_\infty(T)/\rho] \cdot \phi(T)\,dT$

is the rate per unit mass of energy transfer to the stopping medium by charged particles with energies between T and $T + dT$. The total absorbed dose rate is then

$$\dot{D} = \int dT\, \phi(T) \frac{L_\infty(T)}{\rho}, \tag{3.99}$$

where the integration is over all values of T permitted.

REFERENCES

1. "Radiation Quantities and Units," Report 33, International Commission on Radiation Units and Measurements, Washington, D.C., 1980.
2. W. Heitler, *The Quantum Theory of Radiation*, 3rd ed., Oxford University Press, Oxford, 1954.
3. R. D. Evans, *The Atomic Nucleus*, McGraw-Hill, New York, 1955.
4. O. Klein and Y. Nishina, *Z. Phys.* **52**, 853 (1929).
5. E. Storm and H. I. Israel, "Photon Cross Sections from 0.001 to 100 MeV for Elements 1 through 100," Report LA-3753, Los Alamos Scientific Laboratory, Los Alamos, N.M., 1967.
6. F. Biggs and R. Lighthill, "Analytical Approximations for Photon–Atom Differential Scattering Cross Sections Including Electron Binding Effects," Report SC-RR-72 0659, Sandia Laboratories, Albuquerque, N.M., 1972.
7. F. Biggs and R. Lighthill, "Analytical Approximations for Total and Energy Absorption Cross Sections for Photon–Atom Scattering," Report SC-RR-72 0685, Sandia Laboratories, Albuquerque, N.M., 1972.
8. M. J. Berger and S. M. Seltzer, "Tables of Energy Losses and Ranges of Electrons and Positrons," Report NASA SP-3012, National Aeronautics and Space Administration, Washington, D.C., 1964.
9. R. Kinsey (ed.), "ENDF/B-V Summary Documentation," Report BNL-NCS-17541 (ENDF-201), 3rd ed., Brookhaven National Laboratory, Upton, N.Y., 1979.
10. "Neutron Cross Sections," Report BNL-325 and Supplements, Brookhaven National Laboratory, Upton, N.Y., 1958, 1966.
11. J. R. Lamarsh, *Introduction to Nuclear Reactor Theory*, Addison-Wesley, Reading, Mass., 1966, pp. 35, 38.
12. C. M. Lederer and V. S. Shirley (eds.), *Table of Isotopes*, 7th ed., Wiley-Interscience, New York, 1978.
13. D. I. Garber, L. G. Strömberg, M. D. Goldberg, D. E. Cullen, and V. M. May, "Angular Distributions in Neutron-Induced Reactions," 3rd ed., Report BNL-400, Brookhaven National Laboratory, Upton, N.Y., 1970.
14. M. J. Berger, "Distribution of Absorbed Dose around Point Sources of Electrons and Beta Particles in Water and Other Media," Pamphlet 7, *J. Nucl. Med.*, Suppl. 5, 12 (1971).

15. W. H. Barkas and M. J. Berger, "Tables of Energy Losses and Ranges of Heavy Charged Particles," Report NASA SP-3013, National Aeronautics and Space Administration, Washington, D.C., 1964.

16. J. W. Haffner, *Radiation and Shielding in Space*, Academic Press, New York, 1967, p. 168.

PROBLEMS

3.1. A small homogeneous sample of mass m (g) with atomic mass $\mathfrak{A}$ is irradiated uniformly by a constant flux density ϕ (cm^{-2} s^{-1}). If the total cross section for the sample material with the irradiating particles is denoted by σ_t, derive an expression for the fraction of the atoms in the sample that interact during a 1-h irradiation. State any assumptions made.

3.2. Calculate the linear interaction coefficients in pure air at 20°C and 1 atm pressure for a 1-MeV photon and a thermal neutron (2200 m/s). Assume that air has the composition 78% nitrogen, 21% oxygen, and 1% argon by volume. Use data in Table A3.6 for the photon and that in Table A3.8 for the neutron. Use 2.16 b as the 2200-m/s total neutron cross section for argon.

3.3. For ordinary concrete with a composition of that given in Table 11.5, calculate the atomic densities and weight fractions of each elemental species. Using the elemental mass attenuation coefficients of Table A3.6, compute and plot the photon mass attenuation coefficient (μ/ρ) for ordinary concrete as a function of photon energy between 0.01 and 20 MeV. Aluminum is often assumed to have the same photon attenuation properties as ordinary concrete. Compare your results for concrete to those for aluminum and comment on any differences.

3.4. For interpolation in tables of μ/ρ values, one possibility is to use a linear interpolation of ln (μ/ρ) versus ln E. Discuss the merits of this scheme, and compare to other possible simple schemes. Give numerical examples.

3.5. Derive the Compton formula, Eq. (3.11), given that the momentum of a photon of energy E is equal to E/c and the momentum of an electron of kinetic energy T is equal to $(1/c)[T(T + 2m_ec^2)]^{1/2}$.

3.6. Verify Eqs. (3.14) to (3.18).

3.7. Verify Eq. (3.19); that is, given Eq. (3.21), carry out the integration

$$_e\sigma_T = \int_{4\pi} {}_e\sigma_T(\theta_s)\, d\Omega.$$

3.8. From the photon interaction coefficients listed in Appendix 3, determine the photon energies at which, individually, the photoelectric effect and pair production account for one-half of the total attenuation coefficient in air, iron, and lead.

3.9. Demonstrate that $4m_ec^2$ is the threshold energy for triplet production (pair production in the field of an electron).

3.10. Using tabulated values of μ_{Ca} and μ_C for air, given in Table A3.1, determine and plot $\langle \lambda\tau \rangle = f_C$ as a function of E(MeV) over the range 0.01 to 3 MeV. (Over this energy range, bremsstrahlung corrections are negligible.)

3.11 Compute and plot the energy spectrum $F(T)$ of Compton recoil electrons for incident photons of 0.5 and 2.0 MeV. Here $F(T)\,dT$ is the fraction of electrons with energies between T and $T + dT$.

3.12 Derive the relation between the scattering angles in the center-of-mass and laboratory systems for the general inelastic scattering case [see Eqs. (3.68) and (3.69)].

3.13 The differential cross section (mb sr^{-1}) for elastic scattering of a 0.2-MeV neutron from ^{6}Li in the center-of-mass system can be written as

$$\sigma_s(E, \omega_c) = 1.60 - 0.744\omega_c + 1.56\omega_c^2.$$

(a) Calculate the total elastic scattering cross section at this energy.
(b) Calculate the mean cosine of the scattering angle in both the laboratory and the center-of-mass coordinate systems.
(c) Sketch this differential scattering cross section and the corresponding differential cross section $\sigma_s(E, \omega_s)$ in the laboratory coordinate system as functions of the scattering angles.
(d) Calculate the coefficients f_n of Eq. (3.4) for this cross section.
(e) Write an expression for $\sigma_s(E, E', \omega_c)$.

3.14 Consider a neutron inelastic scatter involving the first excited level of ^{56}Fe ($Q = -0.845$ MeV).
(a) What is the minimum value of E for which inelastic scatter may occur?
(b) What is the minimum value of E for which neutrons may be scattered with θ_s as large as 45° and 90°?
(c) Sketch E' versus E for θ_s fixed at 45°.
(d) Sketch ω_c versus E for θ_s fixed at 45°.
(e) Sketch E' versus ω_s for $E = 2$, 1, 0.860363, and 0.860300 MeV.

3.15 The differential neutron elastic scattering cross section (mb sr^{-1} MeV^{-1}) from a nucleus with a nucleus-to-neutron mass ratio A can be approximated by

$$\sigma_s(E, E', \theta_s) = \sum_{n=0}^{N} a_n(E) P_n(\omega_s)\,\delta\left(E' - \frac{E}{(A+1)^2} - (\omega_s + A^2 - 1)^2\right),$$

where ω_s ($\equiv \cos\theta_s$) is the cosine of the scattering angle θ_s in the laboratory system. For iron at $E = 1.0$ MeV it is found that $N = 3$, $a_0 = 191.8$, $a_1 = 161.9$, $a_2 = 167.8$, and $a_3 = 39.9$.
(a) What is the significance of the delta function in the expression above?
(b) Calculate the total elastic scattering cross section at 1.0 MeV in iron.
(c) What is the average cosine of the scattering angle in the laboratory system?
(d) What is the probability a scattered neutron will have a final energy between 0.98 and 1.0 MeV?

3.16 Show that the average neutron energy loss in an isotropic scattering is given by

$$\epsilon_{\text{inel}} = \frac{2EA}{(A+1)^2}\left[1 - \frac{A}{2}\Delta - (1+\Delta)^{1/2} f_1\right],$$

where f_1 is the mean cosine of the scattering angle in the center-of-mass system. [*Hint:* Modify Eq. (3.85) so that the integration is carried out over ω_c.]

3.17. Estimate the production rate of capture gamma photons when a 1-g sample of iron is uniformly irradiated by a thermal neutron flux of 5×10^{11} cm^{-2} s^{-1}. Sketch the energy spectrum of the capture photons.

3.18. When a fast electron moving through air has 5 MeV of energy, what is the ratio, at that energy, of the rate of energy loss by bremsstrahlung to that by collision?

3.19. What thickness of iron is needed to stop a beam of **(a)** 10-MeV electrons, **(b)** 10-MeV alpha particles, and **(c)** 10-MeV protons? Use Eq. (3.93) and compare your values to ranges shown in Figs. 3.16 and 3.17.

3.20. Estimate the range of a 10-MeV tritium nucleus in air.

3.21. A solar flare in 1962 was found to have an energy-dependent proton fluence (in units of protons cm^{-2} MeV^{-1}) given by [16]

$$\Phi(T) = 6.25 \times 10^{16} T^{-5}, \qquad T \leq 500 \text{ Mev}$$

where T is in MeV. What is the energy spectrum of the protons that penetrate the wall of a spacecraft with a wall thickness equivalent to 1 cm of aluminum? Assume that the protons are normally incident on the wall.

4 common radiation sources encountered in shield design

Sources of radiation abound in our technological age. Besides the ubiquitous natural sources of radiation, artificial sources are increasingly evident. In medicine, industry, research, and even in our homes, human-made sources of radiation are commonplace. The proper control of the many sources of radiation and the protection of people and other sensitive systems from this radiation is the principal task of the shielding specialist.

The first task in the analysis of a radiation field or the determination of a shield design is to identify the type of radiation involved, the energy distribution of the radiation, and the strength of the source. Often this information will not be readily available and the shield designers will have to make estimates using their knowledge of the physical nature of the origins of the radiation field. Detailed descriptions and calculations for radiation sources can become quite complex. However, usually only an approximate description of the source radiation will suffice when undertaking shield calculations with the methods presented in this book. By far the majority of shielding problems involve penetrating electromagnetic radiation (gamma or x-ray photons) or neutrons. Although the mechanisms for the production of these two types of radiation are quite distinct, they are not independent since one can give rise to the other. It is therefore important to understand the various generation mechanisms for both these radiations and to be able to estimate, albeit approximately, the amount and energy of the radiation produced.

4.1 NEUTRON SOURCES

4.1.1 Fission Neutrons

Many heavy nuclides will fission on the absorption of a neutron, or even spontaneously, producing several energetic fission neutrons. These fission neutrons are of great importance in many shielding problems both from biological as well as from radiation damage considerations. Fission neutrons may produce secondary radiation sources such as inelastic scattering and capture gamma photons and may transmute stable isotopes into radioactive ones. Consequently, the evaluation of the fission neutron source characteristics is of considerable importance for shield design when fissionable isotopes are present.

Almost all the fast neutrons produced from a fission event are emitted within a few microseconds of the fission event. Only a small fraction (generally less than 1 %) of the total fission neutrons are emitted as *delayed neutrons*, which are produced by the neutron decay of fission products up to many seconds or even minutes after the fission event. Except for very specialized situations, these delayed neutrons, which are emitted with significantly less energy than the prompt neutrons, are of little importance in shield design because of their relatively small yield and low energies. Unless the delayed neutrons are the only neutron source present (e.g., in a circulating fuel reactor), the prompt neutrons totally dominate shielding considerations.

As the energy of the neutron which induces the fission in a heavy nucleus increases, the average number of fission neutrons also increases. Much research has been performed to determine the exact fission neutron yield for many fissionable nuclides because of the importance this parameter plays in the theory of nuclear reactors. In Table 4.1 the average yield of fission neutrons, $\bar{\nu}$, is given for five important fissionable nuclides as a linear fit to the energy E_n of the neutron inducing the fission.

TABLE 4.1 Yield of Fission Neutrons, $\bar{\nu}(E_n)$, as a Function of the Incident Neutron Energy E_n

Fission Species	$\bar{\nu}(E_n)$	E_n Range (MeV)
^{235}U	$\bar{\nu} = 2.432 + 0.066E_n$	$0 \leq E_n \leq 1$
	$\bar{\nu} = 2.349 + 0.150E_n$	$E_n > 1$
^{239}Pu	$\bar{\nu} = 2.867 + 0.148E_n$	$0 \leq E_n \leq 1$
	$\bar{\nu} = 2.907 + 0.133E_n$	$E_n > 1$
^{233}U	$\bar{\nu} = 2.482 + 0.075E_n$	$0 \leq E_n \leq 1$
	$\bar{\nu} = 2.412 + 0.136E_n$	$E_n > 1$
^{238}U	$\bar{\nu} = 2.304 + 0.160E_n$	$E_n \gtrsim 1.5$
^{232}Th	$\bar{\nu} = 1.873 + 0.164E_n$	$E_n \gtrsim 1.4$

Source: *Ref. 1; by permission of Addison-Wesley Publishing Co., Inc.*

Since the advent of fission reactors, many transuranic isotopes have been produced in significant quantities. Many of these isotopes have appreciable spontaneous fission probabilities, and consequently they can be used as very compact sources of fission neutrons. For example, 1 g of ^{252}Cf releases 3×10^{12} neutrons per second, and very intense neutron sources can be made from this isotope, limited in size only by the need to remove the fission heat and by the necessary encapsulation. Properties of the more important spontaneously fissioning isotopes are given in Table 4.2. Almost all of these isotopes decay

TABLE 4.2 Properties of Some Important Spontaneous Fission Neutron Sources

Nuclide	$\bar{\nu}$ Neutrons Per Fission	Neutrons Per (g s)	Half-Life (spontaneous fission)	Half-Life (total)	α Per Fission
^{236}Pu	2.2	3.5×10^{4}	3.5×10^{9} y	2.85 y	1.2×10^{9}
^{238}U	2.3	1.5×10^{-2}	8.19×10^{15} y	4.47×10^{9} y	1.8×10^{6}
^{238}Pu	2.28	2.5×10^{3}	4.77×10^{10} y	87.7 y	5.4×10^{8}
^{240}Pu	2.23	1.0×10^{3}	1.34×10^{11} y	6570 y	2.0×10^{7}
^{242}Pu	2.28	1.7×10^{3}	6.75×10^{10} y	3.76×10^{5} y	1.8×10^{7}
^{242}Cm	2.59	1.7×10^{7}	6.09×10^{6} y	162.8 d	1.4×10^{7}
^{244}Cm	2.82	1.1×10^{7}	1.35×10^{7} y	18.1 y	7.5×10^{5}
^{252}Cf	3.84	3.1×10^{12}	83 y	2.64 y	31.3
^{254}Cf	3.90	8.8×10^{14}	60.5 d	60.5 d	3×10^{-3}
^{254}Fm	4.0	3.2×10^{14}	228 d	3.24 h	1.7×10^{3}

Source: *Refs. 1–5.*

much more rapidly by α emission than by spontaneous fission. Each spontaneous fission half-life listed in this table is the half-life the isotope would have if spontaneous fission were the only decay mechanism. The much shorter total half-life arises from all possible decay processes.

The energy dependence of the fission neutron spectrum has been extensively investigated, particularly for the important isotope ^{235}U. All fissionable nuclides produce a distribution of prompt fission neutron energies which goes to zero at low and high energies and reaches a maximum at about 0.7 MeV. The fraction of prompt fission neutrons emitted per unit energy about E, $\chi(E)$, is often described by the Maxwellian distribution,

$$\chi(E) = 2\pi^{-1/2}T^{-3/2}E^{1/2}e^{-E/T}, \tag{4.1}$$

with the single parameter T. In Fig. 4.1 the measured fission neutron distribution is shown together with the best fit Maxwellian for ^{235}U. The Maxwellian parameter T is related to the average fission neutron energy $\bar{E}$ by

$$T = \tfrac{2}{3}\bar{E}. \tag{4.2}$$

Values for T obtained from Maxwellian fits to fission neutron data for several nuclides are presented in Table 4.3. Very few measurements have been made for

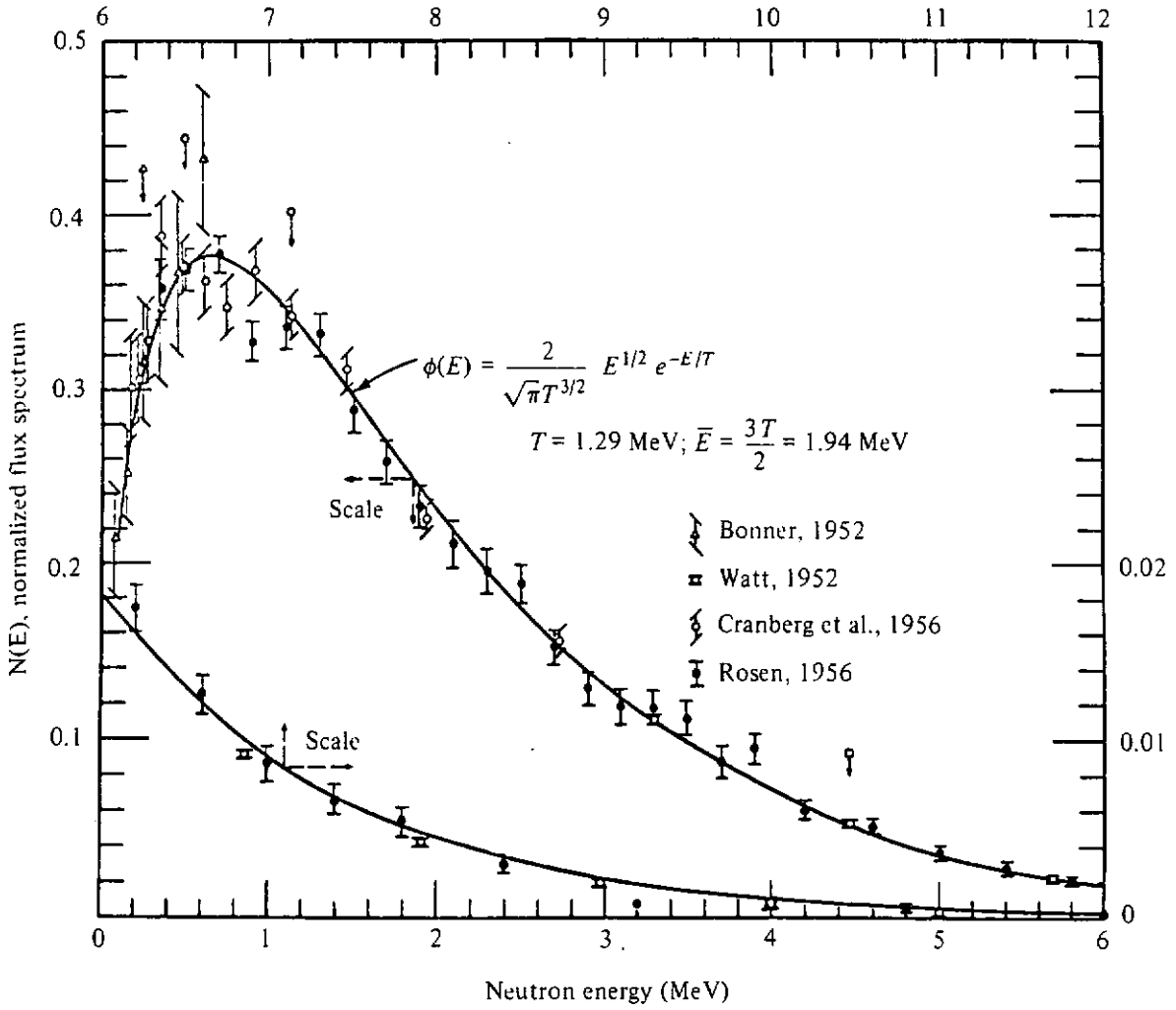

Figure 4.1 Experimental neutron energy spectrum for thermal-neutron induced fission of ^{235}U. Also shown is the Maxwellian fit to the data. (From Ref. 1; by permission of Addison-Wesley Publishing Co., Inc.; adapted from J. A. Grundl, LAMS 2883, Los Alamos Natl. Lab., Los Alamos, NM, 1963)

TABLE 4.3 Maxwellian Parameter T for Prompt Fission Neutron Distributions

Fissionable Isotope	$T = \frac{2}{3}\bar{E}$ (MeV)	Type of Fission
^{233}U	1.306	Thermal
^{235}U	1.290	Thermal
^{239}Pu	1.333	Thermal
^{252}Cf	1.466	Spontaneous
^{244}Cm	1.33	Spontaneous
^{240}Pu	1.27	Spontaneous

Source: *Refs. 1, 3, and 6.*

fast-neutron-induced fission or for isotopes other than ^{233}U, ^{239}Pu, and ^{252}Cf. For other fission neutron spectra, it is expected they can be described by a Maxwellian distribution. From plausible theoretical arguments, the parameter T can be related to the mean number of fission neutrons $\bar{\nu}$ by [7]

$$T(\text{MeV}) = 0.49 + 0.435(1 + \bar{\nu})^{1/2}. \tag{4.3}$$

For shielding studies of neutrons that penetrate thick shields, the relatively few high-energy fission neutrons ($\gtrsim$5 MeV) are of greatest concern. Equation (4.1) best fits the neutron distribution around the peak (0.7 MeV) but may significantly deviate from the actual distribution of fission neutrons at high energies. ^{235}U is the only isotope for which large amounts of experimental data exist for the high-energy portion of the fission neutron distribution resulting from thermal neutron fission. Other fits to ^{235}U data have been made which give closer agreement with the data than that of the simple one-parameter Maxwellian fit. One widely used empirical expression is [8]

$$\chi(E) = 0.4527e^{-E/0.965} \sinh \sqrt{2.29E}, \qquad 0 < E < 20 \text{ MeV}, \tag{4.4}$$

in which E is in units of MeV. If one is interested only in the high-energy tail, the ^{235}U thermal fission spectrum may be approximated by a simple exponential function. Over the range 4 to 14 MeV, a least-squares fit to Eq. (4.4) yields [9]

$$\chi(E) = 1.75e^{-0.766E}. \tag{4.5}$$

This expression deviates less than 10% from Eq. (4.4) over the range of the fit.

Recently a very accurate, three-parameter expression has been proposed for the fission neutron energy spectrum [10]. This expression is capable of describing the small changes in the spectrum arising from different incident neutron energies or from different fissioning isotopes. However, in many shielding applications, the spectrum for thermal-neutron-induced fission of ^{235}U is used, at least as a first approximation, for other fissioning isotopes, although ^{233}U, ^{239}Pu, and ^{252}Cf have somewhat greater high-energy components and consequently their fission neutrons are more penetrating than those of ^{235}U.

4.1.2 Photoneutrons

A gamma photon with energy sufficiently large to overcome the neutron binding energy (about 7 MeV in most nuclides) may cause a (γ, n) reaction. Very intense and energetic photoneutron production can be realized in an electron accelerator where the bombardment of an appropriate target material with the energetic electrons will produce intense bremsstrahlung (see Section 4.3.2) with a distribution of energies up to that of the incident electrons. However, in shielding analyses, most gamma photons encountered have too low an energy and most materials too high a photoneutron threshold for such neutrons to be of concern. Only for a few light elements (see Table 4.4) are the thresholds for photoneutron production sufficiently low that these secondary neutrons may have to be considered. In heavy-water- or beryllium-moderated reactors, the photoneutron source may be very appreciable, and the neutron field deep within a hydrogenous shield is often determined by photoneutron production in the deuterium (which constitutes about 0.015 atom percent of the hydrogen). Capture gamma photons arising from neutron absorption have particularly high

TABLE 4.4 Important Nuclides for Photoneutron Production

Nuclide	Threshold (MeV) ($-Q$ value)	Reaction
^{2}H	2.225	$^{2}H(\gamma, n)^{1}H$
^{6}Li	3.698	$^{6}Li(\gamma, n + p)^{4}He$
^{6}Li	5.67	$^{6}Li(\gamma, n)^{5}Li$
^{7}Li	7.251	$^{7}Li(\gamma, n)^{6}Li$
^{9}Be	1.665	$^{9}Be(\gamma, n)^{8}Be$
^{13}C	4.946	$^{13}C(\gamma, n)^{12}C$

energies ($\sim$7 MeV) and this may cause a significant production of energetic photoneutrons.

The photoneutron source strength S_V at a given location may be calculated from the energy distribution of the photon flux density, $\phi_\gamma(E)$, by

$$S_V = \int_{E_t}^{E_{max}} dE\, \mu_{\gamma,n}(E)\phi_\gamma(E), \tag{4.6}$$

where E_{max} is the maximum photon energy, E_t is the threshold ($= -Q$) for photoneutron production, and $\mu_{\gamma,n}$ is the (γ, n) interaction coefficient. The microscopic cross sections, from which $\mu_{\gamma,n}$ are computed, are shown in Fig. 4.2 for

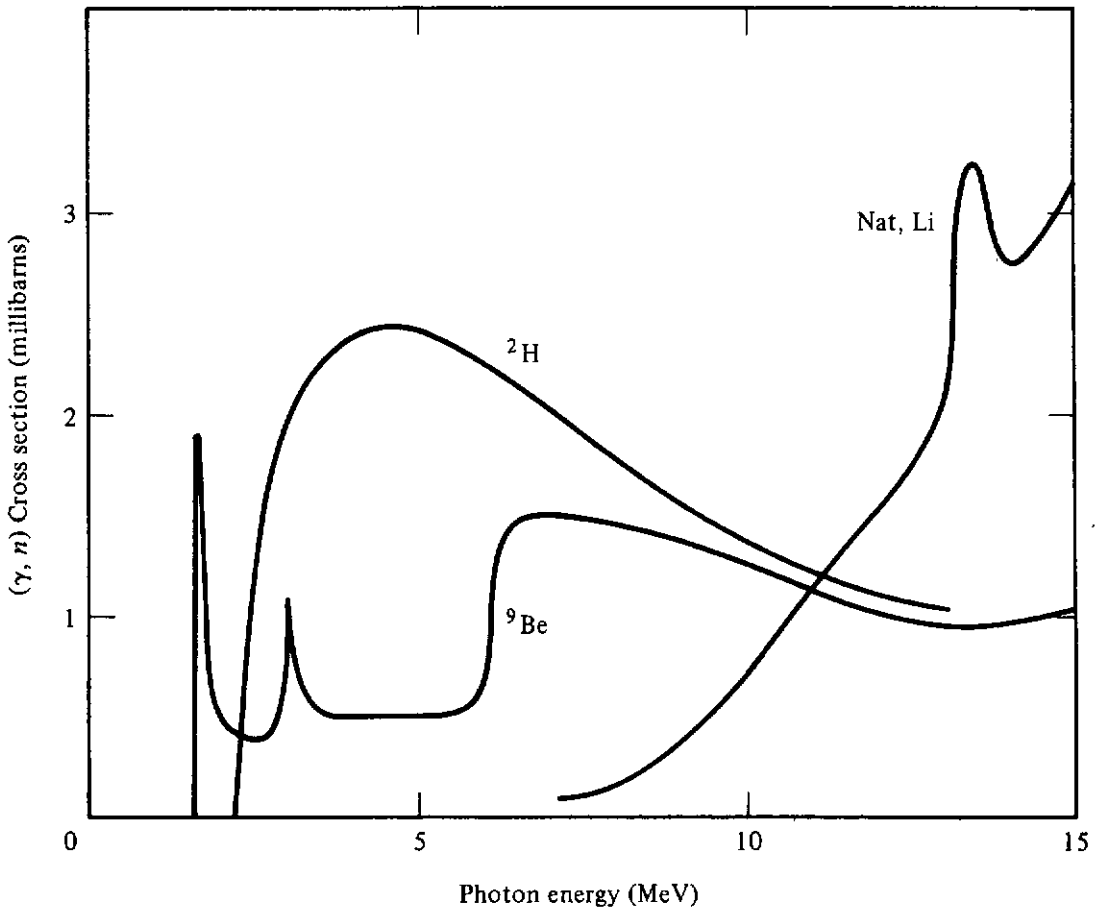

Figure 4.2 Energy dependence of the cross section for photoneutron production for three important materials. (Data from Refs. 3 and 11.)

important photoneutron materials. The energy of the photoneutron can be expressed approximately in terms of the energy of the incident photon. By application of the energy and momentum conservation equations for the (γ, n) reaction, it can be shown that if the incident photon energy E_γ is much less than the energy equivalent of the neutron rest mass ($\sim$931 MeV), the photoneutron energy is [12]

$$E_n = \frac{A-1}{A}\left[E_\gamma + Q - \frac{E_\gamma^2}{1862(A-1)}\right] + E_\gamma\left[\frac{2(A-1)(E_\gamma+Q)}{931A^3}\right]^{1/2}\cos\theta, \tag{4.7}$$

where Q is the Q value for the reaction (negative of the threshold energy), A is the ratio of the target nucleus mass to that of the neutron, and θ is the angle between the photon and neutron directions. As the angle θ varies from 0 to π, it is seen from this result that the neutron energy changes by only a few percent unless A is very small and E_γ is near the threshold energy, $-Q$. In most shielding situations it is sufficient, and safe, to assume that the photoneutrons are emitted isotropically with an energy equal to $E_\gamma + Q$ [or for deuterium, $\frac{1}{2}(E_\gamma + Q)$].

The photoneutron mechanism can be used to create laboratory neutron sources by mixing intimately a beryllium or deuterium compound with a radioisotope that decays with the emission of high-energy photons. Alternatively, the encapsulated radioisotope may be surrounded by a beryllium- or deuterium-bearing shell. The most common laboratory photoneutron source is an antimony–beryllium mixture which has the advantage of being rejuvenated by exposing the source to the neutron flux of a reactor to transmute the stable ^{123}Sb into the required ^{124}Sb isotope (half-life of 60.2 days). Such sources typically contain a mixture of about 30 g of antimony and 8 g of beryllium and yield approximately 30 neutrons per second for 10^6 Bq of ^{124}Sb. The characteristics of several common photoneutron sources are given in Table 4.5.

One very attractive feature of such (γ, n) sources is the nearly monoenergetic nature of the neutrons if the photons are monoenergetic. However, in large sources the neutrons may undergo significant scattering in the source material and thereby degrade the nearly monoenergetic nature of their spectrum. These photoneutron sources generally require careful use because of their inherently large photon emission rates. Because only a small fraction of the high-energy photons actually interact with the source material to produce a neutron (typically 10^{-6}), these sources generate gamma radiation fields that are of far greater biological concern than is the neutron field.

4.1.3 Neutrons from (α, n) Reactions

Many compact laboratory neutron sources use energetic alpha particles from various radioisotopes (emitters) to induce (α, n) reactions in appropriate materials (converters). Although a large number of nuclides will emit neutrons

TABLE 4.5 Characteristics of Some Important (γ, n) Sources

Source	Half-Life	Principal Gamma Photons		Average Neutron Energy[a] (MeV)	Standard Yield[b]
		E (MeV)	Number/ Decay		
$^{24}Na + Be$	15.0 h	2.754	1.00	0.967	3.6
$^{24}Na + D_2O$	15.0 h	2.754	1.00	0.262	7.4
$^{28}Al + Be$	2.24 m	1.779	1.00	0.101	
$^{56}Mn + Be$	2.58 h	1.811	0.29	0.129	0.8
		2.110	0.155	0.397	
		2.52	0.012	0.761	
$^{56}Mn + D_2O$	2.58 h	2.52	0.012	0.147	0.08
		2.657	0.007	0.214	
$^{72}Ga + Be$	14.1 h	1.866	0.07	0.178	1.6
		2.201	0.35	0.475	
		2.491	0.11	0.733	
		2.508	0.19	0.748	
$^{72}Ga + D_2O$	14.1 h	2.491	0.11	0.131	1.9
		2.508	0.19	0.139	
$^{88}Y + Be$	107 d	1.836	0.995	0.151	2.7
		2.734	0.005	0.949	
$^{88}Y + D_2O$	107 d	2.734	0.005	0.252	
$^{116m}In + Be$	54.0 m	2.111	0.20	0.395	0.2
$^{124}Sb + Be$	60.3 d	1.691	0.51	0.022	5.1
		2.091	0.07	0.378	
$^{140}La + Be$	40.2 h	2.521	0.032	0.760	0.07
$^{140}La + D_2O$	40.2 h	2.521	0.032	0.146	0.2
$^{226}Ra + Be$	1622 y	Many		0.68 max.	0.8
$^{226}Ra + D_2O$	1622 y	Many		0.11 max.	0.03
$^{228}Ra + Be$	6.7 y	2.62		0.848	0.9
		1.80		0.119	
$^{228}Ra + D_2O$	6.7 y	2.62		0.195	2.6

[a]From Eq. (4.7), assuming isotropic photoneutron emission.
[b]Number of neutrons emitted from 1 g of Be or D_2O per 10^6 disintegrations of the radionuclide placed 1 cm away.
Source: *Refs. 3, 5, 9, and 13.*

if bombarded with alpha particles of sufficient energy, the energies of the alpha particles from radioisotopes are capable of penetrating the potential barriers of only the lighter nuclei. Of particular interest are those light isotopes for which the (α, n) reaction is exothermic ($Q > 0$) or, at least, has a low threshold energy (see Table 4.6). A neutron source can thus be fabricated by mixing intimately one of these light converter isotopes with a radioisotope which emits energetic alpha particles. Most of the practical alpha emitters are actinide elements, which form intermetallic compounds with beryllium. Such a compound (e.g., $PuBe_{13}$) ensures both that the emitted alpha particles immediately encounter converter

TABLE 4.6 Principal (α, n) Reactions Used for Neutron Sources

Target	Reaction	Reaction Energy (MeV) (Q value)	Threshold Energy (MeV)
Li	$^{6}Li(\alpha, n)^{9}B$	−3.975	6.618
	$^{7}Li(\alpha, n)^{10}B$	−2.791	4.382
Be	$^{9}Be(\alpha, n)^{12}C$	5.702	Exothermic
	$^{9}Be(\alpha, n)3\alpha$	−1.573	2.272
B	$^{10}B(\alpha, n)^{13}N$	1.06	Exothermic
	$^{11}B(\alpha, n)^{14}N$	0.157	Exothermic
C	$^{13}C(\alpha, n)^{16}O$	2.215	Exothermic
F	$^{19}F(\alpha, n)^{22}Na$	−1.950	2.361
Na	$^{23}Na(\alpha, n)^{26}Al$	−2.967	3.484
Mg	$^{25}Mg(\alpha, n)^{28}Si$	2.653	Exothermic
	$^{26}Mg(\alpha, n)^{29}Si$	0.033	Exothermic
Al	$^{27}Al(\alpha, n)^{30}P$	−2.638	3.029

nuclei (thereby producing a maximum neutron yield) and that the radioactive actinides are bound into the source material (thereby reducing the risk of leakage of the alpha-emitting component). Some characteristics of commonly encountered (α, n) sources are listed in Table 4.7.

TABLE 4.7 Characteristics of Some (α, n) Sources

Source	Half-Life	Principal Alpha Energies (MeV)	Average Neutron Energy (MeV)	Optimum Neutron Yield per 10^6 Primary Alphas[a]
^{210}Po/Li	138.4 d	5.305	0.48	1.3
^{239}Pu/Be	24400 y	5.16, 5.15	4.6	60
^{210}Po/Be	138.4 d	5.305	4.5	70
^{238}Pu/Be	86.4 y	5.50, 5.46	4.5	80
^{241}Am/Be	458 y	5.49, 5.44	4.4	75
^{244}Cm/Be	17.6 y	5.81, 5.77	4.3	100
^{242}Cm/Be	163 d	6.12, 6.07	4.1	18
^{226}Ra/Be + daughters	1600 y	7.69, 6.00, 5.49 5.30, 4.78	3.9	500[b]
^{227}Ac/Be + daughters	21.6 y	7.37, 6.71, 6.56 5.90, 5.65	3.9	700[b]
^{241}Am/B	458 y	5.49, 5.44	3	13
^{210}Po/C	138.4 d	5.305	—	0.10
^{241}Am/F	458 y	5.49, 5.44	1.5	4.1
^{210}Po/F	138.4 d	5.305	—	5
^{210}Po/Na	138.4 d	5.305	—	1

[a]Yield for alpha particles incident on a target thicker than the range of the alpha particle.
[b]Yield dependent on proportion of daughters present. Value for ^{226}Ra corresponds to a 22-year-old source (50% contribution for ^{210}Po).

Source: *Refs. 5, 11, and 13.*

The neutron yield from an (α, n) source varies strongly with the converter material, the energy of the alpha particle, and the relative concentrations of the emitter and converter elements. The degree of mixing between converter and emitter and the size, geometry, and encapsulation of the source may also affect the neutron yield. For the most commonly used converter, beryllium, the neutron yield in an optimum mixture can be described by the empirical relation [14]

$$\text{yield} = 0.152E_\alpha^{3.56}\left[1 + \frac{(dT/ds)_e}{(dT/ds)_{\text{Be}}}\right]^{-1}, \tag{4.8}$$

where the yield is the number of neutrons produced per 10^6 alpha particles, E_α is the alpha-particle energy in MeV, and the stopping power ratio is that of the emitter to that of beryllium (see Section 3.9). The thick-target yield of neutrons (i.e., for alpha-particle interactions only with the converter) has the greatest value when beryllium is used as the converter material. Calculated and measured values for this maximum yield [15, 16] vary approximately with the alpha-particle energy E_α as

$$\text{yield} = 0.115E_\alpha^{3.82}, \qquad 3.5 \leq E_\alpha \leq 6.5 \text{ MeV} \tag{4.9}$$

and

$$\text{yield} = E_\alpha^{2.64}, \qquad 6.5 \leq E_\alpha \leq 10.0 \text{ MeV}, \tag{4.10}$$

where E_α is in MeV and the yield is per 10^6 alpha particles. Yields for other converter materials are not as well known. Thick-target yields for a boron or fluorine converter are approximately 30 or 10%, respectively, of that for beryllium, with 3- to 5-MeV alpha particles.

The energy distributions of neutrons emitted from (α, n) sources are continuous below some maximum neutron energy with definite structure at well-defined energies. In Fig. 4.3 calculated neutron energy spectra from beryllium are shown for different alpha-emitting isotopes. The structure in these distributions above 1 MeV can be interpreted in terms of structure in the $^9\text{Be}(\alpha, n)^{12}\text{C}$ cross section, which in turn depends on the excitation state in which the ^{12}C nucleus is left. The peak below 1 MeV in these theoretical distributions arises not from the direct (α, n) reaction, but from the "breakup" reaction $^9\text{Be}(\alpha, \alpha')$ $^9\text{Be}^* \rightarrow {}^8\text{Be} + n$. Notice that as the alpha energy increases, both the fraction of neutrons emitted from the breakup reaction ($E_n < 1$ MeV) and the probability that the product nucleus is left in excited states ($E_n < 6$ MeV) increase, thereby decreasing slightly the average neutron energy (see Table 4.7).

The neutron energy spectra for other converter materials are also continuous, with energy features characteristic of the energy levels of the converter and product nuclei. Generally, the emitted neutrons have lower energies than those from the $^9\text{Be}(\alpha, n)$ reaction, since Q values for all other converter nuclei are smaller. In all (α, n) sources, there is a maximum neutron energy corresponding to the reaction in which the product nucleus is left in the ground state and the neutron appears in the same direction as that of the incident alpha particle ($\theta = 0$). By application of energy and momentum conservation [analogous to Eqs. (3.55) to (3.61)], the maximum neutron energy from an (α, n) source, which

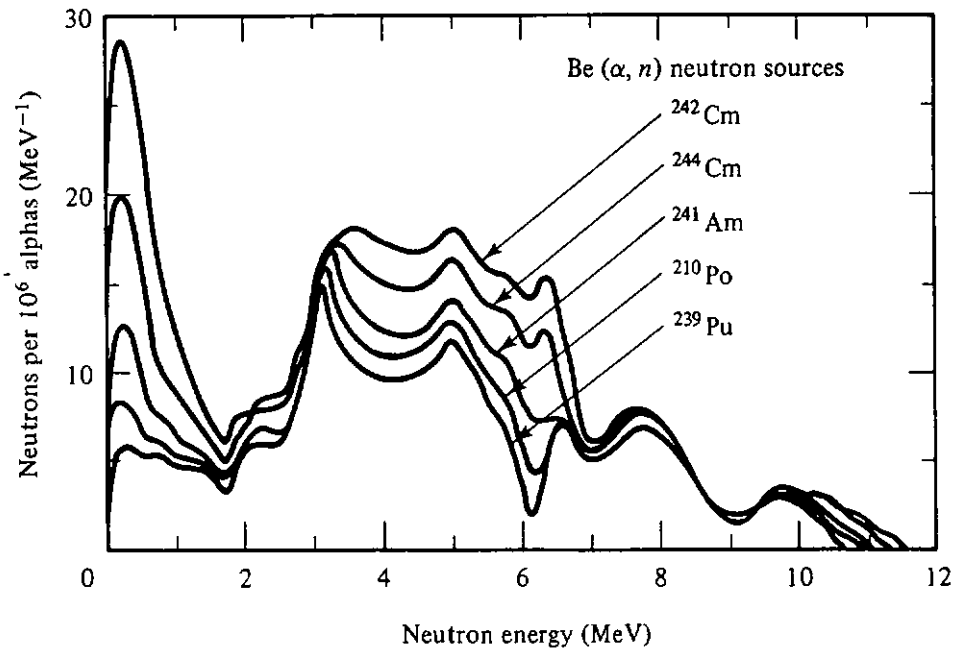

Figure 4.3 Calculated neutron energy spectra induced by alpha particles from different emitters incident on a beryllium target. No energy loss in the emitter is assumed. (After Ref. 15; by permission of the authors and Elsevier North-Holland Publishing Co.)

uses alpha particles of energy E_α, is

$$E_{max} = E_\alpha(A^2 + 3A + 4) + (A + 4)(A + 3)Q + 4\{E_\alpha(A + 3)[E_\alpha A + (A + 4)Q]\}^{1/2}/(A + 4)^2 \tag{4.11}$$

where A is the converter atom/neutron mass ratio and the Q value is for the (α, n) reaction. Thus, unlike fission neutron sources, there are no very high energy neutrons generated in an (α, n) source.

The ideal neutron energy spectrum (such as those in Fig. 4.3) is modified somewhat in actual (α, n) sources. The monoenergetic alpha particles will lose variable amounts of energy through ionization interactions in the source material before inducing an (α, n) reaction. This effectively continuous nature of the alpha-particle energy spectrum tends to smooth out many of the fine features of the ideal neutron spectrum. Further, if the source is physically large as a result of requiring a large activity (e.g., a ^{238}Pu/Be source emitting 10^7 neutrons per second requires about 73 g of plutonium), neutron interactions within the source itself may alter the emitted neutron spectrum. Neutron scattering, $(n, 2n)$ reactions with beryllium, and even neutron-induced fission of the actinide converter will change the neutron energy spectrum slightly. Finally, impurity nuclides which also emit alpha particles, as well as the buildup of alpha-emitting daughters, will affect the neutron energy spectrum. In general, the neutron energy spectrum (as well as the yield) depends in a very complicated way on the composition, size, geometry, and encapsulation of the source. Fortunately, in most shielding applications only approximate energy information is needed and the idealized spectra are often adequate.

4.1.4 Activation Neutrons

A few highly unstable nuclides decay by the emission of a neutron. The delayed neutrons associated with fission arise from such decay of the fission products. However, there are nuclides other than those in the fission product decay chain which also decay by neutron emission. Only one of these nuclides, ^{17}N, is of importance in shielding situations. This isotope is produced in water-moderated reactors by an (n, p) reaction with ^{17}O (threshold energy, 8.0 MeV) with a small cross section of about 5.2 μb averaged over the fission spectrum. The decay of ^{17}N by beta emission (half-life 4.14 s) produces ^{17}O in a highly excited state, which in turn rapidly decays by neutron emission. Most of the decay neutrons are emitted within ± 0.2 MeV of the most probable energy of about 1 MeV, although neutrons with energies up to 2 MeV may be produced.

4.1.5 Fusion Neutrons

Many nuclear reactions induced by energetic charged particles can produce neutrons. Most of these reactions require incident particles of very high energies for the reaction to take place and consequently are of little concern to the shielding analyst. Only near accelerator targets, for example, would such reaction neutrons be of concern.

From a shielding viewpoint, one major exception to the insignificance of charged-particle-induced reactions are those in which light elements fuse exothermally to yield a heavier nucleus and which are accompanied quite often by the release of energetic neutrons. Because of the importance of nuclear fusion as a potentially practical energy source, much research is being performed with these fusion reactions. The resulting fusion neutrons are usually the major (if not the only) source of radiation to be shielded against.[1] The two neutron-producing fusion reactions of most interest in the development of thermonuclear fusion power are

$$^{2}H + {}^{2}H \longrightarrow {}^{3}He\ (0.82\ MeV) + {}^{1}n\ (2.45\ MeV)$$
$$^{2}H + {}^{3}H \longrightarrow {}^{4}He\ (3.5\ MeV) + {}^{1}n\ (14.1\ MeV),$$

whose cross sections are shown in Fig. 4.4. When these reactions are produced by accelerating one nuclide toward the other, the velocity of the center of mass must first be added to the center-of-mass neutron velocity before determining the neutron energy in the laboratory coordinate system. In most designs for fusion power, the velocity of the center of mass is negligible, and a shielder is concerned with only monoenergetic 2.45- or 14.1-MeV fusion neutrons. The 14.1-MeV fusion neutrons are also produced copiously in the detonation of a

[1] Prompt gamma photons are not emitted in the fusion process, and the bremsstrahlung produced by charged-particle deflections are easily shielded by any shielding adequate for protection from the neutrons. On the other hand, activation gamma photons may arise as a result of neutrons being absorbed in the surrounding material (see Section 4.2.5).

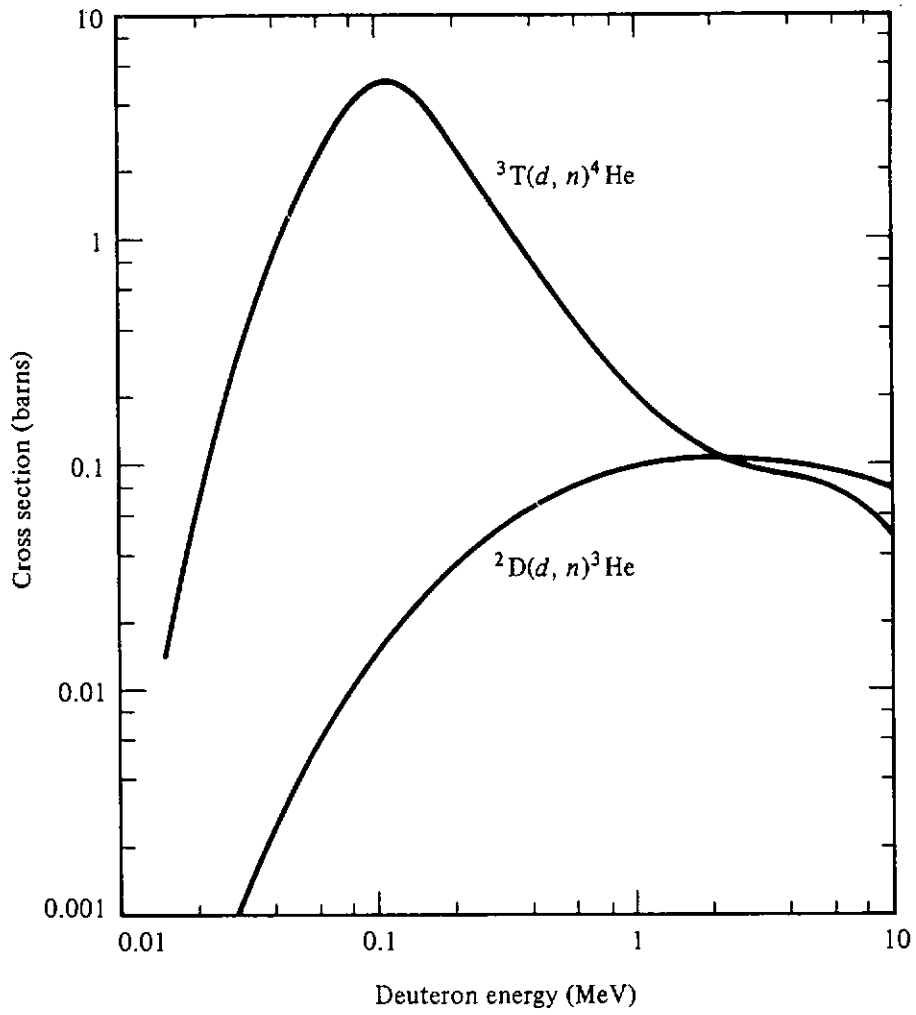

Figure 4.4 Cross sections for the two most easily induced thermonuclear reactions as a function of the incident deuteron energy.

thermonuclear bomb, and consequently, they are of great importance in shield designs for military applications.

From the cross sections of Fig. 4.4, it is found that a beam of relatively low energy deuterons (100 to 300 keV) incident on a deuterium or tritium target can produce a significant number of thermonuclear neutrons. Thus, these D-D or D-T reactions are used in relatively compact accelerators, called "neutron generators," in which deuterium ions are accelerated through a high voltage (100 to 300 kV) and allowed to fall on a thick deuterium- or tritium-bearing target. Typically in such devices, a 1-mA beam current produces up to 10^9 2.5-MeV neutrons per second from a thick deuterium target and up to 10^{11} 14-MeV neutrons per second from a thick tritium target [13].

4.2 SOURCES OF GAMMA PHOTONS

4.2.1 Prompt Fission Gamma Photons

The fission process produces, in addition to neutrons, copious numbers of gamma photons either within the first 50 ns after the fission event (the *prompt fission gamma photons*) or from the subsequent decay of the fission products.

These fission photons are of extreme importance in the shielding and gamma-heating calculations for a reactor. Consequently, much effort has been directed toward determining their nature.

Most investigations of prompt fission gamma photons have centered on the important fissioning isotope ^{235}U. For this nuclide it has been found that the number of prompt fission photons is 7.4 ± 0.8 photons per fission over the energy range 0.3 to 10 MeV [1]; and the energy carried by this number of photons is 7.2 ± 0.8 MeV per fission. Although most of the prompt fission photons have low energies and are consequently of little importance for shielding considerations, they are of concern in gamma-heating problems because they are absorbed locally in the reactor. From 35 to about 660 keV the prompt fission photon yield is roughly constant at 10.5 photons MeV^{-1} $fission^{-1}$. In Fig. 4.5 the prompt fission photon spectrum per fission is shown for ^{235}U and in Table 4.8 a discrete representation of this energy distribution is given. The peaks observed at 15 and 30 keV are caused by photons from the light and heavy

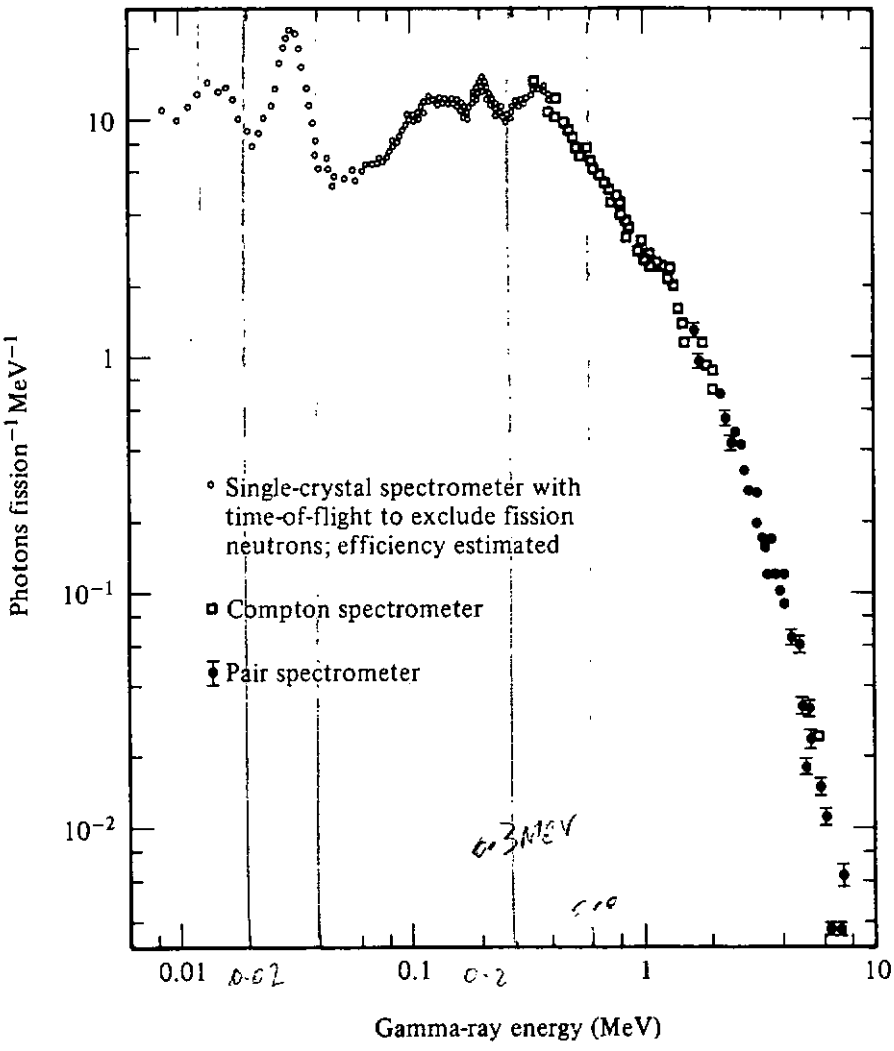

Figure 4.5 Energy spectrum of prompt fission photons emitted within 10^{-7} s after the fission of ^{235}U. The peaks at 15 and 30 keV are x rays from the light and heavy fission fragments, respectively. (From Ref. 11; reproduced by permission of Springer-Verlag New York, Inc.)

TABLE 4.8 Prompt Fission Gamma Photon Spectrum per Fission for ^{235}U as Calculated from Eq. (4.12)

Energy (MeV)	Number of Photons $= \int dE\, \mathfrak{N}(E)$	MeV Fiss^{-1} $= \int dE\, E\mathfrak{N}(E)$
0.3–1[a]	4.8	2.7
1–2	1.6	2.3
2–3	0.51	1.2
3–4	0.18	0.61
4–5	0.062	0.27
5–6	0.022	0.12
6–7	0.0076	0.049
7–8	0.0027	0.020
8–10	~0.0002[b]	0.002[b]
Total[c]	7.2	7.3 MeV/fission

[a]Values below 0.3 MeV can be obtained from Fig. 4.5 as approximately 3 photons fission^{-1} and 0.5 MeV fission^{-1}. These values have large uncertainties; however, photons in this energy range are of little consequence in shield problems. Only for gamma heating must this energy region be considered.

[b]Values obtained from experimental data as quoted in Ref. 11.

[c]Agrees well with measured values of 7.4 ± 0.8 photons per fission and 7.2 ± 0.8 MeV per fission [1].

fission fragments, respectively. The measured energy distribution shown in Fig. 4.5 can be represented by the following empirical fit over the range 0.3 to 7 MeV [1]:

$$\mathfrak{N}(E)\,(\text{photons MeV}^{-1}\,\text{fission}^{-1}) = 6.7e^{-1.05E} + 30e^{-3.8E}, \qquad (4.12)$$

where E is in MeV. The first term of this representation accounts for the high-energy portion of the distribution and the second term for the more abundant low-energy photons.

Very little work has been done to determine the characteristics of prompt fission photons from the fission of nuclides other than ^{235}U. Investigations of ^{233}U, ^{239}Pu, and ^{252}Cf indicate that the prompt fission photon energy spectra for these isotopes resembles very closely that for ^{235}U, and hence for shielding purposes it is reasonable to use the ^{235}U spectrum for other fissioning isotopes.

4.2.2 Gamma Photons from Fission Products

With the widespread application of nuclear fission, one of the important concerns for the shielding analyst is the consideration of the very long lasting gamma activity produced by the decay of fission products. The total gamma energy released by the fission product chains at times greater than 50 ns after fission is comparable to that released as prompt fission gamma photons (i.e., within 50 ns after fission). The decline of the gamma energy release rate as a function of time after fission is illustrated in Fig. 4.6, in which it can be seen that about three-fourths of the delayed gamma energy is released in the first thousand

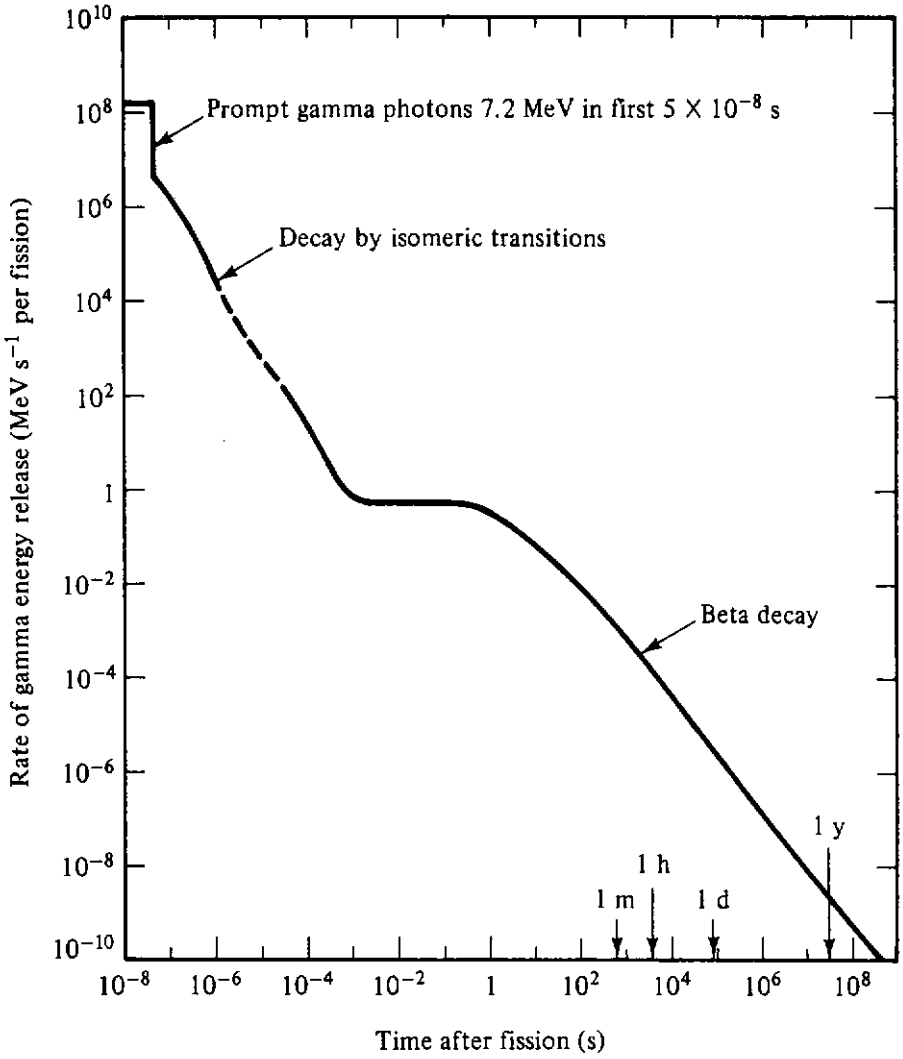

Figure 4.6 Gamma energy release rate from fission as a function of time after fission of ^{235}U.

seconds after fission. In most calculations involving spent fuel, the gamma activity at several months or even years after removal of fuel from the reactor is of interest and only the long-lived fission products need be considered. However, for a circulating-fuel reactor, the gamma activity at times after fission comparable to the circulation time is of interest, while for a pulse reactor or nuclear explosion the entire time range after fission may be of interest.

It has been found that the gamma energy released from fission products is relatively independent of the energy of the neutrons causing the fissions. However, the amount of gamma energy released and the photon energy spectrum depend significantly on the fissioning isotope (see Table 4.9 and Fig. 4.7), particularly in the first 10 s after fission. Generally, fissioning isotopes having a greater proportion of neutrons to protons produce fission-product chains of longer average length, with isotopes richer in neutrons and hence with greater available decay energy. From Fig. 4.8 it is apparent that the photon energy spectrum becomes "softer" (i.e., less energetic) as the time after fission increases. Such behavior is to be expected since energetic gamma photons are emitted

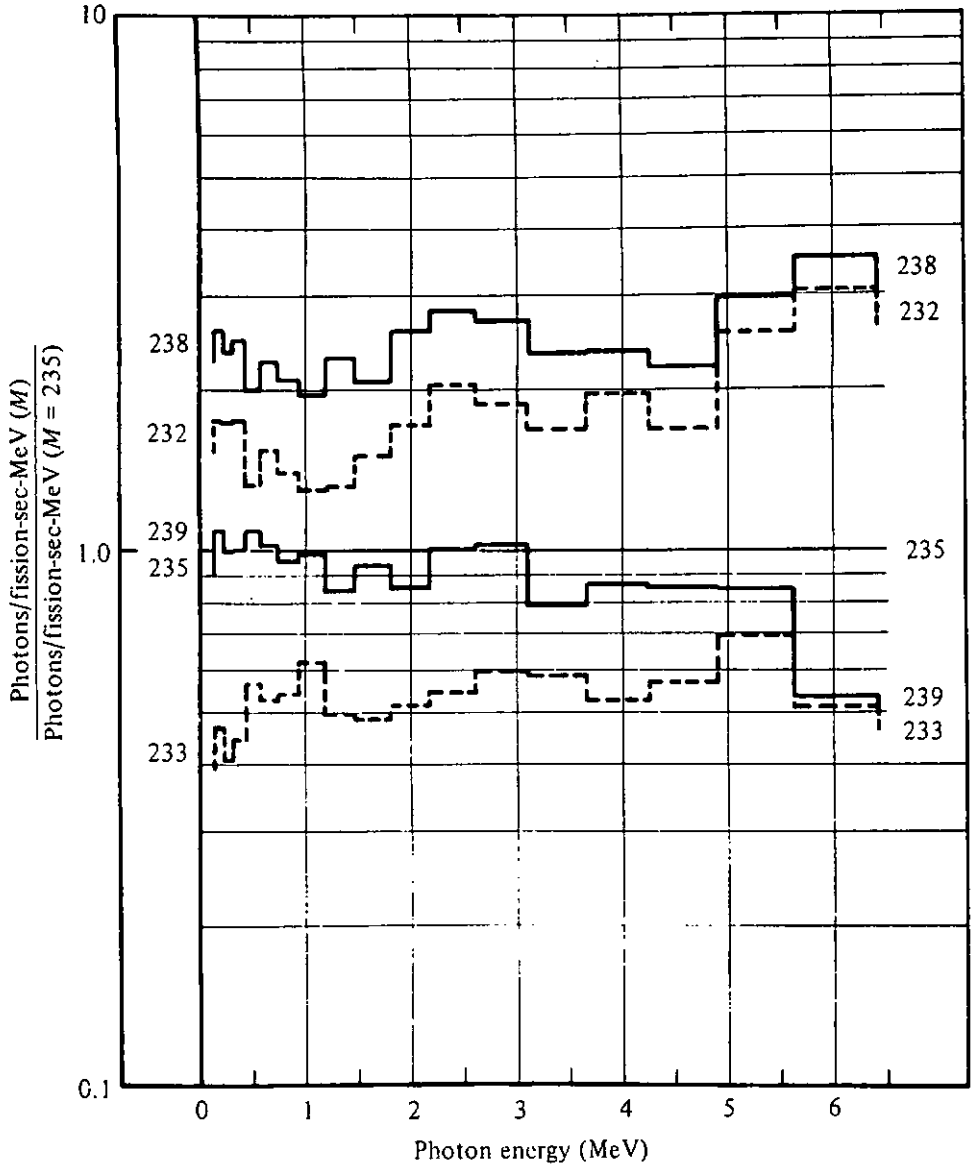

Figure 4.7 Ratios of the gamma spectra of photons emitted by various isotopes in the 0.2- to 0.5-s interval after fission to that of ^{235}U. (From Ref. 1; by permission of Addison-Wesley Publishing Co., Inc.)

TABLE 4.9 Integrated Delayed Gamma Yield and Energy Release[a]

Fission Species[b]	Integrated Gamma Yield (photons/fission for $0.2 < t < 0.5$ s)	Integrated Gamma Yield (photons/fission for $0.2 < t < 45$ s)	Integrated Energy Release (Mev/fission for $0.2 < t < 45$ s)	Total Energy Release (Mev/fission)
^{238}U	1.42	5.50	5.08	10.9
^{232}Th	0.966	5.07	5.04	10.8
^{235}U	0.613	3.31	3.18	6.84
^{239}Pu	0.608	3.26	2.86	6.15
^{233}U	0.312	2.02	1.97	4.24

[a]Integration is over the energy interval 0.1 to 6.5 MeV and time intervals as indicated.
[b]In order of decreasing fission chain length.

Source: *Ref. 1; by permission of Addison-Wesley Publishing Co., Inc.*

generally from short-lived isotopes. Further, from the spectra shown in Fig. 4.8, the expected buildup and decay of particular fission-product activities is evident.

For very approximate calculations the energy spectrum of delayed gamma photons from the fission of ^{235}U may be approximated by [1]

$$\mathfrak{N}(E) = 7.4e^{-1.1E}, \tag{4.13}$$

where $\mathfrak{N}(E)$ is the gamma yield (photons MeV^{-1} $fission^{-1}$) and E is the photon energy in MeV. The time dependence for the total gamma photon energy emission rate $F_T(t)$ (MeV s^{-1} $fission^{-1}$) is often described by the simple decay formula

$$F_T(t) = 1.4t^{-1.2}, \qquad 10\ s < t < 10^5\ s, \tag{4.14}$$

where t is in seconds. More complicated (and accurate) expressions [1] for $F_T(t)$ have been obtained from fits to experimental data, but for preliminary

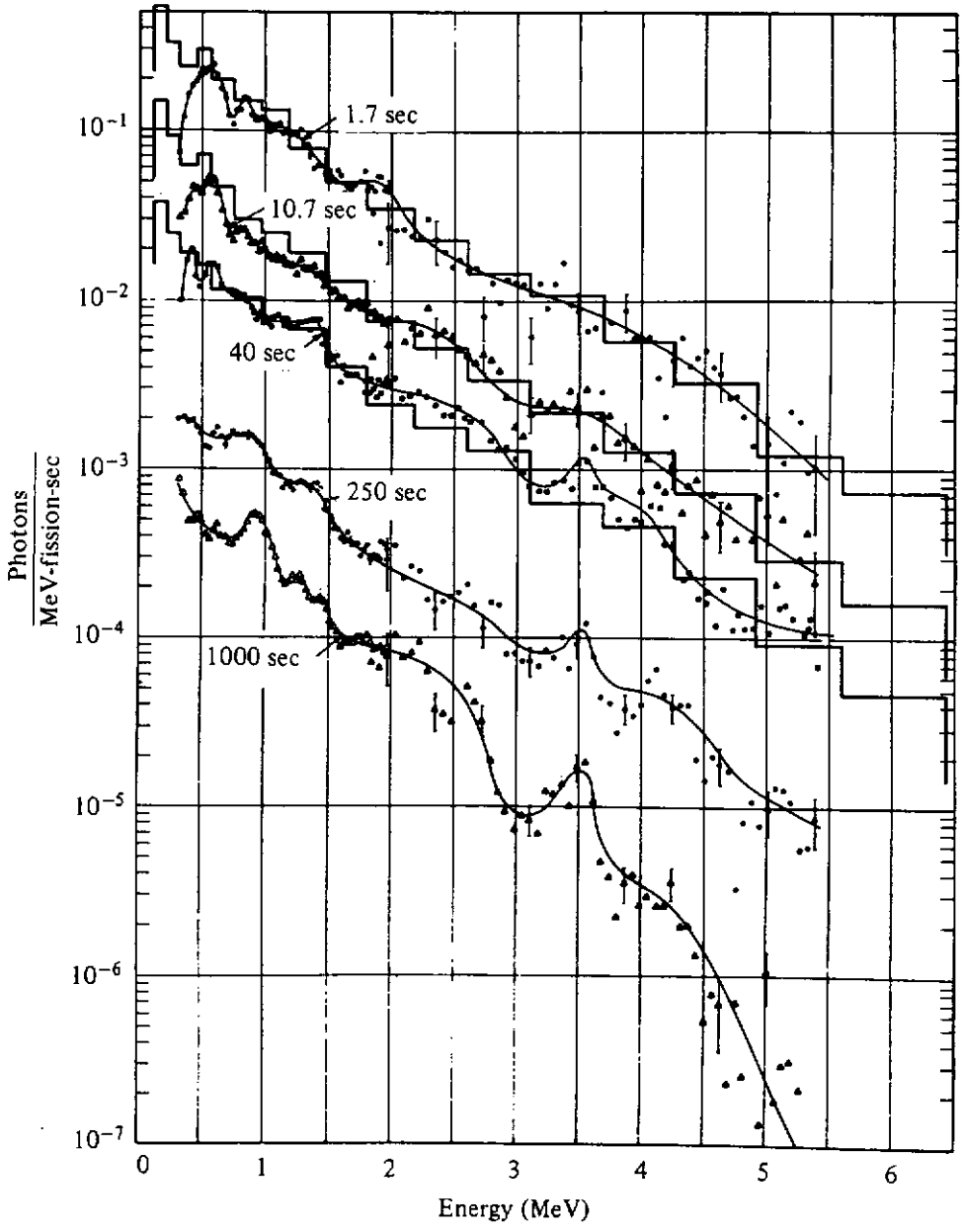

Figure 4.8 Delayed gamma-photon spectra at various times after the fission of ^{235}U. The data points and continuous lines are for thermal-neutron-induced fission, while the histograms are for fast-neutron-induced fission. (From Ref. 1; by permission of Addison-Wesley Publishing Co., Inc.)

calculations Eq. (4.14) is usually adequate. It is observed that both ^{235}U and ^{239}Pu have roughly the same total gamma energy decay characteristics for up to 200 days after the fission, at which time ^{235}U products begin to decay more rapidly until at 1 year after fission the ^{239}Pu gamma activity is about 60% greater than that of ^{235}U.

Often the shield designer is interested in the energy release rate by delayed photon emission, Γ_T, t_s seconds after the shutdown of a fission system which has operated for t_0 seconds at a constant fission rate prior to shutdown. From integration of Eq. (4.14), the energy release rate (MeV s^{-1}), normalized to a fission rate of one per second, is given by

$$\Gamma_T(t_0, t_s) = \int_0^{t_0} dt' \, F_T(t_0 - t' + t_s) = 7.0[t_s^{-0.2} - (t_s + t_0)^{-0.2}]. \tag{4.15}$$

For a given shutdown time, interpolation in operating time is facilitated by the following approximate formula, derived from Eq. (4.15):

$$\Gamma_T(t_0, t_s) \simeq \Gamma_T(t_0', t_s)\frac{1 - (1 + t_0/t_s)^{-0.2}}{1 - (1 + t_0'/t_s)^{-0.2}}. \tag{4.16}$$

For more accurate calculations, the variation with time after fission of the energy spectra of the photons must be taken into account. As in many photon shielding problems, the energy spectra are averaged or integrated over discrete energy intervals and the energy emission rate in each energy group is considered as a function of time after fission [17, 18]. Because of the importance of shielding fission-product sources, extensive computer codes have been developed to compute the abundances and decay rates of the hundreds of fission-product radionuclides. These codes use extensive libraries of radionuclide data and solve the decay and buildup equations for an assembly of any specified fissile composition experiencing any specified power (fission rate) history. The fission-product concentrations, activities, and gamma-photon and beta-particle energy release rates are computed as functions of time for any specified energy-group structure. Further, comparable data may be determined for activation products and transuranic elements. It is the output of these codes, such as ORIGEN [19], that gives accurate source strengths which are needed for detailed shield designs. Sample results are given in Table 4.10. These results are for fission products only and are for thermal-neutron-induced fission of ^{235}U. The results do not account for bremsstrahlung or for neutron absorption, during operation, by previously produced fission products.

Although the codes that solve for the buildup and decay of fission products can give very accurate results, their use requires much effort and expense. As an inexpensive alternative, the energy emission rate $F_j(t)$ by fission products with gamma photons in energy group j at time t after a single fission event may be computed as [20,21]

$$F_j(t) = \sum_{i=1}^{N_j} \alpha_{ij} \exp(-\lambda_{ij} t), \qquad j = 1 \text{ to } 6. \tag{4.17}$$

Values for the parameters α_{ij} and λ_{ij}, $i = 1$ to N_j, are given in Appendix 6

TABLE 4.10 Fission-Product Gamma-Photon Energy Release Rates for Thermal-Neutron-Induced Fission of ^{235}U, Computed Using the ORIGEN Code [19][a]

(a) Single Instantaneous Fission Event

	Energy (MeV)						
$t(y)$	0–1	1–2	2–3	3–4	4–5	5–7.5	7.5–20
1.00(−5)[b]	6.14(−04)	4.93(−04)	1.71(−04)	1.12(−04)	9.59(−05)	1.17(−05)	3.57(−34)
1.00(−4)	7.32(−05)	5.80(−05)	2.71(−05)	3.34(−06)	5.80(−08)	1.18(−10)	9.83(−33)
1.00(−3)	2.97(−06)	2.42(−06)	7.08(−07)	5.70(−08)	2.49(−09)	1.03(−30)	3.62(−32)
1.00(−2)	2.46(−07)	6.57(−08)	4.75(−09)	2.63(−11)	1.20(−17)	1.06(−30)	3.71(−32)
1.00(−1)	1.47(−08)	9.70(−09)	7.37(−10)	6.03(−12)	2.51(−30)	1.06(−30)	3.72(−32)
1.00(0)	4.28(−10)	4.44(−12)	1.09(−11)	3.22(−15)	2.72(−30)	1.15(−30)	4.03(−32)
1.00(+1)	2.09(−11)	3.32(−15)	3.83(−15)	6.61(−18)	3.42(−30)	1.44(−30)	5.07(−32)
1.00(+2)	2.62(−12)	5.16(−18)	3.02(−29)	1.07(−29)	3.49(−30)	1.48(−30)	5.18(−32)
1.00(+3)	2.44(−16)	5.12(−18)	3.02(−29)	1.07(−29)	3.49(−30)	1.47(−30)	5.18(−32)
1.00(+4)	2.29(−16)	4.81(−18)	3.02(−29)	1.07(−29)	3.49(−30)	1.47(−30)	5.18(−32)
(b) Specified Fission Time[c]							
			Operation for 1000 h				
1.00(−5)	1.24(−00)	8.57(−01)	3.10(−01)	5.40(−02)	1.73(−02)	1.96(−03)	1.51(−25)
1.00(−4)	7.34(−01)	4.59(−01)	1.54(−01)	1.82(−02)	3.34(−04)	3.74(−08)	1.38(−25)
1.00(−3)	3.64(−01)	1.67(−01)	1.75(−02)	5.44(−04)	3.63(−05)	3.88(−24)	1.36(−25)
1.00(−2)	1.45(−01)	8.62(−02)	6.49(−03)	4.90(−05)	1.57(−13)	3.88(−24)	1.36(−25)
1.00(−1)	3.58(−02)	1.38(−02)	1.10(−03)	8.60(−06)	9.25(−24)	3.91(−24)	1.37(−25)
1.00(0)	1.27(−03)	1.49(−05)	3.70(−05)	1.09(−08)	9.96(−24)	4.21(−24)	1.48(−25)
1.00(+1)	7.42(−05)	1.13(−08)	1.30(−08)	2.23(−11)	1.24(−23)	5.22(−24)	1.83(−25)
1.00(+2)	9.33(−06)	1.86(−11)	1.09(−22)	3.87(−23)	1.26(−23)	5.32(−24)	1.87(−25)
1.00(+3)	8.79(−10)	1.84(−11)	1.09(−22)	3.87(−23)	1.26(−23)	5.32(−24)	1.87(−25)
1.00(+4)	8.26(−10)	1.73(−11)	1.09(−22)	3.87(−23)	1.26(−23)	5.32(−24)	1.87(−25)

TABLE 4.10 (Cont'd.)

$t(y)$	Energy (MeV)						
	0–1	1–2	2–3	3–4	4–5	5–7.5	7.5–20
			Operation for 10,000 h				
1.00(−5)	1.33(−00)	8.67(−01)	3.10(−01)	5.38(−02)	1.72(−02)	1.95(−03)	1.55(−24)
1.00(−4)	8.24(−01)	4.72(−01)	1.56(−01)	1.81(−02)	3.34(−04)	3.73(−08)	1.42(−24)
1.00(−3)	4.53(−01)	1.80(−01)	1.89(−02)	5.52(−04)	3.63(−05)	3.98(−23)	1.40(−24)
1.00(−2)	2.31(−01)	9.64(−02)	7.71(−03)	5.53(−05)	1.57(−13)	3.98(−23)	1.40(−24)
1.00(−1)	9.68(−02)	1.57(−02)	1.68(−03)	9.72(−06)	9.48(−23)	4.01(−23)	1.41(−24)
1.00(0)	4.52(−03)	9.58(−05)	2.45(−04)	7.84(−08)	1.01(−22)	4.27(−23)	1.50(−24)
1.00(+1)	7.32(−04)	7.93(−08)	8.65(−08)	1.61(−10)	1.22(−22)	5.15(−23)	1.81(−24)
1.00(+2)	9.21(−05)	1.86(−10)	1.07(−21)	3.82(−22)	1.24(−22)	5.24(−23)	1.84(−24)
1.00(+3)	8.79(−09)	1.84(−10)	1.07(−21)	3.82(−22)	1.24(−22)	5.24(−23)	1.84(−24)
1.00(+4)	8.26(−09)	1.73(−10)	1.07(−21)	3.82(−22)	1.24(−22)	5.24(−23)	1.84(−24)
			Operation for 20,000 h				
1.00(−5)	1.33(−00)	8.67(−01)	3.10(−01)	5.38(−02)	1.72(−02)	1.95(−03)	3.22(−24)
1.00(−4)	8.27(−01)	4.72(−01)	1.56(−01)	1.82(−02)	3.34(−04)	3.73(−08)	2.95(−24)
1.00(−3)	4.56(−01)	1.80(−01)	1.91(−02)	5.52(−04)	3.63(−05)	8.29(−23)	2.91(−24)
1.00(−2)	2.34(−01)	9.64(−02)	7.93(−03)	5.54(−05)	1.57(−13)	8.28(−23)	2.91(−24)
1.00(−1)	9.94(−02)	1.57(−02)	1.87(−03)	9.79(−06)	1.97(−22)	8.33(−23)	2.93(−24)
1.00(0)	5.69(−03)	1.32(−04)	3.34(−04)	1.14(−07)	2.08(−22)	8.79(−23)	3.09(−24)
1.00(+1)	1.45(−03)	1.14(−07)	1.18(−07)	2.34(−10)	2.44(−22)	1.03(−22)	3.62(−24)
1.00(+2)	1.82(−04)	3.71(−10)	2.15(−21)	7.63(−22)	2.48(−22)	1.05(−22)	3.68(−24)
1.00(+3)	1.76(−08)	3.68(−10)	2.15(−21)	7.63(−22)	2.48(−22)	1.05(−22)	3.68(−24)
1.00(+4)	1.65(−08)	3.46(−10)	2.15(−21)	7.63(−22)	2.48(−22)	1.05(−22)	3.68(−24)

t (y)	Energy (MeV)						
	0–1	1–2	2–3	3–4	4–5	5–7.5	7.5–20
			Operation for 30,000 h				
1.00(−5)	1.33(−00)	8.67(−01)	3.10(−01)	5.38(−02)	1.72(−02)	1.95(−03)	4.99(−24)
1.00(−4)	8.28(−01)	4.72(−01)	1.56(−01)	1.82(−02)	3.34(−04)	3.73(−08)	4.58(−24)
1.00(−3)	4.58(−01)	1.80(−01)	1.92(−02)	5.52(−04)	3.63(−05)	1.28(−22)	4.51(−24)
1.00(−2)	2.35(−01)	9.64(−02)	8.00(−03)	5.54(−05)	1.57(−13)	1.28(−22)	4.51(−24)
1.00(−1)	1.00(−01)	1.58(−02)	1.95(−03)	9.82(−06)	3.05(−22)	1.29(−22)	4.53(−24)
1.00(0)	6.66−(03)	1.46(−04)	3.66(−04)	1.31(−07)	3.19(−22)	1.35(−22)	4.74(−24)
1.00(+1)	2.14(−03)	1.29(−07)	1.30(−07)	2.68(−10)	3.67(−22)	1.55(−22)	5.45(−24)
1.00(+2)	2.69(−04)	5.57(−10)	3.22(−21)	1.15(−21)	3.72(−22)	1.57(−22)	5.52(−24)
1.00(+3)	2.64(−08)	5.52(−10)	3.22(−21)	1.14(−21)	3.72(−22)	1.57(−22)	5.52(−24)
1.00(+4)	2.48(−08)	5.19(−10)	3.22(−21)	1.14(−21)	3.72(−22)	1.57(−22)	5.52(−24)
			Operation for 40,000 h				
1.00(−5)	1.33(−00)	8.67(−01)	3.10(−01)	5.38(−02)	1.72(−02)	1.95(−03)	6.83(−24)
1.00(−4)	8.29(−01)	4.72(−01)	1.56(−01)	1.82(−02)	3.34(−04)	3.73(−08)	6.26(−24)
1.00(−3)	4.58(−01)	1.80(−01)	1.93(−02)	5.52(−04)	3.63(−05)	1.76(−22)	6.18(−24)
1.00(−2)	2.36(−01)	9.65(−02)	8.03(−03)	5.54(−05)	1.57(−13)	1.76(−22)	6.17(−24)
1.00(−1)	1.01(−01)	1.58(−02)	1.97(−03)	9.84(−06)	4.18(−22)	1.76(−22)	6.20(−24)
1.00(0)	7.54(−03)	1.52(−04)	3.78(−04)	1.38(−07)	4.34(−22)	1.83(−22)	6.44(−24)
1.00(+1)	2.81(−03)	1.36(−07)	1.35(−07)	2.83(−10)	4.91(−22)	2.07(−22)	7.28(−24)
1.00(+2)	3.54(−04)	7.42(−10)	4.29(−21)	1.53(−21)	4.96(−22)	2.10(−22)	7.37(−24)
1.00(+3)	3.51(−08)	7.37(−10)	4.29(−21)	1.53(−21)	4.96(−22)	2.10(−22)	7.37(−24)
1.00(+4)	3.30(−08)	6.92(−10)	4.29(−21)	1.53(−21)	4.96(−22)	2.10(−22)	7.37(−24)

[a]Energy release rates (MeV/s) are given by photon energy group at decay time t (years).
[b]Read as 1.0×10^{-5}.
[c]Data are normalized to unit fission rate, and thus have units (MeV/fission).

for the thermal-neutron-induced fission of ^{235}U and ^{239}Pu. By use of Eq. (4.17), the photon energy emission rates can be calculated readily for a fission system which has experienced any prescribed power history. For example, the energy emission rate Γ_j (MeV s^{-1}) by fission products emitting photons with energies in group j at a time t_s after operation at fission rate P (s^{-1}) for time t_0 is given by

$$\Gamma_j(t_0, t_s) = \int_0^{t_0} dt' \, P(t')F_j(t_s + t_0 - t'). \tag{4.18}$$

For the special case of $P(t)$ being constant (at one fission per second), Eq. (4.17) permits the result above to be reduced to

$$\Gamma_j(t_0, t_s) = \sum_{i=1}^{N_j} \frac{\alpha_{ij}}{\lambda_{ij}} e^{-\lambda_{ij}t_s}(1 - e^{-\lambda_{ij}t_0}). \tag{4.19}$$

Results of calculations performed using the α_{ij} and λ_{ij} coefficients are illustrated in Figs. 4.9 through 4.11. As with the ORIGEN results, these results do not account for bremsstrahlung or for neutron absorption by fission products.

Comparison of the results in Table 4.10 with those in Figs. 4.9 and 4.10 reveals certain differences in energy emission rates, especially for the 4- to 5- and 5- to 7.5-MeV photon energy groups. Energy emission rates in these groups are greater when predicted using the α_{ij} and λ_{ij} parameters than when predicted using the ORIGEN code. These differences are discussed further in Appendix 6.

4.2.3 Capture Gamma Photons

The compound nucleus formed by neutron absorption is initially created in a highly excited state with excitation energy equal to the kinetic energy of the incident neutron plus the neutron binding energy, which averages about 7 MeV.

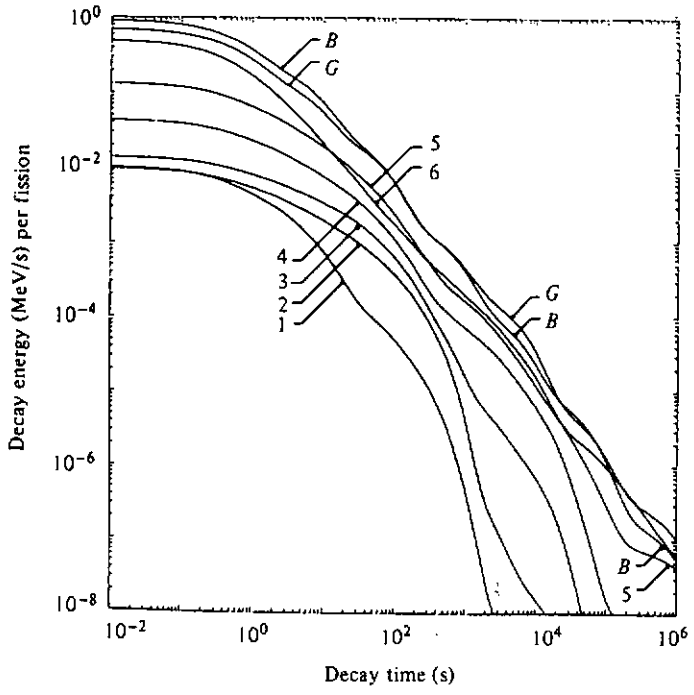

Figure 4.9 Calculated total gamma (G) and beta (B) energy emission rates as a function of time after the fission of ^{235}U. The curves identified by the numbers 1 to 6 are gamma emission rates for photons in the energy ranges (5–7.5), (4–5), (3–4), (2–3), (1–2), and (0–1) MeV, respectively. The plots were obtained from Eq. (4.17) using the data of Appendix A6.

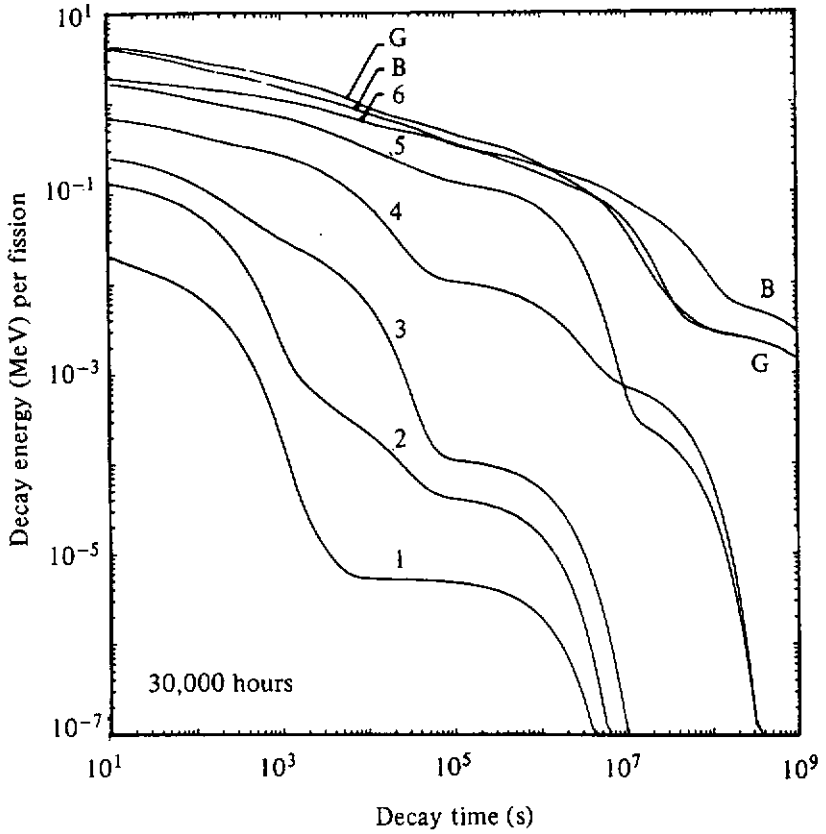

Figure 4.10 Total beta- and gamma-energy emission rates from a ^{235}U sample that has experienced a constant fission rate of one fission per second over a 30,000-h period. The decay time is the time after cessation of irradiation, and the gamma-energy-group structure is the same as in Fig. 4.9. The plots were obtained from Eq. (4.19) using the data of Appendix A6.

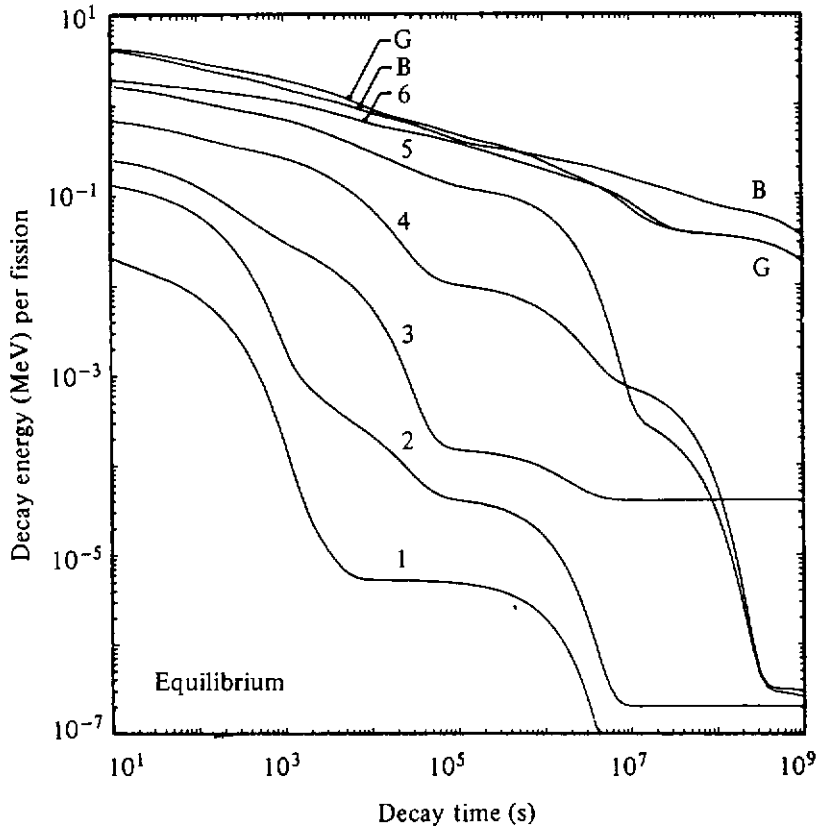

Figure 4.11 Total beta- and gamma-energy emission rates from a ^{235}U sample that has experienced a constant fission rate of one fission per second for effectively an infinite time so that the decay and production of fission products are equal. These data thus represent the "worse-case" situation for estimating radiation source strengths for fission products. The gamma-energy-group structure is the same as that of Fig. 4.9.

The decay of this nucleus, within 10^{-12} s, and usually by way of intermediate states, typically produces several energetic photons. Such capture photons may be intentionally created by placing a material with a high-thermal-neutron (n, γ) cross section in a thermal neutron beam. The energy spectrum of the resulting capture gamma photons can then be used to identify trace elements in the sample. More often, however, capture gamma photons are an undesired secondary source of radiation encountered in neutron shielding. The estimation of the neutron absorption rate and the subsequent production of the capture photons is an important aspect of shielding analyses.

To calculate at some point in a shield the total source strength per unit volume of capture photons of energy E_γ, it is first necessary to know the energy-dependent flux density of neutrons, $\phi(E)$, and the macroscopic absorption coefficient, $\mu_a^i(E) = N^i \sigma_a^i(E)$, where N^i and σ_a^i are the atomic density and microscopic absorption cross section for the ith type of nuclide in the shield medium. If $F^i(E; E_\gamma)\, dE_\gamma$ represents the probability of obtaining a capture photon with energy in dE_γ about E_γ when a neutron of energy E is absorbed in the ith-type nuclide, the production rate per unit volume of capture photons with energy in unit energy about E_γ is

$$S_V(E_\gamma) = \sum_{i=1}^{N} \int_0^{E_{\max}} dE\, F^i(E; E_\gamma) \mu_a^i(E) \phi(E), \tag{4.20}$$

where $E_{\max}$ is the maximum neutron energy and N is the number of nuclide species in the shield material. The detailed calculation of $\phi(E)$ (see Chapters 8 and 10) is generally quite involved, and the (n, γ) cross sections and associated capture gamma spectra are generally poorly known above 10 keV. Thus the evaluation of Eq. (4.20) is rarely attempted in shielding analyses.

Fortunately, in most shielding stituations the evaluation of the capture photon source can be considerably simplified. The absorption cross sections are very small for energetic neutrons, typically no more than a few hundred millibarns for neutrons with energies between 10 keV and 10 MeV, and, when available, they are known with far less certainty than the scattering cross sections. The scattering cross section for fast neutrons is always at least an order of magnitude greater than the absorption cross section, and thus in shielding analysis the absorption of neutrons while they scatter and slow down is often ignored. Hence, to compute the capture photon production rate, only neutrons with energies below 10 keV need be considered. Except in a few materials with isolated absorption resonances in the range 1 to 100 eV, most of the neutron absorption will occur after the neutrons have completely slowed down and assumed a speed distribution which is in equilibrium with the thermal motion of the atoms of the shielding medium. As discussed in Section 3.8, the thermal neutron (n, γ) cross sections may become very large (see Table A3.8), and in practice the capture gamma source calculation is based only on the absorption of thermal neutrons, with the epithermal and high-energy absorptions being neglected. Thus, Eq. (4.20) reduces to

$$S_\gamma(E_\gamma) \simeq \sum_{i=1}^{N} F_{\text{th}}^i(E_\gamma)\bar{\mu}_a^i\phi_{\text{th}}, \tag{4.21}$$

where F_{th}^i is the capture gamma spectrum arising from thermal neutron (n, γ) reactions, $\bar{\mu}_a^i$ the thermal averaged (n, γ) linear absorption coefficient, and ϕ_{th} is the neutron flux density integrated over all thermal energies. The thermal-averaged coefficient $\bar{\mu}_a^i$ may be related to the 2200-m/s cross sections σ_a^i of Table A3.8 by $\bar{\mu}_a^i \simeq \sqrt{\pi}\, N^i\sigma_a^i/2$ [22]. The energy spectra of the capture photons, $F_{\text{th}}^i(E_\gamma)$ (normalized to 100 absorptions), are given in Table A3.9 for important shielding elements.

4.2.4 Gamma Photons from Inelastic Neutron Scattering

The excited nucleus formed when a neutron is inelastically scattered decays to the ground state very rapidly (typically within 10^{-14} s) with the excitation energy being emitted as one or more photons. Because of the constraints imposed by the conservation of energy and momentum in all scattering interactions, inelastic neutron scattering cannot occur unless the incident neutron energy is greater than $(A + 1)/A$ times the energy required to excite the scattering nucleus to its first excited state (see Section 3.7.1). Except for the heavy nuclides, neutron energies above 0.5 MeV are typically required for inelastic scattering. The secondary photons produced by the inelastic scattering of lower-energy neutrons from heavy nuclides are generally not of interest in shielding situations because of their low energies and the ease with which they are attenuated. Only the photons arising from inelastic scattering of high-energy neutrons (above 1 MeV) are usually important in shielding analyses.

The detailed calculation of secondary photon source strengths from inelastic neutron scattering requires knowledge of the fast-neutron flux density, the inelastic scattering cross sections, and spectra of resultant photons, all as functions of the incident neutron energy. The cross sections and energy spectra of the secondary photons depend strongly on the incident neutron energy and the particular nuclide (see Table A3.10). Such inelastic scattering data are known only for the more important nuclides and shielding materials, and even the known data require extensive computerized libraries. Fortunately, in most analyses, these secondary photons are of little importance compared to the eventual capture photons. Although inelastic neutron scattering is usually neglected with regard to its secondary-photon radiation, it will be seen in Chapter 8 that inelastic scattering is a very important mechanism in the attenuation of the fast neutrons, better even than elastic scattering.

4.2.5 Activation Gamma Photons

For many materials, absorption of a neutron will produce a radionuclide with a half-life ranging from a fraction of a second to several years. The radiation produced by the subsequent decay of these activation nuclei may be very signifi-

cant for material that has been exposed to large neutron fluences (e.g., structural components in a reactor core). Most radionuclides encountered in research laboratories, medical facilities, and industry are produced as activation nuclides from neutron absorption in some parent material. Such nuclides decay, usually by beta emission, leaving the daughter nucleus in an excited state which usually decays quickly (within 10^{-7} s) to its ground state with the emission of one or more gamma photons. Thus, the apparent half-life of the photon emitter is that of the parent (or activation nuclide) while the number and energy of the photons is characteristic of the nuclear structure of the daughter.

Although most activation products of concern in shielding problems arise from neutron absorption, there is one important exception in water-moderated reactors. The ^{16}O in the water can be transmuted to ^{16}N in the presence of fission neutrons by an (n, p) reaction with a threshold energy of 9.6 MeV. The activation cross section, averaged over the fission spectrum, is 0.019 mb [11] and although reactions with such small cross sections are usually negligible, ^{16}N decays with a 7.4-s half-life emitting gamma photons of 6.13 and 7.10 MeV (yields of 0.69 and 0.05 per decay). This activity may be very important in coolant channels of large power reactors.

Extensive tabulations of important activation products can be found in many references [3,11]. In Table A3.11, a short compilation of photon yields is given for some important activation nuclides resulting from thermal neutron capture and which are commonly encountered in reactor shield designs. In Appendix 5, photon yields are also presented for many common radionuclides. To calculate the photon activity for a particular activation nuclide, the amount of parent nuclide, the time history of the neutron flux density, and the appropriate activation cross section must be known. Often, decay shemes [23] showing the transition probabilities are used to infer gamma-photon yields. However, it should be emphasized that most of these schemes show only the transition probabilities and not the photon yields; that is, internal conversion and other nonradiative processes are not shown. Consequently, the inferred yields may be somewhat high, particularly for low-energy photons, if such decay schemes are used. Similarly, fluorescence yields cannot be inferred from such compilations, but must be separately determined.

4.2.6 Annihilation Radiation

Positrons, generated either from the decay of radionuclides or from pair production interactions induced by high-energy photons, slow down rapidly in matter (within about 10^{-10} s) and are subsequently annihilated with electrons. The rest mass energy of the electron and positron is emitted in the form of two annihilation photons, each of energy $m_e c^2$ ($= 0.51$ MeV).[2] To a very good

[2]Although the emission of a single photon ($\gtrsim$1.02 MeV) can occur, the probability of this annihilation mechanism is negligible compared to that of the usual two-photon process. [12]

approximation, the annihilation photons can be assumed to originate at the same position at which the positron first appeared since the migration distance of the positron, as it slows down in condensed matter, is usually only a few millimeters at most.

Secondary annihilation radiation arising from pair production can often be neglected in shielding analyses since the primary photons with their much higher energy are responsible for most of the dose rate. For example, the contribution of annihilation radiation to the dose rate for the worst case (10-MeV photons in a medium with $Z \simeq 50$) is less than 7% [24]. Only if information about the photon energy spectrum below 0.51 MeV is required should the annihilation photons be considered. However, for radionuclides that can decay by positron emission, it is necessary to include the annihilation radiation in a shielding analysis.

4.3 SOURCES OF X RAYS

The interaction of photons or charged particles with matter leads inevitably to the production of secondary x-ray photons. The x rays in most shielding applications are usually of low energy ($\lesssim$100 keV) and hence easily attenuated by any shield adequate for the primary radiation. Consequently, the secondary x rays are often completely neglected in analyses involving higher-energy photons. However, for those situations in which x-ray production is the only source of photons, it may be important to estimate the intensity, energies, and resulting exposure rate of the x-ray photons. To make such estimates, it is necessary to understand how the x rays are produced and some characteristics of the production mechanisms. There are two principal methods whereby secondary x-ray photons are generated: the rearrangement of atomic electron configurations leads to "characteristic x rays," and the deflection of charged particles in the nuclear electric field results in "bremsstrahlung." Both mechanisms are discussed below.

4.3.1 Characteristic X Rays

The electrons around a nucleus are arranged in shells or layers, each of which can hold a maximum number of electrons. The two electrons in the innermost shell (K shell) are the most tightly bound, the six electrons in the next shell (L shell) are the next most tightly bound, and so on outward for the M, N, . . . shells. If the normal electron arrangement around a nucleus is altered through ionization of an inner electron or through excitation of electrons to higher-energy levels, the electrons begin a complex series of transitions to vacancies in the lower shells (thereby acquiring higher binding energies) until the unexcited state of the atom is achieved. In each electronic transition, the difference in binding energy between the initial and final state is either emitted as a photon (called a "characteristic x ray") or given up to an outer electron which is ejected from the atom (called an "Auger electron"). The discrete electron energy levels

and the transition probabilities between levels vary with the Z number of the atom, and thus the characteristic x rays provide a unique signature for each element.

The number of x rays with different energies is greatly increased by the multiplicity of electron energy levels available in each shell (1, 3, 5, 7, . . . distinct energy levels for the K, L, M, N, . . . shells, respectively). To identify the various characteristic x rays for an element, many different schemes have been proposed. One of the more popular (but limited and often confusing) uses the letter of the shell whose vacancy is filled together with a numbered Greek subscript to identify a particular electron transition (e.g., $K_{\alpha 1}$ and $L_{\gamma 5}$). In Fig. 4.12 the electron-energy-level diagram is shown for lead, and the more probable and energetic transitions are indicated together with the nomenclature for the associated characteristic x ray. The notation shown in this example is valid for any element; that is, $K_{\beta 1}$ refers to the characteristic x ray produced when an electron from the third energy level of the M shell fills a vacancy in the K shell. Fortunately, in shielding applications such detail is seldom needed, and often only the dominant K series of x rays are considered, with a single representative energy being used for all.

Production of characteristic x rays. There are several methods commonly encountered in shielding applications whereby atoms may be excited and characteristic x rays produced. A photoelectric absorption leaves the absorbing atom in an ionized state. If the incident photon energy is sufficiently high (greater than the binding energy of the K-shell electron, which ranges from 14 eV for hydrogen to 115 keV for uranium), it is most likely (80 to 100%) that a vacancy will be created in the K shell and thus the K series of x rays will dominate the subsequent secondary radiation. These x-ray photons produced from photoelectric absorption are often called "fluorescent radiation" and are widely used to identify trace elements in a sample by bombarding the sample with low-energy photons from a radioactive source or with x rays from an x-ray machine and then observing the induced fluorescent radiation.

Characteristic x rays can also arise following the decay of a radionuclide. In the decay process known as electron capture, an orbital electron (most likely from the K shell) is absorbed into the nucleus, thereby decreasing the nuclear charge by one unit. The resulting K-shell vacancy then gives rise to the K series of characteristic x rays. A second source of characteristic x rays which occurs in many radionuclides is a result of internal conversion. Most daughter nuclei formed as a result of any type of nuclear decay are left in excited states. This excitation energy may be either emitted as a gamma photon or transferred to an orbital electron which is ejected from the atom. Again it is most likely that a K-shell electron is involved in this internal conversion process. The energies and yields of characteristic x rays arising from radioactive decay are tabulated along with gamma photon yields and energies in Appendix 5.

Finally, the passage of charged particles through matter (e.g., alpha or

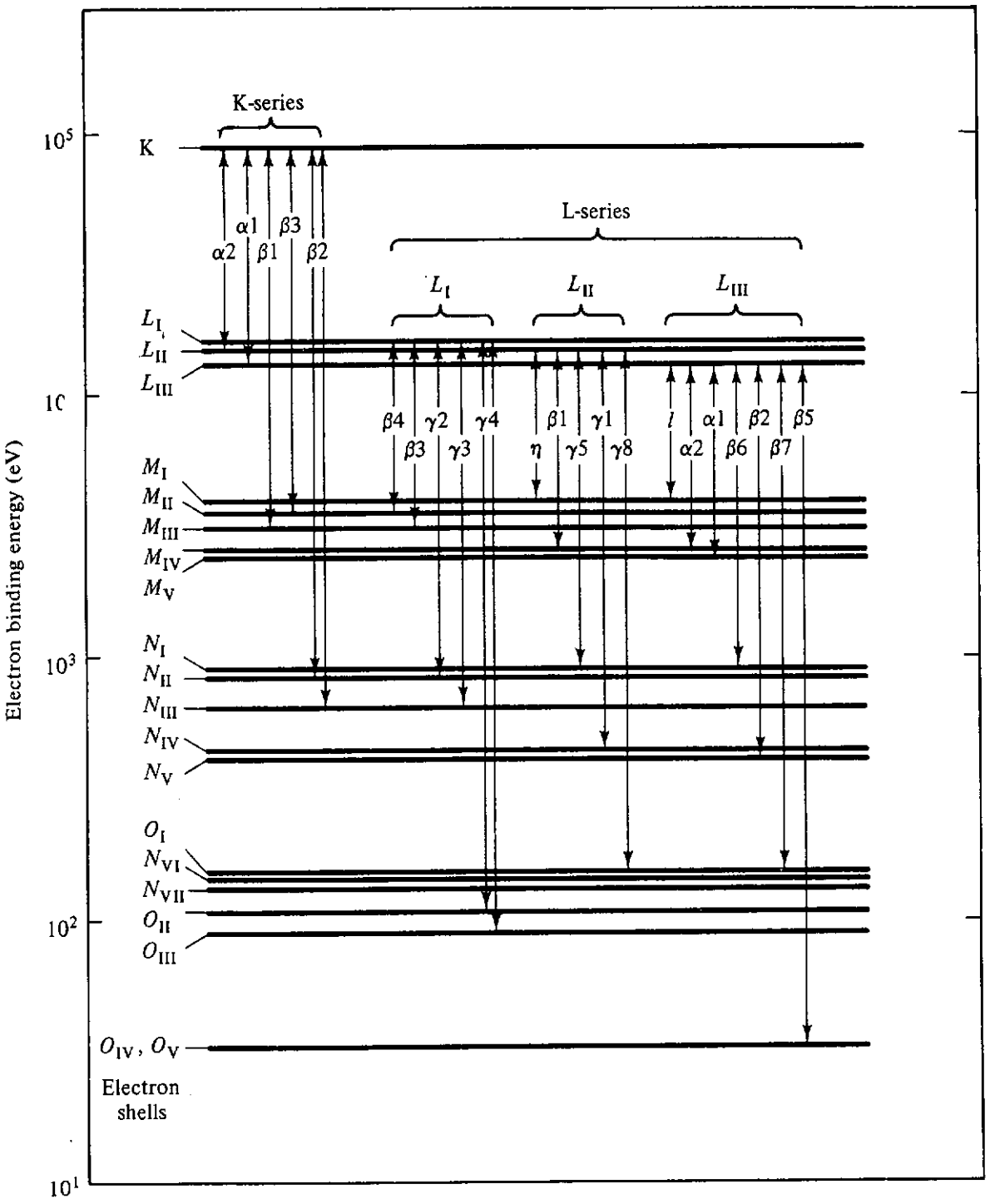

Figure 4.12 X-ray energy-level diagram for lead ($Z = 82$) showing the principal characteristic x-ray transitions and their standard nomenclature. (After Ref. 25.)

beta particles from radioactive decays, secondary electrons from photon interactions, or even charged particles produced by an accelerator) will leave behind many excited and ionized atoms from which characteristic x rays are produced. The calculation of the characteristic x-ray yields from such charged particle interactions is difficult.

Energies of characteristic x rays. To generate a particular series of characteristic x rays, an electron vacancy must be created in an appropriate electron shell. Such vacancies are created only when sufficient energy is trans-

ferred to an electron in that shell so as to allow it to break free of the atom (or at least be transferred to an energy level above all the other electrons). In Chapter 3 it was seen that the photoelectric cross section changed abruptly at well-defined energies (called "edge" energies) corresponding to the ionization or binding energy for electrons in the various shells. Below the edge energy for a shell, vacancies can no longer be created in the shell and the photoelectric cross section therefore becomes smaller since fewer electrons are now available to interact with the incident photon. These shell edge energies increase with the atomic number Z of the atom as a result of the electrons becoming more tightly bound in the atom. The edge energies or ionization energy for different shells (and even for the different electron states within the same shell) can be found in many books on x-ray analysis [25]. An empirical approximation for the K-edge energy, good to within 4% for $Z > 5$, is [26]

$$E_K \text{ (eV)} = 5.706Z^{2.186}. \tag{4.22}$$

The characteristic x rays emitted when electrons fill a vacancy in a shell will always have less energy than that required to create the vacancy. Extensive tabulations of characteristic x-ray energies are available [25], but the accuracies afforded by such tabulations are seldom needed in shielding analyses. The energies of the characteristic x rays for the different elements can be expressed approximately by the simple empirical formula

$$E = CZ^B, \tag{4.23}$$

where the constants B and C are given in Table 4.11 for the more important x rays. From these results it is seen that the K_α x-ray energy varies from only 0.53 keV for oxygen ($Z = 8$) to 6.5 keV for iron ($Z = 26$) to 95 keV for uranium. By comparison, the L series of x rays for uranium occurs at energies around 15 keV. Thus, in most shielding situations, only the K series of x rays from heavy elements are sufficiently penetrating to be of concern.

TABLE 4.11 Values of the Constants B and C Used to Express Characteristic X-Ray Energies as $E = CZ^B$

X Ray	C (eV)	B
$K_{\alpha 1}$	6.474	2.124
$K_{\alpha 2}$	6.622	2.114
$K_{\beta 1}$	6.199	2.145
$K_{\beta 2}$	5.949	2.165
$K_{\beta 3}$	6.293	2.134
$L_{\alpha 1}$	0.4238	2.300
$L_{\beta 1}$	0.1758	2.535
$L_{\beta 2}$	0.3360	2.370

Source: *Data of Ref. 26.*

Intensity of characteristic x rays. The "fluorescent yield" of a material is the fraction of the atoms with a vacancy in an inner electron shell that emit an x ray upon the filling of the vacancy. For vacancies in the K shell, the fluorescent yield is given by [27]

$$\omega_K = (1 + 1.12 \times 10^6 Z^{-4})^{-1}. \tag{4.24}$$

From this result it is seen that the fluorescent yield increases dramatically with the Z number, varying from 0.0036 for oxygen ($Z = 8$) to 0.98 for uranium ($Z = 92$). Thus, the secondary fluorescent radiation is of more concern for heavy materials.

4.3.2 Bremsstrahlung

A charged particle gives up its kinetic energy either by ionizing or exciting atoms along its path or by photon emission as it is deflected (and hence accelerated) by the electric fields of nuclei. The photons produced by the deflection of the charged particle are called bremsstrahlung (literally, "braking radiation"), and may result in a very significant photon radiation field if energetic charged particles are present. For a given type of charged particle, the radiative stopping power, $(dT/ds)_{\text{rad}}$, increases with the particle energy and with the square of the atomic number (Z) of the absorber (see Section 3.9.2), while the collisional (ionization) stopping power, $(dT/ds)_{\text{coll}}$, decreases with particle energy and increases only with the first power of Z (see Section 3.9.1). For a relativistic particle of rest mass M (i.e., $E \gg Mc^2$) it can be shown that the ratio of radiative to ionization losses is approximately [28]

$$\frac{(dT/ds)_{\text{rad}}}{(dT/ds)_{\text{coll}}} \simeq \frac{EZ}{700}\left(\frac{m_e}{M}\right)^2, \tag{4.25}$$

where E is in MeV. From this result it is seen that bremsstrahlung is more important for high-energy particles of small mass incident on high-Z material. In shielding situations, only electrons ($m_e/M = 1$) are ever of importance for their associated bremsstrahlung. All other particles are far too massive to produce significant amounts of bremsstrahlung, and the characteristic x-ray fluorescence arising from their ionizing interactions is the only source of secondary photons ever of interest. Bremsstrahlung from electrons, however, is of particular radiological interest for devices that accelerate electrons (e.g., betatrons, x-ray tubes) or for situations involving radionuclides that emit only beta particles.

Thick-target bremsstrahlung for monoenergetic electrons. The energy distribution of the photons produced by the bremsstrahlung mechanism is continuous up to a maximum energy corresponding to the maximum kinetic energy of the incident charged particles. The exact shape of the continuous bremsstrahlung spectrum depends on many factors, including the energy distribution of the incident charged particles, the thickness of the target, and the amount of bremsstrahlung absorbed in the target and other masking material.

For monoenergetic electrons of energy T_0 (up to several MeV) incident on a target thick compared to the electron range, the energy distribution of the bremsstrahlung, per unit energy and per incident electron, can be approximated by the linear relation [25,28]

$$\mathcal{E}(E) = 2kZ(T_0 - E), \qquad E \leq T_0. \tag{4.26}$$

where $k \simeq 0.7 \times 10^{-3}$ MeV^{-1} and Z is the atomic number of the absorber. Integration of this empirical result over all photon energies gives the total energy emitted as bremsstrahlung per incident electron as

$$E_{\text{br}} = kZT_0^2. \tag{4.27}$$

The fraction of the incident electron energy which is converted into bremsstrahlung is thus

$$Y(T_0) \equiv \frac{E_{\text{br}}}{T_0} = kZT_0, \tag{4.28}$$

which is always a small fraction for realistic shielding situations (see Table 3.1). For example, only 2% of the energy of a 0.5-MeV beta particle, when stopped in lead, is converted into bremsstrahlung.

The angular distribution of bremsstrahlung is generally quite anisotropic and varies with the incident electron energy. Bremsstrahlung induced by low-energy electrons ($\lesssim$100 keV) is emitted predominately at 90° to the direction of the incident electron. As the electron energy increases, the direction of the peak intensity shifts increasingly toward the forward direction, until, for electrons above a few MeV, the bremsstrahlung is confined to a very narrow forward beam. The angular distribution of radiation leaving a target is very difficult to compute since it depends on the target size and orientation. For thin targets the anisotropy of the bremsstrahlung resembles that for a single electron–nucleus interaction, while for thick targets multiple electron interactions and photon absorption in the target must be considered [12].

Bremsstrahlung from beta particles. If the number of incident electrons on a target in unit energy about T (normalized to one electron) is denoted by $\chi(T)$, the energy distribution of the resulting bremsstrahlung intensity can be computed from Eq. (4.26) as

$$\mathcal{E}(E) = 2kZ \int_E^{T_{\max}} \chi(T')(T' - E)\, dT', \tag{4.29}$$

where $T_{\max}$ is the maximum energy of the beta particles. Similarly, the total bremsstrahlung energy per incident electron becomes

$$E_{\text{br}} = kZ \int_0^{T_{\max}} \chi(T')(T')^2\, dT' \equiv kZ(T_{\text{rms}})^2, \tag{4.30}$$

where T_{rms} is the root-mean-square energy of the beta particles. The beta particles from the beta decay of a radionuclide have a characteristic distribution of energies up to a maximum value $T_{\max}$ equal to the beta-decay energy. For such beta particles, the average energy is approximately $T_{\text{av}} \simeq 0.40T_{\max}$ and the rms

energy is $T_{rms} \simeq 0.45T_{max}$ when T_{max} is in the MeV range [28]. Thus, the average total bremsstrahlung energy in MeV emitted per β disintegration becomes

$$E_{br} = kZ(0.45T_{max})^2 \simeq \frac{ZT_{max}^2}{7000} \tag{4.31}$$

with T_{max} measured in MeV. Similarly, the average fraction of the beta-particle energy that is emitted as bremsstrahlung, $f_\beta \equiv E_{br}/T_{av}$, is

$$f_\beta = \frac{kZ(T_{rms})^2}{T_{av}} \simeq \frac{ZT_{max}}{3000}. \tag{4.32}$$

The energy distribution of bremsstrahlung from beta decay can be obtained by evaluating Eq. (4.29). The resulting spectrum is quite different from the straight-line spectrum for monoenergetic electrons, with the beta-decay spectrum being much softer and comparatively less intense at higher energies (see Fig. 4.13). The shape of this spectrum is independent of the electron absorber and is thus characteristic of each β emitter.

Inner bremsstrahlung. During the beta-decay process, the beta particle is accelerated, and consequently, a small amount of bremsstrahlung is emitted. These x rays, called "inner" bremsstrahlung, can be ignored in shielding analyses since only a small fraction of the beta-decay energy, on the average, is emitted as this type of radiation.

4.3.3 X-Ray Machines

The production of x-ray photons as bremsstrahlung and fluorescence occurs in any device that produces high-energy electrons. Devices that can produce significant amounts of x rays are those in which a high voltage is used to accelerate electrons, which then strike an appropriate target material. Such is the basic principle of all x-ray tubes used in medical diagnosis and therapy, industrial applications, and research laboratories.

Although there are many different designs of x-ray tubes for different applications, those shown in Fig. 4.14 are typical for many low to medium voltages ($\lesssim$ 180 kV). The glass tube acts as both an insulator between the anode and cathode and a container for the necessary vacuum through which the electrons are accelerated by the high voltage between the anode and cathode. The anodes of x-ray tubes incorporate a suitable metal upon which the electrons impinge and generate the bremsstrahlung and characteristic x rays. Most of the electron energy is deposited in the anode as heat rather than being radiated away as x rays, and thus heat removal is an important aspect in the design of x-ray tubes. Tungsten is the most commonly used target material because of its high atomic number and because of its high melting point, high thermal conductivity, and low vapor pressure. Occasionally, other target materials are used when different characteristic x-ray energies are desired (see Table 4.12). Generally, the operating conditions of a particular tube (current, voltage, and operating time) are limited

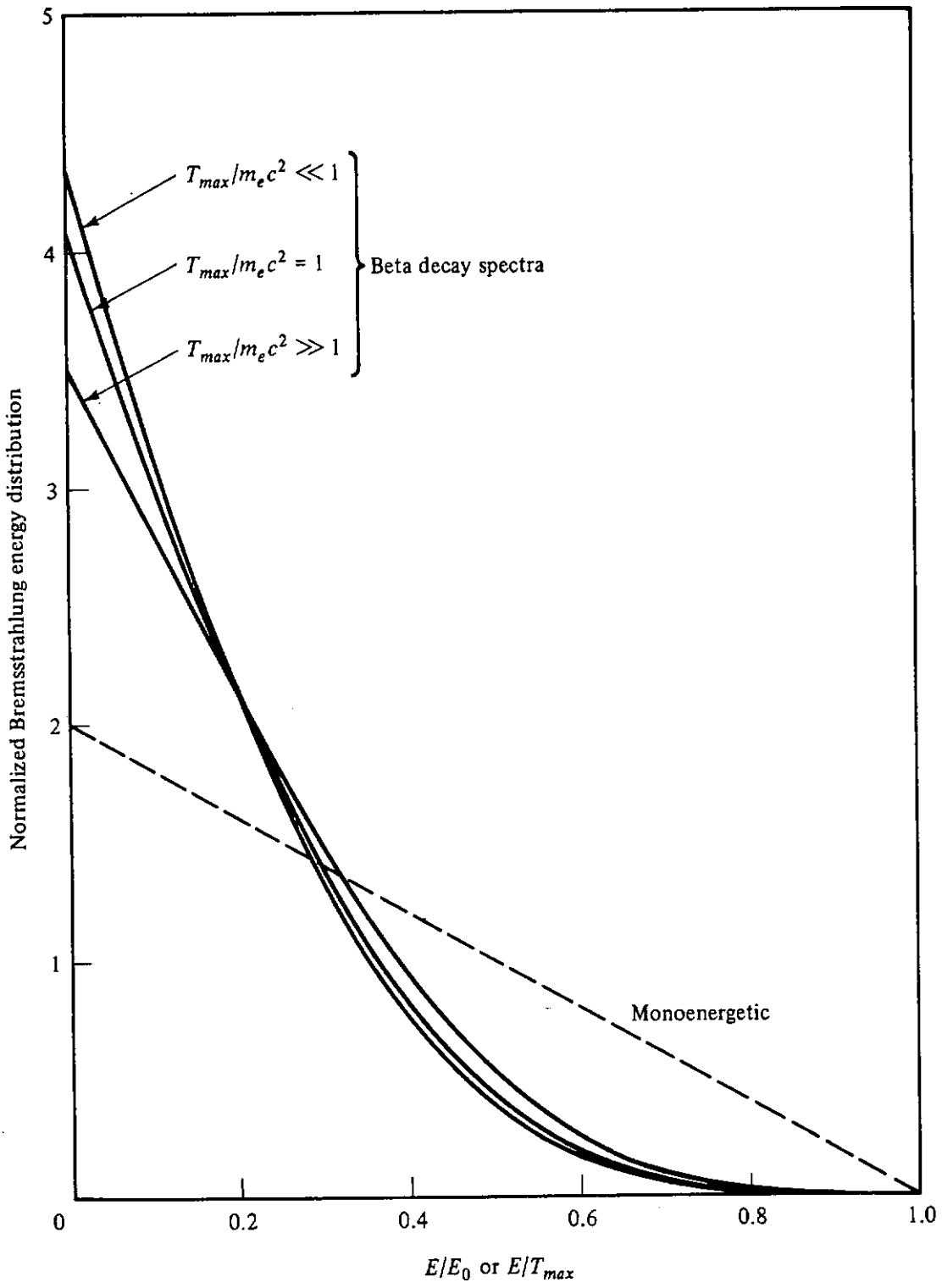

Figure 4.13 Energy distribution of bremsstrahlung for a monoenergetic electron beam of energy T_0 and for beta spectra with maximum energy T_{max}. The area under each curve has been set to unity.

by the rate at which heat can be removed from the anode. For most medical and dental diagnostic units, voltages between 40 and 150 kV are used, while medical therapy units may use 6 to 150 kV for superficial treatments or 180 kV to 50 MV for treatments requiring very penetrating radiation.

The energy spectrum of x-ray photons emitted from an x-ray tube has a continuous bremsstrahlung component up to the maximum electron energy (i.e.,

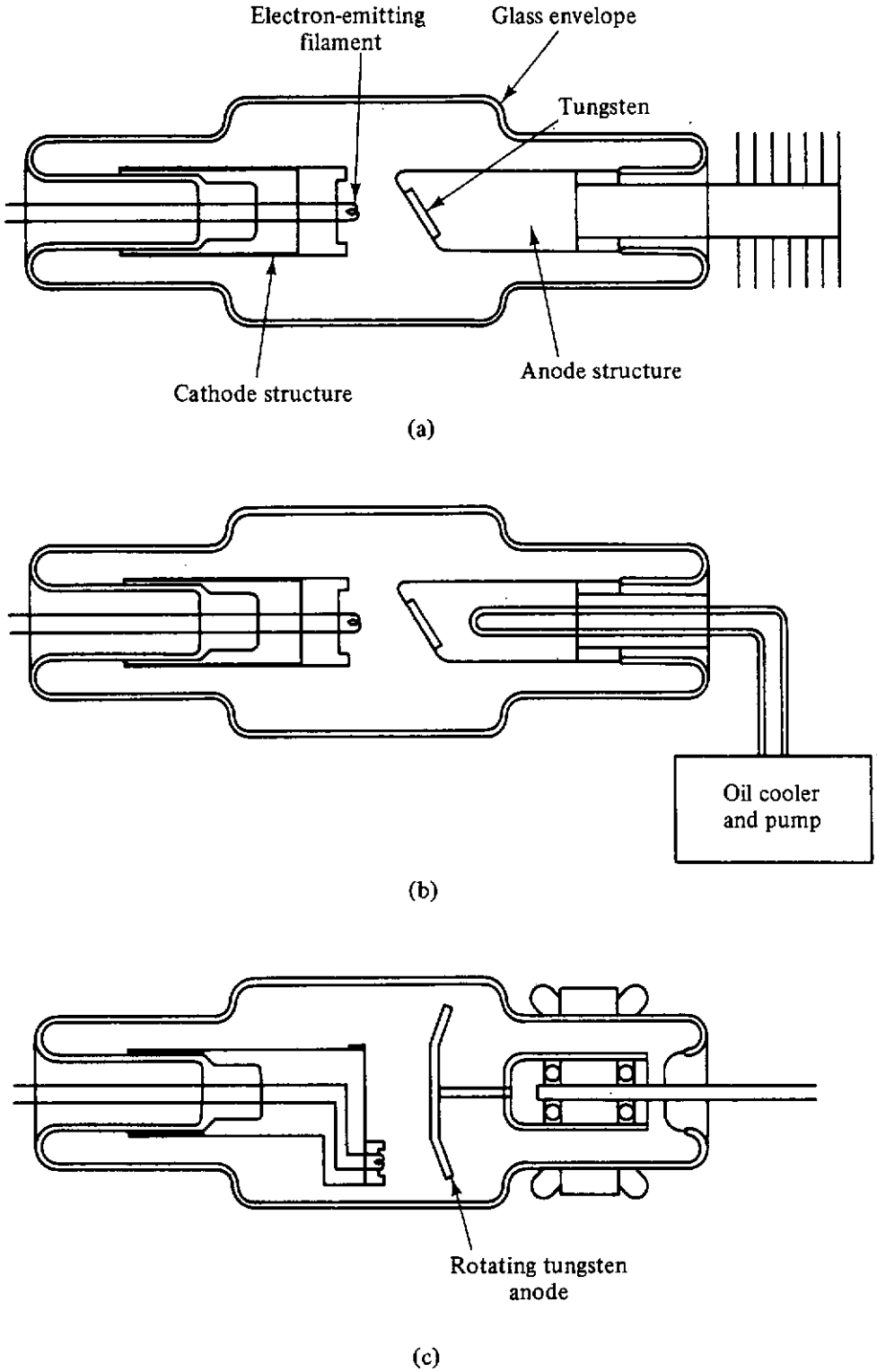

Figure 4.14 Schematic diagrams of typical x-ray tubes showing different methods for dissipating heat in the anode: (a) air cooled; (b) oil cooled; (c) rotating anode. (From Ref. 29; reproduced by permission of McGraw-Hill Publishing Co.)

the maximum voltage applied to the tube). If the applied voltage is sufficiently high as to cause ionization in the target material, there will also be characteristic x-ray lines superimposed on the continuous bremsstrahlung spectrum. In Fig. 4.15 the ideal (i.e., no absorption) energy spectrum of x rays is shown for different tube voltages.

TABLE 4.12 Characteristics of Target Materials Used in X-Ray Tubes

Element	X-Ray Line	Wavelength (10^{-10} m)	Energy (keV)	Excitation Voltage (kV)
Tungsten	$K_{\alpha 1}$	0.2090	59.3182	69.525
	$K_{\beta 1}$	0.1844	67.2443	69.525
	$L_{\alpha 1}$	1.4764	8.3976	10.207
	$L_{\beta 1}$	1.2818	9.6724	11.544
Silver	$K_{\alpha 1}$	0.5594	22.1629	25.514
	$L_{\alpha 1}$	4.1544	2.9843	3.351
Molybdenum	$K_{\alpha 1}$	0.7093	17.4793	20.000
	$K_{\beta 1}$	0.6323	19.6083	20.000
	$L_{\alpha 1}$	5.4066	2.2932	2.520
Copper	$K_{\alpha 1}$	1.5406	8.0478	8.979
	$K_{\beta 1}$	1.3922	8.9053	8.979
Nickel	$K_{\alpha 1}$	1.6579	7.4782	8.333
Cobalt	$K_{\alpha 1}$	1.7890	6.9303	7.709
Iron	$K_{\alpha 1}$	1.9360	6.4038	7.112
Chromium	$K_{\alpha 1}$	2.2897	5.4147	5.989
Aluminum	$K_{\alpha 1}$	8.3393	1.4867	1.560

The characteristic x rays may contribute a substantial fraction of the total x-ray emission. For example, the L-shell radiation from a tungsten target is between 20 and 35% of the total energy emission when voltages between 15 and 50 kV are used [30]. Above and below this voltage range, the L component rapidly decreases in importance. However, even a small degree of filtering of the x-ray beam effectively eliminates the low-energy portion of the spectrum containing the L-shell x rays. The higher-energy K-series x rays from a tungsten target contribute a maximum of 12% of the total x-ray exposure for operating voltages between 100 and 200 kV [30].

From Eq. (4.27) it is seen that the rate at which bremsstrahlung energy is radiated from the target (MeV per second) when bombarded by a current of i amperes of electrons which have been accelerated through a potential of V volts is

$$\dot{E}_{\text{br}} = k\frac{i}{e}Z(10^{-6}V)^2 \simeq 4.4 \times 10^3 iZV^2, \tag{4.33}$$

in which e is the electronic charge. The energy spectrum of this bremsstrahlung is given by Eq. (4.26); however, it is accepted practice in x-ray technology to use the x-ray wavelength λ rather than the photon energy E. Since these two quantities are related by $\lambda = hc/E$, the ideal spectral distribution of bremsstrahlung energy emission rate per unit wavelength, $\dot{\varepsilon}(\lambda)$, is found from Eq. (4.26) to be (Kramer's law)

$$\dot{\varepsilon}(\lambda) = \dot{\varepsilon}(E)\left|\frac{dE}{d\lambda}\right| = k'iZ\left(\frac{\lambda}{\lambda_0} - 1\right)\frac{1}{\lambda^3}, \tag{4.34}$$

where the minimum wavelength $\lambda_0 = hc/V$ and k' is a constant. As the voltage

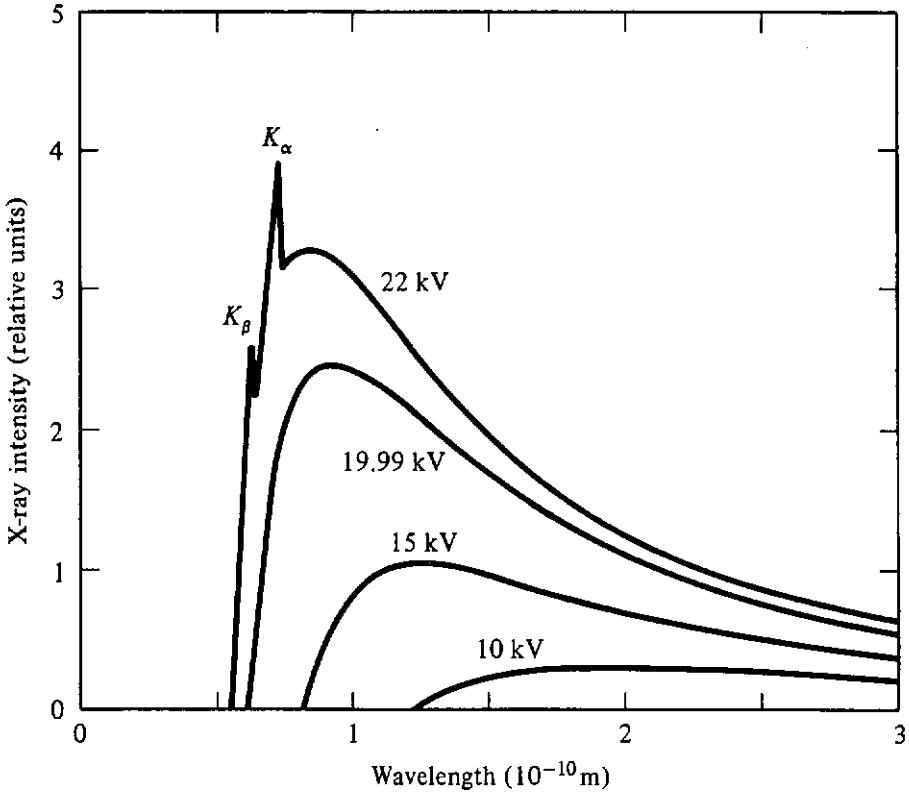

Figure 4.15 Ideal x-ray spectra from molybdenum for different accelerating voltages. The K series of x rays do not appear until the voltage exceeds the critical K-shell ionization energy (20.00 keV). The L series of x rays has wavelengths between 4.3 and 5.4 $\times$ 10^{-10} m and thus do not appear in the spectra above.

increases above the critical voltage for ionization of the target atoms, the emission rate of the characteristic x rays also increases. For voltages up to six times the critical voltage for K-shell ionization, V_K, the emission of the K_α x rays increases approximately as $(V - V_K)^2$ [25].

The shape of the x-ray spectrum from a real x-ray machine often differs considerably from the ideal spectrum discussed above. The high-voltage power supply of most units usually does not provide a constant voltage across the x-ray tube but rather gives a pulsating or fluctuating voltage.[3] This results in fewer high-energy bremsstrahlung photons near the cutoff than would be expected on the basis of the peak voltage alone. In effect, electrons with a distribution of energies up to the peak voltage impinge on the anode and cause a shift of the peak intensity in Fig. 4.15 toward longer wavelengths. On the other hand, the low-energy photons are preferentially absorbed by the target material, the glass envelope of the x-ray tube, and the air outside the tube. In addition, metal filters are often placed in the beam path to absorb preferentially the low-energy photons and thus to shift the spectrum toward higher energies. The strength of the x-ray beam thus depends on the target material, tube voltage, tube current, and the type and amount of filtering experienced by the x rays. Traditionally, the output from a particular x-ray machine is expressed by a parameter $\hat{R}_i$

[3]If a *c*onstant *p*otential is applied to the x-ray tube, the designation "kVcp" is sometimes used, while the *p*eak voltage for a pulsating applied voltage is often indicated by "kVp."

(R mA^{-1} min^{-1}) which is the exposure in the beam (expressed in roentgens) at a specified distance from the tube focal spot (usually 1 m) that would be produced by a 1-mA tube current of 1-min duration. This performance parameter is usually assumed known when making analyses for x-ray shielding around a particular machine since it depends greatly on the operating voltage and the degree of beam filtering. Typical values of $\hat{R}_t$ for tubes with tungsten targets and various degrees of filtering are shown in Fig. 4.16. For a different target

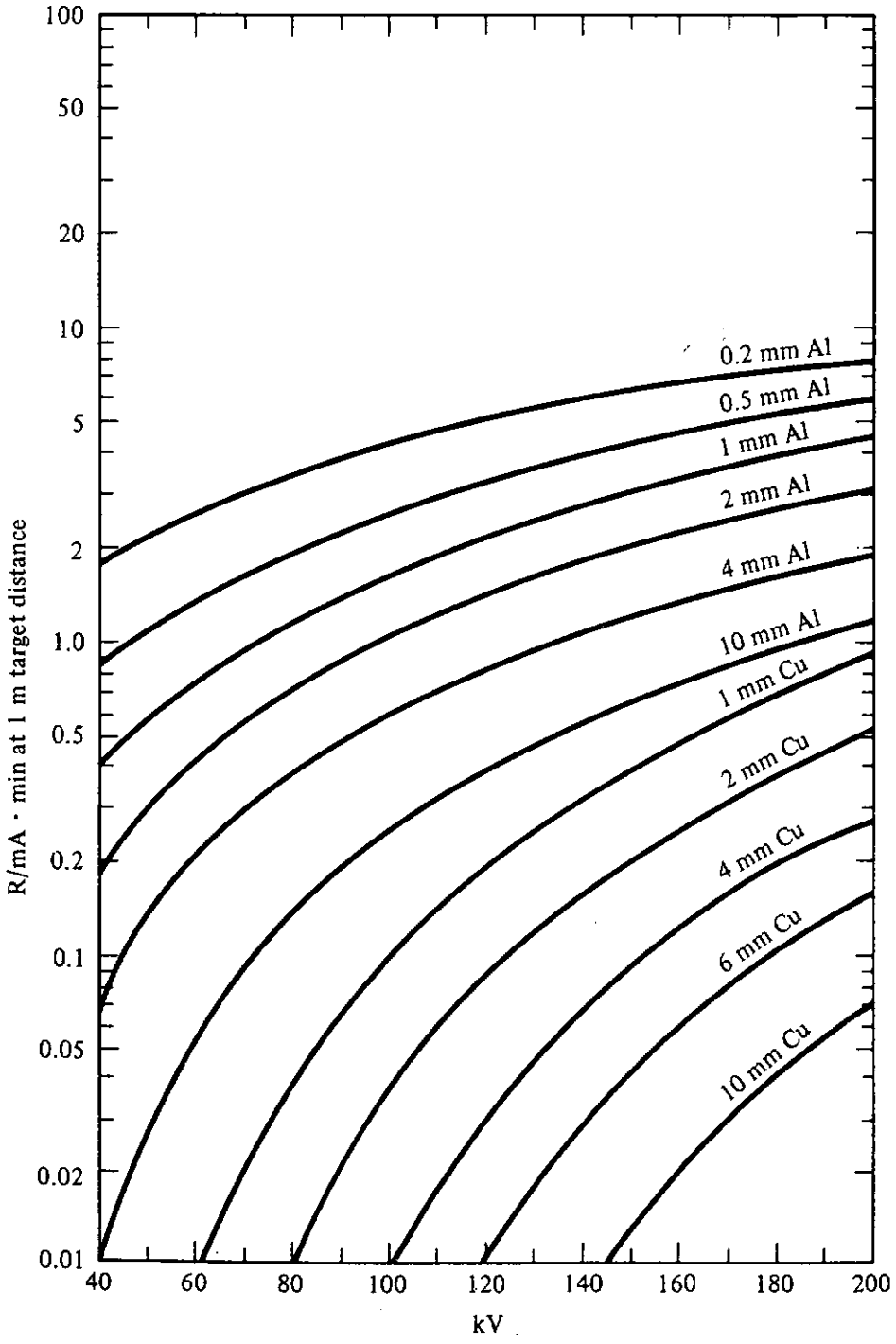

Figure 4.16 Approximate radiation output in R mA^{-1} min^{-1} at a distance of 1 m, measured in air, of the x-ray beam from a tube with a tungsten target for various tube voltages (constant potential) and various degrees of beam filtrations. (From Ref. 31.)

material with atomic number Z, simply multiply these values by $Z/74$ [see Eq. (4.28)]. Values of $\hat{R}_i$ for lower or higher voltages than those of Fig. 4.16 are to be found in Refs. 31 and 32.

REFERENCES

1. G. R. Keepin, *Physics of Nuclear Kinetics*, Addison-Wesley, Reading, Mass., 1965.
2. "Nuclear and Physical Properties of Californium-252," BNL Report 50168 (T-530), Brookhaven National Laboratory, Upton, N.Y., 1969.
3. "Reactor Physics Constants," Report ANL-5800, 2nd ed., Argonne National Laboratory, Argonne, Ill., 1963.
4. C. M. Lederer and V. Shirley, *Table of Isotopes*, 7th ed., Wiley-Interscience, New York, 1978.
5. *Radiological Health Handbook*, U.S. Government Printing Office, Washington, D.C., 1970.
6. P. Guenther, D. Havel, R. Sjoblom, and A. Smith, Report ANL/NDM-19, Argonne National Laboratory, Argonne, Ill., 1976.
7. J. Terrell, *Phys. Rev.* **127**, 880 (1962).
8. L. Cranberg et al., *Phys. Rev.* **103**, 662 (1956).
9. E. P. Blizard and L. S. Abbott (eds.), *Reactor Handbook*, Vol. III, Part B: *Shielding*, 2nd ed., Interscience, New York, 1962.
10. D. G. Madland and J. R. Nix, "New Calculation of Prompt Fission Neutron Spectra and Average Prompt Neutron Multiplicities," *Nucl. Sci. Eng.*, **81**, 213–271 (1982).
11. R. G. Jaeger (ed.), *Engineering Compendium on Radiation Shielding*, Vol. I: *Shielding Fundamentals and Methods*, Springer-Verlag, New York, 1968, Chap. 2.
12. B. T. Price, C. C. Horton, and K. T. Spinney, *Radiation Shielding*, Pergamon, Elmsford, N.Y., 1957.
13. G. F. Knoll, *Radiation Detection and Measurement*, Wiley, New York, 1979.
14. J. B. Marion and J. L. Fowler (eds.), *Fast Neutron Physics*, Interscience, London, 1960.
15. K. W. Geiger and L. Van der Zwan, *Nucl. Instrum. Methods* **131**, 315 (1975).
16. M. E. Anderson and M. R. Hertz, *Nucl. Sci. Eng.* **44**, 437 (1971).
17. J. F. Perkins and R. W. King, *Nucl. Sci. Eng.* **3**, 726–746 (1958).
18. J. F. Perkins, "Decay of U-235 Fission Products," Report RR-TR-63-11, U.S. Army, 1963.
19. O. W. Hermann and R. M. Westfall, "ORIGEN-S: SCALE System Module to Calculate Fuel Depletion, Actinide Transmutation, Fission Product Buildup and Decay, and Associated Radiation Source Terms," Sec. F7 of *SCALE: A Modular Code System for Performing Standardized Computer Analyses for Licensing Evaluation*, Report NUREG/CR-0200, Vol. 2, Oak Ridge National Laboratory, Oak Ridge, Tenn., October 1981. Reference data libraries are from J. C. Ryman, "ORIGEN-S Data Libraries," Sec. M6 of *SCALE: A Modular Code System for Performing Standardized Computer Analyses for Licensing Evaluation*, Report

NUREG/CR-0200, Oak Ridge National Laboratory, Oak Ridge, Tenn., Vol. 3 1983.

20. D. C. George et al., "Delayed Photon Sources for Shielding Applications," *Trans. Am. Nucl. Soc.* **35**, 463 (1980).
21. R. J. LaBauve, T. R. England, D. C. George, and C. W. Maynard, "Fission Product Analytic Impulse Source Functions," *Nucl. Technol.* **56**, 322–339 (1982).
22. J. R. Lamarsh, *Introduction to Nuclear Reactor Theory*, Addison-Wesley, Reading, Mass., 1966.
23. C. M. Lederer, J. M. Hollander, and I. Perlman, *Table of Isotopes*, 6th ed., Wiley, New York, 1968.
24. H. Goldstein, *Fundamental Aspects of Reactor Shielding*, Addison-Wesley, Reading, Mass., 1959.
25. S. Flügge (ed.), *Handbuch der Physik*, Vol. 30, Springer-Verlag, Berlin, 1957.
26. R. D. Dewey, R. S. Mapes, and T. W. Reynolds, "Computed X-Ray Wavelengths," in *Progress in Nuclear Energy*, Series IX: *Analytical Chemistry*, E. A. Elion and D. C. Stewart (eds.), Pergamon, Oxford, 1969.
27. G. R. White, NBS Report 1003, U.S. National Bureau of Standards, Washington, D.C., 1952; as quoted in Ref. 12.
28. R. D. Evans, *The Atomic Nucleus*, McGraw-Hill, New York, 1955.
29. E. F. Kaelble (ed.), *Handbook of X Rays*, McGraw-Hill, New York, 1967.
30. "Radiation Dosimetry: X Rays Generated at Potentials of 5 to 150 kV," ICRU Report 17, International Commission on Radiation Units and Measurements, Washington, D.C., 1970.
31. "Protection against X-Rays up to Energies of 3 MeV and Beta- and Gamma-Rays from Sealed Sources," ICRP Publication 3, International Commission on Radiological Protection, Pergamon, Oxford, 1960.
32. "Protection against ionizing radiation from external sources used in medicine," ICRP Publication 33, International Commission on Radiological Protection, Pergamon, Oxford, 1982.

PROBLEMS

4.1. In neutron shielding analysis, the high-energy neutrons are always of greatest concern. Estimate the fraction of fission neutrons from ^{235}U with energies above 8 MeV.

4.2. In the fission of a heavy nuclide, approximately 160 to 180 MeV of kinetic energy is initially imparted to the fission fragments, which quickly give up their energy by ionizing collisions in the surrounding medium. The remaining 30 to 40 MeV of the fission energy is deposited away from the fission site by prompt and delayed fission gamma photons, neutrons, neutrinos, and β-decay of the fission fragment. What is the rate at which heat must be removed from a 0.1-g sample of ^{252}Cf assuming that all the fission fragments and alpha particles (6.1 MeV) are stopped in the sample or its encapsulation?

4.3. The plutonium generated in a uranium-fueled nuclear reactor is mostly ^{239}Pu.

However, other plutonium isotopes are also produced. Estimate the neutron emission rate as a result of spontaneous fission from a 0.5-kg sample of plutonium which has the following isotopic abundances: ^{242}Pu, 0.1%; ^{241}Pu, 0.05%; ^{240}Pu, 0.9%; ^{239}Pu, 96.22%; ^{238}Pu, 1.5%; ^{237}Pu, 1.2%; and ^{236}Pu, 0.03%.

4.4. For thermal fission of ^{235}U, how many fission neutrons are created when 1 J of fission energy is released?

4.5. The activation product ^{16}N has a 7.4-s half-life and decays with the emission of a 6.13(69%)- or a 7.10(5%)-MeV gamma photon. What are the minimum and maximum neutron energies if the gamma photons induce (γ, n) reactions in a material containing both deuterium and beryllium? Sketch the energy spectrum of the resulting photoneutrons.

4.6. Calculate the neutron emission rate from a 20-GBq point source of ^{124}Sb surrounded by 40 g of beryllium if it is assumed that the ^{9}Be$(\gamma, n)^{8}$Be cross section is about 1 mb (see Fig. 4.2).

4.7. An isotope that decays by ejecting alpha particles with energies 6.82 MeV (10%) and 4.30 MeV (90%) is mixed intimately with a large amount of beryllium. For an (α, n) source using 40 GBq of this mixture, estimate the neutron emission rate and sketch the energy spectrum of the emitted neutrons.

4.8. Estimate the rate at which activation product neutrons from the decay of ^{17}N are produced in a water-moderated, uranium-fueled reactor which is operating at a steady power level of 3000 MW.

4.9. A thermonuclear device (D-T reaction only) is detonated in space with a yield of 1.00 MWd. What is the resulting neutron fluence and energy fluence density of the neutrons 1 km from the detonation point?

4.10. During a pulse of a small experimental reactor, 10 MWs of fission energy is released. Calculate the amount of energy that is released as prompt gamma photons between 5 and 7 MeV.

4.11. Derive Eq. (4.15).

4.12. A new uranium fuel assembly is placed in the outer region of a reactor core, where it generates 3 MW of fission power at a steady rate for 325 days. During a 2-month shutdown of the reactor, this fuel element is then transferred closer to the center of the reactor. After restarting the reactor, the fuel assembly generates a steady power of 7.5 MW for the next 300 days, after which the reactor is once again shut down. The fuel assembly is then removed from service and placed in a storage pool until it is shipped to a reprocessing plant 250 days after the second reactor shutdown. What is the total gamma-energy release rate as well as the energy release rate by gamma photons with energies between 2.0 and 3.0 MeV from the assembly at the time it is shipped for reprocessing?

4.13. A beam of thermal neutrons (10^{10} neutrons cm^{-2} s^{-1}) irradiates a 2-g sample of calcium for 30 s. What is the flux density (in vacuum) of gamma photons with energies greater than 1 MeV at a point 1 m from the sample 2 min after the irradiation ceases? Consider the decay of both ^{47}Ca and ^{49}Ca.

4.14. Cadmium is commonly used to attenuate thermal neutrons because of its large (n, γ) cross section. However, capture gamma photons are produced as a result of the neutron capture. As an example, use Table A3.9 to sketch the energy-dependent flux density of capture photons above 1 MeV at 10 m (in vacuum)

from a point where a thermal neutron beam of 10^8 neutrons s^{-1} is stopped by a cadmium sheet.

4.15. What is the flux density of annihilation photons 2 m (in vacuum) from a 4-MBq point radionuclide source which decays by negatron emission and which emits a single 5-MeV photon per decay if the source is encapsulated by a lead shell 5 mm thick and 12 mm in outside diameter? If the source decayed by positron emission, what would be the flux density of annihilation radiation at the same point?

4.16. Electrons accelerated through a potential of 100 kV strike a gold target. Sketch the spectrum of the resulting x rays first as a function of x-ray energy down to 50 keV and then as a function of wavelength. Show both the bremsstrahlung and characteristic x rays. If the electron beam current and voltage were doubled and the target replaced by an aluminum one, by what percentage would the bremsstrahlung power change?

4.17. Calculate the energy flux density of the bremsstrahlung 1 m (in vacuum) from a small tungsten target bombarded by 10 mA of electrons accelerated through a constant potential of 300 kV. Neglect x-ray absorption and assume isotropic emission of the x rays.

4.18. What is the energy flux density of bremsstrahlung from a 1-Ci source of ^{32}P which is surrounded by lead just thick enough to stop the beta particles? (E_{max} = 1.710 MeV.)

4.19. Calculate the time-averaged bremsstrahlung energy spectrum generated in a x-ray tube to which the voltage in Fig. P4.19 is applied. What is the average power radiated as bremsstrahlung? Compare this to the x-ray output if the tube voltage were constant at V_0.

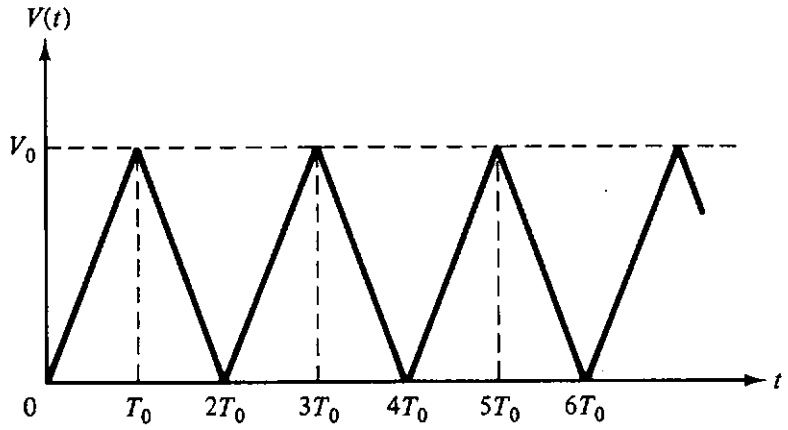

5 detector response functions

Most shielding analysis involves, at least implicitly, a study of the flux density (or fluence) field at pertinent locations with respect to the shield. The locations may be outside or inside the shield. The purpose of such analysis is generally to predict the corresponding responses of some type of detector, and therefore the field information must be converted into the detector responses. Let us designate the detector response by the symbol R; and we can relate R to either a fluence Φ or a flux density ϕ by a multiplier to be called, generally, the *detector response function*, $\mathfrak{R}$.

In its most general form, the detector response is given by[1]

$$R = \int_0^\infty \int_{4\pi} \int_{V_d} \mathfrak{R}(\mathbf{r}_d, E, \boldsymbol{\Omega})\phi(\mathbf{r}_d, E, \boldsymbol{\Omega})\, dV\, d\Omega\, dE, \tag{5.1}$$

where the volume integration is over the sensitive volume V_d of the detector. $\mathfrak{R}(\mathbf{r}_d, E, \boldsymbol{\Omega})$ can be looked upon from a physical point of view as the expected (or average) detector response caused by a particle of energy E traveling in direction $\boldsymbol{\Omega}$ at point $\mathbf{r}_d$, per unit of path length traveled. In general, the explicit representation of the detector response function may be very complicated for a large-volume, directionally dependent detector whose energy dependence varies

[1]In this chapter, time-rate response will be discussed rather than the corresponding time-integrated response. For the latter, one uses fluence rather than flux density in Eq. (5.1). The detector response function defined here is a somewhat simplified form of a more general function which may depend, in addition to those factors specified, on time, previous detector history, or even the magnitude of the response. The present formulation is adequate for the idealized types of detector response shielding specialists normally use in their analyses. Until Section 5.4.4 is reached, the discussion assumes that the flux density is known exactly.

with location within the volume. For analytical purposes, however, most practical detectors can be well represented by one or another of the simple, idealized detectors having response functions as indicated below:

1. Point detector at location $\mathbf{r}_0$, collimated to respond only to radiation with direction $\mathbf{\Omega}_0$:

$$\mathcal{R}(\mathbf{r}_d, E, \mathbf{\Omega}) = \mathcal{R}(E)\delta(\mathbf{r}_d - \mathbf{r}_0)\delta(\mathbf{\Omega} - \mathbf{\Omega}_0). \tag{5.2}$$

2. Point, isotropic detector, at point $\mathbf{r}_0$:

$$\mathcal{R}(\mathbf{r}_d, E, \mathbf{\Omega}) = \mathcal{R}(E)\delta(\mathbf{r}_d - \mathbf{r}_0). \tag{5.3}$$

3. Point, energy-independent, isotropic detector at point $\mathbf{r}_0$:

$$\mathcal{R}(\mathbf{r}_d, E, \mathbf{\Omega}) = \mathcal{R}\,\delta(\mathbf{r}_d - \mathbf{r}_0), \tag{5.4}$$

in which $\mathcal{R}$ is a constant.

Most idealized detector types used in radiation protection practice are of the point, isotropic type; and all the detector concepts described and used in this text are to be considered as such unless a specific statement to the contrary is made. If Eq. (5.3) is substituted into Eq. (5.1), the following somewhat simpler expression results:

$$R(\mathbf{r}_0) = \int_0^\infty \mathcal{R}(E)\phi(\mathbf{r}_0, E)\,dE. \tag{5.5}$$

The concept of detector response embraces such simple isotropic detector types as a flux-density detector (in which case $\mathcal{R} = 1$) and an energy flux-density detector [in which case $\mathcal{R}(E) = E$]. Other detectors used in shielding analysis are generally of a dosimetric nature and have response functions related to energy deposition per unit mass. These are discussed below in detail.

5.1 GENERAL FORMULATION FOR DOSIMETRIC DETECTORS

The basic definition of a cross section (see Sections 3.1 and 3.2) leads to the fundamental rule that, for a sufficiently small volume element ΔV of elemental composition suffused by a field of monoenergetic radiation particles, the number of interactions ΔM which occur per unit time is given by

$$\Delta M = \sigma N \phi\, \Delta V, \tag{5.6}$$

where σ is the microscopic cross section per atom (depending on the type of atom and the energy of the individual particles of radiation) and N is the number of such atoms per unit volume of the medium.

If ϵ is defined as the average amount of energy transferred (a concept to be clarified later) from the radiation field to the medium in a single interaction, it is easy to see that ΔE, the amount of energy transferred per unit time to the medium due to all interactions within ΔV, is given by

$$\Delta E = \epsilon \sigma N \phi\, \Delta V. \tag{5.7}$$

Dosimetric concepts commonly relate to the energy deposition rate per unit of mass, which we will call $\mathcal{G}$; so if the mass of the incremental volume is given by $\rho\,\Delta V$, where ρ is the density of material in ΔV, then

$$\mathcal{G} = \epsilon \frac{\sigma N}{\rho} \phi. \tag{5.8}$$

The function $\mathcal{G}$ is easily established as a point function, since ΔV can be taken to a zero limit (in the stochastic manner discussed in Section 2.1.1) without any consequent change in formula (5.8).

Generalization of the formula to take into account a spectral distribution of particle energies and a mixture of types of atoms, as well as the fact that ϵ will differ for different types of interaction, results in the following equation:

$$\mathcal{G}(\mathbf{r}) = \int_0^\infty \sum_i \frac{N_i(\mathbf{r})}{\rho(\mathbf{r})} \sum_j \sigma_{ji}(E)\epsilon_{ji}(E)\phi(\mathbf{r}, E)\, dE, \tag{5.9}$$

where the dependence on various atoms (or even on various isotopes) is characterized by the subscript i and the specific type of interaction involved is indicated by the subscript j. The units on both sides of this equation must be consistent, of course, or a conversion factor must be introduced to account for any inconsistencies.

If the dosimetric response of interest happens to be precisely the energy deposition rate per unit mass of the medium at the point where the idealized detector is located, the corresponding response function is that portion of the integrand in Eq. (5.9) which multiplies ϕ. That is, for this particular circumstance,

$$R = \mathcal{G} = \int_0^\infty \mathcal{R}(E)\phi(E)\, dE, \tag{5.10}$$

where[2]

$$\mathcal{R}(E) = \sum_i \frac{N_i}{\rho} \sum_j \sigma_{ji}(E)\epsilon_{ji}(E). \tag{5.11}$$

This particular formulation is most directly useful for the type of response called the kerma rate; but it can be used, with precautions, for related responses such as absorbed dose rate and (for photons only) exposure rate.

5.2 RELATIONSHIP OF KERMA RATE AND ABSORBED DOSE RATE: CHARGED-PARTICLE EQUILIBRIUM

The *kerma rate* is determined from Eqs. (5.10) and (5.11), as can be seen from its definition in Section 2.3, as long as ϵ is taken to be the kinetic energy of the secondary charged particles resulting from the interactions of the primary radiation with the atoms in the sensitive volume.

[2]Note that $N_i/\rho = w_i(N_i/\rho_i)$, where w_i is the weight fraction of the ith constituent. (N_i/ρ_i), which may be written $(N/\rho)_i$, depends only on the identity of the ith constituent. For data, see Appendix 3.

At first glance, the foregoing equations appear not to be useful for prediction of *absorbed dose rate*, since this concept requires in principle an accounting of the energy transferred to ionization and related processes along those segments of the tracks of secondary charged particles which lie within the sensitive volume. However, there is frequently a close numerical correspondence between the kerma rate and the absorbed dose rate at a specific location, so that a determination of the kerma rate may be used to estimate the absorbed dose rate to a close approximation.

To appreciate this, one must understand the nature of what is called *charged-particle equilibrium*. This condition is said to exist for a small incremental volume at a given location if, for every charged particle leaving the volume, another of the same type and with the same kinetic energy enters the volume at the same time. Sometimes, one is concerned only with a specific type of charged particle; thus, one may speak, for example, of *electronic equilibrium* (involving only electrons) or *heavy-charged-particle equilibrium*.

This condition is an idealization that is practically impossible to obtain exactly, especially in view of the statistical nature of a radiation field. However, it may be approached under many circumstances, as can be made clear by the following plausible, if not rigorous, analysis.

Consider Fig. 5.1, which depicts all space as divided up into similar increments, of which the shaded one represents the incremental volume of current interest. (The analysis should actually be made on a three-dimensional basis; but the two-dimensional simplification is sufficient to show the principle and is much simpler to draw clearly.) The line marked *a–d* represents a typical track of a secondary charged particle arising from an interaction by a primary particle within the shaded volume. Ionization occurs along this track. (It is made straight in the figure, but this is not necessary to the argument.)

Let us assume that the primary radiation field is practically constant over this entire region—at least over that portion of it extending away from the shaded volume by a distance equal to the range of the most energetic secondary charged particle likely to be produced. If this is so, one might expect, *on the average*, that for every track *a–d* starting from the shaded volume, a similar one starts at a similar point in all nearby volumes with the same energy, proceeding in the same direction and with the same trajectory from start to end of its range. Some of these, which start from surrounding volumes, will penetrate the shaded volume. The kinetic energy of the particle starting at *a* will contribute to the *kerma* at the location of the shaded volume; no other particles shown will make a contribution to this volume. The *absorbed dose*, on the other hand, contributed by the secondary particle from *a* and all similar particles which penetrate the shaded volume come from energy deposited in ionization and related processes along the track segments *a–b*, *b′–c′*, and *c″–d″*. But the energy deposited along *b′–c′* is the same as the particle kinetic energy lost in the track segment *b–c*; similarly, the energy deposited along *c″–d″* is the same as the particle kinetic energy lost along the track segment *c–d*. Thus, as far as the particular interaction

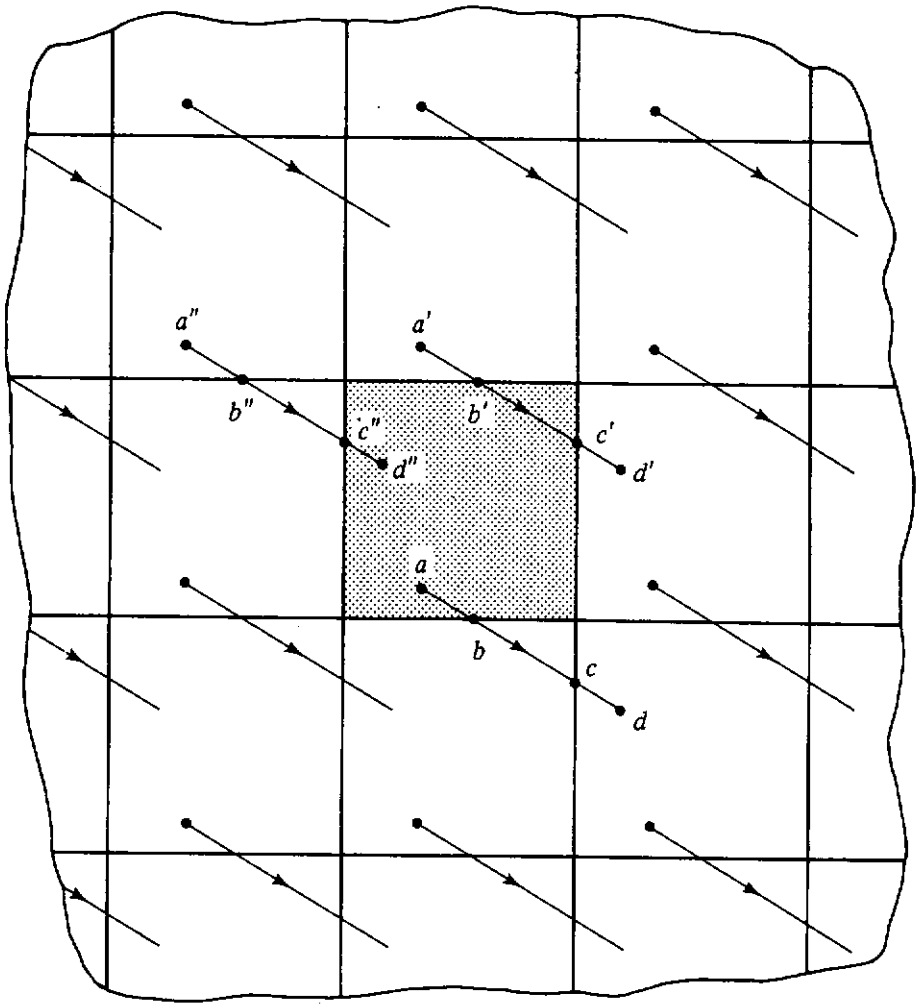

Figure 5.1 All space divided into similar regions (represented by squares) in the vicinity of the incremental volume of primary interest, shown as the shaded square. In each incremental volume, corresponding interaction events for the primary particles are shown, together with lines representing corresponding secondary charged-particle tracks.

shown and corresponding ones nearby are concerned, the contribution to the kerma and the contribution to the absorbed dose are the same. This compensation for lost secondary particles from the volume of interest is then easily generalized to cover *all* interactions in the shaded volume and in the nearby volumes. When such compensation occurs in the shaded volume, there exists what is called "charged particle equilibrium," and under this condition the kerma and absorbed dose would be equal in this volume.

It is easy to see that two separate factors might prevent the establishment of charged-particle equilibrium. In either case, kerma and absorbed dose are not likely to be equivalent.

1. If, within the range of the more energetic charged particles, a boundary exists between the medium containing the shaded volume and another medium of appreciably different properties (which may be the same

material but with a substantially different density), the appropriate correspondence between similar tracks may not be established.

2. If the primary radiation field varies appreciably over the region within the range of the secondary particles around the shaded volume, one cannot expect a close correspondence between interactions and secondary charged particles in the shaded volume and in its nearby elements.

Another circumstance would cause a difference between kerma and absorbed dose. Assume a modification in the depicted figure to the extent that each secondary track, when it reached the point b or b' or b'', was terminated and the remaining kinetic energy in the particle was carried off by a bremsstrahlung photon. In such case, the absorbed dose contribution provided by the segments b'–c' and c''–d'' in the original case would be lost; but the kerma would remain the same as in the original case.

Subject then to the limitations of charged particle equilibrium and negligible bremsstrahlung production, the kerma rate provides a good approximation to the absorbed dose rate. Since determination of kerma rate requires no need for study of the transport of the secondary particles, its analytical determination is much easier than that of absorbed dose and thus there is a strong incentive to use the kerma rate calculation for absorbed dose rate wherever possible. Those who measure absorbed dose by conventional means usually take care to ensure that the measurement process is such as to provide charged-particle equilibrium to a good approximation, so that the measured value can be accurately predicted through calculation of the kerma. This is usually obtained by having a sufficiently thick wall around the sensitive volume.

5.3 NEUTRON KERMA, ABSORBED DOSE, AND DOSE EQUIVALENT RATES

Even though absorbed dose rate is of more biological and engineering significance than kerma rate, it is quite customary to calculate kerma rate when dealing with neutrons. Except within a distance from a boundary equal to the greatest range of the secondary charged particles (heavy particles, with short ranges, usually), one can expect charged-particle equilibrium to exist to a good approximation [1, 2]. Furthermore, the probability of bremmstrahlung carrying off some of the secondary-particle energy is very small for heavy particles. Thus, kerma rate becomes usually a very good approximation to absorbed dose rate for neutrons.

For neutron kerma rate, Eqs. (5.10) and (5.11) apply, modified if one wishes by the notational replacement of $N_i\sigma_{jl}$ with μ_{jl}, the interaction coefficient for the jth type of interaction by a neutron of the given energy with the ith-type atom. For this type of response, ϵ_{jl} refers specifically to the kinetic energy of the charged particle (which may be a recoil nucleus) resulting from this interaction.

The determination of ϵ for use in specifying this response function depends on the reaction (interaction) involved. For neutron elastic scattering, it can be shown that on the average the energy per interaction transferred to kinetic energy of the recoil nucleus is given by

$$\epsilon_{\text{elas}} = \frac{2EA}{(A+1)^2}[1 - f_1(E)], \tag{5.12}$$

where A is the ratio of the mass of the nucleus involved to that of the neutron, and f_1 is the coefficient of the P_1 term in the Legendre expansion of the differential elastic scattering cross section. The coefficient f_1 is also equal to the average cosine of the angle of elastic scattering in the center-of-mass system. Typical values of f_1 for elastic scattering are given in Table 5.1. For isotropic scattering, $f_1 = 0$, and Eq. (5.12) reduces to $\epsilon_{\text{elas}} = 2EA/(A+1)^2$.

TABLE 5.1 Values of the Legendre Coefficient f_1 for the Expansion of the Neutron Elastic Scattering Cross Section for Various Elements

E (MeV)	Element					
	Li	Be	C	O	Si	Fe
6.6282	0.527	0.569	0.220	0.523	0.550	0.790
4.0202	0.340	0.385	0.016	0.372	0.449	0.584
2.4384	0.103	0.017	−0.017	0.022	0.353	0.374
1.4790	0.046	0.222	0.048	0.072	0.287	0.244
0.8970	−0.011	0.166	0.057	0.009	0.217	0.277
0.5441	−0.131	0.045	0.047	0.279	0.152	0.197
0.3300	−0.256	0.036	0.030	−0.109	0.088	0.079
0.2002	0.289	0.024	0.018	0	0.048	0.053
0.1214	0.130	0.015	0.011	0	0.029	0.032
0.0736	0.074	0.010	0.007	0	0.017	0.020
0.0447	0.043	0.006	0.004	0	0.010	0.012
0.0271	0.026	0.004	0.002	0	0.006	0.007
0.0164	0.016	0.002	0.001	0	0.003	0
0.0100	0.010	0.001	0.001	0	0	0

Source: *Ref. 3. Reproduced by permission of Springer-Verlag, New York.*

For neutron inelastic scattering which excites a level of the nucleus by an amount of energy $|Q|$ above the ground state, the average kinetic energy of the recoil nucleus can be shown to be (see Problem 3.9)

$$\epsilon_{\text{inel}} = \frac{2EA}{(A+1)^2}\left[1 - \frac{A}{2}\Delta - f_1(1+\Delta)^{1/2}\right], \tag{5.13}$$

where

$$\Delta \equiv -\frac{|Q|}{E}\frac{A+1}{A}. \tag{5.14}$$

Here f_1 is the Legendre expansion coefficient for inelastic scattering. Coefficients

for inelastic scattering are not as well known as those for elastic scattering and are usually taken as zero, in which case the result above reduces to Eq. (3.86).

Methods of deriving the energy of charged particles and recoil nuclei in connection with the above, as well as other types of possible reactions, are available in the literature (see e.g., Ref. 2). With this information and data on other pertinent variables in Eqs. (5.10) and (5.11), it is possible to determine the response function for various elements and materials of shielding interest. Caswell and Coyne [4] have done this for various tissue-like materials and produced kerma response functions (which they call "kerma factors"). Data for the neutron kerma response function in a four-element approximation to tissue [5] are included in Appendix 3 as Table A3.12.

In order to determine the dose equivalent rate, one must multiply the tissue absorbed dose rate by the average quality factor of all the secondary charged particles within the incremental volume at the specified location.[3] A strict determination of the quality factors demands complete knowledge of the energies of the resulting particles and a careful accounting of the relationship between quality factor and LET (see Table 2.1). It is often satisfactory for practical purposes in determining neutron dose equivalent to assign an overall average quality factor of 10, which is generally a safe estimate [6].

5.4 DOSIMETRIC RESPONSE FUNCTIONS FOR PHOTONS

Equation (5.9) applies to photons, as well as neutrons, but it is usually manipulated so as to appear as

$$\mathcal{G}(\mathbf{r}) = \int_0^\infty \frac{\mu_d(\mathbf{r}, E)}{\rho(\mathbf{r})} E\phi(\mathbf{r}, E)\, dE, \tag{5.15}$$

where μ_d, called the *linear energy deposition coefficient*,[4] is given by

$$\mu_d(\mathbf{r}, E) = \sum_i N_i(\mathbf{r}) \sum_j \sigma_{ji}(E) \frac{\epsilon_{ji}(E)}{E}. \tag{5.16}$$

Since N_i is directly proportional to the density of the ith element in the mixture, one sees that the *mass* energy deposition coefficient μ_d/ρ, like μ/ρ, is independent of the density. For a situation in which the attenuating medium is a mixture of elements in a constant proportion to one another, μ_d/ρ is independent of position, even though there may be density variations within the medium.

For the remainder of this section, we shall ignore the variable $\mathbf{r}$ as an argument, since we are concerned only with the response of a point isotropic detector at a given position. Furthermore, we shall consider the situation only for a monoenergetic flux density, since extension to a polyenergetic spectrum

[3]The basic dose equivalent concept noted here may be referred to as "primitive," to distinguish it from the more complex phantom-related concept discussed later in Section 5.5.

[4]See Section 3.2 for a discussion of average coefficients for compounds and mixtures.

is obvious. This restriction will simplify the algebra without compromising the principles to be developed.

5.4.1 Photon Energy Deposition Coefficients

Up to this point, the term "energy deposition," denoted by ϵ, has been kept somewhat vague, with the value of ϵ imprecise. As one defines ϵ more precisely, one can develop a number of different energy deposition coefficients; and since several different ones are used (sometimes incorrectly) in the shielding literature, it is necessary to explain the distinction between them carefully.

It is desirable for this purpose to review the energy balance for a small incremental volume (ΔV) of a medium interacting with a monoenergetic photon flux density. A slightly simplified picture of the disposition of the energy involved in the photon interactions with the incremental volume is shown in Fig. 5.2(a). From Eqs. (5.15) and (5.16) and from the definitions of the various photon coefficients provided in Chapter 3, one can then derive the related picture of the disposition of energy per unit mass of the medium in the incremental volume as shown in Fig. 5.2(b). One then arrives at the diagrammed relationship expressed in Fig. 5.2(c) in direct proportionality to the diagram in Fig. 5.2(b), by which various energy deposition coefficients are defined conceptually. The mathematical definitions easily follow:

1. μ_a, called the *linear absorption coefficient* [7], is given by
$$\mu_a = \mu - (1 - f_c)\mu_c = \mu_{ph} + \mu_{pp} + f_c\mu_c. \tag{5.17}$$
2. μ'_{tr}, although occasionally used [8], has no previously prescribed name. It very well might be called the *linear pseudo-energy-transfer coefficient* since its use is generally as an alternative to μ_{tr}, defined below. It is given by
$$\mu'_{tr} = \mu_a - (1 - f_{pp})\mu_{pp} = \mu_{ph} + f_{pp}\mu_{pp} + f_c\mu_c. \tag{5.18}$$
3. μ_{tr} is called the *linear energy transfer coefficient* [5], and is given by
$$\mu_{tr} = \mu'_{tr} - (1 - f_{ph})\mu_{ph} = f_{ph}\mu_{ph} + f_{pp}\mu_{pp} + f_c\mu_c. \tag{5.19}$$
4. μ_{en} is called the *linear energy absorption coefficient* [5] and is given by
$$\mu_{en} = (1 - G)\mu_{tr} = (1 - G_{ph})f_{ph}\mu_{ph} + (1 - G_c)f_c\mu_c + (1 - G_{pp})f_{pp}\mu_{pp}, \tag{5.20}$$
where G is the radiative emission constant defined in Section 3.5.4.

Values of the mass energy deposition coefficients, μ_a/ρ, μ_{tr}/ρ, and μ_{en}/ρ, for several elements and mixtures of shielding interest have been extracted from the literature and are provided in Appendix 3. Values for μ'_{tr}/ρ are not generally available and must be determined from its basic definition given here. Values for mixtures of elements are determined from either the number fractions or weight fractions for the individual elemental constituents, just as in the case of mass attenuation coefficients.

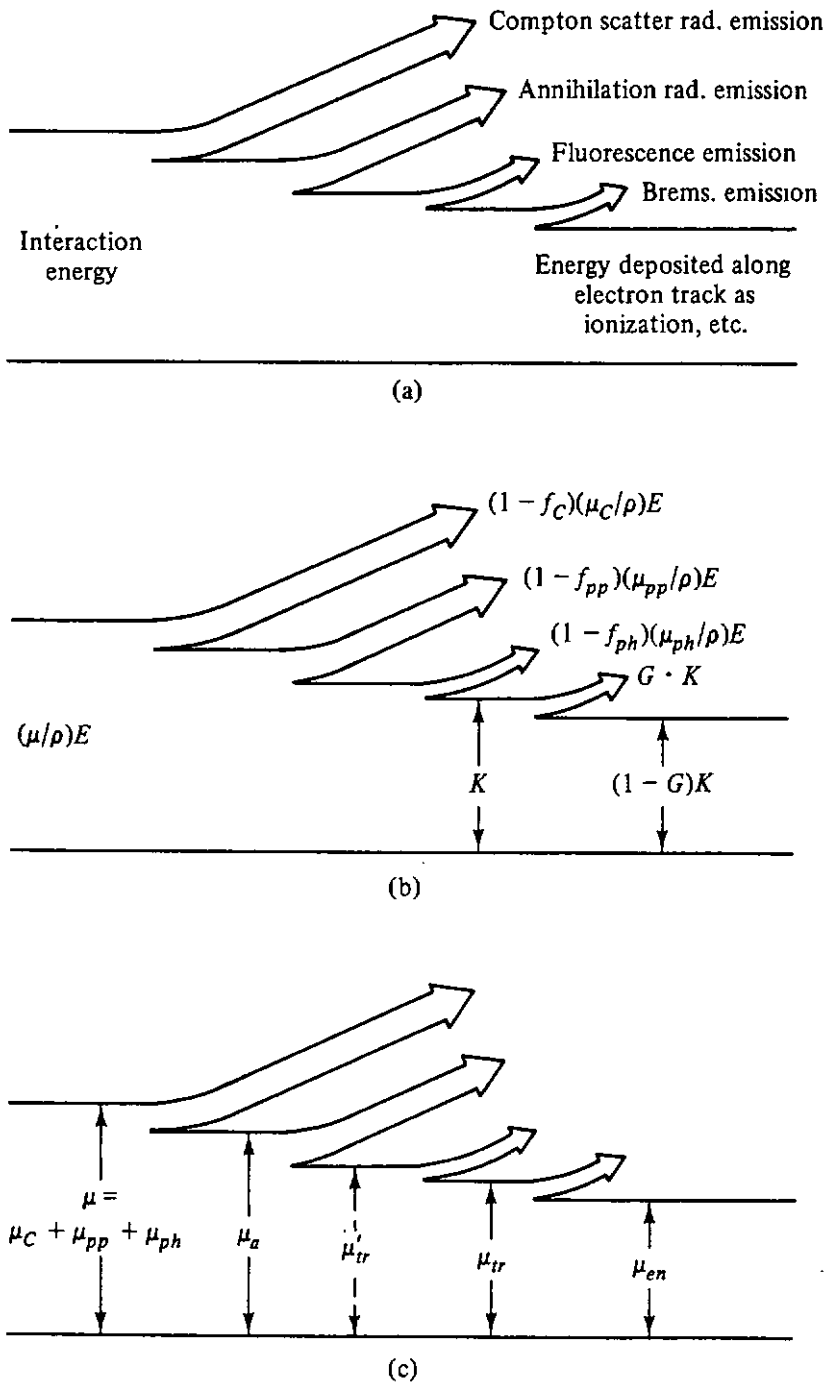

Figure 5.2 Relationships leading to definitions of various energy deposition coefficients for photons. (a) Energy deposition for photon energy involved in the interactions in an incremental volume of material. (b) Formulas for the energy per unit mass of the material in the incremental volume, corresponding to the various energy increments in (a). (c) Linear coefficients defined by their proportionality to the mass energy relationships in diagrams (a) and (b).

5.4.2 Photon Kerma, Absorbed Dose, and Dose Equivalent Rates

The response function for photon detectors of the energy deposition type is easily seen from Eq. (5.15) to be

$$\mathcal{R}(E) = E\left(\frac{\mu_d(E)}{\rho}\right), \tag{5.21}$$

where the proper mass energy deposition coefficient $\mu_d(E)$ to be used depends on exactly which detector response is to be determined, and possibly on other related matters to be discussed later (see Section 5.5).

If ϵ in Eq. (5.16) denotes the average initial kinetic energy of the secondary charged particles (electrons) from photon interactions in the incremental volume, then μ_d is identified as μ_{tr}. With the use of the mass transfer coefficient in Eq. (5.15), the response becomes the photon kerma.

Provided electronic equilibrium exists and there is no bremsstrahlung to remove energy through further photon emission from the secondary charged particles, the photon kerma rate is also a good measure of the absorbed dose rate. This equality between kerma rate and absorbed dose rate for photons is not as nearly universal as it is in the case of neutrons, because the range of the secondary charged particles (electrons) in the photon case may be rather large. In such a case, electronic equilibrium is much more likely to be a poor assumption. Similar considerations relate to the presence of the bremsstrahlung effect; under usual conditions, the secondary electrons arising from photon interactions may be of an energy leading to high secondary-photon yields, especially in high-Z material; but for the secondary heavy particles from neutron interactions, the bremsstrahlung photon yield is negligible.

Under conditions in which kerma rate is not a good approximation for the absorbed dose rate, accurate predictions require taking into account the transport of the secondary charged particles and the production of bremsstrahlung. The production of bremsstrahlung can be taken into account by the substitution in Eq. (5.15) of μ_{en}/ρ for μ_{tr}/ρ as the mass energy deposition coefficient. Such a substitution is easy and should be done generally. In case electronic equilibrium does not exist, at least to a close approximation, there is no way around inclusion of secondary-electron transport in the calculation, a process that compounds the difficulties inherent in analyzing the radiation field and is rarely undertaken if avoidable.

Since the quality factor for electrons is always taken as unity (Section 2.4), the dose equivalent for photon interactions is always numerically given by the absorbed dose, provided that the units are consistent.

The following formulas summarize the response functions, expressed in standard units, for an idealized photon detector. The kerma rate response function, in units of Gy cm^2, is

$$\mathcal{R}_K(E) = 1.602 \times 10^{-10} E\left(\frac{\mu_{tr}(E)}{\rho}\right). \tag{5.22}$$

Under the assumption of electronic equilibrium, the response function for the absorbed dose rate, in units of Gy cm^2, becomes

$$\mathcal{R}_D(E) = 1.602 \times 10^{-10} E\left(\frac{\mu_{en}(E)}{\rho}\right). \tag{5.23}$$

Finally, the response function for the dose equivalent rate, in units of Sv cm^2, is numerically the same as the response function for the absorbed dose rate, in

units of Gy cm^2; so that, in the units prescribed,

$$\mathcal{R}_H(E) = \mathcal{R}_D(E). \tag{5.24}$$

In the formulas above, the unit of E is MeV. In order for the response functions given above to yield a proper result for the detector response when the functions are folded into the flux density, the latter must be expressed in units of cm^{-2} s^{-1}. Units of μ_{tr}/ρ and μ_{en}/ρ are cm^2 g^{-1}.

5.4.3 Photon Exposure Rate

The photon exposure is defined in terms of the electric charge (of either sign) able to be created in air as a result of the interactions in a unit mass of air. The factor W, which gives the energy deposited per ion created, is the connecting link between exposure and the energy deposition per unit mass, $\mathcal{G}$; and, because air is the medium of concern, the subscript i in Eq. (5.9) when used for this purpose must relate to air. Thus, the energy deposition coefficient to be used with Eq. (5.21) must be for air only. (The ΔV in such cases represents conceptually the sensitive volume of an air detector lined with a wall of an air-like substance and embedded in whatever medium the photon exposure field is being determined.) The coefficient to be used should be that related to the kinetic energy of the secondary particles in air, reduced by a factor which takes into account the fact that some of the kinetic energy may be taken away by bremsstrahlung rather than by causing ionization. This coefficient is μ_{en}/ρ.

Fortunately, W is practically constant with respect to electron energy; and it has a value in air estimated at 33.85 eV per ion pair [9]. By this means, the exposure rate can be obtained from the formulas given by Eqs. (5.15) and (5.16), with the use of necessary units conversions and the fundamental definition of the exposure unit of the roentgen (see Section 2.3):

$$\dot{X} = \int_E \mathcal{R}_X(E)\phi(E)\,dE, \tag{5.25}$$

in which the response function, in units R cm^2, becomes

$$\begin{aligned}\mathcal{R}_X(E) = {} & \frac{10^4 \text{ R kg}}{2.58 \text{ C}} \times \frac{1.602 \times 10^{-19} \text{ C}}{\text{ion}} \times \frac{10^6 \text{ ions}}{33.85 \text{ MeV}} \times \frac{10^3 \text{ g}}{\text{kg}} \\ & \times E\left(\frac{\mu_{en}(E)}{\rho}\right)_{air}\end{aligned} \tag{5.26}$$

$$= 1.835 \times 10^{-8}\, E\left(\frac{\mu_{en}(E)}{\rho}\right)_{air} \tag{5.27}$$

This formula requires that E be given in MeV, the mass energy absorption coefficient given in cm^2 g^{-1}, and the flux density spectrum expressed in cm^{-2} s^{-1} MeV^{-1}. In case the flux density spectrum is given in terms of cm^{-2} s^{-1} MeV^{-1} and the exposure rate is desired in R h^{-1}, as is common, the numerical factor above should be multiplied by 3600, to give 6.606×10^{-5}; and the units for $\mathcal{R}_X$ would be changed to R cm^2 s h^{-1}.

5.4.4 Selection of Proper Mass Energy Deposition Coefficients

In spite of the specificity of the energy deposition coefficients given in the formulas of the preceding section, there are frequent occasions in which other selections may be better. *The formulas above are valid provided that the flux density is known exactly.* On the other hand, many analyses of the flux density are carried out on somewhat less exact assumptions than those presumed for the purpose of these formulas.

Figure 5.2 indicates the following photon emission processes which may remove energy from an incremental volume element in which the interactions occur (these photon emissions of course contributing to the overall photon field):

1. Emission of Compton scattered photons
2. Annihilation radiation following pair production
3. Fluorescence radiation
4. Bremsstrahlung

Very often shielding analysts will neglect the less important processes, lower on the list, in their analysis of the photon flux density field at the locations of dosimetric interest. In such cases, this is equivalent to making an approximation that the neglected emission photons are either negligible in number or so weak that they may be considered to be absorbed and deposit their energy at the site of the original interaction.

It has been found that, in case an approximation of this sort has been made, the type of mass coefficient best suited for determining the dose rate response is one that is consistent with the approximation made in the flux density determination [7]. One way to rationalize this rule is as follows. If the approximation used is such as to neglect photon emissions from certain reactions, the calculated flux density at most points will be underestimated. However, the value of μ_a consistent with such an approximation, when used to determine the response function, will be too high. This will thus give a response function which is a little high and, when combined with a flux density which is a little too low, may provide a fairly accurate answer by the principle of "compensating errors." Figure 5.2 is very useful in identifying the proper energy deposition coefficient to use.

In particular, it is usual with current methods in a photon transport calculation for the shield to account only for photons resulting from both Compton scattering and annihilation radiation, implying that fluorescence radiation and bremsstrahlung radiation, if they exist, are absorbed locally. In such case, the coefficient μ'_{tr}/ρ should be used in the response function formulas such as given by Eqs. (5.22) to (5.27).[5] Older calculations have often ignored everything except

[5]If the fluorescence radiation is negligible, μ_{tr} could be reasonably used here since the distinction between μ'_{tr} and μ_{tr} is correspondingly negligible.

the Compton scattering for determining the flux density field, and under such circumstances the use of μ_a/ρ for any and all mass energy deposition coefficients is more proper [10].

5.5 RESPONSE FUNCTIONS FOR EVALUATION OF HAZARDS TO HUMAN BEINGS

Since radiation shielding is widely used for the protection of persons, the detector responses of particular interest are those related to radiation hazards to people. In order to use any of the response functions thus far discussed in computing the detector response ("dose") by Eq. (5.5), it is necessary for the shielding analyst to determine the flux density energy spectrum at every point where the risk is to be evaluated. It has been the custom, especially for photons, to compute the detector response from the *free-field* flux density, that is, in a radiation field uninfluenced by the actual presence of a human body or any approximation to it. Thus, it is still common to study the hazards of a photon field in terms of free-field values of the exposure rate, air kerma rate, or tissue kerma rate.

Nonetheless, it would appear more proper to establish the risk to a human being at some point in a radiation field by assuming that a human body, or a reasonable semblance of one, is present at the position being evaluated. The detector response then should be that obtained at some critical point or points within such a body, and clearly the best suited type of detector response is the dose equivalent.

Unfortunately, the determination of dose equivalent inside the human body, or even a simplified representation of the body (called a *phantom*), greatly complicates the problem of the shielding analyst. First, the total flux density and its spectral distribution (as perturbed by the presence of the body) must be obtained at each critical point within the body or phantom. Next, one must consider the validity of the assumption regarding the equality of absorbed dose and kerma, so that Eqs. (5.23) and (5.24) can be used in the case of photons or Table A3.12 can be used in the case of neutrons. If this assumption is not clearly valid in any specific case, at least to a good approximation, the analyst must follow the transport of the secondary charged particles to see where they dissipate their kinetic energy. Finally, one must select a value for the average quality factor (thereby requiring, possibly, a detailed knowledge of the charged particle spectrum at each point of interest) in order to convert the absorbed dose to dose equivalent.

Fortunately for the shielding analyst, the foregoing process can be avoided by using an approximate procedure which, although it involves the concept of finding the dose equivalent in the human body or a phantom, is much simpler and gives results which only mildly compromise the accuracy of the hazard determination (and even so almost always on the safe side). This simplified procedure uses a phantom response function which, if folded into the *free-field*

flux density spectrum, gives a reasonable estimate of the dose equivalent values at the critical point or points inside the body. Since the free-field data are much easier to obtain than the radiation field inside the actual body, the phantom response function permits a straightforward use of Eq. (5.5) to determine the dose equivalent in the body.

Phantoms of the following types have been studied to provide information of the interaction of both neutrons and photons with idealizations of the human body:

1. A 30-cm slab, laterally infinite, of a homogeneous mixture approximating tissue
2. A cylinder 30 cm in diameter and 60 cm in height composed of a simulated homogenized tissue mixture
3. A 30-cm sphere of a homogenized mixture approximating tissue

The following is a brief explanation of the procedure, somewhat idealized, used for obtaining the phantom response function desired whatever phantom is selected. A broad, parallel, monoenergetic beam of the type of particles under consideration is assumed to be directed on the phantom, usually in a direction that provides the largest values of the response function. At each point in the phantom, absorbed-dose, usually approximated by kerma, values are determined. In this determination, contributions by all secondary charged particles at that position are taken into account; and for each type of charged particle of a given energy the L_∞ value in water and, therefrom, Q are obtained (see Table 2.1). These are then applied to the absorbed-dose contribution from each charged particle to obtain the dose equivalent contribution at the given location. The resulting distribution of absorbed dose and dose equivalent throughout the phantom are then compared, with a view to obtaining that value which is the maximum or otherwise considered to be in the most significant location. The *phantom response function* is then that value of either absorbed dose or dose equivalent divided by the free-field fluence of the incident beam postulated. The ratio of the dose equivalent at the point of greatest significance to the absorbed dose at that point is called the *effective quality factor* (Q_{eff}).[6]

From studies on slab and cylindrical phantoms, several organizations, whose recommendations are highly regarded, have provided such response functions. Prominent among these organizations are the National Council on Radiation Protection and Measurements (NCRP) [11] in the United States, the International Commission on Radiological Protection (ICRP) [12], and the

[6]The data for the phantom rseponse function for absorbed dose and for the effective quality factor are actually of little direct interest to the shielding analyst. However, information on these are given in Table 5.2 to show the reader the intermediate values in the determination of the phantom dose equivalent. Of particular interest is the variation of effective quality factor with neutron energy.

TABLE 5.2 Neutron Response Functional Data for Maximum Absorbed Dose in a Phantom and Corresponding Values of the Effective Quality Factor[a]

Neutron Energy (MeV)	$\mathcal{R}_{D_p}$ (cGy cm^2)	Q_{eff}
2.5(−08)[b]	0.5(−09)	2.3
1.0(−07)	0.6(−09)	2
1.0(−06)	0.6(−09)	2
1.0(−05)	0.6(−09)	2
1.0(−04)	0.6(−09)	2
1.0(−03)	0.5(−09)	2
1.0(−02)	0.5(−09)	2
1.0(−01)	0.8(−09)	7.4
5.0(−01)	1.8(−09)	11.
1.0	3.1(−09)	10.6
2.0	4.3(−09)	9.3
5.0	5.3(−09)	7.8
10.0	6.0(−09)	6.8
20.0	7.2(−09)	6.0
50.0	9.2(−09)	5.0

[a]Prescribed by the ICRP [12].
[b]Read as 2.5×10^{-8}, etc.

American National Standards Institute (ANSI) [13]. Phantom-related response functions provided by these organizations are listed in Tables 5.3 and 5.4.

The maximum value of the dose equivalent in a 30-cm-diameter spherical phantom irradiated with broad, unidirectional, and monoenergetic beams of neutrons or photons has also been studied [14–17]. This maximum dose equivalent is called the *dose equivalent index* as defined by the International Commission on Radiation Units and Measurements (ICRU) [5]. The results of these investigations, summarized in Tables 5.5 and 5.6, provide an alternative for the phantom response function.[7]

Other phantom-related concepts may be used in principle. For example, the ICRP [18] has defined a quantity called the *effective dose equivalent*, which is the weighted sum of the dose equivalent values to several specific organs or tissues of the human body.[8] The application of this concept in some sort of

[7]A common term formerly used by shielding specialists for this type of quantity was *multicollision dose*. This term, however, is now considered unacceptably vague. The term MADE, an acronym for *ma*ximum *d*ose *e*quivalent, has also been used to a limited extent.

[8]The precise definition is given by $H_E = \sum_i w_i H_i$, where H_i is the dose equivalent for the ith organ or tissue and w_i, the weight factor, is assigned the following values: 0.25 for gonads, 0.15 for breast, 0.12 for red bone marrow, 0.12 for lung, 0.03 for thyroid, 0.03 for bone surface, and 0.06 for each of the five remaining organs or tissues receiving the highest dose equivalents.

TABLE 5.3 ANSI-Prescribed Photon Response Functional Data for the Phantom-Related Dose Equivalent

Photon Energy (MeV)	$\mathcal{R}_{H_p}$ (cSv cm^2)
0.1	7.86(−11)[a]
0.15	1.05(−10)
0.2	1.39(−10)
0.25	1.75(−10)
0.3	2.11(−10)
0.35	2.44(−10)
0.4	2.74(−10)
0.45	3.00(−10)
0.5	3.25(−10)
0.55	3.53(−10)
0.6	3.78(−10)
0.65	4.00(−10)
0.7	4.22(−10)
0.8	4.67(−10)
1.0	5.50(−10)
1.4	6.97(−10)
1.8	8.31(−10)
2.2	9.50(−10)
2.6	1.06(−09)
2.8	1.11(−09)
3.25	1.23(−09)
3.75	1.34(−09)
4.25	1.45(−09)
4.75	1.56(−09)
5.0	1.61(−09)
5.25	1.67(−09)
5.75	1.77(−09)
6.25	1.87(−09)
6.75	1.98(−09)
7.5	2.13(−09)
9.0	2.44(−09)
11.0	2.86(−09)
13.0	3.28(−09)
15.0	3.69(−09)

[a]Read as 7.86×10^{-11}, etc.

Source: *Ref. 13.*

detailed anthropomorphic phantom under conservatively selected field conditions can be used to relate the effective dose equivalent rate to the flux density of the incident beam, and this relationship establishes the phantom response function. Response functions related to specific organs in an anthropomorphic phantom are sometimes useful. Still other body- or phantom-related dosimetric

TABLE 5.4 Prescribed Neutron Response Functional Data for the Phantom-Related Dose Equivalent

Neutron Energy (MeV)	$\mathcal{R}_{H_p}$ (cSv cm^2)		
	NCRP	ICRP	ANSI
2.5(−08)[a]	1.02(−09)	1.07(−09)	1.02(−09)
1.0(−07)	1.02(−09)	1.16(−09)	1.02(−09)
1.0(−06)	1.24(−09)	1.26(−09)	1.24(−09)
1.0(−05)	1.24(−09)	1.21(−09)	1.26(−09)
1.0(−04)	1.20(−09)	1.16(−09)	1.16(−09)
1.0(−03)	1.02(−09)	1.03(−09)	1.04(−09)
1.0(−02)	9.9(−10)	9.9(−10)	9.9(−10)
1.0(−01)	6.0(−09)	5.8(−09)	6.0(−09)
5.0(−01)	2.6(−08)	2.0(−08)	2.6(−08)
1.0	3.7(−08)	3.3(−08)	3.7(−08)
2.0	—	4.0(−08)	—
2.5	3.5(−08)	—	3.5−(08)
5.0	4.3(−08)	4.1(−08)	4.3(−08)
7.0	4.1(−08)	—	4.1(−08)
10.0	4.1(−08)	4.1(−08)	4.1(−08)
14.0	5.8(−08)	—	5.8(−08)
20.0	6.3(−08)	4.3(−08)	6.3(−08)
40.0	6.9(−08)	—	—
50.0	—	4.6(−08)	—
100.0	5.0(−08)	5.0(−08)	—

[a]Read as 2.5×10^{-8}, etc.

Source: *Refs. 11, 12, and 13.*

concepts may be established to determine yet other possible response functions relative to the free-field flux density.

The present situation is somewhat unsatisfactory, since a shielding analyst is left with the personal decision as to which of the several available choices for the phantom response function is most authoritative. Fortunately, those given in Tables 5.3 through 5.6 do not differ greatly for a given particle with specified energy. Moreover, the principles involved in using a phantom response function with the free-field flux density are unaffected by minor variations in the response functions themselves. If it is necessary to indicate which response function is utilized in a given situation, it would be appropriate to identify the authority or reference that prescribes the function.

To distinguish detector responses obtained by folding these body- or phantom-related response functions into the free-field flux density from the more primitive free-field dose equivalent concept discussed in Sections 5.3 and 5.4, we adopt the following convention. A dose equivalent response or "biological dose" resulting from the folding of phantom response functional data with

TABLE 5.5 Prescribed Photon Response Functional Data Based on Maximum Dose Equivalent in a 30-cm Sphere Under Parallel-Beam Conditions

Photon Energy (MeV)	$\mathfrak{R}_{H_p}$ (cSv-cm^2)
0.01	7.0 (−10)[a]
0.015	3.1 (−10)
0.02	1.78(−10)
0.03	9.0 (−11)
0.04	6.5 (−11)
0.05	5.3 (−11)
0.06	5.2 (−11)
0.08	5.5 (−11)
0.1	6.4 (−11)
0.15	9.8 (−11)
0.2	1.31(−10)
0.3	1.98(−10)
0.4	2.5 (−10)
0.5	3.1 (−10)
0.6	3.6 (−10)
0.8	4.6 (−10)
1.0	5.6 (−10)
1.5	7.4 (−10)
2.0	9.2 (−10)
3.0	1.20(−09)
4.0	1.42(−09)
5.0	1.62(−09)
6.0	1.83(−09)
8.0	2.2 (−09)
10.0	2.6 (−09)

[a]Read as 7.0×10^{-10}, etc.

Source: *Ref. 17.*

the free-field fluence[9] will be called in this text a *phantom-related dose equivalent*, H_p. If there is any need to specify which set of phantom response functions is used in a calculation of H_p, one must qualify the value by giving information on the phantom response function used, such as, for example, with the phrase "based on the ANSI-prescribed phantom response functions," or whatever.

There still remains some artificiality in the use of response functions based upon uniform-beam interaction with body-sized phantoms when the radiation field may be actually highly variable over a short distance or when the point in the field being investigated is so close to a solid object that a human body could

[9]In principle, *phantom-related tissue absorbed dose* is similarly established. However, for shielding analyses this concept is of much less importance.

TABLE 5.6 Prescribed Neutron Response Functional Data Based on Maximum Dose Equivalent in a 30-cm Sphere Under Parallel-Beam Conditions

Neutron Energy (MeV)	$\mathcal{R}_{H_p}$ (cSv-cm^2)
2.5(−08)[a]	9.5 (−10)
1.0(−06)	1.18(−09)
1.0(−05)	1.16(−09)
1.0(−04)	1.10(−09)
1.0(−03)	9.5 (−10)
1.0(−02)	9.5 (−10)
3.0(−02)	3.1 (−09)
6.0(−02)	6.0 (−09)
1.0(−01)	9.6 (−09)
3.0(−01)	1.10(−08)
5.0(−01)	2.4 (−08)
1.0	3.8 (−08)
2.5	3.4 (−08)
5.0	3.9 (−08)
7.5	4.1 (−08)
10.0	4.1 (−08)
14.0	5.2 (−08)
17.0	6.3 (−08)
20.0	6.5 (−08)

[a]Read as 2.5×10^{-8}, etc.

Source: *Refs. 14–16.*

not be placed there. The usual procedure is to ignore such conceptual difficulties and accept the artificiality of the calculations for the sake of simplification of the required analysis, in the belief that any realistic analysis would not be likely to improve the accuracy of the risk evaluation to an extent worth the additional effort involved.

5.6 CONCLUDING REMARKS

For most radiation protection purposes, the shielding specialist can hardly do better than to use one of the response functions for the prescribed dose equivalent given in Tables 5.3 through 5.6, both for neutrons and for photons. Tradition, however, has led to the popular use of the free-field exposure rate for photons as being adequate for practical purposes. Similarly, free-field kerma rate in a tissue-like detector is sometimes used for neutrons. For shield heating (see Chapter 11), the absorbed dose rate, or the kerma rate as an approximation, is

the appropriate response function for evaluating heat sources in shielding materials [3, 19].

Finally, it should not be forgotten that the proper response function to use is that related to the purpose of a measurement. The detector response more nearly correlated with radiation effects on materials would be the absorbed dose, but this is not universally true. Radiation effects on semiconductors, for example, are related to somewhat more complex physical phenomena than simply energy deposition or ionization. Approaches to treatments of such complexities are given in Chapter 11.

REFERENCES

1. S.-Y. Chen and A. B. Chilton, "Depth–Dose Relationships near the Skin Resulting from Parallel Beams of Fast Neutrons," *Radiat. Res.* **77**, 21–33 (1979).
2. "Neutron Dosimetry for Biology and Medicine," ICRU Report 26, International Commission on Radiation Units and Measurements, Washington, D.C., 1977.
3. A. Foderaro, L. J. Hoover, and J. H. Marable, "Heat Generation by Neutrons," in *Engineering Compendium on Radiation Shielding*, Vol. I., R. G. Jaeger (ed.), Springer-Verlag, New York, 1968, Sec. 7.2.
4. R. S. Caswell and J. J. Coyne, "Kerma Factors for Neutron Energies below 30 MeV," *Radiat. Res.* **83**, 217–254 (1980).
5. "Radiation Quantities and Units," ICRU Report 33, International Commission on Radiation Units and Measurements, Washington, D.C., 1980.
6. "Recommendations of the International Commission on Radiological Protection, Protection against Ionizing Radiation from External Sources," ICRP Publication 15, International Commission on Radiological Protection, Pergamon, Elmsford, N.Y., 1970.
7. J. H. Hubbel and M. J. Berger, "Attenuation Coefficients, Energy Absorption Coefficients, and Related Quantities," in *Engineering Compendium on Radiation Shielding*, Vol. I., R. G. Jaeger (ed.), Springer-Verlag, New York, 1968, Sec. 4.1.
8. E. E. Morris, A. B. Chilton, and A. F. Vetter, "Tabulation and Empirical Representation of Infinite-Medium Gamma-Ray Buildup Factors for Monoenergetic, Point Isotropic Sources in Water, Aluminum, and Concrete," *Nucl. Sci. Eng.* **56**, 171–178 (1975).
9. "Average Energy Required to Produce an Ion Pair," ICRU Report 31, International Commission on Radiation Units and Measurements, Washington, D.C., 1979.
10. H. Goldstein and J. E. Wilkins, Jr., "Calculations of the Penetration of Gamma Rays," NDA/AEC Report NYO-3075, U.S. Government Printing Office, Washington, D.C., 1954.
11. "Protection against Neutron Radiation," NCRP Report 38, National Council on Radiation Protection and Measurements, Washington, D.C., 1971.
12. "Data for Protection against Ionizing Radiation from External Sources: Supple-

ment to ICRP Publication 15," ICRP Publication 21, International Commission on Radiological Protection, Pergamon, Elmsford, N.Y., 1973.

13. "Neutron and Gamma-Ray Flux-to-Dose-Rate Factors," ANSI/ANS-6.1.1-1977 (N666), American National Standards Institute, New York, 1977.
14. S.-Y. Chen and A. B. Chilton, "Calculation of Fast Neutron Depth–Dose in the ICRU Standard Tissue Phantom and the Derivation of Neutron Fluence-to-Dose-Index Conversion Factors," *Radiat. Res.* **78**, 335–370 (1979).
15. A. B. Chilton and Y.-L. Shiue, "Progress Report on Studies Concerning Doses in the ICRU Sphere Resulting from Neutron Beams," Proc. 4th Symp. Neutron Dosimetry, Munich/Neuherberg, June 1-5, 1981, Comm. Eur. Comm., Luxembourg, EUR 7448 EN, Vol. 1, 1981.
16. Y.-L. Shiue and A. B. Chilton, "Calculation of Low-Energy Dose Indices and Depth Doses in the ICRU Tissue Sphere," *Radiat. Res.* **93**, 421–443 (1983).
17. P. J. Dimbylow and T. M. Francis, "A Calculation of the Photon Depth Dose Distributions in the ICRU Sphere for a Broad Parallel Beam, a Point Source, and an Isotropic Field," Report NRPB-R92, National Radiation Protection Board, UKAEA Harwell, Oxfordshire, England, 1979.
18. "Recommendations of the International Commission on Radiological Protection," ICRP Publication 26; published as Annals of the ICRP **1**, No. 3, Pergamon, Elmsford, N.Y., 1977.
19. A. B. Chilton, "Methods for Calculating Radiation-Induced Heat Generation," *Nucl. Eng. Des.* **18**, 401–413 (1972).

PROBLEMS

5.1. Consider the bombardment of a slab of material (bounded by vacuum) by a beam of photons or neutrons. Make a sketch showing qualitatively the ratio of the absorbed dose rate to the kerma rate as a function of depth of penetration into the slab along the direction of the beam. Explain the features of the sketch.

5.2. On the assumption of isotropic scattering in the center-of-mass system, estimate the response function for 0.1-MeV neutrons, where the dosimetric quantity of interest is the kerma rate in water. How does this compare with the corresponding value for tissue given in Table A3.12? Take scattering cross sections for H at this energy to be 12.8 b and for 0 to be 3.5 b. (Only elastic scattering is involved.)

5.3. A small volume of tissue acting as a detector is located in a beam of 1-MeV neutrons which provides a fluence of 10^{13} cm^{-2}. Compute the kerma using the tissue composition of Table A3.12. Then compute the kerma using the response function of the same table. If the same fluence were incident on a phantom (of the type assumed in Table 5.2) in a broad, parallel-beam situation, what would be the maximum value of the absorbed dose in grays? How do you account for the differences among these three answers? [*Note:* The scattering cross sections (elastic) for 1-MeV neutrons are to be taken as 4.3 b for H, 2.6 b for C, 2.0 b for N, and 8 b for O.]

5.4. (a) Plot two curves on log-log paper, one for the neutron tissue kerma per unit fluence and the other for the neutron phantom-related dose equivalent per unit fluence based on the ANSI prescribed response functions. What two principal factors account for the difference between the two curves? Cover the range 0.001 to 2 MeV.

(b) Make a similar plot for photons, assuming that tissue and water have similar characteristics. What accounts for the difference in this case?

5.5. For a fluence of 10^{10} cm^{-2} of 1-MeV photons, evaluate the following:

(a) $X(R)$

(b) K(Gy) in air

(c) K(Gy) in aluminum

(d) K(Gy) in lead

5.6. For a fluence of 10^{10} cm^{-2}, evaluate the following:

(a) K(Gy) for 1-MeV photons in tissue

(b) K(Gy) for 1-MeV neutrons in tissue

(c) H(Sv) for 1-MeV photons

(d) H_p(Sv) for 1-MeV neutrons

5.7. At a certain location, the exposure rate due to 1-MeV photons is 100 R h^{-1}. With the same flux density of 1-MeV photons, what would be the absorbed dose rate in concrete (Gy h^{-1})? State any assumptions made.

5.8. Select at least 10 energies from the first column of Table 5.5. For each of these selected energies, calculate the response function for exposure, in units of R cm^2. From these data, and Table 5.5, determine the ratio of the maximum dose equivalent in a sphere to the free-field exposure under parallel-beam conditions. This ratio is sometimes called C_x and is a function of photon energy. Plot C_x in units of cSv R^{-1} as a function of energy for the range 0.01 to 10 MeV.

5.9. Table 6.2 lists for various radionuclides values of the specific gamma-ray constant, which may be defined as the exposure rate in vacuum at unit distance from a point isotropic source of unit strength. Using data from Appendix 5, verify the table entries for ^{60}Co and ^{137}Cs-^{137m}Ba.

5.10. Using data of Appendix 3 and methods of Chapter 3, compute and plot values of f_C, f_{pp}, and f_{ph} versus the logarithm of photon energy for photon interactions with lead over the energy range 0.01 to 3 MeV. Discuss how the appearance of the graph would change if interactions were with a material of much lower atomic mass. [See Prob. 3.10.]

5.11. A "rule of thumb" for exposure from point sources of photons in air at distances over which exponential attenuation is negligible is as follows:

$$\dot{X} = \frac{6CEN}{r^2},$$

where C is the source strength (Ci), E is the photon energy (MeV), N is the number of photons per disintegration, r is the distance in feet from the source, and $\dot{X}$ is the exposure rate (R h^{-1}).

(a) Reexpress this rule in units of Bq for the source strength and meters for the distance.

(b) Over what range of energies is this rule precise within $\pm 10\%$; $\pm 5\%$?

5.12. **(a)** For at least six neutron energies between 0.01 and 10 MeV, calculate the ratio of the ICRP-prescribed phantom-related absorbed-dose response function (Table 5.2) to the tissue kerma response function (Table A3.12). Draw a graph of the resulting ratio as a function of neutron energy. (As a check, this can be compared with Fig. 15 of the National Bureau of Standards Handbook 63.)

(b) For at least a dozen energies between 2.5×10^{-8} and 50 MeV, calculate the ratio of the ICRP-prescribed phantom-related dose equivalent response function (Table 5.4) to the ICRP-prescribed phantom-related absorbed dose response function (Table 5.2). Draw a graph of the resulting ratio as a function of neutron energy. (As a check, this can be compared with the values for Q_{eff} given in the last column of Table 5.2.)

6 basic concepts in neutral particle penetration

6.1 UNCOLLIDED-PARTICLE ATTENUATION AND MEAN FREE PATH

Consider a uniform, isotropic medium of infinite extent as depicted in Fig. 6.1. A particle[1] at the origin is to be visualized as traveling in the x direction. The probability of it reaching a distance x from the origin without interaction is called $P(x)$; and the probability of it reaching the distance $x + dx$ without interaction is $P(x + dx)$. The probability of it reaching $x + dx$ without interaction is also the product of the probability of it reaching x without interaction multiplied by the conditional probability that if it has reached this distance it will successfully travel the additional distance dx without interaction. As pointed out in Chapter 3, the probability of an interaction in the distance dx is $\mu\, dx$, so that the probability of *not* having an interaction is $(1 - \mu\, dx)$. Thus, it is seen that

$$P(x + dx) = P(x)(1 - \mu\, dx). \tag{6.1}$$

This gives the differential equation

$$\frac{dP(x)}{dx} = -\mu P(x), \tag{6.2}$$

which, with the boundary value that $P(0) = 1$, has the solution

$$P(x) = e^{-\mu x}. \tag{6.3}$$

[1]This chapter applies to the attenuation of photons, neutrons, or any particle for which Eq. (6.3) is obeyed.

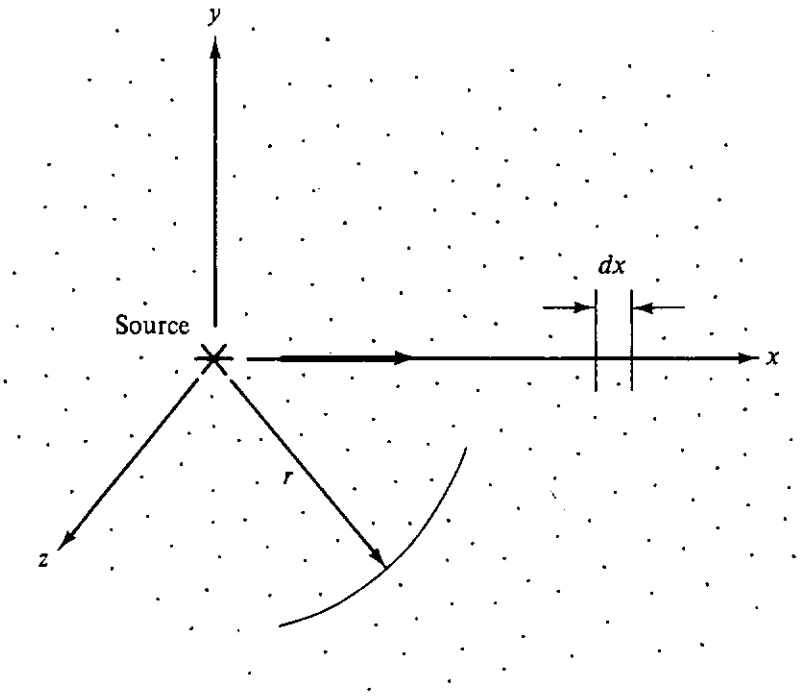

Figure 6.1 Source at the origin of coordinates emitting a particle in the x direction. This may also be considered to illustrate a point isotropic source in an infinite homogeneous medium.

If a monoenergetic parallel beam of particles passes through the y-z plane in the x direction, as shown in Fig. 6.2, the number reaching the distance x without interaction is then $e^{-\mu x}$ times the number of the original particles at $x = 0$. If the flux density of uncollided particles in the beam is $\phi^0(x)$,

$$\phi^0(x) = \phi^0(0)e^{-\mu x}. \tag{6.4}$$

Also, if x is taken as the thickness of a slab shield of uniform composition, as shown in Fig. 6.3, the flux density penetrating the slab is related to the flux den-

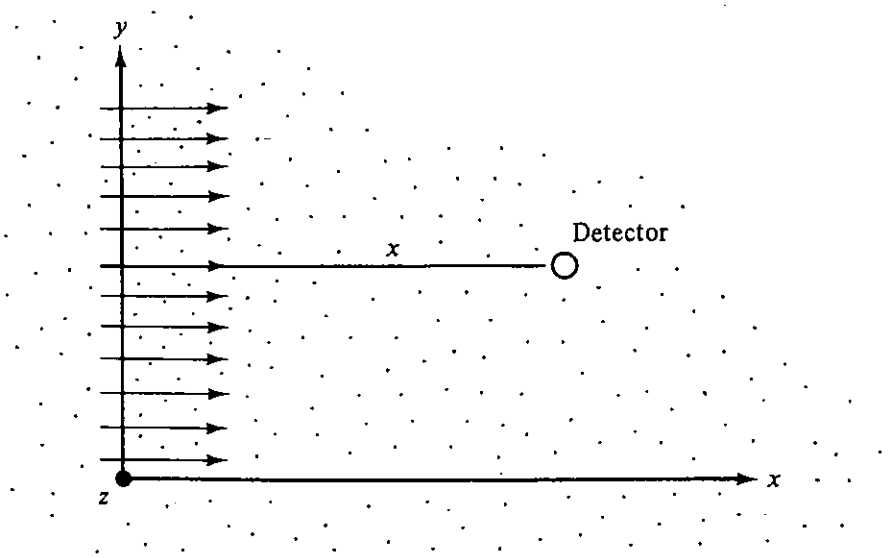

Figure 6.2 Parallel, monoenergetic beam of photons emitted from the y-z plane into the x direction.

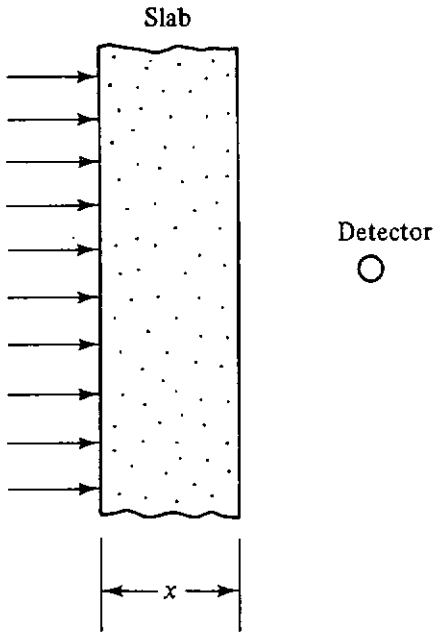

Figure 6.3 Broad, parallel, monoenergetic beam of particles incident normally on the front face of a laterally infinite slab.

sity of a beam normally incident on the slab by the same Eq. (6.4), as is easily seen.

The usual way of determining the particle attenuation coefficient μ is by means of a "narrow-beam" experiment with a setup similar to that in Fig. 6.4. (An early name for μ was the "narrow-beam coefficient.") The arrangement is such that any interaction, whether absorption or scattering, would remove a particle from any appreciable chance of detection. The probability of a particle having a path length between x and $x + dx$ is given by use of Eqs. (6.1) and (6.3) as $P(x) - P(x + dx)$, which equals $\mu e^{-\mu x}\, dx$. Thus, the mean distance traveled by a particle in an infinite uniform medium is

$$x_m = \int_0^\infty x\mu e^{-\mu x}\, dx = \mu^{-1}. \tag{6.5}$$

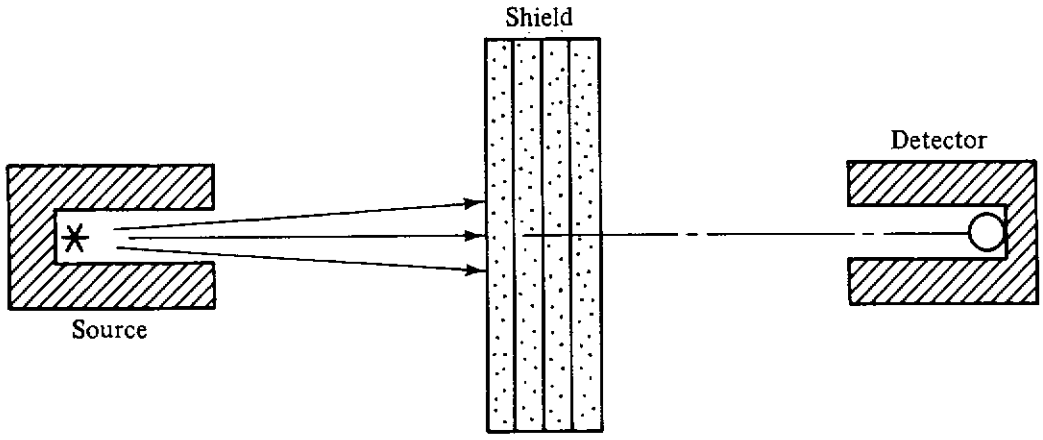

Figure 6.4 Essential elements of an experiment for obtaining the value of the attenuation coefficient ("narrow-beam coefficient") for monoenergetically emitted particles. The collimation in a valid experiment is actually much narrower than presented in this figure, exaggerated for the sake of clarity. The shield thickness is variable by insertion of thin slabs of varying number or thickness into the beam.

This is then the mean length of the path of a particle from a point where it is known to exist to the point where it has its next interaction; and it is commonly called the *mean-free-path length*, abbreviated mfp. The mfp is often a convenient unit of length in the study of photon and neutron transport. Thus, the distance x in ordinary units can be converted into the dimensionless distance μx, the number of "mean-free-path lengths."

Figure 6.5 is a plot of the uncollided flux density for a beam of monoenergetic particles passing from the y-z plane in the x direction. On the semilogarithmic basis shown, the plot becomes a straight line according to Eq. (6.4), with a slope of $-\mu$. At a distance of one mfp from the $x = 0$ plane, it is easily seen that the uncollided flux density is $\phi^0(0)/e$. The mean-free-path length is easily read from the graph as indicated.

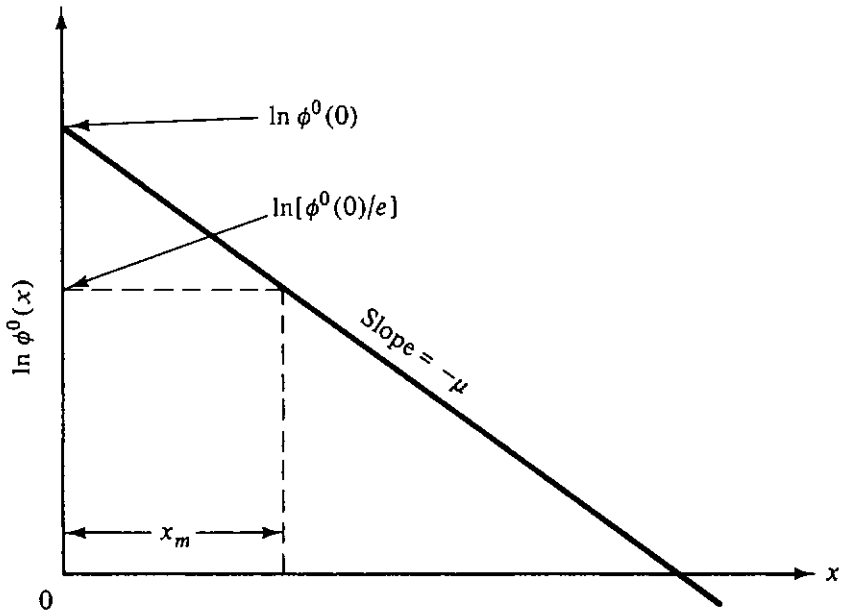

Figure 6.5 Plot of the uncollided particle flux density for a parallel, monoenergetic beam of particles emitted from the y-z plane into the x direction. The scale for the flux density is logarithmic.

If in Fig. 6.1 one visualizes an isotropic point source of monoenergetic particles at the origin, of strength S_p per unit time, the flux density of uncollided particles at some distance r from the source would be the number that would pass through a unit surface area of the sphere of radius r multiplied by the probability per particle of reaching that distance. Thus, in this situation,

$$\phi^0(r) = \frac{S_p}{4\pi r^2} e^{-\mu r}. \tag{6.6}$$

A graph of ln $[r^2\phi^0(r)]$ as a function of r would be just the same as the plot in Fig. 6.5, namely, a straight line with slope $-\mu$.

If one multiplies Eqs. (6.4) and (6.6) by $\mathfrak{R}$, the detector response function at the particle energy, one obtains formulas for R^0, the response of a rate-type

detector sensitive only to uncollided particles or, in general, that portion of a detector response occasioned by the uncollided flux density. For the parallel-beam case,

$$R^0(x) = R_0 e^{-\mu x}, \tag{6.7}$$

where

$$R_0 \equiv R^0(0) = \mathcal{R}\phi^0(0). \tag{6.8}$$

For the point-source case,

$$R^0(r) = \frac{R_1}{r^2} e^{-\mu r}, \tag{6.9}$$

where

$$R_1 \equiv \frac{\mathcal{R}S_p}{4\pi}, \tag{6.10}$$

the detector response at one unit of distance from the source with no attenuating medium present.

The exponential factor in the foregoing equations is slightly complicated if the medium is not homogeneous; that is, μ is no longer a constant but depends on x. If $\mu \equiv \mu(x)$ in Eq. (6.2), the solution to the differential equation becomes

$$P(x) = \exp\left[-\int_0^x \mu(x')\,dx'\right]. \tag{6.11}$$

Thus, the attenuation equations derived for the homogeneous-medium case can be used for the heterogeneous-medium case if μx is replaced by the integral expression given in Eq. (6.11). In the case in which the changes in μ are for discrete laminations or segments of the medium rather than being continuous, the following equivalent replacement is valid:

$$\mu x \longrightarrow \sum_i \mu_i x_i.$$

where the sum represents the total distance in mean-free-path lengths. The distance, in total mean-free-path lengths, is sometimes called the "optical path length," from a similar concept of long standing in the field of optics.

6.2 TOTAL DETECTOR RESPONSE

In the presence of shielding material, the interactions of particles with the medium usually include scattering interactions (and other particle-emitting interactions), which do not absorb all the particle energy but may divert the particle's direction with a loss of some of its energy. In most practical situations, the narrow-beam conditions noted above do not prevail, and it is possible for some of the collided or secondary particles to be scattered or emitted in a direction toward an uncollimated detector. Therefore, in addition to responding to uncollided particles, most detectors will also respond to the so-called "in-scat-

tered" particles. Thus, the total detector response is greater than the response to uncollided particles only.[2]

Figure 6.6 shows, on a semilogarithmic plot, how the total response of a detector might typically vary with respect to distance from a plane source emitting a parallel beam of particles in the x direction in an infinite, homogeneous medium, as illustrated in Fig. 6.2. The response to the uncollided particles is included for comparison purposes; and it is clear from Eq. (6.7) that this is a straight line with slope $-\mu$ on the semilogarithmic plot. Figure 6.7 is a similar plot for the case of a point source in an infinite, homogeneous medium. In this case, the ordinate value plotted is r^2 times the detector response; and again, according to Eq. (6.9), this makes the response to the uncollided particles a straight line with slope $-\mu$. Figures 6.6 and 6.7 look very similar, except that the latter (the point-source case) exhibits a much more pronounced hump in the total response curve near the source, a behavior that is quite common.

It will be noted that in both Figs. 6.6 and 6.7, a length λ_1 is marked off representing the distance from the origin it takes to diminish the value $R(x)$ or $r^2R(r)$ by a factor of e ($= 2.718\ldots$). λ_2 is an additional distance required to diminish the ordinate value by another factor of e. This process can continue indefinitely. In general, λ, called the *relaxation length*, is the additional distance away from the source, starting from any point, required to reduce the detector response (or r^2 times the detector response in the case of a point source[3]) by a factor of e. It is most useful at those distances where the total response line is close to being straight on a semilogarithmic plot and at which λ becomes almost constant.

It should be noted that, whereas the mean-free-path value is separately and precisely established for each separate value of particle energy, the relaxation-length concept does not necessarily require a monoenergetic source.[4] Similarly, it is apparent that different source spectra, differing shield and source configurations, and different detector response functions will usually lead to somewhat different relaxation-length values.

"Layer" concepts, which are similar to the relaxation-length concept, have been defined, generally within the context of a finite shield such as that depicted in Fig. 6.3. The *half-value layer* (or *half-thickness*) is the thickness of that additional layer of shield required to reduce the detector response by a factor of 2. Similarly, a *tenth-value layer* is the additional thickness needed to

[2]Of course, it is possible to have a type of detector biased in some electronic fashion not to accept pulsed responses except of a size given by the uncollided particles. In such a case the total and uncollided responses are the same.

[3]Although rarely used, the term "effective relaxation length" denotes a distance required to reduce $R(r)$ by a factor of e in the point-source case [1].

[4]One unfortunate result of the close correspondence between the relaxation length and the mean free path is that they are often confused. The concepts are distinct in meaning, although closely related; and the values are not the same except for very unusual circumstances, as, for example, when the detector responds only to uncollided photons.

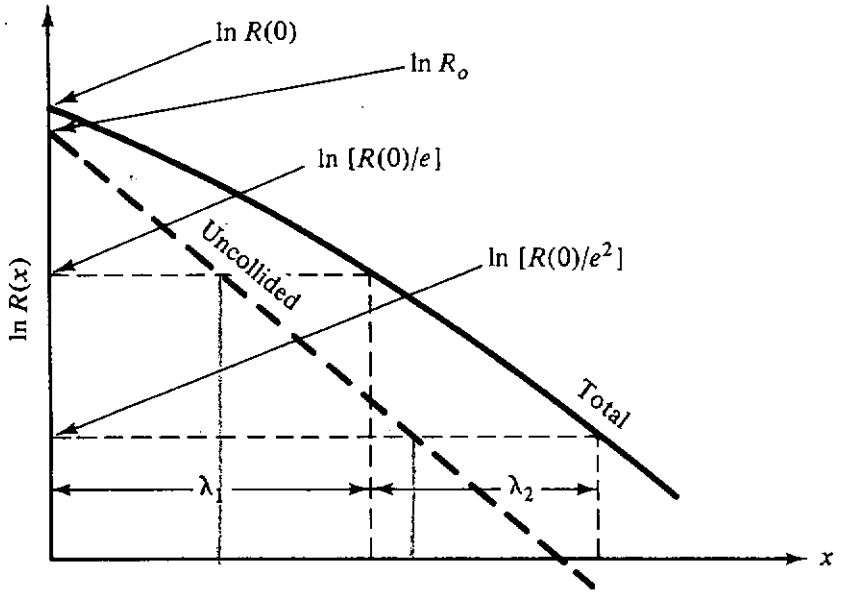

Figure 6.6 Plot of the detector response versus penetration distance in an infinite, homogeneous medium for a plane uniform source. The values λ_1 and λ_2 are for the relaxation lengths at appropriate distances from the source plane. In addition to the total response, the response due to the uncollided particles is shown.

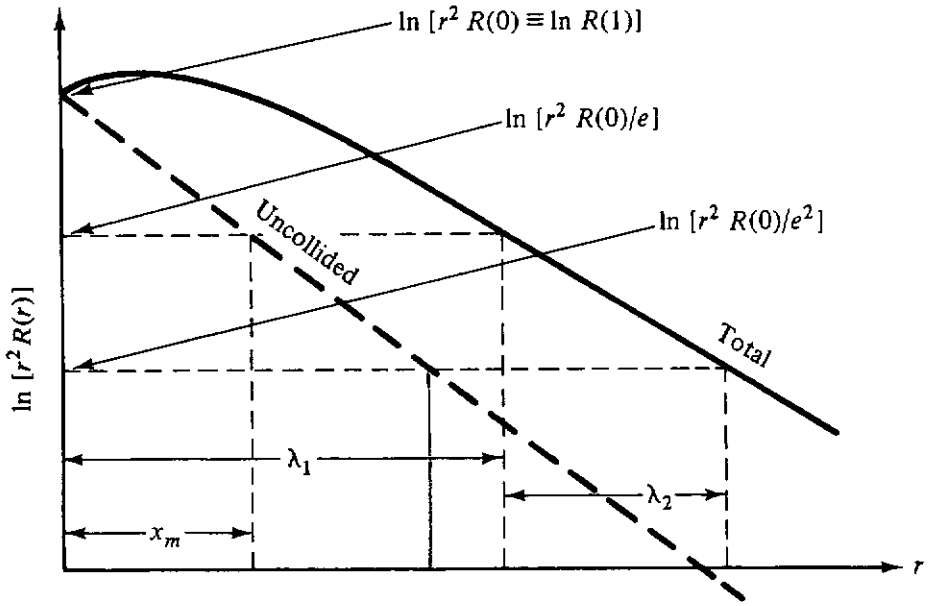

Figure 6.7 Plot of r^2 times the detector response for monoenergetic particles proceeding from a point, isotropic source within an infinite, homogeneous medium. Both the total detector response and the response due only to uncollided radiation are given. Both the mean-free-path distance (x_m) and two values of relaxation length (λ_1 and λ_2) are shown.

reduce the detector response by a value of 10. In principle, it is possible to have layer thicknesses corresponding to any reduction value one might choose, but only the ones mentioned here are common. It follows from what has been said about the relaxation length that the half-value layer or the tenth-value layer

may have different values, depending on the initial value of shield thickness considered.

What has been said thus far, as well as what follows in most of this chapter, is provided in the context of monoenergetic sources. The generalization to sources of mixed energies (*polyenergetic sources*) is straightforward: one simply handles each source emission of a given energy separately and adds the detector responses from all source energy components. With the relaxation-length and layer concepts, however, the detector response results can be analyzed as a composite and need not be broken down into separate monoenergetic source problems. Figure 6.8 is a graph of the detector response from a polyenergetic

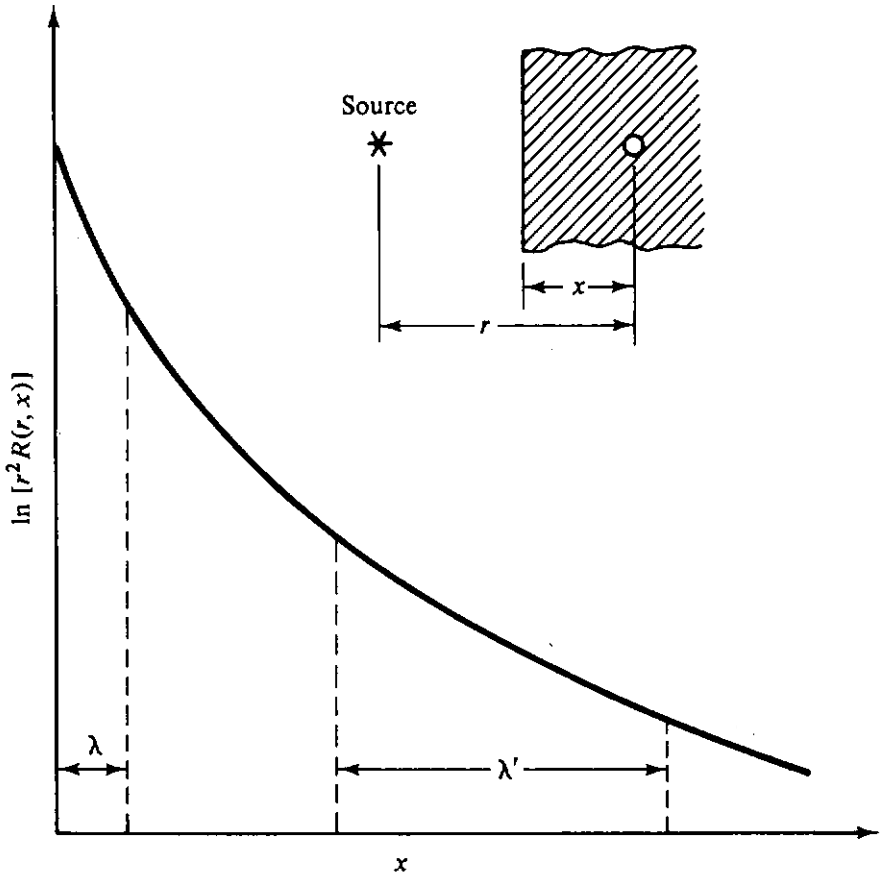

Figure 6.8 Typical detector response curve through a shield for a polyenergetic point source, such as an x-ray machine. λ represents the relaxation length near the source. At some deeper penetration, λ' represents the relaxation length.

source, such as an x-ray machine, on which relaxation lengths are indicated. Note that the curve tends to be concave upward on a semilogarithmic plot. This is due to the fact that the less penetrating "softer" particles tend to be removed from the beam more readily than the more penetrating ones. The result of this is that the relaxation length tends to *increase* with penetration distance for such a case. The same thing is true for half-value or tenth-value layers added onto a shield for polyenergetic sources, at least until almost all the softer components are selectively filtered out.

6.3 APPROXIMATION FORMULAS FOR TOTAL RESPONSE

It is evident from the shape of the total response curves in Figs. 6.6 and 6.7 that the behavior of the total response within appropriate distance ranges may be approximated by a formula of exponential character, similar to one of the formulas for the uncollided component of the response. Use of such a formula would be equivalent to replacing the response curve in one of these figures by a straight line on the semilogarithmic plot. How this is to be done is somewhat arbitrary and depends on the range of distances within which the formula is to be utilized. Thus, formulas of the type given by Eqs. (6.7) and (6.9) may be used to some degree of approximation, provided that R_0 or R_1 are adjusted to equal the intercept of the approximating straight line with the ordinate and the value of the coefficient μ is adjusted to the negative slope of the approximating straight line. Under appropriate conditions, then, it is possible to indicate that

$$R(x) \simeq R_0' e^{-\mu' x} \tag{6.12}$$

for the plane-source case, and

$$R(r) \simeq \frac{R_1'}{r^2} e^{-\mu' r} \tag{6.13}$$

for the point-source case. The primed quantities represent the adjusted parameters.

The parameter μ' is generally called the *effective linear attenuation coefficient* μ_{eff} when one is dealing with photons; and it is often called the macroscopic removal cross section μ_r (or, more properly, the *removal coefficient*) when one is dealing with neutrons, although the latter term is sometimes given a somewhat more restricted meaning (see Section 8.3). There is no specific terminology for R_0' or R_1'. The ratio R_0'/R_0 or R_1'/R_1 has sometimes been called the *initial buildup factor* (B_0), although the term "buildup factor" without the modifier "initial" usually has a more restricted meaning (see Section 7.1).

Finding values for the primed parameters for use in Eq. (6.12) or (6.13) is equivalent to establishing the best straight-line approximation to the curve for total response in Fig. 6.6 or 6.7. There is no rigorous rule for doing this; and one must use an approximation best suited to the circumstances presented in a specific problem. Figure 6.9 indicates some of the possible choices.

It is very clear from Figs. 6.6 and 6.9(a) that if no pronounced hump exists near the origin and the attenuation formula is to be used for penetration from monoenergetic sources only up to a few relaxation lengths, the initial buildup factor ratio would be unity or slightly greater. On the other hand, for deeper penetrations, especially if the hump near the origin is pronounced, this ratio would be much greater than unity. Estimation of μ' is also subject to variation. It is almost always less than μ, and sometimes appreciably so. In the case shown in Fig. 6.9(b), in which the straight-line approximation is tangent to the correct curve at some point, one can obtain the correct value of μ' by one of the following formulas, readily derived from Eqs. (6.12) and (6.13):

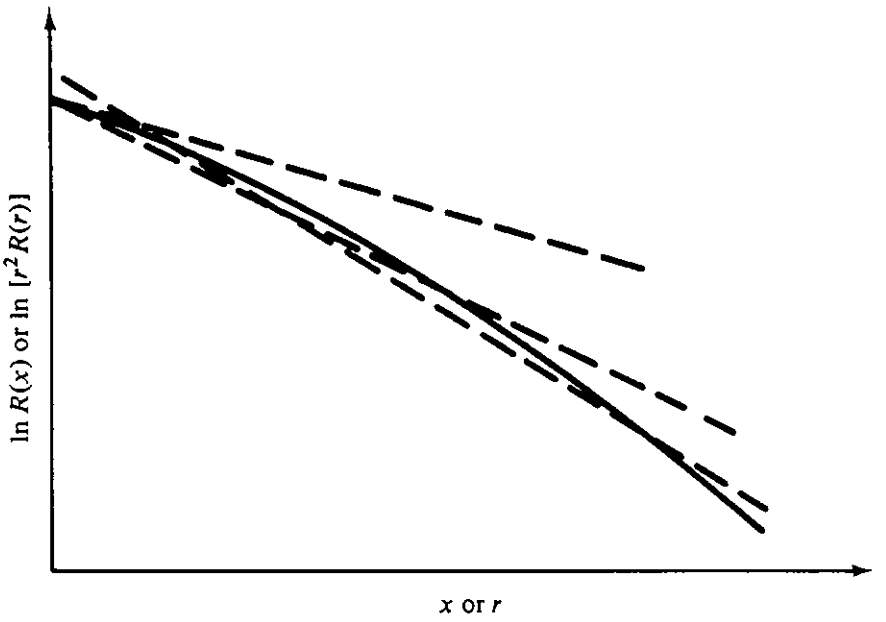

(a)

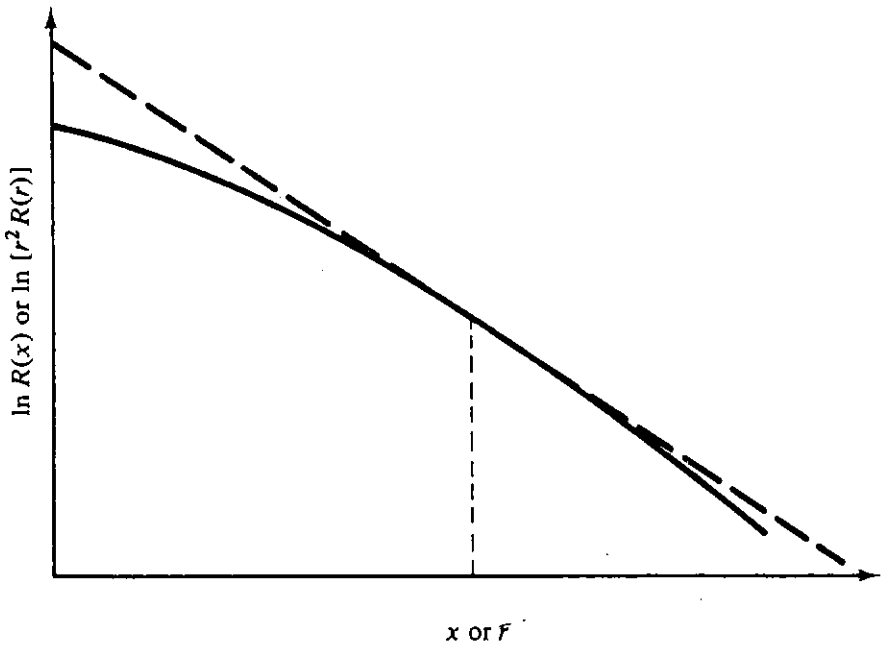

(b)

Figure 6.9 Plots of total detector response which indicate various exponential approximations (straight lines on the semilogarithmic plot): (a) various possible approximations shown as dashed lines; (b) a tangent-line approximation.

$$\mu' = -\frac{dR/dx}{R} \tag{6.14}$$

or

$$\mu' = -\frac{d(r^2R)/dr}{r^2R}. \tag{6.15}$$

The relaxation length, defined as $1/\mu'$ for this tangent approximation, is known as the *local* relaxation length at the point of tangency.

Table 6.1 gives a reasonable set of data on the initial buildup factor and

TABLE 6.1 Values of B_0 ($\equiv R_1'/R_1$) and c ($\equiv \mu'/\mu$) for a Point, Monoenergetic Source of Photons Embedded in Infinite Media[a]

E_0 (MeV)	Water[b]	Concrete	Iron	Lead
		B_0		
0.2	5.5	3.8	2.2	—
0.5	3.7	3.0	2.4	1.4
1.0	2.9	2.6	2.3	1.5
1.5	2.6	2.4	2.2	1.5
2.0	2.4	2.2	2.1	1.5
5.0	1.8	1.8	1.6	1.1
		c		
0.2	0.60	0.72	0.85	—
0.5	0.69	0.73	0.78	0.94
1.0	0.76	0.77	0.79	0.90
1.5	0.79	0.80	0.81	0.89
2.0	0.82	0.82	0.82	0.87
5.0	0.87	0.86	0.85	0.83

[a]These values were obtained by fitting an exponential curve through the exact values at 4 and 7 mean-free-path lengths from the source. The data are specifically for an exposure-type response, but they will serve approximately for all related dosimetric quantities.
[b]These values will serve for *air* also.

effective linear attenuation coefficient for monoenergetic photons from a point source. These data are most useful for shields of several mean free paths in thickness. For broad parallel beams, μ' can be approximated by the use of μ_a (see Section 10.2.1); and, for this case, the initial buildup factor need be only slightly greater than unity.

6.4 RAY ANALYSIS TECHNIQUE

For a "point" source and a "point" detector, the uncollided component of the detector response is caused by particles that travel a straight line or *ray*, between source and detector. Under many circumstances, it is also reasonable to expect that the in-scattered particles which affect the detector also travel in paths which are near this ray. This is partly due to the fact that this path is the shortest distance from source to detector, and partly due to the fact that angular scattering cross-section distributions for neutrons and photons are often peaked strongly forward (see Chapter 3). Under these conditions, one can make a simplified radiation penetration analysis by assuming that *all* the radiation affecting the detector proceeds along the ray between source and detector. As a corollary to this assumption, the material attenuation is treated by means of an exponential

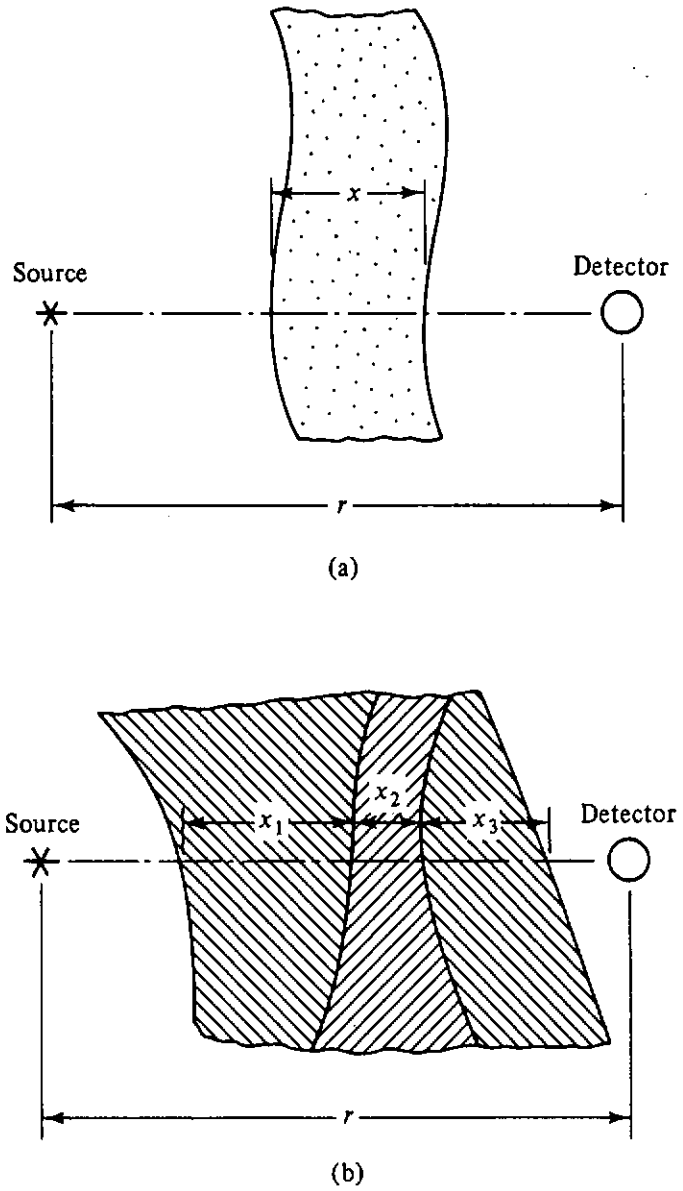

Figure 6.10 Point source and point detector with intervening shield: (a) homogeneous shield; (b) heterogeneous shield. Only a vacuum is assumed to exist outside the shields.

expression whose argument is simply related to the distance along the ray through the shielding material (the distance x in Fig. 6.10, for example).

Since an extended source (line, surface, or volume) can be treated as a collection of point sources that have independent and summable effects on the detector, the point-source formula will be used to derive analytic formulas for the detector response for a variety of standard shapes of extended sources. Use of the derived formulas in practical situations will be indicated by examples and by problems at the end of the chapter. The sources used in these derivations are all monoenergetic, since extension to polyenergetic sources is simply accomplished by summation or integration over the source energies.

It must be observed that since Eqs. (6.9) and (6.13) are of the same form, the formulas to be derived are valid either for the portion of the detector response due to uncollided radiation (in which case they are exact) or to the total detector response including that due to in-scattered radiation (in which case

they are approximate). The detector is always assumed in this section to be isotropic and to measure flux density or a dosimetric quantity based on flux density. As is usual in this text, examples will be based on rate-type detectors.

6.4.1 Basic Point Source

Although the point-source formula is introduced primarily as the basis for developing extended source formulas in this chapter, one must not forget that many sources can be treated as point sources, without the need for further elaboration. X-ray machines are treated as point sources. Radioisotopic sources (pellets or capsules) used in laboratories or medical situations are frequently quite small in size and so treated. In fact, any source for which the source extent is small compared to the distance to the detector can be treated as a point source, as will be seen later (Section 6.4.3).

Both Eqs. (6.9) and (6.13) for a point source, adapted appropriately to include the situation in which the attenuating medium may be finite, as illustrated in Fig. 6.10, can be encompassed in one or the other of the following equations:

$$R = \frac{\hat{R}S_p}{r^2}e^{-kx}, \tag{6.16}$$

for a single homogeneous shielding medium, or, more generally,

$$R = \frac{\hat{R}S_p}{r^2}\exp\left(-\sum_i k_i x_i\right). \tag{6.17}$$

In the equations above, k may represent either μ (in which case R must represent R^0, the response to uncollided particles only) or μ' (i.e., either μ_{eff} for photons or μ_r for neutrons).

R_1 or R_1' in the original formulas has been split into two terms, S_p representing the point-source strength and $\hat{R}$ representing the value of R_1/S_p or R_1'/S_p. In case of the uncollided response or in case the total response is being calculated with an initial buildup factor of unity, $\hat{R}$ has a simple and fundamental meaning: the detector response to the given type of point source at one unit distance from the source, in the complete absence of any attenuating medium, if the source has a strength of unity. For a monoenergetic, isotropic point source, $\hat{R}$ is readily expressed in terms of the detector response function $\mathfrak{R}(E)$ (see Chapter 5) as $\hat{R} = \mathfrak{R}(E_0)/4\pi$, where E_0 is the energy of the source particles. The exact numerical value of $\hat{R}$ depends on the units employed and the type of detector response. A few examples of the more common applications for point isotropic sources will illustrate.

1. If S_p is given in particles per second, r in the denominator of the equation is given in centimeters,[5] and the detector response is the flux density in particles per square centimeter per second, then $\hat{R} = 1/4\pi$ (dimensionless).

[5]It is not necessary for r in the denominator to be of the same units as the length dimension in the exponential factor. The r in the denominator must have length units consistent with those of $\hat{R}$; in the exponent, the length dimension must have units reciprocal to those of k.

2. If the source is a neutron emitter of S_p neutrons per second, r in the denominator is given in centimeters, and the detector response is the phantom-related dose equivalent rate in units of cSv s^{-1}, then $\hat{R}$ is given by the appropriate value of the response function $\mathcal{R}_{H_p}$ from Table 5.4, divided by 4π, with units of cSv cm^2.
3. If the source is a photon emitter of S_p photons per second, r in the denominator is given in centimeters, and the detector response is the phantom-related dose equivalent rate in units of cSv s^{-1}, then $\hat{R}$ is the appropriate value of the response function $\mathcal{R}_{H_p}$ from Table 5.3, divided by 4π, with units of cSv cm^2.
4. If the source is a radioactive element of strength S_p, expressed indirectly by the activity in curies, r in the denominator is given in meters, and the detector response is expressed as exposure rate in units of R h^{-1}, then $\hat{R}$ for the given photons of energy E_i is given by the expression $19.5 n_i E_i (\mu_{en}/\rho)_i^{air}$, where E_i is given in MeV, n_i is the number of photons of energy E_i emitted per disintegration (see Appendix 5), and $(\mu_{en}/\rho)_i^{air}$ is the appropriate value taken from tables in Appendix 3.[6] The units for $\hat{R}$ here are R m^2 Ci^{-1} h^{-1}. The expression given for $\hat{R}$ is readily derived from Eq. (5.27).

In case an initial buildup factor is to be used to account approximately for scattered radiation, the examples above must be modified by multiplication of $\hat{R}$ by this factor.

Although isotropic emission is typical of most sources encountered in shielding analyses, occasionally situations will arise in which the source emission will be anisotropic in direction. Equation (6.16) or (6.17) may still be used;

[6] $\hat{R}$ for this situation has been called the "partial specific gamma-ray constant" and given the symbol Γ_i. The "specific gamma-ray constant" is the sum of the partial constants for all photon energies, and is simply designated as Γ. Table 6.2 gives values of this constant

TABLE 6.2 Values of the Specific Gamma-Ray Constant (Γ) for Certain Radioisotopes

	Γ	
Radioisotope	$\frac{R\ m^2}{Ci\ h}$	$\frac{R\ cm^2}{GBq\ h}$
^{60}Co	1.30	351
^{137}Cs—^{137m}Ba	0.32	86
^{192}Ir	0.500	135
^{198}Au	0.232	62.7
^{226}Ra + daughters	0.825[a]	223[a]

[a]Assumes source encapsulated in platinum with 0.5-mm wall thickness.

Source: *Ref. 2.*

for certain radioisotopes. These are most useful in the present context for radioisotopes ^{137}Cs and ^{60}Co, emitting monoenergetic or nearly monoenergetic photons. Then $\hat{R}$ simply equals Γ.

however, $\hat{R}$ will now depend not only on the detector response but also on its orientation with respect to the source. For example, suppose that the emission from a monoenergetic source is described by $S(\theta, \psi) = S_p f(\theta, \psi)$, where S_p is still the total strength and $f(\theta, \psi)$ is the probability per unit solid angle that radiation is emitted in the direction $\mathbf{\Omega}(\theta, \psi)$. Then the response of a point detector, in the absence of any attenuating material, placed a unit distance from the source, and oriented in the direction $\mathbf{\Omega}_d(\theta_d, \psi_d)$ with respect to the source, is $\hat{R}(E_0; \theta_d, \psi_d)S_p$, where $\hat{R}(E_0; \theta_d, \psi_d) = \mathfrak{R}(E_0)f(\theta_d, \psi_d)$, and $\mathfrak{R}(E_0)$ is the detector response function for radiation of source energy E_0. In most applications in this text, isotropic sources are used; however, in those cases involving anisotropic sources, the angular dependence of $\hat{R}$ will be shown explicitly.

6.4.2 Straight-Line Sources

Isotropic line source in a nonattenuating medium. Straight-line sources are an idealization of such sources as reactor fuel pins or small pipes carrying radioactive fluid. Also, some area and volume sources are conveniently analyzed by being divided up into thin incremental segments, which can be separately treated as straight-line sources.

Three cases are illustrated in Fig. 6.11. In each case the flux density is to be evaluated at perpendicular distance h (cm) from a line source of strength S_L and length L. First consider the location P_1. Let $dR(P_1)$ be the detector response at P_1 due to the line source element dx treated as an isotropic point source:

$$dR(P_1) = \frac{\hat{R}S_L\,dx}{h^2 + x^2}. \tag{6.18}$$

But $x = h\tan\theta$, $h^2 + x^2 = h^2\sec^2\theta$, and $dx = h\sec^2\theta\,d\theta$; thus,

$$dR(P_1) = \frac{\hat{R}S_L\,d\theta}{h} \tag{6.19}$$

and

$$R(P_1) = \frac{\hat{R}S_L\theta_1}{h}, \tag{6.20}$$

where θ_1 must be expressed in radians. Similarly,

$$R(P_2) = \frac{\hat{R}S_L(\theta_1 + \theta_2)}{h}, \tag{6.21}$$

$$R(P_3) = \frac{\hat{R}S_L(\theta_2 - \theta_1)}{h}. \tag{6.22}$$

If the line source is of infinite length, $\theta_1 = \theta_2 = \pi/2$ at P_2 and $R(P_2) = \hat{R}S_L\pi/h$.

Isotropic line source in an attenuating medium. If the space between the line source and the detector is filled with a uniform medium whose attenuating property is characterized by k, Eq. (6.18) becomes

$$dR(P_1) = \frac{\hat{R}S_L\,dx\,e^{-k(x^2+h^2)^{1/2}}}{h^2 + x^2} \tag{6.23}$$

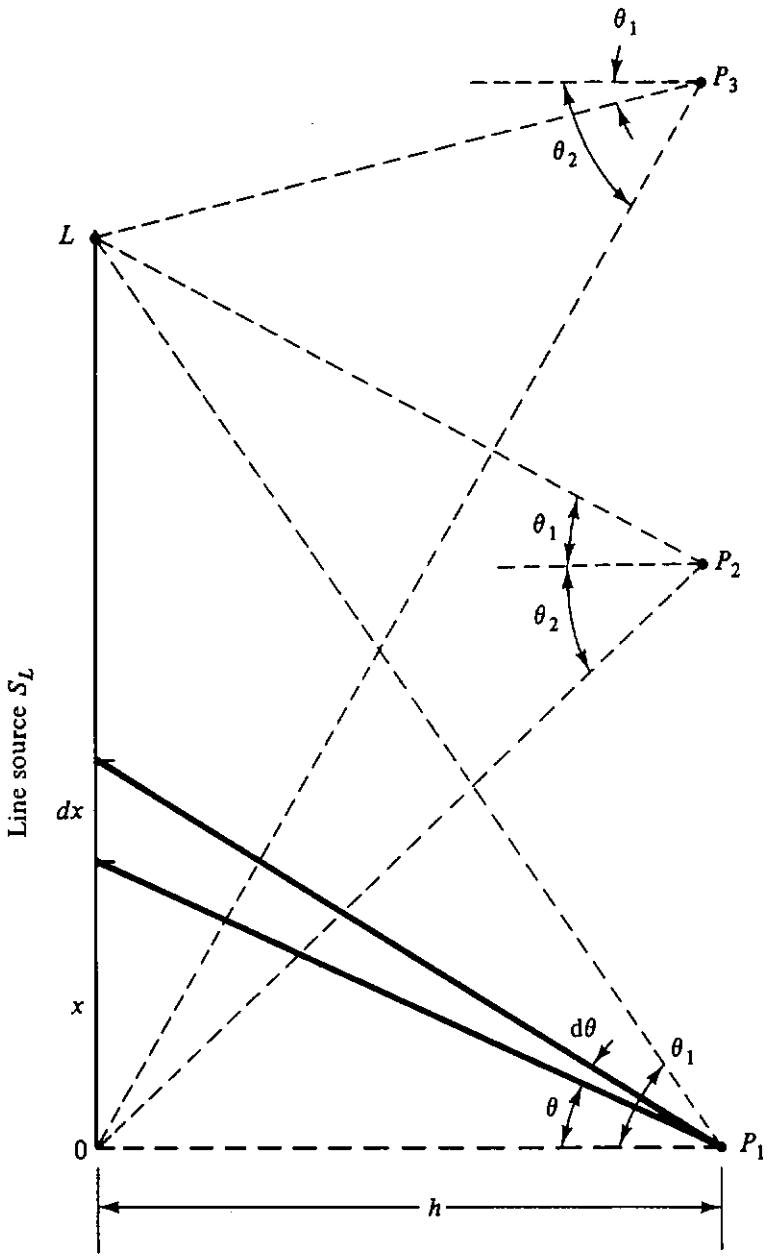

Figure 6.11 Isotropic, straight-line source in a nonattenuating medium. In the three cases illustrated, the angles are defined by lines from the point P normal to the source and to the ends of the source.

or

$$dR(P_1) = \frac{\hat{R}S_L e^{-kh\sec\theta}\, d\theta}{h}, \tag{6.24}$$

and thus

$$R(P_1) = \frac{\hat{R}S_L}{h}\int_0^{\theta_1} d\theta\, e^{-kh\sec\theta} \tag{6.25}$$

$$= \frac{\hat{R}S_L F(\theta_1, kh)}{h}. \tag{6.26}$$

This introduces a special function called the *secant integral* or *Sievert's integral*:

$$F(\theta, b) \equiv \int_0^{\theta} d\theta'\, e^{-b\sec\theta'}. \tag{6.27}$$

Graphs of this function and a brief discussion of its properties are given in Appendix 2. It is known that this function's variation is dominated by a factor θe^{-b}. It is thus possible to express it as

$$F(\theta, b) = \theta e^{-b} \bar{F}(\theta, b). \tag{6.28}$$

Values of $\bar{F}$ are given in Table A2.1 where the variation is seen to be sufficiently slow that linear interpolation is usually satisfactory. Note that using the expression above, θ must be expressed in radians.

By extension, the detector responses at P_2 and P_3 are

$$R(P_2) = \frac{\hat{R}S_L}{h}[F(\theta_1, kh) + F(\theta_2, kh)], \tag{6.29}$$

$$R(P_3) = \frac{\hat{R}S_L}{h}[F(\theta_2, kh) - F(\theta_1, kh)]. \tag{6.30}$$

Line source with slab shield. This geometry is illustrated in Fig. 6.12. The source is shielded by a slab of thickness t with attenuation characterized by coefficient k. (If the slab were made up of layers t_i, each characterized by a coefficient k_i, then $kt \equiv \sum_i k_i t_i$.) By extension of the arguments above,

$$R(P_1) = \frac{\hat{R}S_L}{h}[F(\theta_1, kt)], \tag{6.31}$$

$$R(P_2) = \frac{\hat{R}S_L}{h}[F(\theta_1, kt) + F(\theta_2, kt)], \tag{6.32}$$

$$R(P_3) = \frac{\hat{R}S_L}{h}[F(\theta_2, kt) - F(\theta_1, kt)], \tag{6.33}$$

$$R(P_4) = \frac{\hat{R}S_L}{h}[F(\theta_1, kt) - F(\theta_2, kt)], \tag{6.34}$$

$$R(P_5) = \frac{\hat{R}S_L}{h}[F(\theta_1 + \alpha, kt) - F(\alpha, kt)]. \tag{6.35}$$

6.4.3 Surface Sources

Isotropic disk source in a nonattenuating medium. Surface sources, especially plane sources, are frequently met. The sides or tops of volume sources, such as reactor core assemblies, can be treated as surface sources. Ground contamination by fallout particles constitutes a large plane source, if the contaminant has not penetrated into the ground. Volume sources can often be analyzed as if cut into thin slices, each to be treated as a plane source.

Consider the detector location at distance h from the center of a disk source of uniform strength S_A, as shown in Fig. 6.13. The differential detector response dR is taken to be that due to the source within $d\mathrm{A} = \rho\, d\rho\, d\psi$, treated as a point source

$$dR(P) = \frac{\hat{R}S_A \rho\, d\rho\, d\psi}{r^2}. \tag{6.36}$$

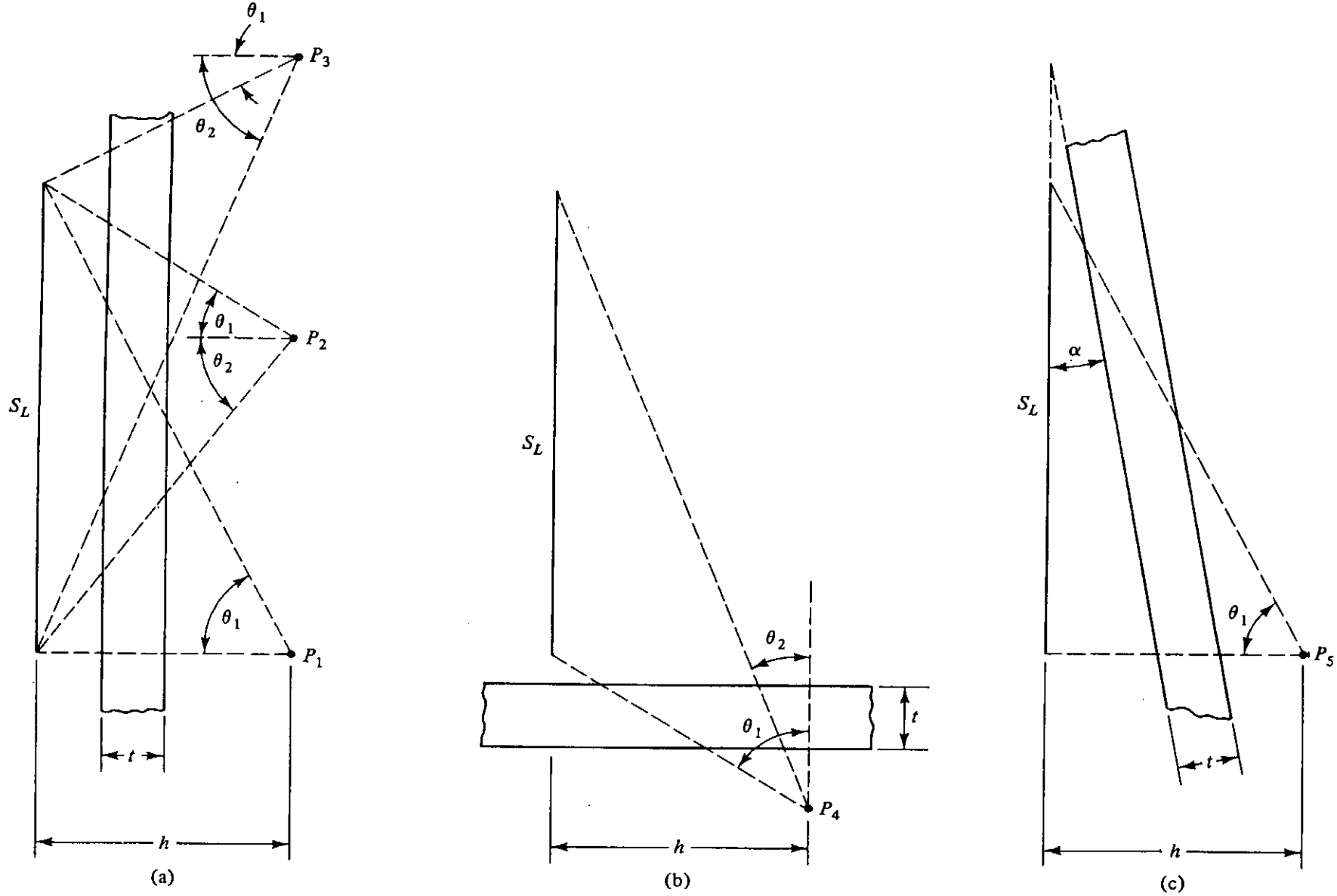

Figure 6.12 Isotropic, straight-line sources with slab shields.

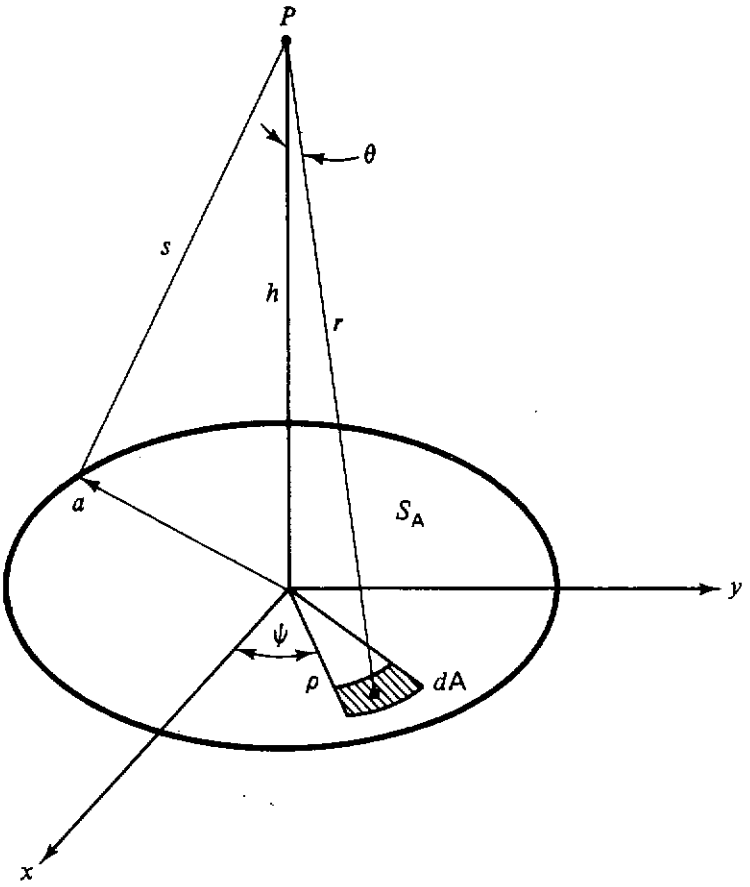

Figure 6.13 Isotropic disk source.

But since $r^2 = h^2 + \rho^2$ and $\rho\, d\rho = r\, dr$

$$dR(P) = \frac{\hat{R} S_A\, dr\, d\psi}{r}. \tag{6.37}$$

Hence,

$$R(P) = \hat{R} S_A \int_0^{2\pi} d\psi \int_h^s \frac{dr}{r} \tag{6.38}$$

$$= 2\pi \hat{R} S_A \ln\left(\frac{s}{h}\right) \tag{6.39}$$

$$= \pi \hat{R} S_A \ln\left(1 + \frac{a^2}{h^2}\right). \tag{6.40}$$

This formula may be approximated for $a \ll h$, since the logarithmic term above can be expanded in the rapidly converging infinite series $(a^2/h^2) - (a^2/h^2)^2/2 + \cdots$. In such a case,

$$R(P) \approx \frac{\pi \hat{R} S_A a^2}{h^2}. \tag{6.41}$$

It is interesting to note that if one inserts the total source strength S, which equals $(\pi a^2) S_A$, one obtains a formula

$$R(P) \approx \frac{\hat{R} S}{h^2}, \tag{6.42}$$

which is the same as the formula for a point source without attenuation [see Eq. (6.16)]. This suggests one of the criteria for judging when an extended source may be treated as a point source: when the distance from the source to the detector is much greater than the spatial extent of the source itself.

If in the formula above a is kept constant and h allowed to approach zero, the value of the detector response approaches infinity. This leads to the conclusion that in a practical situation the idealization represented by this case fails for a point detector at the disk center.

General disk source in a nonattenuating medium. The previous case may be generalized to cover all cases in which the monoenergetic source emission at energy E_0 depends on a power of $\cos\theta$, where θ is the angle between the direction of emission and the normal to the disk plane. These conditions are more likely to apply when the flow rate through a surface is considered as an equivalent source (see Section 2.5). In such a case, the detector response per unit surface area, $\hat{R}S_A$, at one unit of distance from dA in the direction characterized by θ (see Fig. 6.13) is $\mathcal{R}(E_0)j_n^+(m+1)\cos^m\theta/2\pi$, where j_n^+ is the total emission rate per unit area in the source plane into the hemisphere containing the detector. Since $\cos\theta = h/r$, the equation equivalent to Eq. (6.38) becomes

$$R(P) = \frac{\mathcal{R}(E_0)(m+1)j_n^+}{2\pi} h^m \int_0^{2\pi} d\psi \int_h^s \frac{dr}{r^{m+1}}. \tag{6.43}$$

When $m = 0$, this becomes the isotropic disk case (j_n^+ is equivalent to $S_A/2$) and results of the previous case follow immediately.

When $m > 0$, one finds that

$$R(P) = \frac{\mathcal{R}(E_0)(m+1)j_n^+}{m}\left[1 - \left(1 + \frac{a^2}{h^2}\right)^{-m/2}\right]. \tag{6.44}$$

The index m may take on fractional values; however, aside from the value $m = 0$ previously noted, the most usual case is the one where $m = 1$, establishing the "cosine disk source." Thus, for this source in a nonattenuating medium,

$$R(P) = 2\mathcal{R}(E_0)j_n^+\left[1 - \left(1 + \frac{a^2}{h^2}\right)^{-1/2}\right]. \tag{6.45}$$

In the general case, for $m > 0$, it is readily seen that with a finite and $h = 0$,

$$R(0) = \frac{\mathcal{R}(E_0)(m+1)j_n^+}{m}. \tag{6.46}$$

Thus, in general,

$$R(P) = R(0)\left[1 - \left(1 + \frac{a^2}{h^2}\right)^{-m/2}\right]. \tag{6.47}$$

At the opposite extreme, when $h \gg a$, it is easily found by expanding the binomial term that

$$R(P) \simeq R(0)\frac{m}{2}\frac{a^2}{h^2} \tag{6.48}$$

$$= \frac{a^2 \mathcal{R}(E_0)(m+1) j_n^+}{2h^2}, \tag{6.49}$$

which has the same form as Eq. (6.41).

Rectangular surface source in a nonattenuating medium. Consider a rectangular surface source illustrated in Fig. 6.14, with a detector at point P on the axis of symmetry perpendicular to the rectangle. First consider the $\cos^m \theta$ angular dependence described in the preceding paragraph for the disk source. Since $\cos \theta = Z/r$, it is readily shown that

$$R(P) = \frac{2}{\pi} \mathcal{R}(E_0)(m+1) j_n^+ \int_0^{W/2} dx \int_0^{L/2} dy \, Z^m (x^2 + y^2 + Z^2)^{-(m+2)/2}. \tag{6.50}$$

For $m = 1$, corresponding to a cosine plane source, this expression becomes

$$R(P) = \frac{4}{\pi} \mathcal{R}(E_0) j_n^+ \tan^{-1} \left[\frac{\epsilon}{\eta} (1 + \epsilon^2 + \eta^2)^{-1/2} \right], \tag{6.51}$$

in which $\epsilon \equiv W/L$ and $\eta \equiv 2Z/L$. Note that $R(P)$ is proportional to the solid angle at P subtended by the source (Problem 2.8). For Z much greater than W and L, Eq. (6.51) reduces to

$$R(P) \simeq \frac{WL}{\pi Z^2} \mathcal{R}(E_0) j_n^+. \tag{6.52}$$

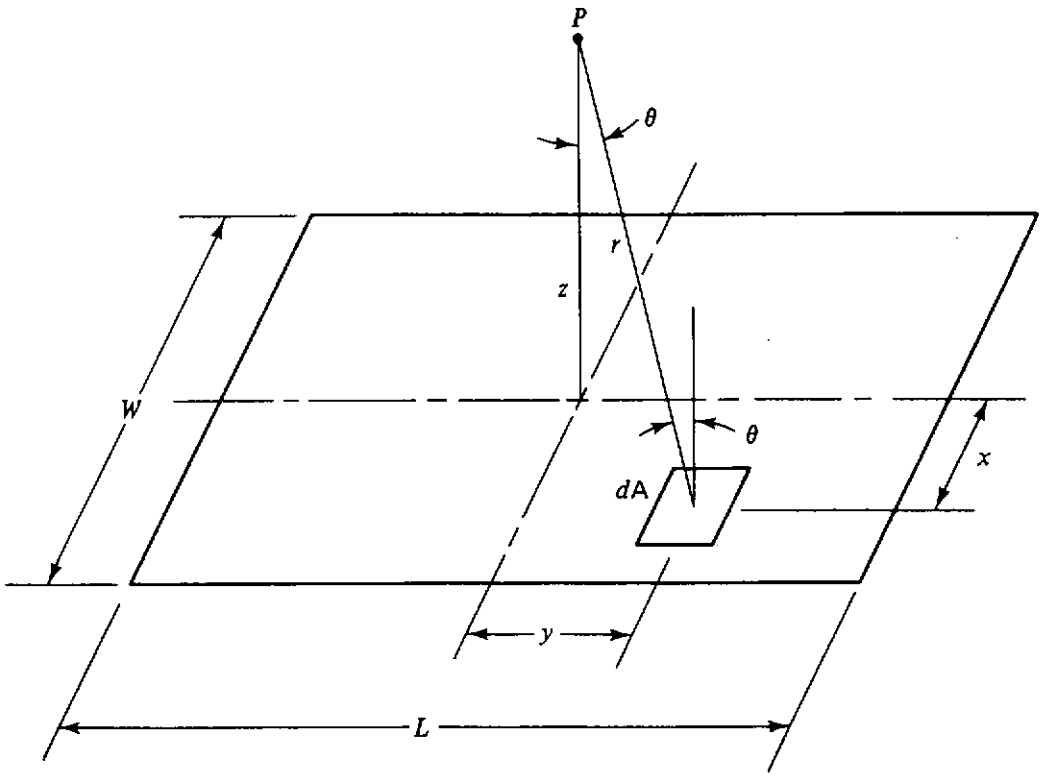

Figure 6.14 Isotropic rectangular plane source.

This is analogous to Eq. (6.42). On the other hand, if Z is zero, which implies a detector in the plane of the source at the center of the rectangle,

$$R(0) = 2\mathcal{R}(E_0)j_n^+ \tag{6.53}$$

and Eq. (6.51) can be revised to appear as

$$R(P) = \frac{2}{\pi}R(0)\tan^{-1}\left[\frac{\epsilon}{\eta}(1+\epsilon^2+\eta^2)^{-1/2}\right]. \tag{6.54}$$

This case is useful, for example, in analyzing the direct radiation from a source at the end of a rectangular duct (see Chapter 9).

Isotropic disk source in an attenuating medium. If the source is in a medium whose attenuating properties are characterized by the coefficient k, Eqs. (6.36) and (6.37) are modified to become

$$dR(P) = \frac{\hat{R}S_A\rho\, d\rho\, d\psi\, e^{-kr}}{r^2} \tag{6.55}$$

$$= \frac{\hat{R}S_A\, dr\, d\psi\, e^{-kr}}{r}. \tag{6.56}$$

Thus,

$$R(P) = \hat{R}S_A\int_0^{2\pi} d\psi \int_h^s \frac{e^{-kr}}{r}\, dr \tag{6.57}$$

$$= 2\pi\hat{R}S_A\int_h^s \frac{e^{-kr}}{r}\, dr. \tag{6.58}$$

At this point we introduce the exponential integral functions

$$E_n(b) \equiv b^{n-1}\int_b^\infty \frac{e^{-t}}{t^n}\, dt, \tag{6.59}$$

where n is zero or a positive integer. Equation (6.58) becomes

$$R(P) = 2\pi\hat{R}S_A[E_1(kh) - E_1(ks)]. \tag{6.60}$$

Graphs and special properties of the exponential integral functions are discussed in Appendix 2. It is known that the variation of these functions is dominated by a factor e^{-b}/b. It is thus possible to express them as

$$E_n(b) = b^{-1}e^{-b}\bar{E}_n(b). \tag{6.61}$$

Values of $\bar{E}_1(b)$ and $\bar{E}_2(b)$ are given in Table A2.2, where the variation is seen to be sufficiently slow that linear interpolation is usually satisfactory.

Many radioactive sources are shaped like small disks, to which this case applies. A circular decontaminated area in the midst of a large fallout field also makes use of these formulas, in a subtractive sense.

Cosine disk source in an attenuating medium. Suppose that the disk source shown in Fig. 6.13 has emission properties such that the strength in various directions from dA is proportional to $\cos\theta$, where θ is the angle between the normal to the disk plane and the direction line from the differential source

area to the detector. In this case, the detector response one unit of distance from dA in the direction characterized by θ is given by $\mathcal{R}(E_0)B_0 j_n^+ \cos\theta\, dA/\pi$. Then the total detector response, from an equation analogous to Eq. (6.58), becomes

$$R(P) = 2\mathcal{R}(E_0)B_0 j_n^+ \int_h^s \frac{he^{-kr}}{r^2}\, dr \tag{6.62}$$

$$= 2\mathcal{R}(E_0)B_0 j_n^+ \left[E_2(kh) - \frac{h}{s}E_2(ks)\right]. \tag{6.63}$$

The top surface of a cylindrical volume source may have emission properties close to being "cosine" in character, and the formula above may be useful when treating it as a "disk source."

Isotropic cylindrical surface sources. Consider the source as depicted in Fig. 6.15. The source surface and the various detectors are embedded

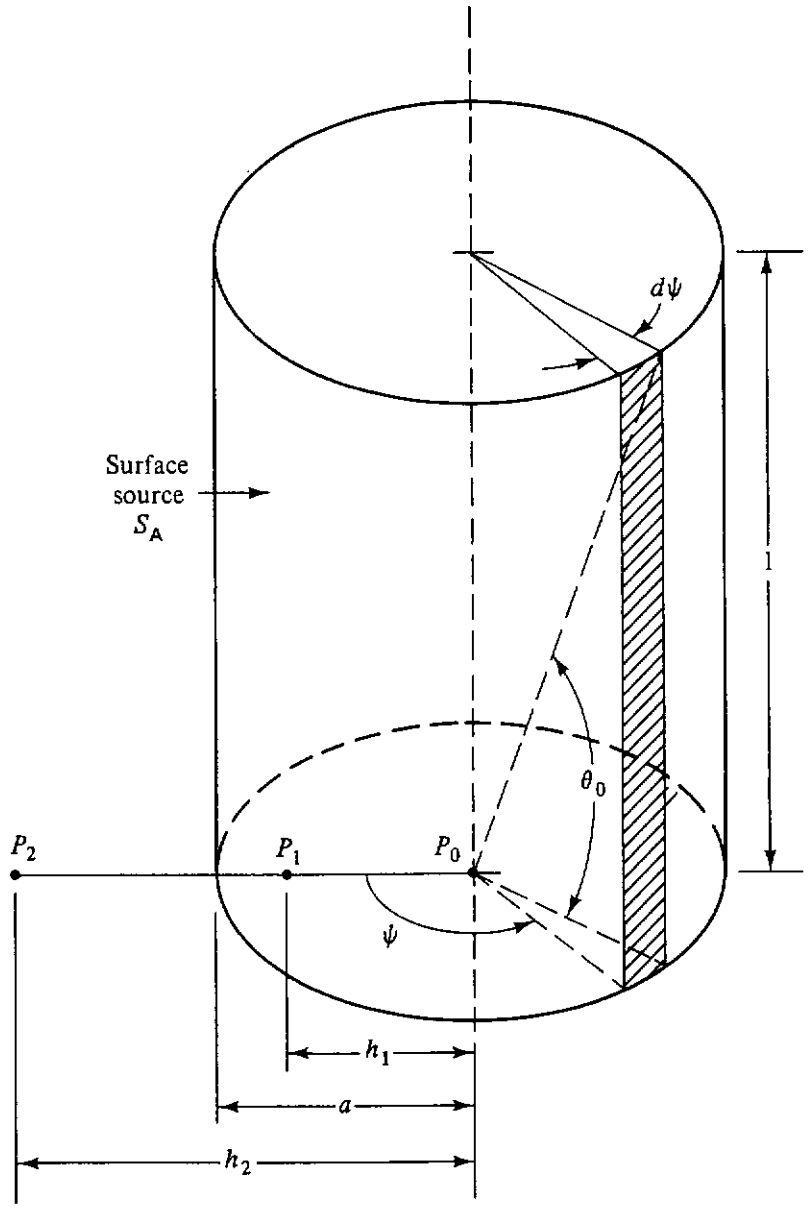

Figure 6.15 Isotropic cylindrical surface source. No sources are on the ends of the cylinder.

in a medium whose attenuation properties are characterized by the parameter k. At point P_0, located on the axis and at the base of the cylinder, the detector response to a differential strip of the surface is given, from Eq. (6.26), by

$$dR(P_0) = \frac{\hat{R}(a\, d\psi\, S_A)}{a} F(\theta_0, ka), \tag{6.64}$$

in which $(a\, d\psi\, S_A)$ is the strength of the strip taken as a line source and $\theta_0 = \tan^{-1}(l/a)$. Then, integration over all values of ψ gives

$$R(P_0) = 2\pi \hat{R} S_A F(\theta_0, ka). \tag{6.65}$$

In the absence of material attenuation ($k = 0$), one easily finds that

$$R(P_0) = 2\pi \hat{R} S_A \theta_0. \tag{6.66}$$

The detector response at P_1 in the absence of an attenuating medium is readily seen to be given by

$$R(P_1) = \hat{R} S_A a \int_0^l \int_{-\pi}^{\pi} \frac{d\psi\, dz}{z^2 + a^2 + h_1^2 - 2ah_1 \cos\psi} \tag{6.67}$$

$$= 2\pi \hat{R} S_A a \int_0^l \frac{dz}{[(z^2 + a^2 + h_1^2)^2 - 4a^2 h_1^2]^{1/2}}. \tag{6.68}$$

By the introduction of a new variable, $\xi = \arctan z/(a - h_1)$, it follows that

$$R(P_1) = \frac{2\pi \hat{R} S_A a}{a + h_1} \int_0^{\theta_1} \frac{d\xi}{[1 - k_1^2 \sin^2 \xi]^{1/2}} \tag{6.69}$$

$$= \frac{2\pi \hat{R} S_A a}{a + h_1} F_e(k_1, \theta_1), \tag{6.70}$$

where $k_1 = 2(ah_1)^{1/2}/(a + h_1)$ and $\theta_1 = \arctan l/(a - h_1)$. Similarly,

$$R(P_2) = \frac{2\pi \hat{R} S_A a}{a + h_2} F_e(k_2, \theta_2), \tag{6.71}$$

where $k_2 = 2(ah_2)^{1/2}/(a + h_2)$ and $\theta_2 = \arctan\, l/(h_2 - a)$. In the equations above, F_e is the incomplete elliptic integral of the first kind (see Appendix 2).

If a slab shield is present between the detector and the source cylinder, the formulation is more complicated. For this case, results are expressible in terms of the W function, which is defined and tabulated elsewhere in the shielding literature [3].

Isotropic spherical surface sources. Consider a spherical surface of radius ρ, having a uniform distribution of isotropic emitters, with strength S_A. The sphere is composed of an attenuating medium characterized by k. The spherical surface dA, in terms of polar coordinates, equals $\rho^2\, d\psi\, d(\cos\theta)$, where θ and ψ are polar and azimuthal angles, respectively, with respect to the center

of the sphere. The detector response at the center is given by

$$R_c = \int_A \frac{\hat{R} S_A e^{-k\rho}\, dA}{\rho^2} \tag{6.72}$$

$$= 4\pi \hat{R} S_A e^{-k\rho}. \tag{6.73}$$

If no attenuating medium exists, then

$$R_c = 4\pi \hat{R} S_A. \tag{6.74}$$

Isotropic spherical surface sources are discussed further in Section 6.6.4 within the context of geometric transformations.

6.4.4 Volume Sources

Uniformly distributed slab source with slab shield. Figure 6.16 illustrates a laterally infinite slab source with a slab shield. Consider first the case in which the source is isotropic and uniformly distributed throughout the

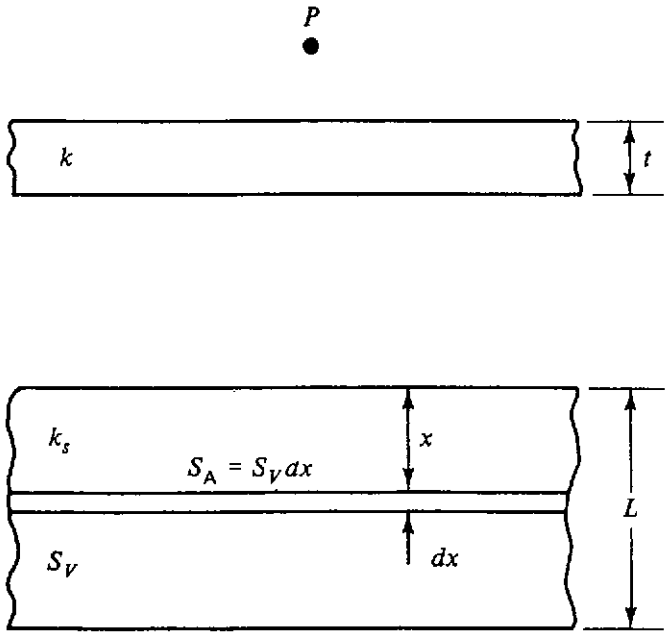

Figure 6.16 Isotropic volumetric source distributed in an infinite slab of thickness L. A slab shield is placed parallel to the source surface.

lower slab with a strength S_V [see also profile (1) of Fig. 6.17]. The source slab is of thickness L and has attenuation properties characterized by the coefficient k_s. The shielding slab has a thickness t and attenuation properties characterized by k. Let $dR(P)$ be the differential detector response at location P due to sources within the portion of the slab within the thickness dx as shown. This differentially thin slab source is treated as a plane source of strength $S_V\, dx$. It follows from Eq. (6.60), with $s \longrightarrow \infty$, that

$$dR(P) = 2\pi \hat{R} S_V E_1(kt + k_s x)\, dx. \tag{6.75}$$

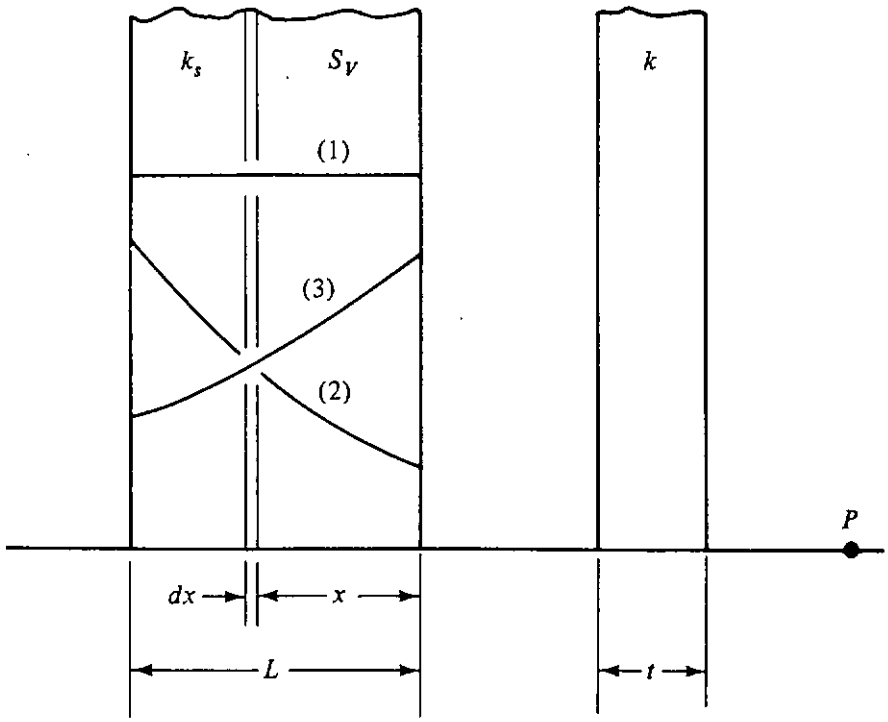

Figure 6.17 Plot of various types of volume source distributions superimposed on the geometric configuration of Fig. 6.16 (rotated by 90°). Profile (1) is for the uniform source case. Profile (2) is for the case in which the source strength increases exponentially with depth into the source slab. Profile (3) is for the exponentially decreasing case.

The total detector response is

$$R(P) = 2\pi\hat{R}S_V \int_0^L E_1(kt + k_s x)\, dx. \tag{6.76}$$

If a change of variable is made, such that $y = kt + k_s x$,

$$R(P) = \frac{2\pi\hat{R}S_V}{k_s} \int_{kt}^{kt+k_sL} E_1(y)\, dy. \tag{6.77}$$

Exponential integral functions have the important property that

$$E_n(y) = -\frac{d}{dy}E_{n+1}(y). \tag{6.78}$$

Thus,

$$R(P) = \frac{2\pi\hat{R}S_V}{k_s}[E_2(kt) - E_2(kt + k_sL)]. \tag{6.79}$$

For an infinitely thick slab (semi-infinite source),

$$R(P) = \frac{2\pi\hat{R}S_V}{k_s}E_2(kt); \tag{6.80}$$

and if the infinitely thick source slab is unshielded,

$$R(P) = \frac{2\pi\hat{R}S_V}{k_s}. \tag{6.81}$$

Cases involving formula (6.81) occur commonly, for example, in situations where radioactivity is uniformly mixed in a body of water or in a large area of ground to a given depth (as in radioactive waste burial), or is created by uniform activation in a large shielding slab.

Exponentially distributed source in slab, with slab shield. Consider now the case depicted in Fig. 6.17, with the source exponentially distributed throughout the source slab. This situation might be encountered, for example, in a problem where the neutron flux density, decreasing exponentially in a slab, gives rise to a source of secondary photons. The distribution could be increasing or decreasing with depth x; however, both subcases are easily handled by the same mathematical apparatus. The volumetric source strength is expressed by a formula of the following general nature:

$$S_V = Ce^{qx}, \tag{6.82}$$

in which q is positive for the increasing distribution [curve (2) in Fig. 6.17] and negative for a decreasing distribution [curve (3)].

For the differential source within the thin portion of the slab of thickness dx, Eq. (6.75) again applies:

$$dR(P) = 2\pi\hat{R}S_V E_1(kt + k_s x)\,dx. \tag{6.83}$$

Substitution of the source strength from Eq. (6.82) and integration gives the detector response at P as

$$R(P) = 2\pi\hat{R}C\int_0^L e^{qx}E_1(kt + k_s x)\,dx. \tag{6.84}$$

The change of variable, $y = kt + k_s x$, gives

$$R(P) = \frac{2\pi\hat{R}C\exp(-qkt/k_s)}{k_s}\int_{kt}^{kt+k_sL}\exp\left(\frac{qy}{k_s}\right)E_1(y)\,dy. \tag{6.85}$$

The integral is easily evaluated with the help of Eq. (A2.20), so that, for $q \neq k_s$ and $t \neq 0$,

$$\begin{aligned} R(P) = \frac{2\pi\hat{R}C}{q}\Big\{&e^{qL}E_1(kt + k_sL) - E_1(kt) \\ &- e^{-(q/k_s)kt}E_1\left((kt + k_sL)\frac{k_s - q}{k_s}\right) + e^{-(q/k_s)kt}E_1\left(kt\frac{k_s - q}{k_s}\right)\Big\}. \end{aligned} \tag{6.86}$$

For $q = k_s$, the detector response becomes [see Eq. (A2.21)]

$$R(P) = \frac{2\pi\hat{R}C}{k_s}\left[e^{k_sL}E_1(kt + k_sL) - E_1(kt) + e^{-kt}\ln\left(1 + \frac{k_sL}{kt}\right)\right]. \tag{6.87}$$

This is, of course, a rare case.

It is of significance to examine the usual case somewhat further. From Eq. (A2.12) one observes that the value of the integrand in Eq. (6.85) is given approximately by $(1/y)\exp[-y(1 - q/k_s)]$. The exponential factor dominates the $1/y$ factor; thus, it is seen that for $q \gg k_s$ and for large values of y, which implies large values of x, the value of the integral is larger than for small values

of y (and x). This means that, under this circumstance, the detector response comes largely from sources deep within the source slab. On the other hand, for $q \ll k_s$ (including a negative q—the decreasing distribution), the opposite is true; and the main contribution to the detector response comes from the sources near the portion of the source slab nearer the detector. For $q \sim k_s$, a more even distribution of contribution importance may be expected. This is of particular significance in connection with neutron shielding, for which case the secondary gamma photons created in a neutron shield may turn out to be more hazardous than the penetration neutrons themselves.

The problem for an exponentially distributed source includes the earlier result for a uniform source distribution [profile (1) in Fig. 6.17]. If one lets q approach zero in Eq. (6.86), it can be shown to reduce to Eq. (6.79).

Finally, in case the outside shield is not present ($t = 0$), Eq. (6.86) becomes

$$R(P) = \frac{2\pi\hat{R}C}{q}\left[e^{qL}E_1(k_sL) - E_1\left(k_sL\frac{k_s - q}{k_s}\right) - \ln\left(\frac{k_s - q}{k_s}\right)\right]. \tag{6.88}$$

Cylindrical volume sources. Figure 6.18 illustrates a uniform cylindrical volume source of strength S_V. If the vertical strip is considered as a line source, it has a line source strength of $(\rho\, d\rho\, d\psi)S_V$. From Eq. (6.20) it is seen that at point P_0 on the axis, if the medium is nonattenuating,

$$\begin{aligned} R(P_0) &= 2\pi\hat{R}S_V\int_0^a \operatorname{arccot}\left(\frac{\rho}{l}\right)d\rho \\ &= 2\pi\hat{R}S_Vl\left[\frac{a}{l}\operatorname{arccot}\left(\frac{a}{l}\right) + \frac{1}{2}\ln\left(1 + \frac{a^2}{l^2}\right)\right]. \end{aligned} \tag{6.89}$$

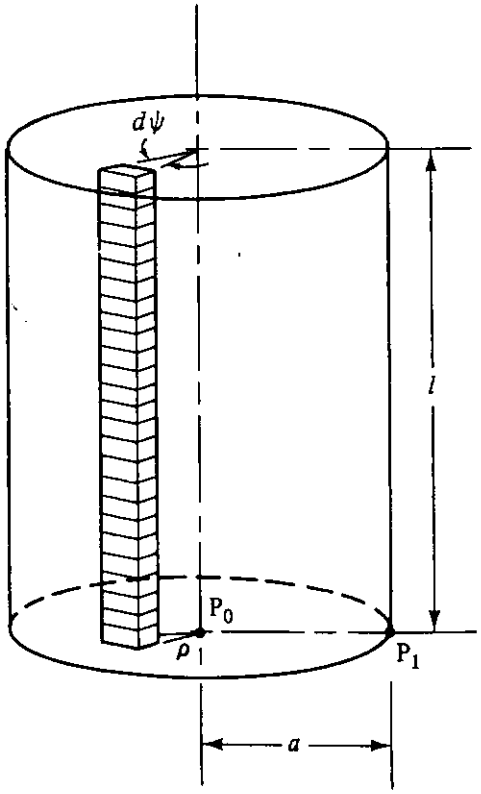

Figure 6.18 Isotropic volume source in the form of a right, circular cylinder.

At point P_1 on the edge of the cylinder, again under the assumption of a non-attenuating medium,

$$R(P_1) = 2\pi\hat{R}S_V \int_0^l \int_0^a \frac{\rho\, dz\, d\rho}{[z^4 + 2z^2(a^2 + \rho^2) + (a^2 - \rho^2)^2]^{1/2}} \tag{6.90}$$

$$= \pi\hat{R}S_V \left\{1 + \frac{2a}{l} - \left[1 + \left(\frac{2a}{l}\right)^2\right]^{1/2} + \ln\left(\frac{1}{2}\left[1 + \left(1 + \frac{4a^2}{l^2}\right)^{1/2}\right]\right)\right\}. \tag{6.91}$$

If an attenuating medium is present, the formulation is more complicated and in general must be expressed analytically in terms of a geometrically elaborate integral requiring solution by numerical techniques on a computer, even though derived as a direct extension of the elementary principles previously discussed. The literature contains a number of tables and graphed functions useful for such problems [3].

Solid cylindrical sources are encountered, for example, in the case of large pipes carrying radioactive material, or from reactor used fuel assemblies in which the radioactive fission products are considered to be smeared out over the cylindrical volume.

Frustrum of a cone. Although the frustrum of a cone seems an unlikely volume source to meet in practice, it is a useful approximation to a cylindrical source when the detector is on the axis of the cylinder, as shown in Fig. 6.19(a), giving a result somewhat higher than that which would actually result from the cylinder.

If the frustrum of the cone is not externally shielded, as shown in Fig. 6.19(b), one can find the differential detector response $dR(P)$ at point P due to the section of the frustrum of thickness dx, treated as a disk source [see Eq. (6.60)] with an area source strength of $S_V\, dx$, to be

$$dR(P) = 2\pi\hat{R}S_V\, dx\, [E_1(k_s x) - E_1(k_s x \sec\theta_0)]. \tag{6.92}$$

Thus,

$$R(P) = 2\pi\hat{R}S_V \int_0^H [E_1(k_s x) - E_1(k_s x \sec\theta_0)]\, dx \tag{6.93}$$

$$= 2\pi\hat{R}\frac{S_V}{k_s}[1 - E_2(k_s H) + \cos\theta_0 E_2(k_s H \sec\theta_0) - \cos\theta_0]. \tag{6.94}$$

If a slab shield of thickness t is interposed between the source and the detector, the response at P can be readily shown to be

$$R(P) = 2\pi\hat{R}\frac{S_V}{k_s}\{E_2(kt) - E_2(k_s H + kt) - \cos\theta_0 E_2(kt \sec\theta_0) + \cos\theta_0 E_2((kt + k_s H)\sec\theta_0)\}. \tag{6.95}$$

Spherical volume sources. For objects as simple as a radioactive pellet or as elaborate as a fluidized-fuel reactor, spherical volume sources are readily visualized.

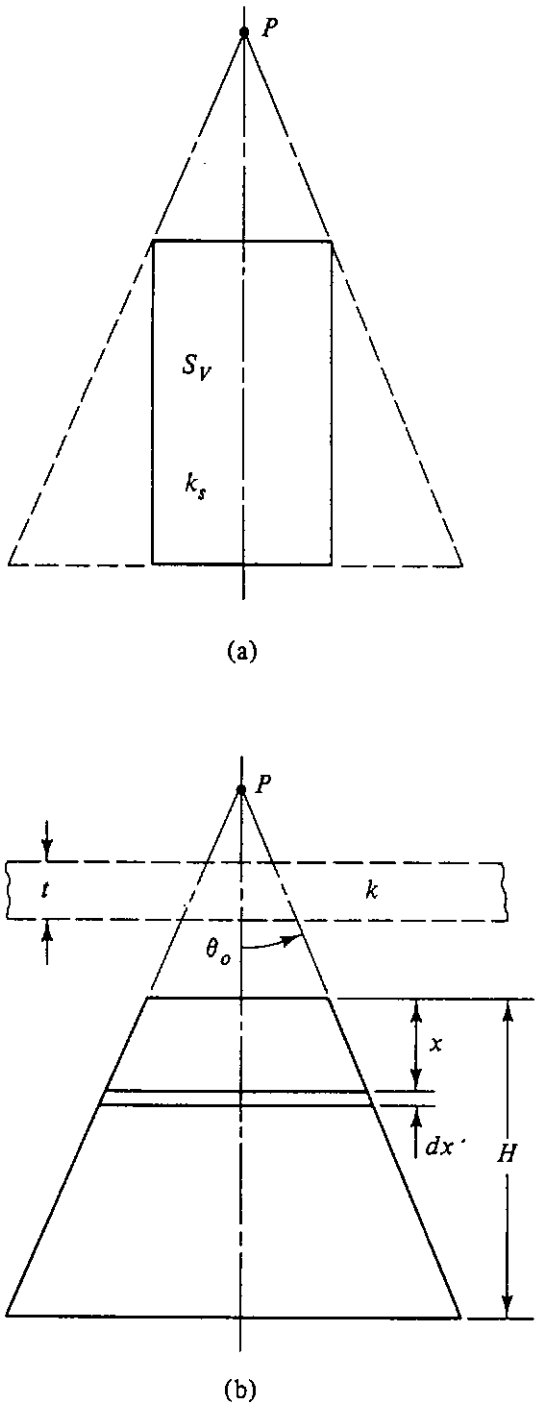

Figure 6.19 Frustrum of a cone as an approximation for a cylindrical volume source.

Consider the spherical volume source illustrated in Fig. 6.20(a) having a source strength of S_V and with attenuation characteristics established by k. The response of a detector at P_4 can be obtained by integration of the response from all differential shells of thickness $d\rho$, each differential response being given by Eq. (6.73) for a shell of surface source strength $S_V\, d\rho$:

$$R(P_4) = 4\pi\hat{R}S_V \int_0^a e^{-k\rho}\, d\rho \tag{6.96}$$

$$= \frac{4\pi\hat{R}S_V}{k}(1 - e^{-ka}). \tag{6.97}$$

Figure 6.20(b) shows how the detector response at P_2 may be obtained, with the use of the same surface source formula modified by the fact that the solid angle subtended by the half angle θ is not 4π but is $2\pi(1 - \cos\theta)$. Since $\cos\theta$

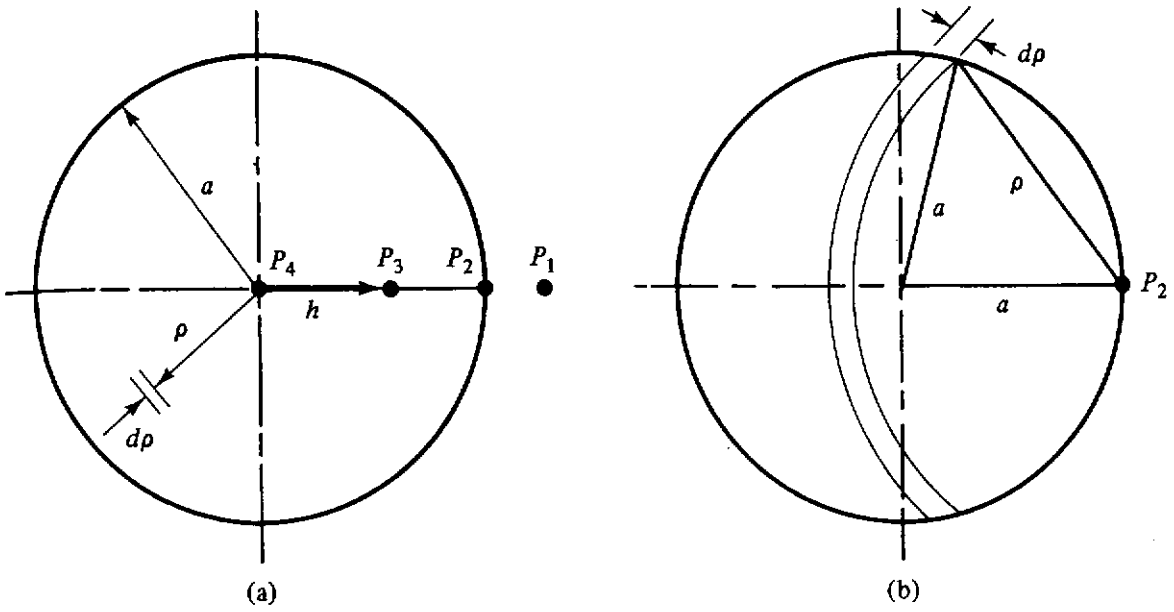

Figure 6.20 Spherical volume source.

may be replaced by $\rho/2a$,

$$R(P_2) = 2\pi\hat{R}S_V \int_0^{2a} \left(1 - \frac{\rho}{2a}\right) e^{-k\rho}\, d\rho \tag{6.98}$$

$$= \frac{2\pi\hat{R}S_V}{k}\left[1 - \frac{1}{2ka}(1 - e^{-2ka})\right]. \tag{6.99}$$

The detector response at P_3 may be obtained by a straightforward but tedious integration of the response from a typical differential volume element of the sphere, to give

$$R(P_3) = \frac{4\pi\hat{R}S_V}{k}\left\{1 - \frac{1}{2}e^{-b} - \frac{1}{2}e^{-b'} - \frac{1}{4kh}[(1 + b)e^{-b} - (1 + b')e^{-b'}] + \frac{bb'}{4kh}[E_1(b) - E_1(b')]\right\}, \tag{6.100}$$

where $b = k(a - h)$ and $b' = k(a + h)$.

The detector response at a location P_1 outside the sphere is not available in closed form but can be expressed in terms of a spherical G function, defined and tabulated elsewhere in the shielding literature [3].

6.5 POINT KERNEL

The ray technique explained and elaborated upon so far in this chapter is a particular branch of a more general approach called the *point-kernel* technique, since the method involves dividing up extended sources into differentially small sources which can be treated independently as point sources. The resulting differential responses become an integrand or "kernel" inside an integral, which then gives total detector response due to the entire extended source.

The point-kernel approach may be explained on two levels. In the broadest and most rigorously correct sense, a differential detector response for a detector

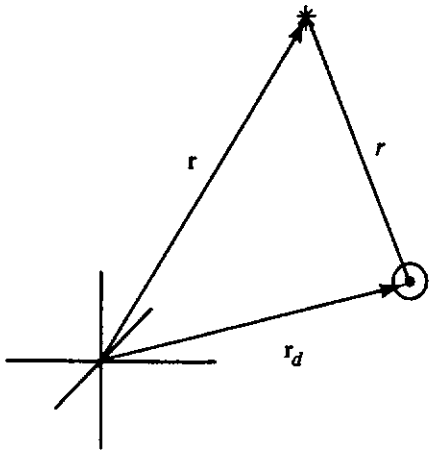

Figure 6.21 Source and detector locations as defined in the "point kernel."

at the point designated by the position vector $\mathbf{r}_d$ (see Fig. 6.21) resulting from a point source of unit strength at a location designated by the position vector $\mathbf{r}$ can be designated as a function $G(\mathbf{r}, \mathbf{r}_d)$; and this function is the "point kernel."[7]

A somewhat simplified point kernel can be defined if one feels justified in making the assumption that the functional relationship of G to its arguments $\mathbf{r}$ and $\mathbf{r}_d$ can be expressed, at least to a satisfactory degree of approximation, solely in terms of r ($\equiv |\mathbf{r} - \mathbf{r}_d|$). Thus, G can be denoted as $G(r)$.

The point-kernel approach—even the simplifed point-kernel approach—is not necessarily hampered by the strictures of the ray approach, such as radiation transport only along the ray and exponential attenuation. An example will suffice to show this. Consider the situation depicted in Fig. 6.22 in which a spherical cavity of essentially nonattenuating material (thin plasma, for example) contains a distributed source, spherically symmetric with respect to the center. At this center is placed the detector. The medium surrounding the cavity is highly reflective to the particles emitted by the source. A ray approach would predict a detector response which is much too low, since the ray technique cannot account for the important reflection contributions. On the other hand, a point kernel can, in principle, be specified so as to account for the backscattering from the wall of the cavity; and since the situation is spherically symmetric, the

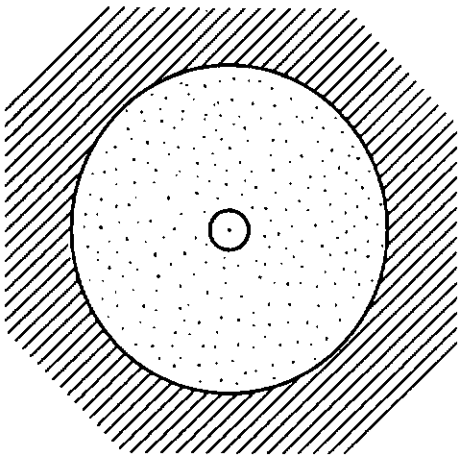

Figure 6.22 Spherical cavity containing a distributed source and a point detector.

[7]The more mathematically minded student will recognize the similarity of G to a Green's function.

simplified point kernel, $G(r)$, is precisely valid to give an exact answer for the detector response.

6.6 GEOMETRIC TRANSFORMATIONS

Many times a shielding problem may be more easily solved if its solution can be related, either rigorously or within a reasonable degree of approximation, to the solution of another problem which is more convenient to solve. In particular, it is often useful to relate detector responses for two cases in which the geometric distribution of the sources differ. This section derives the appropriate equations that transform shielding situations from one type of idealized source distribution to another.

6.6.1 Point to Volumetric and Area-Source Transformations

In general, most transformations of this sort begin with the expression which considers the detector response (dose or dose rate) from a distributed source as a sum, or integral, of responses from differential increments of the distributed source taken as individual point sources. Thus,

$$R = \int_V S_V G(\mathbf{r}, \mathbf{r}_d)\, dV \tag{6.101}$$

for a volume source, or

$$R = \int_A S_A G(\mathbf{r}, \mathbf{r}_d)\, dA \tag{6.102}$$

for an area source. Here, R is the detector response, S_V is the volumetric source strength, S_A is the area source strength, and $G(\mathbf{r}, \mathbf{r}_d)$ is the point kernel for a source at position $\mathbf{r}$ and detector at position $\mathbf{r}_d$ (see Section 6.5). These formulas may be considered as transformations from a point-source response $S_p \cdot G$ to a volumetric or area-source response R, respectively.

The foregoing relations are exact because of the independence of effects of the individual sources. Most of the transformations to follow depend on the validity, either precisely or approximately, of the assumption that the geometric dependence of the point kernel is solely on r, where $r \equiv |\mathbf{r} - \mathbf{r}_d|$. Thus, the simplified point function $G(r)$ is used, unless specifically stated otherwise.

6.6.2 Infinite Plane to Point-Source Transformation

From Eq. (6.57) it is clear that for a detector at a distance z above an infinite plane containing a uniform isotropic area source[8] (see Fig. 6.23),

$$R_{pl}(z) = 2\pi S_A \int_z^\infty rG(r)\, dr. \tag{6.103}$$

[8]For example, if $G(r) = e^{-r/\lambda}/4\pi r^2$, which is proper if the source is expressed in total number of particles per unit time and the detector response is a particle flux density, the result is equivalent to Eq. (6.58).

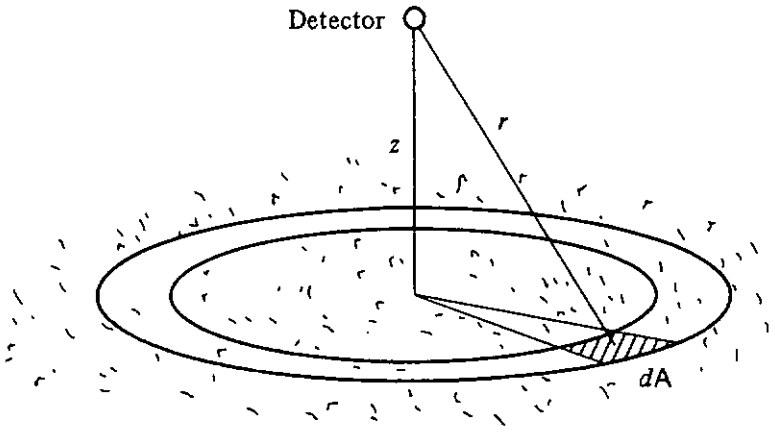

Figure 6.23 Detector above an infinite plane isotropic source.

If one differentiates with respect to z, by Leibnitz's rule, one obtains

$$\frac{dR_{pl}(z)}{dz} = -2\pi S_A[rG(r)]_{r=z} \tag{6.104}$$

or

$$G(r) = -\frac{1}{2\pi S_A}\left[\frac{1}{z}\frac{dR_{pl}(z)}{dz}\right]_{z=r} \tag{6.105}$$

6.6.3 Circular Area (Disk) to Point-Source Transformation

From Eq. (6.102) it is clear that

$$R_{\text{disk}}(z, a) = 2\pi S_A \int_z^{(z^2+a^2)^{1/2}} rG(r)\,dr \tag{6.106}$$

for the detector response on the axis of a flat circular area source (sometimes called a "disk"), where z is the distance from the detector to the center of the disk, a is the radius of the disk, and S_A is the source strength per unit area. This equation is also valid for an annulus source where the distances from the detector on the axis to the outer and inner boundaries of the annulus are the upper and lower limits of the integral, respectively.

By differentiation of Eq. (6.106) (applying Leibnitz's rule) one obtains

$$G(r) = -\frac{1}{2\pi S_A}\left[\frac{1}{z}\frac{\partial}{\partial z}R_{\text{disk}}(z, a)\right]_{z=r} + G((r^2 + a^2)^{1/2}). \tag{6.107}$$

This is valid for any r, thus the last term may be replaced by

$$G((r^2 + a^2)^{1/2}) = \frac{1}{2\pi S_A}\left[\frac{1}{z}\frac{\partial}{\partial z}R_{\text{disk}}(z, a)\right]_{z=(r^2+a^2)^{1/2}} + G((r^2 + 2a^2)^{1/2}). \tag{6.108}$$

Successive applications of this recursion procedure leads to the following expression for $G(r)$:

$$G(r) = -\frac{1}{2\pi S_A}\sum_{\nu=0}^{\infty}\left[\frac{1}{z}\frac{\partial}{\partial z}R_{\text{disk}}(z, a)\right]_{z=(r^2+\nu a^2)^{1/2}} \tag{6.109}$$

This is a useful formula in determining the value of a point kernel from experimental observations made with a circular disk isotropic source, when a

thin disk is considered preferable to a pellet (approximate point source) in order to provide sufficient source strength and minimize self-absorption in the source.

6.6.4 Spherical Surface to Infinite Plane Transformation

As shown in Fig. 6.24, a spherical surface contains a uniformly distributed isotropic area source of strength S_A. The geometric parameters are as indicated. The response at the center of this sphere embedded in a homogeneous infinite medium is given by

$$R_{sph}(z) = S_A \int_A G(r)\, dA \tag{6.110}$$

$$= 2\pi S_A \int_0^{\pi} a^2 \sin\theta G(r)\, d\theta. \tag{6.111}$$

It is easily shown that

$$r^2 = (a + z)^2 + a^2 - 2a(a + z)\cos\theta, \tag{6.112}$$

so that, by differentiation, one obtains

$$r\, dr = a(a + z)\sin\theta\, d\theta. \tag{6.113}$$

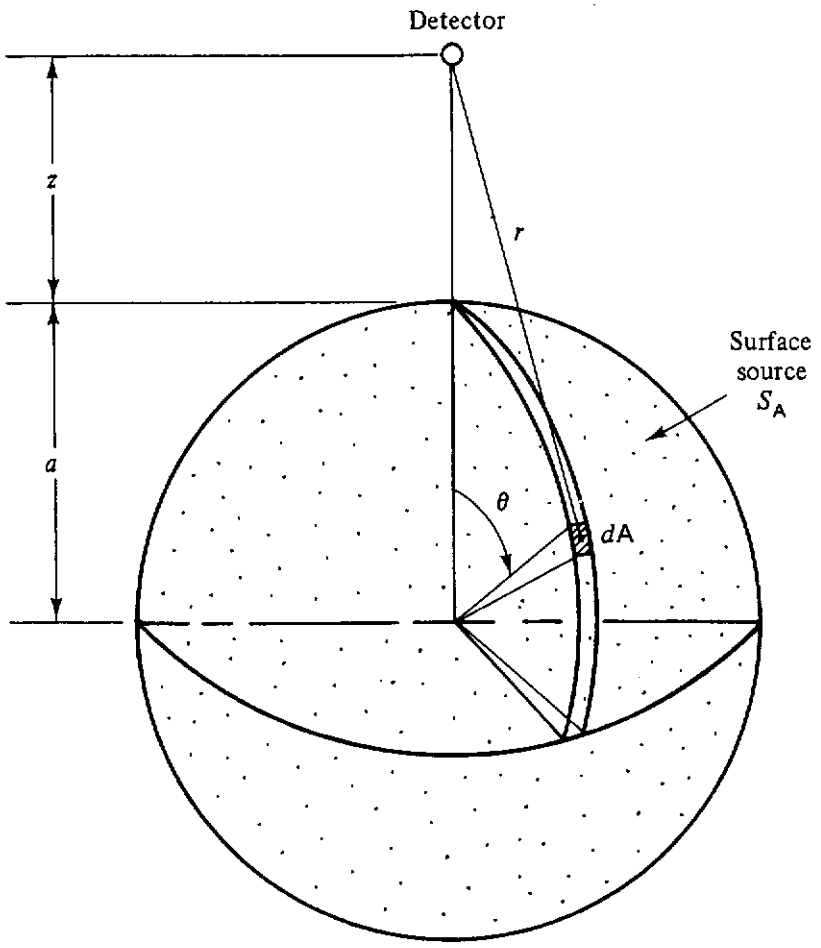

Figure 6.24 Detector outside a spherical surface isotropic source.

With the help of Eq. (6.113), Eq. (6.111) becomes

$$R_{\text{sph}}(z) = 2\pi S_A \frac{a}{a+z} \int_z^{z+2a} rG(r)\, dr$$
$$= \frac{a}{a+z}[R_{pl}(z) - R_{pl}(z+2a)], \tag{6.114}$$

where R_{pl} is the detector response to an infinite plane having the same area source strength as the spherical surface under consideration.

If $a > \lambda$, where λ is the relaxation length for the radiation, the latter R_{pl} term in Eq. (6.114) would be relatively insignificant in amount, so that, in such a case

$$R_{\text{sph}}(z) \approx \frac{a}{a+z} R_{pl}(z). \tag{6.115}$$

If the medium within the spherical surface is appreciably different from the medium outside the surface, one may seriously question the validity of the assumption that $G \equiv G(r)$; therefore, in such a case the transformation represented by Eq. (6.114) may be a poor one. On the other hand, if a is greater than λ both inside and outside, the contribution to the detector response from areas on the side of the sphere away from the detector will be negligible anyway; and Eq. (6.115) is likely to be a good approximation after all.

6.6.5 Cylindrical Surface to Infinite Plane Transformation

For a detector a distance z from an infinitely long cylindrical surface, it is plausible to expect that the detector response would be somewhere between $R_{pl}(z)$ and $R_{\text{sph}}(z)$ [given by Eq. (6.115)], since a cylinder has a one-way curvature —halfway (in a sense) between the zero curvature of the plane and the two-way curvature of the sphere. In fact, the following intermediate equation

$$R_{\text{cyl}}(z) \approx \left(\frac{a}{a+z}\right)^{1/2} R_{pl}(z) \tag{6.116}$$

can be shown to be reasonably valid, within restrictions similar to those for the validity of Eq. (6.115) [4].

6.6.6 Volume to Surface Source Transformation (Elementary)

Consider a semi-infinite, uniformly distributed, isotropic volume source in a homogeneous medium, separated by a surface from another homogeneous, source-free medium. A detector is embedded in the latter medium. The detector response can be made the same if the volume source were replaced by an appropriate area isotropic source distributed on the surface separating the two media; and one need only relate the strength of the equivalent surface source to the strength of the volume source.

This is easily done within the framework of ray theory, involving an assumption of the validity of inverse-square geometric attenuation from a point

source and exponential material attenuation. [This is a more restrictive assumption than that involving simply the point kernel $G(r)$.] Figure 6.25 illustrates a ray from the detector in medium 1 to a typical differential surface area dA. The differential solid angle $d\Omega$ subtended by dA also intercepts a differential portion of the volume source in medium 2. Geometric parameters are as indicated in the figure. Note particularly the angle α between the ray and the normal to the surface at the position of dA.

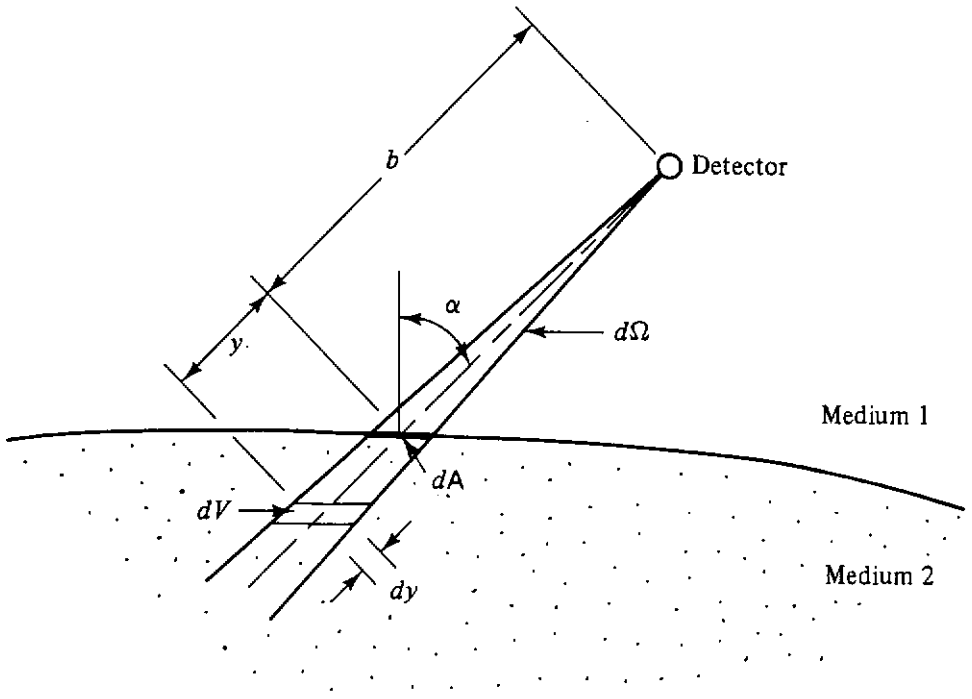

Figure 6.25 Detector above a semi-infinite volume source of homogeneous nature and uniform strength.

S_V is the source strength per unit volume, and $\hat{R}$ is the detector response at 1 unit distance in a vacuum from a unit-strength point source of the same character as is distributed in the volume. Then the contribution from dV is given by

$$d^2R = \frac{S_V \hat{R}\, dV\, e^{-y/\lambda_2} e^{-b/\lambda_1}}{(b+y)^2}, \tag{6.117}$$

where λ_1, the relaxation length in medium 1, is identically equal to $1/k_1$, and λ_2 similarly is $1/k_2$. Since $dV = (b+y)^2\, d\Omega\, dy$,

$$d^2R = S_V \hat{R}\, d\Omega\, e^{-b/\lambda_1} e^{-y/\lambda_2}\, dy. \tag{6.118}$$

The total contribution of all source volume elements within the aperture of $d\Omega$ becomes by integration over y:

$$dR = S_V \hat{R} \lambda_2 e^{-b/\lambda_1}\, d\Omega. \tag{6.119}$$

Assume an equivalent surface source on dA, with strength S_A^{eq} per unit area, such that

$$dR = \frac{S_A^{eq} \hat{R}\, d\text{A}\, e^{-b/\lambda_1}}{b^2}. \tag{6.120}$$

Since $d\mathrm{A} = b^2\, d\Omega \sec \alpha$,

$$dR = S_{\mathrm{A}}^{eq} \hat{R}\, d\Omega \sec \alpha\, e^{-b/\lambda_1}. \tag{6.121}$$

If one equates the two expressions for dR, it becomes evident that

$$S_{\mathrm{A}}^{eq} = S_V \lambda_2 \cos \alpha. \tag{6.122}$$

A physical meaning can be attached to the relationship. The effect on the detector is the same as if all the radiation source within a rectangular prism below $d\mathrm{A}$ of depth $\lambda_2 \cos \alpha$ were brought to the surface and distributed throughout $d\mathrm{A}$ [see Fig. 6.26(a)]. Somewhat more approximately, if $b \gg \lambda_2$, it can be considered that the equivalent area source distributed throughout $d\mathrm{A}$ is made up of all the volume source included within $d\Omega$ to a distance along the ray of λ_2 [see Fig. 6.26(b)].

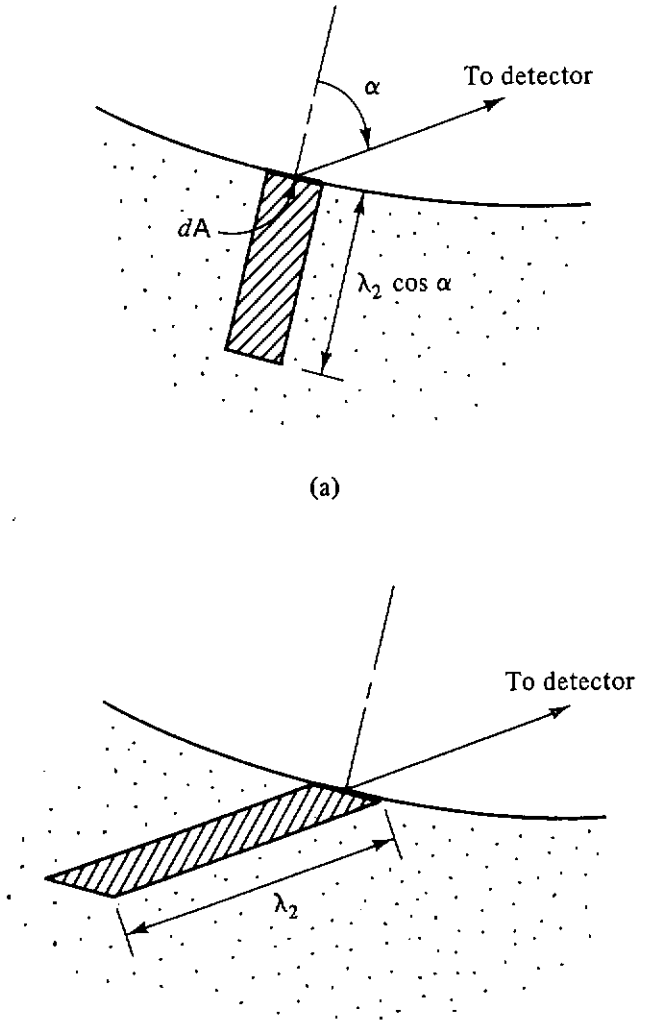

Figure 6.26 Equivalence of volume source and surface source of radiation.

Under practical conditions, medium 2 is not infinite in depth (y does not go to infinity) nor is S_V likely to be constant throughout the medium. However, if the medium is homogeneous and uniform as to source strength for at least several relaxation lengths, the theorem is generally valid to a close approximation.

There are also situations, when one is integrating over all sources to find R, in which one finds that most of the contribution to R comes from parts of the surface for which α is close to 90°. In such cases,

$$S_A^{eq} = S_V \lambda_2 \tag{6.123}$$

can be used throughout the surface to simplify the integration process, without significant loss of accuracy. This would be the case, for example, for a detector above an infinite plane, for which z (detector height above the plane) is much greater than λ_1 (the relaxation length in the medium above the plane).

6.6.7 Volume to Surface Source Transformation (Rigorous)

A much more general and rigorously valid theorem is available for transformation of a volumetrically distributed source to a surface source. It is stated here with reference to Fig. 6.27. (Proof is provided later, in Chapter 10.)

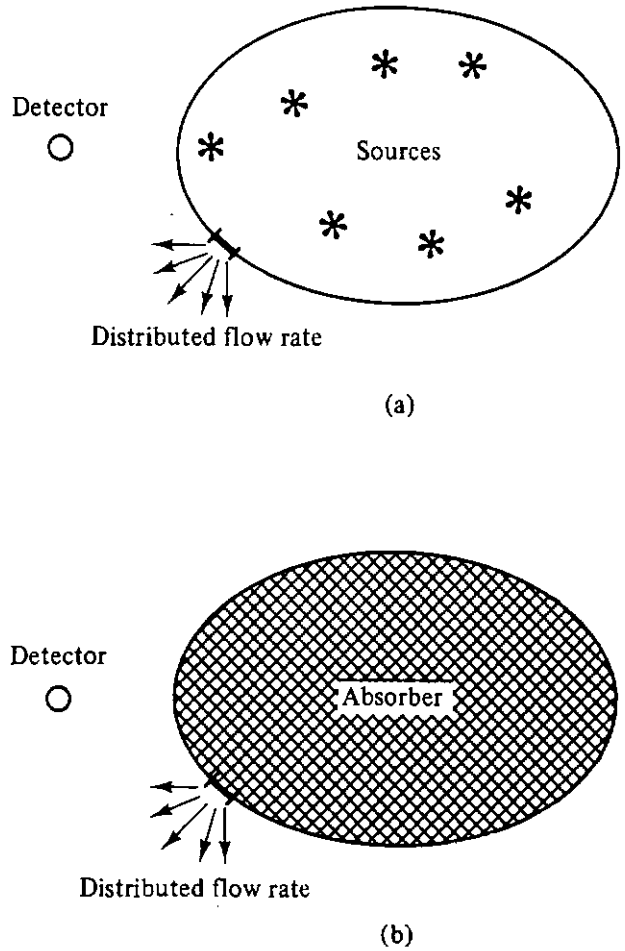

Figure 6.27 Equivalent situations with the same detector responses.

It is supposed that a spatial distribution of matter and radiation sources, discrete or distributed, exists. Call this situation A. A hypothetical closed surface that may surround some of the sources is visualized in this situation. (The surface may seem to surround the detector rather than sources, but in an essential sense this is the same thing.) Assume, for comparison, situation B, in which the detector is the same; the medium and source distribution are the same as in

situation A on the detector side of the closed surface, but on the other side the medium is a perfect absorber. (That is, there is no return across the surface in situation B of radiation going from the detector side to the nondetector side—in some configurations a vacuum on the nondetector side is a possible assumption to ensure this.)

Consider also that in situation B, the entire closed surface provides an area source of such a character that the strength per unit area in each direction and at each energy, $S_A(\mathbf{r}_s, \mathbf{\Omega}, E)$, at each point $\mathbf{r}_s$ on the surface is equal to the flow rate $j_n(\mathbf{r}_s, \mathbf{\Omega}, E)$ at the corresponding point in situation A. Under the conditions above, the detector response for the two situations are the same. This implies that the sources within the closed surface may be replaced by the flow rate they are shown to create at the surface.

Many shielding problems involving a distributed volume source may be greatly simplified by a judicious selection of the closed surface and a knowledge of the flow rate through the surface. For example, a reactor biological shield problem can be solved if the nature of the radiation leakage through the reactor core surface is known with reasonable accuracy from prior transport analysis for the core region. This transformation also shows how one can visualize a beam from a point source far away from a shield as being equivalent to an area source at the face of the shield itself, as illustrated in Fig. 6.28. If one considers the source-to-shield distance as being very large compared with other pertinent dimensions, the shield can be analyzed as if a plane, parallel beam originated at the front face.

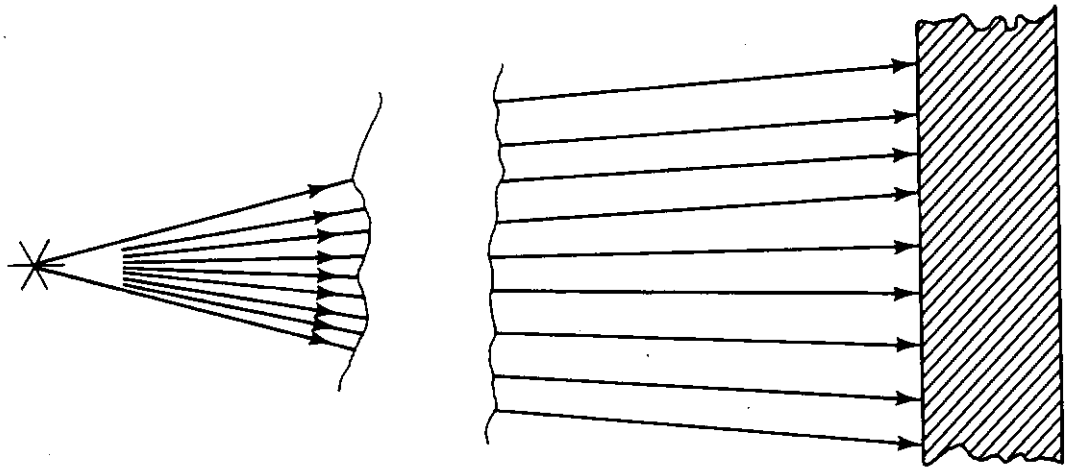

Figure 6.28 Beam from a point source striking a slab.

6.7 SPECIAL CONCEPTS USEFUL FOR DESIGN PURPOSES

The emphasis in most of this text is on *analysis* rather than *synthesis*, on *principles* rather than *practice*. Yet most shielding specialists will sooner or later be required to apply these principles in the context of a design problem. It is desirable at this point to introduce briefly a few concepts particularly applicable to the design process.

The governing concept in any shielding design is the *maximum permissible prescribed dose equivalent* (MPD), sometimes alternatively designated the *maximum permissible exposure* (MPE) if the radiation field consists entirely of photons and if the "dose" is measured in units of exposure (roentgens). The basic shielding requirement then is that the actual prescribed dose equivalent (or exposure) not exceed the MPD (or MPE) during some appropriate period as specified.[9]

Sometimes the shield designer will find that the MPD is given him in a more or less arbitrary fashion; at other times the shielding specialist may be required to use his own best judgment for establishing it. Fortunately, guidance is available under a variety of conditions. For many situations the guidance has been the following:

1. The MPD for a week is given as 1 millisievert for personnel who work in occupations in which a small but definite radiation risk is knowingly accepted ("occupational exposure").
2. The MPD for a member of the general public is taken as one-tenth the value above, or 0.1 millisievert per week ("nonoccupational exposure"). For the average of a large number of members of the general public, the MPD should be further reduced by a factor of 3.
3. The exposure in roentgens is often taken to be comparable to the prescribed dose equivalent with a conversion factor of 100 milliroengtens to 1 millisievert. (See Chapter 5 for more precise conversion factors.)
4. Regardless of the MPD or MPE values given above, a still more basic rule is that all radiation should be reduced to the level *as low as reasonably achievable*. This is the so-called "ALARA" doctrine.

Two subsidiary concepts need to be defined. One is called the *use factor*, U, defined as the fraction of time during which the radiation under consideration is directed at a particular protective shield. The other is called the *occupancy factor*, T, the fraction of time when the radiation is directed toward the protective shield that the position behind the shield, which requires protection, is actually occupied. Both U and T are unity or less; and one can see that their use can increase the allowable value of the transmitted dose rate that is required as a shielding design criterion by the ratio $1/UT$.[10] Some guidance for selection of U and T is available in the literature [2].

[9]Terminology is variable here. The ICRP [5] uses terms such as "recommended limits," "secondary limits," and "authorized limits."

[10]It is common to define the occupancy factor, T, as the fraction of time the position behind the shield is occupied, without any reference to the period that the radiation beam is directed toward the shield in question [2]. However, it is not proper to multiply U and T in the simple fashion as shown in this text unless either the probabilities of occupancy and use are statistically independent or their possible dependency is allowed for by use of the more precise definition given in the body of this text. We prefer the latter approach as being safer.

The term *workload*, with symbol W, is sometimes met as an aspect of the design process. In terms of the concepts introduced in this chapter, W may be the same as $\hat{R}S_p$ if $\hat{R}$ is on an accumulated-dosage basis (usually over a week's time). On the other hand, if $\hat{R}$ is on a time-rate basis, W is given by $\hat{R}S_p t$, where t is the number of units of time in the time interval considered. This would imply a definition of W as the detector response one unit of distance from a given source, accumulated over the prescribed period of time, in the absence of shield or attenuating medium. This specialized terminology will be used in this text only in the special cases where it is commonly employed, such as for medical-facility shielding (see Section 7.5).

The basic principle in design is to see that the "dose" provided a person (or a sensitive piece of equipment) in a specified period of time will not exceed the specified limit for that period of time. For single sources, this may be carried out by use of such formulas as are given in this chapter, suitably modified, as appropriate, by use and occupancy factors. Often these formulas are used in a reverse manner, by setting the response function equal to the limit and then solving for a combination of shield thickness and source-to-detector distance which will just establish this value. The design process may require a technique of "guess and analysis," especially if more than one source is present in a given situation. A series of trial designs may be analyzed in an iterative fashion until a satisfactory design solution is found to be acceptable.

REFERENCES

1. "Glossary of Terms in Nuclear Science and Technology," USAS NI.1-1967, American National Standards Institute, New York, 1967.
2. "Structural Shielding Design and Evaluation for Medical Use of X Rays and Gamma Rays of Energies up to 10 MeV," NCRP Report 49, National Council on Radiation Protection and Measurements, Washington, D.C., 1976.
3. E. P. Blizard, A. Foderaro, N. G. Goussev, and E. E. Kovalev, "Extended Radiation Sources (Point Kernel Integrations)," in *Engineering Compendium on Radiation Shielding*, Vol. I, R. G. Jaeger (ed.), Springer-Verlag, New York, 1968, Chap. 6.
4. H. Etherington (ed.), *Nuclear Engineering Handbook*, McGraw-Hill, New York, 1958, p. 7–95.
5. "Recommendations of the International Commission on Radiological Protection," ICRP Publication 26, published as Annals of the ICRP 1, No. 3, Pergamon, Elmsford, N.Y., 1977.

PROBLEMS

6.1. Verify Eqs. (6.34) and (6.35).

6.2. Consider a uniform line isotropic source of length L and strength S_L on the axis of a cylinder of radius a and attenuation coefficient μ, as shown in Fig. P6.2. There is no attenuation outside the cylinder. Derive an expression for the uncol-

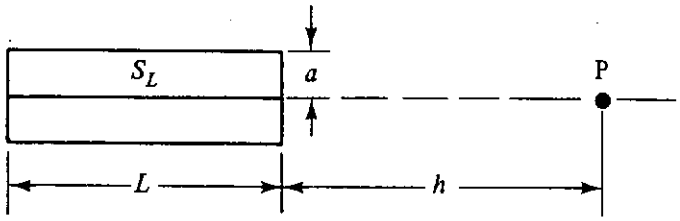

Fig. P6.2

lided flux density at P. Suppose that the source is 10 TBq of ^{60}Co and $L = 10$ cm. Suppose that the cylinder is iron with $a = 1$ cm and $h = 100$ cm. For uncollided photons, evaluate $\dot{K}^0_{\text{air}}$, $\dot{X}^0$, and $\dot{H}^0_p$.

6.3. Consider a 14-MeV neutron generator emitting 10^{10} neutrons per second. The neutrons are created on a disk of 1-cm radius, coated with ^{3}H, bombarded by a beam of 150-keV deuterons. It may be assumed that the neutrons are emitted isotropically. Neglecting air attenuation, evaluate $\dot{H}_p$ at a distance of 100 cm from the source.

6.4. Consider a 37-TBq ^{60}Co source (1.25 MeV) uniformly distributed over a disk of area 1 m^2. A 2-cm-thick sheet of lead covers the source. A detector is located, in air, 50 cm from and on the axis of the disk. For uncollided photons, evaluate ϕ^0, $\dot{K}^0_{\text{air}}$, $\dot{X}^0$, and $\dot{H}^0_p$.

6.5. Verify Eq. (6.69).

6.6. Consider a point isotropic source on the axis of an infinite cylinder of radius R, and with linear attenuation coefficient k. What is the probability for a particle to escape the surface of the cylinder without having had an interaction? [*Hint:* See W. G. Bickley and J. Naylor, *Phil Mag.* **20**, 343–347 (1935).]

6.7. Consider a plane isotropic disk source of uniform strength S_A, radius R, in an infinite medium for which the linear attenuation coefficient is μ. A detector is located distance z from and on the axis of the disk. Derive an expression for the uncollided *angular* flux density $\phi^0(\theta)$ at P. Integrate this to determine the *total* uncollided flux density.

6.8. Consider a laterally infinite slab source of thickness L and uniform volumetric strength S_V (isotropic) in a medium characterized by attenuation coefficient μ. Find an expression for the *angular* distribution of the uncollided flux density at a distance z (in vacuum) from the slab surface.

6.9. A detector is located on the axis of an infinitely long cylindrical surface source of uniform strength S_A. The source and detector are in a nonattenuating medium. Derive an expression for the angular distribution of the flux density at the detector, $\phi(\theta)$, where θ is the polar angle measured with respect to the axis. Integrate $\phi(\theta)$ to obtain the total flux density.

6.10. Consider a uniform isotropic cylindrical surface source in a medium without attenuation. Let the cylinder length equal the diameter. Let ϕ^0 be the uncollided flux density, and ϕ^0_0 the uncollided flux density at the center of the cylinder. Plot ϕ^0/ϕ^0_0 for axial locations within the cylinder and for radial locations within the cylinder at the base and at the midplane.

6.11. Consider a uniform isotropic spherical surface source of strength S_A and radius R in a nonattenuating medium. Let ϕ^0_0 be the flux density at the center of the

sphere. Derive an expression for $\phi^0(r/R)$ where r is the radial distance. Plot ϕ^0/ϕ_0^0 versus r/R for $0 \leq r/R \leq 4$.

6.12. Repeat Problem 6.11 for a spherical volume source of strength S_V in a non-attenuating medium.

6.13. Show that Eq. (6.50) yields

$$R(P) = \frac{3}{\pi}\mathcal{R}(E_0)j_n^+\{(1+\eta^2)^{-1/2}\tan^{-1}[\epsilon(1+\eta^2)^{-1/2}] + \epsilon(\eta^2+\epsilon^2)^{-1/2}\tan^{-1}[(\epsilon^2+\eta^2)^{-1/2}]\} \quad \text{for } m=2,$$

$$R(P) = \frac{8}{3\pi}\mathcal{R}(E_0)j_n^+\{\epsilon\eta(1+\epsilon^2+\eta^2)^{-1/2}[(\epsilon^2+\eta^2)^{-1}+(1+\eta^2)^{-1}] + \tan^{-1}[\epsilon\eta^{-1}(1+\epsilon^2+\eta^2)^{-1/2}]\} \quad \text{for } m=3.$$

6.14 Using the method of Section 6.3, derive approximate values for the total detector responses $\dot{K}_{\text{air}}$, $\dot{X}$, and $\dot{H}_p$ for the conditions of Problem 6.2.

6.15. Using the method of Section 6.3, derive approximate values for the total detector responses $\dot{K}_{\text{air}}$, $\dot{X}$, and $\dot{H}_p$ for the conditions of Problem 6.4.

7 special techniques in photon attenuation

7.1 PHOTON BUILDUP-FACTOR CONCEPT

From Eq. (6.16) it is seen that, in an infinite homogeneous medium, the response of a point detector to uncollided photons at a distance r from a point source of monoenergetic photons is given by the formula

$$R^0(r) = \frac{R_1}{r^2} e^{-\mu_0 r} = \frac{\hat{R} S_p}{r^2} e^{-\mu_0 r}, \tag{7.1}$$

where $\hat{R}$ is the detector response one unit of distance in a vacuum from a point source of unit strength, S_p is the source strength, and μ_0 is the linear attenuation coefficient for photons of the source energy. Figure 7.1(a) shows this situation and a graph of the function $\ln (r^2 R^0)$ versus r, which appears as a straight line with slope $-\mu_0$. Suppose that the total detector response R to both uncollided and scattered photons were known, either on the basis of experimental data or through some accurate calculations. The function $\ln (r^2 R)$ also appears on the graph as the curved line above the straight one. For corresponding values of r, the ratio of the total to uncollided responses, $R(r)/R^0(r)$, is called the *buildup factor* and is denoted by the symbol $B(r)$; thus, Eq. (7.1) is modified to read

$$R(r) = \frac{\hat{R} S_p}{r^2} e^{-\mu_0 r} B(r). \tag{7.2}$$

Although the point-source buildup factor described above is the most useful, the buildup concept can be used in different situations. For example, Fig. 7.1(b) shows a plane slab with a broad, parallel, monoenergetic beam of photons incident on one face and a detector positioned at the opposite face. Here, again, the detector response to uncollided photons is

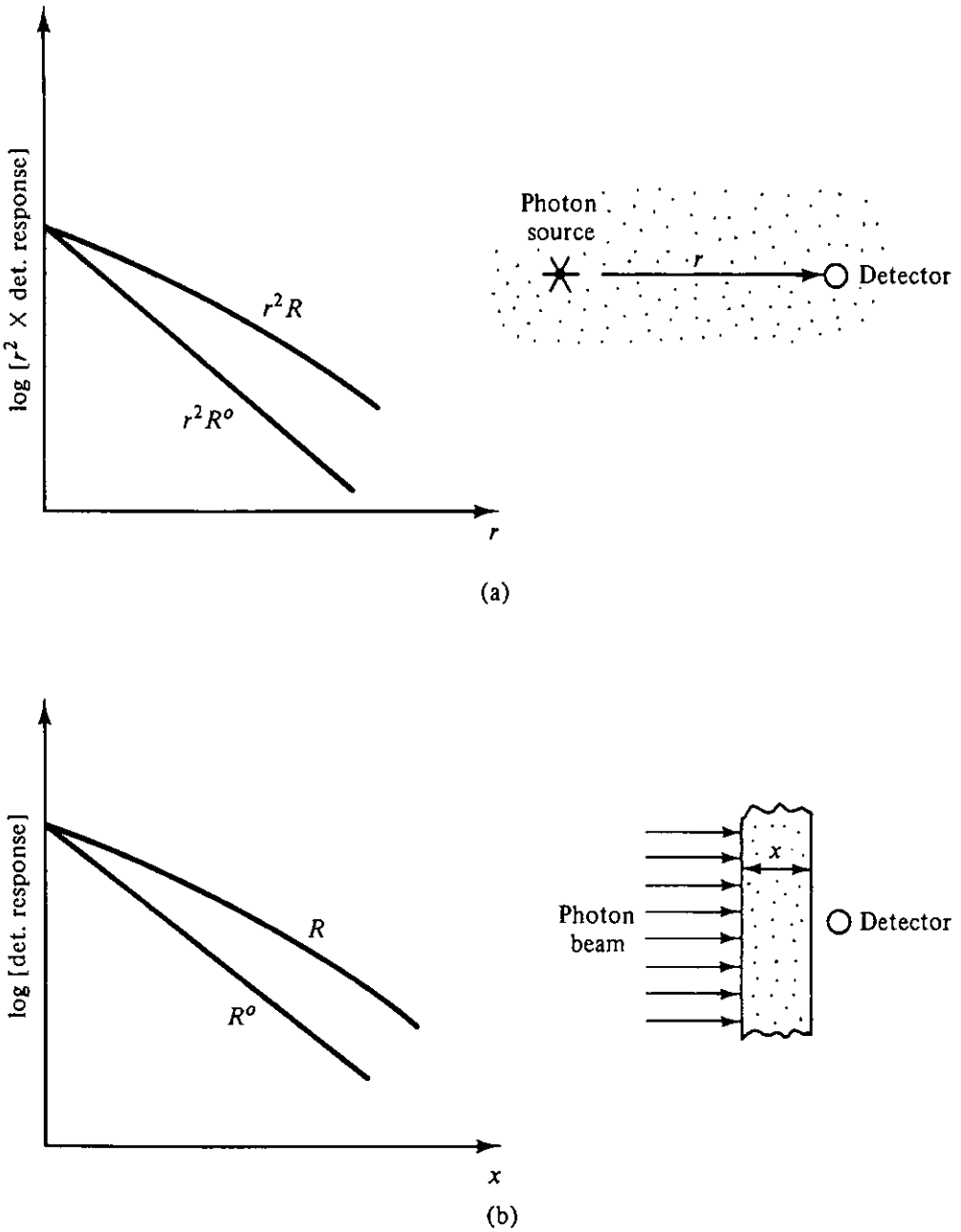

Figure 7.1 (a) Detector response in an infinite medium as a function of distance r from a point source. (b) Detector response behind a slab shield of thickness x illuminated by a parallel beam of radiation.

$$R^0(x) = R_0 e^{-\mu_0 x}, \tag{7.3}$$

where R_0 is the detector response in the absence of the slab (i.e., a vacuum between source and detector). If $R(x)$ is the total detector response (to both collided and uncollided photons), the buildup factor B is again defined as the ratio $R(x)/R^0(x)$; thus, Eq. (7.3) is modified to read

$$R(x) = R_0 e^{-\mu_0 x} B(x). \tag{7.4}$$

It is clear then that, in either case, $R = BR^0$; and because of the comparative ease of calculating R^0 in these and most practical cases, we can readily find the total detector response if only we are fortunate enough to have data for the buildup factors for the situation under consideration.

It is easily seen that, since the response to the in-scattered photons, R^s, is given by $R - R^0$, $R^s = (B - 1)R^0$. From this we note that B can never be less than unity. B can be exactly equal to unity only when the circumstances are such that R^0 is positive while R^s equals zero [this occurs when x equals zero for the case depicted in Fig. 7.1(b)] or when R^s remains finite while R^0 approaches infinity [this occurs for the point source case in Fig. 7.1(a) as r approaches zero].

Buildup factors can be obtained, in principle, by experiment; but since the attenuation and scattering coefficients are known with reasonable accuracy, buildup factors are customarily obtained by solution of the photon transport equation (Chapter 10) and the subsequent folding of the photon flux density at the detector position $\mathbf{r}_d$ into the response function. Thus, from the definition of B, one can easily see that for a specific case the buildup factor will be given by

$$B \equiv \frac{R}{R^0} = \frac{\int_0^{E_0} dE \mathcal{R}(E)\phi(\mathbf{r}_d, E)}{\mathcal{R}(E_0)\phi^0(\mathbf{r}_d)}, \tag{7.5}$$

where $\mathcal{R}(E)$ is the detector response function[1] (see Section 5.4).

Buildup factors are not constants, but rather vary with a number of parameters and specifications of a particular problem, as follows:

1. Distance of penetration through the attenuating medium. Intuition tells one, and it can be rigorously proved, that to free one from concern about density effects the values of buildup factor should depend on $\mu_0 r$ or $\mu_0 x$ (mean-free-path lengths) rather than on linear distances.
2. The geometric configuration of the attenuating medium, source, and detector position.
3. The type of medium, expressed in terms of the atomic charge number Z for elemental materials. For compounds or mixtures, an average Z is often used as the basis for finding values of the buildup factor, although this is somewhat approximate since no single method of averaging is precisely valid in a universal sense.
4. The type of detector response function $\mathcal{R}$.
5. The energy of the source photons, taken to be monoenergetic, and their direction of emission.

The list above implies the possibility of an enormous number of possible cases and huge tables of resulting buildup data. In spite of this possibility, the buildup factor concept has been found exceedingly useful for analysis of photon penetration.

[1]Equation (7.5) shows that in the use of buildup factors to calculate the detector response R, it is necessary to use the appropriate value of $\mathcal{R}(E_0)$, which in turn may require a choice of the proper energy deposition coefficient for the detector, $\mu_d(E_0)$. Section 5.4 provides the proper guidance for this determination. The choice of this coefficient also depends on the degree of approximation used for determination of the flux density, which, for the present purpose, is that used in the calculation of the buildup factors. For the buildup factors given in this text, the methods by which they were calculated generally imply the use of μ_{tr} for μ_d.

The necessity for large tables of data has been greatly reduced by the fact that photon cross sections, at least above the K-edge energies, are smooth functions of source energy and of atomic charge number of the attenuating medium. This property of photon cross sections implies that buildup data are needed only for a few selected values of source energies and elemental types, plus a few common mixtures or compounds. Accurate interpolation for other energies or materials is then possible. Moreover, buildup factors are smooth functions of distance (in terms of the mean-free-path length) and therefore only a few selected values out to the greatest distance of practical importance are needed. Thus, again, accurate interpolation for other distances is possible.

Only a few types of dosimetric response are of major interest: exposure (usually calculated as proportional to air kerma), absorbed dose in the shielding medium (usually calculated as medium kerma), tissue absorbed dose (usually calculated as tissue kerma), energy flow through a shield surface, and prescribed dose equivalent. Furthermore, the buildup factors are usually quite similar for these various types of response, and, as an approximation, one may often be substituted for another if the responses are expected to be nearly equal.

The amount of needed buildup factor data can be further reduced by recognizing that most practical geometric configurations of shield and/or source can be approximated by one or another of a few idealized situations. In view of the great emphasis on the point-kernel approach, as indicated in Chapter 6, the point-isotropic-source type of buildup factor is by far the most useful. Also, it is quite common in the ray approximation to use the point-isotropic, infinite-medium factors even though the shields in practical situations are not infinite and often not homogeneous. It is only necessary to use as the distance argument for the buildup factor the actual number of mean-free-path lengths of medium between the point source and the detector. In most cases, the approximation errors involved are not great.

However, buildup factors are not panaceas for all calculations in photon shielding. Complexities and difficulties in their use are discussed in more detail in Section 7.3.

7.2 BUILDUP-FACTOR VALUES AND EMPIRICAL APPROXIMATIONS

Exposure and material kerma (energy transfer) buildup factors are provided in Appendix 4 for point isotropic sources in homogeneous infinite media of air, water, concrete, iron, and lead [1,2]. The exposure buildup factors are most useful in point-kernel calculations for biological protective shields, while the material kerma buildup factors are useful for shield heating and radiation damage calculations. Other extensive tables of data are available in the literature [3]. Most of these data have been calculated by use of the "moments method" in the case of infinite medium calculations or by Monte Carlo techniques for situations involving medium boundaries (see Chapter 10).

In general, the buildup-factor data provided in this text are found to be accurate within error limits on the order of 10% or better. However, the data for lead at high energies may be considerably less accurate because the calculations on which they are based ignored the possibility of bremsstrahlung interactions. It has been estimated [4] that at energies up to 8 MeV the buildup factors for lead may be too small by factors up to 1.5.[2] It is therefore recommended that, when data are used for lead above 2 MeV, a factor of safety of at least 1.5 be applied to allow for such inaccuracies. This applies specifically to data from Tables A4.7 and A4.8, as well as data derived from the parameters for lead found in Tables A4.9 and A4.10 and in Fig. 7.2.

To reduce the amount of data and to provide an accurate analytical means of interpolation, various empirical formulas have been devised to give a moderately accurate representation of the buildup factor data as a function of distance. A good formula should satisfy the following criteria:

1. The number of independent parameters should be minimized, consistent with the accuracy requirements.
2. The formula should be simple and of a type that lends itself well to inclusion in the integrand of point kernels which are subsequently to be integrated.
3. The formula should reproduce exactly the value of unity for the buildup factor when the distance argument is zero under circumstances for which this is valid.
4. It would also be desirable to provide a formula that permits extrapolation to deep penetration, but this is difficult to do within requirement 2 since the deep penetration trends involve fractional powers of the distance [5].

Formulas for buildup factors that are widely favored and which satisfy the first three of the criteria above are:

Taylor's formula [6]

$$B = Ae^{-\alpha\mu_0 r} + (1 - A)e^{-\beta\mu_0 r}. \tag{7.6}$$

The advantage of this formula is that it fits, without difficulty, into any point kernel which already contains an exponential attenuation function. Values of the parameters A, α, and β for exposure buildup factor data in concrete are given in Appendix 4 and other values can be found in the literature [3,6]. Maximum deviations of formula predictions from the data are also provided in the appendix.

[2]This estimate is based on the use of μ_{en} in the calculation of the uncollided response. If the coefficient μ_{tr} is used for this purpose, in accordance with the footnote following Equation (7.5), partial compensation for ignoring bremsstrahlung may be effected. For example, it is estimated that the correction factor for lead kerma buildup factors at energies around 6–8 MeV can be lowered to about 1.2 because of the difference between μ_{en} and μ_{tr} for lead at that energy, provided the latter coefficient is used in calculating the uncollided contribution.

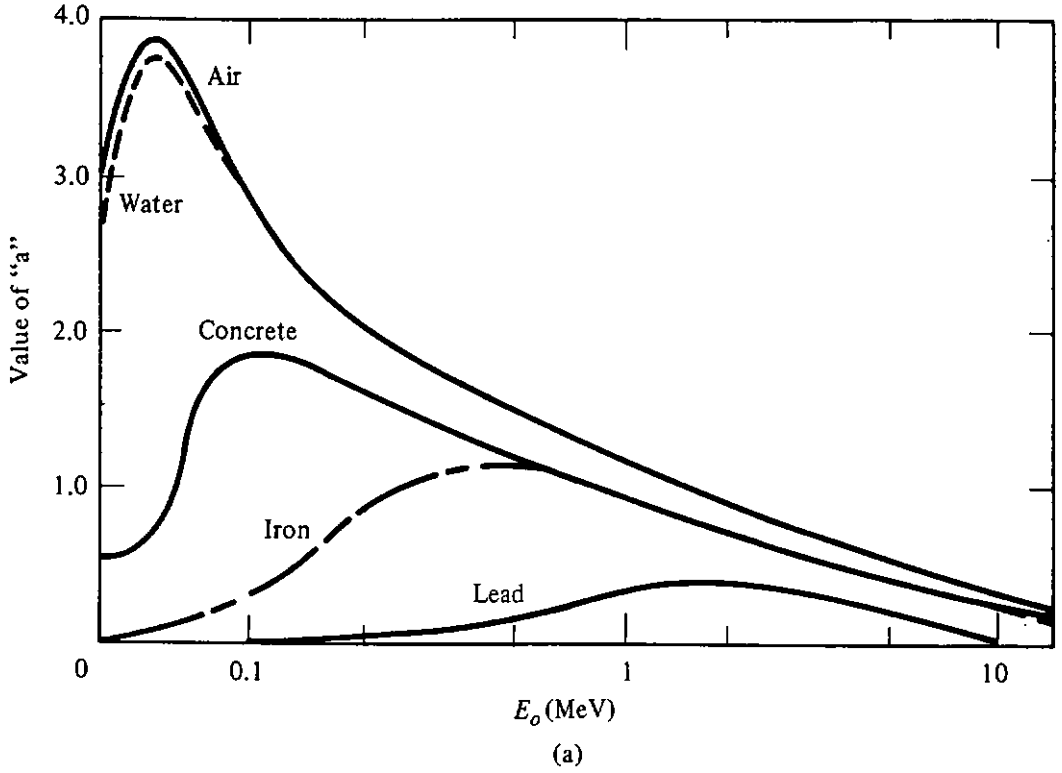

(a)

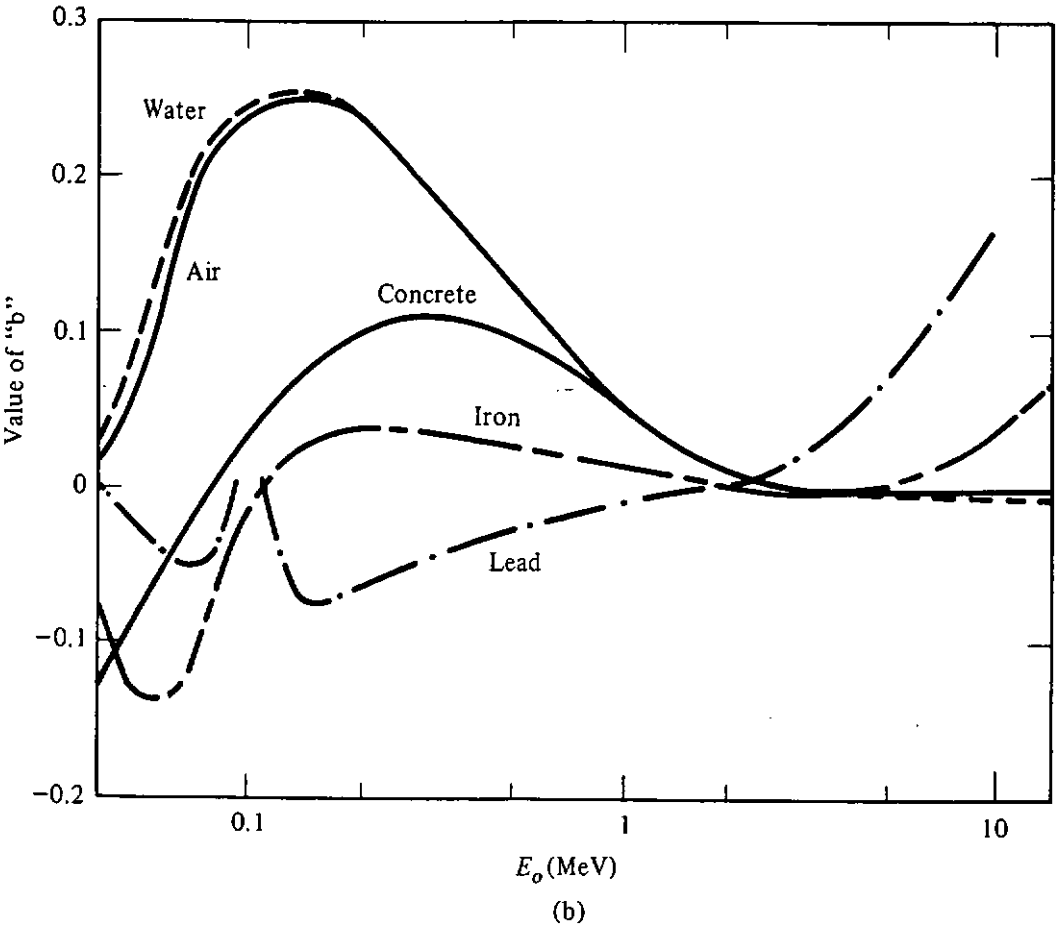

(b)

Figure 7.2 (a) Value of the parameter a in Berger's empirical formula for exposure buildup factors from a point source of monoenergetic photons. (b) Value of the parameter b in Berger's empirical formula for exposure buildup factors from a point source of monoenergetic photons. The curves for air, water, and concrete (slightly smoothed) are based on the data contained in Appendix A4. The curve for lead is based on unpublished calculations of A. B. Chilton, C. M. Eisenhauer, and G. L. Simmons.

The three-parameter Taylor formula provides a better fit to data for high-Z materials than for low-Z materials. Foderaro and Hall [7] have developed an elaboration of the Taylor formula which is closely fitted to the buildup-factor data for water. The formula is

$$B = \sum_{n=1}^{3} A_n \exp(-\alpha_n \mu_0 r), \tag{7.7}$$

with $\sum_{n=1}^{3} A_n = 1$. Values for the parameters A_n and α_n are provided in Table A4.13. The use of this formula is similar to that of the Taylor formula.

Berger's formula [3,8]

$$B = 1 + a\mu_0 r e^{b\mu_0 r}. \tag{7.8}$$

This formula also fits in reasonably well with point-kernel type of calculations. Furthermore, the formulation is such that the contribution from the uncollided radiation is provided by the first term while the second term determines the in-scattered contribution. Even though only two parameters are involved, it is about as a accurate as Taylor's formula. Berger's parameter values are also given in Appendix 4.

Polynomial formula [3]

$$B = \sum_{i=0}^{N} a_i (\mu_0 r)^i. \tag{7.9}$$

Usually, N equals 3, thereby providing reasonable accuracy up to 20 mean-free-path lengths; however, under circumstances involving only a few mean-free-path lengths, an appreciable simplification is provided by making N equal to 1 (linear approximation). Parameter values for this formula are not presented in this text, but are available in the literature [3,9].

The parameters in the formulas above are functions of both initial photon energy (E_0) and (average) atomic number of the medium (Z). For some sets of parameters, the variation with E_0 is sufficiently smooth to permit further empirical approximation of such parameters with E_0 [3]. A graph of the variation with E_0 of the parameters in the Berger formula for exposure buildup factors is given in Fig. 7.2 and permits easy evaluation of the Berger parameters for any source photon energy.

Many of the calculations discussed in Chapter 6, when k is taken to mean μ_0, can be used to predict the total detector response if a buildup factor is included as a part of the point kernel.[3] If in so doing one substitutes an empirical form selected from the list above, it is usually possible to carry the integration completely to an analytic form. This is discussed further in Section 7.4.

[3]The student should be warned that the "effective-μ" approach presented in Section 6.3 is an *alternative* to the buildup-factor approach of this chapter. The two approaches should not be used in conjunction. Whenever the buildup factor is used, the exponential part of the basic attenuation function must contain the linear attenuation coefficient.

7.3 COMPLEX ASPECTS OF THE BUILDUP FACTOR

7.3.1 Buildup Factors When Uncollided Radiation Is Not Dominant

The success of the buildup-factor concept in photon shielding is due not only to the regularities of photon interaction coefficients with energy but also to the fact that the uncollided radiation in most cases is the most penetrating component and therefore tends to dominate the penetration process.[4] (Note that over the most usual range of photon energies, the attenuation coefficient increases as the photon loses energy by successive scatterings; see Fig. 3.5.)

There are circumstances, however, for which the uncollided component clearly does not dominate the penetration phenomenon; and for such situations the use of the uncollided component as the basis for the buildup factor may give buildup factor values which are undesirably large or which do not behave in a manner easily approximated with simple empirical formulas. One such situation, shown in Fig. 7.3, is that of a slab on which a parallel beam is obliquely incident. Table A4.12 provides exposure buildup factors for concrete under this circumstance [10]. It is seen how rapidly the buildup factors increase with increasing shield thickness. One uses such data as these in the manner indicated by the following formula:

$$R(x) = B(\cos\theta_0; \mu_0 x) R_0 e^{-\mu_0 x/\cos\theta_0}. \tag{7.10}$$

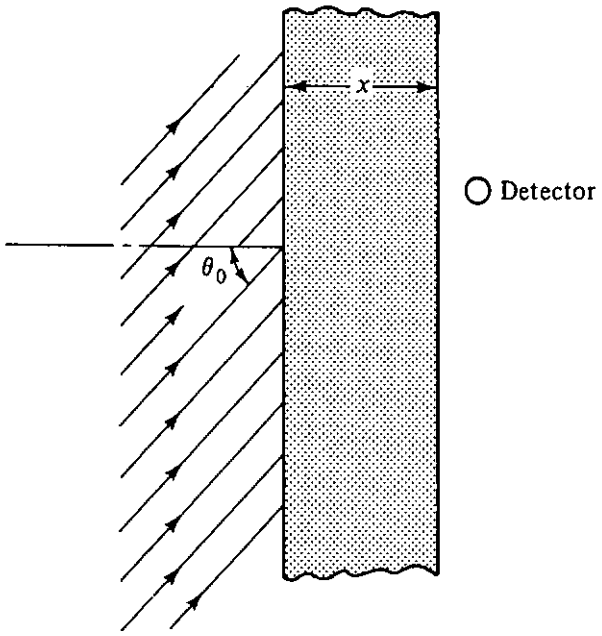

Figure 7.3 Parallel beam obliquely incident on a slab. θ_0 is the angle of obliquity.

[4]The term "dominate" as used here does not mean that the uncollided-component contribution to the detector response is always greater than the in-scattered component. It means, in a somewhat general fashion, that the trends of the total response with distance are more significantly affected by the uncollided radiation behavior than by that of any scattered component of another energy.

Sometimes in cases like this, shielders prefer to use a "pseudo-buildup factor" B' with the property

$$R(x) = B'(\cos\theta_0;\ \mu_0 x)R_0 e^{-\mu_0 x}. \tag{7.11}$$

This formulation, while yielding smaller B' values, is uncommon and no data for this pseudo-buildup factor are included in this text.

7.3.2 Correction for a Shield of Finite Extent

Many times it is the case that a shield is of finite thickness and the use of infinite medium buildup factors may give a value that is higher than it need be. Figure 7.4 gives a means of correcting the infinite medium buildup factor B_∞ so as to obtain the proper buildup factor B_x for a detector behind a shield of finite thickness.

The data on which Fig. 7.4 is based [3,11] are actually for the one-dimensional, rectangular-geometry case in which a monoenergetic beam is normally incident on a front face of a slab (or emitted normally from a plane in an infinite[5] medium). For penetration thicknesses of greater than a few mean-free-path lengths, the data are almost independent of slab thickness (4 mfp is the distance used here). The data graphed imply an energy flux density detector; but since most photon dosimeters have responses closely related to energy flux density,

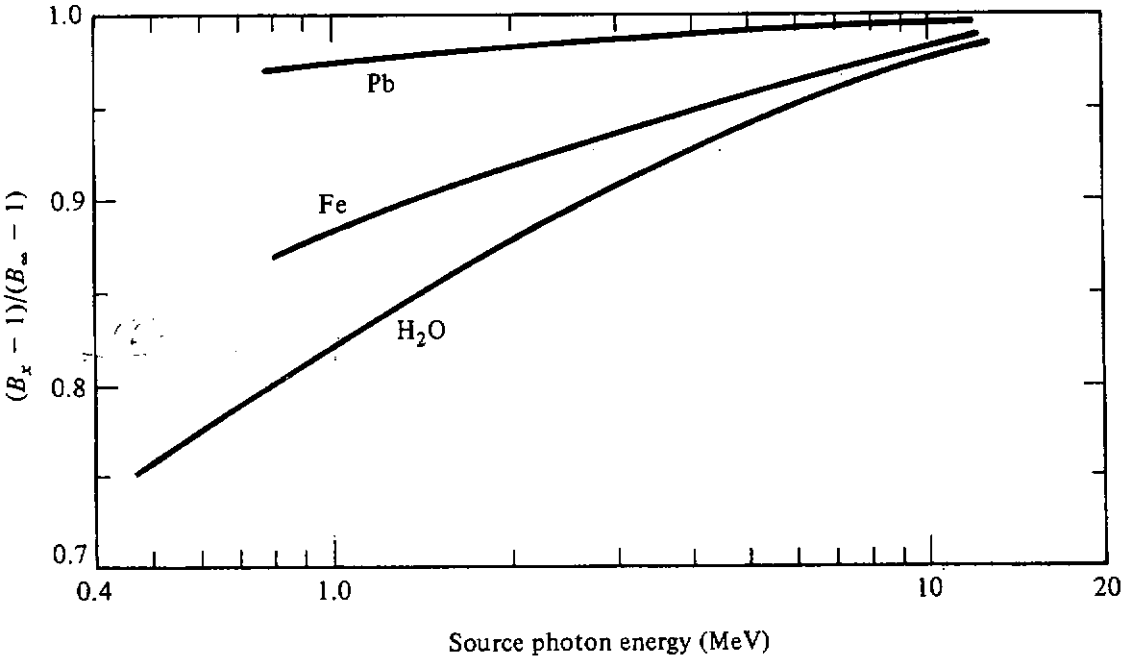

Figure 7.4 Correction factors for buildup factor data for finite-thickness media.

[5]The calculations were actually done for a semi-infinite medium with vacuum to the left of the source plane, but the results are the same for an infinite medium, after several mean-free-path lengths of penetration.

this graph will serve for them also. Through unpublished calculations, S. Y. Chen and A. B. Chilton have shown that the data are rather insensitive to the exact directional distribution of the radiation incident on the front face. They have also shown that data for ordinary concrete are very similar to those provided for a water medium.

The reader must be cautioned, however, that in the case of a shielded source surrounded by a larger enclosure of appreciable thickness the back scattering from the outer enclosure makes the situation between shield and enclosure close to an infinite-medium condition. Under such a condition, the correction for the finite thickness of the shield might better be ignored.

7.3.3 Laminated Shields

The use of the buildup-factor concept for heterogeneous media is of dubious merit, for the most part. The possible combinations are too numerous to calculate. However, it has been found that certain regularities exist which permit the use, at least approximately, of homogeneous-media buildup factors for shields made up of laminations of two or more different types of materials [12]. A commonly used rule for laminations of two different materials, of thicknesses x_1 and x_2, numbered in the direction from source to detector is as follows: If $Z_1 < Z_2$, the overall buildup is approximately equal to the buildup factor B_2 for the higher-Z medium with the use of $\mu_1 x_1 + \mu_2 x_2$ as its argument; if $Z_1 > Z_2$, the overall buildup factor to use is the product $B_1(\mu_1 x_1)$ times $B_2(\mu_2 x_2)$. The laminations should each be at least one mean-free-path length thick, and the source photon energy is used as the energy argument for all tabulated values. (For compounds, Z_1 and Z_2 represent *average* atomic numbers.)

A qualitative justification for this rule of thumb can be provided. It requires a recognition that high-Z materials tend strongly to filter out the low-energy photons produced by scattering more readily than do low-Z materials. (From the tables of attenuation coefficients in App. 3, it is seen that the photoelectric effect dominates the Compton effect at low photon energies and is stronger for high-Z elements than for low-Z elements.) Thus, the photon spectrum upon penetrating high-Z material is relatively "hard," or deficient in low-energy photons. If the low-Z lamination comes first, the photon spectrum emerging from the first low-Z lamination contains a relative abundance of low-energy photons, but these are largely filtered out by the following high-Z lamination, so that the detector "sees" radiation characteristic only of the high-Z material. On the other hand, if the second lamination is of low-Z material, the radiation is relatively hard when it strikes the second lamination and then experiences a softening of the spectrum within the second lamination. When it reaches the detector its nature shows the effect of both the first lamination and the second lamination, requiring recognition of the properties of both laminations when one chooses the composite buildup factor.

More precise methods are available in certain cases. Kalos's empirical

formulas [12,13], for example, have been found to be rather accurate for slabs containing two layers as diverse as water and lead, on which a monoenergetic, parallel beam of photons is normally incident:

1. For $Z_1 > Z_2$, and $0.5 \leq E_0 \leq 10$ MeV:

$$B(\mu_1 x_1, \mu_2 x_2) = B_2(\mu_2 x_2) + \frac{B_1(\mu_1 x_1) - 1}{B_2(\mu_1 x_1) - 1}[B_2(\mu_1 x_1 + \mu_2 x_2) - B_2(\mu_2 x_2)]. \quad (7.12)$$

2. For $Z_1 < Z_2$, and $0.5 \leq E_0 \leq 10$ MeV:

$$B(\mu_1 x_1, \mu_2 x_2) = B_2(\mu_2 x_2) + [B_2(\mu_1 x_1 + \mu_2 x_2) - B_2(\mu_2 x_2)] \times \left\{\frac{B_1(\mu_1 x_1) - 1}{B_2(\mu_1 x_1) - 1} \exp(-1.7\mu_2 x_2) + \frac{(\mu_c/\mu)_1}{(\mu_c/\mu)_2}[1 - \exp(-\mu_2 x_2)]\right\}. \quad (7.13)$$

Other formulas, usually empirical, are available in the literature [14].

7.4 EXTENSION OF POINT-KERNEL TECHNIQUES TO INCORPORATE BUILDUP

If the formulas of Chapter 6 or similar formulas involving a point-kernel approach are used for predicting the response of a detector to uncollided photons, the total response can be obtained, of course, by multiplication of the formulas by an appropriate buildup factor. For an extended source, the buildup factor must be consistent with the source and the shield geometry. However, if the buildup factor is applied to the point kernel *before* the integration leading to the final formula, the *point-source* buildup factor must be used. Since the values of point-source buildup factors are comparatively well known, this is generally the best approach. This suggests, in turn, that the point-source buildup factors should be expressible so as to fit into the integrands in such a fashion that the modified integrand is still as easily integrated as before. The following examples will indicate how this process works.

7.4.1 Isotropic Disk Source in an Attenuating Medium

Equation (6.60), adapted to the uncollided photon flux density, can be multiplied by a buildup factor for the disk source, so that the total detector response would be given by

$$R(P) = 2\pi \hat{R} S_A[E_1(\mu_0 h) - E_1(\mu_0 s)]B_{\text{disk}}(\mu_0 h, \mu_0 s). \quad (7.14)$$

Since, in general, we do not have information on B_{disk}, we discard this approach and insert the point-source buildup factor, which we will simply call B, under the integral sign of Eq. (6.58), so as to obtain

$$R(P) = 2\pi\hat{R}S_A\int_h^s \frac{B(\mu_0 r)e^{-\mu_0 r}}{r}\,dr. \tag{7.15}$$

This expression can be evaluated by numerical methods for any specific problem. However, an analytical formula can be provided by using one of the available empirical formulas for B, requiring in turn that values of the appropriate parameters in the buildup-factor formula be known for photons with the specified source energy. Results for the disk source are given below.

Taylor's formula. Insertion of Eq. (7.6) into expression (7.15) gives

$$\begin{aligned} R(P) &= 2\pi\hat{R}S_A\left[A\int_h^s \frac{e^{-(1+\alpha)\mu_0 r}}{r}\,dr + (1-A)\int_h^s \frac{e^{-(1+\beta)\mu_0 r}}{r}\,dr\right] \\ &= 2\pi\hat{R}S_A\{AE_1([1+\alpha]\mu_0 h) - AE_1([1+\alpha]\mu_0 s) \\ &\quad + (1-A)E_1([1+\beta]\mu_0 h) - (1-A)E_1([1+\beta]\mu_0 s)\}. \end{aligned} \tag{7.16}$$

It is seen from this example that Taylor's formula is a very simple one to use in this fashion, involving no additional complexity in the integration process. It has a minor disadvantage in that one cannot make a simple separation of terms to give the uncollided and in-scattered contributions to the detector response.

Berger's formula. Alternatively, one may insert Eq. (7.8) into Eq. (7.15) to get

$$\begin{aligned} R(P) &= 2\pi\hat{R}S_A\left[\int_h^s \frac{e^{-\mu_0 r}}{r}\,dr + a\mu_0\int_h^s e^{-(1-b)\mu_0 r}\,dr\right] \\ &= 2\pi\hat{R}S_A\left\{E_1(\mu_0 h) - E_1(\mu_0 s) + \frac{a}{1-b}[e^{-(1-b)\mu_0 h} - e^{-(1-b)\mu_0 s}]\right\} \end{aligned} \tag{7.17}$$

The resulting expression is quite simple, and it is easy to separate contributions of the uncollided and in-scattered photons directly from this expression, since the two exponential integral terms give the uncollided component only.

Linear formula. Since the linear formula for the buildup factor is equivalent to the Berger formula with b equal to zero, Eq. (7.17) is easily adapted to this approximation.

7.4.2 Source Slab with Slab Shield

As another example, consider the case illustrated by Fig. 6.17, having a distributed source inside a slab, with an additional shielding slab of the same material between the source and the detector. For the sake of generality, consider the exponential distribution for the source given by Eq. (6.82). As before, the use of Taylor's formula for the buildup factor requires only minor modifications

of Eq. (6.86) and other related formulas. We shall therefore consider only Berger's formula.

The uncollided contribution can be taken directly from Eq. (6.86) by substituting μ_0 for k and k_s. We need to derive in further detail only the scattered contribution, using $(B - 1)$ as the multiplier for this purpose. Equation (6.83) will be the starting point, but it will be necessary to go back to the original point kernel which led to the exponential integral when applying the point-source buildup-factor multiplier. Thus, the response to the scattered photons becomes

$$R^s(P) = 2\pi\hat{R}C \int_0^L dx\, e^{qx} \int_{t+x}^{\infty} (B - 1)\frac{e^{-\mu_0 r}}{r}\, dr. \tag{7.18}$$

Since

$$B - 1 = a\mu_0 r e^{b\mu_0 r} \tag{7.19}$$

in Berger's approximation,

$$R^s(P) = 2\pi\hat{R}Ca\mu_0 \int_0^L dx\, e^{qx} \int_{t+x}^{\infty} e^{-\mu_0' r}\, dr, \tag{7.20}$$

which reduces to

$$R^s(P) = \frac{2\pi\hat{R}Cae^{-\mu_0' t}[1 - e^{-(\mu_0' - q)L}]}{(1 - b)(\mu_0' - q)}, \tag{7.21}$$

where $\mu_0' \equiv \mu_0(1 - b)$.

If $q = \mu_0'$, it is readily shown that

$$R^s(P) = \frac{2\pi C\hat{R}aLe^{-\mu_0' t}}{1 - b}. \tag{7.22}$$

If the source is infinitely thick, there is no finite solution unless $q < \mu_0'$, in which case it can be seen that

$$R^s(P) = \frac{2\pi C\hat{R}ae^{-\mu_0' t}}{(1 - b)(\mu_0' - q)}. \tag{7.23}$$

Finally, if there is no external shielding slab, $t = 0$, and the term $e^{-\mu_0' t}$ drops out of Eqs. (7.21) through (7.23).

7.5 SPECIAL TECHNIQUES FOR MEDICAL FACILITIES

While the buildup-factor approach for calculating shielding effectiveness can be used for all gamma- and x-ray photons, an older but equally acceptable method can be used. In essence, this older method does not separate the attenuation of uncollided photons and the buildup of in-scattered photons but treats the attenuation in a single function. This is illustrated most clearly by formulas and procedures established for shielding of medical facilities [15]. Two slightly different approaches using this method are outlined in the remainder of this chapter.

7.5.1 Shielding of Gamma Irradiators and High-Energy X-Ray Machines

The shielding by a slab of any point source, whether monoenergetic or polyenergetic, can be established in terms of the following formula, a revision of Eq. (7.2):

$$R = \frac{\hat{R}S_p}{r^2} A_f, \tag{7.24}$$

where A_f, called the *attenuation factor*, is defined as the ratio of the detector response with the shield in place to the detector response with the shield absent, all other parameters being the same. Under most practical circumstances, this dimensionless factor can be taken as independent of all geometric variables except the thickness of the slab and the angle of incidence of the ray between source and detector with respect to the shield. The situation assumed for this purpose is one in which the point source is far enough away from the slab shield that the radiation incident upon it is roughly parallel and uniformly illuminates a large portion of the slab surface (see Fig. 6.28). The detector is considered to be close to the exit slab surface. Air or any other medium between source and detector except for the shield itself is taken to have a negligible attenuation effect. (Under these circumstances, for a monoenergetic source the attenuation factor A_f can be well approximated in terms of a slab buildup factor B as [see Eq. (7.10)]

$$A_f = e^{-\mu_0 x \sec\theta_0} B(\cos\theta_0; \mu_0 x), \tag{7.25}$$

where θ_0 is the angle with respect to the slab normal of the incident radiation on the slab of thickness x.)

Experiments have been carried out under these conditions for a number of radioisotopes and slabs of varied materials [15]. Examples of resulting data for A_f for lead and concrete shields are given in Figs. 7.5 and 7.6, respectively, for normal incidence conditions. Figure 7.7 gives curves resulting from experimental measurements of attenuation factors for gamma radiation incident on lead slab shields at oblique angles. Similar curves for obliquely illuminated concrete slab shields can be obtained by using the buildup factors of Table A4.12 and Eq. (7.25). From these results it is seen that for oblique incidence, the attenuation by thin to moderate slab thicknesses ($\lesssim$5 mean free paths) is very insensitive to the angle of incidence for $\theta_0 \lesssim 50°$. To a good approximation, attenuation factors for beams normal to a slab can be used for the slant incidence case, except for extremely oblique incidence and very thick walls, and provided that the slant thicknesses are used as arguments for the attenuation factors.

The graphs for A_f in Figs. 7.5 through 7.7 are based on experiments involving an exposure or an exposure-rate detector. However, the values are not highly sensitive to the precise type of dosimeter, and thus they are approximately valid for all types of "dose." Many additional tabulations and graphs are available in the literature for different materials, source energies, and geometric conditions

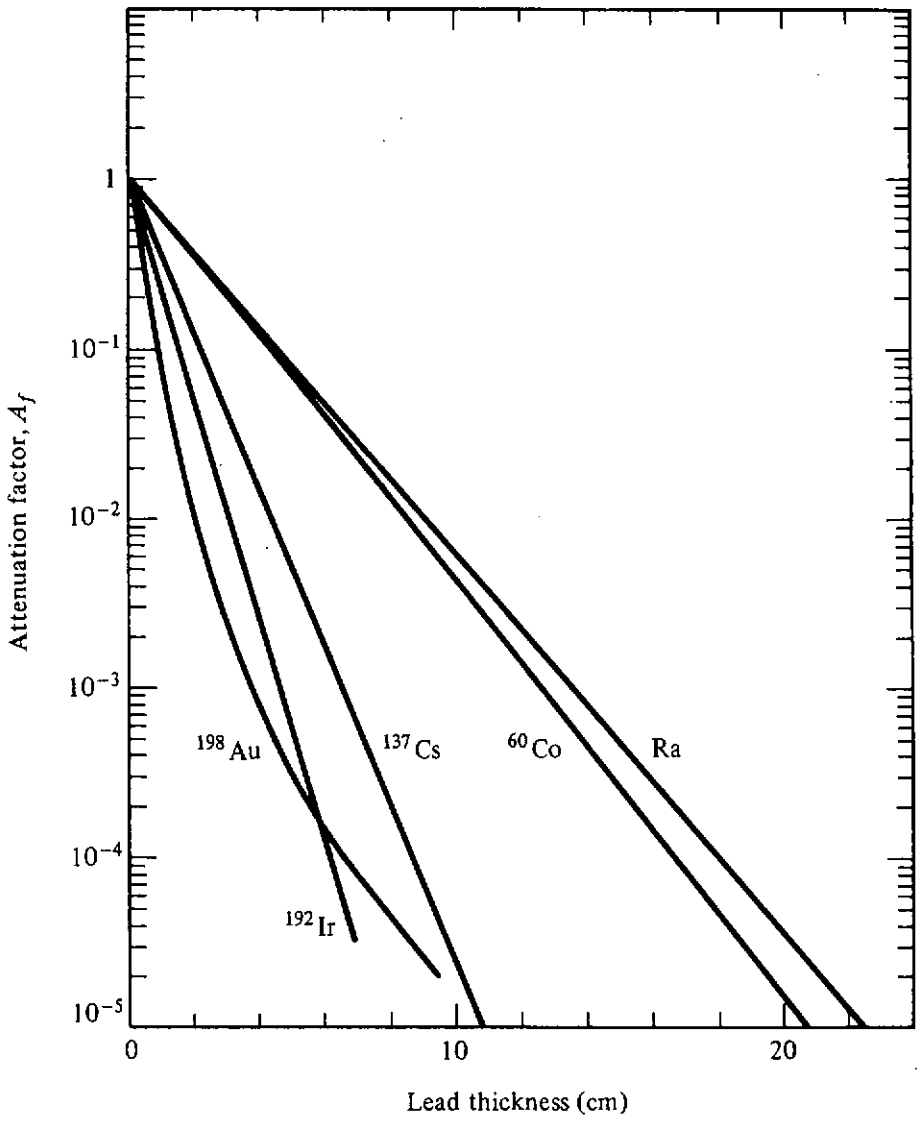

Figure 7.5 Attenuation factor A_f for gamma photons from several radionuclides normally incident on lead slabs. (From Ref. 15; by permission of the National Council on Radiation Protection and Measurements.)

[15–17]. Such attenuation factors provide a very quick means of assessing the effectiveness of a shield.

To apply this simplified method to shielding of gamma-ray or high-energy x-ray beams (> 3 MV) from medical equipment, $\hat{R}S_p$ in Eq. (7.24) is usually taken as the exposure rate in roentgens per hour at 1 m from the source in the primary-photon beam without any intervening shield (except possibly a filter in the equipment itself). Of interest is the exposure a person would experience behind a shield in some prescribed interval of time (usually 1 week). In terms of the "workload" W, the "use factor" U, and the "occupancy factor" T, previously defined (see Section 6.7), Eq. (7.24) becomes

$$X = \frac{WUT}{r^2} A_f. \tag{7.26}$$

Typical weekly workloads for medical installations and recommended values for U and T are given in the literature [15]. If the left side of the equation is

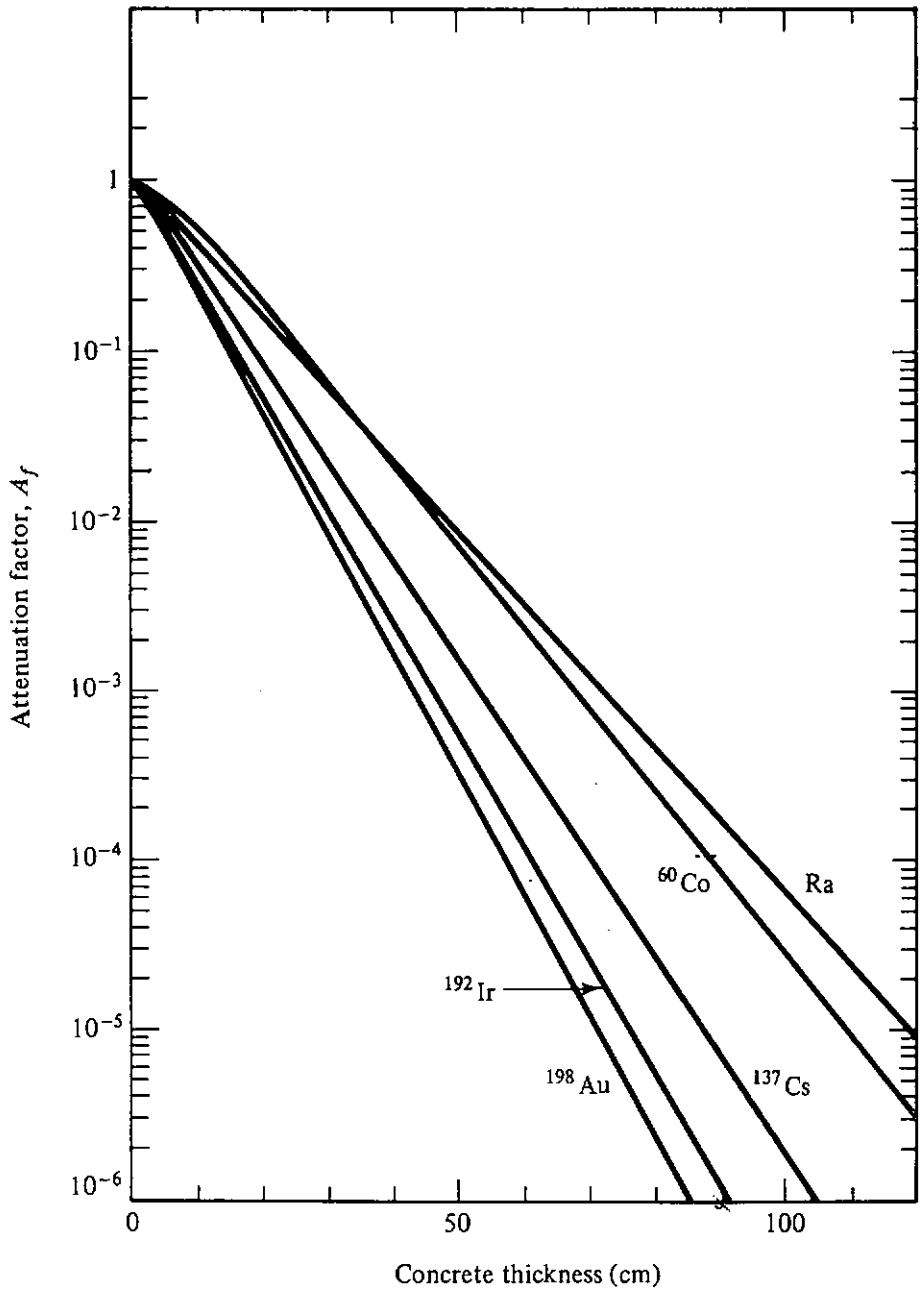

Figure 7.6 Attenuation factor A_f for gamma photons from several radionuclides normally incident on concrete slabs of density 2.35 g cm^{-3}. (From Ref. 15; by permission of the National Council on Radiation Protection and Measurements.)

provided as the prescribed maximum permissible exposure (such as 0.1 R week^{-1}), the equation can then be solved to find the required value of A_f, from which, in turn, the proper shielding thickness can be obtained by use of graphs such as Figs. 7.5 through 7.7.

7.5.2 Shielding of Low- and Intermediate-Energy X-Ray Machines

In Chapter 4 it was seen that the energy spectrum of photons from an x-ray machine is generally quite complex and depends not only on the operating conditions of the tube (peak voltage and current) but also on the target material,

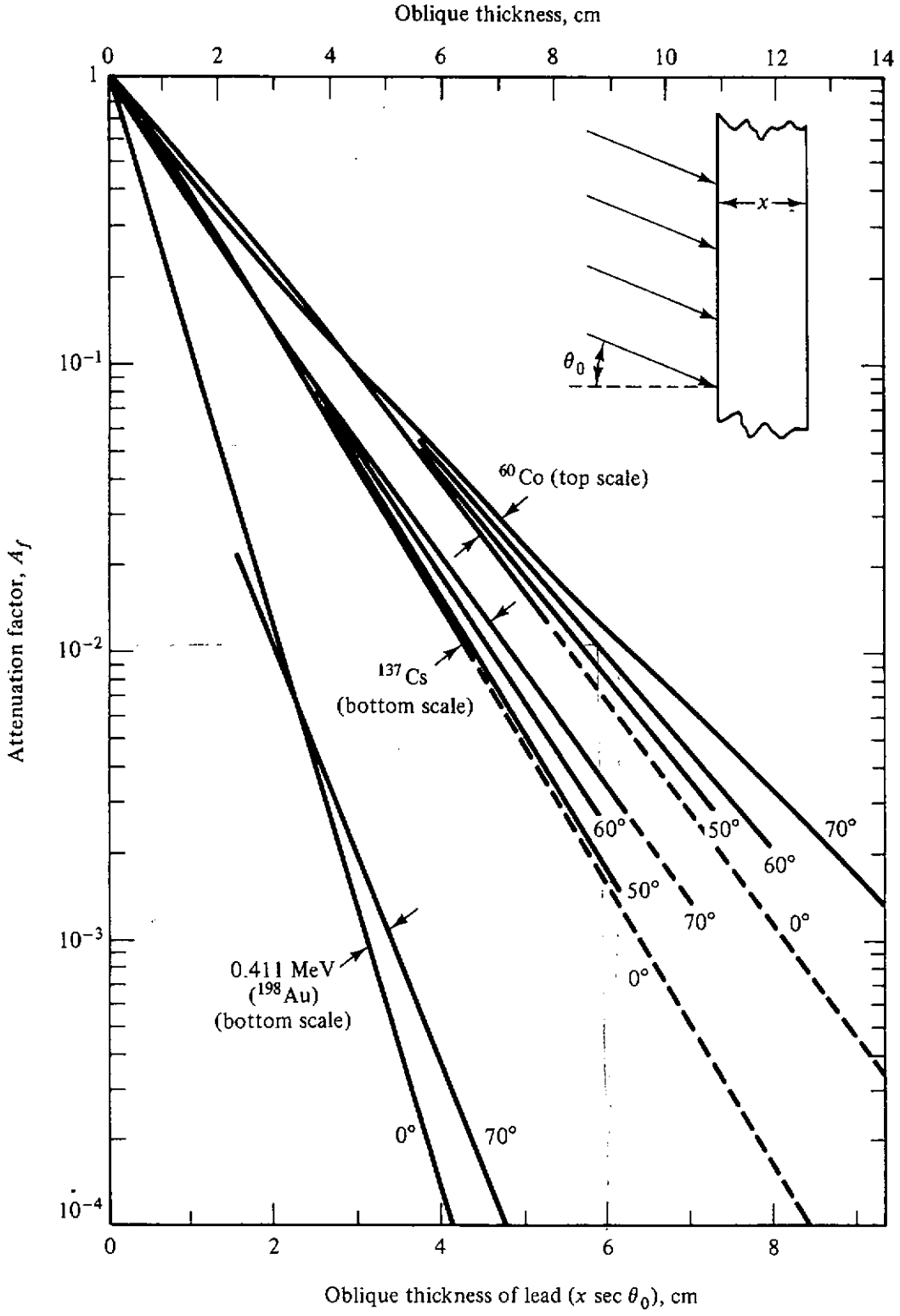

Figure 7.7 Attenuation factors for the transmission of gamma photons from three radionuclide sources through a lead slab. The lead slab is uniformly illuminated at several angles of incidence with respect to the normal. Results for ^{198}Au have been corrected so that only the transmission of the 0.411-MeV gamma photon is shown. (After Ref. 17.)

wave form of the applied voltage, and the amount of filtration afforded by the target, tube walls, and external filters. Because of the inability to calculate accurately the emitted x-ray spectrum, the common practice of decomposing a

polyenergetic photon source into multiple, approximately monoenergetic components and then treating each component separately (with buildup corrections or effective attenuation coefficients) is seldom attempted in x-ray analyses. Rather, a widely accepted approach based on empirical values for attenuation factors has been developed. The success and simplicity of this approach is based on the remarkable property that the rate at which radiation from an x-ray machine is attenuated in a thick shield depends primarily on the voltage applied to the machine. In effect, the initial portion of the shield attenuates preferentially the lower-energy photons until only the high-energy photons (determined by the tube voltage) are left to be attenuated and most of the structure of the original spectrum is lost.

It is customary when dealing with x-ray machines (except for very high voltage devices above 3 MV or machines that do not indicate the current) to specify the emitted radiation in terms of the exposure rate in the beam at a unit distance from the focal point (target) caused by a unit current of electrons. This quantity, $\hat{R}_t$, with typical units R m^2 min^{-1} mA^{-1}, depends on the tube voltage, target material, and amount of beam filtration, and it must either be measured for each machine or estimated from plots such as Fig. 4.16. Thus, instead of prescribing a photon source strength for S_p in Eq. (7.2), the electron beam current i is used to compute the exposure rate in the beam at a distance r from the electron target; that is, Eq. (7.24) becomes

$$\dot{X} = \frac{i\hat{R}_t}{r^2} A_f, \tag{7.27}$$

where A_f is the exposure-rate attenuation factor if a slab shield is placed in the beam before the detector. Because both $\hat{R}_t$ and A_f depend on the radiation "quality" (i.e., spectral shape) as well as on tube voltage and target material, they are usually combined into a single *normalized shielded output factor* $B_f = A_f\hat{R}_t$, which is no longer dimensionless but has the same units as $\hat{R}_t$. This combining of the two factors has the advantage that only one quantity has to be determined for a given design situation rather than both A_f and $\hat{R}_t$. Moreover, often only B_f is of interest; for example, if the exposure rate behind a shield is specified as $\dot{X}$, the required B_f factor can be computed from Eq. (7.27) as

$$B_f = \frac{\dot{X}r^2}{i} \tag{7.28}$$

for any x-ray machine. This normalized shield output factor has been measured for many specific x-ray sources and found, for sufficiently thick shields, to depend mainly on the highest energy x rays in the beam. Thus, B_f can be obtained from a set of universal curves (one for each machine voltage) as a function of the shield thickness for a given material. Figures 7.8 and 7.9 are typical of such curves derived from experimental data for concrete and lead shields. In these figures, B_f is expressed in R m^2 mA^{-1} min^{-1}, and to be consistent i, $\dot{X}$, and r in Eqs. (7.27) and (7.28) must be expressed in milliamperes, roentgens per minute, and meters, respectively.

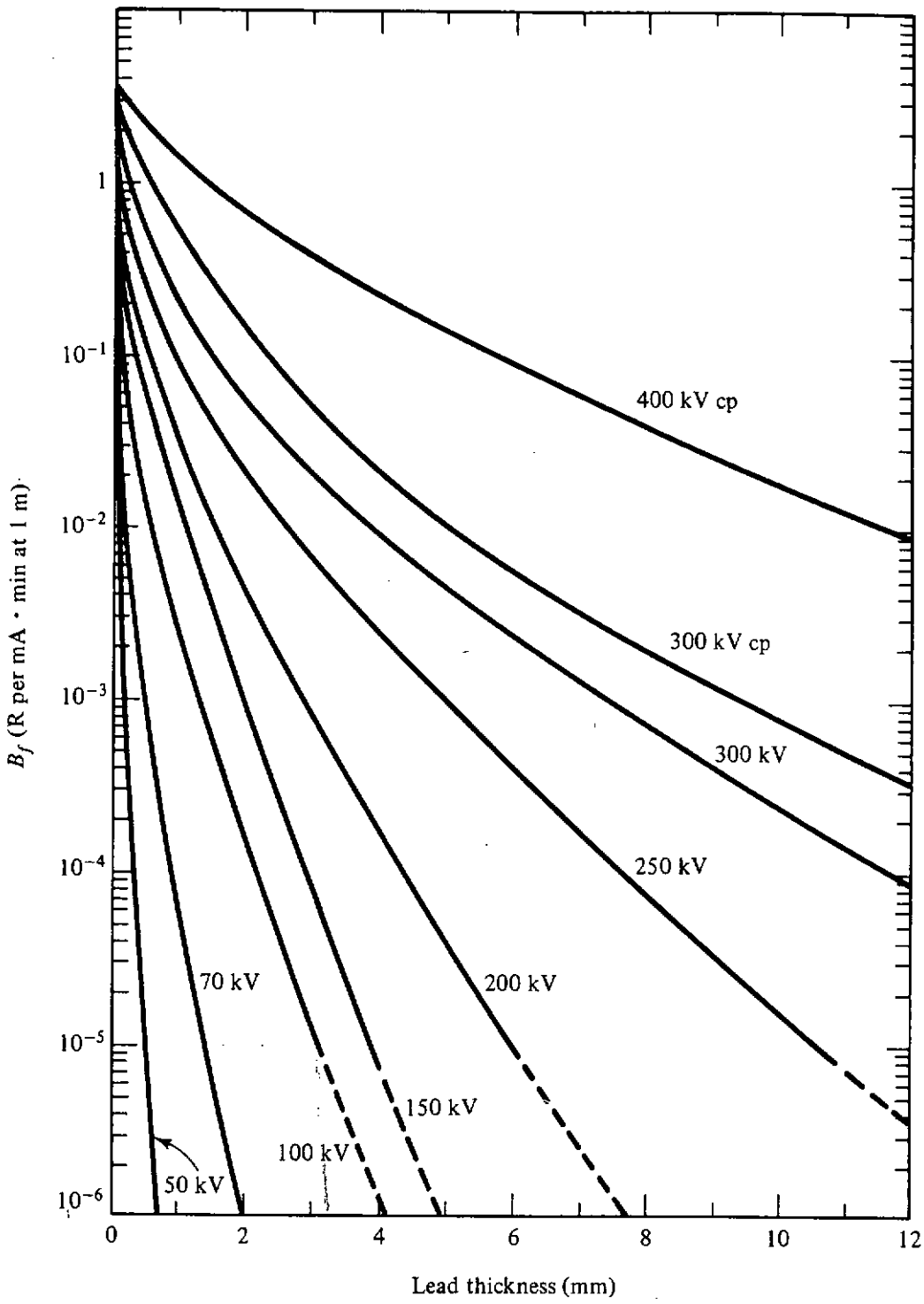

Figure 7.8 Attenuation in lead of x rays produced by various peak potentials (kVp) with a 90° angle between the electron beam and the axis of the x-ray beam. Pulsed waveforms are assumed except for the 300 and 400 kVcp curves which are for a constant potential generator. The x-ray beam filtrations are: 0.5 mm of aluminum for 50 kV; 1.5 mm of aluminum for 70 kV; 2.5 mm of aluminum for 100 and 150 kV; 3 mm of aluminum for 200, 250, and 300 kV; and 3 mm of copper for the 300 and 400 kVcp curves. (After Ref. 15; by permission of the National Council on Radiation Protection and Measurements.)

From Figs. 7.8 and 7.9 it is seen that for a highly filtered beam, B_f (and hence A_f) decreases almost purely exponentially with increasing shield thickness. The asymptotic attenuation coefficients (obtainable from the slopes of the curves

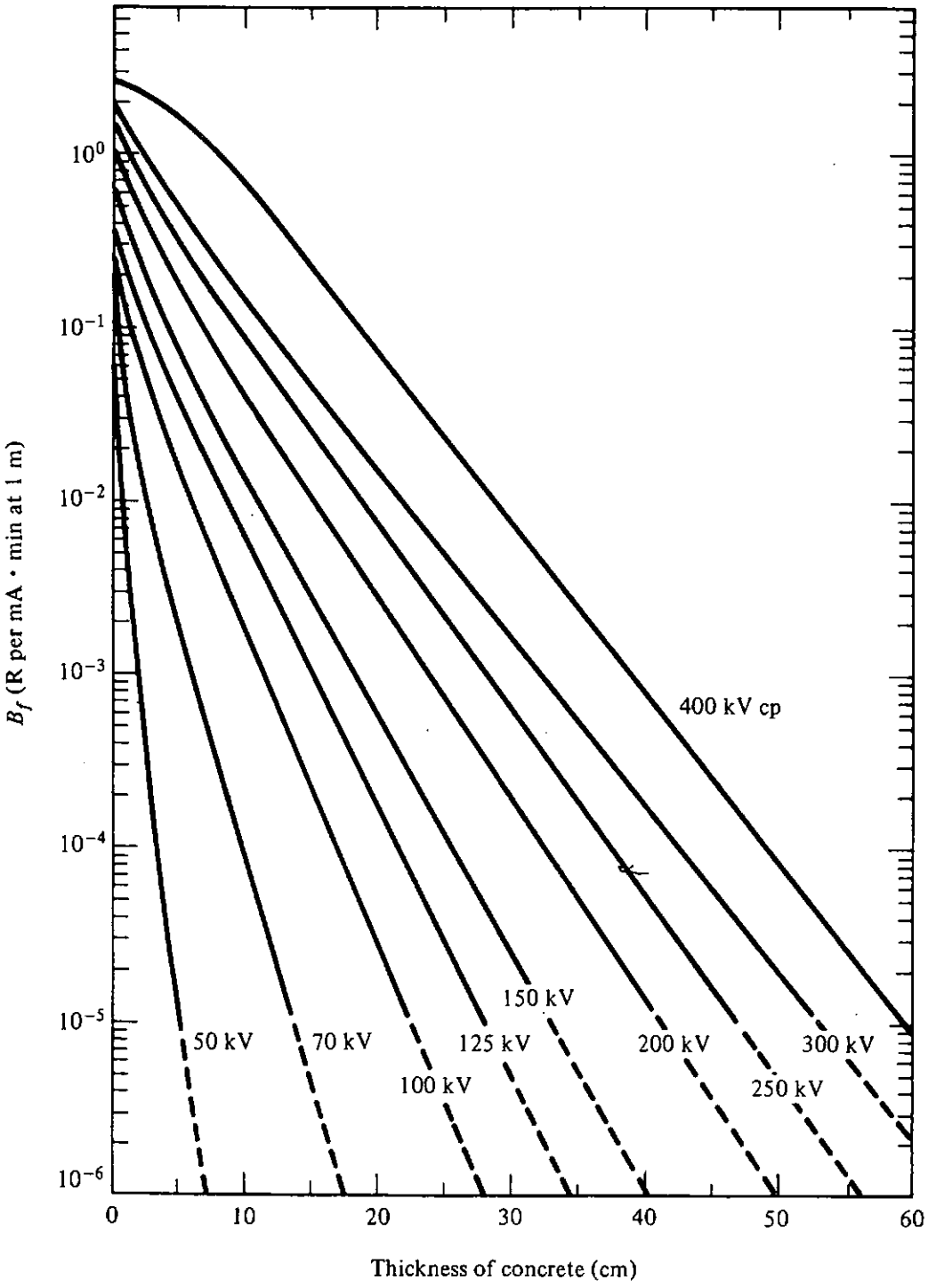

Figure 7.9 Attenuation in concrete of x rays produced by various peak potentials (kVp) with a 90° angle between the electron and x-ray beams. Pulsed waveforms are assumed except for the 400-kVcp curve which assumes a constant potential. The x-ray beam filtrations are: 1 mm of aluminum for 50 kV; 1.5 mm of aluminum for 70 kV; 2 mm of aluminum for 100 kV; 3 mm of aluminum for 125 to 300 kV; and 3 mm of copper for the 400-kVcp curve. Concrete density is 2.35 g cm^{-3}. (Ref. 15; by permission of the National Council on Radiation Protection and Measurements.)

in Figs. 7.8 and 7.9) are seen to depend on only the voltage used to generate the x rays. Rather than use these constant asymptotic attenuation coefficients, it is often more convenient for estimating rapidly the shielding of filtered x rays to

use the associated half-value layer (HVL) or tenth-value layer (TVL) (see Section 6.2). In Table 7.1 values of the HVL and TVL are presented for a wide range of x-ray tube voltages with lead, iron, or concrete shields.

For radiological protection of personnel from medical, dental, and industrial x-ray machines which operate only intermittently, the average exposure over some period of time (usually a week) is of interest rather than the instantaneous exposure rate, which is zero when the machine is idle. To obtain such an average weekly exposure X, Eq. (7.27) is integrated over the time that the machine is in operation during the week to give

$$X = \frac{W}{r^2} B_f, \tag{7.29}$$

where the weekly workload is now defined as $W = it$ (with t being the weekly operating time of the x-ray unit) and is usually expressed in units of mA min.

TABLE 7.1 Half-Value and Tenth-Value Layers[a]

Peak Voltage (kV)	Attenuation Material					
	Lead (mm)		Concrete (cm)		Iron (cm)	
	HVL	TVL	HVL	TVL	HVL	TVL
50	0.06	0.17	0.43	1.5		
70	0.17	0.52	0.84	2.8		
100	0.27	0.88	1.6	5.3		
125	0.28	0.93	2.0	6.6		
150	0.30	0.99	2.24	7.4		
200	0.52	1.7	2.5	8.4		
250	0.88	2.9	2.8	9.4		
300	1.47	4.8	3.1	10.4		
400	2.5	8.3	3.3	10.9		
500	3.6	11.9	3.6	11.7		
1,000	7.9	26	4.4	14.7		
2,000	12.5	42	6.4	21		
3,000	14.5	48.5	7.4	24.5		
4,000	16	53	8.8	29.2	2.7	9.1
6,000	16.9	56	10.4	34.5	3.0	9.9
8,000	16.9	56	11.4	37.8	3.1	10.3
10,000	16.6	55	11.9	39.6	3.2	10.5
Cesium-137	6.5	21.6	4.8	15.7	1.6	5.3
Cobalt-60	12	40	6.2	20.6	2.1	6.9
Radium	16.6	55	6.9	23.4	2.2	7.4

[a]Approximate values obtained at high attenuation for the indicated peak voltage values under broad-beam conditions; with low attenuation these values will be significantly less.

Source: *Ref. 15; by permission of the National Council on Radiation Protection and Measurements.*

Often the x-ray beam is not always pointed at the same shield nor is the area behind a particular shield always occupied continuously. To correct for these considerations, the result above is multiplied by the use factor U for the machine and by the occupancy factor T appropriate for a particular shielded area. With these refinements, the normalized shield output B_f required to reduce the weekly exposure to a specified level is

$$B_f = \frac{X_L r^2}{WUT}, \tag{7.30}$$

where X_L is the maximum allowable exposure for the time period of 1 week. Figures 7.8 and 7.9 (or similar curves) can then be used to find the shield thickness needed to afford the desired level of protection. Attenuation factors for higher and lower voltages than those given can be found in the literature [15].

7.5.3 Shielding for Leakage and Scattered Photons

The procedure above is very useful for the design of shielding against the primary beam of x rays or gamma photons. However, often consideration needs to be given to radiation that leaks through the protective housing around the x-ray tube or to radiation that is scattered from the object being irradiated, usually a patient. Typically, the exposure from leakage radiation and that from scattered radiation are roughly equal for x-ray machines operated at less than 500 kV. However, the leakage radiation is composed of photons of higher energies and hence is more penetrating than is the scattered component. Consequently, the secondary protective barrier for leakage radiation may often be somewhat thicker than that needed for scattered radiation.

Since the leakage radiation is usually highly filtered (most tube housings are lead lined), the use of asymptotic HVL values allows rapid evaluation of the additional shielding requirements against leakage radiation if the exposure rate due to leakage at 1 m from the housing is known. This leakage exposure rate should ideally be measured, but usual design standards limit this leakage to 1 R or to 0.1 R in a hour at 1 m from the source when a therapeutic machine below 500 kV or a diagnostic machine, respectively, is operated at its maximum current. For therapeutic machines operated at 500 kV or above, the leakage at 1 m from the housing is usually designed to be less than 0.1 % of the exposure in the direct beam 1 m from the source [15].

The treatment of scattered x-ray radiation is usually based on a simple and direct, although somewhat crude procedure. Consider the situation depicted in Fig. 7.10. The weekly exposure behind a shield at distance r_2 from the scattering body which is itself a distance r_1 from the beam focus is given approximately by ($U = 1$ for scattered radiation)

$$X = \left(a\frac{F}{400}\right)\frac{WT}{r_1^2 r_2^2} B_f, \tag{7.31}$$

where F is the illuminated area on the scattering body in cm^2 and a is an empir-

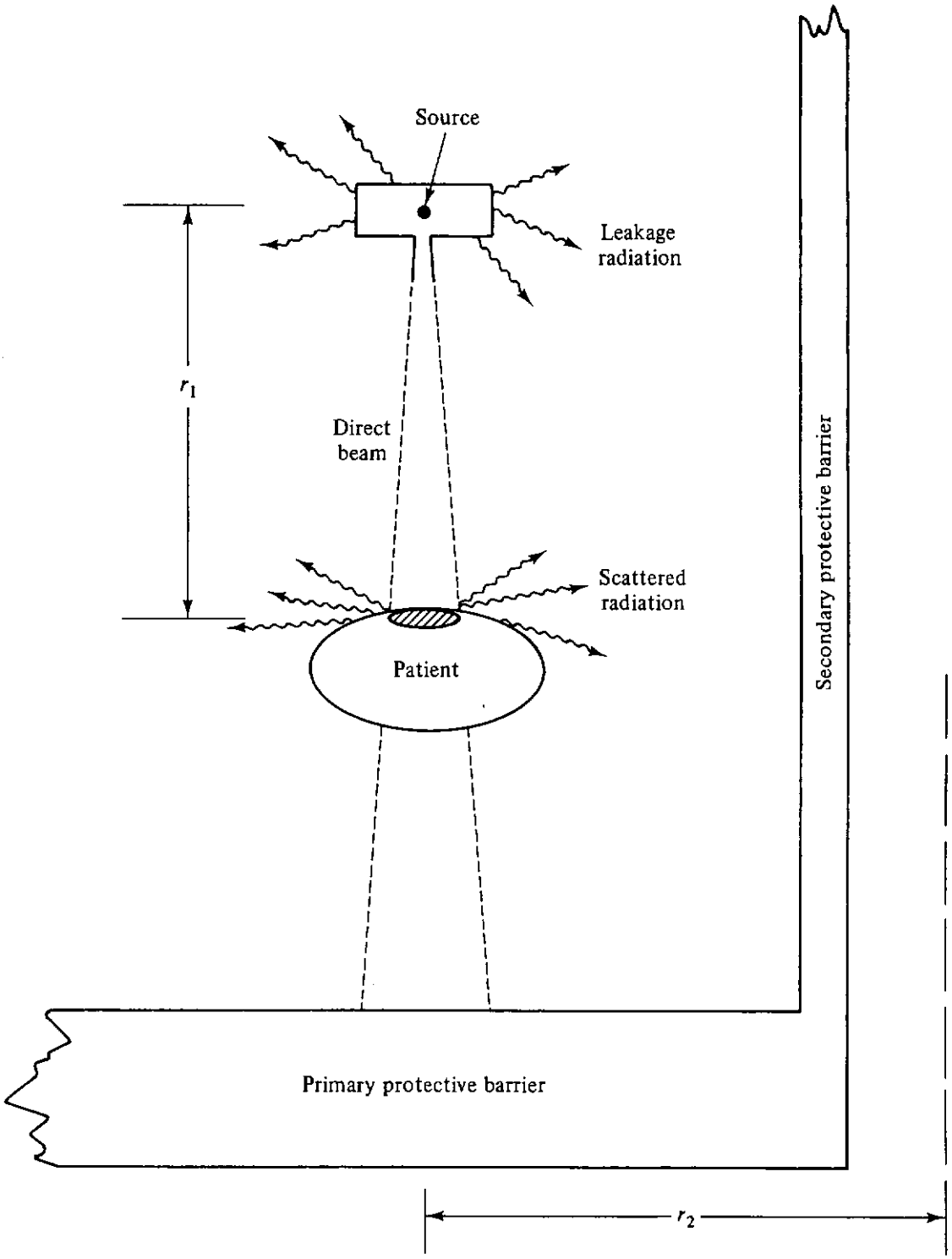

Figure 7.10 Geometry used in describing the shield design for the three sources of radiation (direct, scattered, and leakage) from an x-ray machine or gamma irradiator.

ically determined ratio of the scattered to incident exposure rates.[6] The value of a varies with the photon energy and the angle of scatter, and for 90° scattering with $F = 400\,\text{cm}^2$, a has a value of between 0.0013 and 0.0019 for x rays between 100 and 500 kV and falls off rapidly at lower energies (see Table 7.2).

[6]The ratio a has a close relationship to the more precisely defined albedo function discussed in detail in Chapter 9.

TABLE 7.2 Ratio a of Scattered to Incident Exposure[a]

Source	Scattering Angle					
	30°	45°	60°	90°	120°	135°
X rays						
50 kV	0.0005	0.0002	0.00025	0.00035	0.0008	0.0010
70 kV	0.00065	0.00035	0.00035	0.0005	0.0010	0.0013
100 kV	0.0015	0.0012	0.0012	0.0013	0.0020	0.0022
125 kV	0.0018	0.0015	0.0015	0.0015	0.0023	0.0025
150 kV	0.0020	0.0016	0.0016	0.0016	0.0024	0.0026
200 kV	0.0024	0.0020	0.0019	0.0019	0.0027	0.0028
250 kV	0.0025	0.0021	0.0019	0.0019	0.0027	0.0028
300 kV	0.0026	0.0022	0.0020	0.0019	0.0026	0.0028
4 MV	—	0.0027	—	—	—	—
6 MV	0.007	0.0018	0.0011	0.0006	—	0.0004
Gamma rays						
^{137}Cs	0.0065	0.0050	0.0041	0.0028	—	0.0019
^{60}Co	0.0060	0.0036	0.0023	0.0009	—	0.0006

[a]The scattered radiation is measured at 1 m from a phantom with a field area of 400 cm^2 at the phantom surface. The incident exposure is measured 1 m from the source in the center of the field without the phantom.

Source: *Ref. 15; by permission of the National Council on Radiation Protection and Measurements.*

In applying formula (7.31) to find the B_f of a shield needed for protection against scattered radiation, the appropriate shield thickness is found by using the attenuation curve for the actual tube voltage if it is less than 500 kV. For x-ray machines operating at 1 MV or above, the normalized shield output factor B_f is decreased from that computed from Eq. (7.31) to account for the large increase in machine output as the voltage increases. Consequently, the calculated values of B_f are divided by a factor of 20, 300, and 700 for machines operating at 1, 2, and 3 MV, respectively. The calculation of the shield thickness to give this modified B_f value is obtained from the attenuation curve for a 500-kV machine rather than the actual higher machine voltage. This last approximation implies that the energy spectrum of the x rays is approximately unchanged upon reflection if the tube voltage is less than 500 kV, but if the tube voltage is greater than this value, the spectrum is degraded to one corresponding to 500 kV.

It may be noticed (see Fig. 7.10) that the secondary protective barrier is generally subject to radiation both as leakage from the x-ray machine and as scattered radiation from the patient. The general principles of design with two sources have already been discussed briefly in Section 6.7. In practical applications, a simple, although approximate, method can be employed. The thickness of the secondary barrier is determined separately for the two sources: the greater of the two results is taken as basic. If the barrier thicknesses required by the two

sources separately differ by more than 1 TVL, take the basic value as final; if the difference is less than 1 TVL, add one HVL to the basic value to obtain the required design value.

7.5.4 Adjustment of Attenuation Factors for Density

While it is usual to present empirical data for attenuation factors as a function of the shield thickness x (e.g., Figs. 7.5 through 7.9), it has been found that A_f and B_f depend on the shield material not simply as a function of x but rather as a function of the shield mass thickness ρx. [This dependency is related to the fact that buildup factors and exponential attenuation factors, discussed earlier in this chapter, depend on $\mu x \equiv (\mu/\rho)\rho x$, in which μ/ρ is actually independent of the density.] Thus, if a shield material is used that has a different density but approximately the same average atomic number as that for which attenuation factors are available, the appropriate shield thickness is found by multiplying the graphical value of x by the ratio $\rho_{\text{graph}}/\rho_{\text{actual}}$. Since most structural walls have shielding properties very much like concrete, aside from the density, this rule makes Fig. 7.6 quite generally useful.

REFERENCES

1. C. M. Eisenhauer and G. L. Simmons, "Point Isotropic Buildup Factors in Concrete," *Nucl. Sci. Eng.* **56**, 263–270 (1975).
2. A. B. Chilton, C. M. Eisenhauer, and G. L. Simmons, "Photon Point Source Buildup Factors for Air, Water, and Iron," *Nucl. Sci. Eng.* **73**, 97–107 (1980).
3. A. B. Chilton, "Buildup Factor," in *Engineering Compendium on Radiation Shielding*, Vol. I, R. G. Jaeger (ed.), Springer-Verlag, New York, 1968, Sec. 4.3.1.2.
4. J. P. Kuspa and N. Tsoulfanidis, "Calculations of Gamma-Ray Buildup Factors Including the Contribution of Bremsstrahlung," *Nucl. Sci. Eng.* **52**, 117–123 (1973).
5. U. Fano, L. V. Spencer, and M. J. Berger, "Penetration and Diffusion of X Rays," in *Handbuch der Physik*, Vol. 38/2, S. Flügge (ed.), Springer-Verlag, Berlin, 1959, pp. 660–817.
6. H. Goldstein and J. E. Wilkins, Jr., "Calculations of the Penetration of Gamma Rays," NDA/AEC Report NYO-3075, U.S. Government Printing Office, Washington, D.C., 1954.
7. A. Foderaro and R. J. Hall, "Application of Three-Exponential Representation of Photon Buildup Factors to Water," *Nucl. Sci. Eng.* **74**, 74–78 (1981).
8. M. J. Berger, "Effects of Boundaries and Inhomogeneities on the Penetration of Gamma Radiation," Report NBS-4942, U.S. National Bureau of Standards, Washington, D.C., 1956.
9. M. Metghalchi, "On the Polynomial Form of Gamma-Ray Buildup Factor Functions," *Nucl. Sci. Eng.* **70**, 207 (1979).

10. E. M. Fournie and A. B. Chilton, "Gamma-Ray Buildup Factors for Concrete Slab Shields under Slant Incidence Conditions," *Nucl. Sci. Eng.* **76**, 66–69 (1980).
11. M. J. Berger and J. Doggett, "Reflection and Transmission of Gamma Radiation by Barriers: Semianalytic Monte Carlo Calculation," *J. Res. Natl. Bur. Stand.* **56**, No. 2, 89–98 (1956).
12. H. Goldstein, *Fundamental Aspects of Reactor Shielding*, Addison-Wesley, Reading, Mass., 1959; reprinted by Johnson Reprint Corp., New York, 1971.
13. M. H. Kalos, "A Monte Carlo Calculation of the Transport of Gamma Rays," Report NDA 56-7, Nuclear Development Associates, New York, 1956.
14. D. Bünemann and G. Richter, "Multilayered Shields," in *Engineering Compendium on Radiation Shielding*, Vol. I, R. G. Jaeger (ed.), Springer-Verlag, New York, 1968, Sec. 4.3.2.
15. "Structural Shielding Design and Evaluation for Medical Use of X Rays and Gamma Rays of Energies up to 10 MeV," NCRP Report 49, National Council on Radiation Protection and Measurements, Washington, D.C., 1976.
16. A. B. Chilton, "Broad Beam Attenuation, Homogeneous Mixtures, General," in *Engineering Compendium on Radiation Shielding*, Vol. I, R. G. Jaeger (ed.), Springer-Verlag, New York, 1968, Sec. 4.3.1.
17. F. S. Kirn, R. J. Kennedy, and H. O. Wyckoff, "The Attenuation of Gamma Rays at Oblique Incidence," *Radiology* **63**, No. 1, 94–104 (1954).

PROBLEMS

7.1. Determine the total detector responses $\dot{K}_{air}$, $\dot{X}$, and $\dot{H}_p$ for the situation described in Problem 6.2, using the buildup-factor methods of this chapter. Compare results with the corresponding approximate answers obtained for Problem 6.14.

7.2. Determine the total detector responses $\dot{K}_{air}$, $\dot{X}$, and $\dot{H}_p$ for the situation described in Problem 6.4, using the buildup-factor methods of this chapter. Compare results with the corresponding approximate answers obtained for Problem 6.15.

7.3. The finite medium/infinite medium ratios for the in-scattered contribution, as shown in Fig. 7.4, are all less than unity. Explain why the ratio would be *greater* than unity for a detector that measures the net flow rate through the exit surface of a shield. Predict approximate values for the ratios in such a case.

7.4. A 10,000-GBq ^{137}Cs source is embedded in an infinite, homogeneous medium of air at a pressure of 0.1 MPa, temperature of 20°C, and 30% relative humidity. Using the methods of this chapter, estimate the exposure rate R h^{-1} at a distance of 200 m from the source.

7.5. A 74-GBq ^{60}Co source is to be shipped in a lead cask of cylindrical shape, with dimensions as shown in Fig. P7.5. The source may be approximated as a point source, with a 2-cm clearance radially and axially from the cask walls. Regulations limit $\dot{H}_p$ at the surface of the cask to 1 mSv h^{-1}. Is the cask adequate to meet this limit? Assume emergent photon spectrum to be comprised of only 1 MeV photons.

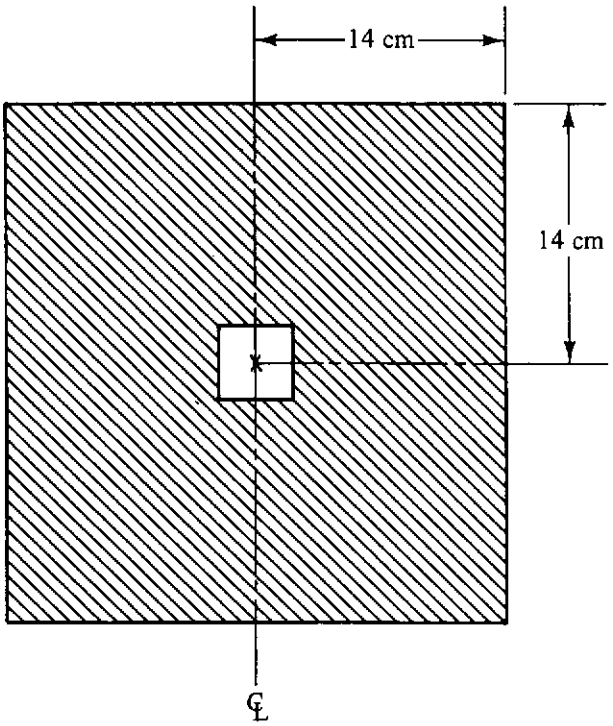

Fig. P7.5

7.6. **(a)** Table A4.2 lists exposure buildup factors for 1-MeV photons in an infinite water medium. Compare values from the table at 1, 4, and 10 mean-free-path lengths with values estimated using the Berger and Foderaro–Hall approximations.

(b) By equating the values for R given in Eqs. (6.13) and (7.2), show that the following approximation applies for a point source in an infinite medium:

$$B(\mu r) \simeq B_0 \exp[(1 - c)\mu r],$$

where $c \equiv \mu'/\mu$ (Table 6.1). Check the accuracy of this formulation at 1, 4, and 10 mean-free-path lengths in water.

7.7. It is desired to design a water well within which is to be stored either a 148-TBq point source of ^{137}Cs or a 37-TBq point source of ^{60}Co, but not both. Which source governs the design of the source well? How deep should the well be if the exposure rate at the water surface is limited to 10 mR h^{-1}?

7.8. A 3.7-TBq photon point source, emitting one 1-MeV photon per disintegration, is to be stored under water in an open pit. The maximum permitted exposure rate at the surface of the water is 2 mR h^{-1}. Estimate the required depth of water above the source. Perform calculations using the Foderaro–Hall form of the buildup factor. Check results using the Berger form of the buildup factor.

7.9. ^{137}Cs has accidentally been distributed over the ground, covering many acres. Nearby is mining slag, primarily $MgSiO_3$, with a density of 2.5 g cm^{-3}. How deep must the slag be spread over the contaminated area to reduce the exposure rate, 2 m above the original grade, by a factor of 100? Buildup factors for slag may be approximated by those for concrete.

7.10. A hot cell employs for source storage a cylindrical water well 1.5 m in diameter and 5 m deep. Suppose that a source encapsulation fails in such a way that

37 TBq of ^{60}Co is dissolved in the water. Estimate the resulting exposure rate 1 m in air above the center of the well. Estimate the necessary thickness for a lead cover plate to limit the exposure rate to 5 mR h^{-1}.

7.11. A point source of 1-MeV photons is shielded radially by 3 mfp of water, followed by 3 mfp of steel, followed by 3 mfp of concrete, bounded by air. What are the linear thicknesses of the shields? Estimate the overall exposure buildup factor at the concrete–air interface.

7.12. In gamma-photon source or detector calibration procedures, both the source and detector are commonly positioned in air above an effectively infinite concrete or earth interface. For precision calibration, it is necessary to account for photon scattering in the concrete or earth as well as in the air. As an example, consider a 0.7-GBq ^{137}Cs source placed 0.05 m above grade and an air-equivalent

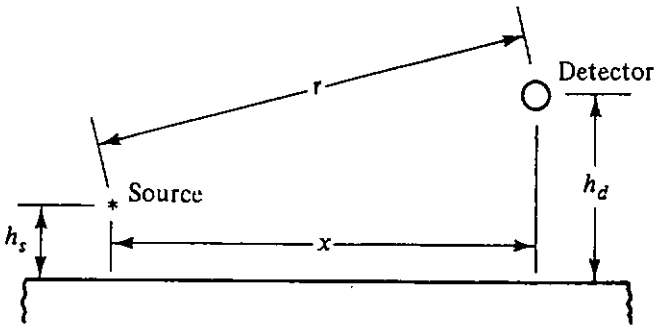

(a)

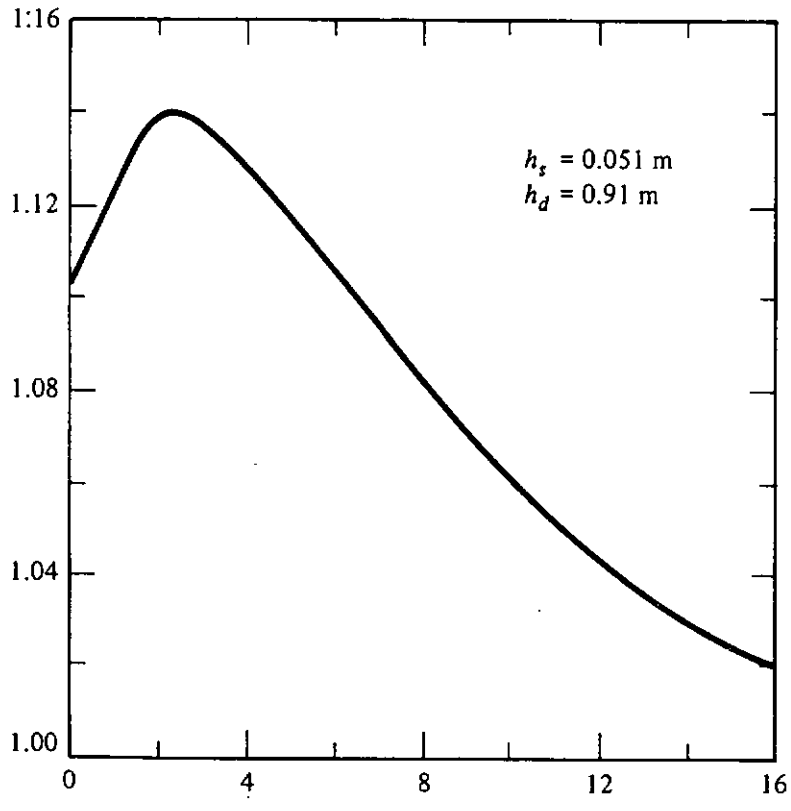

(b)

Fig. P7.12

ion chamber placed 0.91 m above grade. Evaluate the exposure rate (mR h^{-1}) for $x = 5$ m and an air density of 0.001175 g cm^{-3}. The geometry is illustrated in the figure. A procedure has been described in the paper "The Close-In Exposure Field from Point Isotropic Gamma-Ray Source Located at an Air–Ground Interface," *Nucl. Sci. Eng.* 27, 403–410 (1967). The buildup factor accounting for the interface is given by KB_∞, where B_∞ is the infinite-medium-buildup factor and K is a factor depending on x, h_s, and h_d, illustrated in Fig. P7.12. Suggested infinite-medium-buildup factors are:

$$\text{For } {}^{60}\text{Co}: \quad 1 + 0.77(\mu_0 r) + 0.22(\mu_0 r)^2,$$
$$\text{For } {}^{137}\text{Cs}: \quad 1 + 0.92(\mu_0 r) + 0.36(\mu_0 r)^2.$$

7.13. A 250-kVp x-ray therapy unit operates with a tube current of 20 mA for an average of 18 h a week. How thick should a concrete primary protective barrier (density 2.1 g cm^{-3}) be to reduce the weekly exposure in a controlled area 3 m from the tube focus to less than 100 mR? The wall in question has a use factor of $\frac{1}{2}$ assigned to it, and the occupancy factor is unity. What would be the thickness if the wall were made of lead sheet?

7.14. A ^{60}Co gamma-ray irradiator containing a 2-TBq source is directed at a 30-cm-thick concrete wall (density 2.2 g cm^{-3}). If the wall is 7.5 m from the source, what is the exposure rate behind the wall when the irradiator is on?

7.15. The protective housing around the x-ray tube of a therapeutic device is found to limit the leakage radiation at one meter from the tube target to 0.8 R h^{-1} when the machine is operated at 250 kVp with a current of 20 mA. If the machine has a weekly workload of 22,000 mA min, what is the thickness of a concrete (density 2.2 g cm^{-3}) protective barrier 2.8 m from the x-ray tube such that a person behind the barrier receives less than 100 mR in a week? Assume an occupancy factor of unity for the area behind the shield. For the purpose of this problem, ignore the radiation scattered from the patient.

7.16. What is the thickness of a lead barrier necessary to protect from scattered x-ray radiation a controlled area 2.5 m from scatterers (patients)? The patients are positioned 60 cm from the tube focus and the x-ray beam is collimated into a cone of 0.1 sr. The x-ray machine is operated at 300 kVp with a current of 15 mA and has a weekly workload of 15,000 mA min. The barrier adjoins an area with an occupancy factor of unity and the average weekly exposure to personnel in this area must be less than 100 mR. What is the instantaneous exposure rate behind this barrier when the machine is operating? For the purposes of this problem, ignore leakage radiation from the machine.

7.17. A beam from a ^{60}Co irradiator containing a 20-TBq source falls obliquely onto a 40-cm-thick concrete wall (density 2.3 g cm^{-3}) 5 m from the source. Estimate how close to perpendicular incidence the beam may be so that the maximum exposure rate behind the wall is less than 100 mR h^{-1}.

8 special techniques in neutron attenuation

Neutron shielding analyses are often quite complex, involving not only attenuation of primary (or source) neutrons but also production and attenuation of secondary particles. These associated problems include the production of photons during neutron inelastic scattering, slowing down and thermalization of neutrons, capture of thermal neutrons leading to capture gamma photons, and even production of secondary neutrons as a result of fission or $(n, 2n)$ reactions. Neutron shielding analysis might also require consideration of energy deposition in the shielding material, and the resulting thermal and radiation damage effects. Although consideration in detail of all these problems may not be required for a particular application, the analyst must be aware that one of the "secondary" problems may dominate a shield design or analysis. For example, in a thick shield irradiated by fission neutrons, secondary photons become more numerous than fast neutrons deep in the shield, and consequently can contribute far more radiation dose outside the shield than do the transmitted fast neutrons (see Fig. 8.1).

Another complexity of neutron shielding analysis is that none of the associated problems is easily solved using elementary techniques. To obtain accurate results with errors of only a few percent, it is necessary to use sophisticated numerical techniques based on exact descriptions of photon and neutron interactions in the shield. A discussion of these techniques, based on transport theory or Monte Carlo simulation, is deferred to Chapter 10.

In the context of this chapter, source or primary neutrons are the fast neutrons arising from fission or fusion. However, an analyst may also be required to treat lower-energy neutron sources such as neutrons escaping from

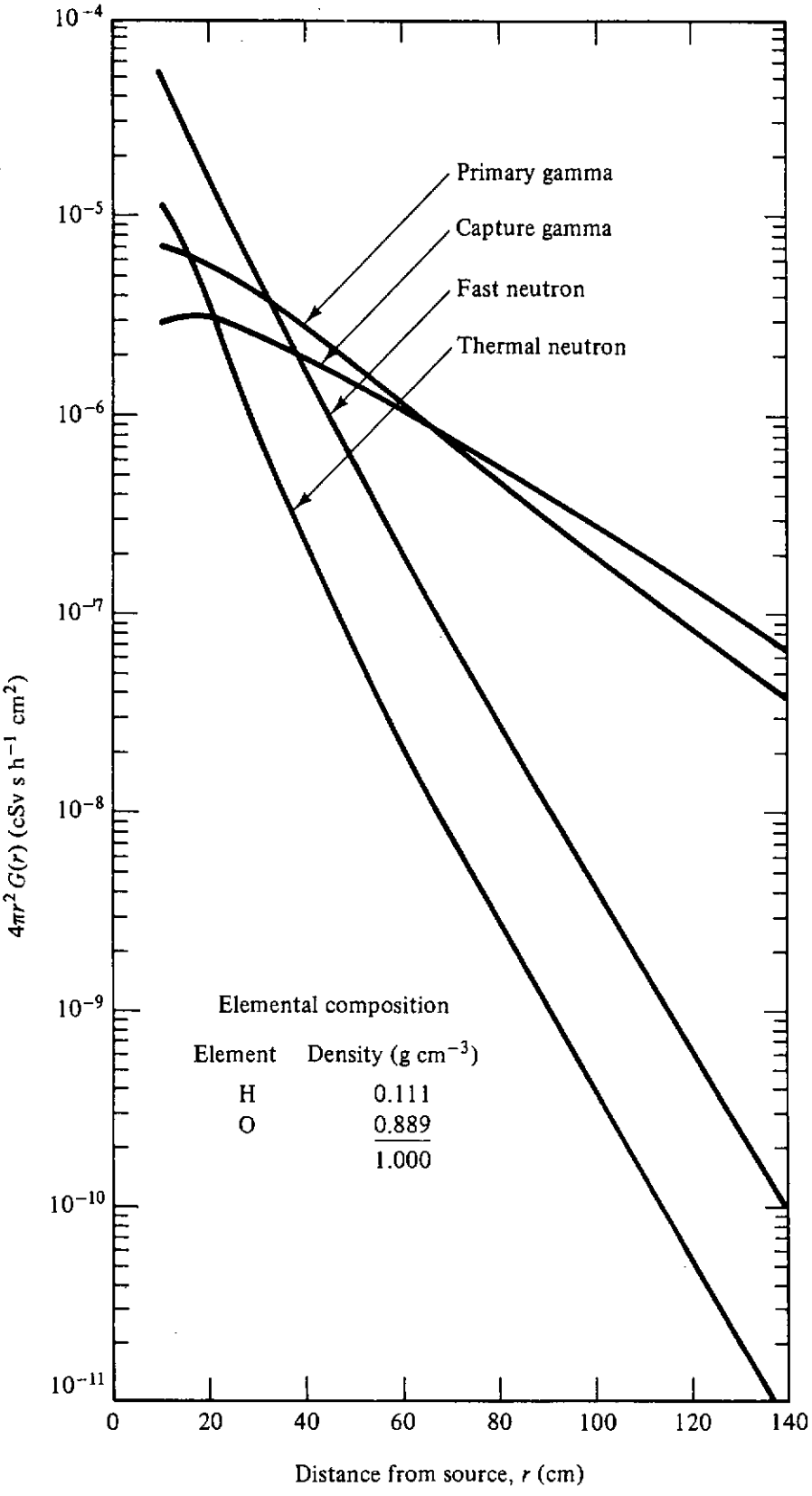

Figure 8.1 Phantom-related dose equivalent kernels $G(r)$, multiplied by $4\pi r^2$, expressed in Sv h^{-1} for a point isotropic ^{252}Cf fission neutron source of unit strength (i.e., 1 neutron s^{-1}) in an infinite water medium. The primary gamma kernel includes photons from the fission products. (From Ref. 1.)

nuclear reactor vessels or from fusion containment structures. Such neutron sources may emit principally thermal neutrons or neutrons of intermediate energies. For two reasons, this chapter concentrates attention on the attenuation of fast neutrons. First, a complete treatment of a fast-neutron shielding problem also requires consideration of neutrons with thermal and intermediate energies that are produced in the shield. Second, as shown in Tables 5.4 and 5.5, the higher-energy neutrons are more significant than the lower-energy neutrons in terms of phantom-related dose equivalent response functions.

Neutron-attenuation calculations in final shield design are performed by use of large computer systems with extensive cross-section libraries. In earlier stages of design, the accuracy afforded by the computer techniques is often not required and a great deal of time and effort can be saved by using semiempirical methods, many of which were developed in the early days of neutron shielding. For example, calculations of fast-neutron attenuation in certain situations may be made with the use of the methods of Chapter 6, that is, by using exponential attenuation with effective attenuation coefficients. Similarly, many secondary-photon calculations can be performed with ray theory (see Section 6.4) once the secondary-photon source strengths have been obtained. The simplified neutron attenuation methods presented in this chapter are often adequate to obtain rough estimates of expected dose rates for many shielding situations. Further, these estimates are valuable tools to aid in the decision as to whether more complex (and expensive) calculations need to be made.

8.1 DIFFERENCES BETWEEN FAST-NEUTRON AND PHOTON FLUX DENSITY CALCULATIONS

For photon attenuation, the use of exponential attenuation and buildup factors is a very powerful and simple technique. However, the extension of these techniques to neutron attenuation problems, although very attractive because of their simplicity, must be done cautiously. The correction of the uncollided flux densities for scattered fast neutrons is generally much more difficult than for the corresponding photon situation. An approximate technique, mentioned in Section 6.3 and developed in detail in this section, is to replace the actual total cross section by an effective *removal cross section* in the uncollided flux density description.

A much better technique, in principle, would be to use the concept of buildup factors to correct the uncollided flux density for scattered neutrons. Unfortunately, the use of neutron buildup factors in this precise way has not been very practical since for neutron problems the buildup of scattered neutrons depends strongly on the material composition, incident neutron energy spectrum, and above all, the geometry of the particular problem. For fast neutrons the probability of scattering is much higher than that of absorption in most materials, and consequently the ratio of scattered neutrons to absorbed neutrons can be very large, especially for shields incorporating heavy nuclides, for which

elastic scattering is not very effective in slowing down the fast neutrons. As a result, neutron buildup factors can assume very large values. Moreover, the size of the system through which the neutrons travel will affect strongly the magnitude of the scattered neutron flux density inside, and the presence of a free surface generally causes a substantial reduction in the neutron flux density near the surface of the shield. This latter effect, not as severe in photon attenuation, prevents the use of infinite-medium buildup factors for a problem involving a finite shield size. Finally, since cross sections can vary dramatically with the neutron energy and from material to material, the buildup of scattered fast neutrons depends sensitively on the exact value of the initial energy of the neutrons as well as the energy dependence of the cross sections for the particular shield material. Furthermore, in contrast to photon scattering, the angular distributions of the scattered neutrons may vary rapidly with the neutron energy. The considerations above imply that buildup factors would have to be calculated for each particular neutron problem, and that general infinite-medium buildup factor tabulations, which are used quite successfully in gamma-ray penetration studies, may introduce serious errors for the fast-neutron problems.

Nevertheless, the concept of a buildup correction is well established in shielding methodology, and many simple models for fast-neutron attenuation include a factor to correct in an approximate manner, for the buildup of scattered fast neutrons. Some of these approximate models are presented in this chapter; however, it must be expected in light of the discussion above that such models will necessarily have a much more restricted range of applicability than do the analogous models for photon attenuation.

8.2 ATTENUATION OF FAST NEUTRONS FROM FISSION SOURCES IN HYDROGENOUS MEDIA

There is one widely encountered situation where the attenuation of a fast-neutron beam can be expected to be somewhat insensitive to the buildup of scattered neutrons. As discussed in Section 3.7.3, elastic scattering from light elements results in a significant portion of the initial kinetic energy being lost, on the average, in a single scattering interaction. In particular, for hydrogen scattering the average energy loss is one-half of the initial neutron energy, and consequently, the scattering of a fast neutron on hydrogen acts essentially as an effective absorption or removal interaction since the neutron will, on the average, be removed from the fast-neutron energy region by a single scatter. Thus, for the deep penetration of fast neutrons, the fast-neutron flux density might be expected to be very nearly equal to that of uncollided fast neutrons deep in an hydrogenous medium. In addition, the cross section for hydrogen in the MeV-energy region increases as the neutron energy decreases and hence a low-energy neutron is much more likely to scatter with hydrogen than would a higher-energy neutron. In effect, this characteristic of the hydrogen cross section implies that, once a fast neutron interacts in an hydrogenous medium, the

subsequent scattering or slowing down interactions will occur relatively near the point of the first scattering interaction.

From the arguments above it is then possible to derive a point kernel for the uncollided fast-neutron flux density in an infinite hydrogeneous medium [2]. Consider a point fission source emitting S_p fission neutrons per second with an energy spectrum given by $\chi(E)$ in an infinite hydrogeneous medium with a hydrogen atom density of N_H cm^{-3}. The uncollided flux density $\phi_H^0(r, E)$ at distance r from the source is (if one neglects, for the moment, any nonhydrogen collisions)

$$\phi_H^0(r, E) = \frac{S_p \chi(E)}{4\pi r^2} \exp\left[-N_H \sigma_H(E) r\right]. \tag{8.1}$$

In Fig. 8.2, the uncollided flux density energy spectrum in water, as given by Eq. (8.1), is shown for a ^{235}U fission neutron energy spectrum. Each one is normalized to unity at the maxima. Notice that, as the distance from the source increases, the energy spectrum of the uncollided neutrons becomes harder with the peak shifting toward the higher energies. Further, the distribution becomes increasingly symmetric as r increases and appears to assume a Gaussian shape at large distances.

Since the total fast-neutron flux density is of interest, Eq. (8.1) must be integrated over all fission energies. To perform such an integration the functional

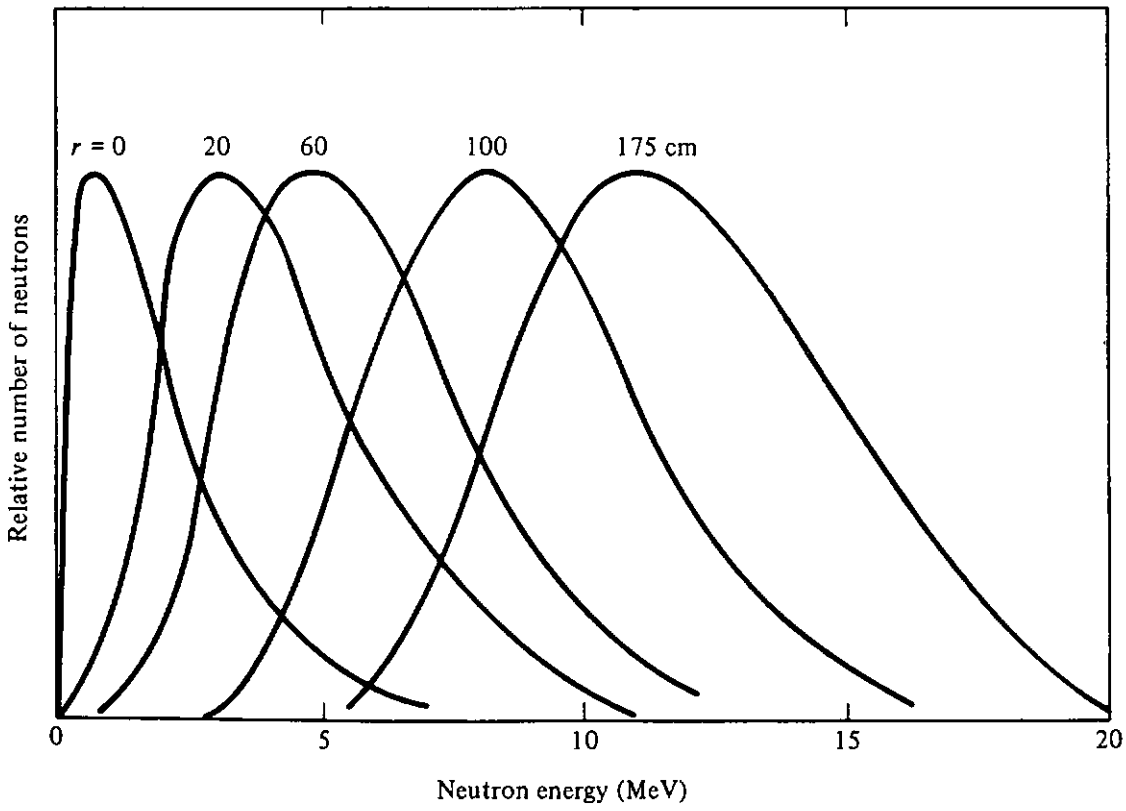

Figure 8.2 Relative distribution of uncollided fission neutrons from a point ^{235}U fission source at various distances into the surrounding water medium. At each distance, the distributions have been adjusted to have the same peak height. In reality, the distributions decrease in amplitude rapidly as r increases. (After Refs. 2 and 3.)

form of $\chi(E)$ and $\sigma_H(E)$ must be used, and because the fast flux is dominated by those neutrons with energies greater than 4 MeV, somewhat simpler forms than those presented in Chapter 4 may be used. To describe the high-energy fission neutrons, several exponential fits to the fission spectrum have been made of the form of Eq. (4.5), that is,

$$\chi(E) \simeq Ae^{-aE}, \tag{8.2}$$

where the fit parameters A and a depend on the fissile isotope and the energy range of the fit (see the first two columns, Table 8.1). For the energy range 2 to

TABLE 8.1 Parameters for the Uncollided Fast-Neutron Flux Density of Eq. (8.16) for Various Point Fissioning Isotopes in Water ($N_H = 0.0670 \times 10^{24}$ cm^{-3})[a]

Isotope	A (MeV^{-1})	a	βA	α	γ
^{233}U (thermal)	1.40	0.714	2.33	0.923	0.580
^{235}U (thermal)	1.43	0.723	2.36	0.928	0.580
^{239}Pu (thermal)	1.36	0.698	2.31	0.914	0.580
^{252}Cf (spontaneous)	1.18	0.630	2.17	0.876	0.580
^{244}Cm (spontaneous)	1.37	0.700	2.31	0.915	0.580
^{240}Pu (spontaneous)	1.47	0.736	2.38	0.934	0.580

[a]Values of a and A for the fission neutron spectrum were obtained by a least-squares fit of Eq. (8.2) to the Maxwellian spectrum of Eq. (4.1) between 6 and 14 MeV.

12 MeV, the hydrogen total cross section (which is essentially the scattering cross section) may be fitted by [4]

$$\sigma_H(E) \simeq BE^{-b}, \tag{8.3}$$

where $B = 5.13 \times 10^{-24}$ cm^2 and $b = 0.725$ when E is in units of MeV.

Substitution of Eqs. (8.2) and (8.3) into Eq. (8.1) yields the following result for the fast-neutron uncollided flux density energy spectrum:

$$\phi_H^0(r, E) = \frac{AS_p}{4\pi r^2} \exp\left[-f(r, E)\right], \tag{8.4}$$

where

$$f(r, E) \equiv N_H BrE^{-b} + aE. \tag{8.5}$$

With this formulation, the energy E_p at which the uncollided flux density has its maximum for a given value of r (or at which f has a minimum) is readily found by setting $f'(\equiv \partial f/\partial E)$ to zero and solving for E_p. The result is

$$E_p = (N_H Bbr/a)^{1/(b+1)}. \tag{8.6}$$

To obtain the total fast-neutron uncollided flux density, Eq. (8.4) must be integrated over energy. This integration can be performed easily, although approximately, by assuming a Gaussian function for the energy distribution of the uncollided neutrons. This Gaussian approximation is equivalent to representing $f(r, E)$ by a second-order Taylor series expansion about E_p; that is,

since $f'(E_p) = 0$,

$$f(r, E) \simeq f(r, E_p) + \tfrac{1}{2}(E - E_p)^2 f''(r, E_p). \tag{8.7}$$

With this approximation, the full width at half maximum, ΔE, of the uncollided distribution is found from Eq. (8.4) to be

$$\Delta E = 2\sqrt{\frac{\ln 4}{f''(r, E_p)}}. \tag{8.8}$$

Substitution of the expression for $f''(r, E_p)$ derived from Eqs. (8.5) and (8.6) yields

$$\Delta E = 2\left(\frac{\ln 4}{(b+1)a^{(b+2)/(b+1)}}\right)^{1/2} [N_H B b r]^{1/2(1+b)}. \tag{8.9}$$

A comparison of the exact peak energies and full widths at half maxima for ^{235}U fission neutrons in water, obtained from Eq. (8.1) with actual values for $\chi(E)$ and $\sigma_H(E)$, to the approximate values given by Eqs. (8.6) and (8.9) is presented in Fig. 8.3. Note that the approximation is remarkably good except for positions near the source ($r < 40$ cm).

Finally, an expression for the total fast-neutron uncollided flux density is obtained by integrating Eq. (8.4) [after incorporating Eq. (8.7)] over the appropriate fast-neutron energy range, E_f, that is,

$$\phi_H^0(r) = \frac{AS_p}{4\pi r^2} e^{-f(r, E_p)} \int_{E_f} dE \exp\left[-\tfrac{1}{2}(E - E_p)^2 f''(r, E_p)\right]. \tag{8.10}$$

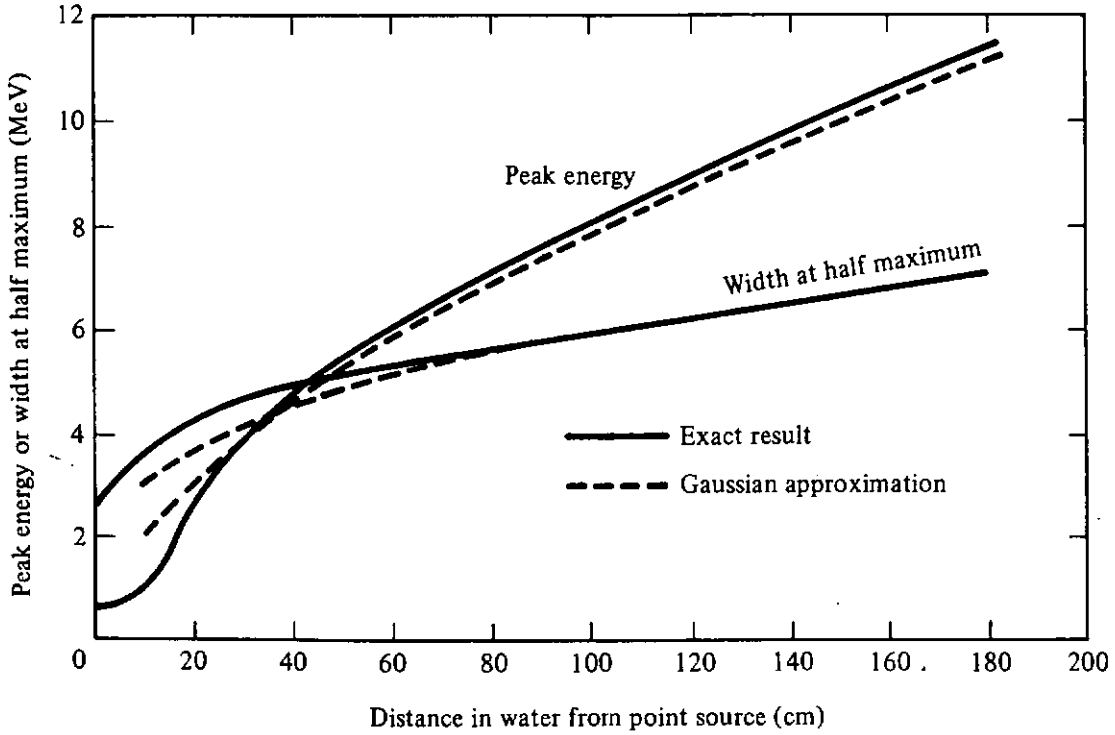

Figure 8.3 Comparison of the peak energy and the half-width for the exact uncollided neutron distribution [Eq. (8.1)] and for the approximate Gaussian model [Eqs. (8.4) and (8.7)] for a point ^{235}U fission neutron source in an infinite water medium. (From Ref. 3.)

For a Gaussian distribution 95.5% of the distribution is between two standard deviations ($\Delta E/\sqrt{\ln 4}$) on either side of E_p. Thus, except for values of r near the source, the range of integration over E in Eq. (8.10) can be extended to the range $(-\infty, \infty)$ without introducing significant error. The resulting integral can now be performed analytically, and the result may be written as

$$\phi_{\mathrm{H}}^{0}(r) = \frac{S_p A \beta}{4\pi r^2} r^{\gamma/2} \exp(-\alpha r^{\gamma}), \tag{8.11}$$

where

$$\gamma \equiv \frac{1}{1+b}, \tag{8.12}$$

$$\beta \equiv \left[\frac{2\pi\gamma(N_H B b)^{\gamma}}{a^{1+\gamma}}\right]^{1/2}, \tag{8.13}$$

and

$$\alpha \equiv \frac{1}{\gamma}\left(\frac{a}{b}\right)^{b\gamma}(N_H B)^{\gamma}. \tag{8.14}$$

Numerical values for these constants are given in Table 8.1 for several fission neutron sources.

The presence of heavier nonhydrogen components in the attenuating medium (e.g., the oxygen in a water shield) will also degrade the fast neutrons in energy, although not nearly as well as the hydrogen. Many fast-neutron experiments have been performed to measure the attenuation of fast fission neutrons in hydrogenous media. Experimentally, it is found that the fast-neutron flux density falls off slightly faster with increasing distance from the source than Eq. (8.11) would indicate. In particular, experimental data for attenuation in water reveal that the spatial distribution of the total fast-neutron flux density can be related to that in hydrogen by

$$\phi^{0}(r) = \phi_{\mathrm{H}}^{0}(r) \exp(-\mu_{r,0} r); \tag{8.15}$$

that is, the nonhydrogen component (oxygen) contributes an exponential attenuation factor. The constant $\mu_{r,0}$ although given the symbol of an attenuation coefficient, is an empirically derived constant to account for the nonhydrogen attenuation. Because of the similarity of this constant to the coefficient in the usual exponential attenuation of uncollided radiation, it is called the *removal* coefficient, although numerically it is usually significantly less than the actual total attenuation coefficient. More will be said about the physical basis of the removal coefficient in the next section. Thus, by correcting for the attenuation of the oxygen, the fast-neutron flux density in water for a point fission source of unit strength ($S_p = 1$ neutron per second) may be written as

$$\phi^{0}(r) = \frac{A\beta}{4\pi r^2} r^{\gamma/2} \exp(-\alpha r^{\gamma} - \mu_{r,0} r). \tag{8.16}$$

The fit of Eq. (8.15) to experimental ^{235}U data in water [4] suggests a value of $\mu_{r,0}$ for oxygen of 0.0308 cm^{-1} (or, equivalently, a microscopic removal cross section of 0.91 b per atom). In Table 8.1, values of the parameters for the

fast-neutron flux density kernel above are given for several fission sources whose fission neutron energy spectra have been represented by the exponential form of Eq. (8.2). From these results it is seen that the total fast-neutron uncollided flux density falls off less rapidly for a ^{252}Cf source than for a ^{235}U source as a consequence of the harder spectrum for ^{252}Cf fission neutrons. Although ^{238}U, ^{233}U, and ^{239}Pu fission neutrons have slightly harder initial fission spectra than those from ^{235}U, the differences are slight and, within the limitations of the present model, kernels for all uranium and plutonium neutron sources may be approximated by the ^{235}U kernel.

It should be emphasized at this point that the fast-neutron flux density kernel of Eq. (8.16) is not adequate for detector-response evaluation since no account is taken of the buildup of small-angle-scattered neutrons. In fact when Eq. (8.16) is expressed in tissue-absorbed dose rate units (1 cm^{-2} s^{-1} $\simeq 1.7 \times 10^{-7}$ Gy h^{-1} in tissue for fast neutrons), the resultant dose rates are about a factor of 8 to 10 lower than the true values. The usefulness of the kernel is to suggest how the uncollided flux density (and hence dose rate) can be expected to vary with distance from the source. Consequently, by fitting the functional form of the kernel to experimental data, one could expect to obtain a reasonably accurate semiempirical result. Such a fitting technique could be expected to lead to better agreement with experiment since the buildup of fast neutrons could be incorporated empirically. One widely used result is that due to Casper [5], who obtained the following fast-neutron tissue-absorbed-dose kernel for a point ^{235}U fission source in water:

$$G(r) = \frac{1.94 \times 10^{-7}}{4\pi r^2} r^{0.349} \exp(-0.422 r^{0.698} - 0.0308 r), \tag{8.17}$$

where r has units of centimeters and G has units of Gy h^{-1} for a source strength of one neutron per second.

Other functional forms have been fit to experimental dose rate data or to values calculated by the more elaborate neutron transport techniques. One particularly simple form for a ^{235}U fission source which can be readily incorporated into analytical kernel calculations (see Chapter 6) expresses the fast-neutron tissue-absorbed-dose kernel for water in terms of exponential functions [6,7], in the same units as used above, as

$$G(r) = \frac{10^{-8}}{4\pi r^2}(8.61 e^{-0.129 r} + 1.04 e^{-0.091 r}). \tag{8.18}$$

Another empirical result, with the same units, which fits the experimental water kernel for absorbed dose in tissue more accurately than do the previous two results and which is valid over a much wider range of r ($0 < r < 300$ cm) is given by [8]

$$G(r) = \frac{9.3 \times 10^{-8}}{4\pi r^2} e^{-br}, \tag{8.19}$$

where

$$b = \left[0.126 - 0.0001773\left(r - \frac{r^2}{600}\right)\right]\left[1 - \left(2 + \frac{r^4}{5000}\right)^{-1}\right]. \qquad (8.20)$$

A comparison of the above three empirical tissue-absorbed-dose point-kernels in water with accurately calculated values is presented in Table 8.2.

TABLE 8.2 Absorbed Dose Rate Kernels in Tissue from a Point ^{235}U Fission Source in Water (D_0) obtained by the Moments Method [8,9]

Distance from Source (cm)	$4\pi r^2 G_0(r)$ Moments Methods (Gy s h^{-1} cm^2)	Ratio to G_0[a]		
		G_1/G_0	G_2/G_0	G_3/G_0
0	0.95×10^{-7}	0	1.016	0.979
10	3.78×10^{-8}	1.026	0.738	0.969
20	8.27×10^{-9}	1.185	0.993	1.041
30	2.55×10^{-9}	1.064	0.970	0.990
60	8.73×10^{-11}	0.936	0.936	0.988
90	3.56×10^{-12}	0.947	1.030	1.053
120	1.99×10^{-13}	0.849	1.027	0.978

[a] G_1 calculated from Eq. (8.17); G_2 calculated from Eq. (8.18); and G_3 calculated from Eq. (8.19).

Kernels in the simple exponential form of Eq. (8.18) are very useful for analytical evaluation of tissue-absorbed doses resulting from distributed fission sources. For example, a disk source is treated in Problem 8.2. More accurate formulas such as Eq. (8.19) generally require numerical integration in treatment of distributed sources.

The dose rate from a plane fission source emitting neutrons only perpendicularly from the source plane, can be obtained directly from the above results by omitting the spherical reduction factor $4\pi r^2$, and replacing r by x, the distance from the source plane. The resultant plane dose rate kernel could be used to approximate conservatively the spatial behavior of the fast flux density or dose rate far from a plane *isotropic* source since only those neutrons which leave the source nearly perpendicularly will survive a deep penetration into the hydrogenous media. Of course, a more accurate approach to this plane isotropic source case would be to use Eq. (8.18) as a point kernel and to integrate over the source plane.

Finally, the emphasis on water as the shielding material in the above dose rate kernels is not because water is the most important type of neutron shielding material today (although it plays an important role in water-moderated reactors), but rather is a result of the historical accident that early shielding research and engineering was motivated by the naval reactor program for which water is obviously an important shielding material. The modification of the water dose rate kernels for other hydrogenous media is discussed in the next section.

8.3 REMOVAL CROSS SECTIONS

In many realistic situations fission neutrons will be attenuated not only by an hydrogenous medium but also by an interposed nonhydrogenous shield (e.g., the wall of a steel pressure vessel). Many experimental data have been obtained for such situations, and under special circumstances the effect of the non-hydrogen component can be very simply accounted for by an exponential attenuation factor, much as was done for the oxygen correction in the preceding section.

An idealized fast-neutron attenuation experiment is shown in Fig. 8.4(a). A plane perpendicular fission source is embedded in an infinite homogeneous hydrogenous medium into which a nonhydrogenous component in the form of

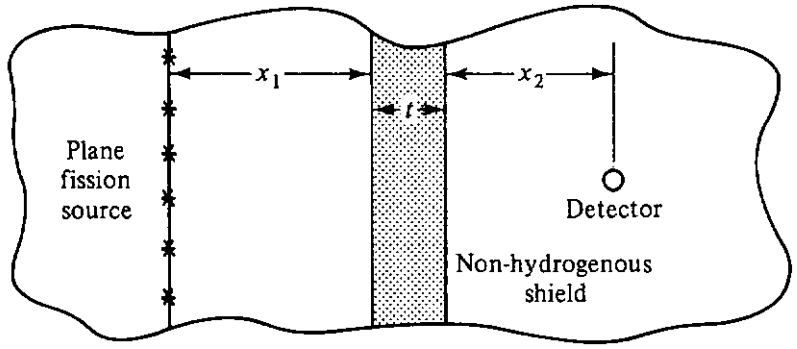

(a)

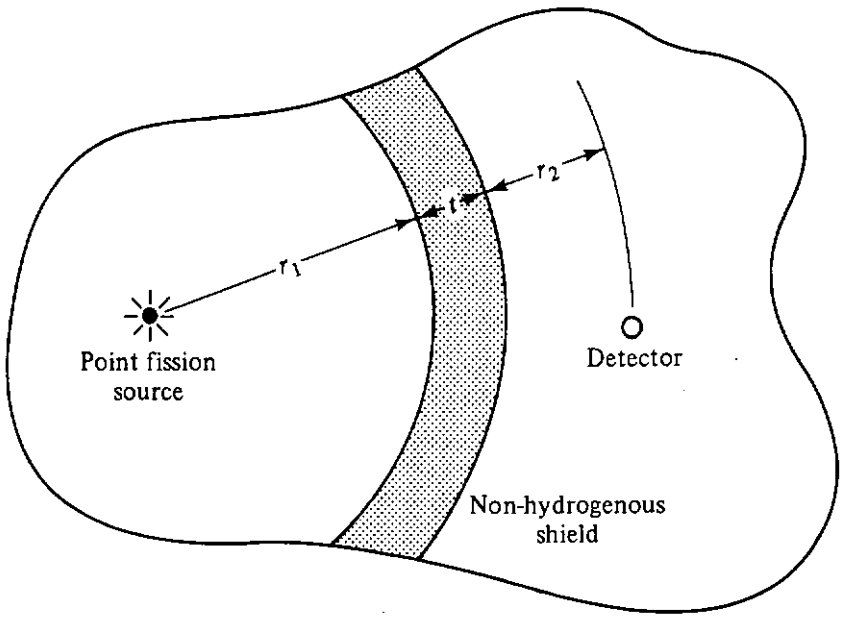

(b)

Figure 8.4 Idealized experimental geometry for the measurement of the removal cross section: (a) plane geometry; (b) spherical geometry. A nonhydrogenous shield of thickness t is placed between the source and detector in an infinite hydrogenous medium.

a homogeneous slab of thickness t can be inserted. Experimental results[1] reveal that, under certain circumstances, the tissue-absorbed dose rate $\dot{D}'$ with the slab in position (i.e., at a distance $x = x_1 + x_2$ of hydrogenous medium *plus* a thickness t of the nonhydrogenous component) is related to the dose rate $\dot{D}$ at a distance x from the source, without the slab, by

$$\dot{D}' = \dot{D}e^{-\mu_r t}, \tag{8.21a}$$

where μ_r is called the *removal coefficient* and is a constant characteristic of the nonhydrogenous component for a given fission neutron energy spectrum. The analogous experiment in spherical geometry, with a point source, is shown in Fig. 8.4(b). In this experiment, with $r = r_1 + r_2$,

$$\dot{D}' = \dot{D}\left(\frac{r}{r+t}\right)^2 e^{-\mu_r t}. \tag{8.21b}$$

Two important restrictions on the experimental arrangement are required for the validity of Eqs. (8.21a) and (8.21b). First, it is important that there be at least 6 g cm^{-2} of hydrogen, equivalent to 50 cm of water, between the nonhydrogenous component and the observation position. Second, the thickness t must be such that $\mu_r t$ is less than 5.

Although the factor $\exp(-\mu_r t)$ in Eqs. (8.21a) and (8.21b) appears to indicate that absorption of neutrons is taking place in the nonhydrogenous component, the primary interactions are scattering interactions in which the fission neutrons are degraded in energy only slightly. However, the hydrogen in the material following the nonhydrogenous component (one of the two experimental restrictions) will moderate or remove the slightly slowed-down neutrons more quickly than those neutrons which traverse the nonhydrogenous component without any energy loss. If, following the nonhydrogenous component, there is sufficient hydrogen to effect the removal of the neutrons which are slightly moderated, the spatial variation of the fast-neutron tissue-absorbed dose rate $\dot{D}$ for the plane geometry case in water can be obtained from one of the kernels of Eqs. (8.17) to (8.19) by replacing r with x and omitting the spherical divergence factor $1/4\pi r^2$. For the spherical geometry case in a water medium, $\dot{D}$ is given directly by one of the kernels of Eqs. (8.17) to (8.19). In Fig. 8.5, experimental results are shown for iron slabs in water. Notice the sharp decline of the fast-neutron flux density just beyond the iron slabs. Only after about 40 cm of further penetration in water is the flux density well described by the removal model implicit in Eq. (8.21a).

If a series of slabs of different materials is inserted into the hydrogenous medium, the removal term $\exp(-\mu_r t)$ of Eqs. (8.21a) and (8.21b) becomes

[1]The actual experimental work was performed, of course, with a finite isotropic plane fission source (e.g., a disk). However, with the use of appropriate point kernel models (see Section 6.6.3), the actual experimental results can be used to deduce the result that would be obtained in the present idealized situation.

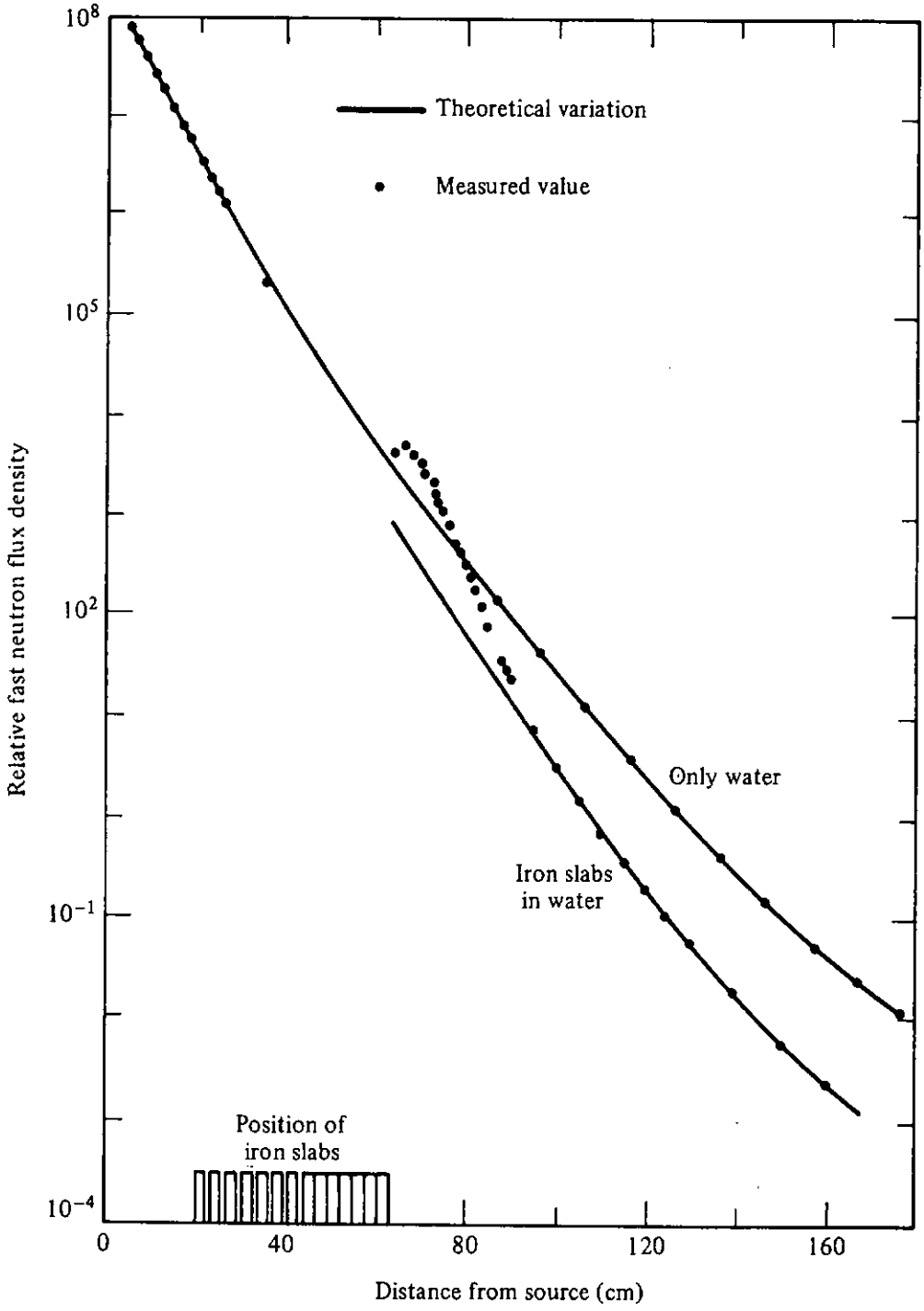

Figure 8.5 Fast-neutron flux density as a function of distance from a ^{235}U fission source plane with and without interposed iron slabs. (After Ref. 3.)

simply $\exp(-\sum_i \mu_{r,i}\, t_i)$, where $\mu_{r,i}$ is the removal coefficient for the ith slab of thickness t_i. Similarly, if a slab of a mixture of elements is inserted, the removal coefficient μ_r for the slab is given by $\sum_i N_i \sigma_{r,i}$, where N_i is the atom density of the ith element with microscopic removal cross section $\sigma_{r,i}$. This additive nature of the relaxation lengths for the nonhydrogen components, which is a direct consequence of Eqs. (8.21a) and (8.21b), has generally been supported by experiment, although some deviations have been noted.

The (n, γ) absorption cross sections for most materials in the MeV-energy

region are negligible and play no significant role in the removal of fast neutrons. Conceptually, the removal cross section is that fraction of the total fast-neutron cross section, averaged over energies of fission neutrons, representing inelastic and elastic scattering through a large scattering angle (i.e., scattering in which there is significant energy loss). Thus, the removal cross section can be expected to be somewhat less than the total cross section. As an approximation, $\mu_r \simeq \frac{2}{3}\bar{\mu}_t$, where $\bar{\mu}_t$ is the average total attenuation coefficient in the energy range 6 to 8 MeV [10].

There is no firm theoretical reason for the removal cross section to be a material constant, and indeed, it might be expected to vary with the fission neutron energy spectrum, slab thickness, amount of hydrogenous material on either side of the slab, and the geometry of the experiment. However, experimental results have shown that for most situations (provided that the slab is less than 5 removal relaxation lengths thick), μ_r can be often taken as a constant for a given incident fission spectrum. In Table 8.3, measured values of removal cross sections for several materials are presented. To obtain removal cross sections for other elements, the following empirical formulas (in units of cm^2/g) have been obtained to permit interpolation between these measured values [12]:

$$\frac{\mu_r}{\rho} = \begin{cases} 0.19Z^{-0.743} & (Z \leq 8) \\ 0.125Z^{-0.565} & (Z > 8) \end{cases} \tag{8.22}$$

or

$$\frac{\mu_r}{\rho} = 0.206\mathcal{A}^{-1/3}Z^{-0.294} \tag{8.23}$$

TABLE 8.3 Measured Microscopic Removal Cross Sections of Various Elements and Compounds for ^{235}U Fission Neutrons

Material	σ_r (b/atom)	Material	σ_r (b/atom)
Aluminum	1.31 ± 0.05	Oxygen	0.99 ± 0.10
Beryllium	1.07 ± 0.06	Tungsten	3.36
Bismuth	3.49 ± 0.35	Zirconium	2.36 ± 0.12
Boron	0.97 ± 0.10	Uranium	3.6 ± 0.4
Carbon	0.81 ± 0.05	Boric oxide, B_2O_3	4.30 ± 0.41[a]
Chlorine	1.2 ± 0.8	Boron carbide, B_4C	4.7 ± 0.3[a]
Copper	2.04 ± 0.11	Fluorothene, C_2F_3Cl	6.66 ± 0.8[a]
Fluorine	1.29 ± 0.06	Heavy water, D_2O	2.76 ± 0.11[a]
Iron	1.98 ± 0.08	Hevimet[b]	3.22 ± 0.18
Lead	3.53 ± 0.30	Lithium fluoride, LiF	2.43 ± 0.34[a]
Lithium	1.01 ± 0.05	Oil, CH_2 group	2.84 ± 0.11[a]
Nickel	1.89 ± 0.10	Paraffin, $C_{30}H_{62}$	80.5 ± 5.2[a]

[a]Removal cross section is in barns per molecule or per group.
[b]90 wt% W, 6 wt% Ni, 4 wt% Cu; cross section is weighted average.
Source: *Refs. 4 and 11; reproduced by permission of John Wiley & Sons, Inc.*

where $\mathcal{A}$ and Z are the atomic mass and atomic number, respectively, for the element of concern.

8.3.1 Extensions of the Removal-Cross-Section Model

Effect of hydrogen following the nonhydrogen shield. In the preceding section it was stated that the applicability of the removal-cross-section model of Eq. (8.21) was dependent on whether there is sufficient hydrogen following the nonhydrogenous component to complete the removal of neutrons which have been degraded slightly in energy. If there is insufficient hydrogen following the nonhydrogenous component, not all the neutrons will be removed, and the removal cross section will appear to have a smaller value. In such a situation the removal cross section is no longer simply a material property, but is also a function of the hydrogen thickness following the nonhydrogen component.

Several experiments have been performed on such hydrogen-deficient shields to determine the effect on the removal cross section [defined by Eq. (8.21)] of the amount of hydrogen following the nonhydrogen component. In Fig. 8.6 some calculated results are shown for a polyethylene and lead or iron system. Notice that after 30 cm of polythylene the removal cross sections approach the values for lead or iron given in Table 8.3. Further, the values of

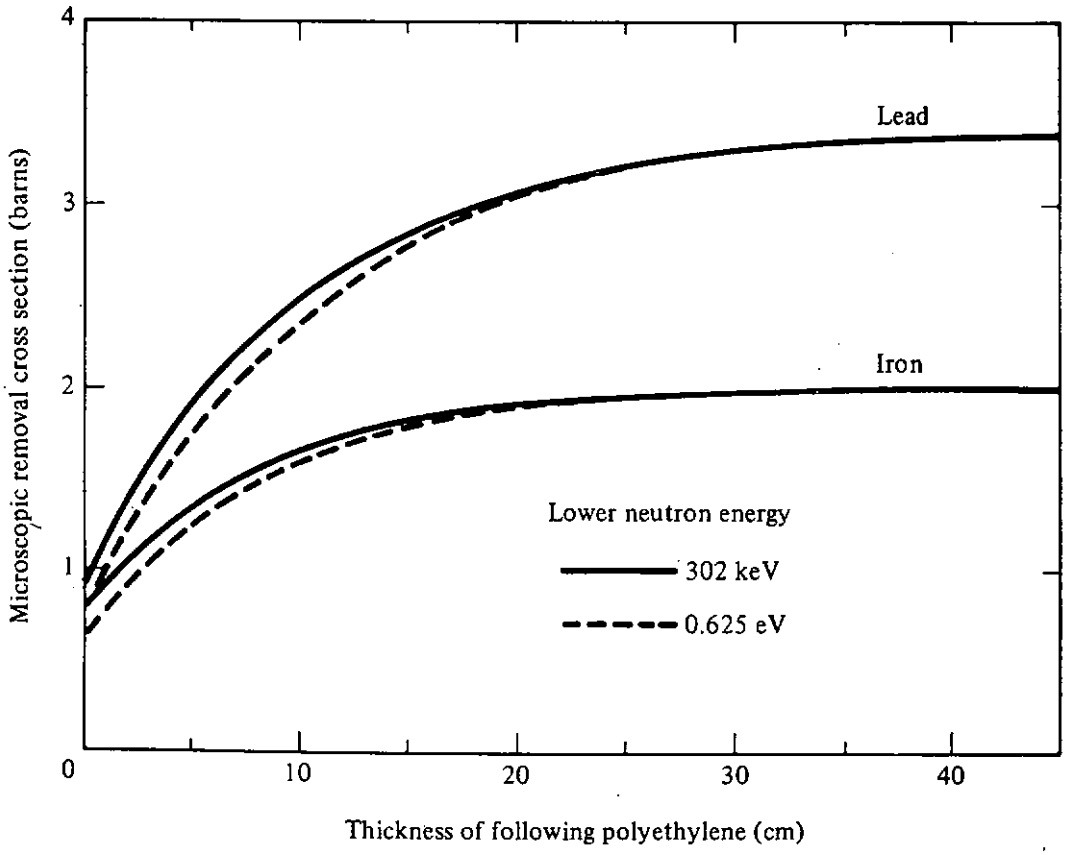

Figure 8.6 Effective microscopic removal cross sections for iron and lead followed by various thicknesses of polyethylene for a point ^{235}U fission neutron source. (From data of Ref. 13.)

these asymptotic removal cross sections are very insensitive to the lower cut-off energy used to define the lower limit of the fast-neutron flux density. However, for hydrogen-deficient shields, the lower cutoff energy yields slightly smaller values for the removal cross section, as would be expected, since the limited hydrogen available is unable to remove all the degraded neutrons and consequently leaves relatively more fast neutrons to penetrate the shield.

Homogeneous shields. For homogeneous systems in which the nonhydrogen material is uniformly dispersed in an hydrogenous medium (e.g., concrete), the removal-cross-section concept can also be applied if the hydrogen concentration is sufficiently high. For such situations, the fast-neutron tissue-absorbed dose rate $\dot{D}(r)$ from a point fission source of strength S_p can be related to the dose rate $\dot{D}_{\mathrm{H}}(r)$ in a pure hydrogen medium of equivalent hydrogen density by the equation

$$\dot{D}(r) = \dot{D}_H(r) \exp\left(-\sum_{i=1}^{N} \sigma_{r,i}^{\mathrm{homo}} \frac{N_A \rho_i}{\mathcal{A}_i} r\right), \tag{8.24}$$

where $\sigma_{r,i}^{\mathrm{homo}}$ is the microscopic removal cross section of the ith nonhydrogen component for a fission neutron source, $\mathcal{A}_i$ and ρ_i are the atomic mass and partial density of the ith component, respectively, and N_A is Avogadro's number. The pure hydrogen dose rate $\dot{D}_{\mathrm{H}}(r)$ in this result can be calculated in terms of a point source dose kernel $G_{\mathrm{H}}(r)$ as $\dot{D}_{\mathrm{H}}(r) = S_p G_{\mathrm{H}}(r)$, where $G_{\mathrm{H}}(r)$ can be inferred from the water kernels of Eqs. (8.17) to (8.20) by eliminating the oxygen contribution and correcting for the different hydrogen atomic density. For example, using Casper's semiempirical kernel of Eq. (8.17), with the oxygen removal term eliminated, $G_{\mathrm{H}}(r)$ can be expressed as

$$G_H(r) = \frac{1.94 \times 10^{-7}}{4\pi r^2} \{(\Upsilon r)^{0.349} \exp\left[-0.422(\Upsilon r)^{0.698}\right]\}, \tag{8.25}$$

where Υ is the ratio of the hydrogen atom density in the mixture to that in pure water. For most elements the homogeneous removal cross section in Eq. (8.24) can be taken equal to the heterogeneous removal cross section [see Table (8.3)], although for lighter elements the homogeneous removal cross sections appear to be 5 to 10% smaller than those for heterogeneous media [14].

For Eq. (8.24) to be valid it is imperative that there be sufficient hydrogen present to remove neutrons degraded in energy by collisions with the heavy component. In Fig. 8.7 the lowest concentration of water required for the validity of Eq. (8.24) is presented as a function of the atomic mass of the nonwater component. Notice that the heavier the nonhydrogen component, the more water is required. It should also be noted that concrete, which is a very important neutron shielding material, is just barely able to pass this criterion. One should be cautious therefore in the application of Eq. (8.24) to a very dry concrete.

Energy-dependent removal cross sections. In many situations the neutron spectrum incident on an hydrogenous shield will not be that of a

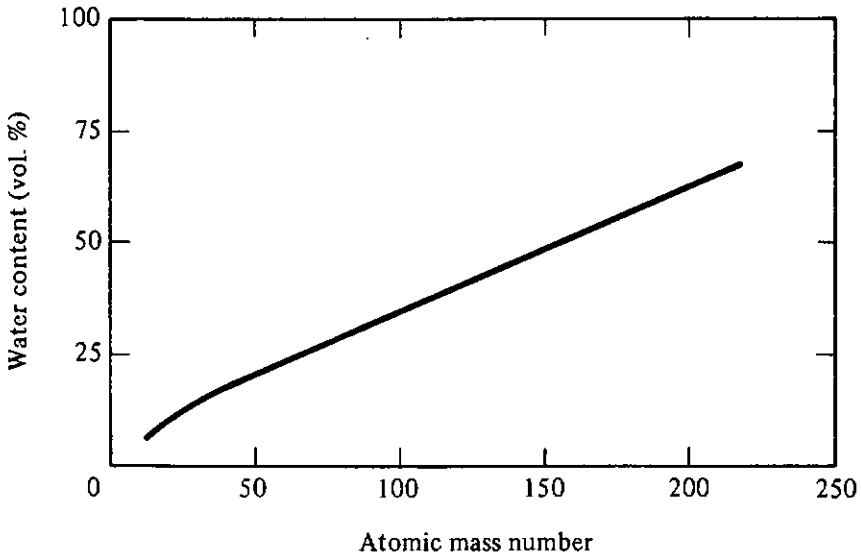

Figure 8.7 Lowest volume concentration of water in a homogeneous mixture containing heavy components with an average atomic mass $\mathfrak{A}$ for Eq. (8.24) to be valid. (From Ref. 13; by permission of Springer-Verlag New York, Inc.)

fission source, but may have a completely different energy dependence, $\chi(E)$, as a result of penetration through other materials or from a difference in the physical source of the fast neutrons (e.g., a fusion reaction). In such situations the removal concept can again be used by employing energy-dependent removal cross sections. As with the fission-spectrum case, it is important that sufficient hydrogen be present to remove those neutrons which have been slightly degraded by collisions with the nonhydrogenous components in the shield. For any point isotropic source of strength S_p and energy spectrum $\chi(E)$, the tissue-absorbed dose rate a distance r away from the source in an infinite homogeneous medium can, by analogy with our previous results, be written as

$$\dot{D}(r) = \int_0^\infty dE\, S_p \chi(E) G_{\mathrm{H}}(r, E) \exp\left[-\sum_{i=1}^{N} \sigma_{r,i}(E)\, \frac{N_A \rho_i}{\mathfrak{A}_i} r\right], \tag{8.26}$$

where $G_{\mathrm{H}}(r, E) \equiv$ neutron dose kernel at a distance r from a unit isotropic source emitting neutrons of energy E in a pure hydrogen medium of density equivalent to that in the shield material

$\sigma_{r,i}(E) \equiv$ microscopic removal cross section of the ith non-hydrogen shield component for neutron energy E

$\mathfrak{A}_i, \rho_i \equiv$ atomic mass and volume density of the ith shield component, respectively

$N_A \equiv$ Avogadro's number

The use of Eq. (8.26) to calculate the dose rate depends on two crucial pieces of information: the hydrogen dose rate kernel, G_{H}, and the energy-dependent removal coefficient $\mu_{r,i}$. As a rough approximation for the energy-dependent hydrogen dose kernel, one may use the following result [14]:

$$G_{\mathrm{H}}(r, E) = \frac{1}{4\pi r^2} \exp\left[-\mu_{\mathrm{H}}(E) r\right][1 + \mu_{\mathrm{H}}(E) r] \mathfrak{R}_D(E), \tag{8.27}$$

which is simply the uncollided dose rate kernel times an approximate buildup-factor correction, $[1 + \mu_H(E)r)]$, times the tissue-absorbed dose response function $\mathcal{R}_D(E)$. Here $\mu_H(E)$ is the total hydrogen attenuation coefficient at energy E. An alternative is to use the following empirical result for the tissue-absorbed dose rate kernel in water for a point monoenergetic neutron source of energy E:

$$G_{H,0}(r, E) = \frac{A_0(E)}{4\pi r^2} \exp[-A_1(E)r - A_2(E)r^2], \tag{8.28}$$

where values of the coefficients A_0, A_1 and A_2 are tabulated in Table 8.4 for several source energies. The monoenergetic dose rate kernels are shown in Fig. 8.8. The pure hydrogen dose rate kernel can then be obtained by correcting for the oxygen removal in water and adjusting the hydrogen atomic density, that is,

$$G_H(r, E) = \frac{A_0(E)}{4\pi r^2} \exp[-A_1(E)\Upsilon r - A_2(E)(\Upsilon r)^2 + \mu_{r,0}(E)\Upsilon r], \tag{8.29}$$

where Υ is the ratio of the hydrogen atom density to that in water, and $\mu_{r,0}(E)$ is the energy-dependent removal coefficient for oxygen in water.

TABLE 8.4 Constants for the Empirical Fit of the Tissue-Absorbed Dose Rate Kernel for a Point Monoenergetic Neutron Source in Water as Given by Eq. (8.28)[a]

Source Energy (MeV)	$A_0\left(\frac{\text{Gy h}^{-1}\text{ cm}^2}{\text{s}^{-1}}\right)$	A_1 (cm^{-1})	A_2 (cm^{-2})	Range of Fit (cm)
2	2.630(−7)[b]	0.1716	0.6274(−3)	10–80
4	3.437(−7)	0.1115	0.3792(−3)	10–110
6	3.105(−7)	0.07953	0.1913(−3)	10–140
8	2.536(−7)	0.06362	0.1634(−3)	10–140
10	2.193(−7)	0.05723	0.1414(−3)	10–140
14	1.952(−7)	0.04925	0.1318(−3)	10–140

[a]These values were obtained by a least-squares fit to results of moments calculations [8,9]. Agreement is within ±10% over the indicated range of each fit.

[b]Read as 2.630×10^{-7}, etc.

A more severe limitation of the energy-dependent removal-cross-section theory is the availability of values for removal cross sections. Only sparse experimental data are available, and those have rather large associated uncertainties. In Fig. 8.9 several energy-dependent removal cross sections are shown and in Table 8.5 neutron removal cross sections are listed for different energies. However, in many cases it is necessary to use theoretical values of removal cross sections. Many investigations have been undertaken to relate the removal cross section to nuclear properties [15,16]. Conceptually, the removal coefficient for an isotope is that portion of the total cross section μ_t which removes the

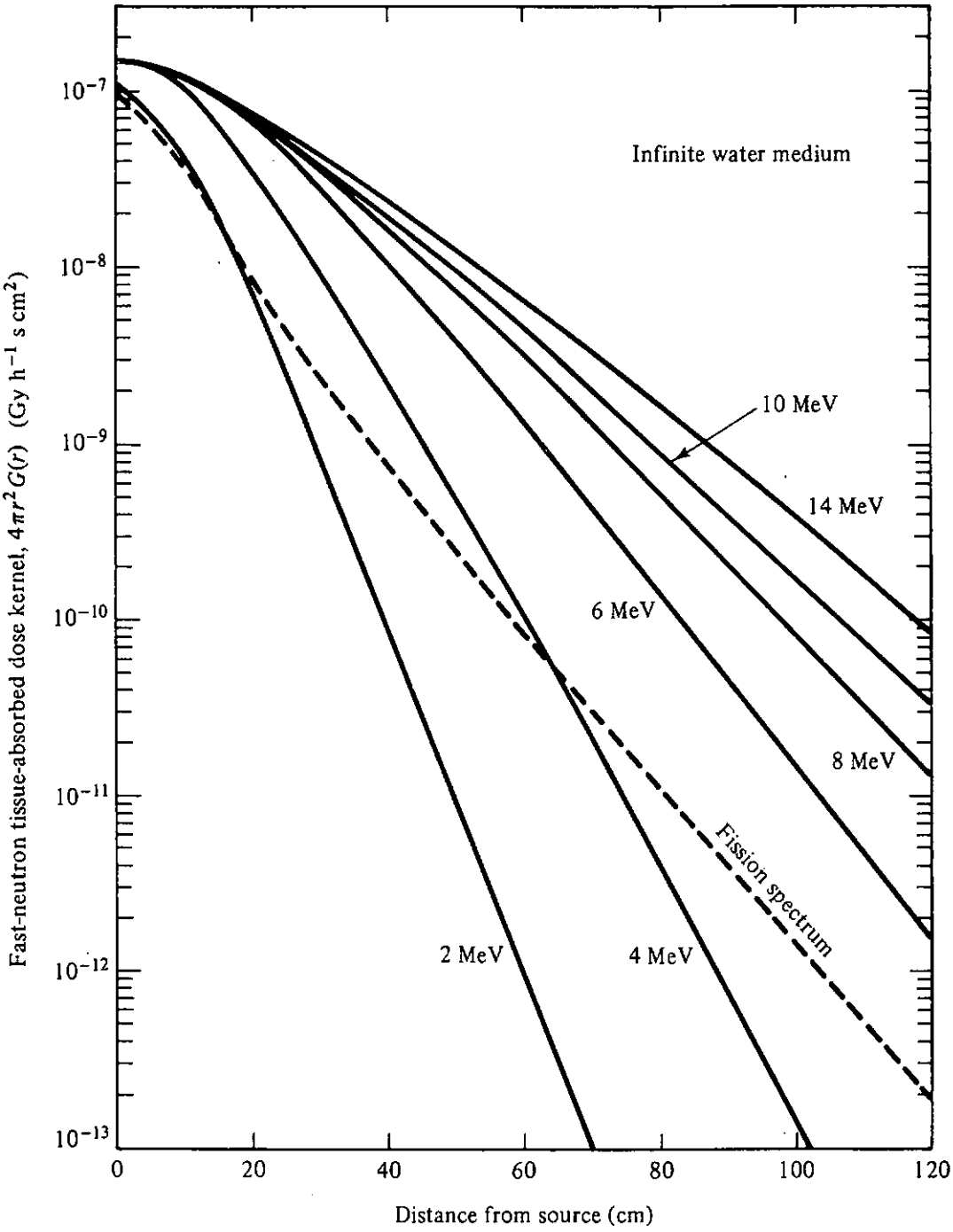

Figure 8.8 Fast-neutron tissue-absorbed dose kernel (multiplied by $4\pi r^2$) expressed in units of Gy h^{-1} for point monoenergetic neutron sources and a point ^{235}U fission source in an infinite water medium. The sources are assumed to have unit strength (i.e., one neutron emitted per second). (After Ref. 9.)

neutron from the energy region of interest. Only elastic scatters at small angles do not appreciably degrade the incident neutron energy. Hence,

$$\mu_r(E) = \mu_t(E) - f(E)\mu_{el}(E), \tag{8.30}$$

where $f(E)$ is the probability an elastic scatter causes negligible energy loss and $\mu_{el}(E)$ is the elastic scattering coefficient. As an approximation, $f(E)$ is often set equal to the mean cosine of the scattering angle in the laboratory coordinate

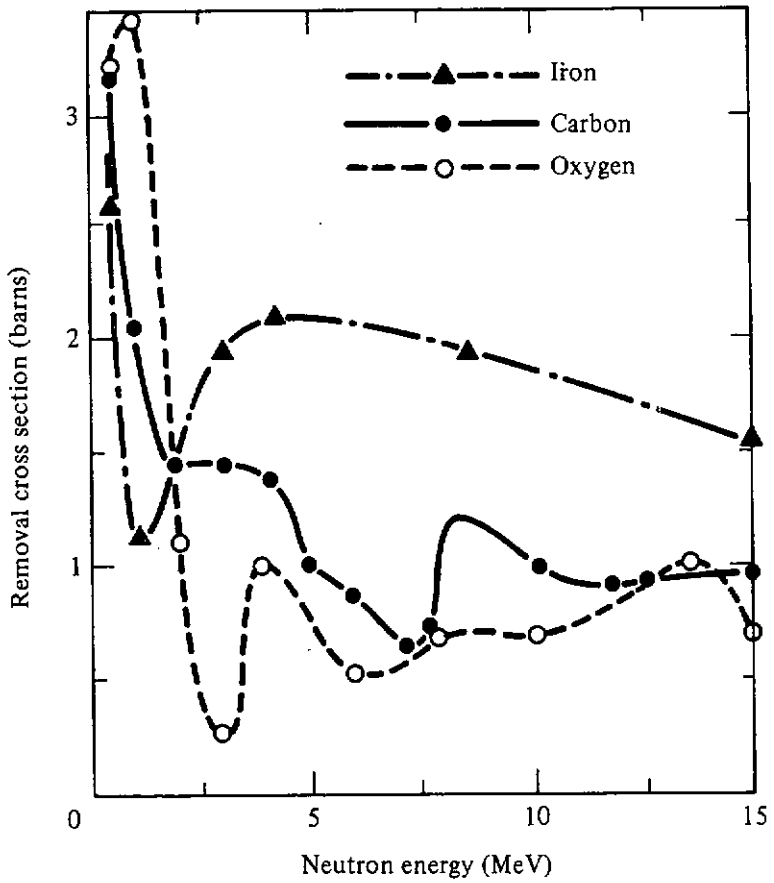

Figure 8.9 Measured values of energy-dependent removal cross sections. (After Ref. 15.)

TABLE 8.5 Energy-Dependent Neutron Removal Cross Sections, $\sigma_r(E)$, for Different Energies and Elements (barns/atom)

	Energy (MeV)				
Element	0.5	1.0	1.2	3	15
Be	—	—	—	2.3 ± 0.2	1.04 ± 0.05
B	—	—	—	1.3 ± 0.1	0.82 ± 0.07
C	3.16 ± 0.25	2.08 ± 0.23	—	1.58 ± 0.02	0.92 ± 0.02
O	—	—	—	0.48 ± 0.19	0.70 ± 0.06
Na	2.5 ± 0.2	2.5 ± 0.3	2.8 ± 0.4	—	—
Al	—	—	—	1.68 ± 0.07	1.24 ± 0.11
S	—	—	—	1.40 ± 0.20	1.58 ± 0.09
Ti	—	—	—	2.4 ± 0.4	1.54 ± 0.04
Fe	2.4 ± 0.5	1.04 ± 0.11	—	1.96 ± 0.04	1.53 ± 0.05
Ni	4.3 ± 0.8	2.0 ± 0.7	—	1.90 ± 0.03	1.59 ± 0.07
Cu	—	—	—	2.3 ± 0.1	1.84 ± 0.10
Zn	—	—	—	1.73 ± 0.11	1.64 ± 0.15
Zr	—	—	—	2.77 ± 0.08	1.90 ± 0.12
W	—	—	—	4.8 ± 0.5	3.63 ± 0.40
Pb	1.2 ± 0.8	2.87 ± 0.63	—	3.72 ± 0.13	3.39 ± 0.18
Bi	—	—	—	3.78 ± 0.33	3.35 ± 0.20

Source: *Ref. 14; by permission of Springer-Verlag New York, Inc.*

system. A somewhat more direct approach is to write Eq. (8.30) as

$$\mu_r(E) = \mu_t - 2\pi \int_{\cos\theta_r}^{1} \mu_{el}(E, \theta_c)\, d(\cos\theta_c), \tag{8.31}$$

where $\mu_{el}(E, \theta_c)$ is the differential elastic scattering cross section per unit solid angle about the scattering angle θ_c in the center-of-mass system (which is approximately equal to the laboratory scattering angle for all but the lightest nuclides). The threshold angle θ_r below which elastic scattering does not degrade the neutron energy sufficiently to remove it from the energy region of interest has been determined by comparison of μ_r from Eq. (8.31) to experimental results. For hydrogen, the best value of $\cos\theta_r$ is 0.45, while for all other nuclides, $\cos\theta_r = 0.6 \pm 0.1$ [17].

Generally, the lack of information for energy-dependent removal cross sections as well as a lack of an accurate hydrogen attenuation dose kernel limit the use of removal-cross-section theory for dose calculations. Of particular concern in shield calculations are those energy regions for which these removal cross sections have minima, that is, those energies for which neutrons can stream through the shield material with little chance of being removed. In practice, more elaborate removal–diffusion models are used to calculate the penetration of nonfission spectra through various shields (see Section 8.5.3). However, for an approximate calculation, Eq. (8.26) may often be useful.

8.4 FAST-NEUTRON ATTENUATION IN NONHYDROGENOUS MEDIA

In nonhydrogenous material, the calculation of the attenuation of fast neutrons is quite difficult, and elaborate numerical procedures based on transport theory or removal–diffusion theory are needed if accurate results are required. For rough estimates of fast-neutron penetration, however, a few empirical results have been obtained which will be outlined in this section.

Important nonhydrogenous materials frequently encountered in shield design include iron, lead, and aluminum used as structural material or for photon shielding. Fast neutrons are attenuated very poorly by these materials. For Po-Be neutrons, relaxation lengths are found to be 16 cm for iron, 24 cm for lead, and 30 cm for aluminum [18]. Hence, fast-neutron attenuation through only a few centimeters of these materials can be neglected for practical purposes.

However, for thick nonhydrogenous shields, fast neutrons may be appreciably attenuated. Beyond a few mean-free-path lengths from a fast-neutron source in an infinite nonhydrogenous medium, the fast-neutron flux density has been observed to decrease exponentially. However, the relaxation length is a characteristic not only of the material but also of the source energy and the lower-energy limit used to define the fast-neutron region (i.e., the "fast group" of neutrons). Specifically, the total fast-neutron flux density, $\phi_\alpha(r)$, above some threshold energy E_α at a distance r greater than 3 mean-free-path lengths from

a point monoenergetic source of strength S_p and energy E_0 in an infinite homogeneous medium can be calculated by [19]

$$\phi_\alpha(r) \equiv \int_{E_\alpha}^{E_0} \phi(r, E)\, dE = \frac{S_p B_0}{4\pi r^2} \exp\left(\frac{-r}{\lambda_r}\right). \tag{8.32}$$

The factor B_0 corrects for the initial buildup (Sec. 6.3) of scattered fast neutrons and, after a few mean-free-path lengths, becomes a constant. Both the initial buildup factor and the relaxation length λ_r are empirical constants and depend on the attenuating material, the source energy, and the threshold energy E_α. In Table 8.6 values of B_0 and λ_r are presented for a few materials.

TABLE 8.6 Initial Buildup Factors and Relaxation Lengths in Different Media for Monoenergetic Neutron Sources[a]

Substance	$E_0 = 4$ MeV		$E_0 = 14.9$ MeV	
	B_0	λ (cm)	B_0	λ (cm)
B_4C ($\rho = 1.67$ g cm^{-3})	2	12.0	2	17.2
C ($\rho = 1.67$ g cm^{-3})	2	11.4	2	19.2
Al ($\rho = 2.7$ g cm^{-3})	2.5	14.1	2.5	15.8
Fe ($\rho = 7.83$ g cm^{-3})	2.5	7.6	2.7	8.2
Pb ($\rho = 11.3$ g cm^{-3})	4	15	2.9	15.3

[a]Energy range for fast-neutron flux density is 1.5 MeV to E_0.

Source: *Ref. 19; by permission of Springer-Verlag New York, Inc.*

If the fast-neutron source is distributed in energy, the technique above can still be applied by dividing the source energy region into several contiguous narrow energy ranges and then considering the neutrons in each range as monoenergetic neutrons governed by Eq. (8.32). Thus,

$$\phi_\alpha(r) = \frac{S_p}{4\pi r^2} \sum_i f_i B_0^i e^{-r/\lambda_r^i}, \tag{8.33}$$

where f_i is the fraction of neutrons emitted in the ith energy range and B_0^i and λ_r^i are the initial buildup factor and relaxation length, respectively, for neutrons at the mean energy of the ith energy range. At large distances into the shield only a few terms in the summation of Eq. (8.33) will be significant, those corresponding to neutrons whose energies are at minima in the total effective nuclear cross section.

The empirical exponential attenuation of the flux density given by the equations above, can also be applied to media composed of a mixture of elements by using a weighted average of the relaxation lengths for the individual components, that is,

$$\lambda_r = \left(\sum_i \frac{\rho_i'}{\rho_i} \frac{1}{\lambda_r^i}\right)^{-1}, \tag{8.34}$$

where λ_r^i is the relaxation distance of the ith material at density ρ_i, and ρ_i' is the actual density of the ith material in the mixture which may be different from ρ_i.

One of the major difficulties in applying the technique above is the lack of empirical data for initial buildup or, more important, for values of the relaxation lengths. Often, values for λ_r are chosen as the reciprocal of the removal coefficient μ_r for neutrons above 3 MeV. In reality, one can expect the relaxation length to be somewhat larger since hydrogen is not present to remove the slightly degraded neutrons. Typically, the removal coefficient should be reduced by a factor of about 2 as a rule of thumb to compute λ_r (see Fig. 8.6). However, the use of such inferred values for the relaxation lengths introduces a great deal of uncertainty in the calculated fast-neutron flux densities, and consequently such estimates must be used cautiously.

For a heavy material inserted as a layer of thickness t in a light ($A < 27$) nonhydrogenous infinite medium, it has been found that an exponential removal correction similar to that used with hydrogenous media can be used. For this case, the total fast-neutron flux density above a certain threshold energy that is produced a distance r from a point monoenergetic source of strength S_p (with the heavy material interposed between source and detector) is given by

$$\phi_\alpha(r) = \frac{S_p}{4\pi r^2}\phi_\alpha^L(r - t)\exp\left[-\hat{\mu}_r(E_0)t\right], \tag{8.35}$$

where $\phi_\alpha^L(r - t)$ is the total fast-neutron flux density above the threshold energy E_α produced at distance $(r - t)$ from the source in a pure medium of the light material [obtained from Eq. (8.32)]. If the threshold E_α is chosen as 1.5 MeV, and a sufficient amount of the light material is present, it has been found that the effective removal coefficient, $\hat{\mu}_r$, is equal to the value measured in water [19]. However, if insufficient light material is present (e.g., less than 30% by volume of graphite), the effective removal coefficient in Eq. (8.31) becomes smaller than the corresponding hydrogenous-medium removal coefficient.

The procedures described in this section for estimating the fast-neutron flux density are, at best, only approximate. For design work, it is necessary to employ more elaborate methods based on the neutron-transport equation (see Chapter 10).

8.5 CALCULATION OF THE INTERMEDIATE AND THERMAL FLUX DENSITIES

The attenuation of fast neutrons in a shield necessarily leads to neutrons with intermediate and, eventually, thermal energies. The resulting intermediate-energy neutrons can contribute appreciably to the transmitted neutron dose rate in a shield, and the thermal neutrons, which are readily absorbed in the shield material, lead to the production of high-energy capture gamma photons. In

many instances, the capture gamma dose rate at the shield surface is the dominant consideration in the shield design. Thus, an important aspect of neutron shield analyses is the calculation of thermal and intermediate neutron flux densities.

The thermal and intermediate neutrons in a shield arise from the thermalization of fast neutrons as well as from thermal and intermediate-energy neutrons incident on the shield's surface. Many elaborate techniques have been developed to compute accurately the thermal and intermediate neutron flux densities; however, two simplified methods, based on diffusion and Fermi age theory, are first presented.

8.5.1 Diffusion Theory for Thermal Neutron Calculations

For hydrogenous shields the fast neutrons are rapidly thermalized once they are removed from the fast group as a result of the higher hydrogen cross section experienced by the removed neutrons. Consequently, as a rough approximation, the neutrons can be assumed to become thermalized at the point at which they are removed from the fast group. In effect, the migration of intermediate energy neutrons is neglected. The diffusion of the thermal neutrons then establishes the thermal-neutron flux density inside the shield. The thermal neutron flux density ϕ_{th} can be calculated by use of the steady-state, one-speed, diffusion model for neutron transport,

$$D\nabla^2\phi_{th}(\mathbf{r}) - \mu_a\phi_{th}(\mathbf{r}) + S_{th}(\mathbf{r}) = 0, \tag{8.36}$$

where D and μ_a are the diffusion coefficient and linear absorption coefficient (macroscopic absorption cross section), respectively, for thermal neutrons.

Neutrons appear in the thermal group as they are lost from the fast group. Thus, the thermal neutron source term in Eq. (8.36) can be determined from the fast-neutron vector current density, $\mathbf{j}_f(\mathbf{r})$, as

$$S_{th}(\mathbf{r}) = -\nabla \cdot \mathbf{j}_f(\mathbf{r}). \tag{8.37}$$

To a good approximation the fast neutrons can be considered to be moving directly away from their source since there is little change in direction from the time the neutron leaves the source until it is removed from the fast region. Also, far from the fast neutron sources, the fast neutrons will all be traveling in approximately the same direction $\boldsymbol{\Omega}$ away from their source, so that $\mathbf{j}_f(\mathbf{r}) \simeq \boldsymbol{\Omega}\phi_f(\mathbf{r})$. Thus, the source of thermal neutrons can be estimated from the fast-neutron flux density as

$$S_{th}(\mathbf{r}) \simeq -\nabla \cdot \boldsymbol{\Omega}\phi_f(\mathbf{r}). \tag{8.38}$$

The vector $\boldsymbol{\Omega}$ is a unit vector away from the fast-neutron source in the direction of fast neutron travel or, equivalently, the direction in which the fast flux density decreases the most rapidly (i.e., opposite to the direction of the gradient of ϕ_f).

For example, consider a plane shield ($0 < x < T$) in which the fast-neutron flux density is represented by an exponential function, or more generally, by

a sum of N exponentials; that is,

$$\phi_f(x) = \sum_{i=1}^{N} \phi_f^i(0) e^{-k_f^i x}. \tag{8.39}$$

where $\phi_f^i(0)$ and k_f^i are adjusted to give the best fit to the given fast-neutron flux density. For this case, the diffusion equation becomes

$$\frac{d^2\phi_{th}(x)}{dx^2} - \frac{\mu_a}{D}\phi_{th}(x) = -\frac{1}{D}\sum_{i=1}^{N} k_f^i \phi_f^i(0) e^{-k_f^i x}, \tag{8.40}$$

whose general solution is

$$\phi_{th}(x) = Ae^{-x/L} + Ce^{x/L} - \sum_{i=1}^{N} \frac{k_f^i \phi_f^i(0)}{(k_f^i)^2 D - \mu_a} \exp(-k_f^i x), \tag{8.41}$$

where $L \equiv (D/\mu_a)^{1/2}$. The constants A and C are then evaluated from the presumably known thermal neutron flux density incident at $x = 0$, and by setting ϕ_{th} to zero at the outer surface of the shield (or equivalently, for thick shields, setting C equal to zero).

Instead of representing the fast-neutron flux density by a sum of exponentials as in Eq. (8.39), the shield could be divided into contiguous regions, with the flux density in each region represented by a single exponential, that is,

$$\phi_f(x) = \phi_f(x_j) e^{-k_f^j (x - x_j)}, \qquad x_j < x < x_{j+1}. \tag{8.42}$$

Such a fit is easily performed by a series of straight-line fits to a plot of $\ln \phi_f(x)$ versus x, and the relaxation constant k_f^j is obtained from

$$k_f^j = \frac{1}{x_j - x_{j+1}} \ln\left[\frac{\phi_f(x_{j+1})}{\phi_f(x_j)}\right]. \tag{8.43}$$

Once the exponential fit of the fast-neutron flux density is obtained for each region, the thermal neutron diffusion equation is solved in each region. The constants of integration are evaluated by requiring the solution and its first derivative to be continuous at the interfaces x_i or equal to specified values of the thermal neutron flux density at the shield surfaces. For preliminary analyses, it is often sufficient to fit the fast-neutron flux density by a single exponential over the whole shield volume. In Table 8.7, values for D and μ_a are presented for

TABLE 8.7 Neutron Properties of Hydrogeneous Shield Materials

Material	Density (g/cm³)	k_f (cm⁻¹)[a]	D (cm)	μ_a (cm⁻¹)
Water	1.0	0.14	0.17	0.022
Ordinary concrete	2.35	0.085	0.65	0.0094
Barytes concrete	3.50	0.125	0.44	0.019
Iron concrete	4.30	0.16	0.29	0.081

[a]Approximate value for fast-neutron attenuations for a single exponential fit by Eq. (8.39). Actual fit values should be used whenever available.

Source: *Ref. 7; reproduced by permission of Wadsworth Publishing Company, Belmont, CA 94002.*

a few important shield materials, together with values of k_f for attenuation of fast neutrons.

8.5.2 Fermi Age Treatment for Thermal and Intermediate-Energy Neutrons

A refinement of the procedure above is to use Fermi age theory to correct for the migration of neutrons as they slow down to thermal energies [4]. Age theory describes the slowing down of neutrons by a continuous energy loss process which results in the same average energy loss as in the actual discrete energy losses from each scattering interaction. With this theory, neutrons are found to be distributed spatially in a Gaussian manner about the point at which they begin to slow down. The number of neutrons slowing down past energy E at location x arising from a plane source with unit strength of fast neutrons with energy E_0 which begin to slow down at location x' is given by [20]

$$q(x, x', \tau(E)) = \frac{e^{-(x-x')^2/4\tau}}{(4\pi\tau)^{1/2}}, \tag{8.44}$$

where, for elastic scattering, the Fermi age $\tau(E)$ is related to the neutron energy E by

$$\tau(E) \equiv \int_E^{E_0} [3\mu_s^2(E)\xi(E)(1 - \omega_0)E]^{-1}\, dE. \tag{8.45}$$

In this definition, ω_0 is the mean cosine of the laboratory scattering angle and $\xi(E)$ is the average logarithmic energy decrement per elastic scatter which can be shown to be given by the following average over all the nuclear species in the medium [20]:

$$\xi(E) = \frac{1}{\mu_s(E)} \sum_i \mu_s^i(E)\xi^i, \tag{8.46}$$

where the superscript i denotes the ith nuclear species. For a nuclide with a nuclear-to-neutron mass ratio A,

$$\xi = 1 - \frac{(A-1)^2}{2A} \ln\left(\frac{A+1}{A-1}\right). \tag{8.47}$$

For $A \gtrsim 10$, it can be shown that $\xi \simeq 2/(A + \frac{2}{3})$.

From its definition in Eq. (8.45), the Fermi age is seen to have units of area and to be a monotonic decreasing function of the neutron energy such that a neutron has zero age at the source energy and a maximum age when it reaches thermal energies. A physical interpretation of $\tau(E)$ is that it is one-sixth the mean-squared displacement from the point at which a neutron begins to slow down in an infinite medium to the location where it acquires energy E. The value of $\tau(E)$ depends on the material composition, the neutron source energy, and the energy E. Typical values for the age of fission neutrons to thermal energies in some materials are: [20] H_2O, 27 cm^2; D_2O, 131 cm^2; Be, 102 cm^2; and C, 368 cm^2. Values for concrete depend sensitively on the composition,

especially on the hydrogen content. For ordinary concrete, values range between 120 and 220 cm^2 [21].

The number of fast neutrons reaching thermal energies per unit time at some point x inside the shield, $S_{th}(x)$, is obtained by convoluting the slowing down kernel of Eq. (8.44) with the rate at which fast neutrons are removed, Eq. (8.38). For plane geometry in a shield of thickness T,

$$S_{th}(x) = \int_0^T \left[-\frac{d\phi_f(x')}{dx'}\right] q(x, x', \tau_{th})\, dx', \tag{8.48}$$

where τ_{th} is the age to thermal energy. If the fast-neutron flux density in the shield is given by $\phi_f(x') = \phi_f(0) \exp(-k_f x')$, the result above reduces to

$$S_{th}(x) = \frac{k_f \phi_f(0)}{2} e^{-k_f(x - k_f\tau_{th})} \left[\operatorname{erf}\left(\frac{T - x}{2\tau_{th}^{1/2}} + k_f \tau_{th}^{1/2}\right) - \operatorname{erf}\left(k_f \tau_{th}^{1/2} - \frac{x}{2\tau_{th}^{1/2}}\right)\right], \tag{8.49}$$

where the error function, erf (x), is defined by

$$\operatorname{erf}(x) = \frac{2}{\pi^{1/2}} \int_0^x e^{-y^2}\, dy. \tag{8.50}$$

The error function approaches $+1$ (or -1) as its argument becomes a large positive (or negative) number. If the shield thickness $T \gg \tau^{1/2}$, then for x far removed from either surface of the shield, the argument of the first error function in Eq. (8.49) is positive and large while the argument of the second error function is large and negative. Thus,

$$S_{th}(x) \simeq k_f \phi_f(0) e^{-k_f(x - k_f\tau_{th})}, \qquad 0 \ll x \ll T. \tag{8.51}$$

If the thermal neutrons are absorbed near the point at which they reach thermal energies, then (in equilibrium) the absorption rate $\mu_a \phi_{th}(x)$ must equal the rate of neutron thermalization $S_{th}(x)$. Thus from Eq. (8.51)

$$\begin{aligned} \phi_{th}(x) &\simeq \frac{k_f}{\mu_a} \phi_f(0) e^{-k_f(x - k_f\tau_{th})} \\ &= \frac{k_f}{\mu_a} \phi_f(x - k_f \tau_{th}). \end{aligned} \tag{8.52}$$

This result implies that inside the shield the thermal neutron flux density is proportional to the fast-neutron flux density displaced toward the source by a *displacement distance* $k_f\tau_{th}$. The thermal neutron flux density inside a shield can thus be expected to parallel the fast-neutron flux density—a result usually observed (see, e.g., Fig. 8.1).

Age theory can also be used to estimate in an approximate manner the energy-dependent flux density $\phi(x, E)$ of neutrons with intermediate energies [22]. The volumetric rate at which fast neutrons slowing down past energy E [or equivalently, reach age $\tau(E)$] deep in a shield is

$$q(x, E) = \int_0^T \left[-\frac{d\phi_f(x')}{dx'}\right] q(x, x', \tau(E))\, dx'. \tag{8.53}$$

If the fast-neutron flux density is again assumed to be attenuated exponentially in the shield, that is, $\phi_f(x') = \phi_f(0) \exp(-k_f x')$, and if $T \gg \tau^{1/2}$, then following the same reasoning used to obtain Eq. (8.51), one finds

$$q(x, E) = k_f \phi_f(0) \exp[-k_f(x - k_f \tau(E))]. \tag{8.54}$$

In an infinite, nonabsorbing medium, the flux density $\phi(E)$ is related to the slowing-down density $q(E)$ by [20]

$$\phi(E) = \frac{q(E)}{\xi(E)\mu_s(E)E}, \tag{8.55}$$

so that for a thick neutron shield (with negligible neutron absorption above thermal energies), the intermediate-energy-neutron flux density can be described approximately by

$$\phi(x, E) = \frac{k_f \phi_f(0)}{\xi(E)\mu_s(E)E} \exp[-k_f(x - k_f \tau(E))]. \tag{8.56}$$

This result can be expressed in terms of the fast-neutron flux density as

$$\phi(x, E) = B(E)\phi_f(x), \tag{8.57}$$

where $B(E)$ is an effective buildup factor for the intermediate-energy neutrons, given by

$$B(E) = \frac{k_f}{\xi(E)\mu_s(E)E} \exp[k_f^2 \tau(E)]. \tag{8.58}$$

It should be noted that this intermediate-energy-neutron buildup factor is independent of position.

8.5.3 Removal–Diffusion Techniques

Although the results of the preceding section are adequate for initial estimates, more accurate techniques are often needed without the effort and expense of a full-scale multigroup transport calculation. Multigroup diffusion theory, which is considerably less expensive and complex to use than transport theory, is remarkably successful at describing the slowing down and thermalization of neutrons in reactor cores. Early attempts at the use of diffusion theory to calculate the neutron flux density deep within a shield met with only limited success [23], although better accuracy was obtained by introducing extraneous renormalization techniques to describe the penetration of the fast neutrons [24,25]. That strict diffusion models should be of limited use to describe fast-neutron penetration and subsequent thermalization is not surprising since diffusion theory requires both the differential scattering cross sections and the angular flux density to be well described by first-order Legendre expansions (i.e., at most, to vary linearly with ω). Such conditions usually hold in a reactor core where the neutron flux density is approximately isotropic; however, the flux density deep within a shield is determined by those very energetic neutrons which are highly penetrating and whose angular distribution is therefore highly anisotropic.

The penetrating fast neutrons are very successfully described by removal theory. The migration of the neutrons, once they are removed from the anisotropic fast group and begin to thermalize, is small compared to the distance traveled by the unremoved neutrons. Further, during thermalization, the flux density becomes more isotropic as more scatters occur. Consequently, one would expect multigroup diffusion theory to be applicable for the description of the slowing-down process and the subsequent diffusion at thermal energies. Thus, one approach to compute the buildup of low-energy neutrons inside a shield is to combine removal theory (to describe the penetration of fast neutrons) with multigroup diffusion theory (to describe the subsequent thermalization and thermal diffusion). This combination of removal and diffusion theory, in many formulations, has proved very successful.

Original Spinney method. The first wedding of removal theory to diffusion theory was introduced by Spinney in 1958 [26]. In the original formulation the fast source region, 0 to 18 MeV, was divided into 18 equal-width energy *bands*. The source neutrons in each band penetrate the shield in accordance with removal theory. The density of removal collisons from all bands is then used as the source of neutrons in the first diffusion *group*. Explicitly, this diffusion source density at $\mathbf{r}$ is given by

$$S_d(\mathbf{r}) = \sum_{i=1}^{18} \int_V \frac{S_V(\mathbf{r}')\chi_i \mu_{r,i}(\mathbf{r}) \exp(-\mu_{r,i}|\mathbf{r} - \mathbf{r}'|)}{4\pi|\mathbf{r}' - \mathbf{r}|^2} dV(\mathbf{r}'), \tag{8.59}$$

where $S_V(\mathbf{r}')$ = production rate of source neutrons per unit volume at $\mathbf{r}'$ in the source region
χ_i = fraction of source neutrons in the ith removal band
$\mu_{r,i}(\mathbf{r})$ = removal coefficient for the ith band at $\mathbf{r}$.

The term $\mu_{r,i}|\mathbf{r} - \mathbf{r}'|$ is the total number of removal relaxation lengths between $\mathbf{r}$ and $\mathbf{r}'$ for a fast neutron in the ith band.

These removal neutrons are inserted as source neutrons into the top energy group of five energy groups, with the fifth group representing the thermal neutrons. The transfer of neutrons from diffusion group to diffusion group is determined by Fermi age theory[20], a continuous slowing-down model, and consequently neutrons can be transferred only to the energy group directly below. Thus, the diffusion group equations are written as

$$\nabla^2\phi_i(\mathbf{r}) - \frac{\mu_{a,i}}{D_i}\phi_i(\mathbf{r}) - \tau_i^{-1}\phi_i(\mathbf{r}) = -\frac{S_i(\mathbf{r})}{D_i}, \tag{8.60}$$

where ϕ_i = flux density for group i
$\mu_{a,i}$ = linear absorption coefficient for group i
D_i = ith group diffusion coefficient
τ_i = square of the slowing-down length from group i to the next lower group $i + 1$, or equivalently, the Fermi age of neutrons starting from group i and slowing down to group $i + 1$; for the thermal group, $\tau_i^{-1} = 0$.

The source term for the ith diffusion group is thus given by

$$S_i(\mathbf{r}) = \begin{cases} S_d(\mathbf{r}) \text{ from Eq. (8.59)}, & i = 1, \\ D_{i-1}\tau_{i-1}^{-1}\phi_{i-1}, & i > 1. \end{cases} \tag{8.61}$$

The group constants are obtained by averaging over the energy range of each group (E_{i+1}, E_i) with a $1/E$ flux-density weighting for the slowing-down groups $(i = 1, \ldots, 4)$ and with a Maxwellian distribution for the thermal group $(i = 5)$. Explicity, for the slowing-down groups, the group constants are given by

$$\mu_{a,i} = \int_{E_{i+1}}^{E_i} \frac{\mu_a(E)}{E}\,dE \Big/ \int_{E_{i+1}}^{E_i} \frac{dE}{E} \tag{8.62}$$

$$D_i = \int_{E_{i+1}}^{E_i} \{3[\mu_{\text{in}}(E) + \mu_{\text{es}}(E)(1 - \omega_0)]E\}^{-1}\,dE \Big/ \int_{E_{i+1}}^{E_i} \frac{dE}{E} \tag{8.63}$$

and τ_i is the Fermi age from E_i to E_{i+1}, namely,

$$\tau_i = \int_{E_{i+1}}^{E_i} \{3[\mu_{\text{in}}(E) + \mu_{\text{es}}(E)(1 - \omega_0)]\mu_t(E)\xi(E)E\}^{-1}\,dE, \tag{8.64}$$

where ω_0 is the mean cosine of the laboratory scattering angle for elastic scattering (Table 5.1), and μ_a, μ_{in}, μ_{es}, and μ_t are, respectively, absorption, inelastic scattering, elastic scattering, and total interaction coefficients. With the assumptions that elastic scattering is isotropic and that inelastic scattering takes place from only a single energy level, E^*, the mean logarithmic energy decrement per scatter, $\xi(E)$, is given by

$$\xi(E) = \left[\mu_{\text{es}}\xi_{\text{es}} + \mu_{\text{in}} \ln\left(\frac{E}{E - E^*}\right)\right] \Big/ (\mu_{\text{es}} + \mu_{\text{in}}), \tag{8.65}$$

where

$$\xi_{\text{es}} = \begin{cases} \dfrac{2}{A + \frac{2}{3}}, & A > 1 \\ 1, & A = 1. \end{cases} \tag{8.66}$$

Improved removal–diffusion models. The original Spinney method described above was quite successful in predicting the low-energy neutron flux densities in the concrete shields around early graphite reactors. However, to obtain better accuracy for a wider range of shield configurations, several obvious improvements could be made. First, more diffusion groups could be used to describe better the continous slowing-down model implied by Fermi age theory. Second, neutrons should be allowed to transfer past intermediate diffusion groups in a single step to account for the possibility of large energy losses in inelastic scattering or elastic scattering from light nuclei. Third, more detail should be given for the removal of fast neutrons from the removal bands to the diffusion groups. Fast-neutron diffusion cannot altogether be neglected, and hence, the upper diffusion groups should overlap the same energy region spanned by the lower-energy removal bands. Further, when neutrons suffer a

removal interaction, they should be allowed to enter any one of several diffusion groups depending on the severity of the removal interaction. This improved description of the removed neutrons would give more information about the fast-neutron flux, an important consideration for radiation damage studies.

Shortly after the introduction of the Spinney method, several variations of it were introduced which implement some or all of the improvements described above [27–29]. The removal band and diffusion group structure as well as the allowed neutron transfers in three of these improved schemes are illustrated in Fig. 8.10.

Perhaps the most widely used version of the removal–diffusion model is the variation used in the NRN code [30]. This version has the most energy detail (30 removal bands and 24 diffusion groups) as well as the most flexibility in describing the transfer of neutrons between energy bands and groups. In this formulation, the ith-group diffusion equation is

$$D_i\nabla^2\phi_i - \sum_{k=i+1}^{24} \mu_{ik}\phi_i - \mu_{a,i}\phi_i + \sum_{j=1}^{i} \mu_{ji}\phi_j + S_i = 0, \tag{8.67}$$

where the first term accounts for leakage, the second term for neutron scattering to lower-energy groups, the third term for absorption, the fourth term for scattering of neutrons into the group from all higher groups, and the last term for the injection of removed neutrons from all the removal bands as source neutrons. The transfer coefficients, μ_{ij}, is calculated from

$$\mu_{ij} = \int_{E_{i+1}}^{E_i} dE \int_{E_{j+1}}^{E_j} dE'\, \mu(E \longrightarrow E')E^{-n} \Big/ \int_{E_{i+1}}^{E_i} dE\, E^{-n}, \tag{8.68}$$

where $\mu(E \longrightarrow E')$ is the differential coefficient for scattering from an energy E into unit energy about E'. The E^{-n} spectrum weighting (the user supplies the value of n) allows for more flexibility in approximating the actual energy dependence of the slowing down flux density. The mean absorption coefficient for group i is denoted by $\mu_{a,i}$, and the group diffusion coefficient is calculated more exactly than by use of Eq. (8.63) from

$$D_i = \int_{E_{i+1}}^{E_i} \frac{dE}{3\mu_{\mathrm{tr}}(E)E} \Big/ \ln\left(\frac{E_i}{E_{i+1}}\right) \tag{8.69}$$

and

$$\mu_{\mathrm{tr}}(E) = \mu_t(E)[1 - \omega_0(E)] - \tfrac{4}{5}\mu_{bl}(E) + \tfrac{9}{5}\mu_{bl}(E)\omega_0(E), \tag{8.70}$$

where μ_{bl} is the coefficient at energy E for either absorption or scatter to an energy below the lower energy limit E_{l+1}.

The removal flux density for the gth removal band, ϕ_g^0, is calculated using energy-dependent removal cross sections [Eq. (8.31)] as

$$\phi_g^0(\mathbf{r}) = \int_V dV(\mathbf{r}') \int_{E_{g+1}}^{E_g} dE \frac{S(\mathbf{r}', E)\exp[-\mu_r(E)|\mathbf{r} - \mathbf{r}'|]}{4\pi|\mathbf{r} - \mathbf{r}'|^2}, \tag{8.71}$$

where the integration is over all differential source volumes $dV(\mathbf{r}')$ and all energies in the gth energy band. The distribution of the source neutron emission

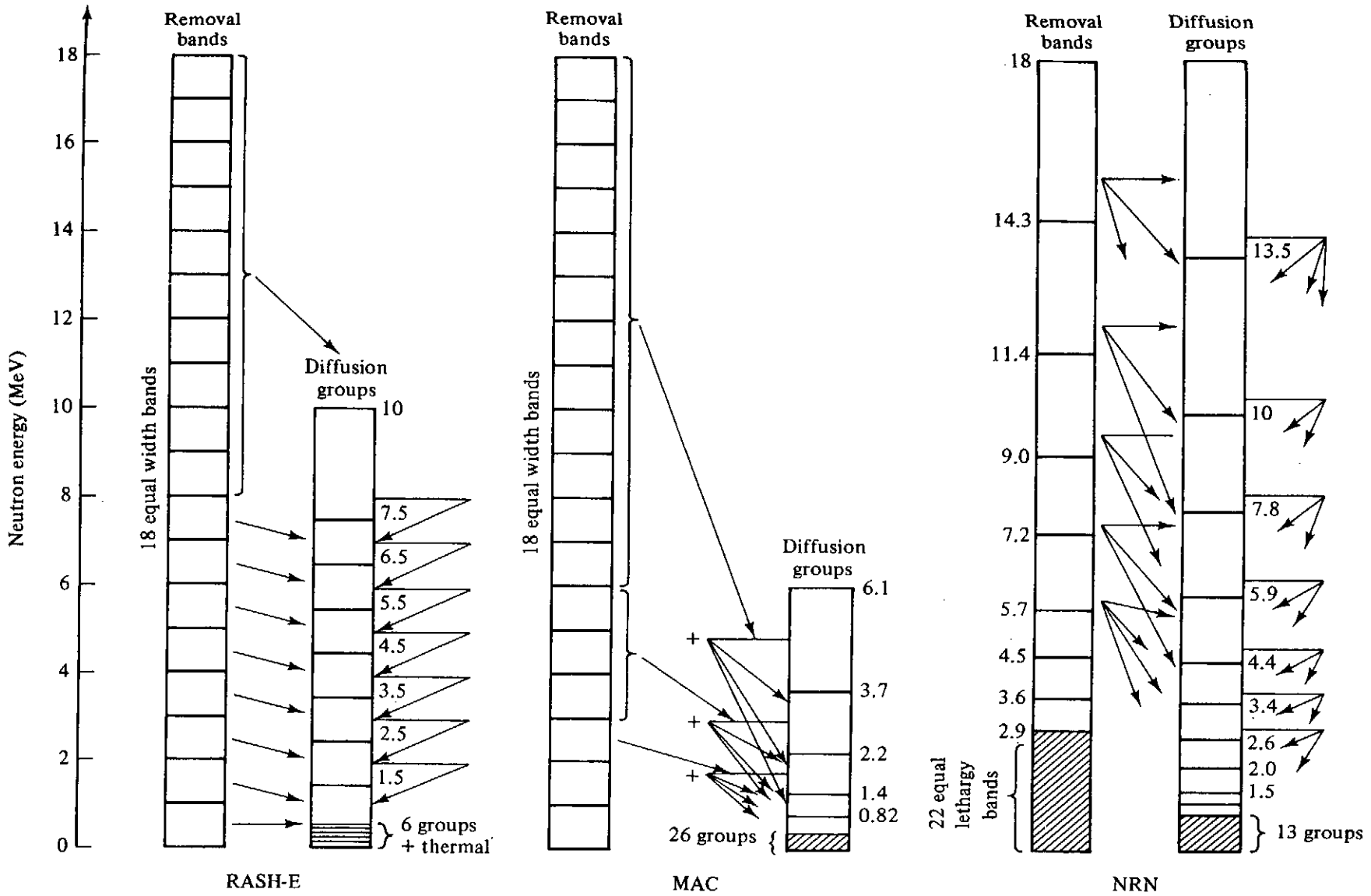

Figure 8.10 Schematic comparison of the neutron transfer between removal bands and the diffusion groups in three improved removal–diffusion models. In RASH-E removed neutrons from one band enter only one diffusion group, and diffusion group transfer is only to the immediate lower group. In MAC, removed neutrons are first added to the neutrons scattering out of one diffusion group, and then the downscatter source terms for many lower groups are calculated from this sum. Removed neutrons in NRN can enter directly several diffusion groups, and transfer from one diffusion group can occur to all lower groups. (Adapted from Ref. 30)

rate is given by $S(\mathbf{r}', E)$. Finally, the rate at which neutrons are introduced into the ith diffusion group from all removal bands per unit volume, S_i, is given by

$$S_i(\mathbf{r}) = \sum_{g=1}^{30} \hat{\mu}_{gi}\phi_g^0(\mathbf{r}), \tag{8.72}$$

where the transfer coefficient from removal band g to diffusion group i, $\hat{\mu}_{gi}$, is calculated from

$$\hat{\mu}_{gi} = \int_{E_{g+1}}^{E_g} dE \int_{E_{i+1}}^{E_i} dE'\, \mu(E \rightarrow E')/(E_i - E_{i+1}). \tag{8.73}$$

For thick shields with attenuation factors as low as 10^{-12}, this removal–diffusion method gives very accurate results even for layered shields, provided that penetration takes place mainly at the source energies [28]. It is least accurate when significant attenuation occurs after diffusion (e.g., water followed by a thick iron shield). The greatest disadvantage of this method is the need to calculate many group and band constants. Nevertheless, the removal–diffusion technique is a very powerful tool for the reactor designer, offering accuracies for many shield configurations comparable to those of the much more expensive neutron transport methods.

8.6 CAPTURE-GAMMA-PHOTON ATTENUATION

Often a significant contribution to the total dose at the surface of a shield is made by capture gamma photons produced deep within the shield as a result of neutron absorption. Another source of secondary photons arises from the inelastic scattering of fast neutrons. These inelastic scattered photons generally have much lower energies than the capture gamma photons and are usually ignored in the analysis of thick shields.

Most neutrons are not absorbed until they are thermalized, and consequently, one needs to consider only the absorption rate of thermal neutrons in most shield analyses.[2] For this reason it is important to calculate accurately the thermal neutron flux density $\phi_{th}(\mathbf{r})$ in the shield. The volumetric source strength of capture photons per unit energy about E is thus given by

$$S_\gamma(\mathbf{r}, E) = \phi_{th}(\mathbf{r})\mu_a(\mathbf{r})f(\mathbf{r}, E), \tag{8.74}$$

where $\mu_a(\mathbf{r})$ is the absorption coefficient at $\mathbf{r}$ for thermal neutrons and $f(\mathbf{r}, E)$ is the number of photons produced in unit energy about E per thermal neutron absorption at $\mathbf{r}$. Although the capture-photon-energy distribution for any material will be composed of a set of monoenergetic photons, a great many different energies can generally be expected as a result of multiple nuclear transitions following neutron capture and the usual presence of many different nuclear species in the shield material. Consequently, the capture-gamma-photon yield

[2]An exception would be the capture gamma photons produced in the core of a fast reactor where the neutrons are captured before they are thermalized.

is usually "binned" into energy groups. Thus, the source strength for the ith energy group of width ΔE_i is

$$S_{\gamma i}(\mathbf{r}) \equiv \int_{\Delta E_i} S(\mathbf{r}, E)\, dE = \phi_{\text{th}}(\mathbf{r})\mu_a(\mathbf{r})f_i(\mathbf{r}), \tag{8.75}$$

where f_i is the number of photons produced in group i per thermal neutron absorbed at $\mathbf{r}$, averaged over all isotopes at $\mathbf{r}$, that is,

$$f_i(\mathbf{r}) = \frac{1}{\mu_a(\mathbf{r})} \sum_m \mu_a^m(\mathbf{r}) f_i^m, \tag{8.76}$$

where the superscript m refers to the mth nuclide and summation is over all nuclear species. The quantity f_i^m is the number of capture photons emitted in group i arising from the absorption of a thermal neutron by the mth nuclide (see Table A3.9).

The calculation of the dose rate from capture gamma photons is based on the distributed source of Eq. (8.75). The calculational procedure is illustrated for an infinite slab shield in which the thermal neutron flux density has been previously obtained (see Fig. 8.11). The slab will generally be composed of laminates, that is, a series of adjacent homogeneous regions. If the thermal

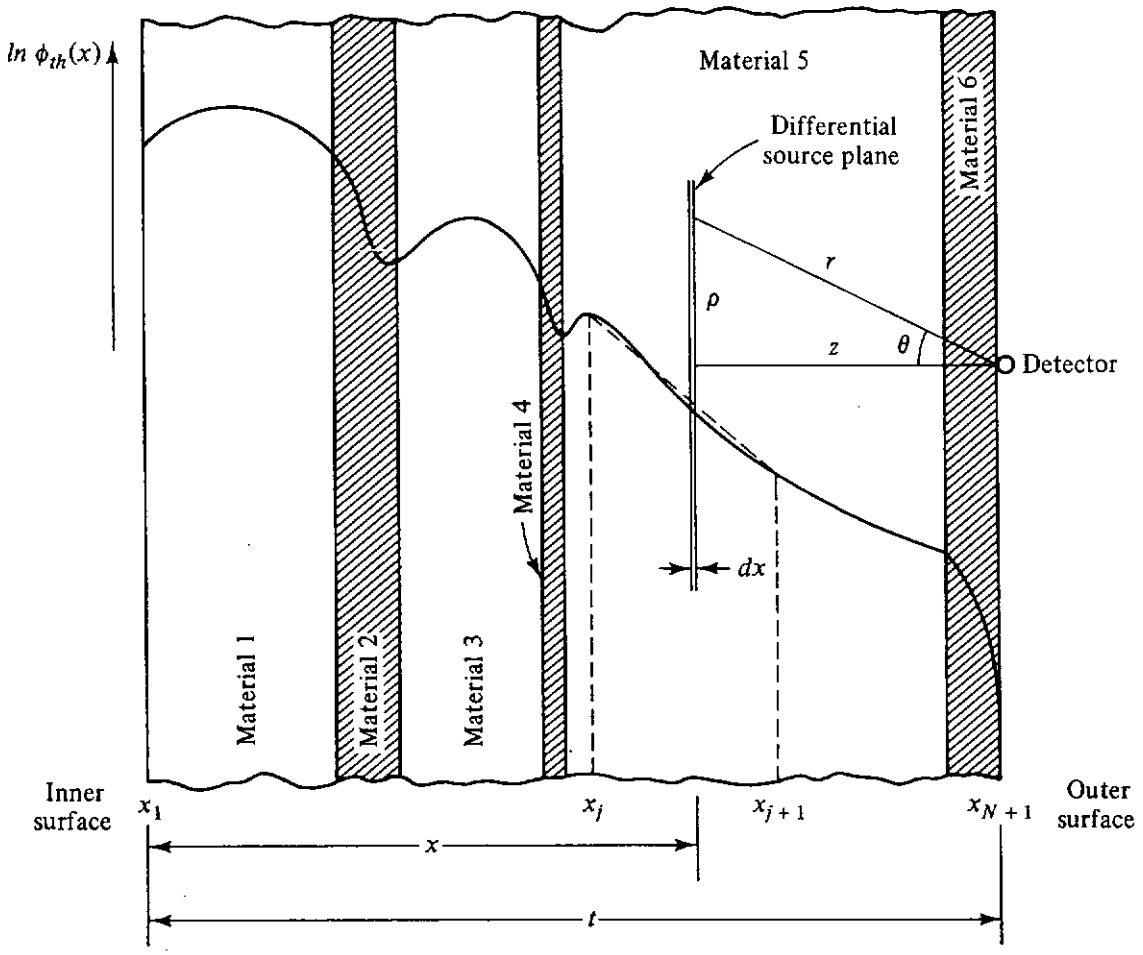

Figure 8.11 Profile of the thermal neutron flux density in a multilaminate shield showing the coordinate system used for calculation of the capture-gamma-photon dose rate at the shield surface.

neutron flux density depends only on the distance into the slab (plane geometry), then with the technique involving the point kernel and point-source buildup factors, the dose rate or detector response R at the shield surface from capture gamma photons in all G groups is (recall the disk source calculation of Section 6.4.3)

$$R(t) = \sum_{i=1}^{G} \mathcal{R}_i \int_0^t dx\, S_{\gamma i}(x) \int_0^\infty d\rho\, B_i(r) 2\pi\rho \frac{\exp(-\mu_i r)}{4\pi r^2}, \tag{8.77}$$

where $\mathcal{R}_i$ is a flux-to-dose rate conversion factor for photons in energy group i, B_i is a composite buildup factor for photons in group i traveling from the source to the detector through the various interposed laminates, and $\mu_i r$ is the total number of mean-free-path lengths for photons in group i between the source and the detector.

Equation (8.77) could be evaluated numerically for a given B_i and $S_{\gamma i}$; however, considerable simplification is possible if we assume functional forms for these two quantities that allow analytical evaluation of the integrals. In particular, the shield is subdivided into N contiguous regions such that each region is composed of a single material and over which the thermal neutron flux density can be fit reasonably well by a single exponential (see Fig. 8.11). Thus, for the jth region bounded by x_j and x_{j+1}, the thermal neutron flux density is represented by

$$\phi_{\text{th}}^j(x) \simeq \phi^j \exp(-k^j x), \qquad x_j < x < x_{j+1}, \tag{8.78}$$

where ϕ^j and k^j are constants. Thus the capture gamma source strength for the ith energy group becomes

$$S_{\gamma i}^j(x) = C_i^j \exp(-k^j x), \tag{8.79}$$

with $C_i^j \equiv \phi^j \mu_a^j f_i^j$, where the superscript j refers to material properties in the jth region and the subscript i refers to the energy group of the photons.

8.6.1 Response Rate from Uncollided Photons

For the case of no buildup ($B = 1$), the integration in Eq. (8.77) can be performed analytically. If the total number of mean-free-path lengths between x_{j+1} and the outer surface is denoted by $\zeta_i^{j+1} = \sum_{m=j+1}^{N} \mu_i^m (x_{m+1} - x_m)$, then the integral over ρ in Eq. (8.77) represents the flux density produced by a disk source at x shielded by $\mu_i^j(x_{j+1} - x) + \zeta_i^{j+1}$ mean-free-path lengths of material. Explicitly, the integral becomes

$$\int_0^\infty d\rho \frac{2\pi\rho}{4\pi r^2} \exp[-\mu_i^j (x_{j+1} - x) \sec\theta - \zeta_i^{j+1} \sec\theta].$$

From the geometry of Fig. 8.11, r and ρ are related by $r^2 = \rho^2 + (t - x)^2$ so that $r\,dr = \rho\,d\rho$. Also, $\sec\theta = r/(t - x)$. As may be seen from the definition of the E_1 function (Appendix 2), the integral above becomes

$$\tfrac{1}{2} E_1(\zeta_i^{j+1} + \mu_i^j (x_{j+1} - x)).$$

With this result and the source representation of Eq. (8.79), Eq. (8.77) becomes

$$R^0(t) = \frac{1}{2}\sum_{i=1}^{G} \mathcal{R}_i \sum_{j=1}^{N} C_i^j \int_{x_j}^{x_{j+1}} \exp\left(-k^j x\right) E_1(\zeta_i^{j+1} + \mu_i^j(x_{j+1} - x))\, dx \tag{8.80}$$

$$= \frac{1}{2}\sum_{i=1}^{G} \mathcal{R}_i \sum_{j=1}^{N} \frac{C_i^j}{\mu_i^j} \exp\left[-k^j\left(x_{j+1} + \frac{\zeta_i^{j+1}}{\mu_i^j}\right)\right] \times \int_{\zeta_i^{j+1}}^{\zeta_i^j} E_1(y) \exp\left(\frac{k^j y}{\mu_i^j}\right) dy. \tag{8.81}$$

This last result can be evaluated using Eq. (A2.20) or can be expressed in terms of the following function, which is often encountered in the field of radiative transfer:

$$F_n(s, a) \equiv \int_0^s E_n(x) e^{ax}\, dx. \tag{8.82}$$

Although this function is tabulated[3], it can be expressed for $n = 1$ in terms of the exponential integral function (which is more widely tabulated) as

$$F_1(s, a) = \begin{cases} \dfrac{e^{as}E_1(s) - E_1(s(1-a)) - \ln|1-a|}{a}, & a \neq 0, 1, \\ e^s E_1(s) + \ln s + \gamma, & a = 1, \\ 1 - E_2(s), & a = 0, \end{cases} \tag{8.83}$$

where $\gamma = 0.5772156\ldots$ (Euler's constant)[3]. Thus, the response rate from uncollided capture gamma photons, Eq. (8.81) (without buildup) becomes

$$R^0(t) = \frac{1}{2}\sum_{i=1}^{G} \mathcal{R}_i \sum_{j=1}^{N} \frac{C_i^j}{\mu_i^j} \exp\left[-k^j\left(x_{j+1} + \frac{\zeta_i^{j+1}}{\mu_i^j}\right)\right] \times \left[F_1\left(\zeta_i^j, \frac{k^j}{\mu_i^j}\right) - F_1\left(\zeta_i^{j+1}, \frac{k^j}{\mu_i^j}\right)\right]. \tag{8.84}$$

This result may be expressed in terms of the E_1 function by using Eq. (8.83), although explicit consideration of all possible singular combinations of the problem parameters leads to a large number of different expressions [31].

8.6.2 Response Rate from Scattered Photons

To estimate analytically the response rate due to the buildup of scattered photons, it is necessary to employ some analytic form for the composite buildup factor. The present analysis assumes the Berger form,

$$B_i(r) = 1 + a_i \mu_i r \exp(b_i \mu_i r), \tag{8.85}$$

with a_i and b_i corresponding to the ith group of photons. The response rate resulting from the buildup of scattered photons is then obtained by inserting the

[3]Often, a will be greater than unity, and hence the argument of the E_1 function will be negative. However, for positive x, we can define $E_1(-x_1) - E_1(-x_2) = Ei(x_2) - Ei(x_1)$ (see Appendix 2) and Eq. (8.83) remains valid.

second term of this buildup factor into Eq. (8.81). The result is

$$R^s(t) = \frac{1}{2}\sum_{i=1}^{G} \mathcal{R}_i a_i \sum_{j=1}^{N} \frac{C_i^j}{1-b_i} \exp\left[-(1-b_i)(\mu_i^j x_{j+1} + \zeta_i^{j+1})\right] \times \int_{x_j}^{x_{j+1}} \exp\left\{-[k^j - (1-b_i)\mu_i^j]x\right\} dx, \tag{8.86}$$

which, as long as $k^j \neq (1-b_i)\mu_i^j$, reduces to

$$R^s(t) = \frac{1}{2}\sum_{i=1}^{G} \mathcal{R}_i a_i \sum_{j=1}^{N} \frac{C_i^j}{(1-b_i)(1-b_i-k^j/\mu_i^j)\mu_i^j} \times \{\exp\left[-(1-b_i)\zeta_i^{j+1} - k^j x_{j+1}\right] - \exp\left[-(1-b_i)\zeta_i^j - k^j x_j\right]\}. \tag{8.87}$$

If in any term, $k^j = (1-b_i)\mu_i^j$, then that term in the inner summation of the result above becomes

$$\frac{C_i^j(x_{j+1}-x_j)}{1-b_i} \exp\left[-(1-b_i)(\mu_i^j x_{j+1} + \zeta_i^{j+1})\right]. \tag{8.88}$$

8.7 NEUTRON SHIELDING BY CONCRETE SLABS

Of all shielding materials, concrete is probably the most widely used because of its relatively low cost and the ease with which it can be cast into large and variously shaped shields. However, neutron attenuation calculations for concrete, especially by the simplified methods presented in this chapter, are usually quite difficult, partly as a result of the variation in elemental compositions of different concretes. Moreover, the hydrogen content of many concretes is often only marginal for the application of removal theory. Neutron transport or Monte Carlo methods generally must be used if accurate results are desired.

Certain specific shielding situations for concrete have been studied extensively; in similar situations, the results of these earlier studies may be used directly instead of repeating the laborious calculations. In Fig. 8.12 the phantom-related dose equivalent rate in an infinite concrete medium arising from a point ^{252}Cf fission source is shown. Comparison of these results to similar results for a water medium (Fig. 8.1) shows that, at large distances from the source, the capture gamma photons again provide a major component of the total dose equivalent rate. However, for a concrete medium, the fast and thermal neutrons are not attenuated nearly as readily as in a water medium, so that after 140 cm of shielding material the fast and thermal neutron dose equivalent rates are still the major components of the total, while, in a water medium, the neutron dose equivalent rates are negligible after the same thickness of shielding.

Another particularly important case is that of a plane slab of ordinary concrete on which a monoenergetic, broad, parallel beam of neutrons is normally incident. This problem has been studied in some detail [32–36] and a brief summary of the most useful results are presented here. In Table 8.8, results are given for a calcareous type of concrete (i.e., one made of sand and aggregate composed

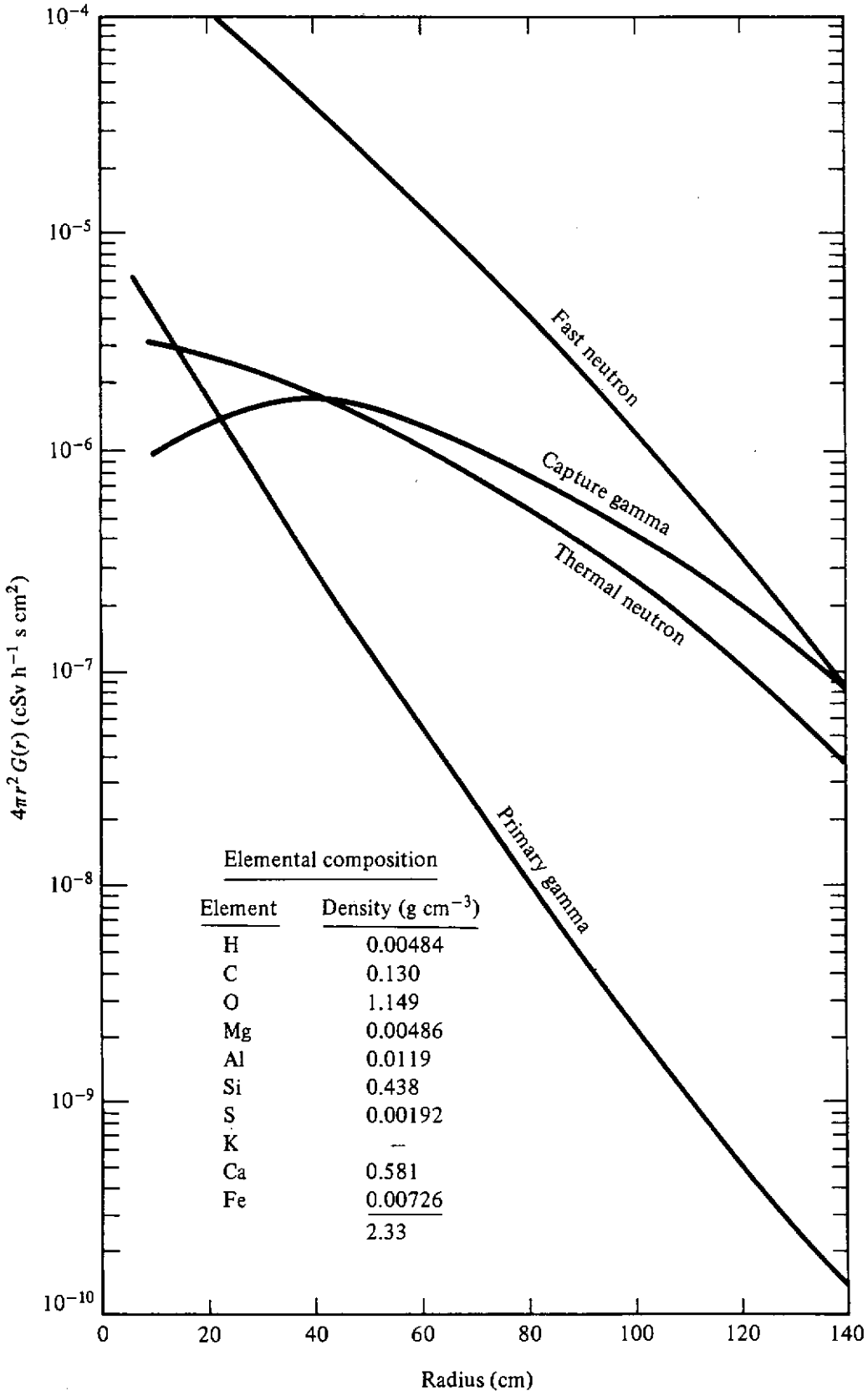

Figure 8.12 Phantom-related dose equivalent kernel ($\times 4\pi r^2$) expressed in units of cSv h^{-1} for a point isotropic ^{252}Cf fission neutron source of unit strength (i.e., 1 neutron s^{-1}) in an infinite ordinary concrete medium. The primary gamma kernel includes photons from fission products. (From Ref. 1.)

TABLE 8.8 Normalized Phantom-Related Dose Equivalent in Units of Sv cm² Behind an Infinite Concrete Slab Uniformly and Perpendicularly Illuminated by a Unit Fluence of Monoenergetic Neutrons[a]

Energy Interval (MeV)		$X = 0$	$X = 50$	$X = 100$	$X = 150$	$X = 200$	$X = 250$	$X = 300$	$X = 350$	$X = 400$
0.0	4.14(−07)	1.0(−11)[b]	1.8(−12)	3.0(−13)	5.1(−14)	9.9(−15)	2.1(−15)	4.6(−16)	1.1(−16)	3.0(−17)
4.14(−07)	1.12(−06)	1.2(−11)	3.1(−12)	4.8(−13)	8.1(−14)	1.6(−14)	3.3(−15)	7.4(−16)	1.7(−16)	4.2(−17)
1.12(−06)	3.06(−06)	1.2(−11)	3.5(−12)	5.5(−13)	9.3(−14)	1.8(−14)	3.8(−15)	8.4(−16)	2.0(−16)	4.8(−17)
3.06(−06)	1.07(−05)	1.2(−11)	3.8(−12)	6.2(−13)	1.1(−13)	2.0(−14)	4.0(−15)	9.2(−16)	2.1(−16)	5.2(−17)
1.07(−05)	2.90(−05)	1.3(−11)	4.0(−12)	6.6(−13)	1.2(−13)	2.1(−14)	4.3(−15)	9.8(−16)	2.3(−16)	5.5(−17)
2.90(−05)	1.01(−04)	1.3(−11)	4.2(−12)	7.3(−13)	1.2(−13)	2.3(−14)	4.4(−15)	9.9(−16)	2.4(−16)	5.8(−17)
1.01(−04)	5.83(−04)	1.3(−11)	4.3(−12)	7.7(−13)	1.3(−13)	2.4(−14)	4.6(−15)	1.0(−15)	2.5(−16)	6.0(−17)
5.83(−04)	3.35(−03)	1.2(−11)	4.4(−12)	8.1(−13)	1.4(−13)	2.5(−14)	5.0(−15)	1.1(−15)	2.6(−16)	6.3(−17)
3.35(−03)	1.11(−01)	3.5(−11)	4.4(−12)	8.0(−13)	1.4(−13)	2.5(−14)	5.0(−15)	1.1(−15)	2.5(−16)	6.1(−17)
1.11(−01)	5.50(−01)	1.6(−10)	7.0(−12)	9.7(−13)	1.7(−13)	3.0(−14)	5.7(−15)	1.3(−15)	2.8(−16)	6.8(−17)
5.50(−01)	1.11	3.1(−10)	2.2(−11)	1.9(−12)	2.9(−13)	4.9(−14)	9.5(−15)	2.0(−15)	4.3(−16)	9.2(−17)
1.11	1.83	3.7(−10)	6.4(−11)	4.9(−12)	5.9(−13)	9.1(−14)	1.7(−14)	3.5(−15)	7.4(−16)	1.8(−16)
1.83	2.35	3.6(−10)	1.2(−10)	1.2(−11)	1.5(−12)	1.9(−13)	3.2(−14)	4.9(−15)	1.3(−15)	2.9(−16)
2.35	2.46	3.5(−10)	1.6(−10)	3.1(−11)	4.6(−12)	6.9(−13)	1.0(−13)	1.7(−14)	3.1(−15)	6.5(−16)
2.46	3.01	3.5(−10)	1.4(−10)	2.3(−11)	3.2(−12)	4.3(−13)	6.3(−14)	1.1(−14)	2.1(−15)	4.4(−16)
3.01	4.07	3.6(−10)	1.3(−10)	1.8(−11)	2.4(−12)	3.3(−13)	5.0(−14)	8.3(−15)	1.6(−15)	3.4(−16)
4.07	4.97	3.7(−10)	1.7(−10)	3.2(−11)	5.0(−12)	7.3(−13)	1.2(−13)	1.8(−14)	3.1(−15)	6.1(−16)
4.97	6.39	3.9(−10)	1.7(−10)	4.0(−11)	7.8(−12)	1.4(−12)	2.3(−13)	3.6(−14)	6.3(−15)	1.2(−15)
6.36	8.19	4.1(−10)	1.7(−10)	4.2(−11)	8.4(−12)	1.6(−12)	2.9(−13)	5.3(−14)	8.9(−15)	1.7(−15)
8.19	10.0	4.2(−10)	1.8(−10)	4.3(−11)	8.9(−12)	1.7(−12)	3.2(−13)	5.9(−14)	1.1(−14)	2.0(−15)
10.0	12.2	4.6(−10)	1.8(−10)	4.3(−11)	8.5(−12)	1.6(−12)	2.8(−13)	5.0(−14)	8.7(−15)	1.7(−15)
12.2	15.0	5.6(−10)	2.1(−10)	5.0(−11)	1.1(−11)	2.0(−12)	3.9(−13)	7.0(−14)	1.3(−14)	2.4(−15)
15.0	25.0	6.2(−10)	5.7(−10)	1.9(−10)	5.6(−11)	1.4(−11)	3.0(−12)	6.0(−13)	1.3(−13)	3.1(−14)
25.0	40.0	7.0(−10)	6.2(−10)	3.1(−10)	1.3(−10)	4.6(−11)	1.4(−11)	4.8(−12)	1.5(−12)	4.2(−13)
40.0	60.0	6.7(−10)	6.2(−10)	3.7(−10)	2.0(−10)	1.0(−10)	4.5(−11)	1.9(−11)	8.2(−12)	3.4(−12)
60.0	80.0	5.9(−10)	6.4(−10)	4.4(−10)	2.6(−10)	1.6(−10)	8.2(−11)	4.3(−11)	2.3(−11)	1.2(−11)
80.0	120.0	5.0(−10)	6.0(−10)	4.6(−10)	3.3(−10)	2.2(−10)	1.4(−10)	8.5(−11)	5.2(−11)	3.1(−11)

[a]Shield mass thickness X is in g cm^{-2} and the elemental composition of the concrete is described in the text.

[b]Read as 1.0×10^{-11}.

TABLE 8.8 (Continued)

Energy Interval (MeV)		$X = 450$	$X = 500$	$X = 550$	$X = 600$	$X = 650$	$X = 700$	$X = 750$	$X = 800$
0.	4.14(−07)	8.0(−18)	2.3(−18)	6.5(−19)	1.8(−19)				
4.14(−07)	1.12(−06)	1.1(−17)	2.6(−18)	6.7(−19)	1.7(−19)				
1.12(−06)	3.06(−06)	1.2(−17)	3.0(−18)	7.6(−19)	1.9(−19)				
3.06(−06)	1.07(−05)	1.3(−17)	3.2(−18)	8.0(−19)	2.0(−19)				
1.07(−05)	2.90(−05)	1.4(−17)	3.3(−18)	8.4(−19)	2.1(−19)				
2.90(−05)	1.01(−04)	1.5(−17)	3.6(−18)	8.8(−19)	2.1(−19)				
1.01(−04)	5.83(−04)	1.5(−17)	3.7(−18)	9.1(−19)	2.2(−19)				
5.83(−04)	3.35(−03)	1.6(−17)	3.8(−18)	9.4(−19)	2.3(−19)				
3.35(−03)	1.11(−01)	1.5(−17)	3.6(−18)	8.5(−19)	2.0(−19)				
1.11(−01)	5.50(−01)	1.7(−17)	4.0(−18)	9.7(−19)	2.3(−19)				
5.50(−01)	1.11	2.0(−17)	4.3(−18)	9.4(−19)	2.1(−19)				
1.11	1.83	4.2(−17)	9.8(−18)	2.4(−18)	5.9(−19)	1.4(−19)			
1.83	2.35	6.7(−17)	1.6(−17)	3.6(−18)	8.3(−19)	1.9(−19)			
2.35	2.46	1.4(−16)	2.9(−17)	6.0(−18)	1.3(−18)	2.8(−19)			
2.46	3.01	9.7(−17)	2.1(−17)	4.6(−18)	1.0(−18)	2.2(−19)			
3.01	4.07	7.5(−17)	1.7(−17)	3.6(−18)	8.0(−19)	1.8(−19)			
4.07	4.97	1.2(−16)	2.5(−17)	5.0(−18)	1.0(−18)	1.9(−19)			
4.97	6.36	2.2(−16)	4.0(−17)	7.4(−18)	1.4(−18)	2.6(−19)			
6.36	8.19	3.1(−16)	5.7(−17)	1.1(−17)	2.0(−18)	3.8(−19)			
8.19	10.0	3.7(−16)	7.0(−17)	1.3(−17)	2.5(−18)	4.8(−19)			
10.0	12.2	3.2(−16)	5.9(−17)	1.2(−17)	2.2(−18)	4.3(−19)			
12.2	15.0	4.6(−16)	8.7(−17)	1.7(−17)	3.2(−18)	6.1(−19)	1.2(−19)		
15.0	25.0	5.8(−15)	1.4(−15)	2.8(−16)	5.7(−17)	1.3(−17)	3.0(−18)	6.7(−19)	1.6(−19)
25.0	40.0	1.2(−13)	3.9(−14)	1.1(−14)	2.8(−15)	7.5(−16)	2.2(−16)	4.8(−17)	1.0(−17)
40.0	60.0	1.4(−12)	5.9(−13)	2.4(−13)	9.5(−14)	3.7(−14)	1.5(−14)	5.3(−15)	2.0(−15)
60.0	80.0	6.0(−12)	2.9(−12)	1.5(−12)	8.2(−13)	3.6(−13)	2.0(−13)	9.2(−14)	4.6(−14)
80.0	120.0	1.9(−11)	1.1(−11)	6.4(−12)	3.6(−12)	2.1(−12)	1.2(−12)	6.5(−13)	3.5(−13)

Source: *Ref. 36.*

largely of limestone).[4] This table gives results of the dose equivalent per unit incident fluence (Sv cm^2) tabulated as a function of the mass thickness $X \equiv \rho x$ of the slab in g cm^{-2}. The tabulated values of the dose equivalent include the contribution from secondary gamma photons created by neutron interaction with the concrete, and all contributions have been calculated on a phantom-related basis by use of conversion factors essentially equivalent to those given in Tables 5.3 and 5.4. No backscatter from any medium behind the slab is included.

The tabulation in terms of mass thickness X permits application of these results to concrete slabs without regard to density. On the other hand, if the proportion of water is changed in this concrete, the attenuation does change, especially for thicker shields. Detailed data must be obtained from the literature [35], but, as an example, it can be shown that a reduction from 5.5% water to 4.5% water requires that the prescribed dose equivalent data of Table 8.8 be multiplied by a factor of about 1.6 for incident neutrons in the energy range 1 to 15 MeV and for shield thicknesses of about 400 g cm^{-2}. A reduction to 3.5% requires a multiplicative factor of about 2.6 under these circumstances; and a reduction to 2.5% implies a factor of about 4.1 [37].

Aside from water variation, the other major change possible in the composition of ordinary concrete is the use of quartz-based sand and aggregate (SiO_2) instead of limestone in ordinary concrete. This siliceous type of concrete allows more dose equivalent penetration than does the same mass thickness of calcareous concrete with the same water content; in general, it has neutron shielding properties about the same as calcareous concrete with about 2% less water (i.e., as if a 5.5% water content had been reduced to 3.5%) [35,37]. Finally, it should be noted that these data are not to be regarded as applying to "heavy concretes," that is, to concretes with minerals containing high-Z elements included as part or all of the aggregate, nor to any other concrete of a composition deviating markedly from those proportions considered "ordinary."

Data are also available for neutron penetration through concrete slabs under slant incidence conditions [35]. In Fig. 8.13 the transmitted phantom-related dose equivalent for several slab thicknesses and incident angles is shown for a slab composed of the same calcareous concrete considered above. These dose-equivalent results, which also include the capture photon contribution, are normalized to a unit incident flow on the slab surface, that is, to an incident beam that irradiates each square centimeter of the surface with one neutron regardless of the beam direction. When normalized in this manner, the transmitted dose equivalent for a given slab thickness is seen to decrease only by a factor of between 2 to 5 as the incident beam changes from normal incidence to

[4]Specifically, the following weight percentages of the various atomic constituents are present in this particular concrete: H, 0.617; C, 17.48; O, 40.92; Mg, 3.26; Al, 1.17; Si, 3.16; Ca, 32.63; Fe, 0.76. On the assumption that the hydrogen is all contained in water, the water content is 5.5% by weight.

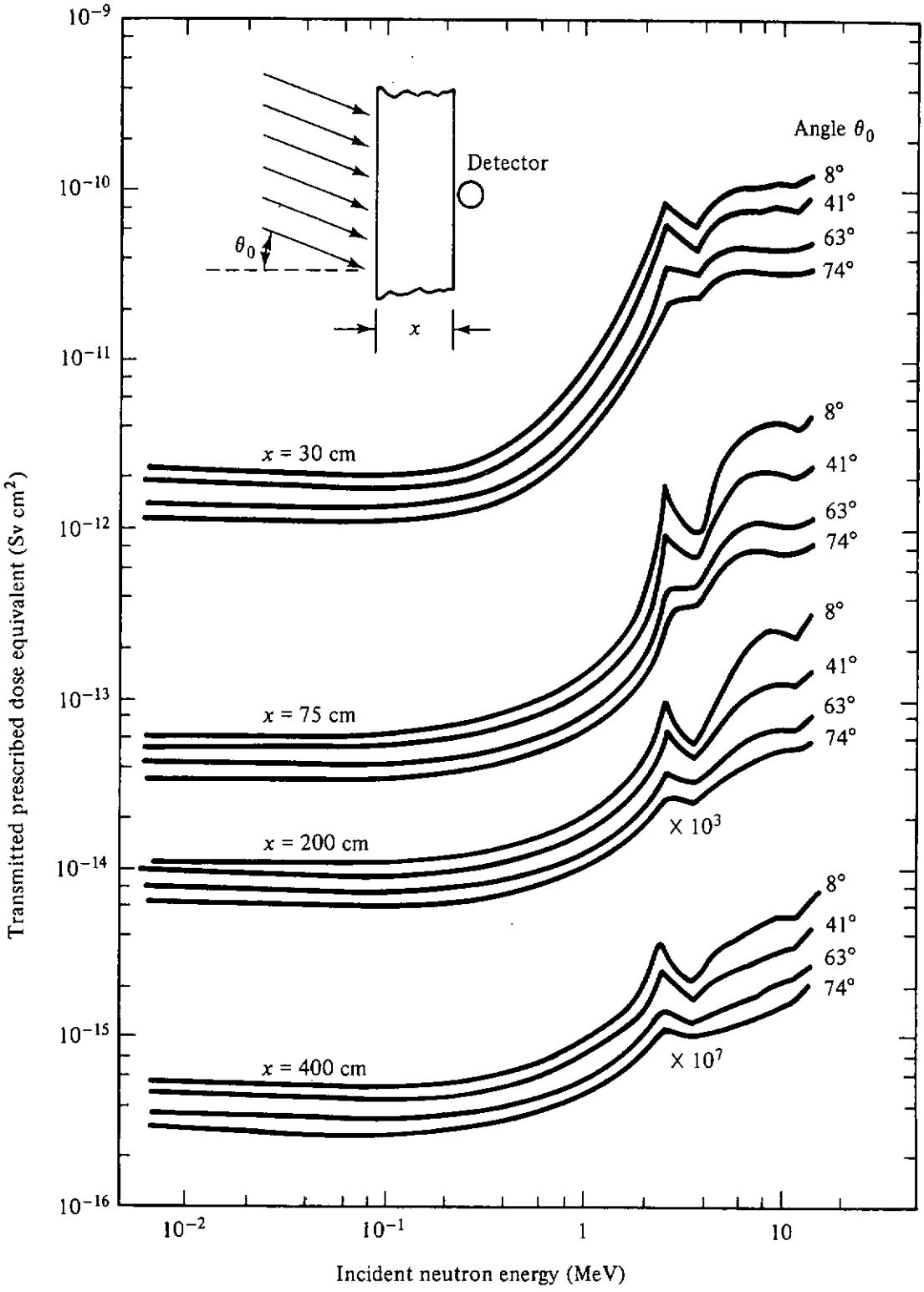

Figure 8.13 Transmitted phantom-related dose equivalent (including the capture-gamma-photon contribution) through a concrete slab illuminated obliquely at four angles as a function of the incident neutron energy. The transmitted dose is normalized to a unit flow on the slab surface. Note that the curves at $x = 200$ cm and $x = 400$ cm have been multiplied by factors of 10^3 and 10^7, respectively. Concrete composition (in 10^{21} atoms cm^{-3}): H, 8.50; C, 20.20; O, 35.50; Mg, 1.86; Al, 0.60; Si, 1.70; Ca, 11.30; and Fe, 0.19; density is 2.31 g cm^{-3} and water (percent by weight) is 5.5%. (From data of Ref. 35.)

a grazing incidence of 75° (from the normal), for a wide range of incident neutron energies. Data for different concretes, incident energies, and incident directions can be found in the original literature.

One final comment on these data is appropriate as a cautionary statement. The tabulated data are based on a compilation of results of theoretical calculations. No experimental verification is available. Under such circumstances, the data should be used with some caution, especially for the greater thicknesses, and a factor of safety of at least 2 is advised.

REFERENCES

1. D. H. Stoddard and H. E. Hootman, "^{252}Cf Shielding Guide," Report DP-1246, E.I. du Pont de Nemours & Co., Savannah River Laboratory, Aiken, S.C., 1971.
2. R. D. Albert and T. A. Welton, "A Simplified Theory of Neutron Attenuation and Its Application to Reactor Shield Design," USAEC Report WAPD-15 (Del.), Westinghouse Electric Corp., Atomic Power Division, Pittsburgh 1950.
3. T. Rockwell (ed.), *Reactor Shielding Design Manual*, D. Van Nostrand, Princeton, N.J., 1956.
4. E. P. Blizard (ed.), *Reactor Handbook*, Vol. III, Part B: *Shielding*, 2nd ed., Interscience, New York, 1962.
5. A. W. Casper, "Modified Fast Neutron Attenuation Functions," USAEC Report XDC-60-2-76, General Electric Corp., Atomic Products Division, Cincinnati, 1960.
6. M. Grotenhuis, "Lecture Notes on Reactor Shielding," Report ANL-6000, Argonne National Laboratory, Argonne, Ill., 1962.
7. S. Glasstone and A. Sesonske, *Nuclear Reactor Engineering*, D. Van Nostrand, Princeton, N.J., 1963.
8. A. Brynjolfsson, "Water," in *Engineering Compendium on Radiation Shielding*, Vol. II, R. G. Jaeger (ed.), Springer-Verlag, New York, 1975, p. 288.
9. H. Goldstein, *Fundamental Aspects of Reactor Shielding*, Addison-Wesley, Reading, Mass., 1959.
10. H. Goldstein and R. Aronson, "Effective Removal Cross Sections—Theory," *React. Sci. Technol.* **4**, 149 (1954) (USAEC Report TID-2015).
11. G. T. Chapman and C. L. Storrs, "Effective Neutron Removal Cross Sections for Shielding," USAEC Report ORNL-1843 (AECD-3978), Oak Ridge National Laboratory, Oak Ridge, Tenn., 1955.
12. L. K. Zoller, "Fast-Neutron Removal Cross Sections," *Nucleonics* **22**, 128 (1964).
13. K. J. Shure, K. A. O'Brien, and D. M. Rothberg, "Neutron Dose Rate Attenuation by Iron and Lead," *Nucl. Sci. Eng.* **35**, 371 (1969).
14. S. G. Tsypin and V. I. Kukhtevich, "Removal Theory," in *Engineering Compendium on Radiation Shielding*, Vol. I, R. G. Jaeger (ed.), Springer-Verlag, New York, 1968, p. 301.
15. H. Gronroos, "Energy Dependent Removal Cross-Sections in Fast Neutron

Shielding Theory," in *Engineering Compendium on Radiation Shielding*, Vol. I, R. G. Jaeger (ed.), Springer-Verlag, New York, 1968, p. 305.

16. J. P. Millot, "Étude de la diffusion des neutrons rapides, section efficace de déplacement," Thesis, Report CEA-2142, Commissariat Énergie Atomique, Paris, 1962.
17. A. Aalto, R. Fräki, and K. Malén, "The Fine Adjustment of the Neutron Penetration in the NRN Method," *Nucl. Sci. Eng.* **22**, 443 (1965).
18. W. W. Dunn, "Transmission of Fast Neutrons through Aluminum, Iron and Lead," Thesis, Air Force Institute of Technology (Armed Services Technical Information Agency 124760), 1957.
19. D. L. Broder and S. G. Tsypin, "Attenuation in Non-hydrogenous Media," in *Engineering Compendium on Radiation Shielding*, Vol. I, R. G. Jaeger (ed.), Springer-Verlag, New York, 1968, p. 325.
20. J. R. Lamarsh, *Introduction to Nuclear Reactor Theory*, Addison-Wesley, Reading, Mass., 1966.
21. "Reactor Physics Constants," ANL-5800, 2nd ed., Argonne National Laboratory, Angonne, Ill., 1963.
22. B. T. Price, C. C. Horton, and K. T. Spinney, *Radiation Shielding*, Pergamon, Elmsford, N.Y., 1957.
23. J. J. Taylor, Report WAPD-23, Westinghouse Corp., 1951; see Ref. 3 for a summary of this technique.
24. J. W. Haffner, as reported by D. K. Trubey, "Removal–Diffusion Combination," in *Engineering Compendium on Radiation Shielding*, Vol. I, R. G. Jaeger (ed.), Springer-Verlag, New York, 1968, p. 270.
25. D. C. Anderson and K. Shure, "Thermal Neutron Flux Distributions in Metal–Hydrogenous Shields," *Nucl. Sci. Eng.* **8**, 260 (1960).
26. A. F. Avery, D. E. Bendall, J. Butler, and K. T. Spinney, "Methods of Calculation for Use in the Design of Shields for Power Reactors," Report AERE-R 3216, Atomic Energy Research Establishment, Oxfordshire, England, 1960.
27. D. E. Bendall, "RASH D—A Mercury Programme for Neutron Shielding Calculations," Report AEEW-M 261, Atomic Energy Weapons Establishment, Winfrith, Dorset, England, 1962.
28. E. G. Peterson, "MAC—A Bulk Shielding Code," USAEC Report HW-73381, Hanford Atomic Products Operation, Hanford, WA 1962.
29. L. Hjärne, "A User's Manual for the N.R.N. Shield Design Method," Report AE-145, AB Atomenergi, Stockholm 1964.
30. J. Butler and A. F. Avery, "Removal–Diffusion Theory," in *Engineering Compendium on Radiation Shielding*, Vol. I, R. G. Jaeger (ed.), Springer-Verlag, New York, 1968, p. 273.
31. P. A. Stevens and D. K. Trubey, "Methods for Calculating Neutron and Gamma Ray Attenuation," in *Radiation Shielding Handbook*, Chap. 3, USAEC Report DASA-1892-3, Oak Ridge National Laboratory, Oak Ridge, Tenn., 1968.

32. R. W. Roussin and F. A. R. Schmidt, "Adjoint S_n Calculations of Coupled Neutron and Gamma-Ray Transport Calculations through Concrete Slabs," *Nucl. Eng. Des.* **15**, 319 (1971).

33. R. G. Alsmiller, Jr., R. R. Mynatt, J. Barish, and W. W. Engle, Jr., "Shielding against Neutrons in the Energy Range 50 to 400 MeV," *Nucl. Instrum. Methods* **72**, 213 (1969).

34. R. W. Roussin, R. G. Alsmiller, Jr., and J. Barish, "Calculations of the Transport of Neutrons and Secondary Gamma-Rays through Concrete for Incident Neutrons in the Energy Range 15 to 75 MeV," *Nucl. Eng. Des.* **24**, 2 (1973).

35. A. B. Chilton, "Effect of Material Composition on Neutron Penetration of Concrete Slabs," Report 10425, U.S. National Bureau of Standards, Washington, D.C., 1971.

36. J. M. Wyckoff and A. B. Chilton, "Dose Due to Practical Neutron Energy Distributions Incident on Concrete Shielding Slabs," Proc. 3rd Int. Congr. IRPA, Washington, D.C., 1973, p. 694.

37. "Radiation Protection Design Guidelines for 0.1–100 MeV Particle Accelerator Facilities," NCRP Report 51, National Council on Radiation Protection and Measurements, Washington, D.C. 1977.

PROBLEMS

8.1. Perform the integration in Eq. (8.10) by extending the integration range to $(-\infty, \infty)$ so as to obtain Eqs. (8.11) to (8.14). How far from the point fission source in a infinite water medium must one be so that less than 5% error is introduced by this approximation? Recall that for a Gaussian (normal) distribution, 95.5% of the area of the distribution is within two standard deviations ($\pm 2\sigma$) of the mean.

8.2. A thin circular plate of natural uranium is immersed into a large water tank and uniformly irradiated by thermal neutrons so that each second 10^8 fissions occur in each square centimeter of the plate. If the diameter of this plate is 100 cm, what is the fast-neutron tissue-absorbed dose rate at a distance of 120 cm from the disk on the axis of symmetry perpendicular to the disk?

8.3. Consider an infinite plane isotropic ^{235}U fission source of strength $S_A = 1\ cm^{-2}s^{-1}$ in an infinite water medium. Estimate the absorbed dose rate in tissue from fast neutrons as a function of distance out to 200 cm from the source plane by **(a)** using Eq. (8.17) for the point kernel, and by **(b)** using Eq. (8.18) for the point kernel. Use Eq. (8.52) to calculate the thermal flux density $\phi_{th}(x)$, and then estimate the tissue-absorbed dose rate at $x = 100$ cm due to capture gamma photons. Note that one 2.23-MeV photon results from a neutron capture by hydrogen with a thermal absorption cross section $\sigma_a = 332$ mb. (For photon calculations, approximate tissue by water.)

8.4. Each of the two situations depicted in Fig. P8.4 involves a point source of fission neutrons surrounded by spherical shells of iron and of water. What is the ratio of the fast-neutron tissue-absorbed dose rate at point P in case A to that at point P in case B? Indicate any assumptions made in your calculations.

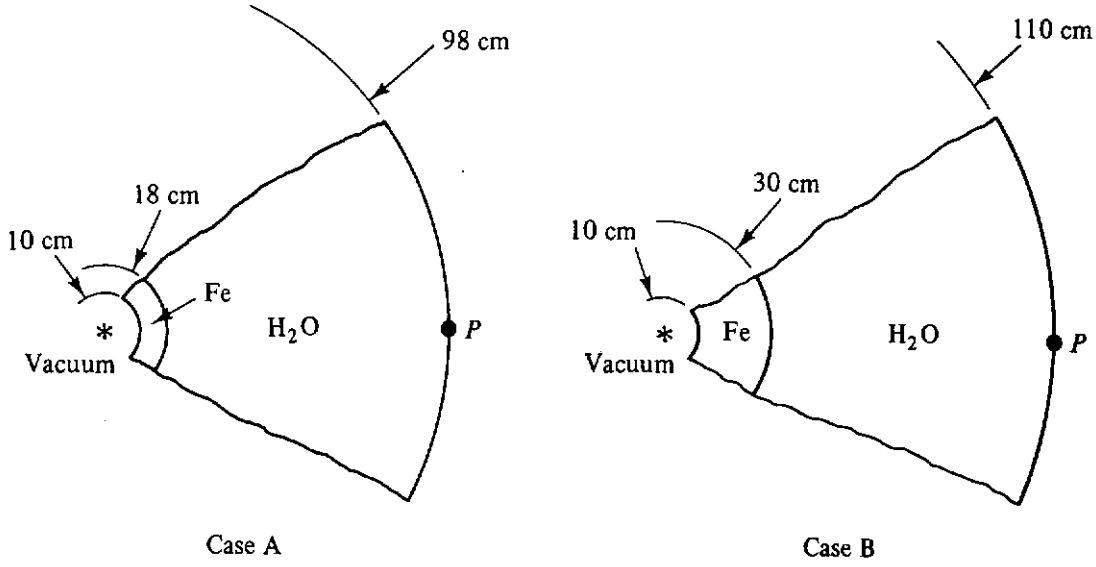

Fig. P8.4

8.5. Compute the linear removal coefficient (for fission neutrons) for soil of density 1.6 g cm^{-3} with the following composition by weight percent: H, 2.80; Si, 29.41; Al, 3.75; K, 1.06; Ca, 0.97; Fe, 1.65; and 0, 60.36.

8.6. What is the linear removal coefficient (for fission neutrons) of uranium carbide (UC_2) with a density of 11.28 g cm^{-3}?

8.7. Estimate the effective microscopic removal cross section (energy independent) of ^{235}U and iron for reactor fast neutrons. Calculate and compare the linear and mass thicknesses of these two materials required to attenuate fast neutrons by a factor of 0.15, when the metal is considered as part of a metal–water combination shield. (Data of Table A3.8 may be useful.)

8.8. Derive an explicit expression for the fast-neutron tissue-absorbed dose rate a distance r (cm) from a point fission source of strength S (neutrons s^{-1}) embedded in a large mass of concrete with the following composition (in 10^{24} atoms cm^{-3}): H, 0.0093; O, 0.0463; C, 0.0065; Si, 0.0099; and Ca, 0.0088.

8.9. A large tank 100 cm thick is filled with a 2% aqueous suspension of B_2O_3, that is, one in which 2 g of B_2O_3 (density 1.84 g cm^{-3}) is suspended in 100 cm^3 of water. Assume that the addition of B_2O_3 to the 100 cm^3 of water does not appreciably change the volume so that 100 cm^3 of suspension result.

(a) What is the linear removal coefficient of B_2O_3 for fission neutrons?

(b) A parallel, collimated beam of fission neutrons of strength 7.7×10^{10} neutrons per cm^{-2} s^{-1} normally illuminates one side of this tank. What is the fast-neutron tissue-absorbed dose rate at the other side if attenuation by the tank walls can be neglected?

(c) What is the tissue-absorbed dose rate in the neutron beam if the tank is removed?

8.10. Estimate the tissue-absorbed-dose point kernel for a point source of 14-MeV neutrons in water by using energy-dependent removal theory. Compare your result to that shown in Fig. 8.8.

8.11. Approximately by what percent is the total fast-neutron flux density above 1.5 MeV reduced if a 20-cm iron slab is inserted into a beam of monoenergetic neutrons with energy of 14.1 MeV?

8.12. The fast-neutron flux density leaking from the outer (plane) surface of a reactor is 3×10^{10} cm^{-2} s^{-1} and the thermal neutron flux density is 10^{11} cm^{-2} s^{-1}. A heavy concrete shield 4 ft thick, which is placed adjacent to the reactor's outer surface, has the following composition: H, 0.023; O, 0.640; Al, 0.027; Si, 0.072; Ca, 0.26; and Fe, 3.39 g cm^{-3}. Estimate the tissue-absorbed dose rate due to thermal neutrons at the outer shield surface. It may be assumed that the fast neutrons are perpendicularly incident on the shield.

8.13. In the 5-m-thick concrete shield (density 2.3 g cm^{-3}) surrounding the pressure vessel of a large reactor, the fast-neutron flux density (cm^{-2} s^{-1}) is observed to vary as

$$\phi_f(x) = 10^9 e^{-0.15x} + 10^7 e^{-0.08x},$$

where x (cm) is the distance into the shield from the inner surface. At the inner surface, the thermal neutron flux density is found to be $\phi_{th} = 2 \times 10^{10}$ cm^{-2} s^{-1}. Plot both the thermal and fast-neutron tissue-absorbed dose rate as a function of distance into the shield. What is the production rate 100 cm into the shield of 2.2-MeV capture gamma photons from hydrogen?

8.14. An isotropic infinite plane source of S_A thermal neutrons cm^{-2}s^{-1} exists on the y-z plane at the origin in an infinite, homogeneous medium. A *gamma* detector is located at a distance x from the neutron source plane in this medium. Derive a formula for the absorbed dose rate in the medium from photons only, in terms of the nuclear properties of the medium.

8.15. A parallel beam of 10^{12} neutrons cm^{-2} s^{-1}, all of 10.75 MeV, strikes a 1-cm-thick steel plate normal to its surface as illustrated in Fig. P8.15. The steel plate is in the form of a round disk with a diameter of 20 cm. What is the exposure rate along the axis 100 cm from the plate due *solely* to gamma photons from inelastic scattering of the neutrons? You may make simplifying assumptions provided that they are clearly stated and provided they introduce errors of less than 20%. Data:

$$\sigma_{inel} = 1.3 \text{ barns for iron at 10.75 MeV},$$

$$\sigma_{total} = 3 \text{ barns for iron at 10.75 MeV}.$$

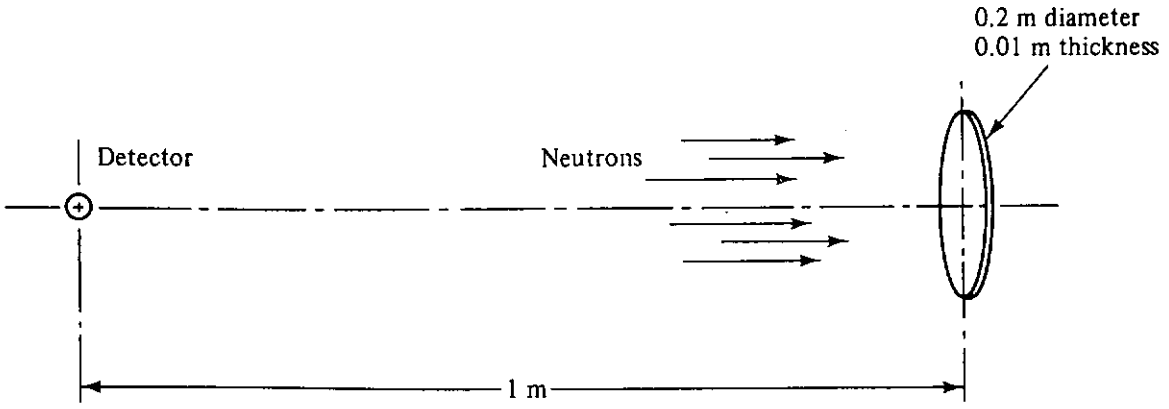

Fig. P8.15

8.16. In Section 8.6, formulas for the capture gamma dose rate behind a slab shield were derived. Consider now a laterally infinite slab illuminated by neutrons uniformly over one surface ($x = 0$) so that the thermal neutron flux density in

the slab varies as $\exp(-kx)$, $k > 0$. The slab thickness t is also very large so that for all practical purposes the slab can be considered to be infinitely thick. Derive formulas for the absorbed dose rate at the front surface of the shield ($x = 0$) due to the secondary gamma photons produced in the shield.

8.17. In a 40-cm-thick iron slab shield, the thermal neutron flux density ($cm^{-2}\ s^{-1}$) varies approximately as

$$\phi_{th}(x) = 10^6 e^{-0.12x},$$

where x is the distance in centimeters from the front face of the shield. Calculate at the exit surface of the slab the exposure rate arising from the production of capture gamma photons in the shield. Perform your calculations first for the uncollided photon component and then for the total detector response.

8.18. A 1-mg source of ^{252}Cf is placed in a large water-filled tank. Estimate, as a function of distance from this source, the absorbed dose rate in tissue due to **(a)** fast neutrons, **(b)** thermal neutrons, **(c)** primary gamma photons, **(d)** capture gamma photons. For photons, the absorbed dose in tissue can be approximated by the absorbed dose in water.

9 approximate techniques under special geometric conditions

9.1 ALBEDO CONCEPT

9.1.1 Differential Number Albedo

The term *albedo* (Latin for "whiteness") is taken from astronomical use and refers to the reflecting characteristics of a surface. Fundamentally, it expresses the ratio of the flow rate of radiation emitted from a small increment of surface to the flow rate of the radiation incident upon that surface under specified conditions. Of course, for neutrons and photons, reflection does not take place exactly at the surface of the medium but results from scattering of the particles by nuclei or electrons within the medium. Furthermore, many scattering interactions may take place within the medium before the incident particle emerges, or is "reflected" from the surface; and thus as a rule the particle does not emerge from exactly the same position on the surface that it entered, as is illustrated in Fig. 9.1. Nevertheless, in radiation shielding calculations in which the character of the incident radiation does not change rapidly over the neighborhood of the increment of surface under consideration, a reasonably accurate assumption can be made that the particles emerging from the incremental area result directly from those incident on that same area. Another common approximation made is that the reflecting medium acts as if it were infinite in depth below the surface. It has been shown that this is an excellent approximation if the medium is of finite thickness greater than two mean-free-path lengths [1,2].

In the discussion that follows it is convenient to assume that the sources and detectors are on the side of the surface away from the reflecting medium

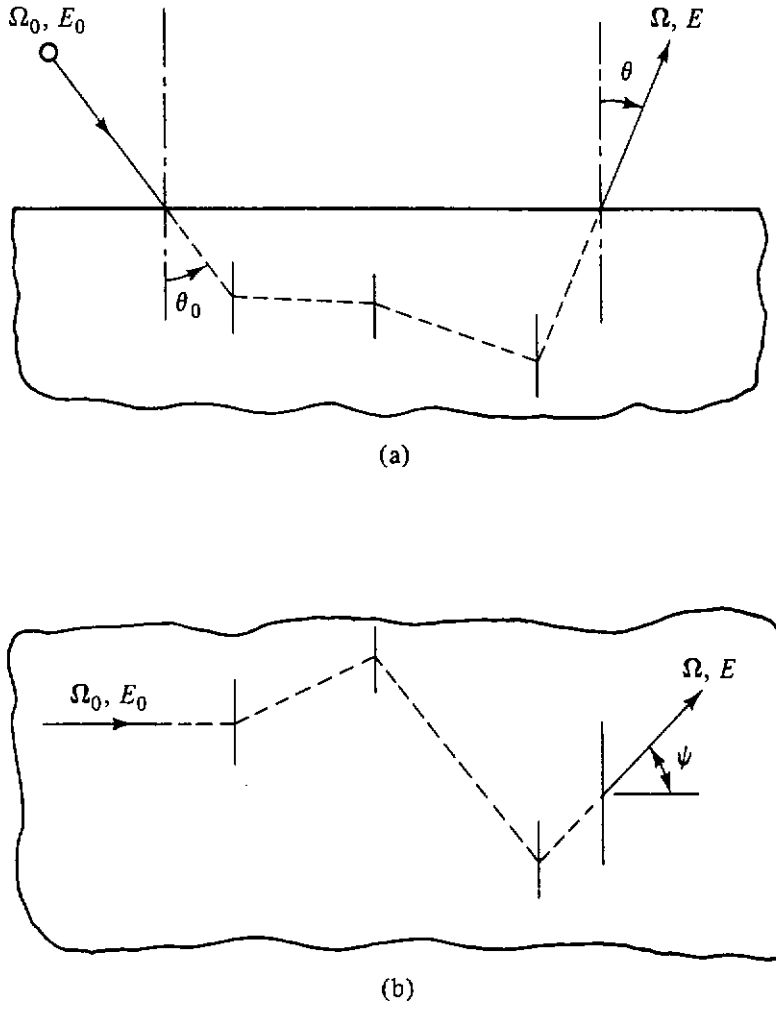

Figure 9.1 Geometry for particle reflection from a scattering medium: (a) View in plane normal to reflecting surface; (b) view in reflecting surface.

and that they are sufficiently close to the surface so that interaction with any medium on the source–detector side of the surface is negligible. Alternatively, one may consider that only a vacuum or very thin medium exists on the source/detector side of the surface.

It is conventional in shielding design and analysis to define albedo in terms of a parallel beam of monoenergetic particles incident on the "reflecting" surface. Figure 9.2 represents the appropriate geometric situation. At the incremental area ΔA in the surface of a reflecting medium, particles of energy E_0 are incident at polar angle θ_0 (with respect to the surface inward normal), with flux density ϕ_0. The flow rate into the surface per unit area is j_{n0}, where

$$j_{n0} = \phi_0 \cos \theta_0. \tag{9.1}$$

Reflected particles emerge from ΔA with differential energy and directional flow rate (per unit surface area) $j_{nr}(E, \theta, \psi)$, where θ is the polar angle with respect to the outward normal, ψ is an azimuthal angle in the surface with respect to the plane established by the incoming radiation direction and the normal, and E is the reflected particle energy. The *differential energy and directional albedo* is then defined as the ratio of the flow rates:

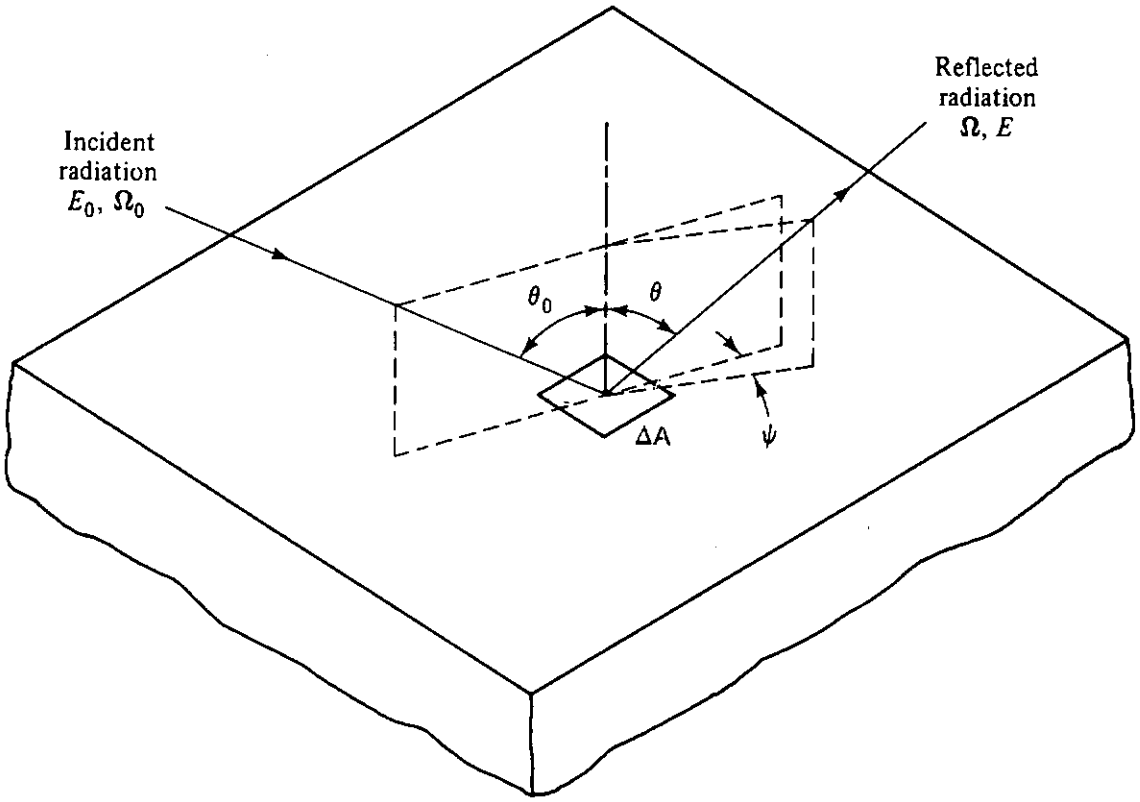

Figure 9.2 Angular and energy relationships in albedo formulation.

$$\alpha(E_0, \theta_0; E, \theta, \psi) \equiv \frac{j_{nr}(E, \theta, \psi)}{j_{n0}} \tag{9.2}$$

This albedo is sometimes given a subscript N to emphasize the fact that it relates to a ratio between particle *number* flow rates. Other types of albedo will be established later.[1]

In case one is not concerned with distinguishing the energies of the outgoing particles, one can define the *directionally differential albedo* by

$$\alpha_N(E_0, \theta_0; \theta, \psi) \equiv \frac{j_{nr}(\theta, \psi)}{j_{n0}}, \tag{9.3}$$

so that

$$\alpha_N(E_0, \theta_0; \theta, \psi) = \int_E \alpha_N(E_0, \theta_0; E, \theta, \psi)\, dE. \tag{9.4}$$

It should be pointed out at this juncture that the albedo values depend on the nature of the reflecting medium as well as the energy and angular variables. Such dependence is often suppressed in the notation unless material variation is of specific concern.

[1]The current literature presents a somewhat confusing array of slightly varied definitions. Selph [2], for example, calls the foregoing concept α_2. His α_1 is a ratio of emergent flow rate to incident flux density, his α_3 is a ratio of emergent flux density to incident flux density. Thus, these three types are simply related as follows: $\alpha_1 = \cos\theta_0\, \alpha_2 = \cos\theta\, \alpha_3$. We avoid this confusion by using only α_N ($\equiv \alpha_2$).

9.1.2 Application and Further Development of the Differential Albedo Concept

An example is appropriate here for development of further aspects of the albedo concept. Figure 9.3 shows a point isotropic source of monoenergetic particles of strength S_p per unit time. The incident flow rate at the location of $d\mathrm{A}$, a differential area within the reflecting surface, is given by

$$j_{n0} = \phi_0 \cos\theta_0 = S_p \frac{\cos\theta_0}{4\pi r_1^2}, \tag{9.5}$$

on the assumption that there is a vacuum above the surface. The flow rate of particles of energy E per unit energy increment and in direction (θ, ψ) per unit solid angle "reflected" from $d\mathrm{A}$ is then given by

$$j_{nr}(E, \theta, \psi)\, d\mathrm{A} = \frac{S_p \cos\theta_0\, \alpha_N(E_0, \theta_0; E, \theta, \psi)\, d\mathrm{A}}{4\pi r_1^2}. \tag{9.6}$$

The reflected flow rate at $d\mathrm{A}$ then acts as a point source for reflected particles which will be detected by a flux density detector in the position shown. The differential flux density at the detector then can be expressed by the following:

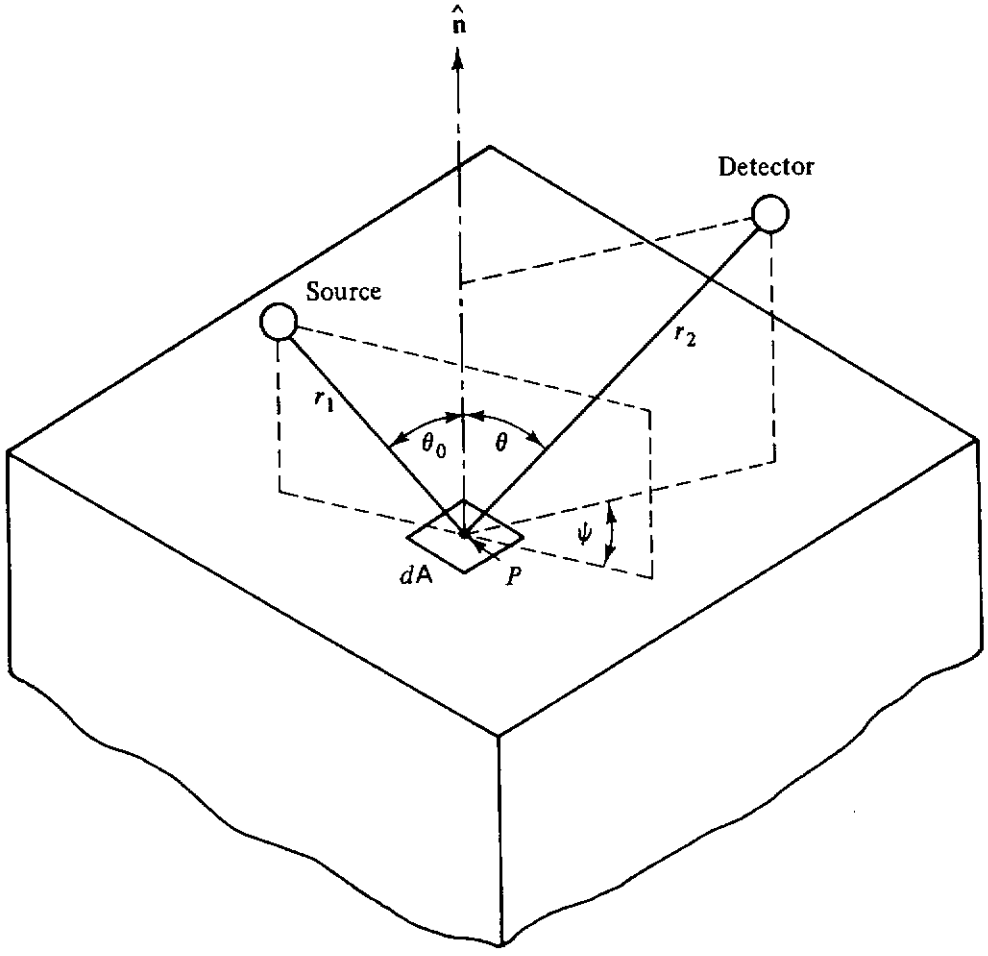

Figure 9.3 Reflection by a differential area of radiation from a point source.

$$d\phi(E) = \frac{S_p \cos\theta_0 \, \alpha_N(E_0, \theta_0; E, \theta, \psi)\, d\mathrm{A}}{4\pi r_1^2 r_2^2}, \tag{9.7}$$

where θ_0, θ, and ψ are functions of the relative positions of the source, the detector, and the differential area dA.

It would generally be of more practical value to convert this result to a differential detector response of a dosimetric type, which can be done by multiplying both sides of the expression above by the appropriate response function $\mathcal{R}(E)$ and integrating over all energy of the reflected particles. Then the detector response to *reflected* radiation from dA becomes

$$dR_r = \frac{S_p \hat{R} \cos\theta_0 \alpha_R(E_0, \theta_0; \theta, \psi)\, d\mathrm{A}}{r_1^2 r_2^2}, \tag{9.8}$$

where $\hat{R}$ is the usual symbol for the detector response one unit distance from a point source of unit strength [in this case, $\mathcal{R}(E_0)/4\pi$] and

$$\alpha_R(E_0, \theta_0; \theta, \psi) \equiv \int_E \frac{\mathcal{R}(E)}{\mathcal{R}(E_0)} \alpha_N(E_0, \theta_0; E, \theta, \psi)\, dE. \tag{9.9}$$

α_R, as defined above, is a differential albedo of a general kind; and it can be made specific by indicating what type of detector is involved, which in turn establishes the ratio $\mathcal{R}(E)/\mathcal{R}(E_0)$. For example, for a flux density detector, $\mathcal{R} = 1$ and α_R becomes α_N as defined in Eq. (9.4); for an energy flux density detector, $\mathcal{R} = E$ and α_R is designated as α_E (called the *energy albedo*); for a detector recording phantom-related dose equivalent rate $\mathcal{R}(E)$ is obtained from one of the Tables 5.3 to 5.6 and α_R becomes α_{H_p}.

Equation (9.8) is the formula of most practical usefulness. The detector response to reflected radiation from a point source is given by integration of this expression over all reflecting area segments "visible" from both the source and the detector. Such integration may sometimes be handled analytically; but usually the albedo function, if known accurately, is sufficiently complicated that numerical summation over small but finite incremental areas is necessary. Although tedious if done by hand, it is readily accomplished by computer.

An alternative form of Eq. (9.8) is sometimes preferred. Since

$$R_0 = \frac{S_p \hat{R}}{r_1^2} \tag{9.10}$$

represents the response to the incident radiation of a detector placed at the location of dA, the basic expression may be written

$$dR_r = \frac{R_0 \cos\theta_0 \, \alpha_R(E_0, \theta_0; \theta, \psi)\, d\mathrm{A}}{r_2^2}. \tag{9.11}$$

This form is useful for certain other situations, for example, one in which the incident radiation is a broad, parallel beam or is directionally dependent. Of course, it must be taken into account that R_0, r_2, θ_0, θ and ψ depend on the location of dA in the reflecting surface.

9.1.3 Total Albedo

Total albedo, $A(E_0)$, is simply the integration of the directionally differential albedo over all reflected directions; thus,

$$A_R(E_0, \theta_0) = \int_0^{2\pi} \int_0^1 \alpha_R(E_0, \theta_0; \theta, \psi)\, d(\cos\theta)\, d\psi. \tag{9.12}$$

Total number albedo A_N is the ratio of the number of particles reflected from unit surface area to the number incident per unit area of the surface. Similarly, the total energy albedo measures the ratio of the radiation energy reflected from a unit area of the surface to the radiation energy incident on a unit area of the surface.

Although the total albedo is not as practically useful a concept as the differential albedo, there are a number of propositions involving the total albedo which have fundamental significance.

1. Conservation of particles requires that $A_N \leq 1$, provided that there are no interactions in the reflecting medium which tend to multiply the number of particles [such as fission or $(n, 2n)$ reactions].
2. Conservation of energy requires that $A_E \leq 1$, provided that there are no interactions in the reflecting medium which transfer more kinetic energy to the particles than is absorbed.
3. For a medium in which the interactions with the particles are either absorptive or scattering, the total albedo has a close relationship with κ, the ratio of the scattering cross section to the total cross section. For $\kappa = 1$ (purely scattering medium), $A_N = 1$; for $\kappa = 0$ (purely absorptive medium), $A_N = 0$. One would expect some sort of general monotonic relationship between κ and total albedo between these two extremes.

9.1.4 Theoretical Approximations to Albedo Functions

Under certain idealizations and simplifications it is possible to derive theoretically certain albedo relations which, although in themselves not highly practical, have led to expressions of a partially empirical nature that are indeed very useful. One approach is as follows. With the help of Fig. 9.4, consider the distribution in the reflecting medium of those scattering events which could lead to emergence from the reflecting surface of particles with energy E, traveling in direction (θ, ψ). This distribution becomes a type of volumetric source; and it can be defined in such a way that $q(x; E, \theta, \psi)\, dE\, d\Omega$ is the rate of interactions per cubic centimeter at depth x leading to scattering of particles into energy range dE at E and into solid angle $d\Omega$ at (θ, ψ), normalized to unit incident surface flow rate of particles having energy E_0 and direction θ_0. (It is noted that q depends on incidence parameters E_0 and θ_0, but this is suppressed for the time being to avoid cumbersome notation.) Since q has been normalized to a unit flow rate input, we can determine the doubly differential number

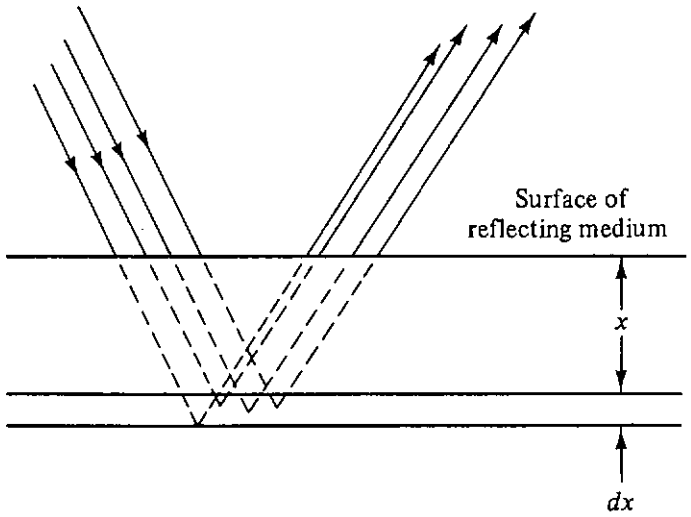

Figure 9.4 Backscattering from single collisions within a scattering medium.

albedo directly as

$$\alpha_N(E_0, \theta_0; E, \theta, \psi) = \int_0^\infty q(x; E, \theta, \psi) e^{-k(E)x \sec\theta}\, dx, \tag{9.13}$$

where k is a general attenuation coefficient such as described in Chapter 6.

Case A. Suppose one can make an assumption that q is approximately constant and independent of x, at least for the first one or two relaxation lengths of depth, for any specified values of E, θ, and ψ. Then q becomes $q(E, \theta, \psi)$, and

$$\alpha_N(E_0, \theta_0; E, \theta, \psi) \simeq \frac{q(E, \theta, \psi)}{k(E)} \cos\theta. \tag{9.14}$$

Furthermore, it is often possible to make an assumption that q is independent of direction, so that we can approximate the source function $q(E, \theta, \psi)$ as $q(E)/4\pi$. This can result, for example, if the particle scattering is isotropic in the laboratory frame of reference. Alternatively, it might result if the scatterings are so numerous that the particle flux has become essentially isotropic. At any rate, under such circumstances the albedo expression becomes

$$\alpha_N(E_0, \theta_0; E, \theta, \psi) \simeq \frac{q(E)}{4\pi k(E)} \cos\theta. \tag{9.15}$$

Modification of the expression above by the ratio of energy-dependent response functions and integration over energy gives a detector response albedo, as previously shown in Eq. (9.9), such that

$$\alpha_R(E_0, \theta_0; \theta, \psi) \simeq Q(E_0, \theta_0) \cos\theta, \tag{9.16}$$

where Q is the collection of all constants and factors in the resulting expression, independent of E, θ, and ψ. The dependence of α_R on the direction and energy of incident particles now is expressed explicitly.

Equation (9.16) shows that under many reasonable conditions the directional distribution of the detector-response albedo function has a simple "cosine"

distribution with respect to the normal to the reflecting surface; and this has become one of the most useful of all assumptions regarding the differential albedo function when no precise data are otherwise available. If the total albedo $A_R(E_0, \theta_0)$ is known or can be reasonably estimated, then the use of the cosine distribution allows us to take as the directionally differential albedo

$$\alpha_R(E_0, \theta_0; \theta, \psi) = \frac{A_R(E_0, \theta_0)}{\pi} \cos \theta. \tag{9.17}$$

Case B. The value of q may not be independent of x, as was the assumption for case A. Under some circumstances, it would be more reasonable to expect the value of q to decrease exponentially with depth as one proceeds along a ray parallel to the direction of the incident radiation, so that $q(x; E, \theta, \psi) = q_0(E, \theta, \psi) \exp(-k_0 x \sec \theta_0)$, where $k_0[\equiv k(E_0)]$ represents the attenuation coefficient for incident particles. Introduction of this into Eq. (9.13) and appropriate integration over depth x gives for this case a result

$$\alpha_N(E_0, \theta_0; E, \theta, \psi) = \frac{q_0(E, \theta, \psi)}{k_0 \sec \theta_0 + k \sec \theta}. \tag{9.18}$$

Subcase B.1. Assume that the albedo process is dominated by single scattering. Since the normalization is to a unit flow rate, corresponding to a flux density of sec θ_0, the value of q_0 easily can be seen to be $\mu_s(E_0, E, \theta_s)$ sec θ_0, where μ_s is the differential energy and direction scattering coefficient for particles of incident energy E_0 and direction θ_0 scattered into the final reflected direction (θ, ψ) and with the reflected energy E.[2] Application of this approximation to Eq. (9.18) gives

$$\alpha_N(E_0, \theta_0; E, \theta, \psi) \simeq \frac{\mu_s(E_0, E, \theta_s)}{k_0} \frac{1}{1 + (k/k_0)(\cos \theta_0/\cos \theta)}. \tag{9.19}$$

Further approximations are possible on occasion. One such is to assume that $k = k_0$, or at least that their ratio is constant and independent of energy. A similar approximation is to assume that the ratio of detector response functions, used in converting from α_N to α_R is approximately unity and can be taken as such. This enables one to derive readily that

$$\alpha_R(E_0, \theta_0; \theta, \psi) \simeq Q(E_0, \theta_0) \frac{\mu_s(E_0, \theta_s)}{1 + (k/k_0)(\cos \theta_0/\cos \theta)}, \tag{9.20}$$

where $\mu_s(E_0, \theta_s)$ is the integral with respect to E of $\mu_s(E_0, E, \theta_s)$, and Q, as before, is the collection of any constants or factors dependent only on the incident parameters E_0 and θ_0.

A similar approach is possible under the assumption that the ratio of detector response functions is approximately E/E_0. In such a case, the formula

[2]The value of θ_s is easily found from the angles θ_0, θ, and ψ by use of the "law of cosines" for spherical triangles, thus:

$$\cos \theta_s = \sin \theta_0 \sin \theta \cos \psi - \cos \theta_0 \cos \theta.$$

becomes

$$\alpha_R(E_0, \theta_0; \theta, \psi) \simeq Q(E_0, \theta_0) \frac{\mu_{se}(E_0, \theta_s)}{1 + (k/k_0)(\cos \theta_0/\cos \theta)}, \tag{9.21}$$

where

$$\mu_{se}(E_0, \theta_s) \equiv \int_E (E/E_0)\mu_s(E_0, E, \theta_s)\, dE. \tag{9.22}$$

The coefficient μ_{se} is called the *energy scattering coefficient*, as distinguished from μ_s, the *particle scattering coefficient* (see Section 3.5.1).

Subcase B.2. Assume that q varies exponentially with depth but that the angular distribution of particles emitted from the differential volume elements (considered as sources) is isotropic, either because the scattering coefficient μ_s is isotropic or because q is dominated by particles which have scattered so many times that correlation with the original preferred direction is lost. In this case, q_0 cannot be specified quite so precisely, but it will be independent of the direction angles (θ, ψ). In such a case it is easily seen that the equation for α_R would be similar to Eq. (9.20) but without the factor μ_s, thus:

$$\alpha_R(E_0, \theta_0; \theta, \psi) \simeq Q'(E_0, \theta_0) \frac{1}{1 + (k/k_0)(\cos \theta_0/\cos \theta)}. \tag{9.23}$$

Case C. This is the case of isotropic scattering of particles without energy loss within the medium in which the ratio of the scattering to the total attenuation coefficients (probability of scattering upon interaction), designated above as κ, is always constant regardless of particle energy. Chandrasekhar [3] has provided an exact solution of the reflected beam strength which can be expressed as a directionally differential albedo in the following form:

$$\alpha_N(\theta_0; \theta, \psi) = \frac{\kappa}{4\pi} \frac{1}{1 + \cos \theta_0/\cos \theta} H(\kappa, \cos \theta_0) H(\kappa, \cos \theta), \tag{9.24}$$

where the H function is tabulated in Appendix 2.

It can be noted from the table of H functions that H is a slowly varying function of its arguments, and it is always between 1 and 3. Thus, for this case, the albedo tends to be roughly isotropic (independent of θ) when $\cos \theta \gtrsim \cos \theta_0$ and roughly cosine dependent when $\cos \theta < \cos \theta_0$.

The integration over all outgoing directions provides a similarly exact expression for total albedo [3]:

$$A_N(\theta_0) = 1 - (1 - \kappa)^{1/2} H(\kappa, \cos \theta_0). \tag{9.25}$$

As can be seen, this has the proper behavior as κ takes on the extreme values of 1 or 0, in accordance with the propositions stated in Section 9.1.3.

9.1.5 Selected Formulas for Gamma Photon Albedo [1,2,4–16]

The fundamental principles discussed in foregoing sections on albedo theory have been adapted to data obtained from measurement or calculation (usually by the Monte Carlo technique) by several investigators. The more

generally useful formulas are presented in this section for gamma photons and in the next section for neutrons.

A generally applicable exposure albedo formula for photons [14] is given by an expression based on the following ideas:

1. The contribution for those photons which have been scattered only once before emerging should be given in the form indicated in Eq. (9.21), with the approximation that k/k_0 equals unity.
2. The contribution from those photons which have been scattered many times before emerging or result from pair production/positron annihilation should be given in the form indicated in Eq. (9.23), with the approximation that k/k_0 is unity.
3. The contribution from those photons scattered only a few times before emerging (which may have directions of emergence only partially correlated with the direction of incidence) should be given by a linear combination the terms for single-scatter contribution and many-scatter contribution.

The resultant expression for exposure albedo (α_X) is of the form

$$\alpha_X(E_0, \theta_0; \theta, \psi) = \frac{C(E_0)_e\sigma_{C_e}(E_0, \theta_s)10^{26} + C'(E_0)}{1 + (\cos\theta_0/\cos\theta)}. \tag{9.26}$$

$_e\sigma_{C_e}(E_0, \theta_s)$ is the Klein–Nishina *energy* scattering cross section [Eq. (3.26)] for photons, as given by application of Eq. (9.22) to Eq. (3.22). Cross sections are to be provided in units of square centimeters in the expression above, and the multiplier of 10^{26} is inserted to allow the parameter C to have values near unity. The parameters C and C' depend not only on energy, as shown, but also on the composition of the reflecting medium. They are usually considered as adjustable so as to allow a fit of the expression above to experimental or Monte Carlo data. Table 9.1 gives values of these parameters for selected values of E_0 and for several common materials.

A more accurate, but more complicated variant of formula (9.26) has been provided [16]:

$$\alpha_X(E_0, \theta_0; \theta, \psi) = F(E_0, \theta_0; \theta, \psi)\frac{C(E_0)_e\sigma_{C_e}(E_0, \theta_s)10^{26} + C'(E_0)}{1 + (\cos\theta_0/\cos\theta)(1 + 2E_0 \operatorname{vers}\theta_s)^{1/2}}, \tag{9.27}$$

in which the factor F is a purely empirical multiplier, given by[3]

$$\begin{aligned} F(E_0, \theta_0; \theta, \psi) = {} & A_1(E_0) + A_2(E_0)\operatorname{vers}^2\theta_0 + A_3(E_0)\operatorname{vers}^2\theta \\ & + A_4(E_0)\operatorname{vers}^2\theta_0 \operatorname{vers}^2\theta \\ & + A_5(E_0)\operatorname{vers}\theta_0 \operatorname{vers}\theta \operatorname{vers}\psi. \end{aligned} \tag{9.28}$$

The square root in the denominator of this formula is an approximate expression for k/k_0, based on the observation that in the range of moderate photon energies the attenuation coefficient is approximately inversely proportional to the square

[3]The versine, which few people remember anymore, is equal to 1 minus the cosine of the angle argument.

TABLE 9.1 Values of Parameters for Eq. (9.26) for the Differential Exposure Albedo of Photons on Various Reflecting Media

Material	E_0 (MeV)	C	C'
Water	0.2	−0.0187	0.1327
	0.662	0.0309	0.0253
	1.00	0.0470	0.0151
	2.50	0.0995	0.0058
	6.13	0.1861	0.0035
Concrete	0.2	0.0023	0.0737
	0.662	0.0347	0.0197
	1.00	0.0503	0.0118
	2.50	0.0999	0.0051
	6.13	0.1717	0.0048
Iron	0.2	0.0272	−0.0100
	0.662	0.0430	0.0063
	1.00	0.0555	0.0045
	2.50	0.1009	0.0044
	6.13	0.1447	0.0077
Lead	0.2	0.0044	−0.0050
	0.662	0.0308	−0.0100
	1.00	0.0452	−0.0083
	2.50	0.0882	0.0001
	6.13	0.1126	0.0063

Source: *Refs. 2 and 14; reproduced by permission of the American Nuclear Society.*

root of the energy [13]. E_0 in this formula is the incident photon energy in MeV. Data for the parameters are available only for two photon energy values on concrete; they are given in Table 9.2.

TABLE 9.2 Table of Parameters for the Modified Albedo Formula [Eq. (9.28)] for Concrete

Parameter	$E_0 =$ 0.662 MeV	$E_0 =$ 1.25 MeV
C	0.0455	0.0710
C'	0.0161	0.0114
A_1	1.512	1.555
A_2	−0.606	−0.629
A_3	−0.641	−0.605
A_4	0.645	0.539
A_5	−0.157	−0.168

Source: *Ref. 16; reproduced by permission of the American Nuclear Society.*

Figure 9.5 shows curves plotted from Eq. (9.28) for selected values of the parameters and geometric variables. The peaks in the curves for high values of the angle of incidence and an azimuthal angle of 0° are due to the relatively large values of ${}_e\sigma_{Ce}$ when the scattering angle θ_s is small.

Other formulas of less accuracy are also available in the literature [2].

9.1.6 Selected Formulas for Neutron Albedo [3,17–21]

The literature abounds with information on neutron albedo and related concepts, and we can only note a few examples that illustrate the principles previously discussed.

Most albedo information in which the incident neutrons are "fast," (i.e., of energy greater than 0.2 MeV) is based on response functions [see Eq. (9.9)] derived from the maximum value of absorbed dose in a phantom. Such albedos will be given the symbol α_{D_p} in this text.

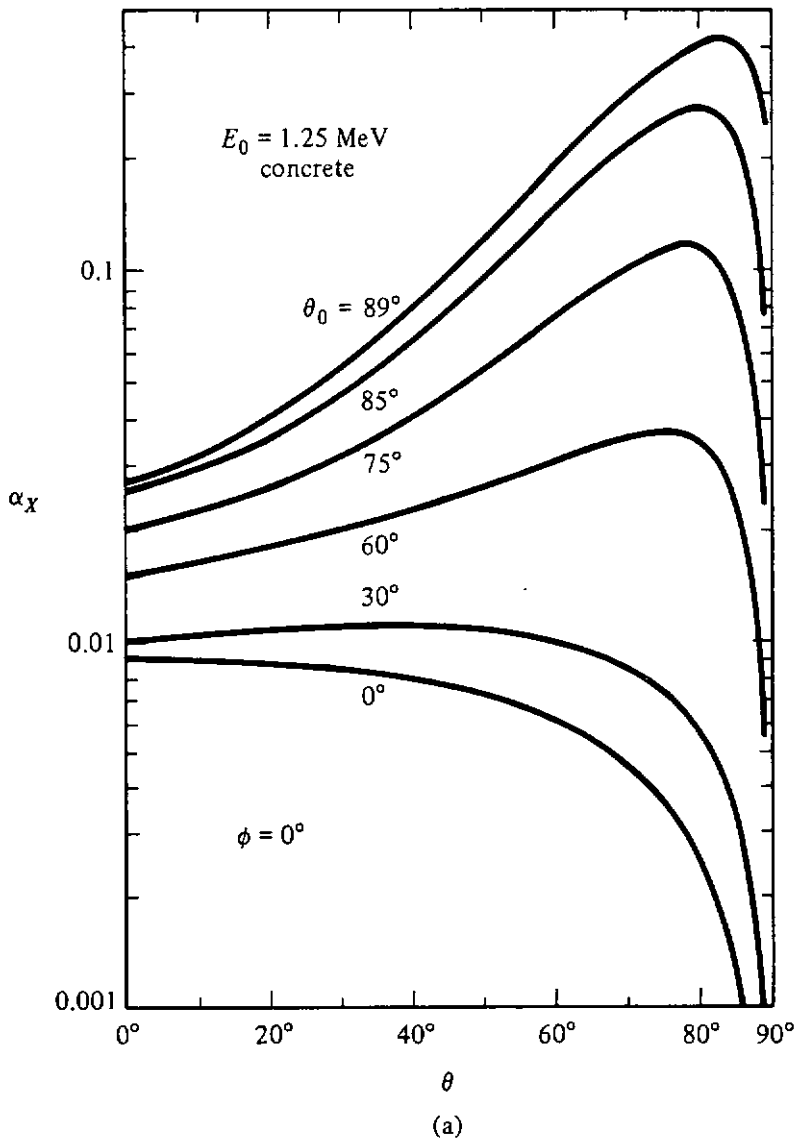

Figure 9.5a Differential exposure albedo, $\alpha_X(E_0, \theta_0; \theta, \psi)$, for reflection of 1.25-MeV photons from concrete: (a) $\psi = 0°$ (Continued)

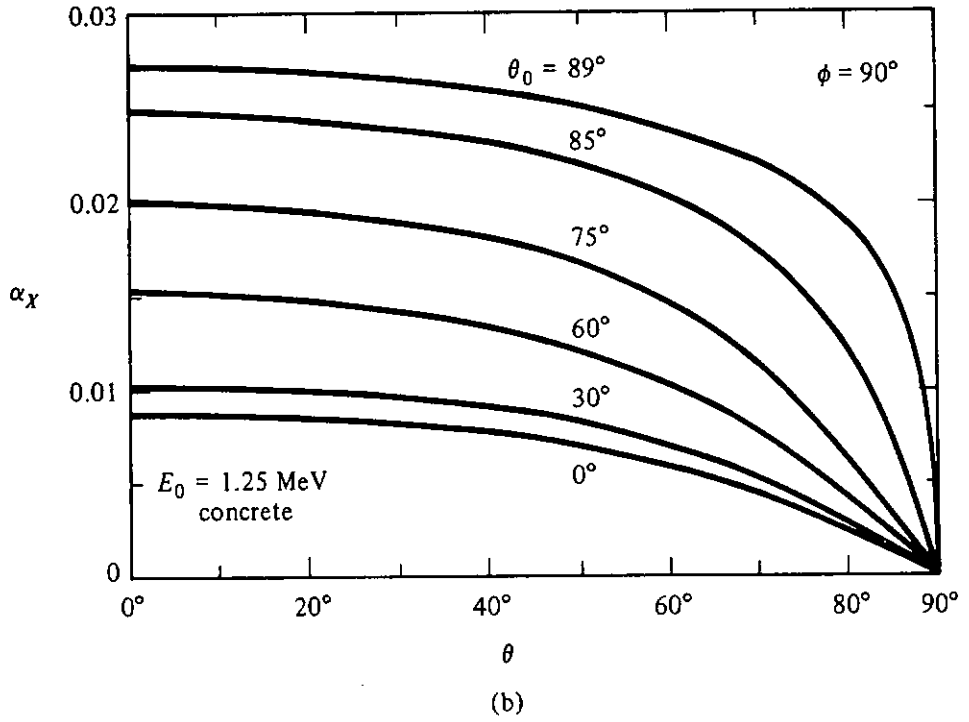

(b)

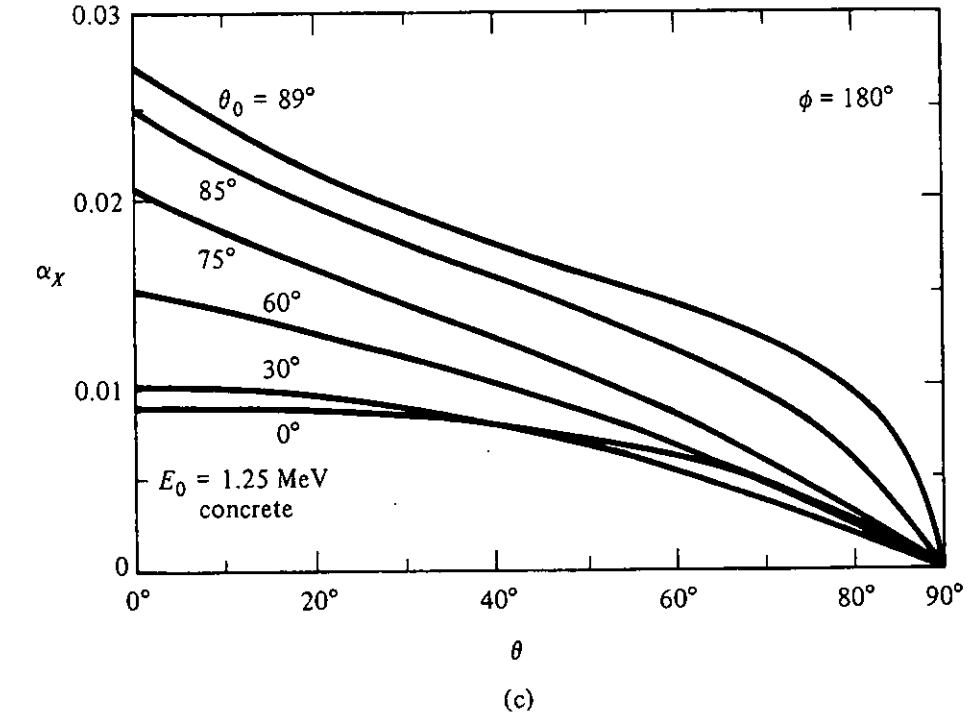

(c)

Figure 9.5b, c (b) $\psi = 90°$; (c) $\psi = 180°$.

A moderately simple formula exists for fast neutrons [22], which is similar in many respects to Eq. (9.26). For this case, it has been assumed that the single-scattered contribution to the albedo conforms to the expression given in Eq. (9.20), the many-scattered contribution conforms to the expression given in Eq. (9.16), and the few-scattered contribution can be considered a linear combination of the two expressions:

$$\alpha_{D_p}(E_0, \theta_0; \theta, \psi) = M(E_0)\cos\theta + \frac{B(E_0) + C(E_0)\cos\theta_s}{1 + Y(E_0)(\cos\theta_0/\cos\theta)}, \qquad (9.29)$$

where the parameters M, B, C, and Y are adjusted to give a good fit to data considered reasonably accurate. These parameters are functions, of course, of the reflecting medium as well as of the incident neutron energy. Values for these parameters, based on Monte Carlo calculations, are given in Table 9.3 for various materials.

In Eq. (9.29) it is clear that the scattering coefficient is expressed by the first two terms of a Legendre expansion with respect to $\cos\theta_s$, so that a moderate degree of anisotropicity in the scattering cross section is taken into account. The factor $Y\ (\equiv k/k_0)$ is assumed to be independent of E.

A simpler, but less accurate, expression has been developed on a largely empirical basis [23], which, in the notation of this text, is given by

$$\alpha_{D_p}(E_0, \theta_0; \theta, \psi) = C(E_0)\,(\cos\theta_0)^{-1/3}\cos\theta. \tag{9.30}$$

Values of C for several different materials are given in Table 9.4.

A particularly noteworthy feature of this formula is its independence of the azimuthal angle ψ. The insensitivity to the azimuthal angle is primarily a consequence of the tendency of neutrons toward isotropicity of scattering in the laboratory frame of reference, and is of course more valid for lower-energy neutrons [23, 24]. Furthermore, a formula such as this is not applicable to media with high hydrogen content, such as water, since neutron scattering on hydrogen nuclei is all forward in the laboratory system.

An interesting empirical observation has been made with respect to the effect of hydrogen on the albedo based on maximum absorbed dose in a phantom[23]. Figure 9.6 shows this total albedo for perpendicularly incident fission neutrons on various reflecting media as a function of the ratio of the macroscopic cross section for hydrogen to the total macroscopic cross section for the material concerned. The fact that a straight line can be drawn through the data points may be somewhat fortuitous; however, there is a crude analogy between this ratio μ_H/μ_t and $(1 - \kappa)$, the ratio of absorption cross section to total cross section. Hydrogen interaction, even though it may be largely scattering, may appear as an absorptive process from the neutron albedo standpoint, especially when the incident beam is perpendicular to the surface, because hydrogen scattering (being forward) serves mainly to drive the neutrons deeper into the medium and decreases their chances of getting out again. Figure 9.6 contains also a line representing Eq. (9.25), permitting one to see how the empirical result is qualitatively consistent with the behavior expected on the basis of the theoretical idealizations discussed in Sections 9.1.3 and 9.1.4.

The simplicity of Eq. (9.30) favorably commends its use; however, it is quite inapplicable to those situations for which a strong azimuthal dependence should be expected, for example, a high-energy neutron beam incident very obliquely on a surface. Such a situation is of particular significance in connection with duct streaming, as is seen in the next section. Even Eq. (9.29), although it provides some azimuthal dependence through the energy-scattering

TABLE 9.3 Energy-Dependent Parameters for the Four-Parameter Formula, Eq. (9.29), of Differential Dose Albedo for Fast Neutrons

		E_0 (MeV)							
Material[a]		0.10	0.25	0.50	1.0	2.0	3.0	5.0	14.0
$M(E_0)$	Fe	0.1401	0.1385	0.1817	0.0797	0.0904	0.1147	0.0756	0.0657
	Al	0.1528	0.1491	0.1523	0.0940	0.1287	0.1020	0.0689	0.0584
	S1	0.0648	0.0687	0.0813	0.0583	0.0547	0.0617	0.0431	0.0269
	S2	0.0746	0.0820	0.0659	0.0505	0.0641	0.0389	0.0311	0.0187
	S3	0.0673	0.0661	0.0693	0.0477	0.0488	0.0407	0.0218	0.0287
	Ct	0.0706	0.0710	0.0834	0.0727	0.0691	0.0810	0.0442	0.0288
$B(E_0)$	Fe	0.0776	0.0672	0.0796	0.0643	0.0863	0.0858	0.0710	0.0575
	Al	0.0488	0.0874	0.0649	0.1008	0.0966	0.1129	0.1017	0.0770
	S1	0.0711	0.0727	0.0793	0.0740	0.0971	0.0836	0.0787	0.0812
	S2	0.0561	0.0514	0.0982	0.0838	0.0972	0.1154	0.1132	0.0788
	S3	0.0615	0.0556	0.1051	0.0633	0.1259	0.1010	0.1042	0.0567
	Ct	0.0819	0.0628	0.0703	0.0676	0.0921	0.0991	0.1214	0.0697
$C(E_0)$	Fe	0.0093	−0.0095	0.0684	−0.0067	−0.0118	0.0140	0.0293	0.0195
	Al	−0.0014	0.0329	0.0112	−0.0381	−0.0101	−0.0122	0.0172	0.0147
	S1	0.0343	0.0292	0.0611	−0.0166	−0.0016	0.0154	0.0177	0.0444
	S2	0.0517	0.0294	0.0671	−0.0295	0.0149	0.0133	0.0289	0.0240
	S3	0.0555	0.0345	0.0964	−0.0118	0.0393	0.0279	0.0212	0.0408
	Ct	0.0406	0.0278	0.0585	−0.0228	0.0189	0.0546	0.0047	0.0235
$Y(E_0)$	Fe	1.1654	1.0115	0.5708	0.9052	0.8566	1.2569	0.9325	1.9877
	Al	0.4868	2.9778	1.2733	1.4044	1.2834	1.4061	1.9476	2.6380
	S1	1.1660	1.1058	1.2315	0.5448	1.1314	1.4523	1.3720	1.8531
	S2	1.0278	0.2818	1.3826	0.7913	1.4744	1.5615	1.8382	1.6692
	S3	1.4170	1.2275	2.5801	0.6001	2.0462	1.7238	1.7486	1.4914
	Ct	1.5033	0.6753	0.8982	0.6403	1.0692	2.3264	2.6435	1.6450

[a]Fe, iron; Al, aluminum; S1, dry desert soil; S2, soil 50% saturated with water; S3, soil 100% saturated with water; Ct, concrete.

Source: *Ref. 22; reproduced by permission of the American Nuclear Society.*

TABLE 9.4 Values of the Constant $C(E_0)$ for the Expression Fitting the Allen et al. [20] Differential Dose Albedo Data for Fast Neutrons Incident on Various Materials

Material	$C(E_0)$ for Incident Energies of:								
	0.1 MeV	0.25 MeV	0.5 MeV	1.0 MeV	2.0 MeV	3.0 MeV	5.0 MeV	14.0 MeV	Fission
Concrete	0.0948	0.1027	0.1062	0.1323	0.1164	0.1030	0.0834	0.0552	0.1110
Dry soil[a]	0.0967	0.0895	0.1002	0.1272	0.1103	0.0979	0.0784	0.0535	0.1050
50% saturated soil[a]	0.0868	0.0957	0.0952	0.1209	0.1074	0.0926	0.0746	0.0533	0.1015
100% saturated soil[a]	0.0778	0.0818	0.0839	0.1054	0.0891	0.0791	0.0644	0.0463	0.0868
Iron	0.1750	0.1752	0.1801	0.1182	0.1477	0.1508	0.1158	0.0802	0.1366

[a]Desert soil.

Source: *Ref. 23.*

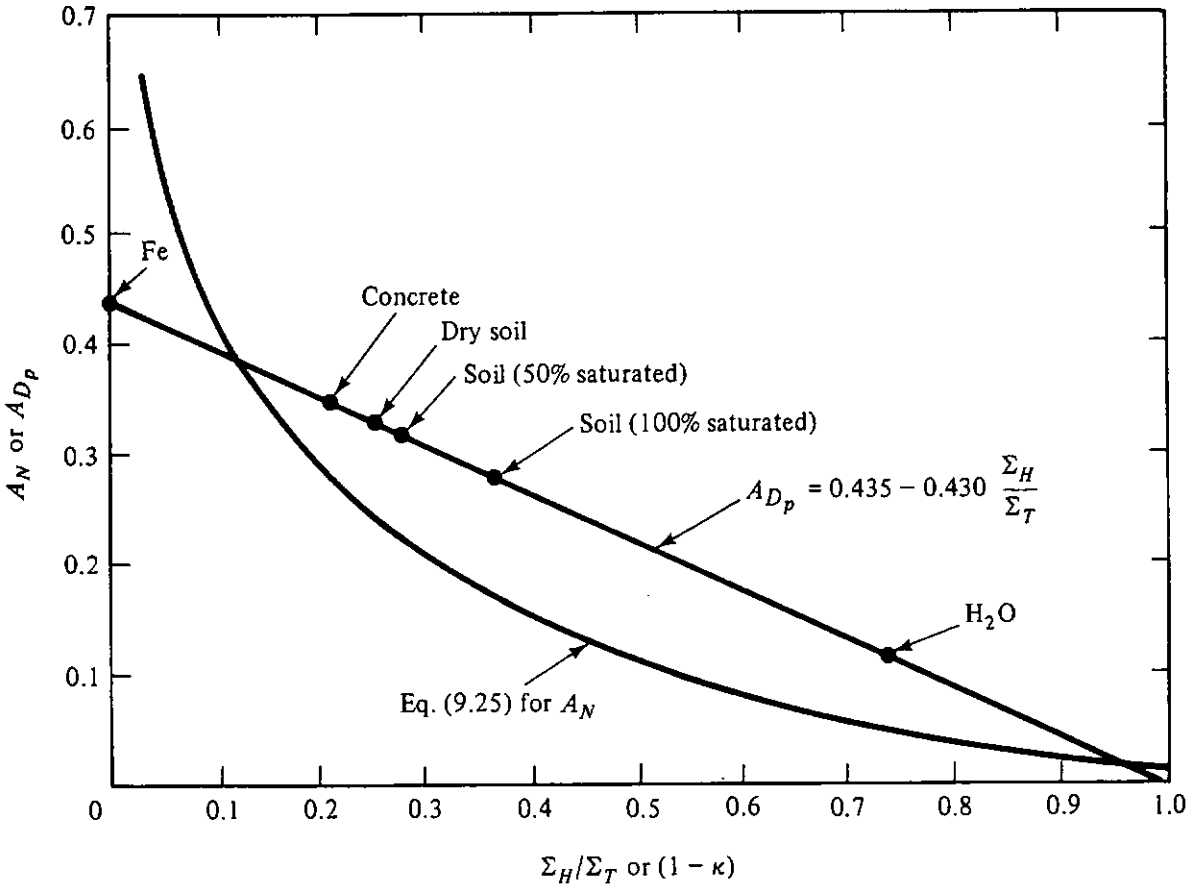

Figure 9.6 Absorbed dose albedo (based on maximum value in a phantom) for fission neutrons ($E_0 > 2$ MeV) normally incident on various media, as a function of Σ_H/Σ_T (older notation for μ_H/μ_t). (Based on data of French and Wells [23].)

function $B + C\cos\theta_s$, does not do this adequately enough to provide high accuracy [22].

A more complicated formula, but one that reproduces Monte Carlo results with discrepancies within about 10%, is the following, based on free-field tissue kerma response functions [18]:

$$\alpha_K(\Delta E_0, \theta_0; \theta, \psi) = \frac{1}{1 + K_1(\cos\theta_0/\cos\theta)} \sum_{m=0}^{8} G_m P_m(\cos\theta_s) + \frac{1}{1 + K_2(\Delta E_0, \theta_0, \theta)/\cos\theta} \sum_{k=0}^{4} B_k P_k(\cos\theta_s), \tag{9.31}$$

in which

$$K_2(\Delta E_0, \theta_0, \theta) = \sum_{i=0}^{2} (\cos\theta)^i \sum_{j=0}^{2} a_{ij}(\cos\theta_0)^j. \tag{9.32}$$

In this equation the symbol ΔE_0 implies that the incident beam does not contain neutrons of a single energy but contains neutrons distributed uniformly throughout a narrow range of energies. The constants in Eq. (9.32) are all functions of the incident energy range as well as of the reflecting medium. Values for the

constants are adjustable, in general, to permit fitting of the expression to data from experiments or Monte Carlo calculations. Values obtained for high-energy neutrons on reinforced concrete are given in Table 9.5.

The two terms in Eq. (9.31) represent the contributions from single collisions and multiple collisions, respectively. Each has a form close to that prescribed by Eq. (9.29). The summation in the first term represents a high order of expansion of the scattering cross section and should therefore bring about reproduction of the single-scattering contribution much more accurately, even for obliquely incident beams.

The fast-neutron albedo formulas given above are not based on precisely the same response function. However, since the albedo concept involves a *ratio* of response functions of the same type, it would not be expected that the albedo would vary much with the dosimetric quantity visualized for the detector measurement [see Eq. (9.9)]. The albedo values therefore for α_{D_p} and α_K should not be substantially different. By the same token, all the formulas above should be useful for predicting α_{H_p}, the albedo that is particularly useful for radiation protection purposes. It has been shown, for example, that Eq. (9.31) would provide data quite useful for the dose equivalent based on the maximum value in a phantom with an error not greater than about 20% [25].

For energies below the "fast" region, albedo functions found in the literature are almost always of the number type, α_N. An equation is available for incident neutrons of intermediate energy [19], but it is of purely empirical character and exhibits little in the way of application of the principles previously brought out in this text.

The behavior of thermal neutrons is sufficiently well represented by the idealizations leading to Eqs. (9.24) and (9.25) that those formulas, using the Chandrasekhar H function (Appendix 2), are believed to be quite accurate for differential and total number albedo. For thermal neutrons on ordinary concrete, the value of parameter κ is taken to be 0.974 [26].

Some older literature exists [2] which gives information on total albedo based on simplified descriptions of neutron interactions in thick media (e.g., by the diffusion approximation). These simplified approximations to neutron transport have been found to be very useful for describing thermal neutron total albedos, but unfortunately offer no information about the directional dependence of the reflected neutrons.

Particularly simple forms for thermal neutron albedo follow the same format as Eq. (9.30). The following formulas are based on empirical approximations to Monte Carlo data obtained for ordinary concrete [27]:

$$\alpha_N(\theta_0; \theta, \psi) = 0.21(\cos\theta_0)^{-1/3} \cos\theta \tag{9.33}$$

and

$$A_N(\theta_0) = 0.66(\cos\theta_0)^{-1/3}. \tag{9.34}$$

TABLE 9.5 Constants for Eqs. (9.31) and (9.32) for the Differential Dose Albedo Data for Fast Neutrons Incident on Concrete

Constant	Value of Constant for ΔE_0 of: 0.2–0.75 MeV	0.75–1.5 MeV	1.5–3 MeV	3–4 MeV	4–6 MeV	6–8 MeV
G_0	6.585(−2)[a]	7.045(−2)	7.211(−2)	7.024(−2)	6.856(−2)	5.899(−2)
G_1	5.048(−2)	4.393(−2)	5.845(−2)	7.452(−2)	8.294(−2)	6.039(−2)
G_2	3.710(−2)	7.088(−2)	5.968(−2)	1.000(−1)	9.517(−2)	7.524(−2)
G_3	1.544(−2)	1.898(−2)	2.729(−2)	5.591(−2)	7.761(−2)	8.140(−2)
G_4	7.837(−3)	2.408(−3)	1.190(−2)	2.646(−2)	4.292(−2)	6.622(−2)
G_5	0	−3.589(−3)	1.000(−3)	−6.908(−4)	1.824(−2)	3.056(−2)
G_6	0	0	4.637(−3)	−8.087(−4)	5.599(−3)	1.595(−2)
G_7	0	0	6.490(−3)	−1.459(−3)	5.288(−3)	1.277(−2)
G_8	0	0	0	−1.809(−3)	1.046(−2)	9.380(−3)
B_0	6.27(−2)	9.00(−2)	8.80(−2)	9.05(−2)	8.744(−2)	6.374(−2)
B_1	1.50(−2)	8.5(−3)	1.30(−2)	2.15(−2)	2.817(−2)	1.382(−2)
B_2	5.3(−3)	9.7(−3)	6.0(−3)	2.30(−2)	2.344(−2)	1.178(−2)
B_3	0	0	0	0	1.779(−2)	1.084(−2)
B_4	0	0	0	0	8.517(−3)	6.801(−3)
K_1	1.0	1.0	1.1	0.9	1.1	1.06
a_{00}	0.36	0.51	0.56	0.60	0.43	0.35
a_{01}	1.29	0.32	0.18	0.15	2.02	0.95
a_{02}	0	1.00	1.32	0.48	−0.38	0
a_{10}	0.06	−0.04	−0.14	−0.61	0.05	0.10
a_{11}	−3.06	−2.46	−2.76	−1.08	−9.13	−2.28
a_{12}	0	0	0	0	5.93	1.11
a_{20}	−0.20	0.05	0.05	0.32	0.04	0
a_{21}	1.68	0.95	1.14	0.30	5.97	0
a_{22}	0	0	0	0	−4.39	0

[a]Read as 6.585×10^{-2}, etc.

Source: *Refs. 2 and 18; by permission of the American Nuclear Society.*

9.1.7 Emission of Secondary Gamma Radiation from Incident Neutrons

Although not strictly an albedo concept, the emergence of secondary gamma photons from a surface on which neutrons are incident has been studied [2,25]. Concrete is the medium most often analyzed in this respect, but the results are somewhat variable because they are sensitive to the exact nature of the concrete. Furthermore, secondary photon production cross sections are not always well known for the various elemental ingredients; and calculational data are therefore not always reliable. A few general observations can be made, however:

1. As far as a dose-type albedo for fast neutrons is concerned, the secondary gamma radiation appears to make negligible contribution.
2. The differential results are essentially independent of azimuthal angle ψ, as might be expected from the assumption that secondary gamma emission from nuclei is practically isotropic.
3. On the basis of surface flow rate output to surface flow rate input, the results are not highly sensitive to $\cos \theta_0$.
4. Variation with respect to polar angle of emergence conforms approximately to $(\cos \theta)^{2/3}$.

9.2 RADIATION STREAMING THROUGH DUCTS

The treatment of radiation streaming through ducts is important throughout shielding design and analysis. Shield penetrations are unavoidable and in many instances radiation streaming is the critical design consideration. Protection against exposure of personnel requires careful placement of ducts and shadow shields.

Except in special cases, the analysis of radiation streaming requires a numerical transport calculation for a particular geometry and source. A common procedure is to use a Monte Carlo method to track particles within the duct and to use an albedo approximation to account for reflection of particles from duct walls. Straight cylindrical and rectangular ducts may be treated, in part, by analytical methods as long as the intensity of the incident radiation is uniform across the duct entrance and symmetrical in angular distribution about the duct axis. The radiation emerging from the duct may be divided into three components: a line-of-sight component, a component of radiation penetrating the duct walls near the entrance, and a component of radiation reflected from the duct walls.

Semiempirical analyses are available for photon penetration of two-legged rectangular ducts and for thermal neutron penetration of articulated cylindrical ducts. This chapter presents only an overview of the radiation streaming prob-

lem. For detailed analyses and case studies, the reader must consult the shielding literature.

9.2.1 Characterization of Incident Radiation

In this chapter, most of the discussion is limited to straight ducts whose first legs are perpendicular to an entrance plane. This entrance plane is considered as the effective source for the radiation entering the duct, and the source strength is assumed to be uniform across the plane of the duct mouth. The formulas developed below are sufficiently general that the source may be considered either as a distributed source of radioisotopic nature, or as a boundary between the duct and a volumetric source of radiation from which radiation emerges toward the duct opening. For an effectively isotropic source plane, the source strength can be referred to as S_A, the total emission rate in all directions per unit area in the source plane. However, because the particles emitted away from the duct opening are of no importance and because the emission is often quite anisotropic in direction (e.g., radiation escaping from a large volumetric source), it is more convenient to refer to the strength of the effective source plane in terms of j_n^+, the particle flow rate per unit area of the source plane that is emitted into the hemisphere toward the duct entrance. For isotropic source planes, j_n^+ is equivalent to $S_A/2$, while, for anisotropic sources, the relation is more complicated.

For a source plane producing a flux density $\phi_0(\theta)$ at the duct entrance, the effective source strength in particles per unit time per steradian per unit area in the source plane is equivalent to (see Section 2.2)

$$j_{n0}(\theta) = \phi_0(\theta) \cos \theta, \tag{9.35}$$

in which the angular distribution of the flux density is assumed to depend only on the angle θ between the normal to the source plane and the direction under consideration. For simplicity in the following subsections, the particles emitted from the source will be assumed to be monoenergetic. The extension to polyenergetic sources is readily accomplished by representing the sources as a sum of essentially monoenergetic components.

Sometimes it is convenient to represent the source as if it were concentrated at the center of the source plane, on the duct axis. If A is the cross-sectional area of the duct, then the equivalent point source angular distribution per steradian is

$$S(\theta) = \mathrm{A} j_{n0}(\theta) = \mathrm{A} \cos \theta \phi_0(\theta). \tag{9.36}$$

With azimuthal symmetry, the source or the flow rate (as an equivalent source) can be characterized by an expansion in integral powers of $\cos \theta$ (see Sections 2.2 and 2.5), starting from the "zeroth" power. Frequently, the expansion can be represented by a single power of $\cos \theta$, and in the discussion to follow, this simplification will be assumed. Equations are expressed in general

terms, using the notation of Chapter 6, which can be easily interpreted in terms applicable either to a radioisotopic source or to a volume leakage flow rate (or flux density).

9.2.2 Line-of-Sight Component for Straight Ducts

The component of radiation streaming directly down a straight duct without interacting with the walls is detected as in the case of a small area source having a detector on its axis. If the duct has no attenuating material in it (air, in practical cases, may be assumed to have no attenuating effect), the formulas of Section 6.4.3 relative to disk or rectangular sources without attenuating medium apply. If the ducts are filled with an attenuating medium, the formulas of that section which consider such attenuation apply.

In a general way (see Fig. 9.7), the detector response at location P on the duct centerline due to incident monoenergetic particles passing through differential area dA in the entrance plane is obtainable from Eq. (2.29):

$$R^{(0)}(P) = \mathcal{R}(E_0) \int \phi_0(\theta) d\Omega = \mathcal{R}(E_0) \int j_{n0}(\theta) \sec\theta \, d\Omega, \tag{9.37}$$

where $\phi_0(\theta)$ is the angular flux density at the duct entrance, taken to be composed of monoenergetic particles of energy E_0, and $j_{n0}(\theta)$ is the corresponding angular flow rate. In Eq. (9.37), the integration is over the solid angle subtended by the source plane at the point P.

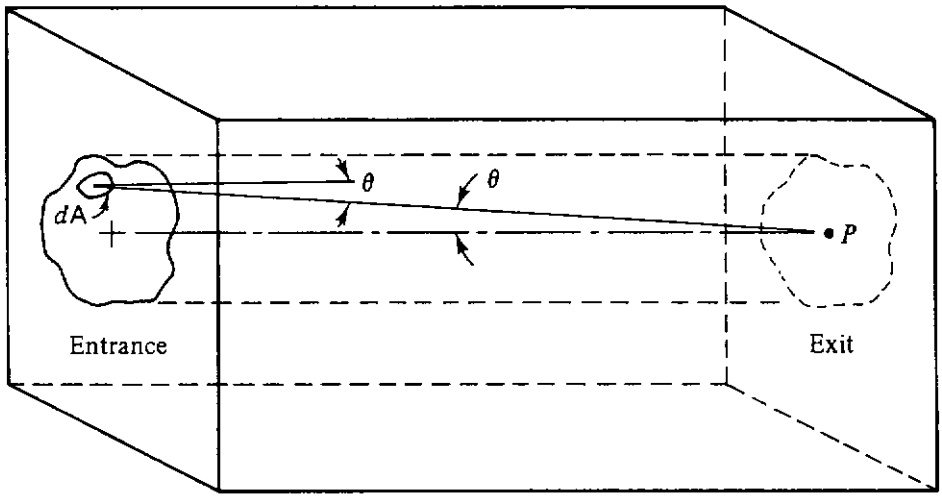

Figure 9.7 Detector response at point P on duct axis due to passage of particles through area dA in duct entrance plane.

Cylindrical duct. For point P on the axis of a cylindrical duct of radius a and length Z, the response can be determined by use of the appropriate equation selected from the sequence from Eqs. (6.38) through (6.49), in which $m = 0$ for an isotropic source or an isotropic flow rate at the source plane, and $m = 1$ for a cosine source or cosine flow rate (isotropic flux density) at the source plane.

Rectangular duct. Evaluation of the line-of-sight component for a rectangular duct is illustrated in Fig. 6.14. The response at point P on the axis of the duct is obtained by use of the appropriate equation selected from the list of equations from Eqs. (6.50) through (6.53), in which the value of m has the same meaning as indicated above for a cylindrical duct source.

9.2.3 Wall-Penetration Component for Straight Ducts

Consider the cylindrical duct illustrated in Fig. 9.8. The duct of length Z and radius a is in a medium with attenuation coefficient k. The wall-penetration component is given by the equation[4]

$$R^{(w)}(P) = (m + 1)\mathcal{R}j_n^+ \int_{\theta_0}^{\pi/2} d\theta \sin\theta \cos^{m-1}\theta \exp[-k(Z \sec\theta - a \csc\theta)], \quad (9.38)$$

where $\theta_0 = \tan^{-1} a/Z$. Equation (9.38) follows from Eq. (9.37) with $j_{n0}(\theta) = [(m + 1)/(2\pi)]j_n^+ \cos^m\theta$ and with the inclusion of the exponential attenuation through the duct wall. This result can be expressed as the ratio of the detector

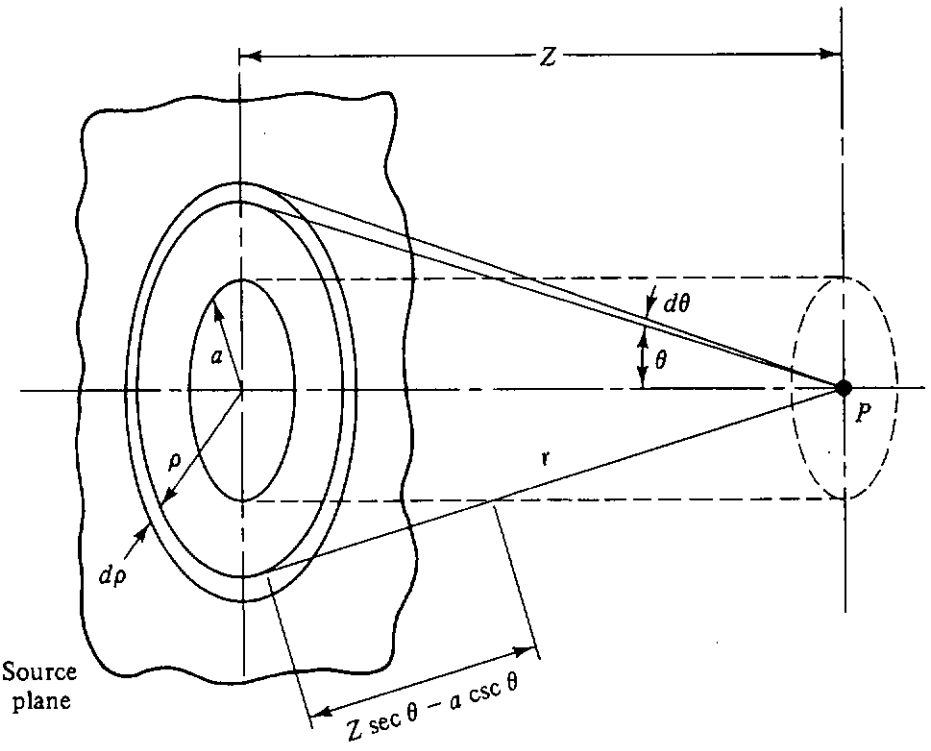

Figure 9.8 Geometry for evaluation of the wall-penetration component of detector response for a straight, cylindrical duct. The particle flow rate in the source plane is $j_n(\theta) = j_n^+(m + 1)\cos^m\theta/2\pi$, where j_n^+ is the total flow rate into the hemisphere toward the duct.

[4]If k is taken to be simply the attenuation coefficient, this treatment leads to a value for the wall-penetration component for uncollided particles. To account approximately for buildup, an effective attenuation coefficient may be applied as discussed in Sections 6.3 and 6.4.

response at point P on the duct axis to that at the duct entrance [Eq. (6.46)]:

$$\frac{R^{(w)}(P)}{R^{(0)}(0)} = m \int_0^{[1+(a/Z)^2]^{-1/2}} dx\, x^{m-1}\, e^{-kZ[x^{-1}-(a/Z)(1-x^2)^{-1/2}]}, \tag{9.39}$$

that is,

$$\frac{R^{(w)}(P)}{R^{(0)}(0)} = f\left(m, kZ, \frac{a}{Z}\right). \tag{9.40}$$

This function has been evaluated by Trubey [28] for $m = 0$ and 1, for $0.1 \leq kZ \leq 5.0$, and for $0.001 \leq a/Z \leq 1$. The result is illustrated in Fig. 9.9 for the case $m = 1$, an isotropic incident flux. Also shown in the figure is the ratio $R^{(0)}(P)/R^{(0)}(0)$ for the line-of-sight component.

These results for a cylindrical duct may be applied to a rectangular duct (Fig. 6.14) if the approximation is made that the solid angle subtended at

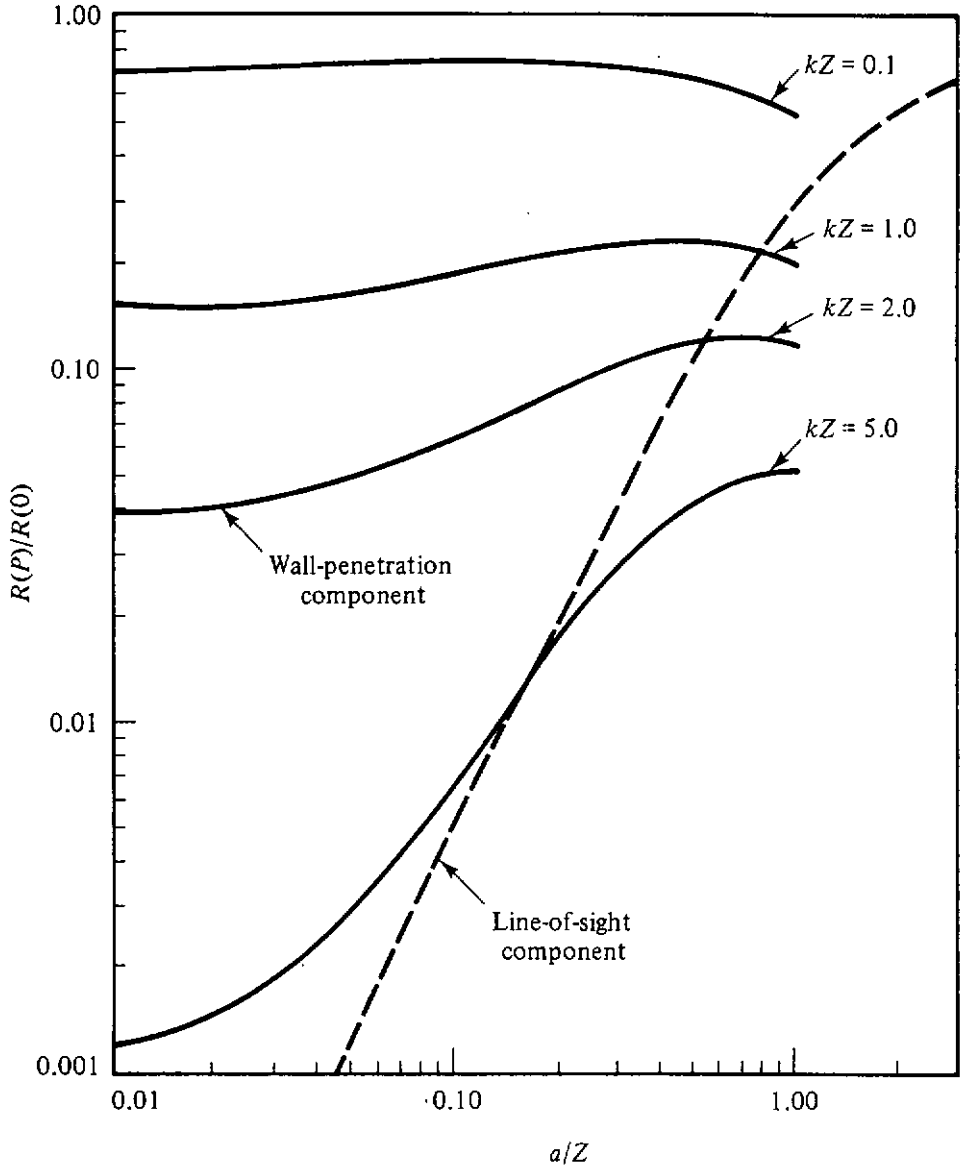

Figure 9.9 Wall-penetration and line-of-sight components of the ratio $R(P)/R(0)$ for uncollided particles at the exit of a cylindrical duct. The flux density at the duct entrance is isotropic.

point P by the rectangular duct entrance is the same as that of an equivalent circular entrance. Under this approximation,

$$\cos\theta_0 = 1 - \frac{2}{\pi}\tan^{-1}[\epsilon\eta^{-1}(1 + \epsilon^2 + \eta^2)^{-1/2}]. \tag{9.41}$$

9.2.4 Single Wall-Reflection Component in Straight, Cylindrical Ducts

This development is only for cylindrical ducts, although numerical results are likely to be similar for rectangular ducts with the same cross-sectional area. It is assumed at this time that the particles entering the duct at the entrance face are or may be considered as coming from a point source on the duct axis. At the moment, only singly reflected particles are taken into account. Single reflection cannot be expected to dominate the total reflected contribution to the detector response at the exit end of the duct under all conditions, as, for example, in the case of thermal neutrons streaming down a long, thin duct. Nevertheless, under many circumstances, the single reflection may be the major part of the total reflected contribution; and an estimate can sometimes be made of the multiple-reflection contribution on the basis of the single-reflection contribution, as will be seen later.

The geometry and notation for this situation are as given in Fig. 9.10. The equivalent point source on the axis is located at point P_0 at the duct entrance and the detector at the other end of the duct at P. Call the point-source strength $S(\theta)$ particles per second per steradian, in recognition of the assumption made here that its angular dependence involves only the angle θ; and further assume that the source particles are monoenergetic. Consider the reflection from the circular strip of area $d\mathrm{A} = 2\pi a\, dz$. That part of the response at location P due

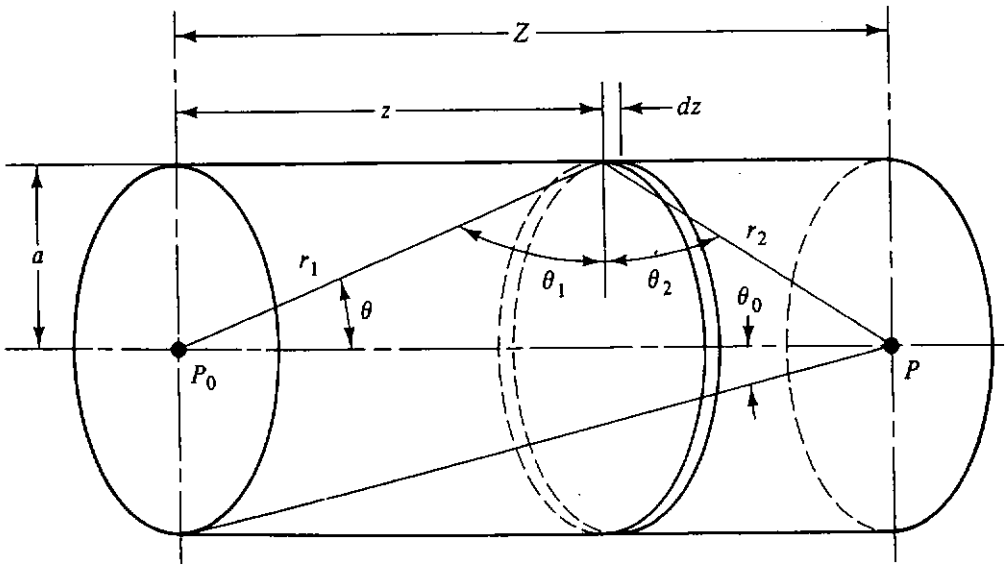

Figure 9.10 Geometry for evaluation of single wall reflection in a straight, cylindrical duct.

to the reflection from area $d\mathrm{A}$ is

$$dR^{(1)}(P) = \mathcal{R}(E_0)\, d\mathrm{A}\, S(\theta) \frac{\cos\theta_1\, \alpha_R(E_0, \theta_1; \theta_2, 0)}{r_1^2 r_2^2} \tag{9.42}$$

in accordance with Eq. (9.8). (Note that the albedo function has zero for the value of the azimuthal angle argument.) This leads directly to

$$R^{(1)}(P) = 2\pi a^2 \mathcal{R}(E_0) \int_0^Z \frac{S(\theta)\alpha_R(E_0, \theta_1; \theta_2, 0)}{r_1^3 r_2^2}\, dz. \tag{9.43}$$

This equation will be applied to three specific cases and one combination case, for illustration.

Case A. Suppose that the source is plane isotropic (isotropic flow rate into the entrance face of the duct), uniformly distributed over the duct entrance plane. One should then take $S(\theta)$ as $a^2 j_n^+/2$, where j_n^+, a constant, has units $\mathrm{cm}^{-2}\,\mathrm{s}^{-1}$. Also, assume for this case that the wall albedo is isotropic, so that $\alpha_R = A_R(E_0)/2\pi$. Equation (9.43) becomes

$$R^{(1)}(P) = \tfrac{1}{2} a^4 \mathcal{R}(E_0) j_n^+ A_R \int_0^Z \frac{1}{(a^2 + z^2)^{3/2}[a^2 + (Z - z)^2]}\, dz; \tag{9.44}$$

or, in terms of the nondimensional variable $t \equiv z/Z$ and the parameter $\beta \equiv a/Z$,

$$R^{(1)}(P) = \tfrac{1}{2}\beta^2 \mathcal{R}(E_0) j_n^+ A_R I_i(\beta), \tag{9.45}$$

where

$$I_i(\beta) \equiv \int_0^1 \frac{\beta^2}{(\beta^2 + t^2)^{3/2}[\beta^2 + (1 - t)^2]}\, dt. \tag{9.46}$$

It can be shown that, for small values of β, $I_i \simeq 1$ (see Problem 9.1). In fact, Fig. 9.11 shows exact values of the integral over a wide range of values of β. One sees that I_i approaches unity as β approaches zero, or Z/a approaches infinity. It is also of significance that most of the value of the integral is obtained for values of t very near zero, which leads to the conclusion that in this case the single-reflection contribution comes largely from portions of the duct very near the source plane.

Case B. As one can generally perceive from Section 9.1, a cosine albedo is more reasonable than an isotropic albedo [see Eq. (9.17)]. If, in the development above, one takes $\alpha_R = A_R(E_0)\cos\theta_2/\pi$, the following equation results:

$$R^{(1)}(P) = 2\beta^3 \mathcal{R}(E_0) j_n^+ A_R I_{c,0}(\beta), \tag{9.47}$$

where

$$I_{c,0}(\beta) \equiv \int_0^1 \frac{0.5\beta^2}{(\beta^2 + t^2)^{3/2}[\beta^2 + (1 - t)^2]^{3/2}}\, dt. \tag{9.48}$$

Values of this integral have also been calculated and found to approach unity as β approaches zero, or Z/a approaches infinity (see Fig. 9.11). The integral above is symmetric between the two limits, and detailed analysis shows

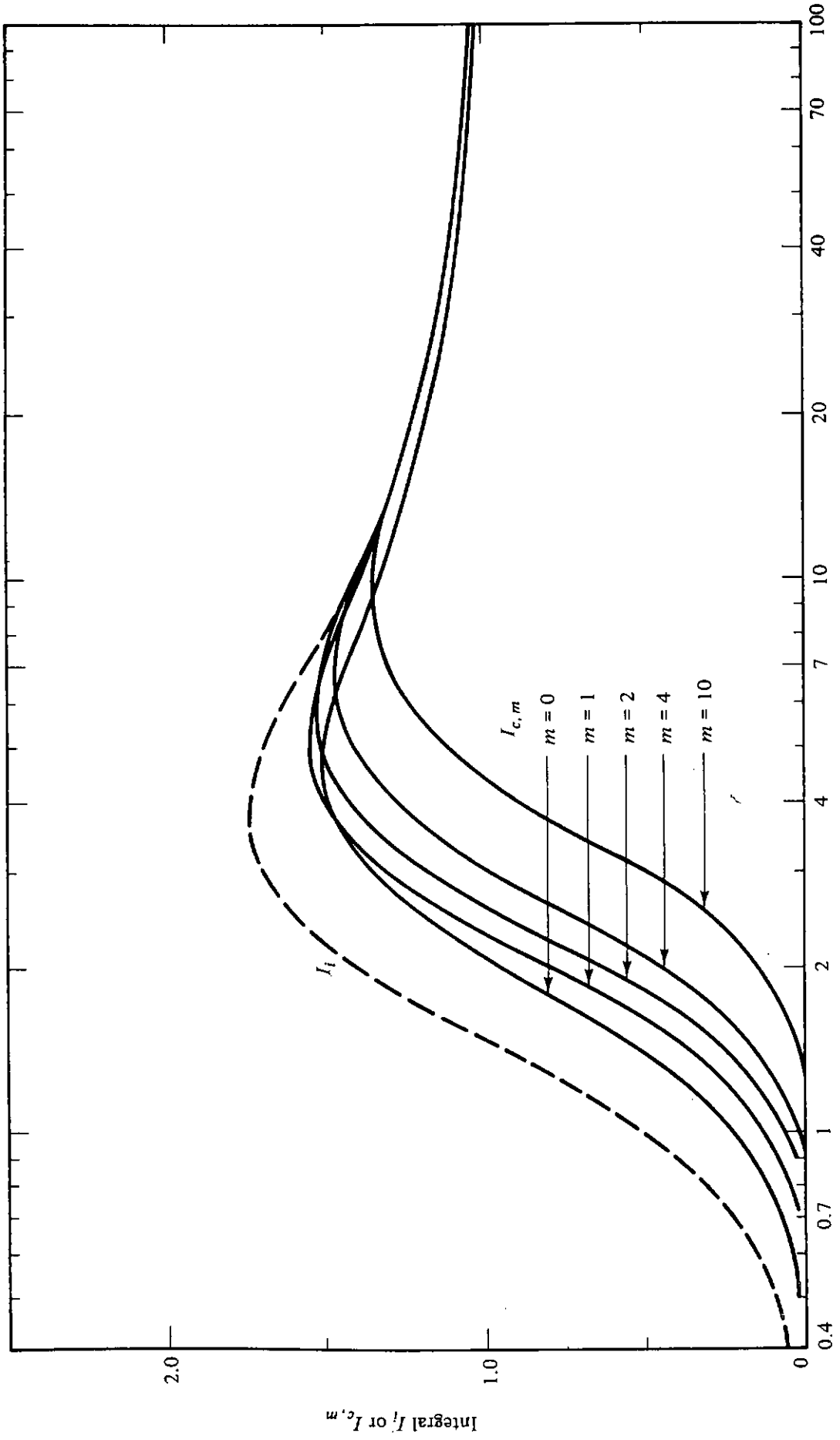

Figure 9.11 Plot of the integrals I_l and $I_{c,m}$ defined by Eqs. (9.46) and (9.51), respectively. As the length of the cylindrical duct becomes much greater than its radius (i.e., as $\beta \equiv a/Z \longrightarrow 0$), both of these integrals approach unity.

that the main contributions to the detector response come equally from locations on the wall near both source and detector.

Combination of cases A and B (Simon–Clifford formula). The Simon–Clifford formula for $R^{(1)}$ was derived[29] on the assumption that the total albedo for the wall is some combination of an isotropic part A_i and a cosine part A_c, so that A_R is to be taken as $A_i + A_c$; then $\alpha_R = (A_i/2\pi) + (A_c \cos\theta_2/\pi)$. In this case,

$$R^{(1)}(P) = \tfrac{1}{2}\beta^2 \mathcal{R}(E_0) j_n^+ [A_i I_i(\beta) + 4\beta A_c I_{c,0}(\beta)]. \tag{9.49}$$

The case above represents early efforts to solve the problem of a straight cylindrical duct through the biological shield of a reactor. The entrance plane for such cases is very near the core or at least the reflector surrounding the core. The assumption of an isotropic plane source at the entrance means an isotropic flow rate leaking from the reactor, which in turn implies a leakage flux density of a secant character. Since the secant function approaches infinity as the angle θ approaches a right angle, this assumption for the source distribution is somewhat suspect. The assumed behavior of the albedo function, somewhere between an isotropic function and a cosine function, is also somewhat crude but is consistent with the slight information available at the time of the Simon–Clifford development.

Case C. This case is somewhat more realistic than the previous cases, and is intended to represent the situation of a straight cylindrical duct through a reactor shield. Suppose that the source is the flow rate of particles in a given energy interval, at the surface of the reactor. Rather than an isotropic flow rate, it is more reasonable to expect the flow rate to be peaked in the outward direction so that $j_{n0}(\theta)$ is proportional to $\cos^m\theta$. Let j_n^+ be the total outward reactor-leaking flow rate at the entrance to the duct. Then the effective point-source strength $S(\theta)$ becomes equivalent to $(a^2/2)(m+1)j_n^+ \cos^m\theta$.

For the albedo function, the cosine distribution of case B, which appears more consistent with formulas such as that of Eq. (9.30), can be tried. Thus, for this case, $\alpha_R = A_R(E_0)\cos\theta_2/\pi$.

Substitution into Eq. (9.43) readily leads to

$$R^{(1)}(P) = (m+2)\beta^3 \mathcal{R}(E_0) j_n^+ A_R(E_0) I_{c,m}(\beta), \tag{9.50}$$

where

$$I_{c,m}(\beta) \equiv \frac{m+1}{m+2}\int_0^1 \frac{dt\, t^m \beta^2}{(\beta^2 + t^2)^{(m+3)/2}[\beta^2 + (1-t)^2]^{3/2}}. \tag{9.51}$$

As before, this quantity can be shown to be approximately equal to 1 for small values of β. Exact values of $I_{c,m}$ for various values of Z/a are given in Fig. 9.11. Detailed analysis of these integrals shows that for $m > 0$, most of the single-reflection contributions to the detector response comes from portions of the duct wall near the detector end.

9.2.5 Multiple Wall-Reflection Component in Straight, Cylindrical Ducts

Simon and Clifford[29] have shown that, for isotropic or cosine albedos (cases A and B, above) and $Z \gg a$, multiple reflection in the walls of cylindrical ducts may be taken into account approximately by replacement of the total albedo A_R with

$$A'_R = \frac{A_R}{1 - A_R}. \tag{9.52}$$

This approximation will be applied to the cases of isotropic and cosine albedos, as an extension of the previous discussion of single reflections in straight cylindrical ducts. This method of approximation has been justified analytically only for an isotropic source or incident flow rate, although it is intuitively appealing as a widely applicable rule, as may be seen from the following analyses.

Case A: Isotropic source, isotropic albedo. For an isotropic incident source of strength $S_A = 2j_n^+(\text{cm}^{-2}\,\text{s}^{-1})$ in the duct entrance plane, the line-of-sight component to the response of a detector in the center of the duct exit is

$$R^{(0)} = \tfrac{1}{2}\beta^2 \mathcal{R}(E_0) j_n^+. \tag{9.53}$$

Substitution of A'_R from Eq. (9.52) for A_R in Eq. (9.45) leads to the following equation for the response to wall-scattered radiation:

$$R^{(s)} = \tfrac{1}{2}\beta^2 \mathcal{R}(E_0) j_n^+ A'_R = R^{(0)} \frac{A_R}{1 - A_R}, \tag{9.54}$$

in which the factor I_t has been taken as unity, since the approximation applies only for $Z \gg a$. The total detector response, $R^{(0)} + R^{(s)}$, is thus

$$R = R^{(0)}(1 + A_R + A_R^2 + A_R^3 + \cdots). \tag{9.55}$$

This result leads to a simple rule that the contributions from successive orders of reflection, including the zeroth order (line-of-sight) component, are in a constant ratio A_R.

Case B: Isotropic source, cosine albedo. Modification of Eq. (9.47) to account for multiple scattering leads to the result that

$$R^{(s)} = R^{(0)} 4\beta A'_R = R^{(1)}(1 + A_R + A_R^2 + \cdots). \tag{9.56}$$

In this case, contributions from successive orders of scattering, but *not* including the zeroth order (line-of-sight) component, are in a constant ratio A_R.

9.2.6 Transmission of Radiation through Two-Legged Rectangular Ducts

An analytical treatment of radiation transmission through multiple-legged ducts of arbitrary cross section is beyond the scope of this text. Approximation techniques that might be employed in such a general case are illustrated here in

the analysis of radiation transmission through two-legged rectangular ducts. Details of the analysis, and refinements to account for lip and corner penetration, have been described by LeDoux and Chilton [30].

The geometry for the analysis is illustrated in Fig. 9.12. The method of analysis is applicable for ducts whose lengths are appreciably greater than widths and heights and whose walls are of uniform composition and at least one mean-free-path thick. The detector response $R(P)$ is evaluated at point P in the center of the duct exit. Radiation incident on the duct is approximated by a point source $S(\theta)$ at the center of the duct entrance. If the angular flux density at the duct entrance is $\phi_0(\theta)$, the point-source strength $S(\theta)$ is taken as the product of the entrance area and $\cos\theta\,\phi_0(\theta)$. The method is applicable to incident radiation whose angular distribution is azimuthally symmetric about the axis of the entrance duct. Although the method is formulated for incident particles monoenergetic at E_0, it may be extended to polyenergetic sources in multigroup or other approximations.

The method is based on the approximation that $R(P)$ consists principally of responses to radiation reflected from prime scattering areas, that is, areas visible to both source and detector and from which radiation may reach the detector after only a single reflection. Four prime areas may be identified in Fig. 9.12. Areas A_1 and A_2 on the walls, and areas A_3 on the floor and ceiling (considering the figure to be a plan view). Reflection from each area is treated as though it occurred from a single point at or near the centroid of the area. Thus, the detector response may be expressed as

$$R(P) = R_1(P) + R_2(P) + 2R_3(P), \tag{9.57}$$

where, according to Eq. (9.8),[5]

$$R_1(P) = \frac{\mathcal{R}(E_0)A_1 S(\pi/2 - \theta_1')\cos\theta_1' \alpha_R(E_0, \theta_1'; 0, 0)}{(r_1 r_2)^2}, \tag{9.58}$$

$$R_2(P) = \frac{\mathcal{R}(E_0)A_2 S(0)\alpha_R(E_0, 0; \theta_2', 0)}{(r_1' r_2')^2}, \tag{9.59}$$

$$R_3(P) = \frac{\mathcal{R}(E_0)A_3 S(\pi/2 - \theta_1'')\cos\theta_1'' \alpha_R(E_0, \theta_1''; \theta_2'', \pi/2)}{(r_1'' r_2'')^2}, \tag{9.60}$$

in which the arguments of the albedo function $\alpha_R(E_0, \theta_0; \theta, \psi)$ are as illustrated in Figs. 9.2 and 9.3.

9.2.7 Approximate Methods for Obliquely Incident Radiation

Transmission of obliquely incident radiation through a long duct may be treated on the basis of the approximation that the detector response is due primarily to radiation reflected from a prime scattering area at the lip of the duct, as illustrated in Fig. 9.13.

[5] $S_p\,\hat{R}$ has been replaced by $S(\theta)\mathcal{R}(E_0)$ for convenience. See the discussion of Section 6.4.1 for an explanation of this preference.

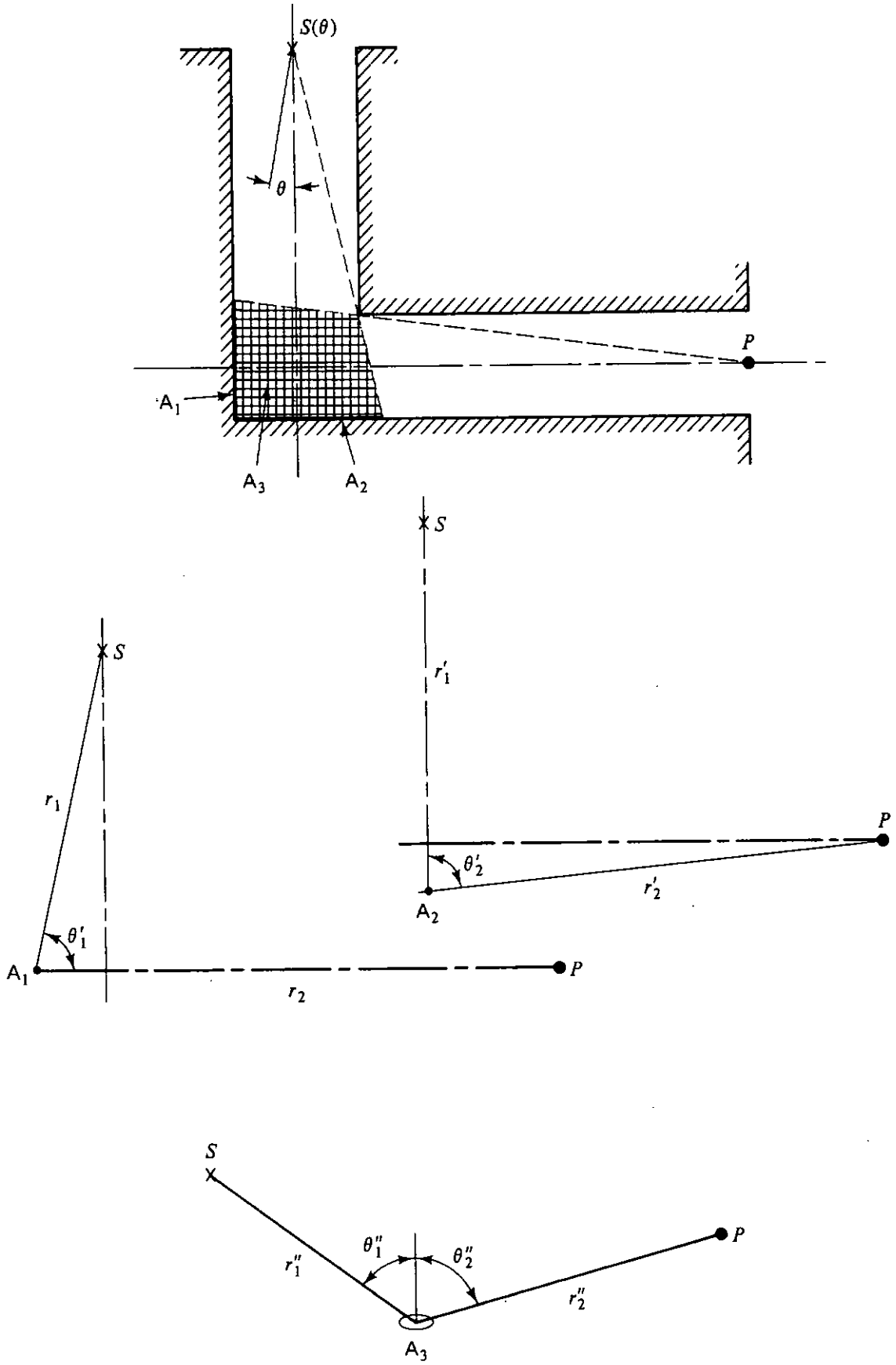

Figure 9.12 Prime scattering areas in radiation transmission through two-legged rectangular ducts.

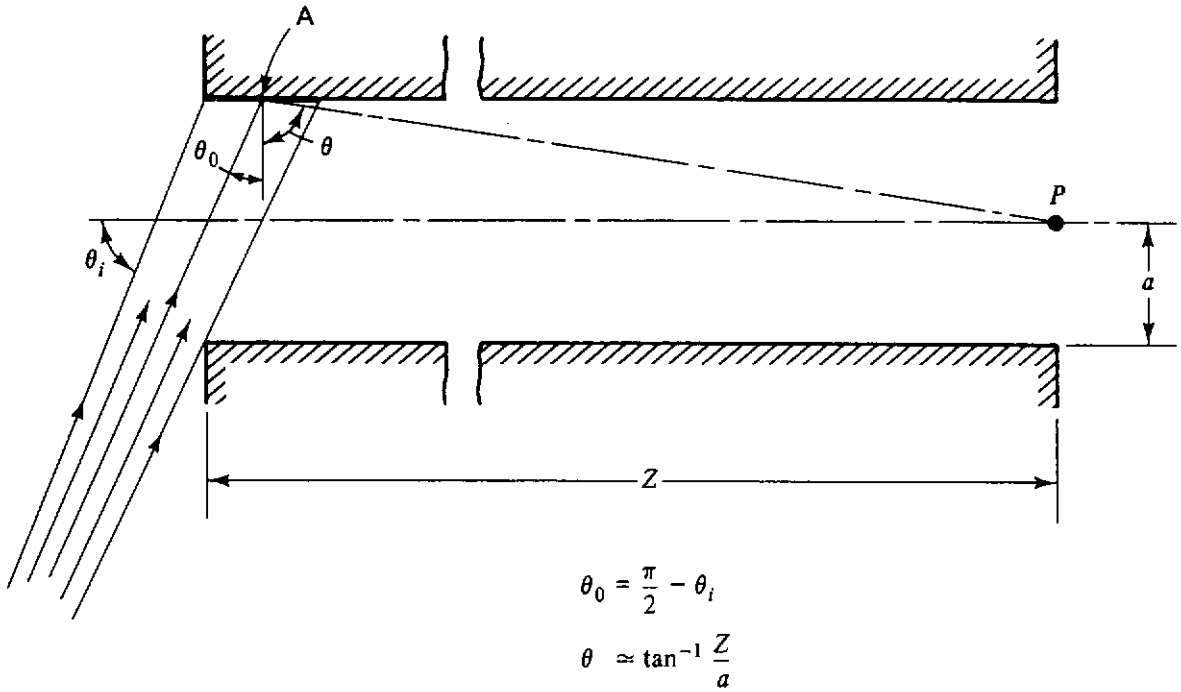

Figure 9.13 Prime scattering areas for radiation incident obliquely on the entrance of a duct.

Suppose that the duct is illuminated by a beam of particles of flux density ϕ_0, at energy E_0, all at angle θ_i to the duct axis. The prime scattering area may be evaluated readily for rectangular ducts with the beam parallel to a pair of walls. For a circular duct of radius a, the area is

$$\mathrm{A} = 4a^2 \cot \theta_i. \tag{9.61}$$

This is the same as the prime scattering area for a duct of square cross section (a by a) into which the incident radiation is parallel to one set of walls and inclined at angle θ_i to the other pair. For this square duct, as well as for the circular duct, the detector response to singly reflected particles may be evaluated approximately by the methods of Section 9.1.2 as

$$R(P) \simeq \frac{\mathfrak{R}(E_0)\mathrm{A}\phi_0 \cos(\pi/2 - \theta_i)\alpha_R(E_0, \pi/2 - \theta_i; \tan^{-1} Z/a, 0)}{Z^2}. \tag{9.62}$$

Use of this equation for a circular duct would be highly approximate. It would tend to underestimate the response because of the use of a single argument, $\pi/2 - \theta_i$, for the angle of incidence on the duct wall. However, there would be a compensating overestimate, in that all particles would be assumed to scatter with no change in azimuth (i.e., $\psi = 0$).

9.2.8 Scaling Laws for Duct Penetration

One might note that the preceding formulas for detector response at the end of a duct are independent of the duct absolute dimensions but depend only on relative dimensions, such as β (or a/Z). This implies an independence of geometric scale, and such a relationship is a good test of the validity of any

formula for duct penetration, whether analytical or empirical in origin. Such a theorem has been provided by Diaz and Chilton [31] and is easily explained, although the rigorous demonstration is beyond the scope of this text.

Consider two duct systems as shown in Fig. 9.14. Two points P_a and P_b are said to be *corresponding* points if the coordinates of P_b in its system are equal to the coordinates of P_a in its system multiplied by the scaling constant, ξ. Then, both the differential and the total radiation flux density (and all detector responses which depend on flux density) are identical at corresponding points in the two duct systems provided that the following circumstances are valid:

1. The two ducts, although differing possibly in volume, are similar geometrically by the scaling constant ξ and have at corresponding points on the respective walls the same or equivalent materials (i.e., materials having the same albedo function).
2. The energy spectrum, the directional distribution, and the strength per

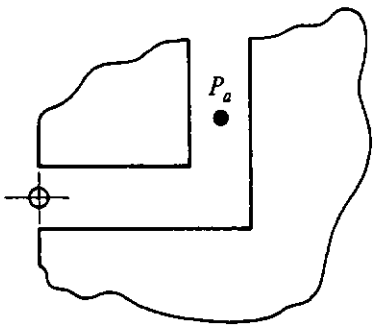

(a)

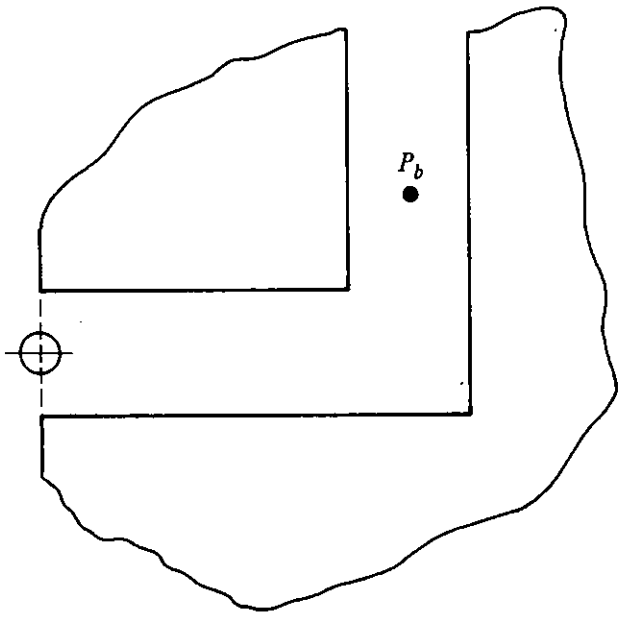

(b)

Figure 9.14 Geometrically similar duct systems, with corresponding points.

unit surface area of the source that introduces the radiation into the duct are identical at corresponding points in the two systems.

3. The radiation transport within the duct walls can be ignored; and radiation emerging from a point of the wall, aside from that introduced as a source, is correlated completely with radiation incident at the same point, by means of an albedo function.

Requirement 3 implies that the dimensions of the duct (such as its width or its diameter) should be appreciably larger than the relaxation distance of the radiation in the wall medium. It also implies that those contributions which involve penetration rather than reflection, such as the wall-penetration at the entrance face or the lip penetration at the intersection edge of two legs of a duct, are not covered by the theorem. (Fortunately, for large ducts, these contributions are usually of secondary importance [30].)

The theorem is independent of the shape of the duct or the number of legs and is particularly useful for extending experimental findings to situations which are geometrically similar but on a different scale. A particularly important example will serve to illustrate this point.

Figure 9.15 shows the results of experiments and calculations carried out by Maerker and Muckenthaler [32] to determine thermal neutron flux densities along the centerlines of one-, two-, and three-legged concrete ducts of 3-ft²

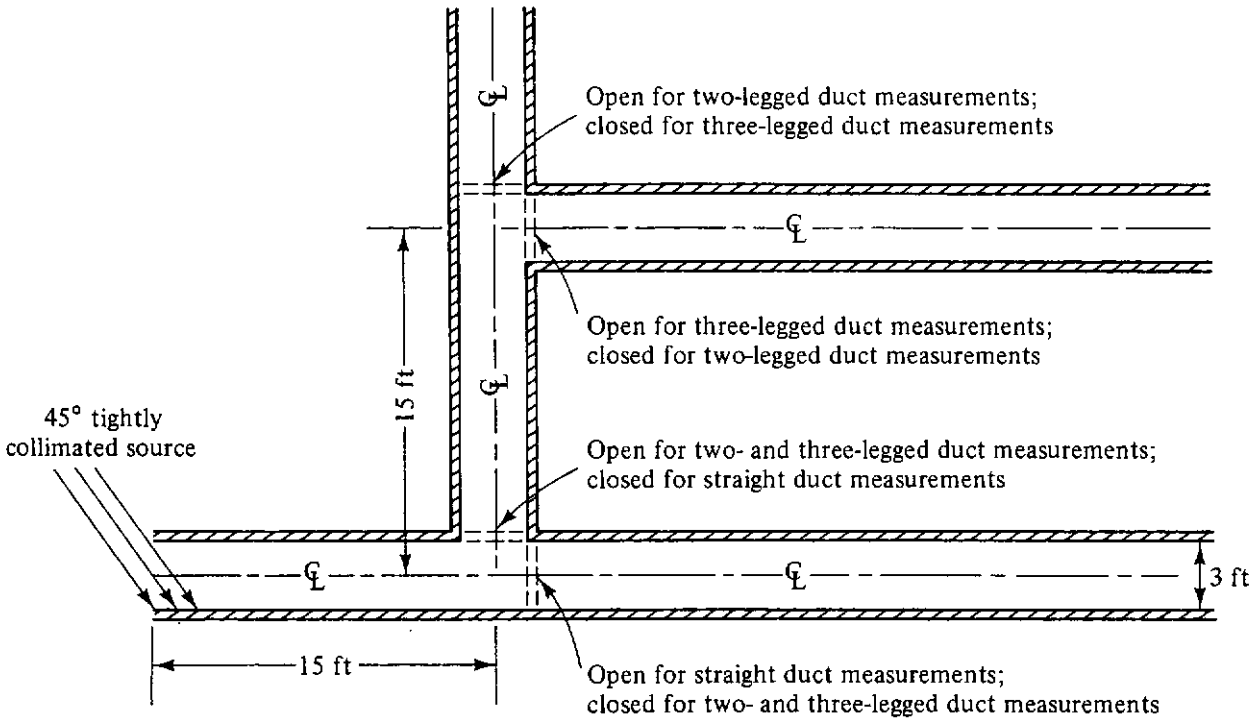

Figure 9.15a Duct system studied by Maerker and Muckenthaler for thermal-neutron streaming along the centerline [32]. (a) Diagram of the concrete duct system with square duct cross section. (Continued) (Reproduced by permission of the American Nuclear Society.)

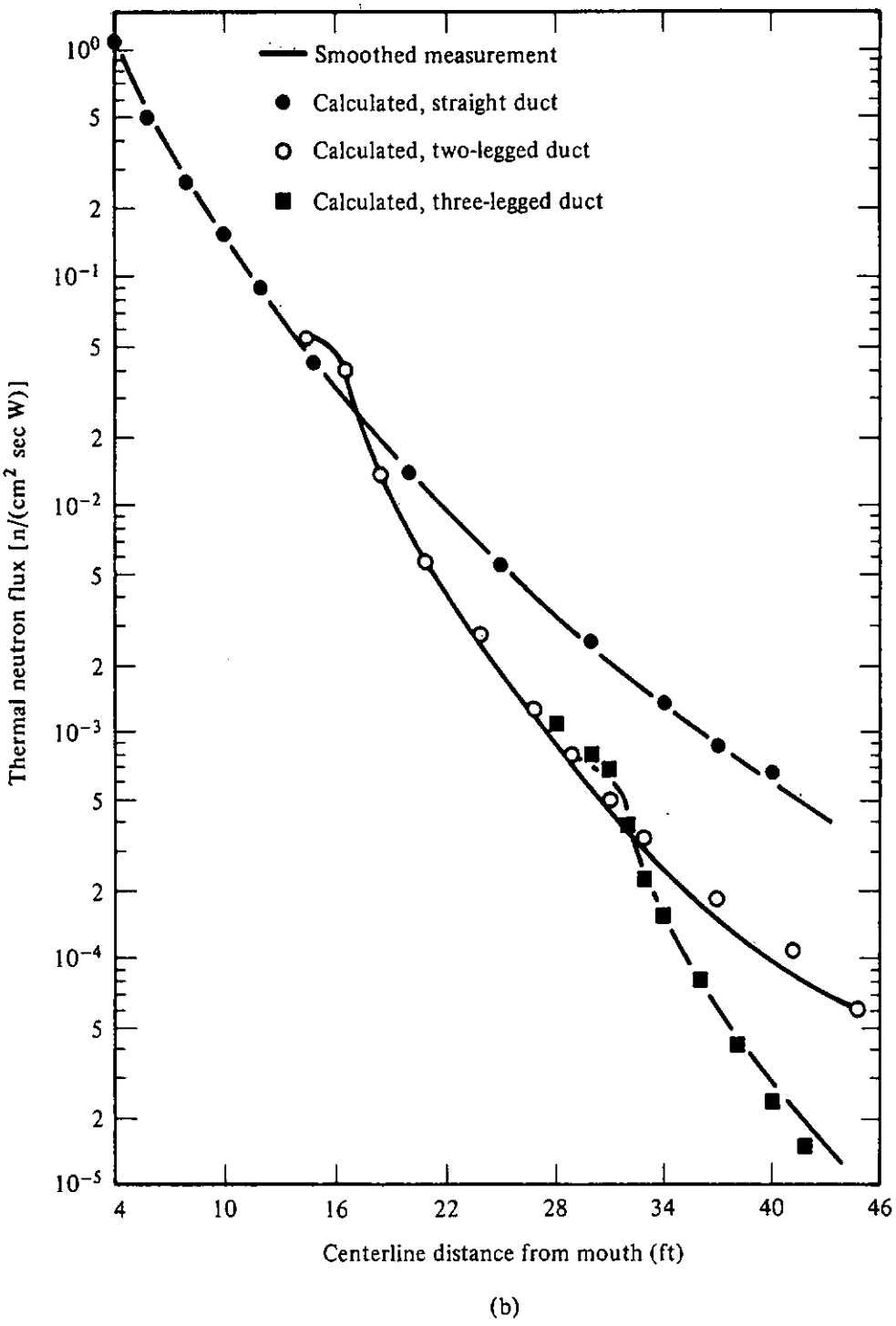

Figure 9.15b (b) Results of measurements and Monte Carlo calculations for thermal-neutron flux density along the centerline of the system, with a flow rate incident on the wall near the entrance of 1.97 thermal neutrons per square centimeter per watt. (Reproduced by permission of the American Nuclear Society.)

cross section. The source in this case is a beam of thermal neutrons parallel to one pair of duct walls (in the plane of the figure) and incident at 45° to the entrance face. The scaling theorem indicates that, with the same beam flux density, the results at corresponding points down the duct system would be the same regardless of duct size (except for very small ducts). For example, if the

neutron flux density per unit power[6] at 24 ft along the centerline from the duct mouth in the 3 ft by 3 ft (0.91 m by 0.91 m) two-legged system in Fig. 9.15 is 2.6×10^{-3} W^{-1} cm^{-2} s^{-1}, the same flux density per watt would exist under the same source condition at a distance of 16 ft (4.9 m) into a two-legged 2 ft by 2 ft (0.61 m by 0.61 m) duct in which the legs are 10 ft (9.1 m) long.

Note that the data displayed in Fig. 9.15 may be even more widely useful than the scaling theorem shows. For one thing, it appears that successive limbs of the composite curve for a multilegged duct are very similar in appearance; and it is easy to postulate without excessive error that there is a single governing curve which is valid for each leg, starting over at the point that one leg ends and another begins. This permits one to put together composite curves for ducts in which the scaled leg lengths (i.e., the duct length/width ratio) are different from the original 5: 1 ratio in one or more legs. Extension of the curves to additional legs is easily visualized.

Similarly, it has been shown [33] that, by the time the neutrons have streamed down toward the end of the second leg or beyond in this (or similar) duct systems, they are all largely thermalized, regardless of the spectrum of the original neutron beam. Thus, at such penetration distances, one may assume that the original energy of each neutron is unimportant; and the curves provided in Fig. 9.15 can be used even for fast-neutron sources. Finally, it has been shown [33] that the wall-produced secondary-gamma absorbed dose rate for a detector at a given point on the centerline is approximately equal to the absorbed dose rate at that point due to the thermal neutrons.

9.3 TREATMENT OF SHIELD HETEROGENEITIES

Analysis of shields containing certain types of inhomogeneities may be carried out within the context of the ray technique (Section 6.4). Examples include small voids or lumps randomly distributed within a continuous phase, and well-defined regions such as ducts transverse to the direction of radiation penetration.

Consider two rays through a shield (Fig. 9.16) containing randomly distributed discontinuous voids in a continuous phase with effective attenuation coefficient k. Ray 1 travels distance t with transmission probability $T_1 = e^{-kt}$. Ray 2 travels distance $t - \delta$ with transmission probability $T_2 = e^{-k(t-\delta)}$. The average path length is $\bar{t} = t - \delta/2$; however, the average transmission probability is

$$\bar{T} = \tfrac{1}{2}(T_1 + T_2) = e^{-k\bar{t}} \cosh\left(\frac{k\delta}{2}\right) > e^{-k\bar{t}}. \tag{9.63}$$

[6]The original source in this experiment was a reactor several hundreds of feet distant, so that the beam coming from it was essentially parallel. The units for the flux density data are per watt of reactor power. The exact power level is unimportant, since it is given for normalization purposes that the flow rate of neutrons initially incident on the side wall near the entrance was 1.97 neutrons per square centimeter per second per watt.

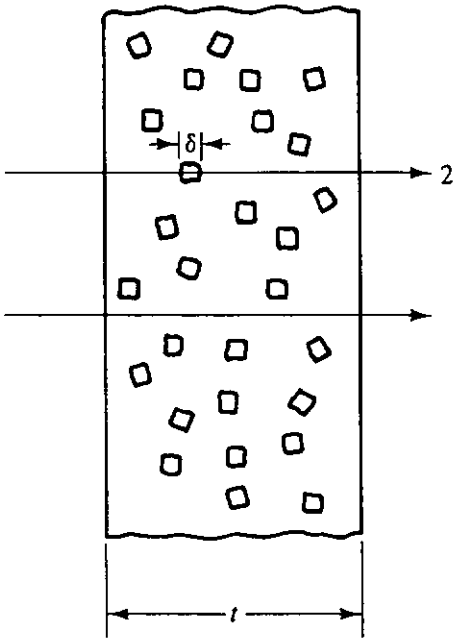

Figure 9.16 Shield containing randomly distributed inclusions.

Thus, in general, ray attenuation probabilities cannot be based on mean path lengths, for there is a *channeling* effect, the neglect of which would result in overestimates of shield effectiveness. This effect does not depend on the randomness of the voids, but is also valid for regular void distributions.

9.3.1 Limiting Case of Very Small Shield Discontinuities

Suppose, in Eq. (9.63) that $\delta \ll k^{-1}$, that is, that dimensions of discontinuities (lumps or voids in this context) are much smaller than radiation relaxation lengths in the continuous phase. In that case, clearly, the channeling effect is negligible. Shield transmission factors may be computed using an average mass attenuation coefficient $(\overline{k/\rho})$. Suppose that k and ρ are the effective attenuation coefficient and density of the continuous phase, whereas k' and ρ' are properties of the discontinuous phase. If v is the volume fraction of the discontinous phase and $\bar{\rho}$ is the average density, the transmission probability is

$$T(t) = e^{-(\overline{k/\rho})\bar{\rho}t}, \tag{9.64}$$

where

$$\overline{k/\rho} = \frac{\rho(1-v)}{\bar{\rho}}\frac{k}{\rho} + \frac{\rho' v}{\bar{\rho}}\frac{k'}{\rho'} = w\left(\frac{k}{\rho}\right) + w'\left(\frac{k'}{\rho'}\right), \tag{9.65}$$

where w and w' are the weight fractions of the continuous and discontinuous phases, respectively. Thus,

$$T(t) = e^{-[(1-v)k+vk']t} = e^{-kt}e^{-(k'-k)vt}. \tag{9.66}$$

Of course, if the average mass attenuation were known directly, as would probably be the case for concrete, for example, then Eq. (9.64) would be used.

9.3.2 Small, Randomly Distributed Discontinuities

Channeling effects have been treated by a statistical technique attributed to Coveyou (see Ref. 34). Suppose that δ is the mean path length of a ray through a discontinuity. The mean transmission probability is

$$\bar{T}(t) = e^{-kt}e^{-(k'-k)vt/\Xi}, \tag{9.67}$$

in which the factor Ξ called the *cross-section effectiveness ratio* is given by the expression

$$\Xi = \frac{(k - k')v\delta}{\ln [ve^{-(k'-k)\delta} + (1 - v)]}. \tag{9.68}$$

For a discontinuity with a convex surfaces, δ is four times the volume divided by the surface area. For various-sized discontinuities, or a discontinuity with a concave or reentrant surface, δ must be evaluated on an ad hoc basis.

9.3.3 Discontinuities of Well-Defined Geometry

Shield discontinuities of well-defined geometry may be taken into account using the ray technique described in Chapter 6. For example, consider the slab shield with a spherical discontinuity illustrated in Fig. 9.17. If $S_V(\mathbf{r}')$ is the strength of a distributed isotropic, monoenergetic source at $\mathbf{r}'$, then the response of a detector at $\mathbf{r}$ is

$$R(\mathbf{r}) = \int_V dV\, S_V(\mathbf{r}')G(\mathbf{r}', \mathbf{r}), \tag{9.69}$$

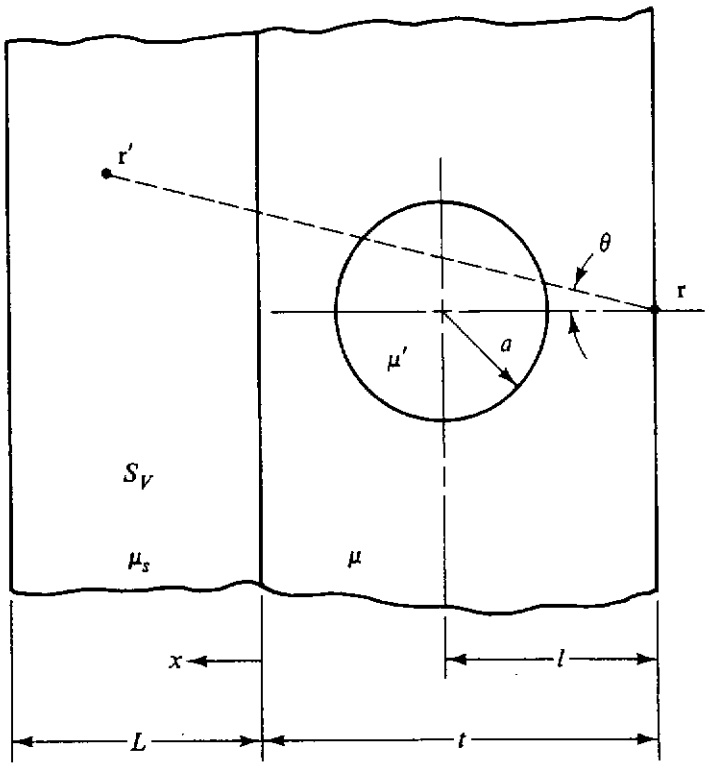

Figure 9.17 Spherical discontinuity in a slab shield, backed by a slab source.

in which the kernel is

$$G(\mathbf{r}', \mathbf{r}) = \frac{\hat{R}T(\mathbf{r}', \mathbf{r})}{|\mathbf{r}' - \mathbf{r}|^2} \tag{9.70}$$

and the transmission function is

$$T(\mathbf{r}', \mathbf{r}) = \exp\left[-\int_0^{-|\mathbf{r}'-\mathbf{r}|} dx\, k(E_0, x)\right]. \tag{9.71}$$

Equation (9.71) is a line integral along the straight-line path between $\mathbf{r}'$ and $\mathbf{r}$. For fast neutrons, an appropriate choice for k would be $(\mu_r/\rho)\rho(x)$. For gamma photons, one choice would be $(\mu_{\text{eff}}/\rho)\rho(x)$. Alternatively, Eq. (9.71) could be modified by using linear attenuation coefficients and buildup factors. In this example, specifically, $|\mathbf{r}' - \mathbf{r}| = (x + t)\sec\theta$, and, for uncollided particles,

$$T(x, \theta) = \exp\left[-\{\mu_s x \sec\theta + \mu[t\sec\theta - 2(a^2 - l^2\sin^2\theta)^{1/2}] + 2\mu'(a^2 - l^2\sin^2\theta)^{1/2}\}\right] \quad \text{for } \theta \leq \sin^{-1} a/l, \tag{9.72}$$

and

$$T(x, \theta) = \exp\left[-(\mu_s x \sec\theta + \mu t \sec\theta)\right] \quad \text{for } \theta > \sin^{-1} a/l. \tag{9.73}$$

Evaluation of the following integral then yields the response at r:

$$R(r) = 2\pi\hat{R}S_V \int_0^L dx \int_0^{\pi/2} d\theta \tan\theta\, T(x, \theta). \tag{9.74}$$

The result is no more than a direct application of the ray technique. However, in this case, as in most, numerical integration is indicated.

REFERENCES

1. M. Leimdörfer, "The Backscattering of Photons," in *Engineering Compendium on Radiation Shielding*, Vol. I, R. G. Jaeger (ed.), Springer-Verlag, New York, 1968, pp. 233–245.
2. W. E. Selph, "Albedos, Ducts, and Voids," in *Reactor Shielding for Nuclear Engineers*, N. M. Schaeffer (ed.), TID 25951, National Technical Information Service, U.S. Dept. of Commerce, Springfield, Va., 1973, Chap. 7.
3. S. Chandrasekhar, *Radiative Transfer*, Dover, New York, 1960, pp. 124–125.
4. M. J. Berger and D. J. Raso, "Monte-Carlo Calculations of Gamma-Ray Back-Scattering," *Radiat. Res.* **12**, 20–37 (1960).
5. M. J. Berger and D. J. Raso, "Backscattering of Gamma-Rays," Report 5982, 2nd ed., U.S. National Bureau of Standards, Washington, D.C., 1960.
6. M. B. Wells, "Differential Dose Albedos for Calculation of Gamma-Ray Reflection from Concrete," Report RRA-T46, Radiation Research Associates, Fort Worth, TX 1964.
7. L. G. Haggmark, T. H. Jones, N. E. Scofield, and W. J. Gurney, "Differential Dose-Rate Measurements of Backscattered Gamma-Rays from Concrete, Aluminum, and Steel," *Nucl. Sci. Eng.* **23**, 138–149 (1965).
8. B. P. Bulatov and E. A. Garusov, "^{60}Co and ^{198}Au γ-Ray Albedo of Various

Materials," *At. Energ.* **5**, 631 (1958); and *J. Nucl. Energy, Part A: React. Sci.* **11**, 159–164 (1960).

9. B. P. Bulatov and O. I. Leipunskii, "The Albedo of γ-Rays and the Reflection Build-up Factor," *Sov. J. At. Energy* **7**, 1015–1017 (1961).
10. B. P. Bulatov and N. F. Andrushin, "Gamma-Ray Energy and Number Albedos," *Sov. J. At. Energy* **22**, 307–308 (1967).
11. T. Hyodo, *Nucl. Sci. Eng.* **12**, 178 (1962).
12. H. Fujita, K. Kobayashi, and T. Hyodo, "Backscattering of Gamma-Rays from Iron Slabs," *Nucl. Sci. Eng.* **19**, 437–440 (1964).
13. M. J. Barrett and J. Waldman, "Experimental Gamma-Ray Backscattering by Various Materials," Report TO-B 64-68, Technical Operations Research, Boston, 1964.
14. A. B. Chilton and C. M. Huddleston, "A Semi-empirical Formula for Differential Dose Albedo for Gamma Rays on Concrete," *Nucl. Sci. Eng.* **17**, 419 (1963).
15. A. B. Chilton, C. M. Davisson, and L. A. Beach, "Parameters for C-H Albedo Formula for Gamma Rays Reflected from Water, Concrete, Iron, and Lead," *Trans. Am. Nucl. Soc.* **8**, 656 (1965).
16. A. B. Chilton, "A Modified Formula for Differential Exposure Albedo for Gamma Rays Reflected from Concrete," *Nucl. Sci. Eng.* **27**, 481–482 (1967).
17. M. Leimdörfer, "The Backscattering of Neutrons," in *Engineering Compendium on Radiation Shielding*, Vol. I, R. G. Jaeger (ed.), Springer-Verlag, New York, 1968, pp. 330–345.
18. R. E. Maerker and F. J. Muckenthaler, "Calculation and Measurement of the Fast-Neutron Differential Dose Albedo for Concrete," *Nucl. Sci. Eng.* **22**, 455–462 (1965).
19. W. A. Coleman, R. E. Maerker, F. J. Muckenthaler, and P. N. Stevens, "Calculation of Doubly Differential Current Albedos for Epicadmium Neutrons Incident on Concrete and Comparison of the Reflected Subcadmium Component with Experiment," *Nucl. Sci. Eng.* **27**, 411–422 (1967).
20. F. J. Allen, A. Futterer, and W. Wright, Reports BRL-1148 (1961); BRL-1190 (1963); BRL-1189 (1963); BRL-1199 (1963); BRL-1204 (1963); BRL-1224 (1963); and BRL-1238 (1964); U.S. Army Ballistic Research Laboratory, Aberdeen Proving Ground, Md.
21. R. E. Maerker and F. J. Muckenthaler, "Measurements and Single-Velocity Calculations of Differential Angular Thermal Neutron Albedos for Concrete," *Nucl. Sci. Eng.* **26**, 339 (1966).
22. Y. T. Song, C. M. Huddleston, and A. B. Chilton, "Differential Dose Albedo for Fast Neutrons," *Nucl. Sci. Eng.* **35**, 401–405 (1969).
23. R. L. French and M. B. Wells, "An Angular Dependent Albedo for Fast-Neutron Reflection Calculations," Report No. RRA-M31, Radiation Research Associates Fort Worth, TX, 1963.
24. Y. T. Song, "Fast Neutron Streaming through Two-Legged Concrete Ducts," Report TR-354 (AD-457746), Naval Civil Engineering Laboratory, Port Hueneme, CA 1965.
25. G. P. Cavanaugh, "A Calculation and Analysis of Albedos Due to 14 MeV

Neutrons Incident upon Concrete," Ph.D. thesis, University of Illinois at Urbana-Champaign, 1975.

26. L. V. Spencer, J. A. Diaz, and E. Moses, "Neutron Penetration in Cylindrical Ducts," Report NBS 8542, U.S. National Bureau of Standards, Washington, D.C., 1964.
27. M. B. Wells, "Reflection of Thermal Neutrons and Neutron-Capture Gamma Rays from Concrete," Report RRA-M44, Radiation Research Associates, Fort Worth, TX, 1964.
28. D. K. Trubey, "A Calculation of Radiation Penetration of Cylindrical Duct Walls," Report ORNL-CF-63-2-64, Oak Ridge National Laboratory, Oak Ridge, Tenn., 1963. See also: W. E. Selph and H. C. Claiborne, "Methods for Calculating Effects of Ducts, Access Ways, and Holes in Radiation Shields," Report ORNL-RSIC-20, Oak Ridge National Laboratory, Oak Ridge, Tenn., 1968.
29. A. Simon and C. E. Clifford, "The Attenuation of Neutrons by Air Ducts in Shields," *Nucl. Sci. Eng.* **1**, 156–166 (1956).
30. J. C. LeDoux and A. B. Chilton, "Gamma Ray Streaming through Two-Legged Rectangular Ducts," *Nucl. Sci. Eng.* **11**, 362–368 (1959).
31. J. Diaz and A. B. Chilton, "Modeling Relationships for Radiation Transport within Ducts and Other Cavities in Shields," *Nucl. Sci. Eng.* **35**, 283–285 (1969).
32. R. E. Maerker and F. J. Muckenthaler, "Neutron Fluxes in Concrete Ducts Arising from Incident Thermal Neutrons: Calculation and Experiment," *Nucl. Sci. Eng.* **29**, 444–454 (1967).
33. R. E. Maerker and F. J. Muckenthaler, "Neutron Fluxes in Concrete Ducts Arising from Incident Epicadmium Neutrons: Calculations and Experiments," *Nucl. Sci. Eng.* **30**, 340–354 (1967).
34. W. R. Burrus, in *Engineering Compendium on Radiation Shielding*, Vol. I, R. G. Jaeger (ed.), Springer-Verlag, New York, 1968, p. 491.

PROBLEMS

9.1. Consider a point isotropic photon source placed on the plane interface between air (with negligible attenuation) and a semi-infinite reflecting slab. An exposure rate detector is located at distance r in air from the source on a normal to the slab. Estimate the ratio of the exposure rate due to reflected photons to the direct (uncollided) exposure rate for the cases below. Make the approximation that all reflected photons enter and emerge from the slab at the location of the source.

(a) A ^{137}Cs source and a concrete slab
(b) A ^{137}Cs source and a lead slab
(c) A ^{60}Co source and a concrete slab
(d) A ^{60}Co source and a lead slab

9.2. A thick concrete slab, 0.5 × 0.6 m, is placed with reference to a detector and a source as illustrated in Fig. P9.2. A shielding wall prevents any direct radiation reaching the detector. Air scattering is to be ignored and there are no scattering surfaces other than the concrete slab. Estimate the detector response for the following cases:

(a) A 2-GBq ^{137}Cs source and an exposure rate detector [use Eq. (9.26)]
(b) A 1-GBq ^{60}Co source and an exposure rate detector [use Eq. (9.27)]
(c) A point isotropic neutron source of energy 14 MeV and strength 10^9 s^{-1}, and measurement of tissue absorbed dose rate based on maximum value in a phantom
(d) A point isotropic neutron source of energy 2 MeV and strength 10^9 s^{-1}, and measurement of tissue absorbed dose rate based on maximum value in a phantom

You may make the approximation that the reflecting slab is of infinitesimal area. If you do so, justify the approximation.

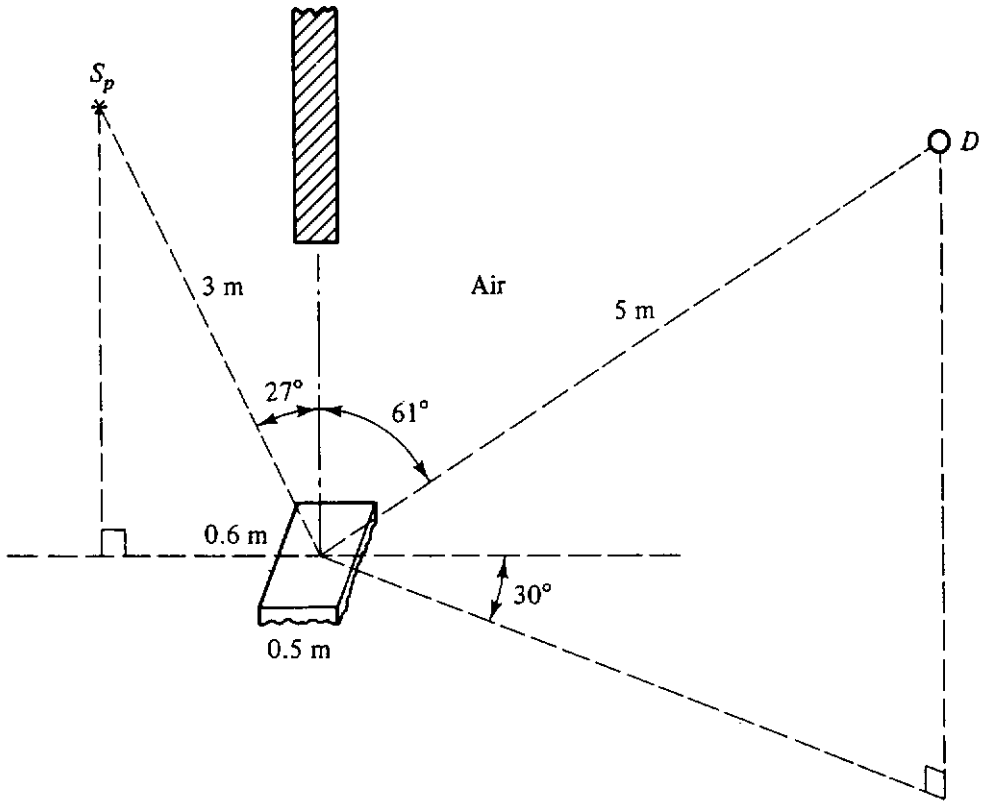

Figure P9.2

9.3. Suppose that the source and detector of Problem 9.2 were reversed in position. Would the estimated response rates remain the same under the approximation that the reflecting slab is infinitesimal in area? Under an exact treatment, would the estimated response rates remain the same?

9.4. A spherical room of radius R has concrete walls which are much thicker than the mean-free-path length of photons in concrete. The only source in the room is a massless point source of monoenergetic photons. The radius of the room is such that the scattering and absorption of photons in the air in the room can be neglected. Let ϕ_r be the flux density of reflected photons at a point very near the source, and resulting from scattering in the walls of the room. Let the radius of the room now change to a value of ξR, where ξ is a geometric scaling factor. Still neglecting scattering and absorption in the air of the room, determine the ratio of the flux density of reflected photons in the scaled configuration to that in the original configuration. First assume the source and response location to be at

the center of the sphere and treat only single reflection from the wall. Then generalize to consider an off-center source and multiple wall-scattered photons.

9.5. Consider an infinitely broad parallel beam of neutrons normally incident from the vacuum side of an infinite plane bounding two semi-infinite regions, one of vacuum and one of concrete. The incident flux density is ϕ_0. The differential directional and total number albedos are respectively α_N and A_N. The reflected flux density ϕ_r is to be evaluated at normal distance h, in vacuum, from the plane.

(a) Prove that the isotropic assumption for albedo (i.e., $\alpha_N = A_N/2\pi$), leads to an infinite answer for the reflected flux density. (This leads to a suspicion that the completely isotropic assumption for albedo is not correct in reality.)

(b) Assume a cosine distribution for α_N (i.e., $\alpha_N = A_N \cos\theta/\pi$) and find the total reflected flux density measured by the detector. Show that the result is independent of distance h.

9.6. For all the cases below, assume that the incident particles have individual energies of 2 MeV. Assume an incident polar angle with respect to the normal of 30°, an exit polar angle with respect to the normal of 45°, and an exit azimuthal angle of 90°. Particles uniformly illuminate the concrete surface at the plane interface between two semi-infinite regions, one of concrete, one of vacuum.

(a) Evaluate the differential directional exposure albedo, $\alpha_X(E_0, \theta_0; \theta, \psi)$, using Eq. (9.26).

(b) Evaluate and compare differential directional absorbed dose albedos for neutrons using Eqs. (9.29) and (9.30).

(c) Using Eq. (9.30), evaluate the total albedo A_{D_p} for absorbed dose in tissue based on maximum value in a phantom.

9.7. Consider the integrals defined by **(a)** Eq. (9.46), **(b)** Eq. (9.48), and **(c)** Eq. (9.51). Prove that, for long cylindrical ducts ($\beta \ll 1$), values of the integral approach unity. (*Hint:* Divide the integral into two parts, one from 0 to $\frac{1}{2}$ and the other from $\frac{1}{2}$ to 1.)

9.8. Consider single wall reflection in straight cylindrical ducts, as discussed in Section 9.2.4. Prove the assertion made as to what part of the duct wall is most important in providing the single-reflection component of the response, for

(a) Case A, isotropic incident flow rate—isotropic albedo

(b) Case B, isotropic incident flow rate—cosine albedo

(c) Case C, isotropic incident flux density—cosine albedo

9.9. Consider a two-legged rectangular duct with a 90° bend, as illustrated in Fig. 9.13. Duct walls are concrete. Dimensions are 3 m × 3 m. The first leg is 10 m long (to the axis of the second leg). The second leg is 15 m long (from the axis of the first leg). At the entrance plane 1-MeV photons have a flux density ϕ^+, isotropic within the 2π solid angle directed toward the duct entrance, that is,

$$\phi_0(\theta) = \frac{\phi^+}{2\pi} \qquad (\text{cm}^{-2}\,\text{s}^{-1}\,\text{sr}^{-1}),$$

where angle θ is measured from the axis of the first leg. At the entrance plane, the exposure rate, $R_0 = \phi^+ \mathcal{R}(E_0)$, is 1 R/h. Estimate the exposure rate $R(P)$ at the center of the duct exit plane.

9.10. Suppose that 5-cm-diameter spheres of heavy rock ($\rho' = 4.5\ \text{g cm}^{-3}$) are dispersed randomly throughout a matrix of cement mortar ($\rho = 2.1\ \text{g cm}^{-3}$), to

the extent that the volume fraction of the rock equals 0.4. This mixture is used to make a photon shield of 25-cm thickness. Take μ_{eff}/ρ for both spheres and matrix material to be the same and given by μ_a/ρ for ordinary concrete. The shield is placed in a broad, parallel beam of 1-MeV photons which is normally incident on it. If the exposure rate in the absence of the shield is 20 R h^{-1}, what is the exposure rate behind the shield when it is in place?

(a) Solve on the assumption that the shield acts as a homogeneous mixture.

(b) Solve taking into account the heterogeneous nature of the shield.

10 the transport description of radiation penetration

10.1 TRANSPORT EQUATION

For many shielding situations in which particle scattering or production of secondary radiation (e.g., fission neutrons or annihilation photons) is important, the approximate methods of the earlier chapters may not be capable of describing the radiation field with sufficient accuracy. The exact description of the radiation particles (neutrons or photons) that takes into account all the possible particle-medium interactions and the effects of medium composition and geometry is the realm of *transport theory*. In its most general form, transport theory is a special branch of statistical mechanics which deals with the interaction of one species of particles (the radiation field) with another species (the shielding medium).

The shielding analyst would ideally like to know the distribution of photons or neutrons everywhere in the shielding medium. For most applications the steady-state spatial and energy distribution of the particle density, $n(\mathbf{r}, E)$, is all that is needed.[1] Unfortunately, there is no equation for this quantity that holds rigorously in all situations. The simplest equation which accurately describes the particle distribution in a medium is for the *differential energy and directional flux density* $\phi(\mathbf{r}, E, \mathbf{\Omega})$ (see Section 2.1.2). This quantity has the physical interpretation of being the expected number of particles at point $\mathbf{r}$ with energies in unit energy at E and with directions of travel within a unit solid

[1] The time dependence of the radiation field is usually assumed to be that of the primary radiation sources, and time delays caused by the finite speed of the radiation particles can usually be ignored in shielding applications.

angle which cross a unit area perpendicular to the direction $\mathbf{\Omega}$ in a unit time. In terms of the particle number density distribution $n(\mathbf{r}, E, \mathbf{\Omega})$ (the expected number of particles per unit volume at $\mathbf{r}$ with energies in unit energy about E and moving in a unit solid angle about $\mathbf{\Omega}$), one has

$$\phi(\mathbf{r}, E, \mathbf{\Omega}) = vn(\mathbf{r}, E, \mathbf{\Omega}), \tag{10.1}$$

where v is the particle speed (see Section 2.1.1). For photons $v = c$, the speed of light, while for nonrelativistic neutrons $v = (2E/m)^{1/2}$.

To obtain an equation for $\phi(\mathbf{r}, E, \mathbf{\Omega})$, consider the particle balance in an arbitrary volume V with a closed surface S for those particles with energies in dE about E moving in $d\Omega$ about the direction $\mathbf{\Omega}$. In a steady-state radiation field, the net rate at which particles are lost (either by leaving or entering the volume V, or by changing their energy or direction of travel) must exactly be balanced by the rate secondary or source particles are introduced into V with the required energy and direction of motion. Thus the particles of the radiation field must satisfy the following balance relation to maintain the steady state:

$$(a) + (b) - (c) - (d) = 0, \tag{10.2}$$

where (a) is the net number of particles flowing out of V across S in a unit time, (b) is the total number of particles suffering collisions in V in a unit time, (c) is the number of secondary particles in dE about E moving in $d\Omega$ about $\mathbf{\Omega}$ that are produced by all particle–medium interactions in V in a unit time, and (d) is the number of particles in dE about E moving in $d\Omega$ about $\mathbf{\Omega}$ that are introduced in V in a unit time by "external" or true sources (i.e., sources of particles that are independent of the particle population). The desired equation for $\phi(\mathbf{r}, E, \mathbf{\Omega})$ is then obtained by expressing mathematically each component of this balance relation in terms of the differential flux density.

From the definition in Section 2.1.4 of the *doubly differential flux density vector*, $\mathbf{j}(\mathbf{r}, E, \mathbf{\Omega}) \equiv \mathbf{\Omega}\phi(\mathbf{r}, E, \mathbf{\Omega})$, the quantity $\hat{\mathbf{n}} \cdot \mathbf{j}(\mathbf{r}, E, \mathbf{\Omega})\, dE\, d\Omega$ physically represents the number of particles in dE about E traveling in $d\Omega$ about $\mathbf{\Omega}$ which cross a unit area (with unit normal $\hat{\mathbf{n}}$) in a unit time at point $\mathbf{r}$. Thus term (a) of the balance relation may be expressed mathematically as

$$(a) = \left[\int_S dS\, \hat{\mathbf{n}} \cdot \mathbf{\Omega}\phi(\mathbf{r}, E, \mathbf{\Omega})\right] dE\, d\Omega, \tag{10.3}$$

which can be expressed as a volume integral upon application of the Gauss integral theorem, namely

$$(a) = \left[\int_V dV\, \nabla \cdot \mathbf{\Omega}\phi(\mathbf{r}, E, \mathbf{\Omega})\right] dE\, d\Omega. \tag{10.4}$$

Since the ∇ operator affects only the spatial variables and not $\mathbf{\Omega}$ (i.e., $\mathbf{r}$ and $\mathbf{\Omega}$ are independent variables), this last result may be finally written as

$$(a) = \left[\int_V dV\, \mathbf{\Omega} \cdot \nabla\phi(\mathbf{r}, E, \mathbf{\Omega})\right] dE\, d\Omega. \tag{10.5}$$

The total interaction rate, term (*b*) of Eq. (10.2), is

$$(b) = \left[\int_V dV\, \mu(\mathbf{r}, E)\phi(\mathbf{r}, E, \mathbf{\Omega})\right] dE\, d\Omega, \tag{10.6}$$

where μ is the total interaction coefficient (or macroscopic cross section). If it is assumed that the secondary particles appear at the position where the causal interaction (fission, scatter, positron production, atomic excitation, etc.) occurs, term (*c*) can be written as

$$(c) = \left[\int_V dV \int_0^\infty dE' \int_{4\pi} d\Omega'\, \mu_s(\mathbf{r}, E' \to E, \mathbf{\Omega}' \to \mathbf{\Omega})\phi(\mathbf{r}, E', \mathbf{\Omega}')\right] dE\, d\Omega, \tag{10.7}$$

where $\mu_s(\mathbf{r}, E' \to E, \mathbf{\Omega}' \to \mathbf{\Omega})\, dE\, d\Omega$ is the probable number of secondary particles at point $\mathbf{r}$ with energies in dE about E in direction $d\Omega$ about $\mathbf{\Omega}$ produced by an incident particle of energy E' traveling in direction $\mathbf{\Omega}'$ per unit path length of the incident particle. Finally, if $S(\mathbf{r}, E, \mathbf{\Omega})$ denotes the production rate of particles from non-radiation-induced sources with energies in dE about E in $d\Omega$ about $\mathbf{\Omega}$ per unit volume about point $\mathbf{r}$, the balance relation Eq. (10.2) can be written mathematically as

$$\int_V \Big[\mathbf{\Omega} \cdot \nabla\phi + \mu\phi - \int_0^\infty dE' \int_{4\pi} d\Omega'\, \mu_s(\mathbf{r}, E' \to E, \mathbf{\Omega}' \to \mathbf{\Omega})\phi(\mathbf{r}, E', \mathbf{\Omega}') + S(\mathbf{r}, E, \mathbf{\Omega})\Big] dV = 0. \tag{10.8}$$

However, the volume V is arbitrary, and hence the integrand of Eq. (10.8) must be identically zero; therefore,

$$\mathbf{\Omega} \cdot \nabla\phi(\mathbf{r}, E, \mathbf{\Omega}) + \mu(\mathbf{r}, E)\phi(\mathbf{r}, E, \mathbf{\Omega}) = \int_0^\infty dE' \int_{4\pi} d\Omega'\, \mu_s(\mathbf{r}, E' \to E, \mathbf{\Omega}' \to \mathbf{\Omega})\phi(\mathbf{r}, E', \mathbf{\Omega}') + S(\mathbf{r}, E, \mathbf{\Omega}). \tag{10.9}$$

This integrodifferential equation for $\phi(\mathbf{r}, E, \mathbf{\Omega})$ is known as the transport equation or the linearized Boltzmann equation (named after L. Boltzmann, who first derived it over a century ago). The equation serves as a precise description of the radiation field in all neutron- or photon-shielding situations. However, in the derivation above, several implicit assumptions have been made. The radiation particles are assumed to be point particles that stream in straight lines between collisions, which occur at distinct points in the system (i.e., the associated wavelength of the particle and the interaction distance between the particle and the atoms of the medium are assumed to be very small compared to the mean-free-path length of the particle and the size of the system). Also, all internal structure (e.g., spin or polarization) of the diffusing particles has been ignored. More important, the transport equation is linear because all photon–photon or neutron–neutron interactions have been neglected. For virtually all shielding applications, these assumptions are quite valid and the transport equation of Eq. (10.9), or a variant thereof, is the basis of most of the large shielding codes which are routinely used today.

The form of the transport equation given above is quite general and applies to any geometry, to either photons or neutrons, and allows for all types of particle–medium interactions (all of whose probabilities are encompassed by the interaction coefficients μ and μ_s). To solve this equation for the differential energy and directional flux density $\phi(\mathbf{r}, E, \mathbf{\Omega})$, one must specify (1) the coordinate system used (so that the streaming term $\mathbf{\Omega} \cdot \nabla\phi$ can be expressed explicitly), (2) the coefficients μ and μ_s (which depend on the material composition of the shielding medium and the interactions of interest), (3) the distribution of the true sources $S(\mathbf{r}, E, \mathbf{\Omega})$ which usually arise from the presence of radionuclides in the medium, and (4) the boundary conditions which determine the incident flux density at the edges of the shielding medium. In the following subsections, different forms for the transport equation in various geometries for neutrons and for photons are derived and some of their important properties discussed.

Unfortunately, exact analytical solutions of the transport equation are known for only the simplest cases, none of which is directly applicable to realistic shielding problems. Consequently, much effort has been directed toward the development of approximations to the transport equation which can then be solved by numerical techniques or, for the simplest approximations, even by analytical methods. In the next sections, some of the more useful approximations and methods for their solutions are reviewed. The purpose of these reviews is to acquaint the reader with the essence of the approximations and the ideas behind the methods used for their solution. It is not intended to present the full detail needed to describe the algorithmic details of the computational methods based on these approximations. Readers interested in these details as well as other approximations are referred to books devoted to transport theory, for example, Ref. 1.

10.1.1 Explicit Form for the Three Basic Geometries

While the choice of the spatial and directional coordinate system is independent of the transport problem, geometric symmetries which may be present can often be more easily expressed in one coordinate system than another. If the problem has any spatial symmetry, the proper choice of the coordinate system usually allows the elimination of one or more of the independent spatial variables. Although many coordinate systems are possible, results are presented below for the three most commonly encountered ones: rectangular (Cartesian), spherical, and cylindrical.

The basic difficulty in writing the transport equation for a particular geometry is expressing the leakage or streaming term $\mathbf{\Omega} \cdot \nabla\phi(\mathbf{r}, E, \mathbf{\Omega})$ in terms of the variables of the coordinate system. If the distances s and t are measured along the directions of $\mathbf{\Omega}$ and $\nabla\phi$, respectively, and if Θ is the angle between these two vectors (see Fig. 10.1), then since $\nabla\phi = d\phi/dt$, $dt/ds = \cos\Theta$, and $\mathbf{\Omega}$ is a unit vector

$$\mathbf{\Omega} \cdot \nabla\phi = \cos\Theta \frac{d\phi}{dt} = \cos\Theta \frac{ds}{dt}\frac{d\phi}{ds} = \frac{d\phi}{ds}. \tag{10.10}$$

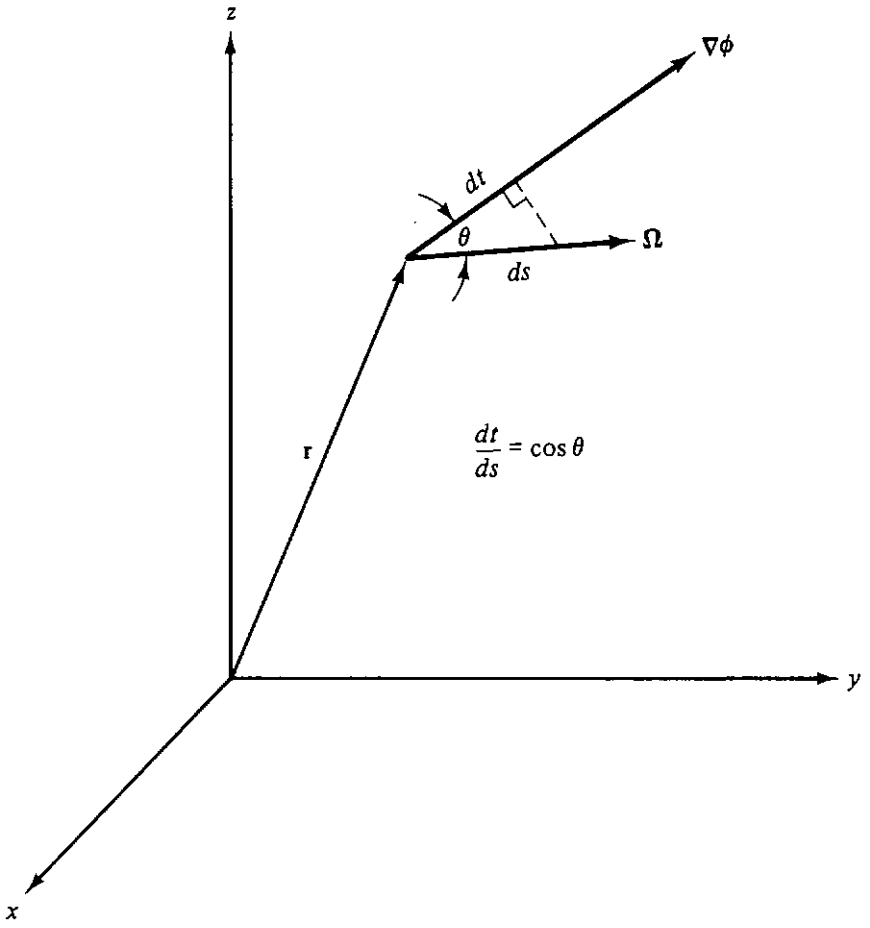

Figure 10.1 Orientation of the unit vector $\boldsymbol{\Omega}$ and the gradient of $\phi(\mathbf{r}, E, \boldsymbol{\Omega})$.

Thus $\boldsymbol{\Omega} \cdot \nabla\phi$ is the rate of change of ϕ along the direction of particle travel $\boldsymbol{\Omega}$ (i.e., $d\phi/ds$). To calculate the explicit expression for the streaming term $\boldsymbol{\Omega} \cdot \nabla\phi$ in any geometry, one needs only to evaluate $d\phi/ds$ in terms of the spatial and angular variables of the particular geometry.

As an example, consider the rectangular (Cartesian) spatial coordinate system for $\mathbf{r}$ and spherical coordinate system for $\boldsymbol{\Omega}$ shown in Fig. 10.2. Thus, the streaming term

$$\boldsymbol{\Omega} \cdot \nabla\phi(\mathbf{r}, E, \boldsymbol{\Omega}) = \frac{d\phi(x, y, z, E, \theta, \psi)}{ds}$$

$$= \frac{\partial\phi}{\partial x}\frac{dx}{ds} + \frac{\partial\phi}{\partial y}\frac{dy}{ds} + \frac{\partial\phi}{\partial z}\frac{dz}{ds} + \frac{\partial\phi}{\partial\theta}\frac{d\theta}{ds} + \frac{\partial\phi}{\partial\psi}\frac{d\psi}{ds}. \quad (10.11)$$

From Fig. 10.2 the following variations of x, y, z, θ, and ψ with distance s along $\boldsymbol{\Omega}$ are found:

$$\frac{dx}{ds} = \sin\theta\cos\psi = \sqrt{1-\omega^2}\cos\psi$$

$$\frac{dy}{ds} = \sin\theta\sin\psi = \sqrt{1-\omega^2}\sin\psi$$

$$\frac{dz}{ds} = \cos\theta = \omega$$

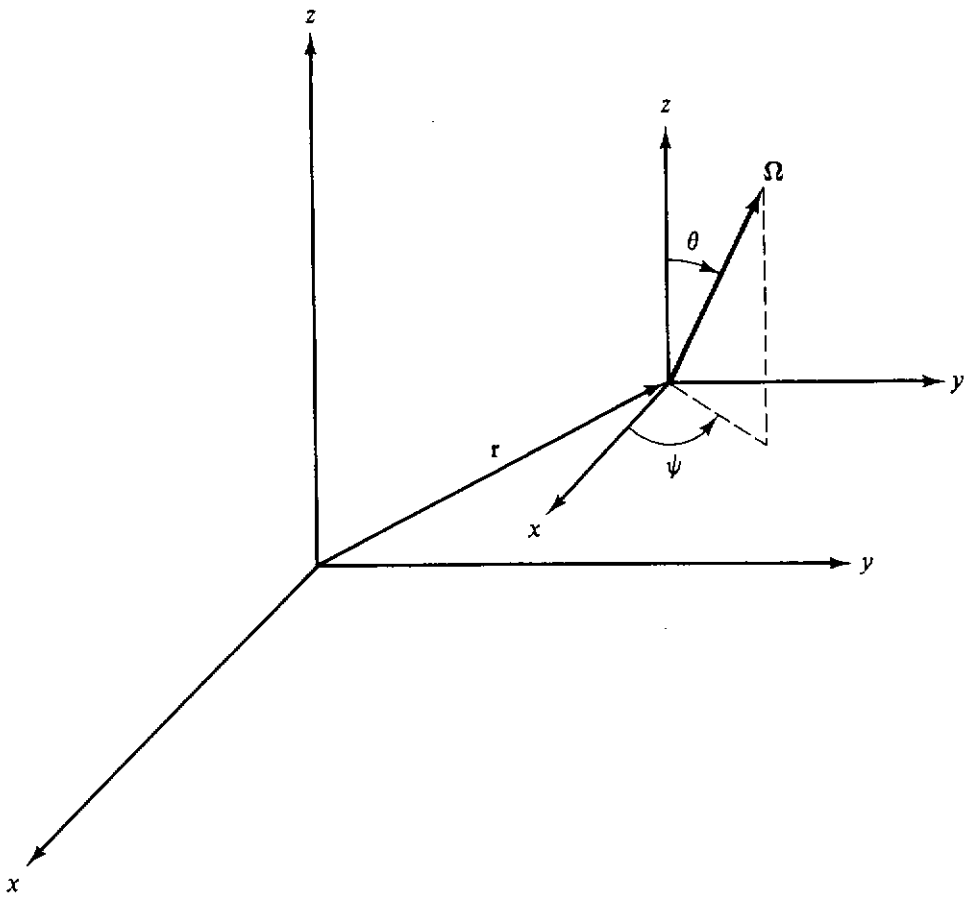

Figure 10.2 Rectangular coordinate system for $\mathbf{r}(x, y, z)$ and the spherical coordinate system used for $\boldsymbol{\Omega}(\theta, \psi)$.

$$\frac{d\theta}{ds} = \frac{d\psi}{ds} = 0,$$

where $\omega \equiv \cos\theta$. Thus, from Eq. (10.11) the streaming term becomes

$$\boldsymbol{\Omega} \cdot \nabla\phi = \sqrt{1-\omega^2}\left(\cos\psi \frac{\partial\phi}{\partial x} + \sin\psi \frac{\partial\phi}{\partial y}\right) + \omega \frac{\partial\phi}{\partial z}. \tag{10.12}$$

For the special case in which the sources and material properties do not depend on x or y (e.g., an infinite homogeneous slab perpendicular to the z axis with laterally uniformly distributed sources), the flux density ϕ varies only with z, ω (or θ), and, in general, ψ. Thus, the derivatives $\partial\phi/\partial x$ and $\partial\phi/\partial y$ in Eq. (10.12) vanish, and

$$\boldsymbol{\Omega} \cdot \nabla\phi = \omega \frac{\partial\phi(z, E, \omega, \psi)}{\partial z}. \tag{10.13}$$

This particularly simple form will be used throughout this chapter to illustrate various approximation techniques for treating the transport equation. For other geometries the explicit form of the streaming term in the transport equation is more complicated. In Table 10.1 explicit forms for the streaming term are given for the three widely used geometries shown in Fig. 10.3.

TABLE 10.1 Analytical Forms of $\Omega \cdot \nabla\phi$ in Common Orthogonal Geometries

Geometry	Spatial Variables	Angular Variables[a]	$\Omega \cdot \nabla\phi$
Rectangular	z	ω	$\omega \dfrac{\partial\phi}{\partial z}$
	z, x	$\omega, \eta,$	$\omega \dfrac{\partial\phi}{\partial z} + \eta \dfrac{\partial\phi}{\partial x}$
	x, y, z	ω, η, ξ	$\omega \dfrac{\partial\phi}{\partial z} + \eta \dfrac{\partial\phi}{\partial x} + \xi \dfrac{\partial\phi}{\partial y}$
Cylindrical[b]	r	ψ, ξ	$\dfrac{\omega}{r} \dfrac{\partial(r\phi)}{\partial r} - \dfrac{1}{r} \dfrac{\partial(\eta\phi)}{\partial\psi}$
	r, θ	ψ, ξ	$\dfrac{\omega}{r} \dfrac{\partial(r\phi)}{\partial r} + \dfrac{\eta}{r} \dfrac{\partial\phi}{\partial\theta} - \dfrac{1}{r} \dfrac{\partial(\eta\phi)}{\partial\psi}$
	r, z	ψ, ξ	$\dfrac{\omega}{r} \dfrac{\partial(r\phi)}{\partial r} + \xi \dfrac{\partial\phi}{\partial z} - \dfrac{1}{r} \dfrac{\partial(\eta\phi)}{\partial\psi}$
	r, θ, z	ψ, ξ	$\dfrac{\omega}{r} \dfrac{\partial(r\phi)}{\partial r} + \dfrac{\eta}{r} \dfrac{\partial\phi}{\partial\theta} + \xi \dfrac{\partial\phi}{\partial z} - \dfrac{1}{r} \dfrac{\partial(\eta\phi)}{\partial\psi}$
Spherical[c]	r	ω	$\dfrac{\omega}{r^2} \dfrac{\partial(r^2\phi)}{\partial r} + \dfrac{1}{r} \dfrac{\partial[(1-\omega^2)\phi]}{\partial\omega}$
	r, θ	ω, ψ	$\dfrac{\omega}{r^2} \dfrac{\partial(r^2\phi)}{\partial r} + \dfrac{\eta}{r \sin\theta} \dfrac{\partial(\sin\theta\phi)}{\partial\theta} + \dfrac{1}{r} \dfrac{\partial[(1-\omega^2)\phi]}{\partial\omega} - \dfrac{\cot\theta}{r} \dfrac{\partial(\xi\phi)}{\partial\psi}$
	r, θ, ζ	ω, ψ	$\dfrac{\omega}{r^2} \dfrac{\partial(r^2\phi)}{\partial r} + \dfrac{\eta}{r \sin\theta} \dfrac{\partial(\sin\theta\phi)}{\partial\theta} + \dfrac{\xi}{r \sin\theta} \dfrac{\partial\phi}{\partial\zeta} + \dfrac{1}{r} \dfrac{\partial[(1-\omega^2)\phi]}{\partial\omega} - \dfrac{\cot\theta}{r} \dfrac{\partial(\xi\phi)}{\partial\psi}$

[a] θ, ψ, and ζ are in radians.

[b] $\omega = (1-\xi^2)^{1/2} \cos\psi$, $\eta = (1-\xi^2)^{1/2} \sin\psi$; ψ is the angle of revolution about the ξ axis.

[c] $\eta = (1-\omega^2)^{1/2} \cos\psi$, $\xi = (1-\omega^2)^{1/2} \sin\psi$; ψ is the angle of revolution about the ω axis.

Source: *Ref. 2; by permission of Gordon & Breach Science Publishers, Inc.*

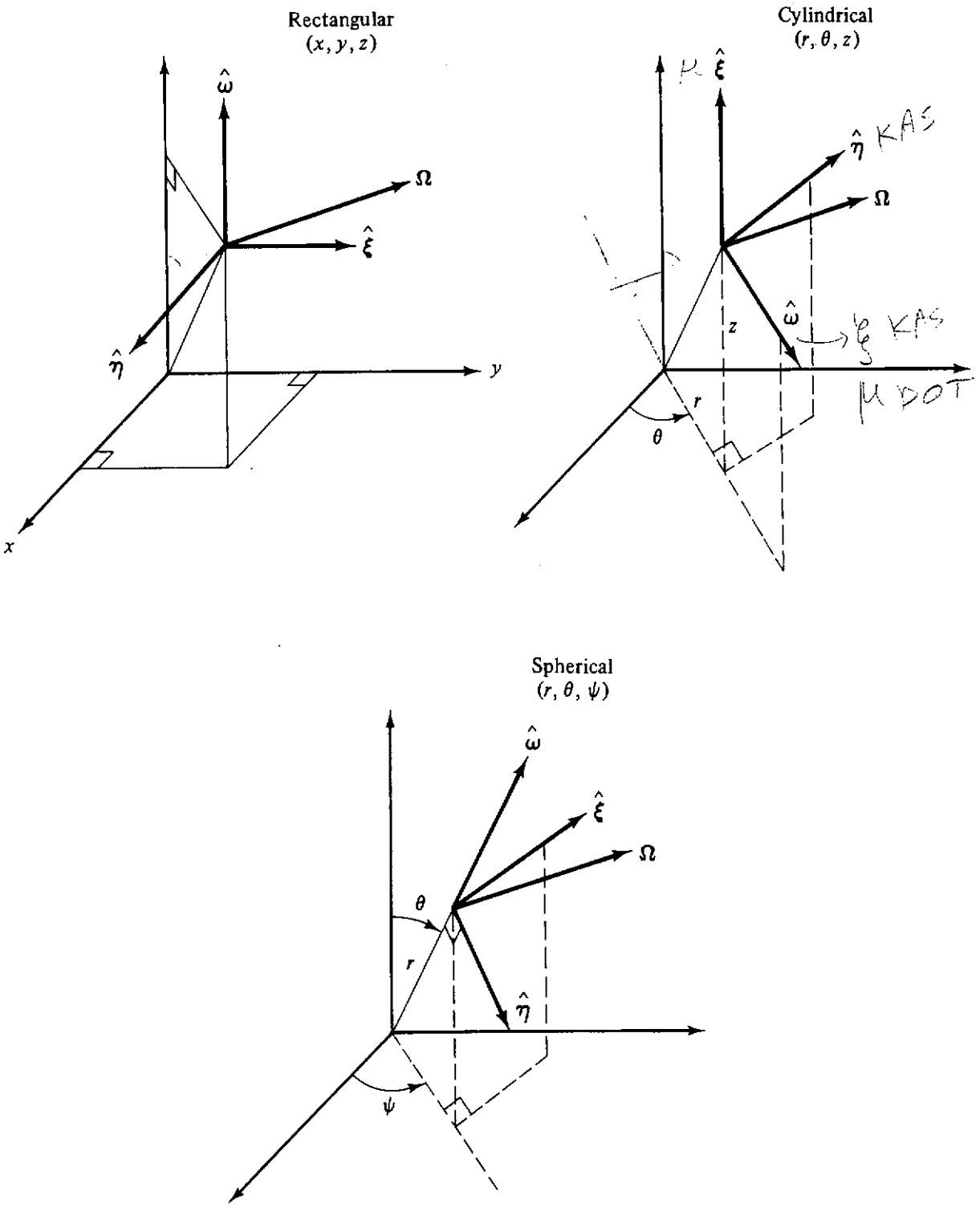

Figure 10.3 Coordinate systems for the three most commonly used geometries with the transport equation. The quantities $\hat{\omega}$, $\hat{\eta}$, and $\hat{\xi}$ are unit vectors for a local coordinate system (generally functions of the position coordinate system) with respect to which exist the directional cosines $\omega = \hat{\omega} \cdot \mathbf{\Omega}$, $\eta = \hat{\eta} \cdot \mathbf{\Omega}$, and $\xi = \hat{\xi} \cdot \mathbf{\Omega}$. (Adapted with permission of Gordon & Breach Science Publishers, Inc.)

10.1.2 Transport Equation for Photons

For most photon-transport calculations the quantity of interest is the *doubly differential energy flux density*, $I(\mathbf{r}, E, \mathbf{\Omega}) \equiv E\phi(\mathbf{r}, E, \mathbf{\Omega})$, often called simply the "radiation intensity" (see Section 2.1.5). The transport equation, Eq. (10.9), upon multiplication by E on both sides, may be written as

$$\mathbf{\Omega} \cdot \nabla I(\mathbf{r}, E, \mathbf{\Omega}) + \mu(\mathbf{r}, E) I(\mathbf{r}, E, \mathbf{\Omega}) = \int_0^\infty dE' \int_{4\pi} d\Omega' \frac{E}{E'} \mu_s(\mathbf{r}, E' \to E, \mathbf{\Omega}' \to \mathbf{\Omega}) I(\mathbf{r}, E', \mathbf{\Omega}') + ES(\mathbf{r}, E, \mathbf{\Omega}). \tag{10.14}$$

In most photon-shielding analyses, only the three dominant photon–medium interactions (Compton scattering, pair production, and photoelectric absorption) need be considered. Even pair production can be completely ignored if the source photon energies are not significantly above the pair production threshold of 1.02 MeV. Fluorescent radiation following photoelectric absorption is also often ignored if information about the low-energy photons is not wanted. Such low-energy photons are usually assumed, for simplicity of treatment, to be absorbed at the place where they originate. Similarly, any bremsstrahlung photons created by the passage of fast recoil electrons (or positrons) through the medium are usually ignored in photon-shielding calculations. The total interaction coefficient $\mu(\mathbf{r}, E)$ is the sum of the coefficients for the three dominant interaction mechanisms [Eq. (3.31)]. The secondary photon production kernel μ_s can then be written as the sum of the contributions from the three types of interactions as

$$\mu_s(\mathbf{r}, E' \to E, \mathbf{\Omega}' \to \mathbf{\Omega}) = \mu_C(\mathbf{r}, E' \to E, \mathbf{\Omega}' \to \mathbf{\Omega}) + \frac{1}{4\pi} \mu_{pp}(\mathbf{r}, E') 2\delta(E - m_e c^2) + \frac{1}{4\pi} \mu_{ph}(\mathbf{r}, E') \mathfrak{N}(\mathbf{r}, E, E'), \tag{10.15}$$

where $\mathfrak{N}(\mathbf{r}, E, E')$ is the number of photons in unit energy about E emitted per photon of energy E' absorbed in a photoelectric interaction at $\mathbf{r}$. It is assumed above that the fluorescence and annihilation radiation are emitted isotropically at the point where the primary photon is absorbed.

The treatment of photon transport problems is considerably easier than that of neutron transport problems in one important respect. Unlike neutron cross sections, the photon cross sections vary smoothly with energy and material composition and do not exhibit, for the most part, any sudden resonances as occur for neutron interactions. Only at low photon energies ($\lesssim$100 keV) where electron binding effects become important does the photoelectric cross section display any discontinuities. As a result, analytical or empirical expressions may be used to obtain cross-section values for any photon energy or for any material. Such empirical expressions serve as the basis for most photon-cross-section libraries. Neutron-cross-section libraries, on the other hand, depend almost exclusively on measured data.

Many modern numerical techniques for obtaining the radiation intensity from the transport equation are based on the transport equation as written in Eq. (10.14). However, it is often convenient to use the photon wavelength (expressed in Compton units) $\lambda \equiv m_e c^2/E$ rather than the energy variable E. The main reason for this transformation is that the free electron approximation for photon scattering is widely used to compute $\mu_C(\mathbf{r}, E' \rightarrow E, \mathbf{\Omega}' \rightarrow \mathbf{\Omega})$ and, as was seen in Chapter 3, this photon scattering model is expressed much more simply in terms of λ and λ' than in terms of E and E'. Moreover, the energy spectrum (or its derivatives) of scattered photons arising from a monoenergetic source have discontinuities at $\lambda = \lambda_0 + 2$, $\lambda = \lambda_0 + 4, \ldots$, where λ_0 is the source photon wavelength. The spectral locations of these discontinuities are not so easily expressed in the energy variable.

To express Eq. (10.14) in terms of the wavelength λ, observe that since $E\phi(\mathbf{r}, E, \mathbf{\Omega}) = \lambda\phi(\mathbf{r}, \lambda, \mathbf{\Omega})$, $I(\mathbf{r}, E, \mathbf{\Omega}) = I(\mathbf{r}, \lambda, \mathbf{\Omega})$. Further, $ES(\mathbf{r}, E, \mathbf{\Omega}) = \lambda S(\mathbf{r}, \lambda, \mathbf{\Omega})$ and

$$\mu_s(\mathbf{r}, E' \rightarrow E, \mathbf{\Omega}' \rightarrow \mathbf{\Omega})\, dE = -\mu_s(\mathbf{r}, \lambda' \rightarrow \lambda, \mathbf{\Omega}' \rightarrow \mathbf{\Omega})\, d\lambda. \tag{10.16}$$

Equation (10.14) then becomes

$$\begin{aligned} &\mathbf{\Omega} \cdot \nabla I(\mathbf{r}, \lambda, \mathbf{\Omega}) + \mu(\mathbf{r}, \lambda) I(\mathbf{r}, \lambda, \mathbf{\Omega}) \\ &= \int_0^\infty d\lambda' \int_{4\pi} d\Omega' \frac{\lambda}{\lambda'} \mu_s(\mathbf{r}, \lambda' \rightarrow \lambda, \mathbf{\Omega}' \rightarrow \mathbf{\Omega}) I(\mathbf{r}, \lambda', \mathbf{\Omega}') + \lambda S(\mathbf{r}, \lambda, \mathbf{\Omega}). \end{aligned} \tag{10.17}$$

If the atomic and electron densities at $\mathbf{r}$ are denoted by $N(\mathbf{r})$ and ${}_eN(\mathbf{r})$, respectively, and if the photon scattering description of Eq. (3.22) is used for the scattering process, then the kernel μ_s can be written as

$$\begin{aligned} \mu_s(\mathbf{r}, E' \rightarrow E, \mathbf{\Omega}' \rightarrow \mathbf{\Omega}) &= {}_eN(\mathbf{r}) {}_e\sigma_C(\lambda', \lambda, \mathbf{\Omega} \cdot \mathbf{\Omega}') + \frac{N(\mathbf{r})}{4\pi} \sigma_{\mathrm{pp}}(\mathbf{r}, \lambda') 2\delta(\lambda - 1) \\ &\quad + \frac{N(\mathbf{r})}{4\pi} \sigma_{\mathrm{ph}}(\mathbf{r}, \lambda') \mathfrak{N}(\mathbf{r}, \lambda, \lambda'), \end{aligned} \tag{10.18}$$

where the spatial dependence of σ_{pp}, σ_{ph}, and $\mathfrak{N}$ is due only to atomic composition variations. If the medium is homogeneous in composition, although not necessarily in density, then ${}_eN(\mathbf{r}) = ZN(\mathbf{r})$. Thus, the kernel becomes

$$\begin{aligned} \mu_s(\mathbf{r}, \lambda' \rightarrow \lambda, \mathbf{\Omega}' \rightarrow \mathbf{\Omega}) &\equiv \mu_s(\mathbf{r}, \lambda' \rightarrow \lambda, \mathbf{\Omega}' \cdot \mathbf{\Omega}) \\ &= \frac{N(\mathbf{r}) {}_e\sigma_T}{2\pi} [F(\lambda', \lambda)\delta(1 - \mathbf{\Omega} \cdot \mathbf{\Omega}' + \lambda - \lambda') + F_{\mathrm{iso}}(\lambda', \lambda)], \end{aligned} \tag{10.19}$$

where from Eq. (3.22),

$$F(\lambda', \lambda) = \frac{3}{8}\left(\frac{\lambda'}{\lambda}\right)^2 \left[\frac{\lambda}{\lambda'} + \frac{\lambda'}{\lambda} + (\lambda - \lambda')(\lambda - \lambda' - 2)\right] Z, \tag{10.20}$$

and where the isotropic component of the kernel is given by

$$F_{\mathrm{iso}}(\lambda', \lambda) = \frac{1}{2 {}_e\sigma_T} [2\sigma_{\mathrm{pp}}(\lambda')\delta(\lambda - 1) + \sigma_{\mathrm{ph}}(\lambda')\mathfrak{N}(\lambda, \lambda')], \tag{10.21}$$

with ${}_e\sigma_T$ representing the microscopic Thomson cross section [Eq. (3.21)]. Often the isotropic component F_{iso} resulting from annihilation and fluorescent radiation is ignored in transport calculations, leaving only the Compton scattering to describe the secondary photon production. However, for a problem with high-energy photons, annihilation radiation may be important and techniques have been devised which make it possible to include both Compton scattering and annihilation radiation in transport calculations.

In the description of photon transport above, several possible photon interactions have been ignored or approximated. Such a treatment is not as cavalier as one might first suppose (see Section 5.4.4). In shielding calculations, one is concerned primarily with the deposition of photon energy and, ultimately, the "dose" arising from this deposition. The details of the photon flux density are not generally of great concern. Thus, since the fluorescence radiation is small both in total amount and individual photon energy, it is sufficiently accurate in the estimation of a dose to assume that the entire energy of the photoelectric event is carried away by the photoelectron. Bremsstrahlung is generally a minor component, and its neglect implies that all the kinetic energy of the secondary electrons is transferred to the medium directly. Similarly, the neglect of pair production and subsequent annihilation radiation is not unreasonable if the pair production cross section is small enough. It should be noted that for none of these approximations is the principle of energy conservation violated. These approximations simply result in energy being deposited in a somewhat different location than would be predicted by a more rigorous calculation.

10.1.3 Transport Equation for Neutrons

The description of the transport of neutrons is fundamentally identical with that used for photons. However, for neutrons the variation of the cross sections in the transport equations is much more erratic for different neutron energies or medium compositions. Moreover, fast neutrons tend to make far more scatters while propagating through a medium than do photons, and consequently the details of the scattering cross sections can become very important. Because of the constraints of conservation of energy and momentum in a scattering process, the scattering kernels for neutron transport (as for photon transport) are often highly anisotropic in the scattering angle. Moreover, scattering cross sections are different for each scattering isotope and for each inelastic scattering level of a given isotope. Thus, the scattering kernel encountered in a rigorous description of neutron transport can be very much more complicated than the Compton scattering cross section used in photon transport problems (where only free electron scattering usually need be considered).

If $\sigma_{ij}(E' \rightarrow E, \mathbf{\Omega}' \rightarrow \mathbf{\Omega})$ denotes the doubly differential microscopic scattering cross section of the ith nuclear species in which the nucleus is left in its jth excited state, the transport equation of Eq. (10.9) can be written as

$$\boldsymbol{\Omega} \cdot \nabla\phi(\mathbf{r}, E, \boldsymbol{\Omega}) + \sum_{i=1}^{M} N_i(\mathbf{r})\sigma_i(E)\phi(\mathbf{r}, E, \boldsymbol{\Omega})$$

$$= \sum_{i=1}^{M} \sum_{j=0}^{L_i} \int_0^\infty dE' \int_{4\pi} d\Omega'\, N_i(\mathbf{r})\sigma_{ij}(E' \to E, \boldsymbol{\Omega}' \to \boldsymbol{\Omega})\phi(\mathbf{r}, E', \boldsymbol{\Omega}') + S(\mathbf{r}, E, \boldsymbol{\Omega}), \tag{10.22}$$

where $N_i(\mathbf{r})$ is the atomic concentration of the ith isotope with total microscopic cross section $\sigma_i(E)$. The index j refers to the final energy level of the scattering nucleus ($j = 0$ implies elastic scattering, i.e., scattering that leaves the nucleus in the ground state). A total of M nuclear species is considered, the ith of which has $L_i + 1$ scattering levels. The source term S is assumed to include all secondary neutron production processes exclusive of scattering (e.g., fission and $(n, 2n)$ reactions) as well as non-neutron-induced sources [e.g., spontaneous fission, (γ, n), (α, n) reactions]. In most shielding calculations, fission and $(n, 2n)$ reactions can be ignored so that $S(\mathbf{r}, E, \boldsymbol{\Omega})$ is independent of the neutron flux density $\phi(\mathbf{r}, E, \boldsymbol{\Omega})$.

Usually of most importance in the transport equation for fast neutrons is the accurate specification of the scattering source term, which, for deep penetration problems typically encountered in shielding analyses, can be expected to exhibit strong directional anisotropy. From the results of Section 3.7.2, the doubly differential microscopic scattering cross section may be written explicitly as

$$\sigma_{ij}(E' \to E, \boldsymbol{\Omega}' \to \boldsymbol{\Omega}) \equiv \sigma_{ij}(E' \to E, \boldsymbol{\Omega}' \cdot \boldsymbol{\Omega})$$

$$= \frac{\sigma_{ij}(E')}{2\pi(1 - \alpha_i)E'\sqrt{1 + \Delta_{ij}}} \sum_{n=0}^{N} (2n + 1) f_n^{ij}(E') P_n(\omega_c^{ij}) \delta(\boldsymbol{\Omega}' \cdot \boldsymbol{\Omega} - \omega_s^{ij}(E', E)), \tag{10.23}$$

where

$$\omega_c^{ij} \equiv \frac{(E/E')(A_i + 1)^2 - (1 + A_i^2) - A^2\Delta_{ij}}{2A_i\sqrt{1 + \Delta_{ij}}}, \tag{10.24}$$

$$\omega_s^{ij}(E', E) \equiv \frac{1}{2}\left[(A_i + 1)\sqrt{\frac{E}{E'}} - (A_i - 1)\sqrt{\frac{E'}{E}} - \frac{Q_{ij}A_i}{\sqrt{EE'}}\right], \tag{10.25}$$

$$\Delta_{ij} \equiv \frac{Q_{ij}(A_i + 1)}{E'A_i}, \tag{10.26}$$

and Q_{ij} represents the Q value for a scattering interaction which leaves the ith isotope in its jth excited state. The total cross section $\sigma_{ij}(E')$ and the Legendre scattering coefficients f_n^{ij} must be obtained from cross-section compilations based on experimental data since no comprehensive theoretical expressions exist analogous to the Klein–Nishina cross section for photons. Generally for inelastic scattering ($j > 0$) the scattering is often assumed to be isotropic in the center-of-mass system (i.e., $f_n^{ij} = 0$ for $n > 0$). Of course, f_0^{ij} always equals unity.

Finally, the infinite range of the E' integration in the scattering source term in Eq. (10.22) can be reduced by noting that for fast neutrons $\sigma_{ij} = 0$ if the final energy E is greater than the initial energy E'. Further, for the scattered neutron to have an energy E, the energy of the incident neutron, E', must be

such that $E^{ij}_{\min} \leq E' \leq E^{ij}_{\max}$, where $E^{ij}_{\min}$ and $E^{ij}_{\max}$ are found by solving Eq. (3.71) for E with $\cos\theta_c = \pm 1$, namely[2]

$$E^{ij}_{\max} = \frac{E}{(A_i - 1)^2}[\sqrt{A_i^2 - A_i(A_i - 1)Q_{ij}/E} + 1]^2 \tag{10.27}$$

and

$$E^{ij}_{\min} = \frac{E}{(A_i - 1)^2}[\sqrt{A_i^2 - A_i(A_i - 1)Q_{ij}/E} - 1]^2. \tag{10.28}$$

For the special case of hydrogen ($A_i = 1$ and $L_i = 0$), the results above reduce to $E_{\max} = \infty$ and $E_{\min} = E$. Thus the infinite integration range for E' in the scattering source term may be replaced by integration over the interval $(\epsilon_{ij}, \eta_{ij})$ where $\epsilon_{ij} = \min(E_0, E^{ij}_{\min})$, $\eta_{ij} = \min(E_0, E^{ij}_{\max})$, and E_0 is the maximum energy of neutrons in the system.

In the description of neutron scattering above, it is assumed that the scattering nuclei are at rest and unbound so that neutrons always lose energy upon scattering. This assumption is very good for fast and epithermal neutrons for which the thermal motion of and interatomic forces between the scattering atoms can be neglected. However, for thermal neutrons, the thermal motion of the scattering isotopes can cause the neutrons to gain or lose energy upon scattering and thus the above results are no longer valid. The detailed description of low-energy neutron interactions is very complex and beyond the scope of this book. Fortunately, for practical transport shielding calculations, the flux density of thermal neutrons can be treated as a single monoenergetic group of neutrons whose interaction with the medium is described by appropriate "thermal-averaged" cross sections.

Inelastic scattering can often be ignored in many transport calculations involving neutrons with energies less than a few MeV. In this case the transport equation assumes a much simpler form:

$$\begin{aligned}\boldsymbol{\Omega} \cdot \nabla\phi(\mathbf{r}, E, \boldsymbol{\Omega}) + \sum_{i=1}^{M} N_i(\mathbf{r})\sigma_i(E)\phi(\mathbf{r}, E, \boldsymbol{\Omega}) \\ = S(\mathbf{r}, E, \boldsymbol{\Omega}) + \frac{1}{2\pi}\sum_{i=1}^{M}\int_E^{E/\alpha_i} dE' N_i(\mathbf{r})\sigma_s^i(E' \to E)\int_{4\pi} d\Omega' \\ \cdot \delta\left(\boldsymbol{\Omega} \cdot \boldsymbol{\Omega}' - \frac{A_i + 1}{2}\sqrt{\frac{E}{E'}} + \frac{A_i - 1}{2}\sqrt{\frac{E'}{E}}\right)\phi(\mathbf{r}, E', \boldsymbol{\Omega}'),\end{aligned} \tag{10.29}$$

where, with $\alpha_i \equiv (A_i - 1)^2/(A_i + 1)^2$,

$$\sigma_s^i(E' \to E) = \frac{\sigma_s^i(E')}{(1 - \alpha_i)E'}\sum_{n=0}^{N}(2n + 1)f_n^i(E')P_n\left(\frac{(E/E')(A_i + 1)^2 - (1 + A_i^2)}{2A_i}\right). \tag{10.30}$$

For isotropic scattering in the center-of-mass system ($N = 0$), this result reduces to

$$\sigma_s^i(E' \to E) = \frac{\sigma_s^i(E')}{(1 - \alpha_i)E'}. \tag{10.31}$$

[2]Note that, in this context, the E and E' symbols of Eq. (3.71) must be reversed.

In many early investigations of fast-neutron transport, a quantity proportional to the logarithm of the neutron energy was used rather than the neutron energy itself. This quantity, roughly analogous to the use of the Compton wavelength in photon transport, is called the neutron *lethargy*, defined as

$$u \equiv \ln\left(\frac{E_0}{E}\right), \tag{10.32}$$

where E_0 is any arbitrary energy reference (usually taken as the highest neutron energy in the system under consideration). This lethargy variable, besides having a much smaller variation from fast to thermal energies than does the energy variable, permits easier computation of many flux-related quantities (e.g., scattering rate) in idealized systems. However, most modern neutron-shielding transport calculations use the energy variable directly.

10.1.4 Implications of the Transport Equation

Since the transport equation, Eq. (10.9), accurately describes the propagation of photons or neutrons in a medium, it is not surprising that many fundamental properties of radiation fields can be inferred from this equation. In this section several important properties are presented; and although the proof of some is well beyond the scope of this book, their use can often simplify greatly the analysis of radiation fields.

Existence and uniqueness. The question of existence of a solution of the time-dependent transport equation can be answered for various restrictions on the cross sections and source distributions. From physical grounds, a subcritical system must have a nonnegative spatially continuous solution. Further, one intuitively expects such a solution to be unique, that is, if one solution is obtained which satisfies the transport equation and all the boundary conditions, it must be the only solution. For most shielding problems, the question of criticality is not of concern since seldom is fission- or photon-stimulated emission of significance. Generally, scattering is the only secondary-particle-producing reaction of consequence. Under these conditions the existence and uniqueness of a solution to the transport equation is assured if all sources and incident boundary flux densities are specified [3].

Spatially uniform flux density. In an infinite homogeneous medium with uniformly distributed sources, the flux density is independent of position. More surprisingly, it is not always necessary to have a uniform density in the medium in order to have a uniform flux density. The statement of this result (known as Fano's theorem [4]) is as follows:

> The angular and energy-dependent flux density, $\phi(\mathbf{r}, E, \boldsymbol{\Omega})$, in an infinite medium is independent of position $\mathbf{r}$ if (1) the medium composition is everywhere the same except for variations in density, (2) the energy spectrum and angular distribution of sources is independent of $\mathbf{r}$, and (3) the strength of the sources is everywhere proportional to the local density.

The proof of this statement is readily obtained from the transport equation, which may be written as

$$\begin{aligned}&\mathbf{\Omega} \cdot \nabla\phi(\mathbf{r}, E, \mathbf{\Omega}) + \mu(\mathbf{r}, E)\phi(\mathbf{r}, E, \mathbf{\Omega}) \\ &\quad = S(\mathbf{r}, E, \mathbf{\Omega}) + \int_0^\infty dE' \int_{4\pi} d\Omega' \mu_s(\mathbf{r}, E' \to E, \mathbf{\Omega}' \cdot \mathbf{\Omega})\phi(\mathbf{r}, E', \mathbf{\Omega}').\end{aligned} \tag{10.33}$$

Divide by the local density $\rho(\mathbf{r})$ and note that for a single type of medium μ/ρ, μ_s/ρ, and S/ρ are independent of $\mathbf{r}$, to obtain

$$\frac{1}{\rho(\mathbf{r})} \mathbf{\Omega} \cdot \nabla\phi(\mathbf{r}, E, \mathbf{\Omega}) = -\frac{\mu}{\rho}\phi + \int_0^\infty dE' \int_{4\pi} d\Omega' \frac{\mu_s}{\rho}\phi(\mathbf{r}, E', \mathbf{\Omega}') + \frac{S}{\rho}. \tag{10.34}$$

Consider a tentative solution for the flux density that satisfies the following equations without any $\mathbf{r}$ dependence:

$$\frac{\mu}{\rho}(E)\phi(E, \mathbf{\Omega}) = \int_0^\infty dE' \int_{4\pi} d\Omega' \frac{\mu_s}{\rho}(E' \to E, \mathbf{\Omega}' \cdot \mathbf{\Omega})\phi(E', \mathbf{\Omega}') + \frac{S}{\rho}(E, \mathbf{\Omega}). \tag{10.35}$$

This equation yields a positive solution for $\phi(E, \mathbf{\Omega})$ which also satisfies Eq. (10.33) for any given value of $\mathbf{r}$, and since there can be only one solution to the transport equation, it must be the only solution. Thus ϕ must be independent of $\mathbf{r}$ and is given by the solution of Eq. (10.35).

Plane-density variations. For a plane parallel (slab) geometry in which the material properties and source distributions vary only with one spatial dimension (perpendicular to the plane interfaces), the spatial dependence of the flux density will also depend only on this dimension. The flux density in such a slab of thickness T is thus determined from the transport equation

$$\begin{aligned}&\omega \frac{\partial\phi(x, E, \mathbf{\Omega})}{\partial x} + \mu(x, E)\phi(x, E, \mathbf{\Omega}) \\ &\quad = S(x, E, \mathbf{\Omega}) + \int_0^\infty dE' \int_{4\pi} d\Omega' \mu_s(x, E' \to E, \mathbf{\Omega}' \cdot \mathbf{\Omega})\phi(x, E', \mathbf{\Omega}'),\end{aligned} \tag{10.36}$$

subject to specified incident flux densities at the slab surface [i.e., $\phi(0, E, \mathbf{\Omega})$ for $\omega > 0$ and $\phi(T, E, \mathbf{\Omega})$ for $\omega < 0$ are given]. The variation of the interaction coefficients with x complicates somewhat the solution of Eq. (10.36). However, if the material in the medium is everywhere the same and the coefficients vary with x only because of plane-density variations, it is possible to transform this problem into an equivalent problem in a homogeneous medium.

If distance is measured in terms of mass thickness into the medium,

$$\tau(x) \equiv \int_0^x \rho(x')\, dx', \tag{10.37}$$

Eq. (10.36) becomes, upon dividing through by the density ρ,

$$\omega \frac{\partial\phi(\tau, E, \mathbf{\Omega})}{\partial\tau} + \frac{\mu}{\rho}\phi(\tau, E, \mathbf{\Omega}) = \frac{S(\tau, E, \mathbf{\Omega})}{\rho(\tau)} + \int_0^\infty dE' \int_{4\pi} d\Omega' \frac{\mu_s}{\rho}\phi(\tau, E', \mathbf{\Omega}'), \tag{10.38}$$

where $\phi(\tau, E, \mathbf{\Omega}) \equiv \phi(x(\tau), E, \mathbf{\Omega})$. If the material is the same everywhere in the medium, then μ/ρ and μ_s/ρ are independent of position. Further, the flux density in any other plane system of the same material but with arbitrary plane density variations will be determined by this same transport equation. In particular, consider a plane system of the same material but with constant density ρ_h and of the same mass thickness in width, $\tau_T = \rho_h T_h$, and with the same boundary conditions. The flux density ϕ_h for this special homogeneous case is thus determined by

$$\omega \frac{\partial \phi_h(\tau, E, \mathbf{\Omega})}{\partial \tau} + \frac{\mu}{\rho_h} \phi_h(\tau, E, \mathbf{\Omega}) = \frac{S_h(\tau, E, \mathbf{\Omega})}{\rho_h} + \int_0^\infty dE' \int_{4\pi} d\Omega' \frac{\mu_s}{\rho_h} (E' \to E, \mathbf{\Omega}' \cdot \mathbf{\Omega}) \phi_h(\tau, E', \mathbf{\Omega}'), \tag{10.39}$$

with the same incident flux densities $\phi(0, \mathbf{\Omega})$ for $\omega > 0$ and $\phi(\tau_T, \mathbf{\Omega})$ for $\omega < 0$. If one chooses the internal source distribution S_h for this homogeneous problem as

$$S_h(\tau, E, \mathbf{\Omega}) = \frac{S(\tau, E, \mathbf{\Omega})\rho_h}{\rho(\tau)}, \tag{10.40}$$

where S is the source distribution of the original problem with plane-density variations, then Eq. (10.39) becomes identical to Eq. (10.38). Thus, since the boundary conditions are the same for both problems, the two solutions must be identical [i.e., $\phi(\tau, E, \mathbf{\Omega}) = \phi_h(\tau, E, \mathbf{\Omega})$].

For the replacement of a problem with plane-density variations by an equivalent homogeneous problem with sources modified by Eq. (10.40), the material must be the same everywhere in the medium. For example, problems of radioisotopes dispersed in the atmosphere which exhibit plane-density variations with altitude could be treated by an equivalent problem with constant density. While such plane-density variations are rarely encountered in shielding analyses, it is often possible to use this equivalence in an approximate manner to simplify photon transport problems with plane variations in density *and* composition provided that the average Z number is roughly constant throughout the medium. Under this assumption of negligible variation of the average Z number throughout a medium, the quantities μ/ρ and μ_s/ρ will be essentially independent of position despite plane variations in density and material composition. Hence, a large plane source of photons on the ground could be modeled by a homogeneous medium with an effective plane source if the μ/ρ for air and earth were considered sufficiently similar.

Scaling of radiation fields. Many radiation penetration problems are so complex (e.g., very unsymmetric geometric configurations and source placements) that calculational methods often cannot treat them without unacceptable simplifications to the problem or inordinate calculational effort. For such problems, a mock-up experiment may be the best approach to determine the radiation field of interest. However, a full-scale experimental mock-up of a large

structure may be prohibitively expensive, and one would ideally like to use a smaller-scaled model.

The manner in which one should scale such an experiment can be determined from the transport equation. If position in the full-scale and scaled situations are denoted by $\mathbf{r}$ and $\mathbf{r}'$, respectively, the "corresponding positions" in the two systems are defined by

$$\mathbf{r} = \xi \mathbf{r}', \tag{10.41}$$

where ξ is the constant scaling parameter. The flux density ϕ in the original full sized system is then given by

$$\begin{aligned} &\mathbf{\Omega} \cdot \nabla \phi(\mathbf{r}, E, \mathbf{\Omega}) + \mu(\mathbf{r}, E)\phi(\mathbf{r}, E, \mathbf{\Omega}) \\ &\quad = S(\mathbf{r}, E, \mathbf{\Omega}) + \int_0^\infty dE' \int_{4\pi} d\Omega'\, \mu_s(\mathbf{r}, E' \to E, \mathbf{\Omega}' \cdot \mathbf{\Omega})\phi(\mathbf{r}, E', \mathbf{\Omega}'), \end{aligned} \tag{10.42}$$

while the flux density $\tilde{\phi}$ in the scaled system with cross sections $\tilde{\mu}$ and $\tilde{\mu}_s$ and a source distribution $\tilde{S}$ is given by

$$\begin{aligned} &\mathbf{\Omega} \cdot \tilde{\nabla} \tilde{\phi}(\mathbf{r}', E, \mathbf{\Omega}) + \tilde{\mu}(\mathbf{r}', E)\tilde{\phi}(\mathbf{r}', E, \mathbf{\Omega}) \\ &\quad = \tilde{S}(\mathbf{r}', E, \mathbf{\Omega}) + \int_0^\infty dE' \int_{4\pi} d\Omega'\, \tilde{\mu}_s(\mathbf{r}', E' \to E, \mathbf{\Omega}' \cdot \mathbf{\Omega})\tilde{\phi}(\mathbf{r}', E', \mathbf{\Omega}'). \end{aligned} \tag{10.43}$$

The relation between the gradient operators in the two systems is

$$\begin{aligned} \nabla &= \hat{\mathbf{i}} \frac{\partial}{\partial x} + \hat{\mathbf{j}} \frac{\partial}{\partial y} + \hat{\mathbf{k}} \frac{\partial}{\partial z} \\ &= \hat{\mathbf{i}} \frac{dx'}{dx} \frac{\partial}{\partial x'} + \hat{\mathbf{j}} \frac{dy'}{dy} \frac{\partial}{\partial y'} + \hat{\mathbf{k}} \frac{dz'}{dz} \frac{\partial}{\partial z'} \\ &= \xi \left[\hat{\mathbf{i}} \frac{\partial}{\partial x'} + \hat{\mathbf{j}} \frac{\partial}{\partial y'} + \hat{\mathbf{k}} \frac{\partial}{\partial z'} \right] \equiv \xi \tilde{\nabla}. \end{aligned} \tag{10.44}$$

If one now requires that the interaction coefficients and sources at corresponding positions be also scaled (such as by a change in density) so that

$$\tilde{\mu}(\mathbf{r}', E) = \xi \mu(\mathbf{r}, E), \tag{10.45}$$

$$\tilde{\mu}_s(\mathbf{r}', E' \to E, \mathbf{\Omega}' \cdot \mathbf{\Omega}) = \xi \mu_s(\mathbf{r}, E' \to E, \mathbf{\Omega}' \cdot \mathbf{\Omega}), \tag{10.46}$$

and

$$\tilde{S}(\mathbf{r}', E, \mathbf{\Omega}) = \xi S(\mathbf{r}, E, \mathbf{\Omega}), \tag{10.47}$$

Eq. (10.43) then becomes

$$\begin{aligned} &\mathbf{\Omega} \cdot \nabla \tilde{\phi}(\mathbf{r}', E, \mathbf{\Omega}) + \mu(\mathbf{r}, E)\tilde{\phi}(\mathbf{r}', E, \mathbf{\Omega}) \\ &\quad = S(\mathbf{r}, E, \mathbf{\Omega}) + \int_0^\infty dE' \int_{4\pi} d\Omega'\, \mu_s(\mathbf{r}, E' \to E, \mathbf{\Omega} \cdot \mathbf{\Omega}')\tilde{\phi}(\mathbf{r}', E', \mathbf{\Omega}'). \end{aligned} \tag{10.48}$$

This equation for $\tilde{\phi}$ (which can also be thought of as a function of $\mathbf{r}$) is the same as the transport equation for the unscaled flux density ϕ. Thus, if the boundary conditions at corresponding points in the two systems are made equal, then, from the uniqueness property of the solution of the transport equation, the

solutions of Eqs. (10.42) and (10.48) must be identical at corresponding positions, that is,

$$\tilde{\phi}(\mathbf{r}', E, \mathbf{\Omega}) = \phi(\mathbf{r}, E, \mathbf{\Omega}). \tag{10.49}$$

This equivalence between the original system and the scaled mockup is the justification for performing less expensive experiments with models. In such an experiment, if the dimensions are reduced by a factor of ξ (> 1), interaction coefficients and volumetric source strengths (per unit unscaled volume) must be increased by a factor ξ. However, the energy and directional dependence of the scaled and unscaled cross sections and sources must be the same. For example, substitution of iron in a scaled model of a concrete structure will approximately increase μ and μ_s for photons by a constant factor, although the energy dependence will be changed slightly, particularly at low energies.

Volume-to-surface source transformation. A method was presented in Chapter 6 for obtaining the flux density (or a detector response) in a restricted region of some larger space. In this method, the original problem, which allowed arbitrary source and material distributions throughout the space, was transformed into an equivalent problem in which the region of interest was surrounded by an effective surface source and the rest of the space not of interest was replaced by a perfect absorber. This equivalence seems physically reasonable since the distribution of particles in the smaller restricted region should be independent of the origin of the particles entering that restricted region. It is of no concern to the region of interest whether the particles were born at the surface from an effective surface source, or whether they were born far from the region and subsequently underwent many interactions before entering the region of interest. The connection between these two equivalent problems is that the incident flow rate on the bounding surface of the restricted region, $\hat{\mathbf{n}} \cdot \mathbf{\Omega}\phi(\mathbf{r}_s, E, \mathbf{\Omega})$, $\hat{\mathbf{n}} \cdot \mathbf{\Omega} < 0$, in the original problem must equal the effective surface source strength $S_A(\mathbf{r}_s, E, \mathbf{\Omega})$ in the equivalent problem, where $\hat{\mathbf{n}}$ is the unit normal out of the restricted region at any given point $\mathbf{r}_s$ of the surface. In this section a rigorous development [3] of this transformation is presented.

Consider a problem in which a region V (the "region of interest") has a surface source $S_A(\mathbf{r}_s, E, \mathbf{\Omega})$ at a point on the boundary given by $\mathbf{r}_s$ (see Fig. 10.4). If one chooses a local coordinate system with the origin on the surface with x measured along the outward normal $\hat{\mathbf{n}}$, and y and z measured along $\hat{\mathbf{t}}_y$ and $\hat{\mathbf{t}}_z$, normals tangential to the surface, the transport equation, in the neighborhood of a point on the bounding surface, can be written as

$$\mathbf{\Omega} \cdot \hat{\mathbf{n}} \frac{\partial \phi}{\partial x} + \mathbf{\Omega} \cdot \hat{\mathbf{t}}_y \frac{\partial \phi}{\partial y} + \mathbf{\Omega} \cdot \hat{\mathbf{t}}_z \frac{\partial \phi}{\partial z} + \mu\phi = S_V(\mathbf{r}, E, \mathbf{\Omega}) + S_A(\mathbf{r}, E\,\mathbf{\Omega})\,\delta(x)$$

$$+ \int_0^\infty dE' \int_{4\pi} d\Omega'\, \mu_s(\mathbf{r}, E' \rightarrow E, \mathbf{\Omega}' \rightarrow \mathbf{\Omega})\phi(\mathbf{r}, E', \mathbf{\Omega}'). \tag{10.50}$$

where S_V describes any sources other than the surface source S_A. Upon integrating this equation along x from $-\epsilon$ to ϵ and taking the limit as $\epsilon \rightarrow 0$, one obtains

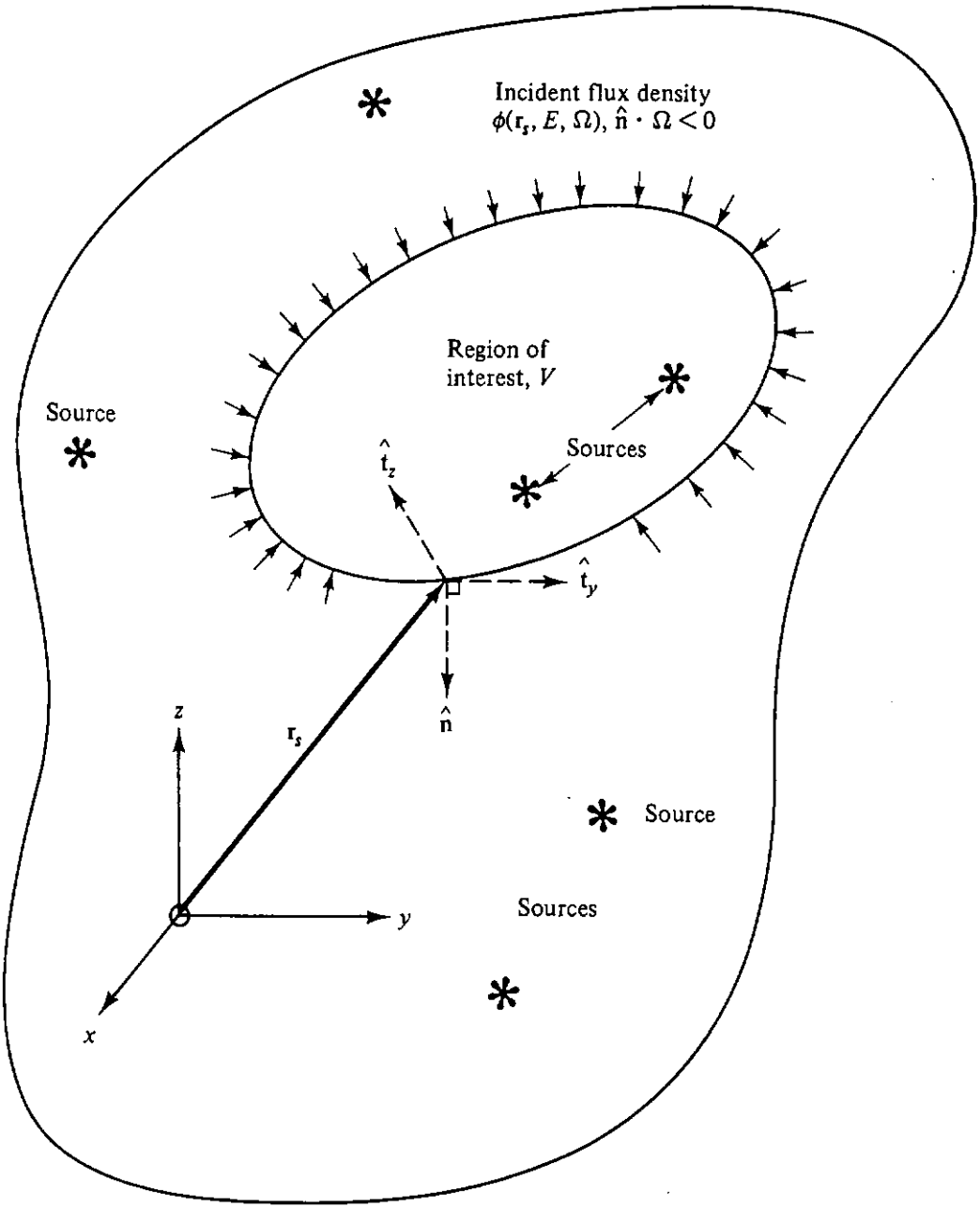

Figure 10.4 Geometry for the transformation to a smaller region of interest.

$$\mathbf{\Omega} \cdot \hat{\mathbf{n}} [\phi^+(\mathbf{r}_s, E, \mathbf{\Omega}) - \phi^-(\mathbf{r}_s, E, \mathbf{\Omega})] = S_A(\mathbf{r}_s, E, \mathbf{\Omega}') \tag{10.51}$$

where $\phi^{\pm}$ denotes the angular flux density on the positive (outward) and negative (inward) sides of the surface. From the definition of the differential flux density vector, $\mathbf{j}(\mathbf{r}, E, \mathbf{\Omega}) \equiv \mathbf{\Omega}\phi(\mathbf{r}, E, \mathbf{\Omega})$, this relation reduces to

$$j_n^+(\mathbf{r}_s, E, \mathbf{\Omega}) - j_n^-(\mathbf{r}_s, E, \mathbf{\Omega}) = S_A(\mathbf{r}_s, E, \mathbf{\Omega}), \tag{10.52}$$

where $j_n^{\pm} = \hat{\mathbf{n}} \cdot \mathbf{j}^{\pm}$ is the component of the current density vector along the direction $\hat{n}$ at the outside (+) and on the inside (−) of the surface. Thus, it is seen that the effect of the surface source is to cause a discontinuity or "jump" in the normal component of the current density vector across the source plane.

In the original problem, there is no surface source on the boundary of the

region of interest, but as a result of the sources inside and outside the region of interest, an angular flux density $\phi(\mathbf{r}_s, E, \mathbf{\Omega})$ is established at the boundary. If the material and sources outside the region of interest were now to be altered arbitrarily, but somehow the incident angular flux density at the boundary were still held equal to $\phi(\mathbf{r}_s, E, \mathbf{\Omega})$, $\hat{\mathbf{n}} \cdot \mathbf{\Omega} < 0$, the flux density inside the region of interest would be unchanged since the solution of the transport equation in a region is uniquely determined by the material and sources in the region and by the incident boundary conditions [3]. In particular, if the medium outside the region of interest were replaced by a perfect absorber the flux density would vanish outside the region of interest. To maintain the same incident neutron profile at the boundary of the region of interest, it is thus necessary to place a surface source on the boundary whose strength from Eq. (10.52) must be

$$S_A(\mathbf{r}_s, E, \mathbf{\Omega}) = -j_n^-(\mathbf{r}_s, E, \mathbf{\Omega}) = -\hat{\mathbf{n}} \cdot \mathbf{\Omega}\phi^-(\mathbf{r}_s, E, \mathbf{\Omega}), \qquad \hat{\mathbf{n}} \cdot \mathbf{\Omega} < 0, \tag{10.53}$$

since $j_n^+ = \phi_n^+ = 0$.

It should be noted that the terms "inside" and "outside" in the discussion above are quite relative. The region of interest could equally well be the region outside the closed boundary of Fig. 10.4, while the region inside the closed boundary can be replaced by a perfect absorber with a surface source, given by Eq. (10.53), placed on the boundary.

This volume-to-surface source transformation is a very useful device for simplifying practical transport calculations. For example, the calculation of the radiation field in a biological shield caused by radiation leaking from a reactor core would generally be very difficult if the core and shield had to be treated simultaneously. However, the foregoing transformation would allow one to decouple the core region from the shield region if the radiation leaking from the core (and incident on the shield) could first be determined. Often only an approximate knowledge of the incident particle flow rate from the core is sufficient to obtain an adequate estimate of an effective surface source strength. The core is then conceptually replaced by a perfect absorber, so that calculations only in the biological shield need be performed.

10.2 APPROXIMATIONS TO THE TRANSPORT EQUATION

The transport equation discussed in the preceding section presents a very detailed description of the radiation field in a medium. Often such detail is not necessary since one seldom needs the complete spatial, directional, and energy dependence of the radiation. Consequently, several approximations of the transport equation which give less information about the radiation field are widely used. Moreover, these approximations usually greatly simplify the description of particle transport and reduce the computational effort needed to calculate properties of the radiation field. In this section three of the most important simple approximations to the transport equation are discussed.

10.2.1 Exponential Attenuation

Many of the techniques presented in this book have been based on radiation being attenuated exponentially as it traverses a medium. This exponential attenuation is rigorously true only for the uncollided radiation—a fact readily inferred from the transport equation. For a homogeneous, source-free medium, the transport equation for the uncollided flux density ϕ^0 can be written as

$$\mathbf{\Omega} \cdot \nabla\phi^0(\mathbf{r}, E, \mathbf{\Omega}) + \mu(E)\phi^0(\mathbf{r}, E, \mathbf{\Omega}) = 0, \tag{10.54}$$

since no scattered particles are included in the uncollided flux density. In Section 10.1.1 it was shown that $\mathbf{\Omega} \cdot \nabla = d/ds$, where s is measured along the direction $\mathbf{\Omega}$. Thus, if the uncollided flux density is known at point $\mathbf{r}$, the flux density at any other point $\mathbf{r}'(\equiv \mathbf{r} + s\mathbf{\Omega})$ is found from Eq. (10.54) to be

$$\phi^0(\mathbf{r} + s\mathbf{\Omega}, E, \mathbf{\Omega}) = \phi^0(\mathbf{r}, E, \mathbf{\Omega}) \exp[-\mu(E)s]. \tag{10.55}$$

Although the total flux density (uncollided plus scattered) is not generally attenuated in a purely exponential manner, there are several situations in which exponential attenuation may be a good approximation. For high-energy photon and neutron problems, the scattering cross sections tend to be very anisotropic and peaked in the forward direction and thus may be approximated by

$$\mu_s(\mathbf{r}, E' \rightarrow E, \mathbf{\Omega}' \cdot \mathbf{\Omega}) \simeq \mu_s(\mathbf{r}, E' \rightarrow E)\,\delta(\mathbf{\Omega}' \cdot \mathbf{\Omega} - 1). \tag{10.56}$$

This "straight-ahead approximation" implies that a particle does not appreciably change its direction of travel upon scattering. With this approximation, the transport equation, Eq. (10.9), for a source-free medium becomes

$$\begin{aligned}\mathbf{\Omega} \cdot \nabla\phi(\mathbf{r}, E, \mathbf{\Omega}) + \mu(\mathbf{r}, E)\phi(\mathbf{r}, E, \mathbf{\Omega}) &= \int_0^\infty dE' \int_{4\pi} d\Omega'\, \mu_s(\mathbf{r}, E' \rightarrow E)\phi(\mathbf{r}, E', \mathbf{\Omega}')\delta(\mathbf{\Omega}' \cdot \mathbf{\Omega} - 1) \\ &= \int_0^\infty dE'\, \mu_s(\mathbf{r}, E' \rightarrow E)\phi(\mathbf{r}, E', \mathbf{\Omega}).\end{aligned} \tag{10.57}$$

If one is interested in a detector response R, given the detector response function $\mathcal{R}(E)$, that is,

$$R(\mathbf{r}, \mathbf{\Omega}) \equiv \int_0^\infty dE\, \mathcal{R}(E)\phi(\mathbf{r}, E, \mathbf{\Omega}), \tag{10.58}$$

then integration of Eq. (10.57) with respect to energy after multiplication by $\mathcal{R}(E)$ gives

$$\mathbf{\Omega} \cdot \nabla R(\mathbf{r}, \mathbf{\Omega}) + \int_0^\infty dE\, \mathcal{R}(E)[\mu(\mathbf{r}, E) - \hat{\mu}_s(\mathbf{r}, E)]\phi(\mathbf{r}, E, \mathbf{\Omega}) = 0, \tag{10.59}$$

where a weighted scattering coefficient is defined as

$$\hat{\mu}_s(\mathbf{r}, E') \equiv \int_0^\infty dE\, \frac{\mathcal{R}(E)}{\mathcal{R}(E')}\, \mu_s(\mathbf{r}, E' \rightarrow E). \tag{10.60}$$

Equation (10.59) may be rewritten as

$$\mathbf{\Omega} \cdot \nabla R(\mathbf{r}, \mathbf{\Omega}) + \bar{\mu}_a(\mathbf{r}, \mathbf{\Omega}) R(\mathbf{r}, \mathbf{\Omega}) = 0, \tag{10.61}$$

with an effective absorption coefficient defined as

$$\bar{\mu}_a(\mathbf{r}, \mathbf{\Omega}) \equiv \int_0^\infty dE\, \mathcal{R}(E)[\mu(\mathbf{r}, E) - \hat{\mu}_s(\mathbf{r}, E)]\phi(\mathbf{r}, E, \mathbf{\Omega})/R(\mathbf{r}, \mathbf{\Omega}). \tag{10.62}$$

If the energy dependence of $\phi(\mathbf{r}, E, \mathbf{\Omega})$ is approximately separable from the angular dependence, then $\bar{\mu}_a$ becomes independent of $\mathbf{\Omega}$ and can be evaluated knowing only the energy dependence of ϕ. In practice, one could approximate $\bar{\mu}_a$ from its definition by assuming some reasonable energy spectrum. This problem of calculating $\bar{\mu}_a$ without first knowing $\phi(\mathbf{r}, E, \mathbf{\Omega})$ is a special case of a macroscopic group-cross-section (coefficient) evaluation, which is discussed in greater detail in Section 10.2.3. With s measured along the direction of $\mathbf{\Omega}$, Eq. (10.61) can be integrated along $\mathbf{\Omega}$ to give

$$R(\mathbf{r} + s\mathbf{\Omega}, \mathbf{\Omega}) = R(\mathbf{r}, \mathbf{\Omega}) \exp\left[\int_0^s \bar{\mu}_a(\mathbf{r} + s'\mathbf{\Omega}, \mathbf{\Omega})\, ds'\right], \tag{10.63}$$

which for a homogeneous medium reduces to

$$R(\mathbf{r} + s\mathbf{\Omega}, \mathbf{\Omega}) = R(\mathbf{r}, \mathbf{\Omega}) e^{-\bar{\mu}_a s}. \tag{10.64}$$

Thus in the straight-ahead approximation, the detector response R is seen to attenuate exponentially along the path of particle travel.

This straight-ahead approximation leads one to expect that a beam of radiation will be attenuated in an approximately exponential fashion whenever the penetration of radiation is dominated by small-angle scattering. For example, the penetration of fast neutrons in an hydrogenous medium is controlled by the streaming of uncollided and small-angle-scattered neutrons both because the scattering cross sections tend to be peaked in the forward scattering direction in the laboratory coordinate system and because any large-angle scatter degrades the neutron energy to such an extent that it is subsequently thermalized rapidly and removed from the fast energy region. Hence, one would expect the removal of fast neutrons in such a medium to exhibit an exponential behavior. Similarly, for high-energy gamma photons (whose scattering cross section is highly forwarded peaked) penetrating through a medium composed of heavy nuclides, any photons scattered through large angles will be degraded in energy and subsequently attenuated rapidly. Thus, the deep penetration of these photons will be governed by small-angle-scattered photons, which in turn can be expected to attenuate exponentially with some effective attenuation coefficient.

Finally, an exponential attenuation behavior can often be expected deep within a shield from more fundamental considerations. Many investigations have explored the characteristics of the transport equation; and for certain approximations, such as constant cross sections or the multigroup model (see Section 10.2.3), the flux density, sufficiently far from boundaries or sources, will inherently attenuate in an exponential manner. However, the calculation of the exact value of the appropriate attenuation coefficient in terms of the material cross sections is generally very complicated.

10.2.2 Diffusion Approximation

For most shielding applications the angular detail of the flux density is not needed. Rather, the directionally integrated flux density $\phi(\mathbf{r}, E)$ is all that is often desired. Although no rigorous equation exists for this quantity, it is possible to obtain an approximate equation for it. This approximation, known as the diffusion equation, is generally much simpler to solve numerically or analytically than is the rigorous transport equation; and consequently diffusion theory is often applied to shielding problems, particularly those involving neutron transport.

Although the diffusion approximation may be derived directly from a particle balance requirement [5], it is more instructive to derive it from the transport equation and to see explicitly the inherent approximation. For simplicity, consider the transport equation in plane geometry in which the angular flux density is azimuthally symmetric [i.e., $\phi(x, E, \omega, \psi) = \phi(x, E, \omega)$]. If the sources are then assumed to be isotropic so that $S(x, E, \omega, \psi) = S(x, E)/4\pi$, the transport equation becomes

$$\omega \frac{\partial \phi(x, E, \omega)}{\partial x} + \mu(x, E)\phi(x, E, \omega) = \frac{S(x, E)}{4\pi} + \int_0^\infty dE' \int_{-1}^{1} d\omega' \int_0^{2\pi} d\psi' \, \mu_s(x, E' \to E, \mathbf{\Omega}' \cdot \mathbf{\Omega})\phi(x, E', \omega'). \tag{10.65}$$

To eliminate the ω dependence, integrate over all directions to obtain the "continuity" equation

$$\frac{\partial j_x(x, E)}{\partial x} + \mu(x, E)\phi(x, E) = \int_0^\infty dE' \, \mu_s(x, E' \to E)\phi(x, E') + S(x, E), \tag{10.66}$$

where the following directionally integrated quantities have been defined (see Sections 2.1.3 and 2.1.4):

$$j_x(x, E) \equiv 2\pi \int_{-1}^{1} d\omega \, \omega\phi(x, E, \omega) \tag{10.67}$$

$$\phi(x, E) \equiv 2\pi \int_{-1}^{1} d\omega \, \phi(x, E, \omega) \tag{10.68}$$

and

$$\mu_s(x, E' \to E) \equiv \int_0^{2\pi} d\psi \int_{-1}^{1} d\omega \, \mu_s(x, E' \to E, \mathbf{\Omega}' \cdot \mathbf{\Omega}). \tag{10.69}$$

Because of the assumed azimuthal symmetry in the flux density, the y and z components of the current density vector $\mathbf{j}(x, E)$ are zero; that is, there is no net flow rate through surfaces perpendicular to the y and z directions.

By this integration of the transport equation over all directions, an equation for the angularly integrated flux density ϕ has been obtained; however, the current component j_x (net flow rate through the y-z plane) also appears in this result, and thus another equation for j_x is needed. To this end, multiply the

transport equation, Eq. (10.65), by ω and integrate the result over all ω. The result, called the "current equation," is

$$\frac{\partial}{\partial x}\int_{-1}^{1} d\omega\, \omega^2\phi(x, E, \omega) + \frac{\mu(x, E)j_x(x, E)}{2\pi} = \int_0^\infty dE' \int_{-1}^{1} d\omega'\, \phi(x, E', \omega')\int_0^{2\pi} d\psi' \int_{-1}^{1} d\omega\, \omega\mu_s(x, E' \to E, \mathbf{\Omega}' \cdot \mathbf{\Omega}). \tag{10.70}$$

To simplify the last term, expand the scattering kernel in Legendre polynomials as

$$\mu_s(x, E' \to E, \mathbf{\Omega}' \cdot \mathbf{\Omega}) = \frac{1}{4\pi}\sum_{l=0}^{\infty}(2l + 1)\mu_{sl}(x, E' \to E)P_l(\mathbf{\Omega}' \cdot \mathbf{\Omega}), \tag{10.71}$$

where the expansion coefficients are given by [see Eq. (A2.30)]

$$\mu_{sl}(x, E' \to E) = 2\pi \int_{-1}^{1} d\omega_s\, P_l(\omega_s)\mu_s(x, E' \to E, \omega_s). \tag{10.72}$$

Notice that $\mu_{s0}(x, E' \to E) = \mu_s(x, E' \to E)$, the differential scattering coefficient with respect to energy. Upon use of the addition theorem of Eq. (A2.32) to express $P_l(\omega_s)$ [$\equiv P_l(\mathbf{\Omega}' \cdot \mathbf{\Omega})$] in terms of ω, ω', ψ, and ψ', the last term of Eq. (10.70) reduces to

$$\int_0^\infty dE' \int_{-1}^{1} d\omega'\, \omega'\phi(x, E', \omega')\mu_{s1}(x, E' \to E) = \frac{1}{2\pi}\int_0^\infty dE'\, \mu_{s1}(x, E' \to E)j_x(x, E'). \tag{10.73}$$

Thus, Eq. (10.70) becomes

$$2\pi\frac{\partial}{\partial x}\int_{-1}^{1} d\omega\, \omega^2\phi(x, E, \omega) + \mu(x, E)j_x(x, E) = \int_0^\infty dE'\, \mu_{s1}(x, E' \to E)j_x(x, E'). \tag{10.74}$$

Equations (10.66) and (10.74), are exact; but they contain three unknowns: $\phi(x, E)$, $j_x(x, E)$ and the second angular moment of the flux density. To reduce the number of unknowns to two so that these equations may be solved for the angularly integrated flux density $\phi(x, E)$, it is necessary to approximate one of the dependent variables in terms of the other two. In the diffusion approximation, the first term in Eq. (10.74) is approximated by assuming the flux density can be represented by a two term truncated Legendre polynomial expansion, that is,

$$\phi(x, E, \omega) \simeq \frac{1}{4\pi}\sum_{i=0}^{1}(2i + 1)\phi_i(x, E)P_i(\omega) = \frac{\phi_0}{4\pi} + \frac{3}{4\pi}\omega\phi_1, \tag{10.75}$$

where

$$\phi_0(x, E) \equiv 2\pi \int_{-1}^{1} d\omega\, \phi(x, E, \omega) = \phi(x, E), \tag{10.76}$$

$$\phi_1(x, E) \equiv 2\pi \int_{-1}^{1} d\omega\, \omega\phi(x, E, \omega) = j_x(x, E). \tag{10.77}$$

Thus, the second angular moment is approximated by

$$2\pi \int_{-1}^{1} d\omega\, \omega^2 \phi(x, E, \omega) \simeq \tfrac{1}{3}\phi(x, E). \tag{10.78}$$

The last term in the current equation, Eq. (10.74), can be written more compactly by defining the mean cosine of the scattering angle, $\bar{\omega}_s$, as

$$\mu_s(x, E)\bar{\omega}_s(x, E) \equiv \frac{1}{j_x(x, E)} \int_0^\infty dE'\, \mu_{s1}(x, E' \to E) j_x(x, E'). \tag{10.79}$$

To evaluate this expression approximately without first knowing $j_x(x, E)$, the energy transfer is commonly neglected in the anisotropic scattering component [i.e., $\mu_{s1}(x, E' \to E) \simeq \mu_{s1}(x, E')\delta(E' - E)$], so that the right-hand side of Eq. (10.79) becomes simply $\mu_{s1}(x, E)$.

With Eqs. (10.78) and (10.79), the current equation finally assumes the form

$$[\mu(x, E) - \mu_s(x, E)\bar{\omega}_s(x, E)] j_x(x, E) = -\frac{1}{3} \frac{\partial \phi(x, E)}{\partial x}, \tag{10.80}$$

or, equivalently,

$$j_x(x, E) = -D(x, E) \frac{\partial \phi(x, E)}{\partial x}, \tag{10.81}$$

where the "diffusion coefficient" $D(x, E)$ is defined by

$$D(x, E) \equiv \tfrac{1}{3}[\mu - \mu_s \bar{\omega}_s]^{-1}. \tag{10.82}$$

This relation between the particle current component and the integrated flux density is known as "Fick's law of diffusion" and states that the flow or diffusion of particles is away from regions with higher particle densities. Finally, elimination of $j_x(x, E)$ between Eqs. (10.81) and (10.66) gives the desired equation for the integrated flux density, namely,

$$\begin{aligned} -\frac{\partial}{\partial x}\left[D(x, E) \frac{\partial \phi(x, E)}{\partial x} \right] + \mu(x, E)\phi(x, E) \\ = S(x, E) + \int_0^\infty dE'\, \mu_s(x, E' \to E)\phi(x, E'). \end{aligned} \tag{10.83}$$

This result is called the "energy-dependent diffusion equation," and is considerably simpler, and hence easier to solve, than the original transport equation. Although the derivation above was for the simplest geometry, the same derivation can be extended to more general geometries [1,6]. In general geometry, the diffusion equation assumes the form

$$\begin{aligned} -\nabla \cdot D(\mathbf{r}, E)\nabla\phi(\mathbf{r}, E) + \mu(\mathbf{r}, E)\phi(\mathbf{r}, E) \\ = S(\mathbf{r}, E) + \int_0^\infty dE'\, \mu_s(\mathbf{r}, E' \to E)\phi(\mathbf{r}, E'), \end{aligned} \tag{10.84}$$

with the approximate relation between the current density vector and the flux density given by

$$\mathbf{j}(\mathbf{r}, E) = -D(\mathbf{r}, E)\nabla\phi(\mathbf{r}, E). \tag{10.85}$$

From the derivation above it is seen that the essential approximation, Eq. (10.75), constrains the angular flux density to vary at most linearly with

ω. Deep in a medium, the flux density is often composed of multiply scattered particles and hence can be expected to be nearly isotropic in direction. For such cases the diffusion approximation should be valid. However, near a free surface or a source, the flux density is quite anisotropic in direction and not at all well represented by a simple linear variation. For these situations the diffusion approximation may be poor. For example, near a point source, the flux density as calculated by diffusion theory varies as $1/r$, while transport theory gives the correct $1/r^2$ variation [3].

The energy-dependent diffusion approximation is often combined with an energy-multigroup approximation (see Section 10.2.3) to eliminate the energy variable, thereby making this model even more amenable to numerical solution. The multigroup diffusion model is widely used because of its simplicity and it often gives remarkably good results, particularly for neutron problems (see the removal–diffusion models in Chapter 8). However, for problems near interfaces or sources [where the approximation of Eq. (10.75) is poor] or for particles which undergo few scatters and have highly anisotropic scattering cross sections, this diffusion model can result in serious errors in the flux densities.

10.2.3 Multigroup Approximation

The steady-state transport equation of Eq. (10.9) is generally far too complex to solve even by numerical techniques. Even if the number of spatial and angular variables were reduced by using a simple geometry, the energy variability of the cross sections generally precludes solving the transport equation except for unrealistically simple cross-section models (e.g., constant cross sections). To make the transport equation more amenable to numerical and analytical analysis, it is usual to consider an approximation of the transport equation in which the energy variable has been removed.

By far the most common method to eliminate the energy variable in the transport equation is to use the "energy multigroup approximation." In this method the entire particle energy range $(0, E_0)$, where E_0 is the highest energy for the particles, is subdivided into G contiguous energy intervals or groups (E_g, E_{g-1}), $g = 1, 2, \ldots, G$, in which E_g $(< E_{g-1})$ is the lowest energy of the gth group. Equation (10.9) is then integrated over the gth energy interval to obtain

$$\begin{aligned}\boldsymbol{\Omega} \cdot \nabla \phi_g(\mathbf{r}, \boldsymbol{\Omega}) + \mu_g \phi_g(\mathbf{r}, \boldsymbol{\Omega}) \\ = \sum_{g'=1}^{G} \int_{4\pi} d\Omega' \, \mu_{g'g}(\mathbf{r}, \boldsymbol{\Omega}' \to \boldsymbol{\Omega}) \phi_{g'}(\mathbf{r}, \boldsymbol{\Omega}') + S_g(\mathbf{r}, \boldsymbol{\Omega}),\end{aligned} \tag{10.86}$$

where the gth group flux density and source are defined as

$$\phi_g(\mathbf{r}, \boldsymbol{\Omega}) \equiv \int_{E_g}^{E_{g-1}} dE \, \phi(\mathbf{r}, E, \boldsymbol{\Omega}), \tag{10.87}$$

$$S_g(\mathbf{r}, \boldsymbol{\Omega}) \equiv \int_{E_g}^{E_{g-1}} dE \, S(\mathbf{r}, E, \boldsymbol{\Omega}), \tag{10.88}$$

and the group total and scattering transfer coefficients are defined as

$$\mu_g \equiv \frac{1}{\phi_g(\mathbf{r}, \mathbf{\Omega})} \int_{E_g}^{E_{g-1}} dE\, \mu(\mathbf{r}, E)\phi(\mathbf{r}, E, \mathbf{\Omega}) \tag{10.89}$$

and

$$\mu_{g'g} \equiv \frac{1}{\phi_{g'}(\mathbf{r}, \mathbf{\Omega}')} \int_{E_g}^{E_{g-1}} dE \int_{E_{g'}}^{E_{g'-1}} dE'\, \mu_s(\mathbf{r}, E' \to E, \mathbf{\Omega}' \to \mathbf{\Omega})\phi(\mathbf{r}, E', \mathbf{\Omega}'). \tag{10.90}$$

Equation (10.86) is an exact result and this multigroup equation is equivalent to the original energy-dependent transport equation. However, to evaluate the "group constants" μ_g and $\mu_{g'g}$ from Eqs. (10.89) and (10.90), it is seen that the energy-dependent flux density must, in principle, first be known! Moreover, these group cross sections obtain a spatial and directional dependence from both the flux density and the energy-dependent interaction coefficients.

The great value of the multigroup equations arises when the group cross sections can be approximated without first knowing the flux density $\phi(\mathbf{r}, E, \mathbf{\Omega})$. For example, it is often assumed that the energy dependence of ϕ can be separated as $\phi(\mathbf{r}, E, \mathbf{\Omega}) \simeq W(E)\phi(\mathbf{r}, \mathbf{\Omega})$ so that the group coefficients become

$$\mu_g(\mathbf{r}) \simeq \int_{E_g}^{E_{g-1}} dE\, \mu(\mathbf{r}, E)W(E) \Big/ \int_{E_g}^{E_{g-1}} dE\, W(E) \tag{10.91}$$

and

$$\mu_{g'g}(\mathbf{r}, \mathbf{\Omega}' \to \mathbf{\Omega}) \simeq \int_{E_g}^{E_{g-1}} dE \int_{E_{g'}}^{E_{g'-1}} dE'\, \mu_s(\mathbf{r}, E' \to E, \mathbf{\Omega}' \to \mathbf{\Omega})W(E') \Big/ \int_{E_{g'}}^{E_{g'-1}} dE\, W(E). \tag{10.92}$$

For very fine energy meshes, the weight function $W(E)$ may be assumed constant over each group so that the group coefficients may be directly computed from the approximations above [the weight W in Eqs. (10.91) and (10.92) cancels out]. For broader groups, various approximations for $W(E)$ are used. In the MeV energy range $W(E)$ is often taken as the fission spectrum (if fission neutrons are being considered), while in the epithermal range an E^{-1} slowing-down spectrum is often chosen for $W(E)$ [6]. A more accurate way to evaluate the group coefficients for a particular problem is first to simplify the geometry of the problem and use a very fine multigroup mesh on this associated simplified problem, with constant weighting for the fine-group coefficients evaluation. The simplified problem is then solved and the resulting flux density is then used as the weighting function in the computation of coarse-group coefficients for the actual problem. In effect, the fine-group coefficients are "collapsed" or reduced to a broad-group set.

The same multigroup approximation can be used to eliminate the energy variable of the energy-dependent diffusion equation. If Eq. (10.84) is integrated over each energy group, one obtains

$$-\nabla \cdot D_g(\mathbf{r})\nabla\phi_g(\mathbf{r}) + \mu_g(\mathbf{r})\phi_g(\mathbf{r}) = \sum_{g'=1}^{G} \mu_{g'g}(\mathbf{r})\phi_{g'}(\mathbf{r}) + S_g(\mathbf{r}), \tag{10.93}$$

where the following group constants have been defined:

$$\phi_g(\mathbf{r}) \equiv \int_{E_g}^{E_{g-1}} \phi(\mathbf{r}, E)\, dE, \tag{10.94}$$

$$\mu_g(\mathbf{r}) \equiv \frac{1}{\phi_g} \int_{E_g}^{E_{g-1}} \mu(\mathbf{r}, E)\phi(\mathbf{r}, E)\, dE, \tag{10.95}$$

$$\mu_{g'g}(\mathbf{r}) \equiv \frac{1}{\phi_{g'}} \int_{E_g}^{E_{g-1}} dE \int_{E_{g'}}^{E_{g'-1}} dE'\, \mu_s(\mathbf{r}, E' \rightarrow E)\phi(\mathbf{r}, E'), \tag{10.96}$$

$$D_g(\mathbf{r}) \equiv \int_{E_g}^{E_{g-1}} dE\, D(\mathbf{r}, E)\, \nabla\phi(\mathbf{r}, E) \Big/ \int_{E_g}^{E_{g-1}} dE\, \nabla\phi(\mathbf{r}, E). \tag{10.97}$$

Again, if these group constants are to be evaluated a priori, some approximation for the flux density must be made.

The generation of group coefficients (or macroscopic cross sections) for photon- and neutron-transport problems is an important research area which blends both art and science. Many different codes have been developed to compute group constants for various transport and diffusion problems. The elimination of the energy variable by the multigroup approximation enables numerical solutions for realistic transport or diffusion problems to be obtained from Eq. (10.86) or (10.93). Many powerful multigroup transport and diffusion codes for one-, two-, and even three-dimensional geometries are available. Nevertheless, the user of these codes should always remember that group coefficients are only approximations, and that the results of a multigroup transport calculation should be verified by experience, experiment, or an analysis of the sensitivity of the results to changes in the group coefficients.

10.3 METHOD OF MOMENTS

In most calculations based on the transport equation, the energy dependence of the particles (neutrons or photons) is treated in an approximate manner, usually with an energy multigroup approximation, as explained in the preceding section. Such approximate energy treatment is necessary to reduce the complexity of the transport equation so that sufficient detail in the spatial dependence of the flux density can be obtained.

However, there are transport problems with geometry sufficiently simplified that it is possible to obtain much more detail in the energy dependence of the flux density. A powerful method to determine the spatial *and* energy distribution of neutrons or photons originating from point, plane, or line sources in an infinite medium is the "method of moments" [7,8]. In this computational method the transport equation is first used to obtain the spatial and angular moments of the flux density, and then the flux density is reconstituted from these moments. To illustrate the basics of this method, consider the transport of neutrons or gamma photons in an infinite homogeneous medium with an infinite uniform

plane source at $x = 0$. If the source depends only on the polar angle, $\cos^{-1}\omega$, the angular flux density must be azimuthally independent [i.e., $\phi(x, E, \omega, \psi) = \phi(x, E, \omega)$]. For this situation the transport equation may be written as

$$\omega \frac{\partial \phi(x, E, \omega)}{\partial x} + \mu(E)\phi(x, E, \omega) = \int_0^\infty dE' \int_{4\pi} d\Omega'\, \mu_s(E' \to E)\, \delta(\boldsymbol{\Omega} \cdot \boldsymbol{\Omega}' - \omega_s(E', E))\phi(x, E', \omega') + S(E, \omega)\, \delta(x), \quad (10.98)$$

where μ_s and ω_s are, respectively, the energy scattering kernel and that function of the particle energies before and after scattering which equals the cosine of the scattering angle [given by Eq. (3.60) for neutron scattering and readily derivable from Eq. (3.11) for photon scattering]. For neutron slowing-down problems or photon scattering, the kernel $\mu_s(E' \to E)$ vanishes if $E > E'$ (i.e., particles always lose energy when scattering). Thus, the lower limit of the E' integral may be replaced by E without any loss of generality. Further, for any realistic source there is always a maximum source energy E_0. Thus, $\phi(x, E, \omega) = 0$ if $E > E_0$, and the upper limit of the E' integral may be replaced by E_0.

Rather than calculate $\phi(x, E, \omega)$ from the transport equation above, the method of moments seeks the angular Legendre moments $\phi_l(x, E)$ defined such that

$$\phi(x, E, \omega) \equiv \frac{1}{4\pi} \sum_{l=0}^{\infty} (2l + 1)\phi_l(x, E)P_l(\omega), \quad (10.99)$$

where $P_l(\omega)$ is the Legendre polynomial of order l (see Appendix 2). The orthogonality properties of these polynomials give the moments as [after multiplying Eq. (10.99) by $P_m(\omega)$ and integrating over 4π steradians]

$$\phi_m(x, E) = 2\pi \int_{-1}^{1} (d\omega)P_m(\omega)\phi(x, E, \omega). \quad (10.100)$$

To obtain an equation for these Legendre moments, multiply the transport equation by $P_l(\omega)$ and integrate over all ω, that is,

$$\int_{-1}^{1} d\omega\, P_l(\omega)\left[\omega \frac{\partial \phi}{\partial x} + \mu\phi - S\, \delta(x)\right] = \int_E^{E_0} dE'\, \mu_s(E' \to E) \int_{-1}^{1} d\omega \int_{-1}^{1} d\omega' \int_0^{2\pi} d\psi'\, P_l(\omega)\, \delta(\boldsymbol{\Omega} \cdot \boldsymbol{\Omega}' - \omega_s(E', E))\phi(x, E', \omega'). \quad (10.101)$$

Substitute for ϕ from the expansion (10.99) and use the recursion relation for Legendre polynomials, Eq. (A2.23), to evaluate the left-hand side of Eq. (10.101) in terms of the Legendre moments ϕ_l. To evaluate the right-hand side, first expand the delta function as a Legendre polynomial series using Eqs. (A2.29) and (A2.30). The result is

$$\delta(\boldsymbol{\Omega} \cdot \boldsymbol{\Omega}' - \omega_s(E', E)) = \frac{1}{4\pi} \sum_{l=0}^{\infty} (2l + 1)P_l(\omega_s(E', E))P_l(\boldsymbol{\Omega} \cdot \boldsymbol{\Omega}'). \quad (10.102)$$

Since the cosine of the scattering angle is given by

$$\mathbf{\Omega} \cdot \mathbf{\Omega}' = \omega\omega' + \sqrt{1-\omega^2}\sqrt{1-\omega'^2}\cos(\psi - \psi'), \tag{10.103}$$

the addition theorem for Legendre polynomials, Eq. (A2.32), can be used to expand $P_l(\mathbf{\Omega} \cdot \mathbf{\Omega}')$ in Eq. (10.102). By thus expressing the delta function in terms of $P_l(\omega)$, $P_l(\omega')$, $P_l^m(\omega)$, $P_l^m(\omega')$ and $\cos[m(\psi - \psi')]$, the right-hand side of Eq. (10.101) is readily evaluated by using the orthogonality properties of the Legendre polynomials. In this manner Eq. (10.101) reduces to

$$\begin{aligned}\frac{l+1}{2l+1}\frac{\partial\phi_{l+1}(x,E)}{\partial x} + \frac{l}{2l+1}\frac{\partial\phi_{l-1}(x,E)}{\partial x} + \mu(E)\phi_l(x,E) \\ = \int_E^{E_0} dE'\, P_l(\omega_s(E',E))\mu_s(E' \to E)\phi_l(x,E') + S_l(E)\,\delta(x),\end{aligned} \tag{10.104}$$

where the source angular moments are defined by

$$S_l(E) = 2\pi\int_{-1}^{1} S(E,\omega)P_l(\omega)\,d\omega. \tag{10.105}$$

The next step in the moments method is to reduce further Eq. (10.104) by introducing the following spatial moments of $\phi_l(x, E)$, that is,

$$\phi_{nl}(E) \equiv \frac{1}{n!}\int_{-\infty}^{\infty}\phi_l(x,E)x^n\,dx, \qquad n, l \geq 0, \tag{10.106}$$

with the definition $\phi_{-1,n} \equiv \phi_{n,-1} = 0$. Thus, multiplication of Eq. (10.104) by $x^n/n!$ and integration of the result over all x yields for $n, l = 0, 1, 2, \ldots,$

$$\begin{aligned}\mu(E)\phi_{nl}(E) = \int_E^{E_0} dE'\, P_l(\omega_s(E',E))\mu_s(E' \to E)\phi_{nl}(E') + S_l(E)\,\delta_{n0} \\ + \frac{1}{2l+1}[(l+1)\phi_{n-1,l+1}(E) + l\phi_{n-1,l-1}(E)].\end{aligned} \tag{10.107}$$

To obtain this result, the spatial derivative terms have been integrated by parts; and the fact that the flux density exponentially vanishes at large distances from the source implies that $\lim_{|x|\to\infty} x^n\phi_l(x) = 0$. It is this requirement that the integrand in Eq. (10.106) vanish at the end points of the spatial integration that makes the extension of the method of moments to finite systems very difficult, since for such systems the integrand does not vanish at the surface.

Equation (10.107) represents an infinite set of interlinked integral equations for the moments ϕ_{nl}. To obtain these moments equations no approximations have been made, and consequently they are equivalent to the original transport equation. To evaluate $\phi_{nl}(E)$ from Eq. (10.107), one previously must have evaluated $\phi_{n-1,l-1}$ and $\phi_{n-1,l+1}$. For dose rate calculations, only the angularly integrated flux density is needed [i.e., $\phi_0(x, E)$]; but to evaluate its moments [$\phi_{n0}(E)$, $n = 0, 1, 2, \ldots$] some of the higher angular moments must also be calculated. The calculational scheme for recursively extracting the moments $\phi_{n0}(E)$ is shown in Fig. 10.5. In general, to obtain n spatial moments of $\phi_0(x, E)$ requires $n(n+1)/2$ solutions of Eq. (10.107).

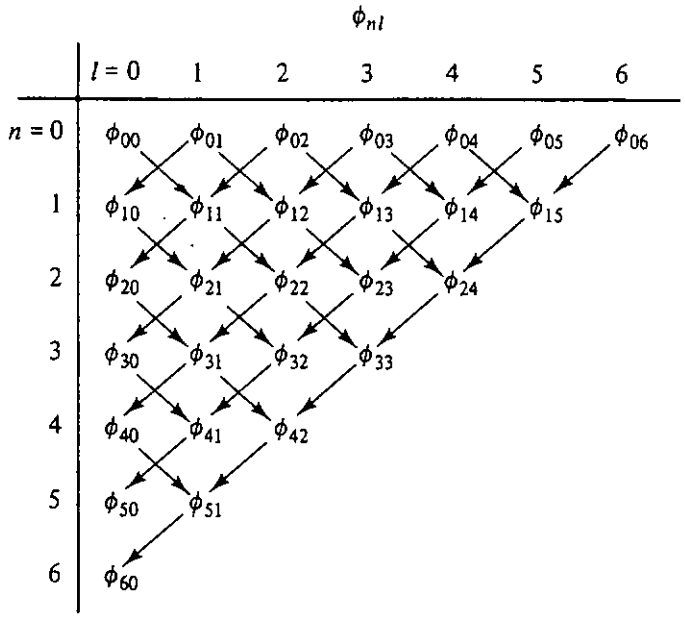

Figure 10.5 Calculational scheme for solving the moments equations.

The numerical solution of the moments equations for the ϕ_{nl}'s is usually approached differently for neutrons than for photons. For photon transport problems, the scattering kernel is a smoothly varying function of its arguments; and if, as is usually done, the free-electron scattering cross section is used, the kernel is easily evaluated for any E and E'. Consequently, Eq. (10.107) can be solved directly for $\phi_{nl}(E)$ (given $\phi_{n-1,l+1}$ and $\phi_{n-1,l-1}$ from a previous step) by numerically evaluating the integral and by using a discrete energy mesh. On the other hand, neutron scattering kernels are characteristically rapidly varying (typically displaying a resonance structure) and they must be determined experimentally. Only for the case of hydrogen scattering are the cross sections sufficiently smooth to permit the numerical solution of the moments equation in the same manner as is used for photons. For neutron problems, various simplified models are frequently used to describe neutron slowing down and to evaluate approximately the integral term in Eq. (10.107). Once the integral term is approximated by some simpler expression, the moment equations can then be solved numerically.

The next step in the method of moments is to use the spatial-angular moments $\phi_{nl}(E)$ to construct the angular moments $\phi_l(x, E)$. In principle, all the moments ϕ_{nl}, $n = 0, 1, 2, \ldots$, are needed to reconstruct ϕ_l; however, just as a truncated Legendre expansion of most functions is a good approximation, it seems reasonable that the first few ϕ_{nl} moments should be sufficient to give a good representation of ϕ_l, especially for ϕ_0. The construction of ϕ_l from a finite number of the ϕ_{nl}'s introduces the major approximation into the method of moments. Several methods for the approximate reconstruction of the angular moments have been proposed. The two most common methods are outlined below.

The most widely used reconstruction approximation is referred to as the "polynomial expansion method," and assumes that the angular moments can be written as

$$\phi_l(x, E) = f(x)g_l(x, E). \tag{10.108}$$

Here the "trial" function $f(x)$ represents an approximate spatial variation of $\phi_l(x, E)$ and is chosen by the analyst. For example, one might expect the flux density, far from the source, to vary in the same manner as the uncollided flux density. If the choice of $f(x)$ is a good approximation of the spatial variation of ϕ_l, the function $g_l(x, E)$ will be a slowly varying function of position, which in turn can be expanded as

$$g_l(x, E) \simeq \sum_{j=0}^{N} g_{lj}(E)p_j(x), \tag{10.109}$$

where $p_j(x)$ is a polynomial of degree j. If good choices are made for $f(x)$ and $p_j(x)$, one would expect that a very low-order (small N) expansion would suffice. The coefficients $g_{lj}(E)$ are then determined by equating the first $N + 1$ spatial moments of the right-hand side of Eq. (10.108) to the $N + 1$ known moments ϕ_{nl}, $n = 0, 1, \ldots, N$.

The evaluation procedure for the $g_{lj}(E)$ coefficients is considerably simplified if the $p_j(x)$ polynomials are chosen to be the set of orthogonal polynomials on the interval $(-\infty, \infty)$ with weight function $f(x)$, that is,

$$\int_{-\infty}^{\infty} p_i(x)p_j(x)f(x)\,dx = \delta_{ij}. \tag{10.110}$$

Thus, substitution of Eq. (10.109) into (10.108) and use of the orthogonality condition above gives

$$g_{li}(E) = \int_{-\infty}^{\infty} \phi_l(x, E)p_i(x)\,dx, \qquad i = 0, 1, 2, \ldots, N, \tag{10.111}$$

which, since $p_i(x)$ is a polynomial of degree i, can be evaluated as a linear combination of the first $i + 1$ spatial moments of $\phi_l(x, E)$ (i.e., the known ϕ_{nl}'s). Finally, once the $\phi_l(x, E)$ are computed, the energy and angular distribution of $\phi(x, E, \omega)$ can be found from Eq. (10.99) after truncating the summation.

In many calculations, such as the dose rate variation in the medium, only $\phi_0(x, E)$ is needed. For photon problems, calculations are usually performed using monoenergetic sources. Moreover, the choice of a suitable trial function is relatively straightforward [8] (e.g., the uncollided flux density), and the polynomial reconstruction technique gives excellent results. However, for neutron penetration problems the choice of the trial function is usually very difficult, and as a result the polynomial reconstruction technique is harder to apply and typically requires much higher orders of the polynomial expansions and hence more calculated $\phi_{nl}(E)$ moments than for the photon case.

A second widely used technique for reconstructing the Legendre moments

of the flux density is termed the "method of undetermined parameters." In this method, it is assumed that $\phi_l(x, E)$ can be expanded as

$$\phi_l(x, E) = \sum_{i=1}^{M} a_i(E) h_i(x), \tag{10.112}$$

where $h_i(x)$ are functions which exhibit the generally expected spatial variation of ϕ_l but which contain M' (≥ 1) undetermined parameters. For example, one may suppose that the flux density decreases exponentially with distance from the source so that an obvious choice for the h_i would be $\exp(-b_i x)$. The $a_i(E)$ are also undetermined parameters which give the energy dependence of $\phi_l(x, E)$. Multiplication of Eq. (10.112) by $x^n/n!$ and integration of the result over all x gives

$$\phi_{nl}(E) = \frac{1}{n!} \sum_{i=1}^{M} a_i(E) \int_{-\infty}^{\infty} x^n h_i(x)\, dx, \qquad n = 0, 1, 2, \ldots \tag{10.113}$$

The integrals in the summation above are performed analytically if the form chosen for h_i permits or numerically if analytic evaluation is not possible. To solve Eq. (10.113) for the M parameters a_i, and the MM' parameters of the h_i functions requires $M(M' + 1)$ moments ϕ_{nl} to be obtained from Eq. (10.107).

The great advantage of reconstructing ϕ_l by the method of undetermined parameters is the flexibility permitted by the choice of the $h_i(x)$ functions. This reconstruction method has been most widely used in neutron penetration studies primarily because the polynomial expansion method, which historically has been mostly applied to photon problems, generally gives poor results for neutron problems as a result of the difficulty in selecting an appropriate trial function.

The moments method is perhaps the most powerful method for obtaining detailed calculations of the energy spectrum in an infinite medium. Almost all calculations of buildup factors for photons have been based on moments solutions. The moments method can be applied to point, line, and plane sources with arbitrary angular distributions. In the actual application of this method, many clever refinements are employed which have not been included in the description above. For example, the uncollided flux density is usually separated from the collided flux density, and many symmetry properties are used to reduce the number of moments needed [8]. Usually, the spatial variable is made dimensionless by measuring distance in mean-free-path lengths and the energy variable is replaced by the Compton wavelength λ for photon calculations and by the lethargy variable u for neutron calculations [7]. Finally, many other more sophisticated methods and improvements for the reconstruction of the angular moments from the spatial-angular moments have been devised [9].

A major disadvantage of the method of moments is its practical restriction to infinite-medium problems. For finite systems the flux density at the surfaces of the medium must be known—information that is not generally known. This method is best applied at distances far from the source since it is usually much

easier to guess the approximate spatial dependence of the flux density far from the source than near the source. Finally, calculations for the complete flux density $\phi(x, E, \omega)$ are generally much more difficult than for the angularly integrated flux density $\phi_0(x, E)$, since to compute $\phi(x, E, \omega)$ requires evaluation of the higher Legendre moments, which in turn requires far more spatial-angular moments ϕ_{nl}.

10.4 DISCRETE-ORDINATES METHOD

The discrete-ordinates method is a name given to several closely related techniques for obtaining approximate solutions to the transport equation. The principal feature in all these methods is the discretization of the angular variable $\mathbf{\Omega}$ such that particles are represented as streaming only along a finite number of directions $\mathbf{\Omega}_i$ rather than in all possible directions as allowed by the transport equation. This so-called "nodal" approach is in contrast to the approach used in the method of moments, in which the angular dependence of the flux density was continuous and was represented by a Legendre polynomial expansion. In the most modern and powerful of the discrete-ordinates techniques, the spatial variables are also discretized and numerical methods are used to obtain the flux density at all the spatial and angular mesh points [1,6]. Further, the energy multigroup approximation is almost always used to eliminate the energy variable.

To illustrate the basic ideas of this powerful method, the discrete-ordinates technique is presented here for the simplest case of one-dimensional plane geometry with azimuthal symmetry. The same ideas are applicable to other geometries even with more than one spatial dimension; however, these extensions become algebraically much more complicated without introducing any additional principles of the discrete-ordinates method. The azimuthally symmetric flux density for group g, $\phi_g(x, \omega)$, in a homogeneous slab of thickness T is given by the following form of the transport equation [see Eq. (10.86)]:

$$\omega \frac{\partial \phi_g(x, \omega)}{\partial x} + \mu_g \phi_g(x, \omega) = \sum_{g'=1}^{g} 2\pi \int_{-1}^{1} d\omega' \mu_{g'g}(x, \omega' \rightarrow \omega) \phi_{g'}(x, \omega') + S_g(x, \omega)$$
$$0 \leq x \leq T, \quad g = 1, 2, \ldots, G, \qquad (10.114)$$

where incident flux densities at the slab surfaces, $\phi_g(0, \omega)$ for $\omega > 0$, and $\phi_g(T, \omega)$ for $\omega < 0$, and any distributed nonscattering sources, S_g, are specified.

The first step in the discrete-ordinates method is to select a finite set of directions $\{\omega_i\}$, $i = 1, \ldots, N$, and a set of corresponding quadrature weights $\{w_i\}$, $i = 1, \ldots, N$ such that the scattering source integral in Eq. (10.114) may be approximated by numerical quadrature as

$$\int_{-1}^{1} d\omega' \mu_{g'g}(x, \omega' \rightarrow \omega) \phi_{g'}(x, \omega') \simeq \sum_{i=1}^{N} w_i \mu_{g'g}(x, \omega_i \rightarrow \omega) \phi_{g'}(x, \omega_i). \qquad (10.115)$$

The particular choice of the sets $\{\omega_i\}$ and $\{w_i\}$ depend on how well the flux density is to be integrated by the quadrature technique above. If there is some reason to believe $\phi_g(x, \omega)$ has some special feature (e.g., the particles are all moving in some narrow range of ω), then a particular choice of quadrature ordinates and weights may be indicated. However, in most cases no prior knowledge of the flux density is available, and most often one chooses ω_i's and w_i's based on a Gauss quadrature procedure, in which the ω_i's are the N zeros of the Nth Legendre polynomial [i.e., $P_N(\omega_i) = 0$] and the corresponding quadrature weights are given by

$$w_i = \frac{2(1 - \omega_i)^2}{[(N + 1)P_{N+1}(\omega_i)]^2}. \tag{10.116}$$

This choice of ω_i and w_i has the remarkable property that the scattering integral approximation (10.115) will be exact if $\mu_{g'g}(x, \omega' \to \omega)\phi_g(x, \omega')$ is a polynomial in ω' of degree $2N - 1$ or less [1]. No higher-degree polynomial can be exactly integrated by any N-point quadrature procedure. Thus, the choice of a Gaussian quadrature for Eq. (10.115) is optimum *for polynomials*. Although $\phi_g(x, \omega)$ is generally not a polynomial, Gauss quadrature is usually used since the flux density can be adequately approximated by a polynomial of sufficiently high degree.

The next step in the discrete-ordinates method is to obtain a set of N equations for $\phi_g^i(x) \equiv \phi_g(x, \omega_i)$. Such equations can be obtained from the transport Eq. (10.114) in a number of ways, thus giving rise to different discrete-ordinate formulations [3]. For instance, Eq. (10.114) may be integrated over N angular subintervals (e.g., ω_{i-1} to ω_i, $i = 1, \ldots, N$) and a variety of approximations used to express these ω integrals in terms of the $\phi_g^i(x)$ (e.g., a linear variation in ω between the ω_i ordinates). However, for the present plane-geometry case the required N equations for the $\phi_g^i(x)$ can be obtained directly by simply evaluating Eq. (10.114) at each ω_i, namely,[3]

$$\omega_i \frac{\partial \phi_g^i(x)}{\partial x} + \mu_g \phi_g^i(x) \simeq Q_g^i(x), \qquad i = 1, \ldots, N \tag{10.117}$$

where the total source Q_g^i is defined as

$$Q_g^i(x) \equiv \sum_{g'=1}^{g} 2\pi \sum_{j=1}^{N} w_j \mu_{g'g}(x, \omega_j \to \omega_i)\phi_{g'}^j(x) + S_g^i(x). \tag{10.118}$$

These N equations are the "discrete-ordinates equations" which must be solved for $\phi_g^i(x)$.

For simple cases the discrete-ordinates equations (10.117) may be solved directly in a semianalytical manner. This was the procedure used in the original

[3]This procedure is equivalent to integrating the transport equation over a small ω subinterval whose central point is ω_i. These ω integrals are then approximated by the integrand at the interval midpoint ω_i. For more general geometries in which $\Omega \cdot \nabla\phi$ includes angular derivatives, this procedure is usually used to generate the discrete-ordinates equations.

development of the discrete-ordinates method by Wick and Chandrasekhar [10]. For example, in a one-group model with isotropic scattering and no internal source S_g, the solution of Eqs. (10.117) may be written as (after the dropping of the subscript g)

$$\phi^i(x) = \frac{\mu_s}{2\mu} \sum_{k=1}^{N} A_k[1 + \xi_k \omega_i]^{-1} e^{-\xi_k \mu x}, \tag{10.119}$$

where the constants A_k are determined from appropriate boundary conditions and the constants ξ_k are the N solutions of

$$1 - \frac{\mu_s}{2\mu} \sum_{j=1}^{N} w_j[1 + \xi_k \omega_j]^{-1} = 0. \tag{10.120}$$

Such analytic solutions of the discrete-ordinates equations are available only for simple cases. Even when available, these solutions are notoriously difficult to evaluate numerically if N is large ($\gtrsim 20$).

The most widely used method to solve the discrete-ordinates equations of Eq. (10.117) is to discretize the spatial variable and reduce the discrete-ordinates equations to equations which give the flux density only at the spatial and angular nodes. For the present case, divide the slab into K intervals by a mesh $\{x_k\}$, where $x_0 = 0$ and $x_K = T$ (see Fig. 10.6). Integration of Eq. (10.117) over the kth spatial interval (x_k, x_{k+1}) gives

$$\omega_i[\phi_g^i(x_{k+1}) - \phi_g^i(x_k)] + \mu_g \int_{x_k}^{x_{k+1}} \phi_g^i(x)\, dx = \int_{x_k}^{x_{k+1}} Q_g^i(x)\, dx, \tag{10.121}$$
$$i = 1, \ldots, N, \quad k = 0, 1, \ldots, K-1.$$

To evaluate the integrals in this result, it is assumed that the mesh width $\Delta x_k \equiv x_{k+1} - x_k$ is sufficiently small so that the integrands can be approximated

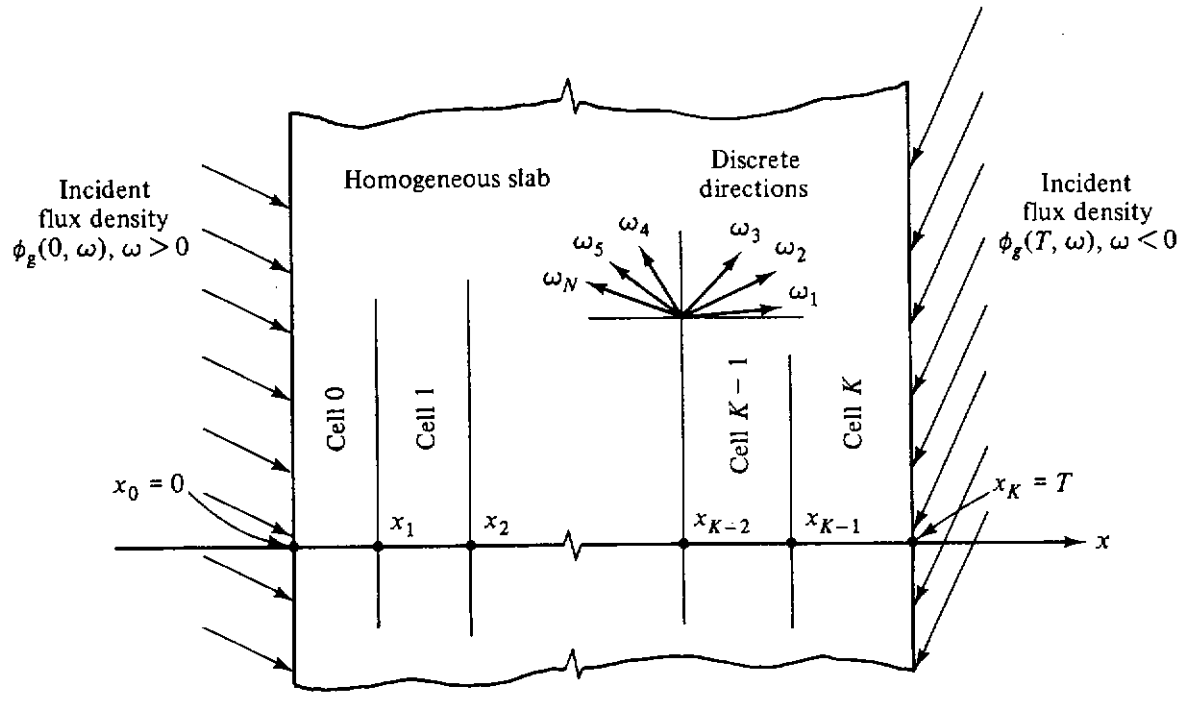

Figure 10.6 Geometry for application of the discrete-ordinates method in a slab.

by their value at the mesh cell midpoint $x_{k+1/2} \equiv (x_{k+1} + x_k)/2$. Thus, Eq. (10.121) is approximated as

$$\omega_i \frac{\phi_g^i(x_{k+1}) - \phi_g^i(x_k)}{\Delta x_k} + \mu_g \phi_g^i(x_{k+1/2}) \simeq Q_g^i(x_{k+1/2}). \tag{10.122}$$

This finite-difference equation relates the values of the flux densities at the mesh cell boundaries and the cell midpoints. However, since $i = 1, \ldots, N$ and $k = 0, \ldots, k - 1$, Eq. (10.122) represents $K \times N$ linear equations in $2K \times N$ unknown angular flux densities at the cell boundaries and midpoints. (Incident flux densities at the outer surfaces of the slab, x_0 and x_K, are assumed known from the boundary conditions.) Thus, to solve Eq. (10.122) for the flux densities it is first necessary to reduce the number of unknowns by relating the cell-centered densities $\phi_g^i(x_{k+1/2})$ to the mesh boundary values. This reduction can be performed in a number of ways, but the simplest and most commonly used method is to assume

$$\phi_g^i(x_{k+1/2}) = \frac{\phi_g^i(x_k) + \phi_g^i(x_{k+1})}{2}. \tag{10.123}$$

Now there are as many linear equations as unknown flux densities.

The solution of Eqs. (10.122) and (10.123) for the flux densities is complicated by the fact that the source term $Q_g^i(x_{k+1/2})$ generally depends also on the flux densities [see Eq. (10.118)]. For small K and N these linear equations can be solved directly. However, it is usual to use an iterative solution scheme which is especially applicable to more complicated cases in curved, multidimensional geometry. This iterative solution is begun by guessing an initial value for the source Q_g^i at each spatial cell midpoint. Then substitution of Eq. (10.123) into (10.122) allows one to eliminate the cell-centered densities and to solve for $\phi_g^i(x_{k+1})$ in terms of $\phi_g^i(x_k)$ as

$$\phi_g^i(x_{k+1}) = \frac{1 - \mu_g \Delta x_k/2\omega_i}{1 + \mu_g \Delta x_k/2\omega_i} \phi_g^i(x_k) + \frac{\Delta x_k}{\omega_i(1 + \mu_g \Delta x_k/2\omega_i)} Q_g^i(x_{k+1/2}), \tag{10.124}$$

or for $\phi_g^i(x_k)$ in terms of $\phi_g^i(x_{k+1})$ as

$$\phi_g^i(x_k) = \frac{1 + \mu_g \Delta x_k/2\omega_i}{1 - \mu_g \Delta x_k/2\omega_i} \phi_g^i(x_{k+1}) - \frac{\Delta x_k}{\omega_i(1 - \mu_g \Delta x_k/2\omega_i)} Q_g^i(x_{k+1/2}). \tag{10.125}$$

These two results then permit the evaluation of the flux densities at all internal spatial mesh boundaries by starting at one of the slab surfaces (where the inward density is given) and sweeping inward along the direction of particle travel (constant ω_i) from mesh boundary to mesh boundary. Equation (10.124) is used for particles streaming to the right ($\omega_i > 0$) starting with the given $\phi_g^i(x_0) \equiv \phi_g(0, \omega_i)$ and evaluating successively $\phi_g^i(x_1), \phi_g^i(x_2), \ldots, \phi_g^i(x_K)$. Similarly, Eq. (10.125) is used for particles streaming to the left ($\omega_i < 0$) starting with the incident $\phi_g^i(x_K) \equiv \phi_g(T, \omega_i)$ and successively computing $\phi_g^i(x_{K-1}), \phi_g^i(x_{K-2})$,

. . . , $\phi_g^i(x_0)$. Once the flux densities in all directions have been found at all cell boundaries, the cell-centered densities are computed from Eq. (10.123) and new and improved estimates of the sources $Q_g^i(x_{k+1/2})$ are computed from Eq. (10.118). This procedure of iteratively computing the flux densities from Eqs. (10.124) and (10.125) and then a revised source estimate from Eq. (10.118) is continued until the computed flux densities converge.

Various procedures can be used to accelerate the convergence and so to reduce the number of iterations required [1,11]. This reduction in the required number of iterations for convergence is particularly important for large problems involving many mesh cells and discrete directions as would be encountered in large multidimensional systems. Moreover, the number of mesh cells and the number of discrete ordinates needed to give an adequate result are not independent. From Eqs. (10.124) and (10.125) it is seen that to ensure the left-hand side is always positive the mesh spacing and discrete ordinates must be chosen so that $|\mu_g \Delta x_k/2\omega_i| < 1$. Thus, the maximum cell width Δx_k is controlled by the smallest cosine of the polar angle, $\min |\omega_i|$, (i.e., the direction closest to $\pi/2$). If more discrete directions are used, the number of spatial cells needed will generally increase. For large systems many mean-free-path lengths thick, as are typically encountered in shielding problems, the number of spatial cells may consequently become very large.

The discrete-ordinates method described in this section has become one of the most powerful tools for the shielding analyst. Unlike the moments method, it is directly applicable to finite-sized systems. (In fact, to apply the discrete-ordinates methods to an infinite system it is necessary to approximate the system by a large finite medium.) However, the major advantage of the discrete-ordinates method is that it is easily extended to heterogeneous multidimensional systems and curved coordinate systems. The same discrete-ordinates procedure illustrated here for a simple one-dimensional plane geometry problem can be applied to a more complex situation [1,2,6]. A spatial and directional mesh is created for the system, and the appropriate form of the transport equation is then integrated over each spatial and directional cell. The solution of the resulting difference equations is then accomplished by introducing an approximation that relates cell-centered flux densities to those on the boundaries [analogous to Eq. (10.123)] and an iterative procedure between the source and flux density calculation is then used. Computer codes based on the discrete-ordinates method are widely available to treat one-, two-, and even three-dimensional problems in the three basic geometries (rectangular, spherical, and cylindrical) with an arbitrary number of energy groups [12–14].

Although discrete-ordinates calculational methods are widely used by shielding analysts, these methods do have their limitations. Most restrictive is the requirement that the problem geometry must be one of the three basic geometries (rectangular, cylindrical, or spherical) with boundaries placed along coordinate planes. Problems with irregular boundaries and material distributions are difficult to solve accurately with the discrete-ordinates method. In multi-

dimensional geometries, the discrete-ordinates methods often produce spurious oscillations in the spatial distribution of the predicted flux density (the so-called "ray effect") as an inherent consequence of the angular discretization. Finally, the discretization of the angular and spatial variables introduces numerical truncation errors, and it is necessary to use sufficiently fine angular and spatial meshes to obtain flux densities which are independent of the mesh size. For multidimensional situations in which the flux density is very anisotropic in direction and in which the medium is many mean-free-path lengths in size (typical of many shielding problems), the computational effort to obtain an accurate discrete-ordinates solution can become very large.

10.5 MONTE CARLO METHOD

If one could determine the exact path each particle makes and energies it assumes while passing through a medium in its random-walk fashion, one could, in principle, calculate many useful quantities by averaging over a large number of individual particle histories so as to minimize the stochastic effects of the individual particle interactions. For example, the probability that a particle in a certain energy range will be absorbed in a given volume could be estimated by computing the proportion of all particles that terminate in the specified volume with the required energy. This concept of using a large number of particle histories (each of which is random in nature) to estimate some average particle behavior is the essential feature of the Monte Carlo method.

In Monte Carlo calculations the particle tracks or histories are generated by simulating the random nature of the particle interactions with the medium. This procedure can in principle be done mathematically without the need for computational tools, but the process is so tedious that a computer is almost a necessity for doing any practical problem. One does not even need to invoke the transport equation for the more elementary operations; all one needs are complete mathematical expressions of the probability relationships which govern the track length of an individual particle between interaction points, the choice of an interaction type at each such point, the choice of a new energy and a new direction if the interaction is of a scattering type, and the possible production of additional particles. These are all stochastic variables; and one needs a complete understanding of the physics of the various processes a particle undergoes in its lifetime from the time it is given birth by the source until it is either absorbed or leaves the system under consideration, in order to make selections of specific values for these variables.

The process of deciding on a specific value of some stochastic variable is generally based on the selection of a number at random from a uniformly distributed set of integers, say, from 1 to some large maximum number, N. A simple way to do this would be to use a nonbiased roulette wheel which can be used to pick at random any number from 1 to N. This invokes pictures of

gambling at Monte Carlo, hence the name of this method. For our purposes the process is more elaborate and more suited to computing machinery, but the principle is similar.

The experience a particle undergoes from the time it leaves its source until it is absorbed or passes out of the system is called its *history*. The process of following a given number of particle histories on the computer can be accomplished in a way completely analogous to the actual physical process of particle transport through a medium. This direct simulation of the physical situation is called *analog Monte Carlo*. (It is common to allow the elimination of unimportant and insignificant processes in the computation and to establish some degree of idealization of the system geometry, within the meaning of the term "analog.") On the other hand, it is possible to use a Monte Carlo process to solve a problem which is physically much different from the one of basic interest, under circumstances for which it can be proved that the resulting answer (say, a detector response) to the altered procedure is the same as that to the original problem, or else has some known relationship to it so that the solution of the basic problem can be obtained indirectly. This use of an associated but altered procedure is called a *non-analog Monte Carlo* procedure.

10.5.1 Random Numbers and Pseudo-Random Numbers

For purposes of selection of a stochastic variable, one would like random access to the infinite set of numbers in the continuum between zero and unity. This can be adequately simulated by use of a random set of integers between 1 and a very large number N, each of which is then divided by N, so as to obtain the set $1/N, 2/N, \ldots, N/N$. (Of course, for practical purposes N should be much larger than the number 36, the highest available on a roulette wheel.)

Storing these random numbers in the computer is out of the question, since N usually is taken to be even larger than the capacity of the entire memory of the computer. Furthermore, devising a method of random access is not simple. It is much more practical to devise a simple mathematical technique for sequentially generating integers which will be uniformly spaced (considering the entire set) between 1 and N and which will *appear* to be ordered in a random manner within that interval. Such numbers are called *pseudo-random* numbers. They are used as if they were random and can indeed pass many of the statistical tests for randomness. However, each one in the list depends in a hidden way on the one (or perhaps a few) immediately preceding it in the list, and hence it cannot be said to be truly random, since randomness demands that selection of any number be completely independent of the value of the previous selection or selections.

The generation of random numbers is almost always tailored to the type of computer, in particular to the size of the largest number which it can hold. Most commercial computers include a random (actually, pseudo-random) number generator in their software packages, either as integers in the range from

1 to its largest (N), as fractional numbers uniformly distributed between 0 and 1 (obtained by the technique of dividing by N), or both. A common means of generating such numbers in the integral range from 1 to N is by means of the following formula:

$$\rho_n = c\rho_{n-1} (\text{mod } N), \tag{10.126}$$

where ρ_n is the nth number on the list, ρ_{n-1} is the previous number, and c is a constant multiplier.[4] The original seed number ρ_0 and the multiplier c are somewhat arbitrary and are selected by the user. The values of ρ_0, c, and the last pseudo-random number generated, ρ_{n-1} are retained in the computer memory so that a new pseudo-random number ρ_n can be obtained whenever the subroutine for the random number generation is called on. If desired, ρ_n is divided by N, to give the corresponding proper fraction between 0 and 1. The length of the list of numbers which are produced before the cycle begins to repeat itself is called the *cycle length*. Obviously, the cycle length should be much longer than the total number of pseudo-random numbers likely to be needed in a single computation or any group of Monte Carlo computations whose answers are likely to be intercompared. The numbers selected for ρ_0 and c are subject to some constraints, but there is some freedom of choice. Some choices are better than others, as shown by Coveyou and MacPherson [15]. A reasonable pair of choices best suited to a computer with 36 bits per word (one of which is reserved for the sign), which therefore can accept a number N up to size 2^{35}, is to choose $\rho_0 = 2^{35} - 1$ and $c = 5^{15}$. It can be proved [16] that the cycle length of this sequence is 2^{33}.

For the remainder of this section, an appropriate set of pseudo-random numbers is assumed to be available from a subroutine of the computer; and the theory will be presented in terms of what will be termed "random numbers," uniformly spaced between 0 and 1, and randomly selected when needed, even though this is not strictly true.

10.5.2 Selection Techniques for Given Stochastic Variables

Figure 10.7 shows a *probability density function* (pdf), $f(x)$ defined such that the probability a randomly selected value of x is between x_1 and x_2 is given by

$$P\{x_1 < x < x_2\} = \int_{x_1}^{x_2} f(x)\, dx. \tag{10.127}$$

It is assumed that x may be any value between the limits a and b, either of which may be minus or plus infinity, respectively. Corresponding to $f(x)$, there is a *cumulative probability distribution* (cpd), $F(x)$, defined by

$$F(x) \equiv \int_a^x f(x')\, dx'. \tag{10.128}$$

[4]The symbol (mod N) means that the result of the multiplication, $c\rho_{n-1}$, is divided by N and the *remainder* resulting from the division is then kept as ρ_n.

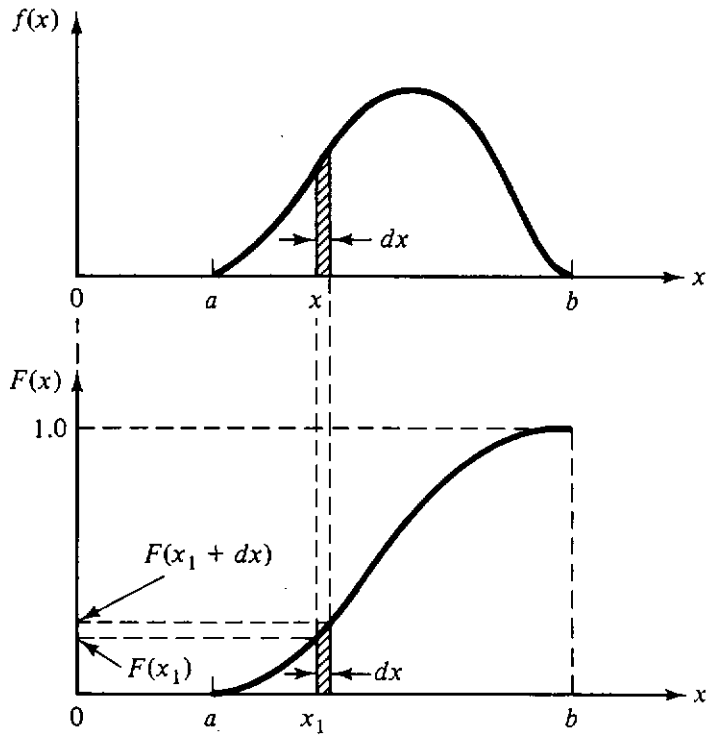

Figure 10.7 Graphs of the probability density function and its corresponding cumulative probability distribution.

The probability that the randomly selected value of x is less than x_1, $P\{x < x_1\}$, is thus given by $F(x_1)$. It is easily seen that the function $F(x)$ is monotonically increasing with x if $f(x)$ is a properly normalized pdf between a and b, with $F(a) = 0$ and $F(b) = 1$.

In the Monte Carlo process it is necessary to generate random values of some variable x (e.g., path length) which, from the physics of the particle interaction process, has some distribution $f(x)$; that is, a histogram of a large number of such randomly generated x values should approach $f(x)$ in shape. One of the major aspects of using the Monte Carlo method is to generate efficiently values of stochastic variables with a specified distribution. Three methods for accomplishing the generation of such random variables are reviewed below.

Cumulative distribution method. This simple method begins by selecting a number ρ_i randomly between 0 and 1. Then the desired value of x_i distributed as $f(x)$ is obtained by solving

$$F(x_i) = \rho_i, \tag{10.129}$$

that is,

$$x_i = F^{-1}(\rho_i), \tag{10.130}$$

where F^{-1} is the function obtained by solving Eq. (10.129) for x_i.

The validity of this or any other procedure can be established by showing that the probability of obtaining a value of x within the interval between some fixed value x and $x + dx$ is $f(x)\,dx$ [i.e., x is distributed as $f(x)$]. For the cpd method, one notes that the value of x_i corresponds to the random number ρ_i;

and the probability of x_i being between x and $x + dx$ is the same as

$$P\{F(x) < \rho_i < F(x + dx)\} = F(x + dx) - F(x) \tag{10.131}$$

$$= \int_x^{x+dx} f(x')\,dx' = f(x)\,dx. \tag{10.132}$$

As an example, consider a particle starting from a given interaction point (or source point) in a certain direction through a medium of constant interaction properties (i.e., of constant μ). Then, by Eqs. (6.1) to (6.5), the values of the path lengths have a pdf

$$f(s) = \mu e^{-\mu s}, \tag{10.133}$$

with s between 0 and infinity. Upon integration it is found that

$$F(s) = 1 - e^{-\mu s}. \tag{10.134}$$

When this cpd is equated to $1 - \rho_i$ in order to find a value s_i, one finds that[5]

$$s_i = \frac{-(ln\ \rho_i)}{\mu}. \tag{10.135}$$

Rejection technique. The cpd method presents difficulties if the pdf, $f(x)$, cannot be integrated analytically to obtain $F(x)$ or, even if $F(x)$ can be easily obtained, $F^{-1}(\rho)$ is difficult to obtain analytically. An alternative approach in such cases is the *rejection technique*. Consider Fig. 10.8, which graphs $f(x)$, assumed to be difficult to work with, and a similar but simpler probability distribution function, $g(x)$, between the same limits. The latter function is taken to have an easily obtainable cpd, $G(x)$, which can in turn be easily inverted to give $G^{-1}(\rho)$. Note that

$$F(x) = \int_a^x h(x')g(x')\,dx', \tag{10.136}$$

where

$$h(x) \equiv \frac{f(x)}{g(x)}. \tag{10.137}$$

If $g(x)$ is a close approximation to $f(x)$, $h(x)$ does not deviate markedly from unity. At any rate, $g(x)$ must be chosen so that $h(x)$ does not exceed some maximum bounding value, h_{max}, in the interval a to b. (It is more efficient, but not mandatory, to make h_{max} the actual maximum value of h between the limits a and b.)

The rejection technique proceeds as follows:

1. Select a random number ρ_i.
2. Obtain a tentative value of x from the equation $x_t = G^{-1}(\rho_i)$.
3. Select another random number ρ_{i+1}.

[5]Since values for $1 - \rho_i$ are also uniformly distributed over the interval 0 and 1, $1 - \rho_i$ can legitimately be used instead of ρ_i, and by so doing one sometimes makes the resulting equation a little simpler.

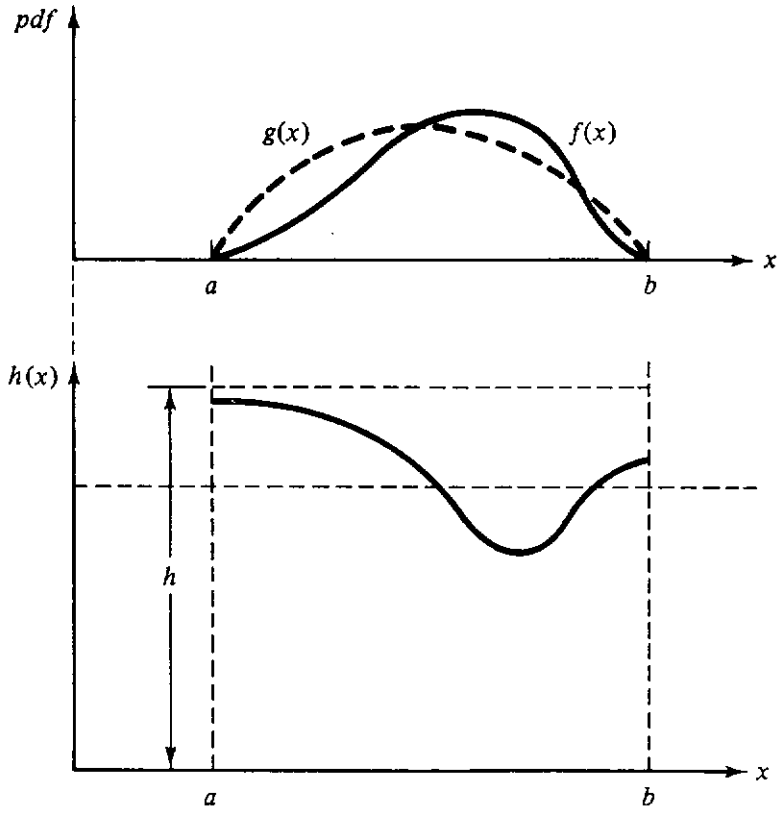

Figure 10.8 Graphs of the probability density function $f(x)$ and a more tractable pdf $g(x)$ which approximates $f(x)$. The ratio $h(x) = g(x)/f(x)$ is plotted in the lower figure. Here $h_{\max}$ is any finite upper bound for $h(x)$, but in practice should not greatly exceed the maximum value of $h(x)$.

4a. If $\rho_{i+1} > h(x_i)/h_{\max}$, *reject* the value x_i and continue to repeat the process above with new pairs of random numbers until an acceptable value is obtained.[6]

4b. If $\rho_{i+1} < h(x_i)/h_{\max}$, *accept* x_i as the appropriate value of x.

The proof of validity of this technique requires recognition of the possibility of an indefinite number of trials before success is achieved. In particular, the probability that the value x_j will be found and accepted between x and $x + dx$ can be found as follows:

$$
\begin{aligned}
&P\{x < x_j < x + dx\} \\
&\quad = P\{x_{t1} \text{ accepted as } x_j \mid x < x_{t1} < x + dx\} \cdot P\{x < x_{t1} < x + dx\} \\
&\qquad + P\{x_{t1} \text{ rejected}\} \cdot P\{x_{t2} \text{ accepted as } x_j \mid x < x_{t2} < x + dx\} \qquad (10.138) \\
&\qquad\qquad \cdot P\{x < x_{t2} < x + dx\} \\
&\qquad + P\{x_{t1} \text{ rejected}\} \cdot P\{x_{t2} \text{ rejected}\} \cdots \\
&\quad = \sum_{i=1}^{\infty} \left(\prod_{k=1}^{i-1} P\{x_{tk} \text{ rejected}\} \right) \cdot P\{x_{ti} \text{ accepted as } x_j \mid x < x_{ti} < x + dx\} \\
&\qquad\qquad \cdot P\{x < x_{ti} < x + dx\}. \qquad (10.139)
\end{aligned}
$$

[6]The probability that ρ_{i+1} exactly equals $h(x_i)/h_{\max}$ is ignored here and throughout this section. This probability is negligible, in principle; but in practical calculations using pseudo-random numbers, the situation may arise on very rare occasions. In such case, it is arbitrary whether to group the "equal" case with the "less than" or "greater than" case.

The probability of *not* obtaining an acceptance of x_{tk} on the kth trial is

$$\int_a^b g(x)\left[1 - \frac{h(x)}{h_{\max}}\right] dx = \int_a^b g(x)\,dx - \int_a^b \frac{f(x)}{h_{\max}}\,dx = 1 - \frac{1}{h_{\max}}. \tag{10.140}$$

Thus,

$$P\{x < x_j < x + dx\} = \sum_{i=1}^{\infty} \left(1 - \frac{1}{h_{\max}}\right)^{i-1} \cdot \frac{h(x_j)}{h_{\max}} \cdot [g(x_j)\,dx]. \tag{10.141}$$

Upon summing the infinite geometric progression, one obtains

$$P\{x < x_j < x + dx\} = h_{\max} \cdot \frac{h(x_j)}{h_{\max}} \cdot [g(x_j)\,dx] = f(x_j)\,dx. \tag{10.142}$$

Alternative-pdf technique. It sometimes happens that the pdf for a process is somewhat cumbersome to use, but it can be split into two separate functions, each of which is separately handled more easily. (They must never have negative values, however.) Let us suppose, for example, that

$$f(x) \equiv f_1(x) + f_2(x). \tag{10.143}$$

The basic function $f(x)$ is normalized to unit area between a and b, but f_1 and f_2 are not. They can, however, be turned into normalized probability functions as follows. Let

$$A_1 \equiv \int_a^b f_1(x)\,dx, \tag{10.144}$$

and

$$A_2 \equiv \int_a^b f_2(x)\,dx. \tag{10.145}$$

Then, since $f(x)$ is properly normalized,

$$A_1 + A_2 = 1. \tag{10.146}$$

If one now defines

$$g_1(x) \equiv \frac{f_1(x)}{A_1} \tag{10.147}$$

and

$$g_2(x) \equiv \frac{f_2(x)}{A_2}, \tag{10.148}$$

then

$$f(x) \equiv A_1 g_1(x) + A_2 g_2(x), \tag{10.149}$$

where g_1 and g_2 are properly normalized pdf's in their own right.

A value of x can be selected by the following procedure:

1. Select a random number ρ_i.

2a. If $\rho_i < A_1$, use $g_1(x)$ as the pdf for selecting a value of x.

2b. If $\rho_i > A_1$, use $g_2(x)$ as the pdf for selecting a value of x.

The proof of the validity of this procedure is simple. The probability that x_j will be found and accepted between x and $x + dx$ can be found as follows:

$$P\{x < x_j < x + dx\} = P\{g_1 \text{ selected}\} \cdot g_1(x_j)\,dx + P\{g_2 \text{ selected}\} \cdot g_2(x_j)\,dx \quad (10.150)$$

$$= A_1 g_1(x_j)\,dx + A_2 g_2(x_j)\,dx \quad (10.151)$$

$$= f(x_j)\,dx. \quad (10.152)$$

This method can be generalized to more than two separate functions, as long as the rule of having no negative values for the functions between the limits is maintained.

10.5.3 Example of a Monte Carlo Calculational Approach

Several aspects of the Monte Carlo method are most easily explained in the context of a specific example. Figure 10.9(a) shows a infinite slab upon which is incident a broad parallel beam of monoenergetic gamma photons at angle θ_0 with the normal to the face of the slab. The photon energy is assumed for simplicity to be below the pair-production threshold, say at 1 MeV. The detector is considered initially to be a differential area on the exit face which measures the exit particle fluence at that point. (Conversion to other dosimetric responses can follow later.)

Geometric transformation. Rather than trying to follow a large number of particles picked at random from the infinitely broad incident beam, most of which would miss the detector area anyway, it is more rewarding to solve a slightly different problem which, however, gives the same result. This is

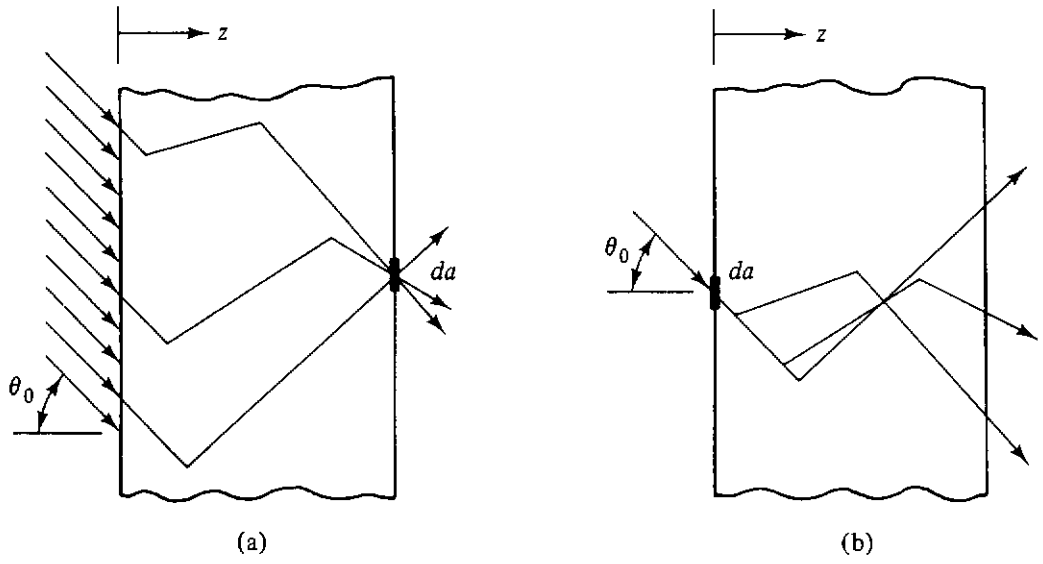

Figure 10.9 (a) Slab illuminated by a broad beam of particles on one side with a small detector on the other side. (b) Transformed but equivalent situation with the illumination on a small area but with the detector spread over a large area on the opposite face.

shown in Fig. 10.9(b) as a pencil of radiation incident at the same energy and angle on a differential area on the incident face, with the entire exit face considered the detector measuring the exit particle fluence. A rigorous proof that these two situations yield the same result will not be given, but it is intuitively obvious that on the average every track in the first situation which goes through the detector has a corresponding track in the second situation, as shown in the figures. Since the starting point for each particle history is the same in the second situation and the particles have a much better chance of passing through the detector in the latter case, we have departed from the strictly analogue approach to one which is much more efficient but which gives the same expected result.

Tracking. Consider the starting point for each history to be the origin. The distance traveled by the first particle to its first collision point is obtained by generating a random number and using Eq. (10.135). The z coordinate of the first interaction point is readily obtained as $s \cos \theta_0$. (The x and y coordinates could also be found but are irrelevant, since the problem is essentially a one-dimensional one.)

At this point, one notes that the photon may have either an absorption (photoelectric) reaction or a scattering (Compton) reaction. Another random number is called forth, and if it is less than μ_C/μ, the interaction is taken to be the scattering one; if larger, the interaction is an absorption and the photon history ends at that point.

If the photon is scattered, its change in energy and direction is customarily obtained by first making a random selection of the new photon wavelength, by use of the free-electron scattering approximation, Eq. (3.37), suitably normalized and rearranged into a form [17] which can be sampled according to the techniques previously described. An appropriate random variable for this random selection is

$$r \equiv \frac{\lambda_s}{\lambda_i}, \tag{10.153}$$

the ratio of the scattered to incident wavelength. If λ is measured in Compton wavelength units, the limits on r, after scattering, are 1 to $1 + (2/\lambda_i)$. Then define

$$f(r) = [A_1 h_1(r) g_1(r) + A_2 h_2(r) g_2(r)]K, \tag{10.154}$$

where

$$A_1 = \frac{\lambda_i + 2}{9\lambda_i + 2} \tag{10.155}$$

$$A_2 = \frac{8\lambda_i}{9\lambda_i + 2} \tag{10.156}$$

$$h_1(r) = 4\left(\frac{1}{r} - \frac{1}{r^2}\right) \tag{10.157}$$

$$h_2(r) = [r^{-1} + (1 - r\lambda_i + \lambda_i)^2]/2 \tag{10.158}$$

$$g_1(r) = \frac{\lambda_i}{2} \tag{10.159}$$

$$g_2(r) = (\lambda_i + 2)(2r^2) \tag{10.160}$$

and K is a collection of parameters independent of r. Note also that $h_{1\max}$ and $h_{2\max}$ can both be made equal to unity.[7] The technique for choosing r is simply a combination of those described in the preceding section, and is depicted in the logic diagram shown in Fig. 10.10. Once r is selected, λ_s is obtained, from which the scattered photon energy is obtained, if desired. From the Compton relationship [Eq. (3.11)], the scattering angle θ_s is obtained. There is no preferred azimuthal angle of scatter about the incident photon direction, so that ψ_s is easily chosen as 2π times another random number.

It is necessary at this time to refer the new photon direction to the angle coordinate system with respect to the basic fixed coordinate system of the slab.

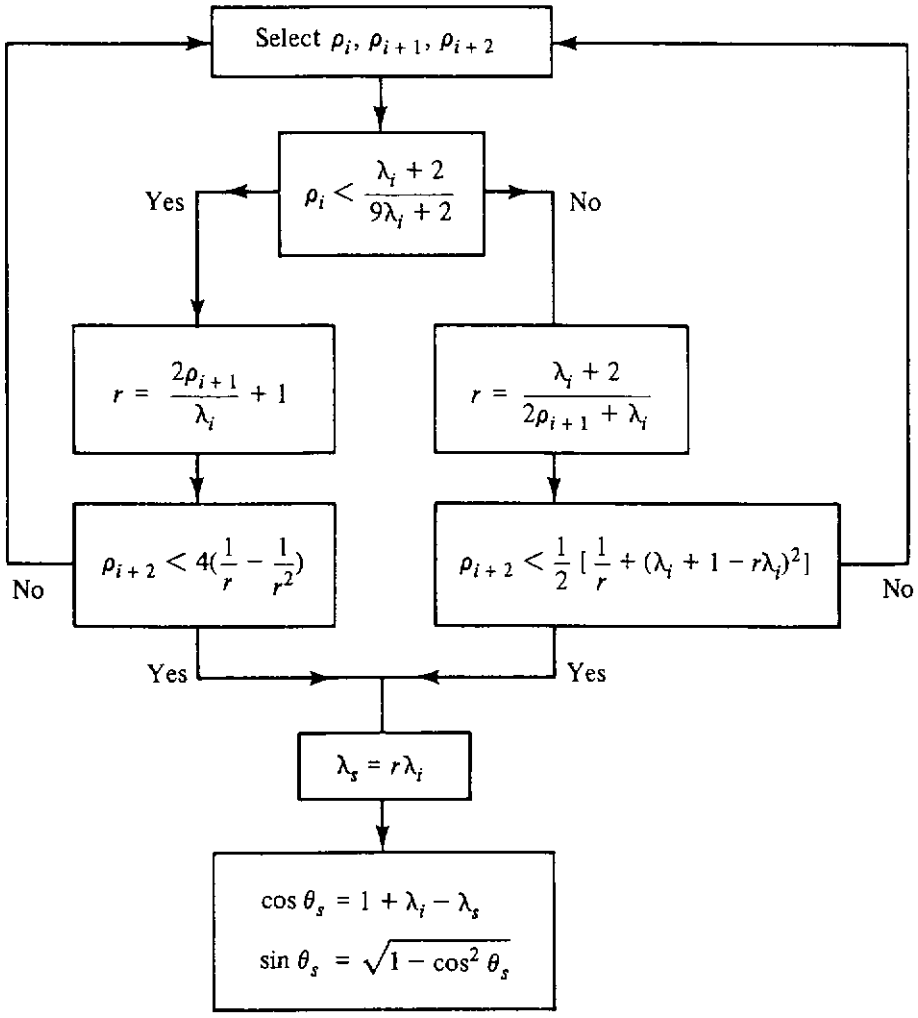

Figure 10.10 Logic diagram for photon wavelength change, based on a pdf derived from the Klein–Nishina scattering formula.

[7]According to the method explained previously, one should combine K with each of the h-functions. However, in the rejection technique, $h(r)$ is actually used in connection with the ratio $h(r)/h_{\max}$ only; and since K is a multiple of both, it can be safely ignored.

Knowledge of the original direction angles $(\theta, \psi)_{\text{old}}$ and the scattering angles (θ_s, ψ_s) allows calculation of the new direction angles $(\theta, \psi)_{\text{new}}$, by the use of standard formulas from spherical trigonometry. This transformation of coordinates to the basic reference coordinate system will not be discussed here in further detail.

Using these techniques, the photon is followed until it passes out of the slab (has a selected track length taking it outside the slab) or until it is absorbed. One then repeats this process for many other source particles thereby generating a large number of histories.

Scoring. A history makes a contribution to the flow at the exit face whenever a track passes through that face. This implies a fluence contribution proportional to $1/\cos\theta$, where θ refers to the polar angle of the track as it crosses the exit face. An alternative way of scoring fluence is to use the definition of internal track length per unit volume. Thus, the detector may be considered a slice of the slab at its exit face. For a very thin slice, say Δz in thickness, the fluence contribution is practically proportional to $\Delta z/\cos\theta$, since the chance of an interaction within Δz is small enough to be ignored.

The total score, or statistical estimate of the fluence, is the sum of the contributions from each history, including, of course, the zero contributions for those histories which end before passing the exit face. The seeming difficulty of finding the proper proportionality constant for either of the foregoing approaches to estimating the detector response is avoided by normalizing the result to the value that would occur in the absence of the slab shield, thus obtaining an attenuation factor, A_f. This normalizing value would be proportional to $n/\cos\theta_0$ for the first approach noted above, where n is the total number of source photon histories, and proportional to $n\,\Delta z/\cos\theta_0$ for the track-length estimator. Thus, the final estimate of attenuation factor for either scoring technique is given by

$$A_f = \frac{1}{n}\cos\theta_0 \sum_{i=1}^{n} \frac{1}{(\cos\theta)_i}, \tag{10.161}$$

where the ith contribution under the summation sign is taken as zero for tracks that never cross the exit face.

Since the contributions to the normalized detector response constitute a statistical distribution for the sample of n histories taken randomly from the infinite number of possible histories that could be followed, the formula (10.161) is a sample mean and becomes an estimate of the "true" value (the mean for the infinite population). Similarly, it may have a sample standard deviation which can be used as an estimator of the population standard deviation, and more important, as an estimator of the probable error for the sample mean.[8]

[8]The statistical niceties of Monte Carlo scoring are beyond the scope of this text. It may be mentioned, however, that the $1/\cos\theta$ estimator, given above, can be proved to have a standard deviation approaching infinity as n approaches infinity. In spite of this, it is still a practical estimator for the mean value [18].

Once the fluence estimations have been determined they are easily turned into estimations of dosimeter response by use of an appropriate response function, such as prescribed in Chapter 5.

10.5.4 Nonanalog Techniques in Tracking

The Monte Carlo technique has two disadvantages. It is inherently slow, so that it requires relatively large computer resources, and it provides only a statistical estimate of the correct answer rather than a precise value. The cure for an answer with a large probable error (standard deviation of the sample mean) in an analog calculation is to increase the number of histories; but the error decreases as the inverse of the square root of the number of histories, so that the computer time required may become very great for a specified small probable error. Fortunately, there are special techniques available for reducing the error without unduly increasing the computer effort, for decreasing the computer effort without appreciably increasing the error, or for even making a reasonable reduction in both error and computer effort.

The central concept for improving the efficiency of the Monte Carlo process is to ascribe to each particle a *weight* or numerical value of its importance to the desired detector response. In the actual physical situation or in the direct analogue mathematical simulation, the weight of each particle is unity. However, this is not necessary. If each particle is given some arbitrary weight or importance value, and if the detector response (e.g., fluence) is defined as the sum of all weights of the particles contributing to the detector response, the transport description of the particles is unchanged. Thus in a Monte Carlo simulation, the scoring of the particles at the detector must be modified from just the sum of the particles' score to the sum of the particles' weighted scores.

The use of weights can greatly increase the flexibility of scoring and sampling procedures available to the analyst. For any single step in the Monte Carlo process involving the probability of survival of a particle or of its reaching a certain point, the result of the sampling process (insofar as its effect on the final answer is concerned) may be taken as the product of the probability of occurrence for the event times the particle weight (the expectation). Thus, if a probability density function $f(x)$ describes some random process, one is allowed to use some simpler probability density function $g(x)$; however, the ultimate expectation of the process must be left unchanged and therefore must have the value $w_b g(x)h(x)$, where $h(x) \equiv f(x)/g(x)$ and w_b is the particle's weight *before* entering the process being considered. The function $g(x)$ as previously stated in Section 10.5.2, can be somewhat arbitrarily chosen although it should not deviate too markedly from $f(x)$ and should have the nature of a proper probability density function. Whereas in the analog case the use of $g(x)$ instead of $f(x)$ is compensated by the subsequent testing for rejection or acceptance, in the weighting technique the value of x selected is accepted without further ado, but the particle weight after the process, w_a, is obtained by multiplying

its previous weight w_b by $h(x)$, where the argument is the value of x selected. This weighting thus preserves the proper expectation value. The function $h(x)$ is said to be the *weight-adjustment factor* (waf).

Another example of the usefulness of weighting is in the avoidance of the absorption process for a particle. Since particles absorbed in the medium give zero contribution to the final answer, one intuitively has the feeling that a history terminating in this way is in a sense a waste of computer time. To avoid a zero contribution, one may change the probability of scatter from μ_s/μ to unity, as long as one compensates by the use of μ_s/μ as a weight-adjustment factor (waf).

A process known as *Russian roulette* takes advantage of the weighting process. If a particle for one reason or another, such as location in the system or direction of travel, appears to have little chance of making a relatively significant contribution to the detector response, one may decide to subject it arbitrarily to a probabilitic process to decide whether it is "killed" or "survives." For example, a random number could be selected; and, if it should be less than $\frac{1}{2}$, the particle would be "killed." Otherwise, it would be continued, but with the application of a waf of 2. In general, if the criterion for continuing a particle history should be that a random number be less $1/m$, the waf would be m. The value of m should be selected with care, and $m = 2$ is generally a conservative choice.

The opposite of this process is called *splitting*. Should a particle be in a very favorable position or direction of travel for making an appreciable contribution to the detector response, it is useful to split it into two (or m) particles each having the same characteristics as the original one except that the weight of each of the new particles is one-half (or $1/m$) the weight of the original particle. This process, of course, requires setting aside the split particles in the computer memory so that they can be subsequently recalled and followed to their final terminations. If continual splitting is allowed, an avalanching of particles can result, and the "traffic control" in the computer program for the storage and recall of particles waiting to have their histories followed can become somewhat elaborate.

Many of the foregoing techniques can be classed together under the general term *biasing*. It is permissible, in principle, to change a probability or to modify a pdf (or to "bias" it) in such a way as to make the particle go into a more preferred direction and maintain a more preferred characteristic—but this biasing must be compensated for by an appropriate weight adjustment factor. Such procedures must be done with discretion, however. It is not a good idea to let the detector response end up being dominated by a few particles with very high weights, nor at the opposite extreme should one spend a lot of computational effort on a large proportion of particles with very low weights. Experience and judgment must be the guide in using the more sophisticated biasing techniques, in which the literature abounds.

Weighting also plays an important role in neutron problems, where it is necessary to sample randomly from the neutron differential scattering cross

sections. Because of the empirical nature of these cross sections, it is difficult to treat them as elegantly as is possible for the corresponding scattering cross section for photons (see Section 10.5.3). The neutron scattering cross section as a function of the scattering angle θ_s is most commonly represented by a truncated Legendre polynomial expansion,

$$f(\omega_s) = \frac{1}{2} + \frac{1}{2} \sum_{n=1}^{N} (2n + 1) f_n P_n(\omega_s), \tag{10.162}$$

where $\omega_s = \cos \theta_s$. A simple approach for sampling from this pdf is to take the first term as an approximating pdf [i.e., let $g(\omega_s) = \frac{1}{2}$]. This choice requires selecting $\omega_s = 1 - 2\rho_i$ and then the use of $h(\omega_s) \equiv f(\omega_s)/g(\omega_s)$ as a waf. More elaborately, one could take the first two terms of the $f(\omega_s)$ above as the approximating pdf $g(x)$, which would involve the solution of a quadratic equation for the selection of ω_s. Other techniques are possible.

An inherent problem with expressing scattering probabilities as a truncated Legendre series is that negative values of $f(\omega_s)$ may occur for certain values of ω_s. Such unrealistic values could be a result of faulty cross-section information; but they generally will occur even if the cross-section information is exact, as a result of inherent oscillations in low-order Legendre expansions. Fortunately, in the technique just outlined, it is never necessary to identify $f(\omega_s)$ as a pdf; however, one must ensure that $g(\omega_s)$ is a proper probability function with no negative values. The expanded scattering cross section, $f(\omega_s)$, appears only as part of $h(\omega_s)$ which is used solely for weight-adjustment purposes. One must be prepared, however, to accept a negative weight once in a while. For most problems, these negative contributions are small and easily drowned out when combined with a large number of positive contributions. On rare occasions, negative values for angular fluences may still result for certain directions. These negative values must be recognized as an artificiality of the process caused by the approximation of the scattering cross section by a truncated Legendre expansion.

10.5.5 Other Special Techniques

Techniques related to the source. The problem of selecting a starting point for a uniform broad, parallel-beam source in the slab problem of Section 10.5.3 was avoided by the transformation of the problem to one with an effective point source. If this technique is found not to be applicable because of geometric or other complexities, one must treat a broad-beam source by establishing finite boundaries to the source. These boundaries, if artificially selected, should be such that the chance of a particle, which starts outside the selected boundaries, will affect the detector is comparatively small. At the same time, the boundaries should be no broader than necessary so as to include only the significantly contributing source particles. The starting location of any source particle selected should be by a random process such that the probability of coming from any incremental area is proportional to the size of that area. If the bounding figure is rectangular in the x-y plane, as in Fig. 10.11(a), the loca-

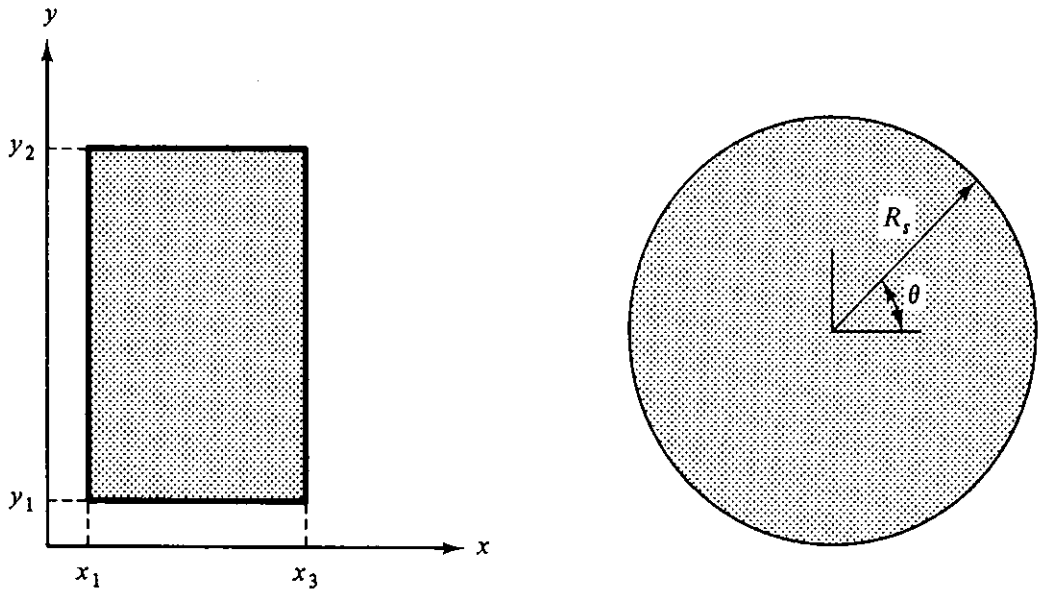

Figure 10.11 Face view of plane sources: (a) a rectangular source; (b) a circular source. Particle scattering points must be randomly chosen in these source planes.

tion of a source point for the beginning of a particle history can be taken with $\{x, y\}$ coordinates equal to $\{x_1 + \rho_i(x_3 - x_1),\ y_1 + \rho_{i+1}(y_2 - y_1)\}$. If the bounding figure is a circle around the origin as in Fig. 10.11(b), the source point can be taken with $\{r, \theta\}$ coordinates $\{R_s\sqrt{\rho_i}, 2\pi\rho_{i+1}\}$,[9] where R_s is the radius of the bounding circle. Alternatively, the (x, y) coordinates within the circle can be obtained by $\{R_s(1 - 2\rho_i), R_s(1 - 2\rho_{i+1})\}$; but the choice must be rejected if $x^2 + y^2 > R_s^2$, and another trial made with new random numbers as in the standard rejection approach.

Once the starting source point is found, a starting direction must be established. For a parallel beam, this is provided by the statement of the problem. On the other hand, for a plane source with a distribution of starting directions, the problem requires further random selection for the starting direction. (The plane may not contain the original source, but the flow at the plane in the inward direction can be treated as the source.)

If the particles are coming from *isotropic* point sources uniformly distributed over the plane (or if the inward-directed passage is isotropic with respect to flow), the (ω_0, ψ_0) distribution is also uniformly random, so that one can take for a given particle $\omega_0 = \rho_i$ and $\psi_0 = 2\pi\rho_{i+1}$. (The reference plane for the aximuthal angle ψ_0 can be arbitrarily chosen.) If the source has a *cosine* distribution inward (or if it is isotropic with respect to fluence at the plane), then ω_0 must be chosen from a pdf $f(\omega_0) = 2\omega_0$ between 0 and 1, to give $\omega_0 \equiv \cos\theta_0 = \sqrt{\rho_i}$.

[9]An easy way to obtain the square root of a random number between zero and one is to select two (practically) uncorrelated random numbers between zero and one and then to use the larger of the two [17].

A point, isotropic source in a uniform, homogeneous medium (either infinite or spherical about the source point) can be most efficiently treated by a transformation similar to the plane-to-point transformation in Section 10.5.3. That is, rather than analyze the situation for a source emitting isotropically in all directions and a point detector at distance r, one could obtain the same answer by analyzing the situation where the particles are initially emitted from the point all in the same direction and the detector becomes the entire spherical surface at the radius r (or, if track length is used for estimating fluence, the detector becomes a thin shell placed at radius r from the source point). See Fig. 10.12.

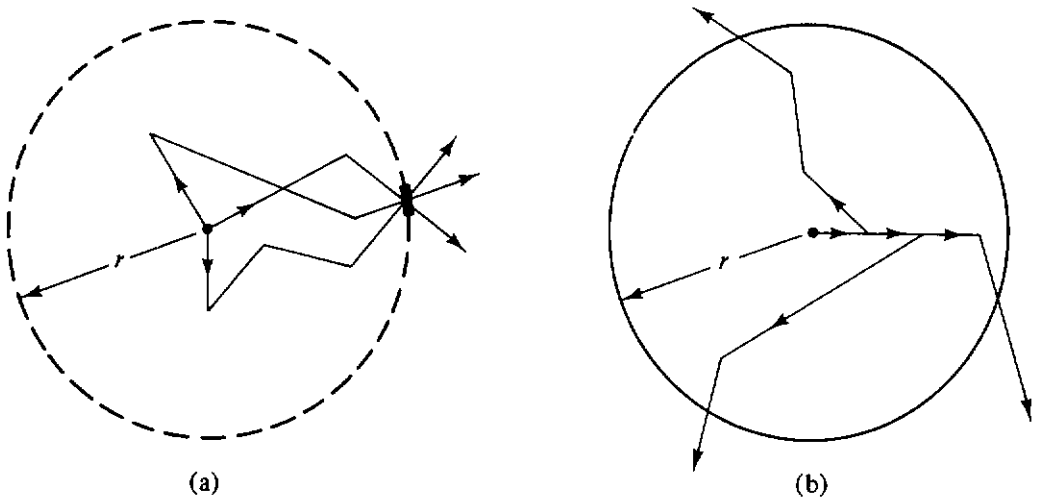

Figure 10.12 (a) A point isotropic source with a small flow detector at a distance r. (b) The transformed and equivalent situation with the source emitting in only one direction and the detector spread out over the entire spherical surface of radius r.

Techniques related to the detector. It is always more statistically accurate to replace a series of random selection processes with a formula for the mean value for the result of these processes, if known. The *no-further-collision estimator* for the in-scattered fluence is an example. Assume a detector at a given point (or a very small detector volume) in space at point $\mathbf{r}_d$. Consider a particle having some interaction at point $\mathbf{r}$. The mean value of the probability distribution of possible contributions of this particle interacting at $\mathbf{r}$ without further interactions, to the fluence at the detector point is easily shown to be

$$w \frac{\mu_s}{\mu} \frac{p(\mathbf{\Omega} \rightarrow \mathbf{\Omega}_d)}{|\mathbf{r}_d - \mathbf{r}|^2} \exp\left[- \int_0^{|\mathbf{r}_d - \mathbf{r}|} \mu(s)\, ds \right],$$

where μ_s is the scattering cross section, μ is the total cross section, $p(\mathbf{\Omega} \rightarrow \mathbf{\Omega}_d)$ is the probability per steradian that a particle moving in direction $\mathbf{\Omega}$ before interaction will, if scattered, scatter in the direction toward the detector (e.g., equals $1/4\pi$ for an isotropic scatter in the laboratory system), and w is the weight of the particle before the interaction. The variable s in the above expression is the distance along a straight line from the interaction point to the detector point.

More advanced treatments of the Monte Carlo technique use this estimate to good advantage [19]. The total detector fluence is the sum of this individual estimator for every interaction point. Note that the track length is not used as an estimator if this last-flight estimator is used, even if the track should go through the detector volume.

There is one problem associated with the last-flight estimator: for interaction points very close to the detector point, the denominator in the expression becomes very large. This is a matter of great concern if the detector is actually embedded within the interacting medium, but of no importance if the detector is outside the shield of attenuating material. Various efforts have been made to cure this defect in the first case [19,20].

10.5.6 Final Remarks

Monte Carlo is an important method, both for checking results by other methods and for making analyses under conditions which are not suited for any other method, especially for complex shield geometries. It is considered by many of the more traditional analysts as a "brute force" method, requiring less of analytical skill and more of sheer computer time and capacity. In a sense this is true yet there is great room for ingenuity in doing a Monte Carlo problem in such a way as to minimize the computer effort and the statistical error simultaneously. The greatest difficulty in this method is its application to very thick shields; however, even here techniques have been developed, such as path stretching [21], to permit its successful use.

The techniques discussed in this text are by no means exhaustive, but are intended to serve as an introduction to this important method. The student is referred to a large amount of literature for more extensive treatment of this subject [8,22].

REFERENCES

1. J. J. Duderstadt and W. R. Martin, *Transport Theory*, Wiley, New York, 1979.
2. B. G. Carlson and K. D. Lathrop, "Transport Theory, the Method of Discrete Ordinates," in *Computing Methods in Reactor Physics*, H. Greenspan, C. N. Kelber, and D. Okrent (eds.), Gordon and Breach, New York, 1968.
3. K. M. Case and P. F. Zweifel, *Linear Transport Theory*, Addison-Wesley, Reading, Mass., 1967.
4. U. Fano, "Note on the Bragg–Gray Cavity Principle for Measuring Energy Dissipation," *Radiat. Res.* **1**, 237 (1954).
5. J. R. Lamarsh, *Introduction to Nuclear Reactory Theory*, Addison-Wesley, Reading, Mass., 1966.
6. G. I. Bell and S. Glasstone, *Nuclear Reactor Theory*, Van Nostrand Reinhold, New York, 1970.

7. H. Goldstein, *Fundamental Aspects of Reactor Shielding*, Addison-Wesley, Reading, Mass., 1959.
8. U. Fano, L. V. Spencer, and M. J. Berger, "Penetration and Diffusion of X Rays," in *Handbuch der Physik*, Vol. 38/2, S. Flügge (ed.), Springer-Verlag, Berlin, 1959.
9. L. V. Spencer and U. Fano, "Calculation of Spatial Distributions by Polynomial Expansion," *J. Res. Natl. Bur. Stand.* **46**, 446 (1951).
10. S. Chandrasekhar, *Radiative Transfer*, Dover, New York, 1960.
11. S. Nakamura, *Computational Methods in Engineering and Science*, Wiley, New York, 1977.
12. T. R. Hill, "ONETRAN: A Discrete Ordinates Finite Element Code for the Solution of the One-Dimensional Multigroup Transport Equation," Report LA-5990-MS, Los Alamos Scientific Laboratory, Los Alamos, N.M., 1975.
13. F. R. Mynatt et al., "DOT III Two-Dimensional Discrete Ordinates Transport Code," Report ORNL-TM-4280, Oak Ridge National Laboratory, Oak Ridge, Tenn., 1973.
14. K. D. Lathrop, "THREETRAN: A Program to Solve the Multigroup Discrete Ordinates Transport Equation in (x, y, z) Geometry," Report LA-6333-MS, Los Alamos Scientific Laboratory, Los Alamos, N.M., 1976.
15. R. R. Coveyou and R. D. MacPherson, "Fourier Analysis of Uniform Random Number Generators," *J. Assoc. Comp. Mach.* **14**, 100–119 (1967).
16. J. M. Hammersley and D. C. Handscomb, *Monte Carlo Methods*, Barnes & Noble, New York, 1964.
17. H. Kahn, "Applications of Monte Carlo," Report AECU-3259, The Rand Corp., Santa Monica, Calif., 1954.
18. F. H. Clark, "Variance of Certain Flux Estimators Used in Monte Carlo Calculations," *Nucl. Sci. Eng.* **27**, 235–239 (1967).
19. M. H. Kalos, "On the Estimation of Flux at a Point by Monte Carlo," *Nucl. Sci. Eng.* **16**, 111–117 (1963).
20. T. J. Jordan, "Adanced Monte Carlo Concepts in Radiation Shielding Calculations: Methods and Applications," *Nucl. Eng. Des.* **13**, 415–422 (1970).
21. L. B. Levitt, "The Use of Self-Optimized Exponential Biasing in Obtaining Monte Carlo Estimates of Transmission Probabilities," *Nucl. Sci. Eng.* **31**, 500–504 (1968).
22. G. G. Biro, "Application of the Monte Carlo Method to Shielding," in *Engineering Compendium on Radiation Shielding*, Vol. I, R. G. Jaeger (ed.), Springer-Verlag, New York, 1968, Sec. 3.1, pp. 101–124.

11 material and structural considerations in shield design

The primary objective in shield design, the limitation of radiation intensities to prescribed levels, may be met by many combinations of materials and geometric configurations. The particular combination of materials and their arrangement specified in a final shield design is influenced by many factors other than just the attenuation properties of the shield. To achieve a final shield design, the designer must also consider material and construction costs, structural strength, maintenance, safety, and weight and space limitations. The physical environment of the shield may also influence the design. For example, high temperatures may impose thermal stresses in the shield or may cause unacceptable dehydration in a concrete shield. For these reasons, the shield designer must know the thermal properties of the shield materials. The ease and safety of fabrication requires familiarity with the mechanical properties of the shield materials. Similarly, safety and maintenance aspects of the shield require that the designer be aware of special chemical and physical properties of the shield materials.

Although many shields are intended as biological shields to minimize exposure of personnel in radiation environments, other shields are designed to protect sensitive equipment. An important example of this latter type of shield is the thermal shield placed around a reactor core to reduce radiation damage and thermal stresses in a pressure vessel. Thus, the shield designer must be aware not only of biological effects of radiation, but also of radiation effects on material properties.

Many of these concomitant factors that influence a final shield design are treated on the basis of the analyst's experience or require the skills and experience of material, structural, or other experts. The shielding analyst will often

have to interact with other design groups, and thus it is important that the shield designer be aware of these associated design problems and the principles used for their analysis. Although a detailed description of all influencing factors is beyond the scope of this text, this chapter is intended to give an introduction to several of the more important principles. One special note: this chapter includes topics from several areas of science and engineering which have well-established notational conventions. Rather than to introduce nonstandard notation simply to avoid reusing previously defined symbols, we choose to employ conventional notation in this chapter and to define the meaning of each symbol when it first occurs.

11.1 MATERIAL PROPERTIES

11.1.1 Selection Criteria

Economic considerations. In a very rough sense, the protection provided by a shield depends not so much on the nature of the material as it does on the mass thickness (mass per unit cross-sectional area) between the source and the person or object protected. Thus, the same degree of protection might be provided by a thin lead shield, a thicker steel shield, a thicker yet concrete shield, or a much thicker water-filled shield. If there were no constraints on shield volume or weight, the choice of material would be based on a balance between material and construction costs with due consideration given to maintenance costs and salvage value. On the other hand, shield volume and weight very often influence other installation costs. For example, the volume and weight of the biological shield of a nuclear reactor influence the required foundation support and the size of the containment building. Furthermore, a shield may itself have a structural function and it must at least support its own weight. Thus, shield design must be integrated with all other design aspects of an installation.

Optimization techniques specifically applicable to shield design have received little attention [1–3]. The *Engineering Compendium on Radiation Shielding*, for example, devotes only 12 pages specifically to this subject in a total of 1451 pages in three volumes (see Ref. 3). The reason for this lack of attention is addressed by Butler [4]. He points out that, in the conceptual stage of shield design, there is usually insufficient detail to justify a comprehensive optimization study. At later stages in design, an optimization study is not justified because of excessive constraints having been introduced as a result of factors unrelated to shielding design.

Fabrication, maintenance, and occupational safety. Construction or fabrication cost is of course an important factor in selecting a shielding material, but maintenance costs should not be overlooked. A water-filled shield, while an attractive option from the viewpoint of construction costs, may

in the long run require substantial maintenance expenditures. Neither should the salvage value of the shield be ignored. The choice of lead as a shield may appear unfavorable from the viewpoint of material cost. However, for relatively short-term shielding requirements, the salvage value of the lead may mitigate the high initial cost. Occupational health and safety, especially during construction, are often important factors in the selection of materials. If the use of lead requires casting or cutting, its toxicity, especially if it is in aerosol form, must be taken into account. Uranium, beryllium, and their compounds also are toxic, while uranium metal, graphite, and paraffin present a flammability hazard.

Mechanical and thermal properties. In the design of a shield for protection of structural materials and in cases where materials serve dual shielding and structural functions, the designer must be concerned with the effects of radiation on mechanical properties and with heating and consequent thermal stresses due to absorption of radiation. These concerns are especially acute in the design of the steel containment vessel and concrete biological shield of a nuclear power plant. Neutron and gamma radiation from the reactor core can cause severe temperature gradients, which may introduce thermal stresses in the containment vessel and shield as well as dehydrate the concrete in the biological shield. Radiation damage, especially that due to fast neutrons, can embrittle structural steel and increase the likelihood of abrupt failure. Thermal effects and radiation damage are thus important concerns of the shield designer in protecting structural materials and are the principal topics covered in this chapter.

11.1.2 Thermal and Mechanical Properties of Structural and Shielding Materials

Mechanical properties. The basic tensile properties of a metal may be described in terms of the results of a uniaxial tensile test. A bar or rod specimen is subjected to axial tension, and the stress and strain are recorded up to the point of fracture. The nominal stress, or engineering stress, is the applied force per unit *initial* cross sectional area of the specimen. The strain ϵ is the fractional elongation of the specimen. Representative stress–strain diagrams for steel are illustrated in Fig. 11.1. Initially, the deformation of the specimen is elastic and the stress is given by $\sigma = \epsilon E$, where E is Young's modulus of elasticity. Beyond a certain *elastic limit*, deformation is plastic and a permanent strain is introduced. The *yield strength* σ_Y is the stress at the elastic limit or, if the elastic limit is not well defined, the stress at some prescribed strain, usually 0.2%. The maximum engineering stress sustained by the specimen is the *ultimate tensile strength* (UTS). Strength under compression is characterized by *compressive strength*, the maximum stress, based on original area, which the material is capable of developing short of failure. For materials such as ceramics, which fail by shattering, the compressive strength is well defined. For other materials, it must be defined in terms of a specified degree of distortion.

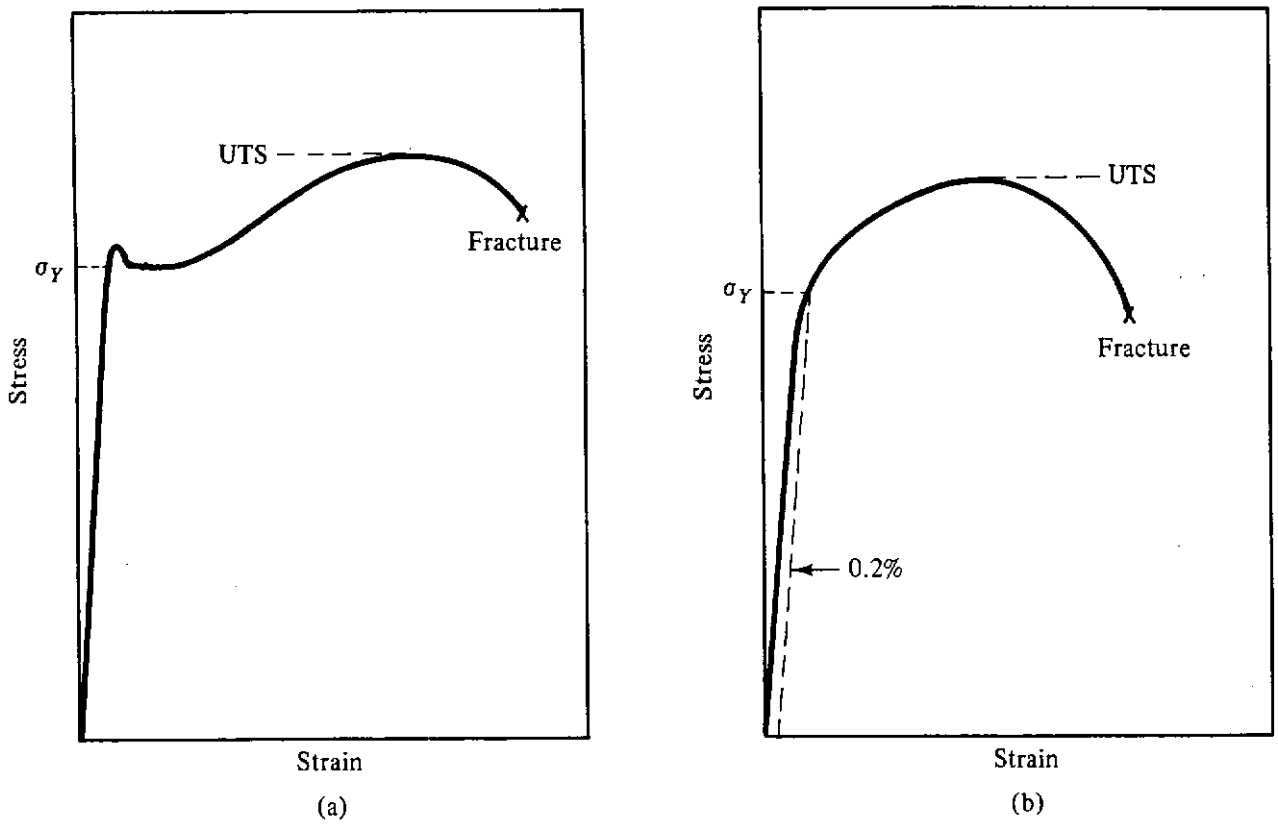

Figure 11.1 Representative stress–strain relationships: (a) ferritic steel; (b) austenitic steel.

Ductility is defined as the ability of a material to deform plastically prior to fracture. Measures of ductility are the strain at fracture or the fractional reduction in cross-sectional area of a test specimen at fracture. *Hardness*, by contrast, is the resistance of a material to plastic deformation, usually by indentation, and is closely correlated with yield strength. *Toughness* is the ability of a metal to absorb energy and deform plastically before fracturing. It is usually measured in terms of the energy absorbed in fracturing a notched specimen.

Fatigue strength is the maximum stress than can be sustained for a specified number of cycles without failure, the stress being completely reversed within each cycle. The *fatigue limit*, applicable to ferritic steel, is the stress below which an apparently infinite number of cycles can be sustained. *Creep* is long-term strain occurring at elevated temperature at a stress below the normal-temperature yield strength. *Creep strength* is the stress that would cause a specified creep strain in a given time at constant temperature.

In general, mechanical properties are sensitive to material temperature and the state of applied stresses. These factors must be considered when applying mechanical-property data in component design.

Thermal properties. *Heat capacity*, *thermal conductivity*, and *temperature coefficient of expansion* are the thermal properties of most importance in shield design. The latter is defined as the fractional change in dimension per unit temperature change in an unconstrained material.

11.1.3 Properties of Selected Shielding Materials

Lead. For photon shielding, commercially available lead (> 99.9% pure) is commonly used. However, pure lead has poor structural properties and is not suitable for high-temperature situations. To increase its strength, lead is often alloyed with antimony. Lead shields are relatively easy to fabricate, since lead may be cast, extruded, rolled, machined, and welded. Casting requires special care because of the 3.85% decrease in density upon solidification and because of the toxicity of lead fumes. Lead is resistant to chemical corrosion, and because of its high density it is widely used for photon shielding when limitations on shield thickness are important, even though it is a relatively expensive material. Thermal and mechanical properties are given in Table 11.1.

TABLE 11.1 Thermal and Mechanical[a] Properties of Lead and Uranium

Property	Lead[b]	Uranium
Melting point (°C)	327.4	1133
Density (g cm^{-3}) (25°C)	11.34	19.05
Specific heat (J g^{-1} K^{-1})		
20–25°C	0.129	0.117
100°C	0.132	—
Thermal conductivity (W m^{-1} K^{-1})		
20–25°C	35	24
100°C	34	27
200°C	32	30
Coefficient of thermal expansion (10^{-6} K^{-1})	29	7–15[c]
Modulus of elasticity (MPa)	1.4×10^4	1.7×10^5
Poisson ratio	0.40–0.45	0.21
Yield strength (MPa)	5.5	190
Ultimate tensile strength (MPa)	13.1	390
Elongation in 2 in.	30–47%	~4%
Reduction in area	100%	~10%
Compressive strength (MPa)	~17	—

[a]Average mechanical properties for cast metal at room temperature.

[b]"Corroding" grade.

[c]Anisotropic wrought alpha phase. For single crystals: (2 to 27) $\times$ 10^{-6} K^{-1}, depending on orientation.

Source: *Refs. 3 and 5.*

Uranium. Because of its high density, depleted uranium is an excellent photon shield material, although it is active chemically and oxidizes upon exposure to air. Its fabrication is difficult and hazardous because of its pyrophoric nature. The structural properties of uranium are similar to those of steel, and it is often alloyed with elements such as molybdenum to improve its mechanical and corrosion-resistance properties. Its structural use is complicated because of its large and anisotropic thermal expansion coefficient. Obviously, uranium

shielding is not suitable in neutron environments. Properties of uranium are given in Table 11.1.

Tungsten. Because of its high density (19.3 g cm^{-3}), and high melting temperature (3410°C), pure tungsten is an excellent material for shielding high energy photons in high-temperature environments. Because of its high cost and difficulty of fabrication, tungsten is usually used only for small shield components near the source.

Steel. Steel is widely used for photon shielding because of its excellent structural, thermal, and chemical properties, its ease of fabrication, and its favorable shielding properties. For photon shielding, but not for neutron shielding, the attenuation properties of steel can be taken as those of pure iron (density 7.87 g cm^{-3}). In Tables 11.2 and 11.3 are listed properties of steels widely used in the nuclear industry. The alloy steels are representative of those used for pressure vessels while the stainless steels are characteristic of those used for cladding fuel and pressure vessels and for reactor-core support components.

Miscellaneous metals. Aluminum, zirconium, and beryllium are often used in conjunction with radiation shields, especially as nuclear reactor components. Their properties of interest to shield designers are given in Table 11.4. The 6061 alloy of aluminum (1.0% Mg, 0.6% Si, 0.25% Cu, 0.25% Cr) is widely used in industry because of its good strength, weldability, and corrosion resistance. The Zircaloy 2 and 4 alloys are commonly used as cladding for fuel elements because of their good high-temperature properties and low thermal neutron absorption cross sections. Zircaloy 2 contains 1.5% Sn, 0.15% Fe, 0.1% Cr, and 0.05% Ni. Zircaloy 4 has the same composition, but without the Ni. Beryllium is often used as a reflector or moderator, or as the converter in a neutron source. The metal and its compounds are extremely toxic.

Concrete. Concrete is the most versatile and widely used shielding material. It is relatively inexpensive, is easily formed into complex-shaped shields, has good structural properties, and can be used to shield against both neutrons and photons. Concrete is prepared from a mixture, by weight, of about 13% cement, 7% water (including water in the aggregate), and 80% aggregate. Many different types of concrete can be prepared by varying the nature of the aggregate (see Table 11.5). For example, to improve photon-attenuation properties, scrap iron or iron one may be incorporated with a sand-and-gravel aggregate. Addition of boron compounds to the aggregate can greatly improve the thermal neutron absorption qualities of a concrete.

The hydrogen content in concrete is important to its utility as a neutron shield. Virtually all the hydrogen in concrete is in the form of water which is present not only as *fixed water* (i.e., water of hydration in the cement and aggregate) but also as *free water* in the pores of the concrete. At elevated tem-

TABLE 11.2 Weight Percentages of Alloying Elements in Various Steels (Heat Analysis)

	C	Mn	Si	Cr	Ni	Mo	P	S
Alloy steels								
ASTM A212B	0.30–0.35	0.85–1.20	0.15–0.30				0.035 max.	0.040 max.
ASTM A302B	0.20–0.25	1.15–1.50	0.15–0.40			0.45–0.60	0.035 max.	0.040 max.
ASTM A302C	0.20–0.25	1.15–1.50	0.15–0.40		0.40–0.70	0.45–0.60	0.035 max.	0.040 max.
ASTM A508(C12)	0.27 max.	0.50–1.00	0.15–0.40	0.15–0.40	0.50–1.00	0.55–0.70	0.025 max.	0.025 max.
ASTM A533B	0.25 max.	1.15–1.50	0.15–0.40		0.40–0.70	0.45–0.60	0.035 max.	0.040 max.
SAE 4130	0.28–0.33	0.40–0.60	0.20–0.35	0.80–1.10		0.15–0.25	0.040 max.	0.040 max.
SAE 4340	0.38–0.43	0.60–0.80	0.20–0.35	0.70–0.90	1.65–2.00	0.20–0.30	0.040 max.	0.040 max.
Stainless steels								
AISI 304	0.08 max.	2.00 max.	1.00 max.	18.0–20.0	8.00–12.0			
AISI 304L	0.03 max.	2.00 max.	1.00 max.	18.0–20.0	8.00–12.0			
AISI 316	0.08 max.	2.00 max.	1.00 max.	16.0–18.0	10.0–14.0			
AISI 316L	0.03 max.	2.00 max.	1.00 max.	16.0–18.0	10.0–14.0	2.00–3.00		
AISI 347[a]	0.08 max.	2.00 max.	1.00 max.	17.0–19.0	9.00–13.0			

[a]Sum of cobalt and tantalum concentrations is less than 10 times the carbon concentration.
Source: *Refs. 5–7.*

TABLE 11.3 Typical Room-Temperature Mechanical and Thermal Properties of Alloy and Stainless Steels

Property	Alloy Steel[a]	Stainless Steels		
		304 and 304L	316 and 316L	347
Melting point (°C)	~1540	1400–1450	1370–1450	1400–1430
Density (g cm^{-3}) (25°C)	7.86	7.9	8.0	8.0
Specific heat (J g^{-1} K^{-1}) (0–100°C)	0.46	0.50	0.50	0.50
Thermal conductivity (W m^{-1} K^{-1})				
25°C	33–52	—	—	—
100°C	—	16	16	16
Coefficient of thermal expansion (10^{-6} K^{-1}) (20–100°C)	11.7	17	16	17
Modulus of elasticity (MPa)	2×10^5	2×10^5	2×10^5	2×10^5
Poisson ratio	0.3	0.3	0.3	0.3
Yield strength (MPa)	345	210–240	210–240	240
Tensile strength (MPa)	550–690	550–590	540–590	630
Elongation	16–20%	55%	55%	50%
Reduction in area	30–50%	65%	65%	65%

[a]Tensile strength, yield strength, and percent elongation are for ASTM A533, A302B and C steels. Other values are nominal.

Source: *Refs. 5–7.*

TABLE 11.4 Thermal and Mechanical[a] Properties of Beryllium, Zirconium, and Aluminum Alloy

Property	Aluminum 6061-T6	Zirconium	Beryllium[b]
Melting point (°C)	582–649	1852	1277
Density (g cm^{-3}) (20°C)	2.70	6.489	1.848
Specific heat (J g^{-1} K^{-1})			
20°C	—	0.28	1.9
20–100°C	—	—	1.8–2.2
100°C	0.96	—	—
Thermal conductivity (W m^{-1} K^{-1}) (20–25°C)	150	21	150
Coefficient of thermal expansion (10^{-6} K^{-1}) (20–200°C)	24.3	6–7	13.3
Modulus of elasticity (MPa)	2.6×10^4	$\sim 1 \times 10^5$	3×10^5
Poisson ratio	0.33	—	0.024–0.030
Yield strength (MPa)	280	~200	190–260
Ultimate tensile strength (MPa)	310	~350	230–350
Elongation in 2 in.	17%	—	1–3.5%

[a]Representative mechanical properties at room temperature.

[b]Vacuum hot-pressed powder.

Source: *Refs. 3 and 5.*

TABLE 11.5 Typical Compositions of Representative Concretes After Curing

Type:	Ordinary	Magnetite[a]	Barytes[b]	Magnetite and steel	Limonite and steel[c]	Serpentine[d]
Density (g cm^{-3}):	2.35	3.53	3.35	4.64	4.54	2.1
Element	Partial Density (g cm^{-3})					
H	0.013	0.011	0.012	0.011	0.031	0.035
O	1.165	1.168	1.043	0.638	0.708	1.126
Si	0.737	0.091	0.035	0.073	0.067	0.460
Ca	0.194	0.251	0.168	0.258	0.261	0.150
C						0.002
Na	0.040					0.009
Mg	0.006	0.033	0.004	0.017	0.007	0.297
Al	0.107	0.083	0.014	0.048	0.029	0.042
S	0.003	0.005	0.361			
K	0.045		0.159		0.004	0.009
Fe	0.029	1.676		3.512	3.421	0.068
Ti		0.192		0.074		
Cr		0.006				0.002
Mn		0.007				
V		0.011		0.003	0.004	
Ba			1.551			

[a]Magnetite ($FeO \cdot Fe_2O_3$) as aggregate.

[b]Barytes, a $BaSO_4$ ore, as aggregate.

[c]Limonite, a hydrated Fe_2O_3 ore, plus steel punchings, as aggregate.

[d]Serpentine ($3MgO \cdot 2SiO_2 \cdot 2H_2O$) as aggregate; a concrete usable at high temperatures with minimal water loss.

Source: *Ref. 8. Extracted from American National Standard ANSI/ANS-6.4-1977 with permission of the publisher, the American Nuclear Society.*

peratures both may be lost, thereby greatly reducing the ability of the concrete to attenuate fast neutrons. At ambient temperatures, free water may be lost slowly over time by diffusion and evaporation. Typically, the free water is initially about 3% by weight of the concrete, and this water is lost by evaporation during curing of the concrete. Over a 20- to 30-year period at ambient temperatures, half the fixed water may be lost [3]. This dehydration is much more rapid at elevated temperatures. General design criteria for ordinary concrete for protection not only against dehydration but also against thermal stresses are as follows [3]:

Maximum ambient temperature:	
Gamma-photon shields	149°C
Neutron shields	71°C
Serpentine	400°C
Maximum internal temperature:	
Gamma-photon shields	177°C
Neutron shields	88°C
Serpentine	425°C
Maximum ΔT from internal heating	6°C
Maximum temperature gradient	1°C/cm

Concrete has good compressive strength; however, it is very weak in tension and it is necessary to embed steel reinforcement rods within the concrete to provide strength under tension. Radiation damage, resulting in some gas evolution from the dissociation of water and reduction in compressive strength, is generally not a severe problem. Dehydration and thermal stresses resulting from the absorption of radiation are usually far more limiting.

Comprehensive discussions of the technology of concrete as a shielding material may be found in Refs. 3 and 9. Standards are also available for the design and analysis of concrete shields[8]. Thermal and mechanical properties of several concretes used in shielding are given in Table 11.6.

Soil and gravel. When space is not a limitation but cost is, earth or gravel shields provide an alternative to more costly shields. In high-radiation environments, the shielding properties of soils and gravels for photons are not highly sensitive to the composition and water content. However, for neutron shielding, the water content is a very important factor. The composition is also important from the viewpoint of activation and capture-gamma-photon production. Table 11.7 gives soil compositions based on (1) average composition of the earth's crust, (2) a composite of 19 analyses from a wide variety of soil classes, and (3) a U.S. average from 28 analyses.

Water in soil is present as bound water (water of hydration), hygroscopic water, capillary water, and gravitational water (e.g., rainwater prior to its flow to a dryer soil where it can be held as capillary or hygroscopic water). The capillary water is easily evaporated and ordinarily should be neglected in

TABLE 11.6 Typical Mechanical and Thermal Properties of Representative Concretes, After Curing

Property	Ordinary	Barytes	Limonite and Steel	Serpentine
Density ($g\ cm^{-3}$)	2.2–2.4	3.5	4.3–4.5	2.1–2.2
Specific heat ($J\ g^{-1}K^{-1}$)	0.65	0.52	0.70	—
Thermal conductivity[a] ($W\ m^{-1}\ K^{-1}$)	0.88	1.6	2.8–3.6	0.9
Coefficient of thermal expansion ($10^{-6}\ K^{-1}$)	14	—	7	32
Tensile strength (MPa)	2–3	2		
Compressive strength (MPa)	38	25–29	38	13–16

[a]Values for concrete only. Reinforcing steel will lead to a considerably greater effective thermal conductivity.

Source: *Refs. 3 and 9.*

TABLE 11.7 Composition, Dry-Weight Percent Basis, of Representative Soils

Element	Global Average[a]	Composite Average[b]	U.S. Average[c]
O	47.33	50.90	50.2 ± 2.2
Si	28.1	39.20	26.5 ± 9.2
Al	8.24	5.00	6.7 ± 2.9
Fe	5.09	2.20	5.5 ± 9.0
Mn			0.07 ± 0.06
Ti			0.45 ± 0.43
Ca	3.65	1.29	5.0 ± 6.6
Mg	2.11		1.3 ± 1.5
K	2.64	1.41	1.4 ± 0.7
Na	2.84		0.6 ± 0.5

[a]This is a mixture approximating the relative abundance of the eight most common elements in the earth's crust [3].

[b]This is a mixture based on the average composition of 19 soil samples taken from a variety of soil classes [10].

[c]These are means and standard deviations of compositions of 28 soils selected from throughout the United States [11]. The total does not add to 100%.

shield design. Representative ranges of soil water content (percent of dry weight) are as follows[11]: sand (0–10), sandy loam (5–20), loam (8–25), silty loam (10–30), dry loam (14–30), and clay (15–30).

Graphite. High-purity, reactor-grade graphite is a good shield material for slowing down fast neutrons and, when impregnated with boron, it makes a very effective medium for capturing neutrons. Because of its excellent high-

temperature properties, graphite is well suited for neutron shielding under conditions of high temperatures and high flux densities. At high temperatures, some outgassing occurs and graphite, normally inert, will be oxidized by air, steam, or carbon dioxide. Under neutron irradiation, the strain energy due to crystal-lattice damage (Wigner energy) is stored and, if the graphite is not carefully annealed, an autocatalytic release of this energy can occur if the temperature is allowed to reach a critical level.

Graphite, as commonly manufactured by an extrusion process, is anisotropic, and certain properties are directional, differing between with-grain (parallel to extrusion axis) and cross-grain (transverse to extrusion axis) orientations (Table 11.8). Upon irradiation at temperatures below 300°C, graphite

TABLE 11.8 Typical Room-Temperature Mechanical and Thermal Properties of Nuclear-Grade Graphite

Density (g cm^{-3})	1.70	
Specific heat (J g^{-1} K^{-1})	0.720	
Thermal conductivity (W m^{-1} K^{-1})	170	(with grain)
	130	(across grain)
Coefficient of thermal expansion (K^{-1})	2×10^{-6}	(with grain)
	4×10^{-6}	(across grain)
Modulus of elasticity (MPa)	1.0×10^{4}	(with grain)
	7.7×10^{3}	(across grain)
Compressive strength (MPa)	41	
Tensile strength (MPa)	9.7	

Source: *Refs. 3 and 9.*

contracts along the extrusion axis and expands transversely to the axis. Contraction in all directions occurs at irradiation temperatures in excess of 300°C.

Air. In many shielding situations, the attenuation properties of air can be neglected, that is, the air can be treated as if it were replaced by a vacuum. There are some situations, though, when this approximation is not valid: when air is the only shielding medium present, and when the distances involved are more than a few meters.

The composition of atmospheric air, by weight and volume, is given in Table 11.9. In most cases dry air can be treated as an ideal gas of molecular

TABLE 11.9 Principal Constituents of the Atmosphere

Constituent	Volume Fraction	Weight Fraction
N_2	0.7808	0.7552
O_2	0.2095	0.2315
CO_2	0.00033	0.0005
A	0.00934	0.0129

weight 28.97. Density of dry air at 0°C and 1 atmosphere pressure is 0.001293 g cm^{-3}. The variation of density, pressure, and temperature with elevation z up to 10,000 m above sea level is approximately exponential [12] and can be taken as:

$$\rho(z_2) = \rho(z_1) \exp [-0.00011(z_2 - z_1)], \tag{11.1}$$

$$p(z_2) = p(z_1) \exp [-0.00014(z_2 - z_1)], \tag{11.2}$$

$$T(z_2) = T(z_1) \exp [-0.000026(z_2 - z_1)]. \tag{11.3}$$

In some shielding and dosimetry calculations, it is necessary to evaluate the density of moist air. Humidity is often given as relative humidity, the ratio of the partial pressure of the water vapor in the air to the saturation vapor pressure at the same temperature. From this information, the partial pressures of air and water may be determined and the density determined using the ideal gas law.

Special-purpose shielding materials. A wide variety of special-purpose materials, many proprietary, are available for shielding purposes. Most are otherwise conventional materials into which are incorporated either boron for neutron shielding, or lead for photon shielding.

Boron carbide B_4C, is a widely used shielding material. It may be used alone, as a powder (density about 1.2 g cm^{-3}), or hot-pressed (sintered) with densities as high as 2.5 g cm^{-3}. Boron is also commonly incorporated in graphite in concentrations up to about 4% by weight. Boral is an alloy of boron carbide in aluminum (up to 50% by weight) and clad with aluminum. Properties of these materials are listed in Table 11.10. Borated plastics and wood-based particle board are also widely used in special neutron shielding applications.

TABLE 11.10 Properties of Boron Carbide, Boral, and Borated Graphite

	B_4C	Boral (50% B_4C)	Borated Graphite
Density (g cm^{-3})	2.51	2.5	1.48
Specific heat (J g^{-1} K^{-1})	1.2 (25–125°C)	0.73	—
Thermal conductivity (W m^{-1} K^{-1})	120 (100°C)	43 (95°C)	25 (100°C)

Source: *Ref. 3.*

Special glass windows are commercially available for use in shielding. These are usually silica glasses (density 2.5 to 2.7 g cm^{-3}) to which about 1 to 2% CeO_2 is added for color stability. Addition of lead may result in a final density as high as 6.2 g cm^{-3}.

11.2 RADIATION DAMAGE

Protection of structural materials or sensitive equipment against radiation damage is often a principal goal in shield design. In this section, the damage mechanisms are briefly discussed for indirectly ionizing radiation (neutrons and photons).

Primary damage mechanisms are of two types: atomic displacements resulting in lattice defects, and changes at the molecular level. The former is the key damage mechanism in metals, the latter in nonmetals. A combination of both mechanisms is important for electrical components such as semiconductors and insulators. Although radiation induces changes in most materials, radiation damage is not always the limiting factor in shielding usage. For example, irradiation criteria for concrete are determined by internal heating rather than by radiation damage.

11.2.1 Damage Mechanisms

Effects at the molecular level. Molecular effects originate with ionization and excitation along the tracks of secondary charged particles. Subsequent events lead to the production of charge carriers as well as mobile and reactive ionic, molecular, and free-radical species. Ultimately, there arise a variety of chemical changes.

Water is dissociated by ionizing radiation, with products including H_2, O_2, and H_2O_2. Yields for each are on the order of one molecule per 100 eV of energy absorbed. The chemistry is complex and is sensitive to the pH, the presence of solutes and dissolved gases in the water, and the nature of the primary radiation.

Organic materials, liquid and solid, may be very sensitive to radiation. Effects include polymerization, cross-linking, and chemical decomposition accompanied by gross changes in physical properties.

Two important irradiation effects in hydrocarbons are gas evolution and viscosity increase. Aromatic hydrocarbons, because of their electronic structure, are relatively resistant to radiation. Saturated aliphatic hydrocarbons evolve H_2 under irradiation with yields of about 5 molecules per 100 eV of energy absorbed. Lubricating oils experience a 10 to 20% increase in viscosity at an absorbed dose of 10^6 Gy and a 75 to 500% increase at 5×10^6 Gy [3].

The more radiation resistant plastics are those which are aromatic based (e.g., polystyrene) or those which cross-link (e.g., polyethylene). Less resistant are those which suffer polymer-chain breakage (e.g., Lucite, Teflon, and butyl rubber). The yields for H_2-evolution are 3.1 molecules per 100 eV for polyethylene and only 0.08 for polystyrene. Polyethylene retains 80% of its strength at about 10^7 Gy, polystyrene at about 10^8 Gy. On the other hand, Lucite retains only half its strength at 10^5 Gy [3].

Atomic displacements. Crystal lattice damage, through production of vacancies and interstitial atoms (point defects), results from neutron interactions, including (n, α) reactions and, only to a far lesser extent, from photon interactions. It is this type of damage that affects the mechanical properties of metals. Certain types of damage, such as swelling due to void formation and radiation-induced (or radiation-enhanced) creep in stainless steel are effected by point defects. Other types of damage, such as increase of yield strength and reduction of ductility, are effected principally by clusters or agglomerates of defects, called displacement spikes. In steel for pressure vessels, the concern is with loss in ductility, especially as related to brittle fracture (see below).

Production of vacancies and interstitial atoms represents a transfer from neutron kinetic energy to potential energy stored within the crystal lattice. Both vacancies and interstitials, especially the latter, are mobile at sufficiently high temperature and their recombination is facilitated by annealing. Recovery of the potential energy as heat is of little consequence except in graphite, where, because of low thermal conductivity, positive feedback may lead to an uncontrolled energy release (Wigner effect) with potentially catastrophic results.

Combined effects. Damage arises in insulators and semiconductors as a result of atomic displacements, whereby point defects serve as charge-carrier donors and traps. Transient effects in these materials are analogous to molecular effects. Irradiation creates secondary-electron charge carriers, and thus affects electrical properties.

Helium formation. Helium is produced in neutron-irradiated materials as a result of (n, α) reactions with ^{10}B or other nuclides, and in reaction chains such as $^{58}Ni + n \rightarrow {}^{59}Ni$, and $^{59}Ni + n \rightarrow {}^{56}Fe + {}^{4}He$. Helium-bubble formation is highly sensitive to temperature. For example, in stainless steels, no bubbles are formed below 650°C. Above 800°C, bubbles do form along grain boundaries and cannot be removed by annealing. Helium formation in the high-temperature and fast-neutron environment of a sodium-cooled nuclear reactor core is responsible for embrittlement of stainless steel cladding of fuel elements. Helium formation is also of concern in the design of the inner walls of fusion power reactors.

11.2.2 Dose–Effect Relationships

For assessment of either photon or neutron damage, the energy spectrum of the primary-particle fluence, $\Phi(E)$, must in principle be known. In most circumstances, rate effects are negligible and damage from photons and neutrons is additive. For photon irradiation, effects are insensitive to the energy spectrum of secondary electrons and the extent of damage is proportional to the absorbed dose. On the other hand, for neutron irradiation, secondary charged particles

may include electrons, protons, alpha particles, and recoil atoms—with a wide range of linear-energy-transfer (LET) values.[1]

Energy spectra of the fluences of each type of charged particle must be evaluated. By expressing the fluences, not as functions of charged-particle energy T, but as functions of LET (given the symbol L, with units MeV/cm), they may be combined into an overall LET spectrum $\Phi_s(L)$ defined in such a way that $\Phi_s(L)\,dL$ is the fluence of *all* secondary charged particles with LET between L and $L + dL$.

Effects at the molecular level. The extent of radiation damage may be evaluated by using a damage response function $\mathcal{R}$, a function of the LET of secondary charged particles, with units of the amount of damage per unit of energy deposited in the irradiated material. Very often the response function is expressed in the radiation-chemistry nomenclature of a "G value," defined as the number of molecules affected per unit energy (usually 100 eV) locally deposited along the charged-particle tracks. In this context, the extent of the damage R is the number of molecules affected per unit volume of material, and is given by

$$R = \int_0^\infty dL\, L\mathcal{R}(L)\Phi_s(L). \tag{11.4}$$

For photon irradiation, $\mathcal{R}$ is independent of L for secondary electrons, and R may be determined equivalently by definite integrals over the LET spectrum of *secondary* electrons or the energy spectrum of *primary* photons, that is,

$$R = \mathcal{R}\int_0^\infty dL\, L\Phi_s(L) = \mathcal{R}\int_0^\infty dE\, E\mu_{tr}(E)\Phi(E). \tag{11.5}$$

In terms of the absorbed dose D, R is thus equal to $\mathcal{R}D\rho$, where ρ is the density of the material, and R is the effect per unit *volume*.

Atomic displacements and helium production in metals. Neutron damage to metals is more pronounced for higher-energy neutrons. Early efforts at correlating dose and effect relied on expressing the extent of the damage as a function of the fluence of fast neutrons (e.g., neutrons with energies greater than some value such as 0.1 or 1.0 MeV). An important property of ferritic steels is the nil-ductility transition (NDT) temperature, below which failure may occur abruptly by brittle fracture. Figure 11.2 illustrates a correlation of the increase in NDT temperature as a function of fast-neutron fluence. It has long been observed, though, that such correlations do not adequately account for the energy spectrum of the neutrons. Measurements made in one neutron environment could not be used in another environment without

[1]The importance of LET in assessment of radiation effects is discussed in Section 2.4 in the context of biological effects.

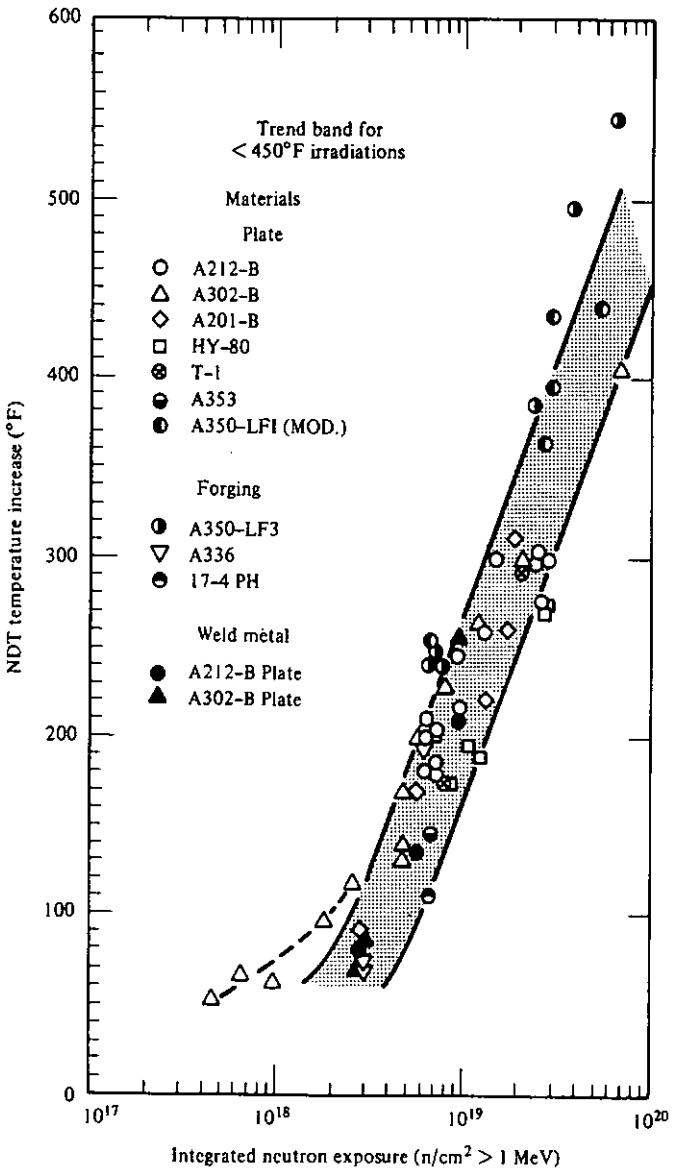

Figure 11.2 Increase in nil ductility transition (NDT) temperatures of steels irradiated at temperatures below 450°F (232°C). (After Ref. 13; copyright © 1973 by the Massachusetts Institute of Technology. Reprinted by permission of the MIT Press, Cambridge, MA.)

application of large safety factors and consequent design penalties. Much more satisfactory results have been obtained using a response-function formulation.

An analytical approach to the response-function formulation is based on the hypothesis that damage is a function of the average concentration of point defects and that the average point-defect concentration is proportional to the number of atomic displacements (vacancy-interstitial pairs) produced by neutron irradiation, per atom in the metal. Thus, the extent of damage, R, is a function of the displacements per atom, N_d, given by

$$N_d = \int_0^\infty dE\, \mathfrak{R}_d(E)\Phi(E). \tag{11.6}$$

The response function $\mathfrak{R}_d(E)$ is also called the displacement cross section, $\sigma_d(E)$, defined as

$$\sigma_d(E) \equiv \int_T dT\, \sigma(E, T)\nu(T), \tag{11.7}$$

where $\sigma(E, T)\, dT$ is the cross section for production of a recoil atom with energy between T and $T + dT$ as a result of a scattering interaction by a neutron of energy E (see Section 5.3). The quantity $\nu(T)$ is the total number of displacements produced as a result of a primary-knock-on atom (PKA) being produced with energy T. Various models have been developed for the evaluation of $\nu(T)$, and the interested reader is referred to Refs. 14 to 16. The mean number of displacements $\bar{\nu}(E)$ per PKA produced by neutrons of energy E is just the ratio of $\sigma_d(E)$ to $\sigma_s(E)$ (the scattering cross section). Figures 11.3 and 11.4 illustrate

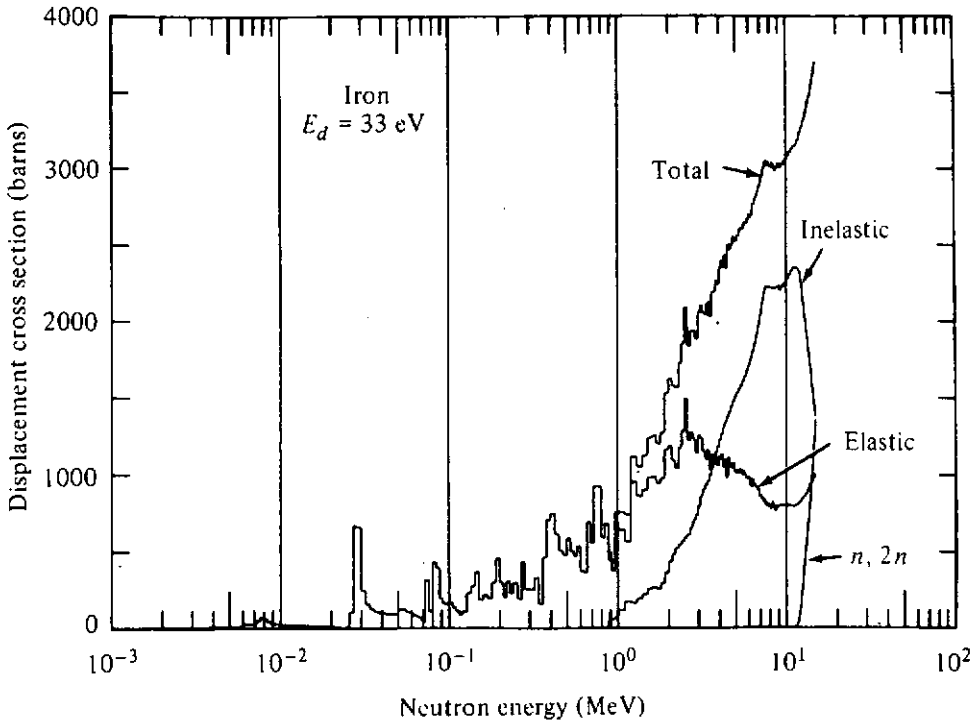

Figure 11.3 Displacement cross section for iron. (After Ref. 16; reproduced by permission of the American Nuclear Society.)

$\sigma_d(E)$ and $\bar{\nu}(E)$ for iron. That (n, γ) reactions are important for low-energy-neutron irradiation is illustrated in Fig. 11.5, which shows the displacement cross section for stainless steel (18% Cr, 10% Ni). Figure 11.6 illustrates correlation of NDT temperature increase with N_d.

Unfortunately, the displacement-cross-section approach to response functions for radiation damage in metals is inadequate in three important respects. First, many types of damage are not well correlated with N_d. Damage extent, rather than being a function of average point-defect concentration, depends on the concentration of defect clusters, or displacement spikes, produced locally in the vicinity of PKA events. Second, no account is taken of the thermal environment during and after irradiation. Certain effects are countered by annealing, while other effects only occur at high temperature. Third, no account

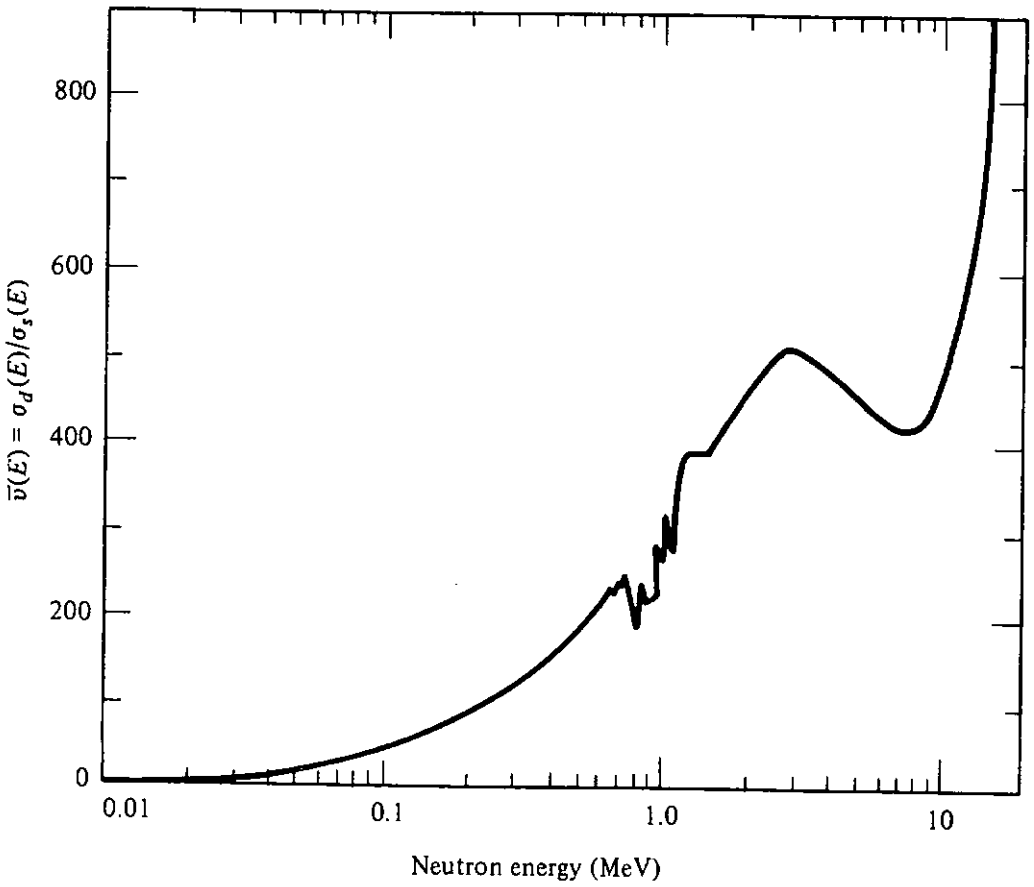

Figure 11.4 Mean number of displacements per PKA in iron, as a function of neutron energy. $\bar{\nu}$ is the ratio of the displacement cross section to the elastic scattering cross section. (After Ref. 16.)

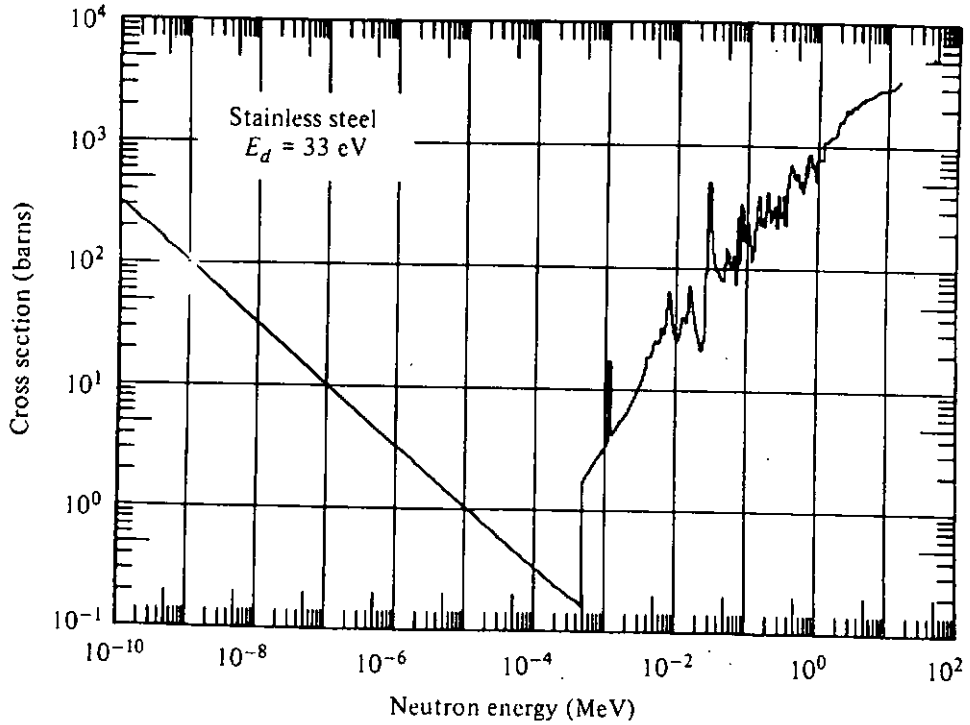

Figure 11.5 Displacement cross section for stainless steel (18% Cr, 10% Ni), including the effects of (n, γ) reactions. (After Ref. 16; reproduced by permission of the American Nuclear Society.)

is taken of helium production. The presence of helium, itself leading to certain effects, promotes other effects. For these reasons, strictly empirical response functions [18–23], also called "damage cross sections," have been derived for various types of damage under prescribed thermal conditions. With this approach, the extent of damage, R, is given by

$$R = \int_E dE\, \mathfrak{R}_{df}(E)\Phi(E). \tag{11.8}$$

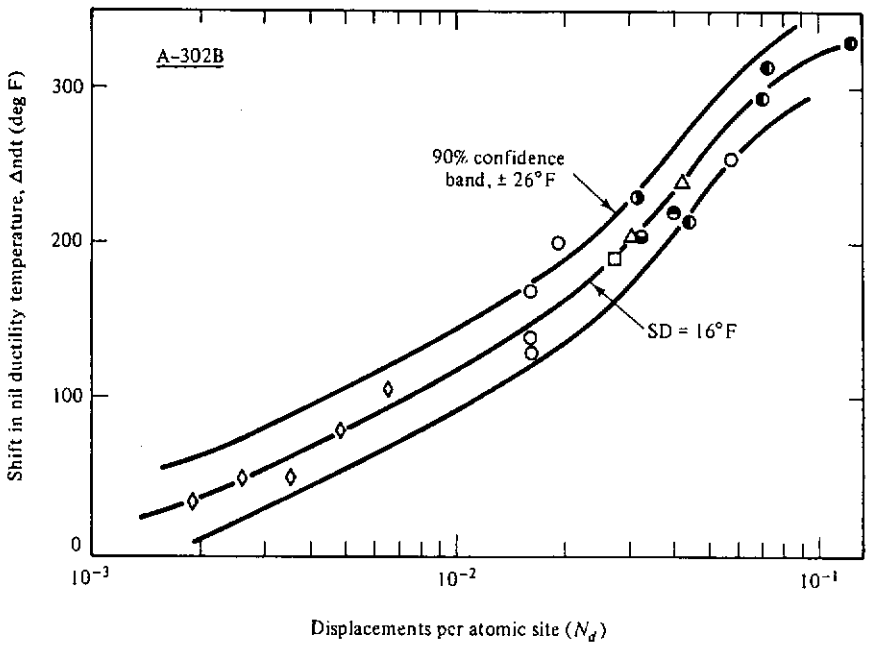

(a)

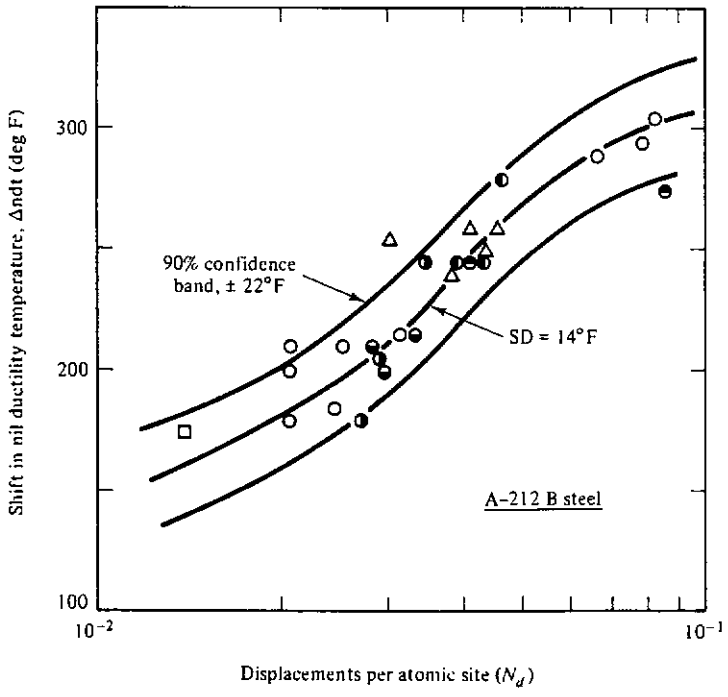

(b)

Figure 11.6 Shifts in nil ductility transition (NDT) temperatures as functions of calculated displacement densities: (a) A-302B steel; (b) A-212B steel. (After Ref. 17; reproduced by permission of the American Nuclear Society.)

Figure 11.7 illustrates the NDT-damage response function for one type of steel at low temperature.

The three approaches to dose-effect relationships may be illustrated and compared in the following example: What fluence of 1-MeV neutrons is required to produce an increase of 150°F (83°C) in the NDT temperature of A-302B steel? From Fig. 11.7, $\mathcal{R}_{df}$ is about 6×10^{-18} °F cm^2, and Φ is thus $150/6 \times 10^{-18}$ or about 3×10^{19} cm^{-2}. From Fig. 11.3, at $E = 1$ MeV, σ_d (for iron) is about 700 barns. From Fig. 11.6, N_d is 0.02. Since $N_d = \sigma_d \Phi$, then $\Phi = 0.02/700 \times 10^{-24}$ or about 3×10^{19} cm^{-2}. Figure 11.2 simply indicates that, for a typical neutron energy spectrum in a reactor, a fluence of about 7×10^{18} cm^{-2} ($E > 1$ MeV), leads to a 150°F increase in the NDT temperature.

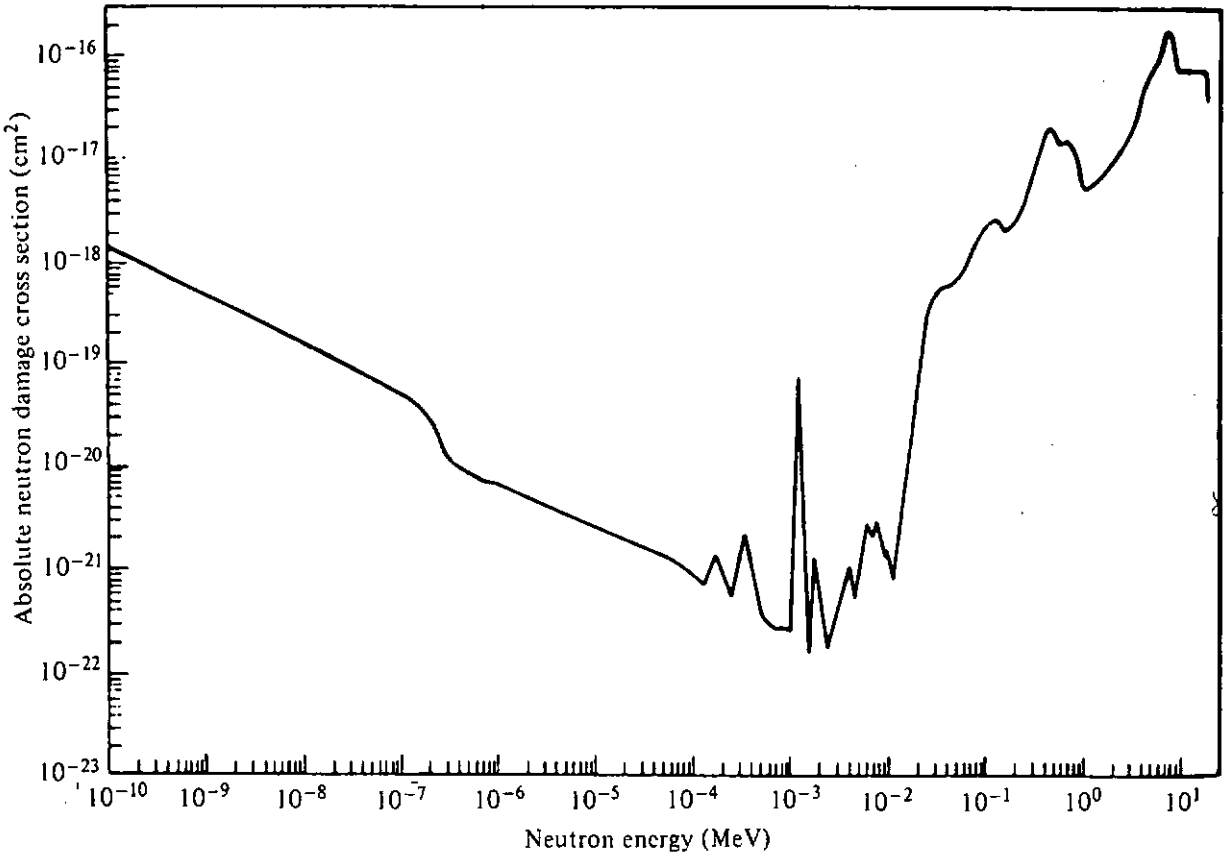

Figure 11.7 Absolute damage cross section for the irradiation of A-302B steel at temperatures less than 240°F (116°C), expressed as °F change in nil ductility transition (NDT) temperature per unit neutron fluence (cm^{-2}). (After Ref. 18; reproduced by permission of North-Holland Publishing Co.)

11.2.3 Radiation-Induced Property Changes in Structural Steel

Under fast-neutron irradiation, all steels experience radiation-induced hardening and embrittlement. While of very great consequence for materials in or near the core of a nuclear reactor, these effects are also important for reactor containment vessels. It is in the design and analysis of these vessels that the shielding specialist may interact with mechanical-design specialists. Radiation

damage is sensitive to the energy spectrum of the neutron fluence and to material cross sections for neutron interactions, and this information is in the domain of the shielding specialist.

Steels bombarded by fast neutrons also experience swelling and radiation-induced creep. These effects are also of great consequence for materials in or near the reactor core, but not of such great consequence for containment vessel performance. For a discussion of these effects, the reader may consult Ref. 24.

Failure by fracture of a stressed metal may result from two general mechanisms. Ductile fracture, or stress rupture, occurs following plastic deformation at local stresses in excess of the ultimate tensile strength. Brittle fracture, in contrast, occurs abruptly with relatively slight plastic deformation. It is characterized by cleavage along characteristic planes within the metal grains, along grain boundaries, or in secondary phases.

Low-carbon structural steels, which have the ferritic body-centered-cubic crystal structure, exhibit a ductile–brittle transition temperature below which brittle fracture occurs. The NDT temperature is highly sensitive to metallurgical treatment. It is typically near 0°C, but may range from -70 to $+20$°C. As indicated earlier, neutron irradiation increases the NDT temperature, and this is a concern for reactor vessels exposed for many years to neutron irradiation. The neutron fluence to which the vessel is to be exposed during its lifetime must be taken into account in the metallurgical, fabrication, operational, and surveillance specifications for the vessel.

The embrittlement of low-carbon structural steel is quite distinct from that occurring in the stainless steels of the austenitic face-centered-cubic crystal structure. In the former, thorough annealing will restore ductility. In the latter, embrittlement due to helium-bubble formation, as well as carbide precipitation at grain boundaries, is promoted by neutron irradiation at high temperatures and is not relieved by annealing.

11.3 THERMAL EFFECTS

Neutron and photon heating of radiation shields or construction materials is of concern not only because of the introduction of thermal stresses but also because of other deleterious effects on materials. An example of the latter concern is the dehydration of concrete at temperatures above about 90°C.

In the discussion below, it is assumed that the energy spectrum $\phi(\mathbf{r}, E)$ of the flux density of neutrons or photons is known throughout the attenuating medium. This includes photons from neutron capture, inelastic scattering, and fission.

11.3.1 Heat Generation Rates in Shields

For direct heating by photons, the volumetric heat generation rate $q(\mathbf{r})$ is the absorbed dose rate multiplied by the density, which gives an energy deposition rate per unit volume (see Chapters 2 and 5 for a definition and discussion of

the concept of "absorbed dose"). To the extent that the kerma rate is a good approximation for the absorbed dose rate,

$$q(\mathbf{r}) = \int_0^\infty dE\, E\mu_{tr}(E)\phi(\mathbf{r}, E), \tag{11.9}$$

where, of course, μ_{tr} must correspond to local materials and densities. The choice of the proper deposition coefficient, μ_{tr} or otherwise, is governed by the method of evaluating $\phi(\mathbf{r}, E)$. For a discussion of this, the reader is referred to Sections 5.2 and 5.6. If only the uncollided flux density is known, a buildup factor may be used in the evaluation of $q(\mathbf{r})$.

For direct heating by neutrons, the volumetric heat generation rate may be computed as

$$q(\mathbf{r}) = \int_0^\infty dE\, \epsilon\mu(E)\phi(\mathbf{r}, E). \tag{11.10}$$

Here the coefficient μ is the interaction coefficient, dependent on local materials and density. The energy ϵ is the mean kinetic energy per interaction transferred from the neutron to secondary charged particles (including recoil atoms). In many cases, elastic scattering is the principal neutron interaction mechanism, and ϵ may be evaluated according to Eq. (5.12). Inelastic scattering may be taken into account using Eq. (5.13). In some cases, charged particle reactions such as the $^{10}B(n, \alpha)$ and $^{16}O(n, \alpha)$ reactions must be taken into account and ϵ includes the energy of the recoil charged particle as well as that of the residual nucleus.

A common shielding situation is one in which neutrons or photons are incident on the surface of an infinite slab shield. For this case, the particles responsible for internal heat generation are typically attenuated exponentially with distance into the shield, so that the heat generation rate can be expressed approximately as

$$q(x) = q_0 e^{-\mu' x}, \tag{11.11}$$

where x is the depth of penetration into the shield and μ' is an effective attenuation coefficient.[2] In stituations where this approximation is inadequate, piecewise exponential functions, or a sum of exponential functions, may be used to represent the heat generation rate.

11.3.2 Temperature Distributions in Shields

Here it is assumed that conduction is the sole mechanism for heat transport within the shield. Convective and radiative heat transport may cool the boundaries of the shield. Steady-state conductive heat transport is described by Fourier's law,

$$\nabla \cdot k(\mathbf{r}, T)\nabla T(\mathbf{r}) = -q(\mathbf{r}), \tag{11.12}$$

[2]To avoid confusion in this chapter with the symbol k for thermal conductivity, μ' rather than k is used to denote a general attenuation coefficient.

in which T is the temperature and k the thermal conductivity. Boundary conditions needed to specify a unique solution of Eq. (11.12) can usually be modeled by the following idealized conditions:

1. *Convective:* $\hat{\mathbf{n}} \cdot (-k\nabla T) = h(T - T_0)$, where T_0 is an external temperature, h is a convective heat transfer coefficient, and $\hat{\mathbf{n}}$ is a unit outward vector normal to the boundary. For example, suppose that the boundary is the inner surface of the pressure vessel in a nuclear power plant. Then T_0 would be the coolant temperature and h the appropriate heat transfer coefficient for turbulent convective heat transfer.
2. *Isothermal:* $T = T_0$, where T_0 is the boundary temperature. For example, suppose that, in the convective case 1, h is very large. Then, setting $T = T_0$ is an excellent approximation.
3. *Adiabatic*: $\hat{\mathbf{n}} \cdot (-k\nabla T) = 0$, that is, no transfer of heat at the boundary. For example, consider the boundary between the outer (cooler) surface of a shield and the atmosphere. The convective heat transfer coefficient h in case 1 would likely be very low and an adiabatic boundary condition would be an appropriate approximation.
4. *Radiative*: In special cases, radiative heat transfer may be an important heat loss mechanism at a boundary. Then, $\hat{\mathbf{n}} \cdot (-k\nabla T)$ at the boundary would be proportional to the fourth power of the difference between the temperature of the boundary and the temperature of a body to or from which heat is being transmitted radiatively.

As an illustration of the temperature distribution in internally heated solids, consider the one-dimensional problem of a slab of thickness L (Fig. 11.8) in which the volumetric heat generation rate is given by Eq. (11.11). The heat generation rate may be expressed in terms of the product of an effective energy transfer coefficient μ_a and the energy flux density I_0 incident on the slab. It is assumed that the thermal conductivity of the shield is uniform and independent of temperature. Temperature distributions in the slab shield are evaluated for three sets of boundary conditions.

Case A: Isothermal inner boundary, adiabatic outer boundary. In this case, $T(0) = T_0$, a constant, and $dT(x)/dx = 0$ at $x = L$. From Eq. (11.12),

$$\frac{d^2T(x)}{dx^2} = -\frac{q(x)}{k}. \tag{11.13}$$

Integration of this equation from x to L, and application of the boundary condition at $x = L$ yields

$$\frac{dT(x)}{dx} = \frac{1}{k}\int_x^L dx''\, q(x''). \tag{11.14}$$

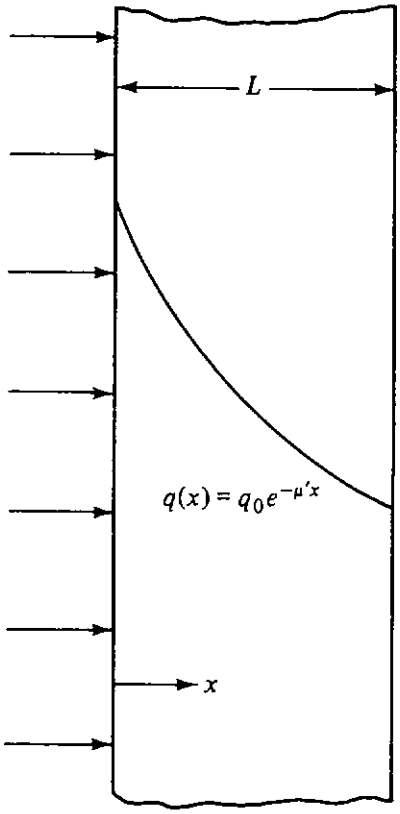

Figure 11.8 One-dimensional rectangular geometry for the case of a slab experiencing an exponentially varying rate of internal heat generation.

A second integration, from 0 to x, and application of the boundary condition at $x = 0$ yields

$$T(x) = T_0 + \frac{1}{k}\int_0^x dx' \int_{x'}^L dx'' \, q(x''), \tag{11.15}$$

which, after substitution of $q(x)$ from Eq. (11.11), gives the final result,

$$T(x) = T_0 + \frac{q_0}{k\mu'^2}(1 - e^{-\mu' x} - \mu' x e^{-\mu' L}). \tag{11.16}$$

The temperature increase $\Delta T(x) \equiv T(x) - T_0$ may be expressed in dimensionless form as

$$\frac{\Delta T}{\theta} = 1 - e^{-\mu' x} - \mu' x e^{-\mu' L}, \tag{11.17}$$

in which

$$\theta \equiv \frac{q_0}{k\mu'^2}. \tag{11.18}$$

The maximum temperature increase occurs at $x = L$ and has the value

$$\frac{\Delta T_{\max}}{\theta} = 1 - (1 + \mu' L)e^{-\mu' L}. \tag{11.19}$$

Case B: Isothermal outer boundary, adiabatic inner boundary. In this case, $T(L) = T_L$, a constant, and $dT(x)/dx = 0$ at $x = 0$. The temperature difference $\Delta T(x) = T(x) - T_L$ is given by

$$\frac{\Delta T(x)}{\theta} = \mu' L - \mu' x - e^{-\mu' x} + e^{-\mu' L}, \tag{11.20}$$

which, at $x = 0$, has the maximum value

$$\frac{\Delta T_{\max}}{\theta} = \mu' L - 1 + e^{-\mu' L}. \tag{11.21}$$

Case C: Isothermal inner and outer boundaries. In this case, $T(0) = T_0$ and $T(L) = T_L$. In the absence of internal heat generation, the temperature distribution is

$$T_c(x) = T_0\left(1 - \frac{x}{L}\right) + T_L\left(\frac{x}{L}\right). \tag{11.22}$$

The temperature increase $\Delta T(x) \equiv T(x) - T_c(x)$, with internal heat generation, is given by

$$\frac{\Delta T(x)}{\theta} = 1 - e^{-\mu' x} - \frac{x}{L}(1 - e^{-\mu' L}). \tag{11.23}$$

The maximum value

$$\frac{\Delta T_{\max}}{\theta} = 1 - \frac{1 - e^{-\mu' L}}{\mu' L}\left(1 + \ln \frac{\mu' L}{1 - e^{-\mu' L}}\right) \tag{11.24}$$

occurs at

$$x = \frac{1}{\mu'} \ln \frac{\mu' L}{1 - e^{-\mu' L}}. \tag{11.25}$$

In Fig. 11.9, the incremental temperature profiles normalized to the maximum temperature change are shown for the three cases above. From Fig. 11.10 it is

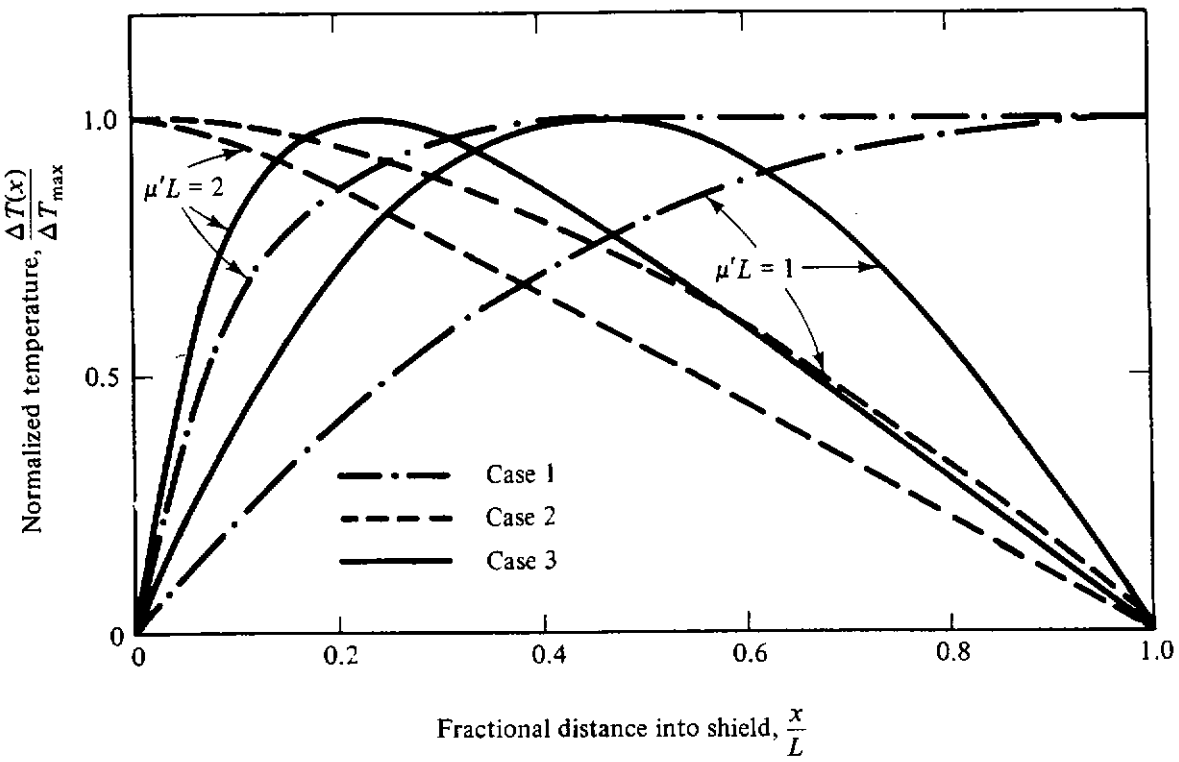

Figure 11.9 Normalized incremental temperature profiles in a slab shield of thickness L with internal heat generation decreasing as $e^{-\mu' x}$ with distance x into the shield. Case 1: isothermal boundary at $x = 0$, adiabatic boundary at $x = L$. Case 2: adiabatic boundary at $x = 0$, isothermal boundary at $x = L$. Case 3: both boundaries isothermal.

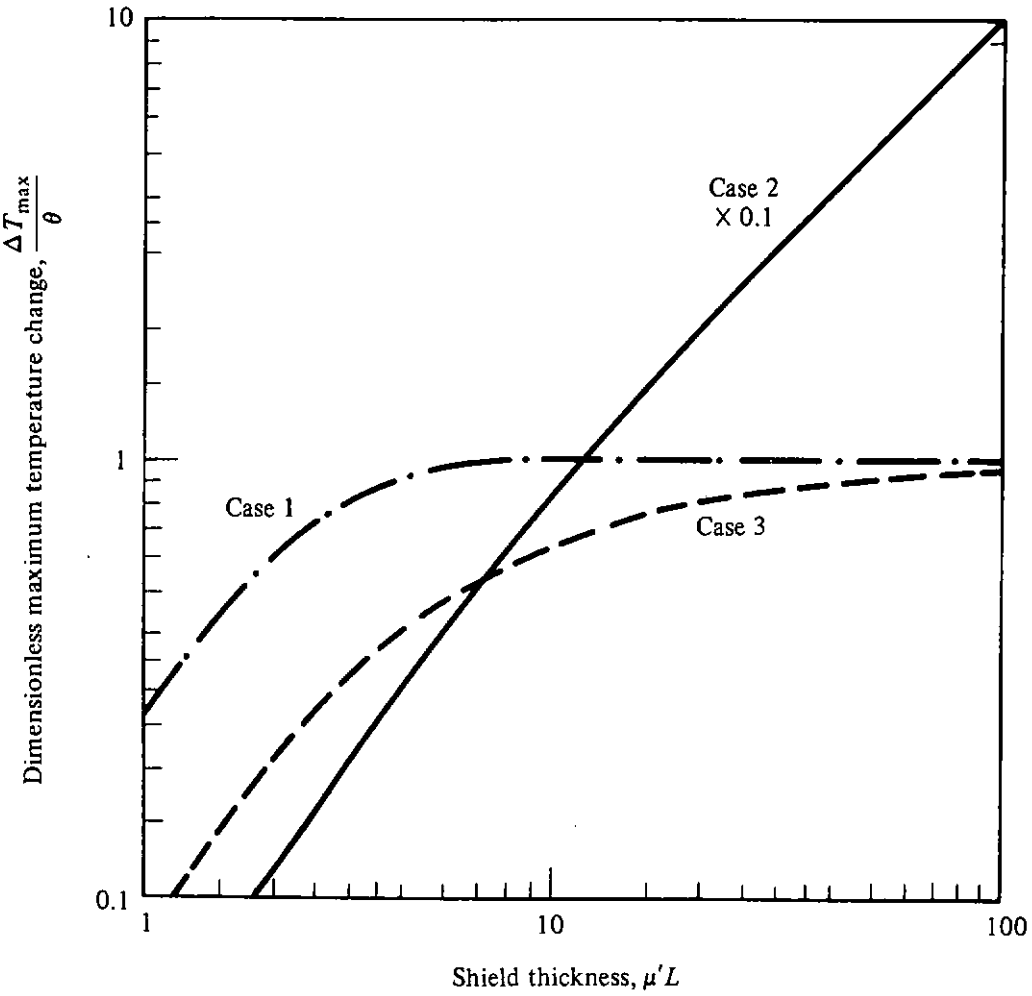

Figure 11.10 Normalized maximum temperature increase in a slab shield with internal heat generation decreasing as $e^{-\mu' x}$ with distance x into the shield, shown as a function of the product of the shield thickness L and the exponential coefficient μ'. Cases 1, 2, and 3 are as in Fig. 11.9.

seen that the maximum incremental temperature change, $\Delta T_{max}/\theta$, is limited as the slab thickness increase for cases A and C; however, for case B, the maximum change increases as L increases.

Consider now the case of the cylindrical shell illustrated in Fig. 11.11. For large radii of curvature—for example, in a reactor pressure vessel or

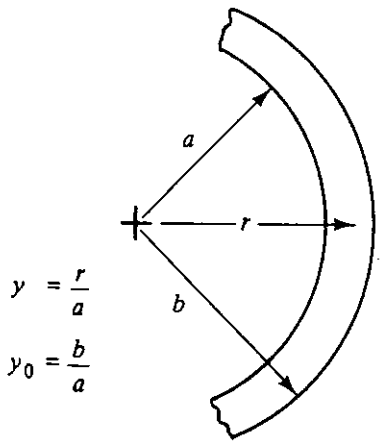

Figure 11.11 Axially symmetric cylindrical geometry for the case of a cylindrical shell experiencing internal heat generation.

biological shield—temperature profiles may be computed approximately using the results above for one-dimensional rectangular geometry. The equations above may be applied directly, with the substitution of $r - a$ for x and $b - a$ for L. In terms of the dimensionless distance parameters $y = r/a$ and $y_0 = b/a$, temperature profiles may be expressed in the dimensionless form $\Delta T/\theta = f(y)$:

Case A: Isothermal inner boundary, adiabatic outer boundary

$$\frac{\Delta T}{\theta} = 1 - e^{-\mu' a(y-1)} - \mu' a(y-1)e^{-\mu' a(y_0-1)}. \tag{11.26}$$

Case B: Isothermal outer boundary, adiabatic inner boundary

$$\frac{\Delta T}{\theta} = \mu' a(y_0 - y) - e^{-\mu' a(y-1)} + e^{-\mu' a(y_0-1)}. \tag{11.27}$$

Case C: Isothermal inner and outer boundaries

$$\frac{\Delta T}{\theta} = 1 - e^{-\mu' a(y-1)} - \frac{(y-1)}{(y_0-1)}[1 - e^{-\mu' a(y_0-1)}]. \tag{11.28}$$

In the third case, the temperature profile in the absence of internal heating is

$$\frac{\Delta T}{\theta} = \frac{T(y) - T_b}{T_a - T_b} = \frac{\ln(y_0/y)}{\ln(y_0)}. \tag{11.29}$$

11.4 THERMAL-MECHANICAL INTERACTIONS

11.4.1 Stress–Strain Relationships

Consider a material under uniaxial stress σ (Fig. 11.12). A positive (negative) value of σ implies tension (compression). The strain, or fractional elongation, under elastic deformation is (see Section 11.1.2)

$$\epsilon_1 = \frac{\sigma_1}{E}, \tag{11.30}$$

in which E is Young's modulus of elasticity. Elastic deformation may be expected

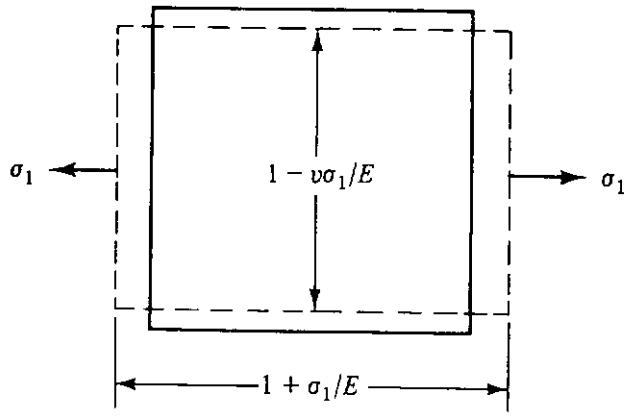

Figure 11.12 Material, initially of unit dimension, under uniaxial stress σ_1.

at stresses up to the yield strength. Accompanying the elongation along the axis of stress is a contraction transverse to the axis. Under compression (negative values of σ and ϵ) a contraction along the stress axis is accompanied by an elongation transverse to the axis. The transverse strain is

$$\epsilon_2 = \frac{-\nu\sigma_1}{E}, \tag{11.31}$$

in which ν is the Poisson ratio. For elastic media that deform at constant volume (e.g., rubber), ν has a maximum value of 0.5, while for metals and concrete, ν is about 0.3 and 0.17, respectively.

Now consider the strain in an isotropic medium due to two orthogonal stresses (Fig. 11.13). In this case

$$\epsilon_1 = \frac{\sigma_1 - \nu\sigma_2}{E}, \tag{11.32}$$

$$\epsilon_2 = \frac{\sigma_2 - \nu\sigma_1}{E}. \tag{11.33}$$

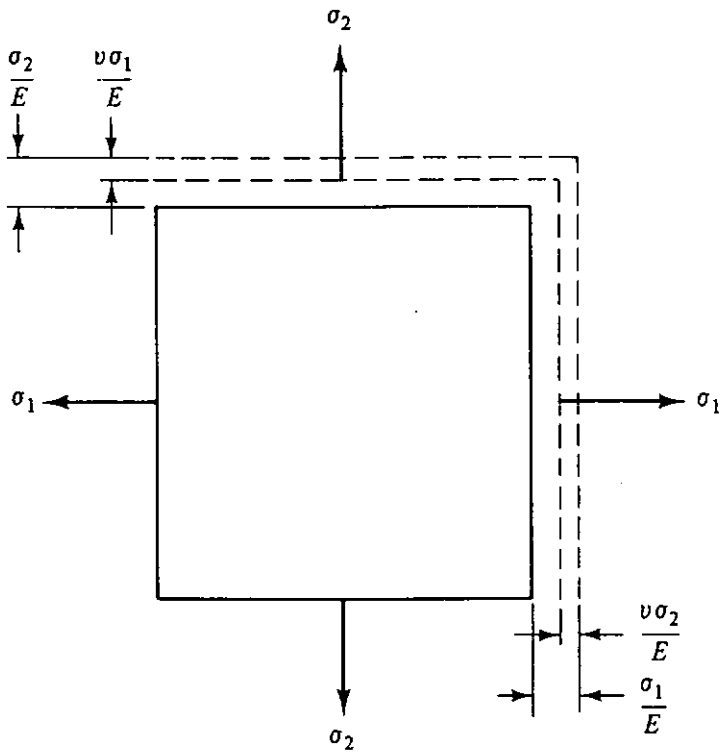

Figure 11.13 Material subjected to two orthogonal stresses σ_1 and σ_2.

These equations may be solved for the stresses, giving

$$\sigma_1 = \frac{(\epsilon_1 + \nu\epsilon_2)E}{1 - \nu^2}, \tag{11.34}$$

$$\sigma_2 = \frac{(\epsilon_2 + \nu\epsilon_1)E}{1 - \nu^2}. \tag{11.35}$$

Similarly, for three orthogonal stresses in an isotropic medium, the stress–strain relations become

$$\epsilon_i = \frac{\sigma_i - \nu(\sigma_j + \sigma_k)}{E}, \tag{11.36}$$

where $i, j, k = 1, 2, 3$ and $k \neq i \neq j \neq k$. The three equations represented by Eq. (11.36) may be solved for the stresses, yielding

$$\sigma_i = \frac{[\epsilon_i(1 - \nu) + \nu(\epsilon_j + \epsilon_k)]E}{(1 + \nu)(1 - 2\nu)}. \tag{11.37}$$

In general, there are also shear stresses that act tangentially on the surface of a test volume and lead to twisting and bending in addition to compression and expansion. There are relations between the shear stresses and strains analogous to those presented above for the normal stresses and strains, but in the simple applications presented below, it is possible to choose the coordinate axes as the principal stress axes and thus to ensure that the shear stresses are zero. For a more detailed treatment, the reader is referred to Refs. 25 to 27.

Although a complete analysis can describe the state of stress throughout a medium, it is still necessary to determine whether or not the stresses are sufficiently high to cause material failure. Most yield tests are uniaxial, in which case $\sigma_1 = \sigma_Y$, the yield strength, and $\sigma_2 = \sigma_3 = 0$. For multiaxial stresses, there are two widely applied criteria. The first, the von Mises yield criterion, predicts yielding when the differences between the principal stresses are related to the uniaxial yield strength as follows:

$$\sigma_Y = \left[\frac{(\sigma_1 - \sigma_2)^2 + (\sigma_2 - \sigma_3)^2 + (\sigma_1 - \sigma_3)^2}{2}\right]^{1/2}. \tag{11.38}$$

An alternative criterion, used with the ASME Boiler and Pressure Vessel Code, predicts yielding when the maximum shear stress $\tau_{max} \equiv (\sigma_{max} - \sigma_{min})$ exceeds $\sigma_Y/2$, where τ_{max} and τ_{min} are the maximum and minimum algebraic values of the principal stresses. This maximum shear stress criterion is usually somewhat more conservative than the von Mises criterion.

11.4.2 Principles of Thermal Stress Analysis

Consider a two-dimensional test body of unit size (see Fig. 11.14) that experiences a uniform increase ΔT in its temperature. The resulting fractional increase in dimension is $\alpha\ \Delta T$, where the *linear coefficient of thermal expansion*

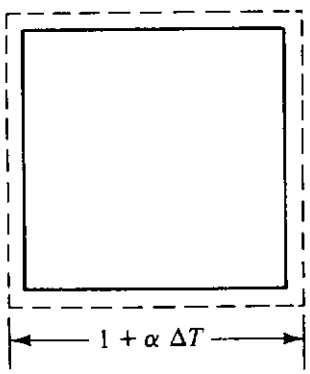

Figure 11.14 Two-dimensional, unconstrained test object, initially of unit dimensions, subjected to a uniform increase ΔT in temperature.

is $\alpha \equiv (1/L)\, dL/dT$ and L is any reference dimension of the body. For an isotropic material, α is solely a material property and is thus independent of the thermal expansion axes. Typical values for shielding materials are given in Tables 11.1 to 11.4 and 11.6. When thermal expansion arises from a change ΔT in an unconstrained body, no thermal stresses are generated in the body.

Now suppose that the same temperature increase ΔT occurs when the test body is constrained against expansion or contraction in the y direction (see Fig. 11.15). The constraints impose a strain equivalent in magnitude to the unconstrained thermal expansion, that is,

$$\epsilon_2 = -\alpha\, \Delta T \tag{11.39}$$

as a result of the stress

$$\sigma_1 = -\alpha E\, \Delta T. \tag{11.40}$$

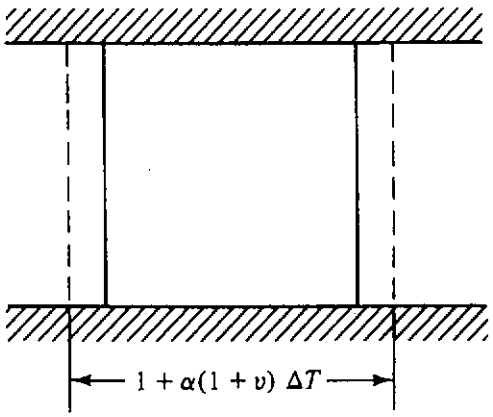

Figure 11.15 Two-dimensional test object, initially of unit dimensions, constrained in one dimension, and subjected to a uniform increase ΔT in temperature.

As a result of this stress in the y direction, the x dimension is further altered (in addition to its thermal expansion) so that the displacement in the x direction of one face with respect to the other is

$$\epsilon_1 = (1 + \nu)\alpha\, \Delta T. \tag{11.41}$$

However, since the body is free to expand or contract in the x direction, $\sigma_1 = 0$.

Constraint of the test body in both dimensions (Fig. 11.16) results in equal strains $\epsilon_1 = \epsilon_2 = -\alpha\, \Delta T$ arising from the temperature change. The resulting stresses, from Eqs. (11.34) and (11.35), are thus

$$\sigma_1 = \sigma_2 = \frac{-\alpha E\, \Delta T}{1 - \nu}. \tag{11.42}$$

In a three-dimensional body, constrained from movement in all directions, the thermal stresses are found from Eq. (11.36) to be

$$\sigma_1 = \sigma_2 = \sigma_3 = \frac{-\alpha E\, \Delta T}{1 - 2\nu}. \tag{11.43}$$

When a body undergoes a temperature change, strains arise both from stresses and from thermal expansion. Accordingly, the general isothermal stress–strain relation of Eq. (11.36) must be modified to account also for normal strains arising from thermal expansion. This generalization is simply

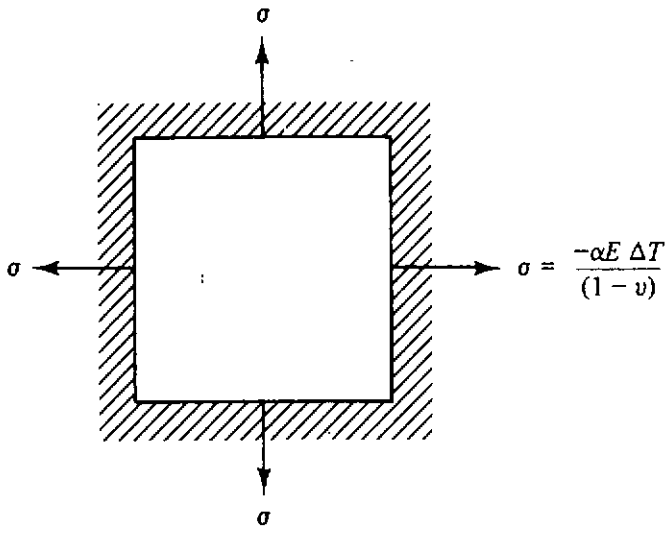

Figure 11.16 Two-dimensional test object, constrained in both directions, and subjected to a uniform increase ΔT in temperature.

$$\epsilon_i = \frac{1}{E}[\sigma_i - \nu(\sigma_j + \sigma_k)] + \alpha\,\Delta T \tag{11.44}$$

where $i, j, k = 1, 2, 3$, $k \neq i \neq j \neq k$, and where $\Delta T = T - T_0$ is the temperature change from some reference temperature T_0 at which the normal strains are said to be zero. By solving this equation for the normal stresses, one obtains

$$\sigma_i = \frac{E}{(1+\nu)(1-2\nu)}[\epsilon_i(1-\nu) + \nu(\epsilon_j + \epsilon_k) - (1+\nu)\alpha\,\Delta T]. \tag{11.45}$$

Finally, it should be noted that not all temperature changes result in thermal stresses. For a totally unconstrained body, no normal stresses are induced if all second-order derivatives of the temperature (e.g., $\partial^2 T/\partial x^2$, $\partial^2 T/\partial x\,\partial y$) vanish everywhere in the body. In particular, $\nabla^2 T$ must vanish, which implies from Eq. (11.12) that no source be present ($q_0 = 0$) and that the system be in steady state. Equivalently, no thermal stresses exist if $T(x, y, z)$ is at most linear in x, y, and z; for example, $T = ax + by + cz + dxy + e$, where a through e are independent of position.

11.4.3 Thermal Stresses in a Slab Shield

Radiation absorbed in a shield acts as an internal heat source, which in turn can induce significant thermal stresses in the shield. To illustrate this problem, consider a slab shield of thickness L in which has been established a one-dimensional temperature difference $\Delta T(x) \equiv T(x) - T_0(x)$ with respect to the profile $T_0(x)$ at which no thermal stresses are assumed to exist (see Fig. 11.8). The calculation of the thermal stresses is quite complex, especially near the y and z boundary planes, at which σ_y ($\equiv \sigma_2$) and σ_z ($\equiv \sigma_3$) are assumed to vanish (i.e., the slab is assumed to expand freely in all directions). However, if only the stresses away from the y and z boundaries are desired, a simple approximate method may be used to solve the stress–strain relations.

First, imagine that the y and z faces of the shield are restrained so that $\epsilon_y = \epsilon_z = 0$. Then, since the x dimension is free to expand, σ_x ($\equiv \sigma_1$) $= 0$ for all x. Under these conditions, the stress–strain relations, Eq. (11.44), become

$$\epsilon_x = \frac{-\nu(\sigma_y + \sigma_z)}{E} + \alpha\,\Delta T(x), \tag{11.46}$$

$$\epsilon_y = 0 = \frac{\sigma_y - \nu\sigma_z}{E} + \alpha\,\Delta T(x), \tag{11.47}$$

$$\epsilon_z = 0 = \frac{\sigma_z - \nu\sigma_y}{E} + \alpha\,\Delta T(x). \tag{11.48}$$

By symmetry, $\sigma_y = \sigma_z$, and thus, from Eq. (11.48),

$$\sigma_y = \sigma_z = -\frac{\alpha\,\Delta T(x)}{1-\nu}. \tag{11.49}$$

The average stress in the y or z direction is thus

$$\bar{\sigma}_i \equiv \frac{1}{L}\int_0^L dx\,\sigma_i(x) = -\frac{\alpha E}{1-\nu}\,\overline{\Delta T}, \qquad i = 2, 3, \tag{11.50}$$

where $\overline{\Delta T}$ is the average temperature change $(1/L)\int_0^L T(x)\,dx$ caused by the incident radiation.

To relate the results above to the actual situation in which the slab is free to expand in the y and z directions, imagine that the restraints are released in such a manner so as to maintain the slab shape while reducing to zero the *average* surface stress on the y and z surfaces. The final distribution of stress along the surface (and in the slab) is that given by Eq. (11.49) less the average stress given by Eq. (11.50):

$$\sigma_i(x) = \frac{E}{1-\nu}[\overline{\Delta T} - \Delta T(x)], \qquad i = 2, 3. \tag{11.51}$$

By St. Venant's principle,[3] this stress profile also equals the stress profile that occurs sufficiently far from the y or z boundaries when these boundaries are totally free.

In addition to the thermal stresses arising in a shield, the shield may have sufficient bulk or bear a substantial load so that a gravitational or mechanical stress must be added to the stress in the vertical direction. If the shield bears a compressive load P, then away from the y or z boundaries, the stress in the vertical direction is $\sigma_y(x) - P/\mathrm{A}$, where A is the horizontal cross-sectional area of the slab.

As an example of this analysis, consider a slab shield with isothermal boundaries at T_0. For a radiation heat source given by Eq. (11.11), the temperature profile across the slab is obtained from Eqs. (11.22) and (11.23), with

[3]St. Venant's principle states that at distances substantially greater than the thickness, the pattern of stresses and displacements depends only on the total force applied at the boundary and not on the way the force is distributed across the boundary.

$T_L = T_0$, as

$$\frac{\Delta T(x)}{\theta} = 1 - e^{-\mu' x} - \frac{x}{L}(1 - e^{-\mu' L}). \tag{11.52}$$

The average temperature increase is found to be

$$\frac{\overline{\Delta T}}{\theta} = 1 - (1 - e^{-\mu' L})\left(\frac{1}{2} - \frac{1}{\mu' L}\right). \tag{11.53}$$

Thus, the stresses in the shield become $\sigma_x = 0$, $\sigma_y = \sigma_z + P/A$ and, from Eq. (11.51),

$$\sigma_z = \frac{\alpha E \theta}{1 - \nu}\left[e^{-\mu' x} + (1 - e^{-\mu' L})\left(\frac{1}{2} + \frac{x}{L} + \frac{1}{\mu' L}\right]\right. . \tag{11.54}$$

In Fig. 11.17, this stress, in dimensionless units $\sigma_z(1 - \nu)/(\alpha E\theta)$, is shown for various slab thicknesses. Notice that near the shield surface the stresses are tensile while the interior of the slab is under compression. Concrete is very weak in tension and thus to prevent failure, the use of reinforcing steel is called for.

11.4.4 Thermal Stresses in a Hollow Cylinder

Radiation can cause thermal stresses not only in shields but also in exposed nonshield components such as piping and reactor pressure vessels. Because the properties of steel change under irradiation (Section 11.2.3), it is important to analyze steel components which normally operate under high stresses in radiation environments or which may experience thermal shocks as a result of abrupt changes in ambient temperature. The complete analysis of piping and pressure vessels is beyond the scope of this text. However, the shield analyst may interact with those performing mechanical analyses, and thus, this section is ended with a brief presentation of the basic concepts used in analysis of stresses in hollow cylinders.

Consider the hollow cylinder depicted in Fig. 11.18. Azimuthal symmetry and axial invariance is assumed (i.e., ΔT is a function only of the radius r). Stresses and strains are identified by the subscripts r, t, and z, for radial, tangential, and axial components. These are functions only of r. Interior and exterior pressures are, respectively, p_i and p_0.

A force balance in the radial direction on the element of volume shown in Fig. 11.18 reveals that

$$\sigma_t - \sigma_r - r\frac{d\sigma_r}{dr} = 0. \tag{11.55}$$

From the figure, it is evident that, if $u(r)$ is the radial displacement, then

$$\epsilon_r = \frac{du}{dr}, \tag{11.56}$$

$$\epsilon_t = \frac{u}{r}. \tag{11.57}$$

Equations (11.55) to (11.57), applied to Eq. (11.45), yield the following linear

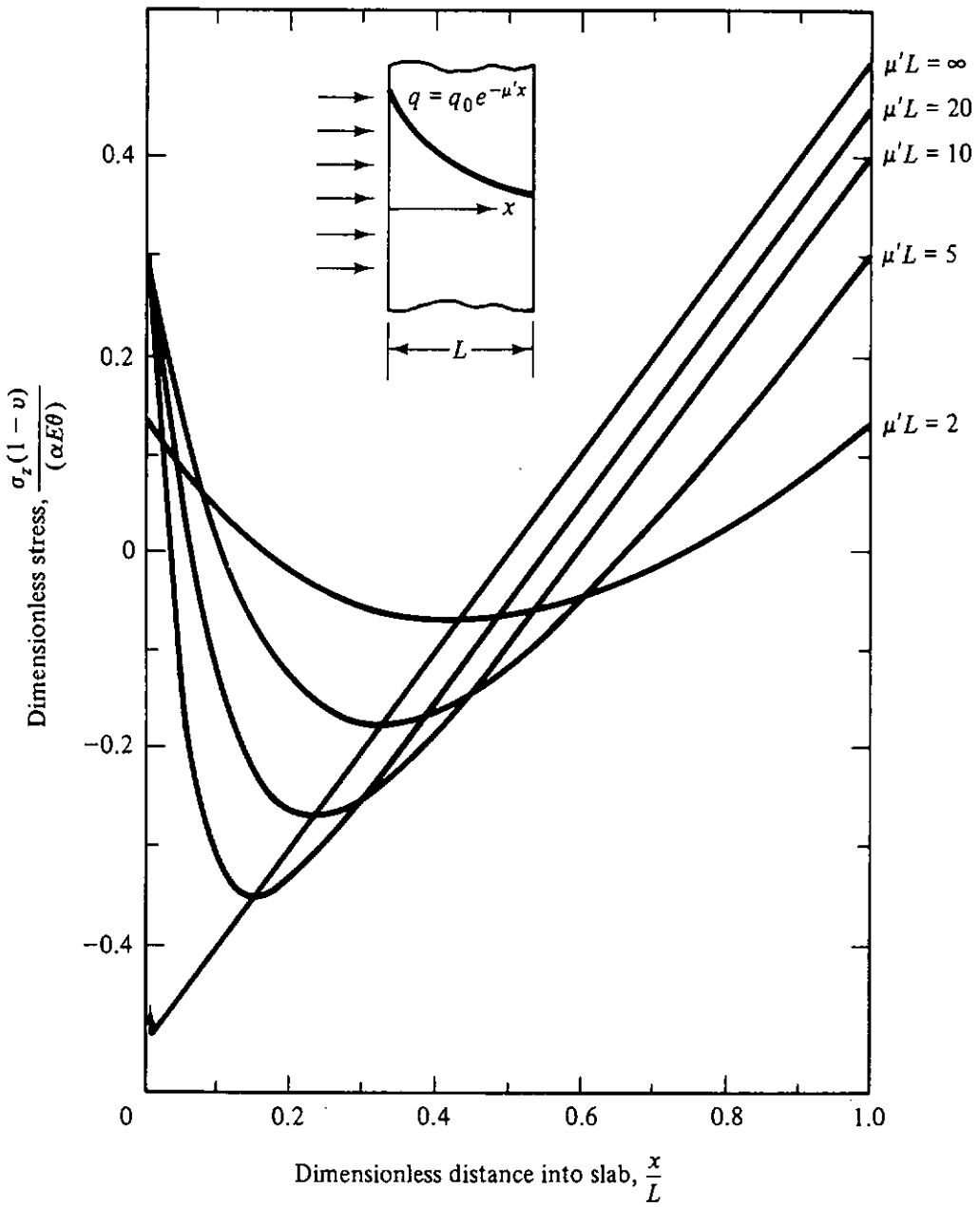

Figure 11.17 Dimensionless thermal stresses in a slab with isothermal boundaries and with internal heat generation decreasing exponentially with distance x into the slab.

differential equation for $u(r)$:

$$\frac{d}{dr}\left[\frac{1}{r}\frac{d(ru)}{dr}\right] = \frac{1+\nu}{1-\nu}\alpha\frac{d\,\Delta T}{dr}. \tag{11.58}$$

This equation has the solution

$$u(r) = \frac{1+\nu}{1-\nu}\frac{\alpha}{r}\int_a^r dr\, r\,\Delta T + C_1 + \frac{C_2}{r}, \tag{11.59}$$

in which the constants C_1 and C_2 must be evaluated from boundary conditions on σ_r, and on specification of conditions for σ_z or ϵ_z. Linearity of the problem allows separation of the stresses into two components: static stresses, evaluated with $\Delta T = 0$ and the boundary conditions $\sigma_r(a) = -p_i$ and $\sigma_r(b) = -p_0$;

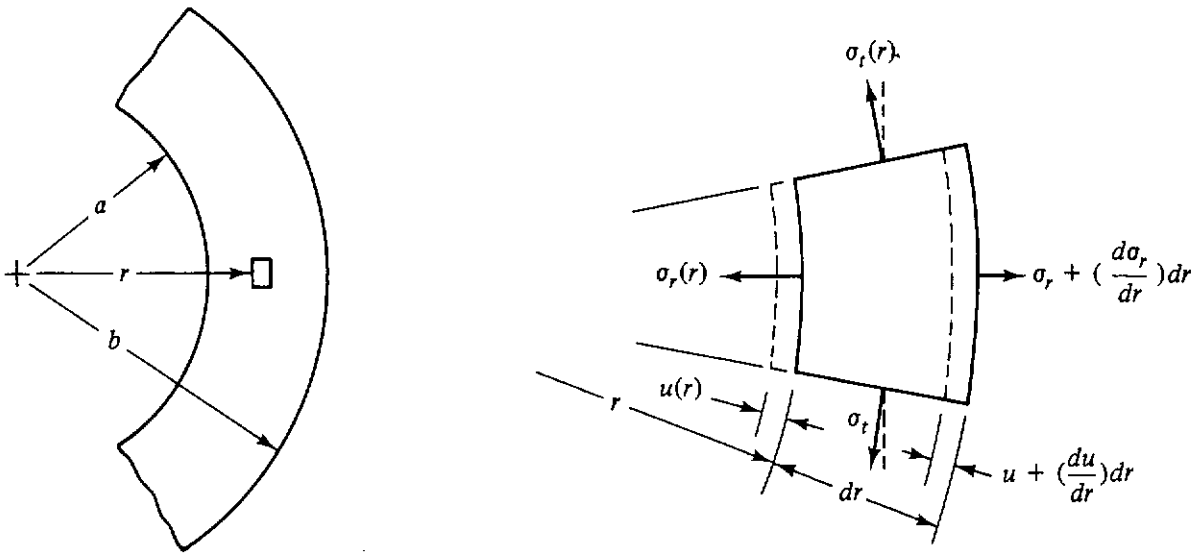

Figure 11.18 Stresses and displacements for an element of a cylindrical shell subjected to static and thermal stresses.

and thermal stresses, evaluated with the prescribed ΔT but with $\sigma_r(a) = \sigma_r(b) = 0$. For a finite cylinder, there is a choice between two specifications for σ_z and ϵ_z. If the ends of the cylinder are restrained, then $\epsilon_z = 0$. On the other hand, if the ends of the cylinder cylinder are unrestrained, then $\int_a^b dr\, r\sigma_z(r) = 0$. The stresses are conveniently expressed in terms of the dimensionless variables introduced in Section 11.3.2: $y = r/a$, $y_0 = b/a$, and $\Delta T(y) = \theta f(y)$.

Static stresses

$$\sigma_r = \frac{p_i - y_0^2 p_0 - (p_i - p_0)(y_0/y)^2}{y_0^2 - 1}, \tag{11.60}$$

$$\sigma_t = \frac{p_i - y_0^2 p_0 + (p_i - p_0)(y_0/y)^2}{y_0^2 - 1}, \tag{11.61}$$

$$\sigma_z = \frac{2\nu(p_i - y_0^2 p_0)}{y_0^2 - 1}, \tag{11.62}$$

if ends are restrained; and

$$\sigma_z = 0, \tag{11.63}$$

if ends are unrestrained. In the usual case, $p_0 \ll p_i$, for which condition

$$\sigma_r = \frac{-p_i(y_0^2 - y^2)}{y^2(y_0^2 - 1)}, \tag{11.64}$$

$$\sigma_t = \frac{+p_i(y_0^2 + y^2)}{y^2(y_0^2 - 1)}, \tag{11.65}$$

$$\sigma_z = \frac{2\nu p_i}{y_0^2 - 1}, \tag{11.66}$$

if ends are restrained. Note that σ_r is everywhere compressive, having its maximum value, $-p_i$, at $y = 1$. The tangential, or hoop, stress is everywhere

tensile, also having its maximum value at $y = 1$. The maximum shear stress, too, occurs at $y = 1$ and has the value

$$\tau_{max} = \frac{p_i y_0^2}{y_0^2 - 1}. \tag{11.67}$$

Thermal stresses

$$\sigma_r' \equiv \frac{(1-\nu)\sigma_r}{\alpha E\theta} = \frac{1}{y^2}\left[\frac{y^2-1}{y_0^2-1}\int_1^{y_0} dy\, yf(y) - \int_1^{y} dy\, yf(y)\right], \tag{11.68}$$

$$\sigma_t' \equiv \frac{(1-\nu)\sigma_t}{\alpha E\theta} = \frac{1}{y^2}\left[\frac{y^2+1}{y_0^2-1}\int_1^{y_0} dy\, yf(y) + \int_1^{y} dy\, yf(y) - y^2 f(y)\right], \tag{11.69}$$

and, for unrestrained cylinder ends,[4]

$$\sigma_z' \equiv \frac{(1-\nu)\sigma_z}{\alpha E\theta} = \frac{1}{y^2}\left[\frac{2y^2}{y_0^2-1}\int_1^{y_0} dy\, yf(y) - y^2 f(y)\right]. \tag{11.70}$$

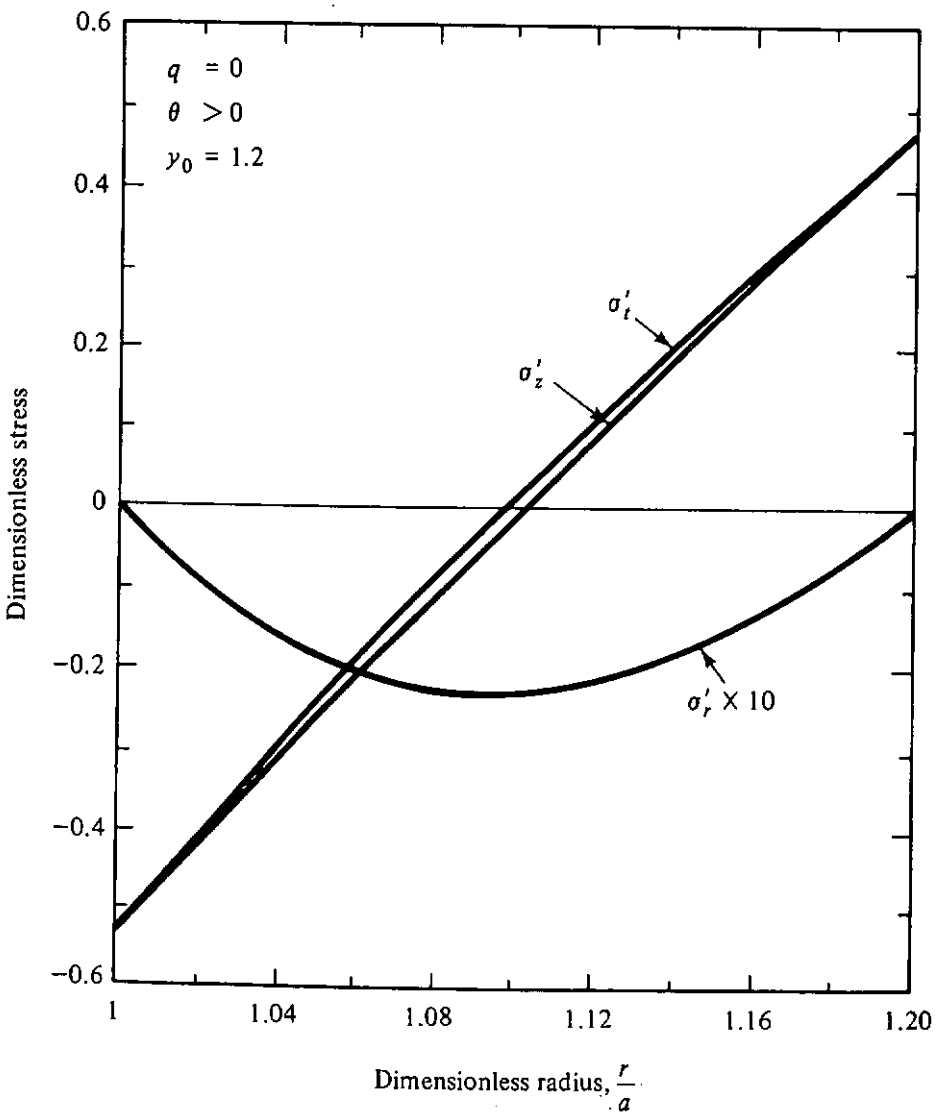

Figure 11.19 Dimensionless thermal stresses in a cylindrical shell with no internal heat generation. The characteristic temperature is $\theta \equiv T(a) - T(b) > 0$.

[4]For restrained ends, the integral term is multiplied by ν.

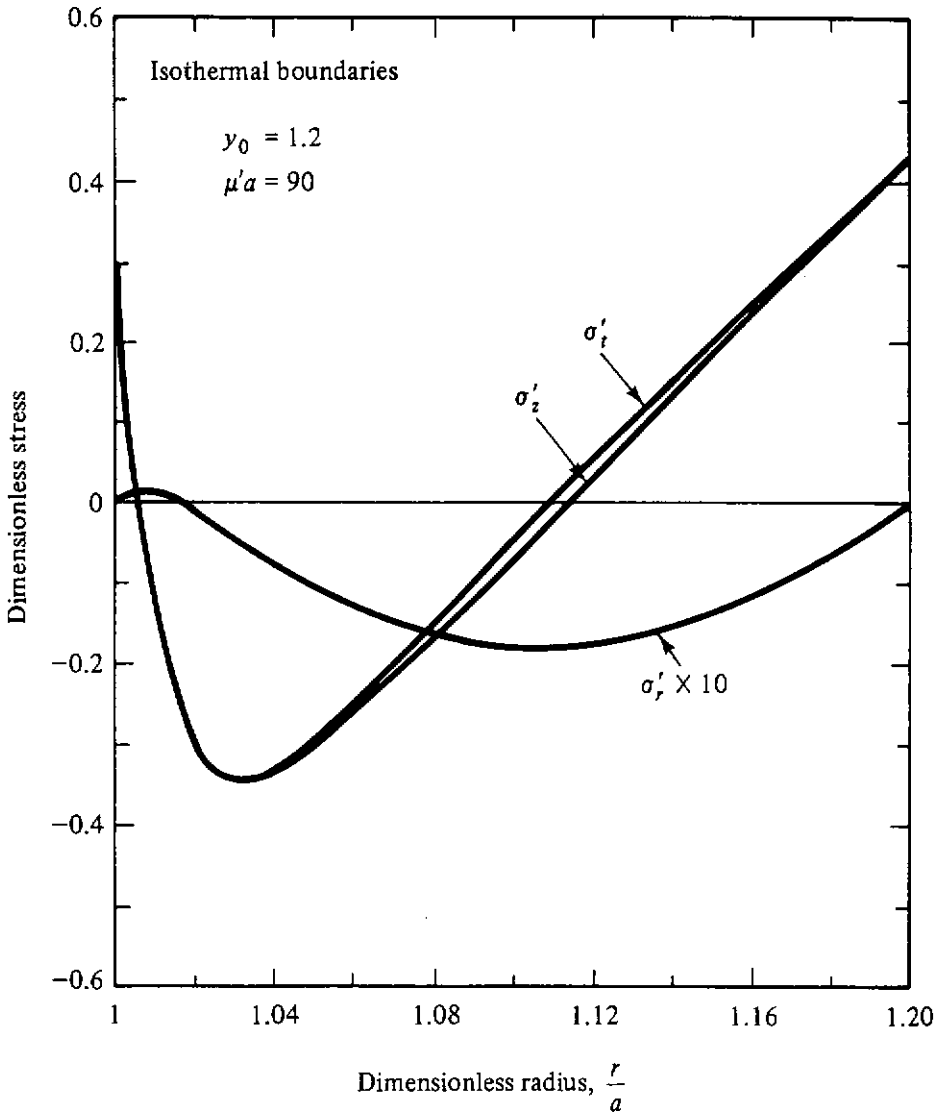

Figure 11.20 Dimensionless thermal stresses in a cylindrical shell with equal boundary temperatures and with internal heat generation decreasing exponentially with radius. The characteristic temperature is $\theta \equiv q_0/k\mu'^2$.

These results are illustrated in Figs. 11.19 to 11.22 for the special temperature profiles discussed in Section 11.3.2 and for unrestrained cylinder ends. For the conduction profile with no internal heat generation, Eq. (11.29), $\theta = T(a) - T(b)$, and

$$\sigma_r' = \frac{1}{2}\left[\frac{\ln y}{\ln y_0} - 1 + \frac{y_0^2 - y^2}{y^2(y_0^2 - 1)}\right], \tag{11.71}$$

$$\sigma_t' = \frac{1}{2}\left[\frac{\ln y}{\ln y_0} - 1 + \frac{1}{\ln y_0} - \frac{y_0^2 + y^2}{y^2(y_0^2 - 1)}\right], \tag{11.72}$$

$$\sigma_z' = \frac{\ln y}{\ln y_0} - 1 + \frac{1}{2\ln y_0} - \frac{1}{y_0^2 - 1}, \tag{11.73}$$

for unrestrained ends. Figure 11.19 illustrates these stresses for the case $y_0 = 1.2$. For θ positive (i.e., $T_a > T_b$), the radial thermal stress is everywhere relatively small and compressive. The tangential and azimuthal stresses are compressive near the inner, hotter, boundary and tensile near the outer boundary.

With the boundaries held at fixed temperatures, but with exponential internal heat generation, the temperature profile of Eq. (11.26) is superimposed and the thermal stresses are as illustrated in Fig. 11.20. Note that the tangential and axial tensile stresses near the outer, cooler boundary add to those resulting from the imposed temperatures at the boundary.

Now consider the cases of the one boundary insulated with the other held at constant temperature, with exponential heat generation. The temperature profiles are those of Eqs. (11.27) and (11.28). The resultant thermal stresses are illustrated in Figs. 11.21 and 11.22 for the case $y_0 = 1.2$ and $\mu' a = 90$. Note

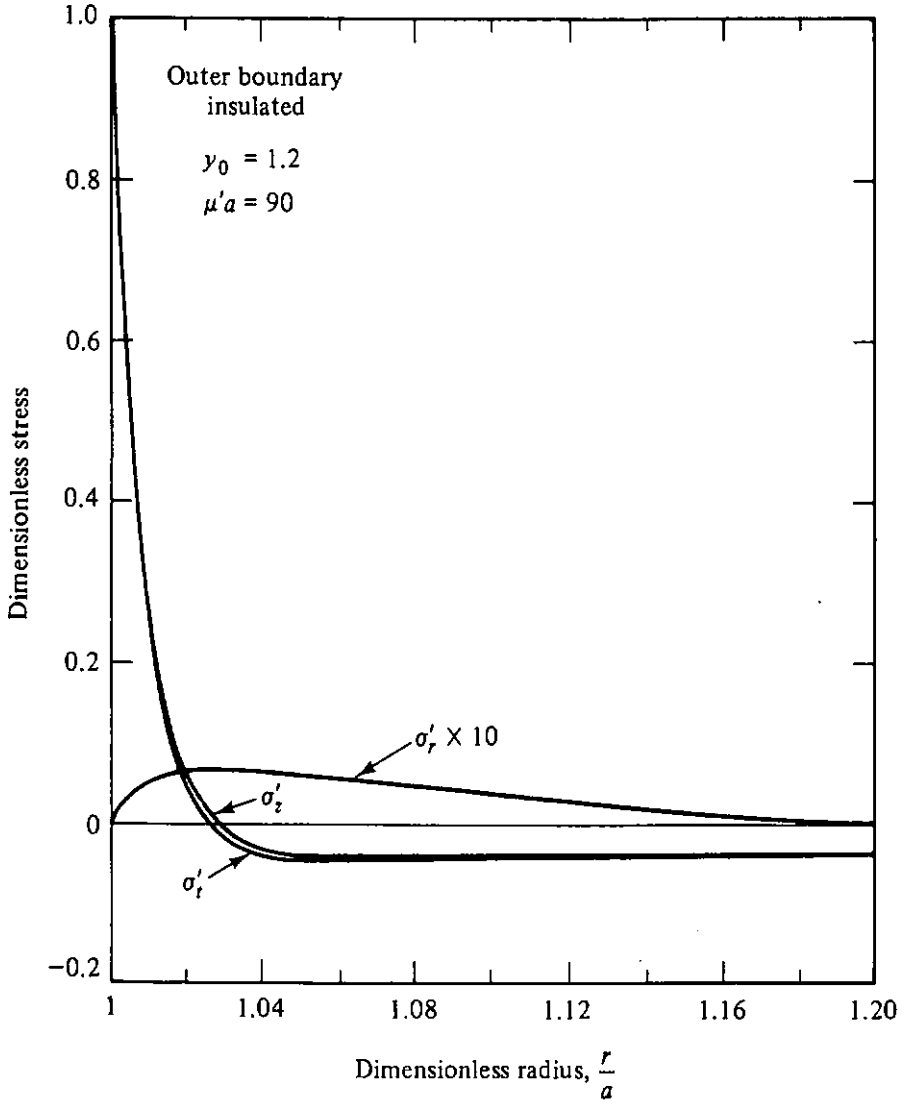

Figure 11.21 Dimensionless thermal stresses in a cylindrical shell with the inner boundary at fixed temperature and the outer boundary adiabatic and with internal heat generation decreasing exponentially with radius. The characteristic temperature is $\theta \equiv q_0/k\mu'^2$.

the order-of-magnitude difference between the maximum stresses in the two cases, those for the insulated boundary being the greater. For the insulated inner boundary, the thermal stresses augment the static stresses, whereas for the insulated outer boundary, the thermal stresses oppose the static stresses.

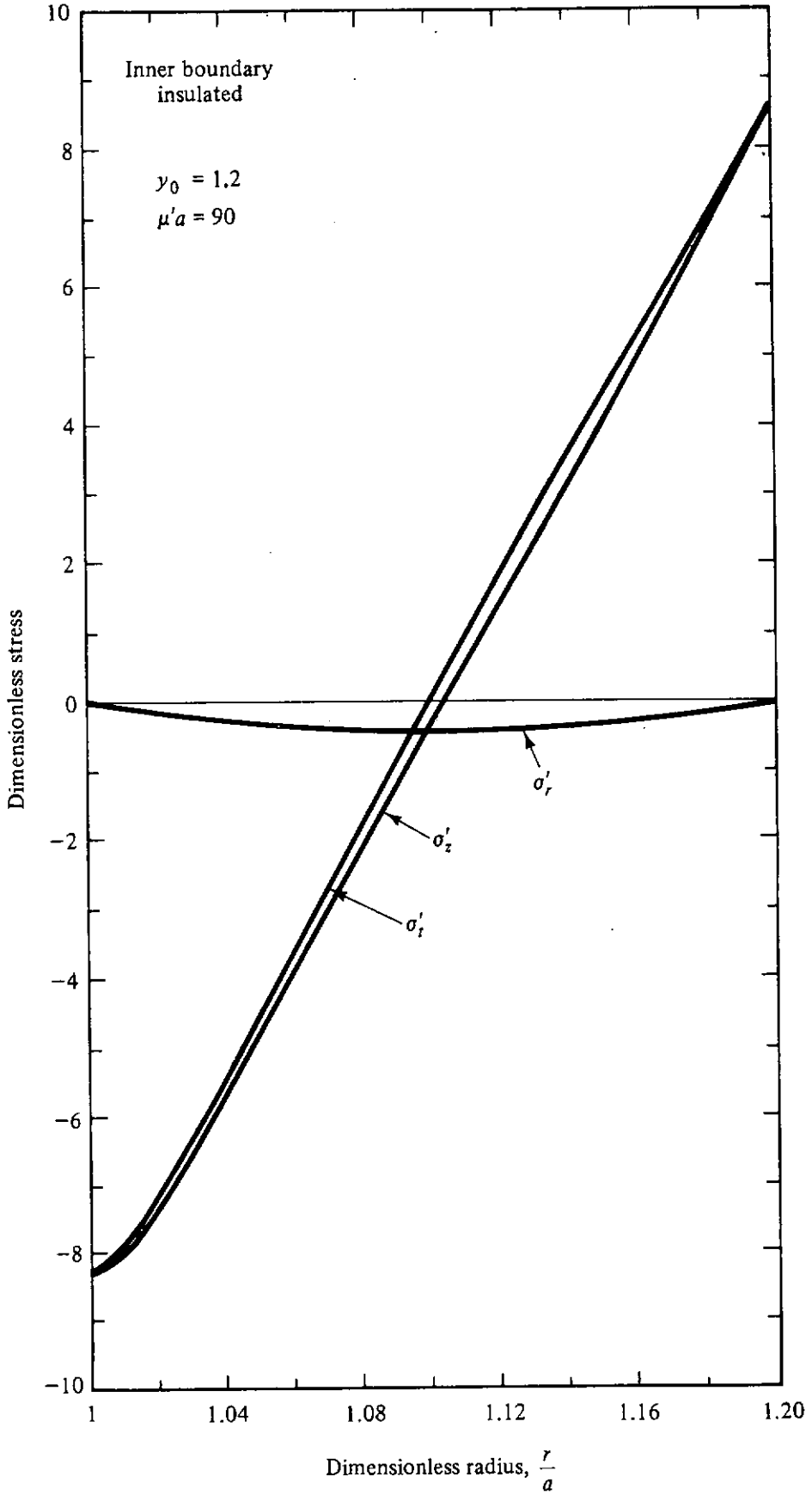

Figure 11.22 Dimensionless thermal stresses in a cylindrical shell with the inner boundary adiabatic and the outer boundary at fixed temperature and with internal heat generation decreasing exponentially with radius. The characteristic temperature is $\theta \equiv q_0/k\mu'^2$.

REFERENCES

1. E. P. Blizard (ed.), *Reactor Handbook*, Vol. III, Part B: *Reactor Shielding*, Interscience, New York, 1962.
2. N. M. Schaeffer (ed.), *Reactor Shielding for Nuclear Engineers*, TID-25951, National Technical Information Service, U.S. Dept. of Commerce, Springfield, Va., 1973.
3. R. G. Jaeger (ed.), *Engineering Compendium on Radiation Shielding*, Vol. II: *Shielding Materials*, Springer-Verlag, New York, 1975.
4. J. Butler, "The Evolution of Shielding Methods and Data—A Continuing Process of Adjustment to Changing Project Needs," in *Nuclear Reactor Shielding*, R. W. Roussin et al. (eds.), Science Press, Princeton, New Jersey, 1977, p. 18.
5. T. Lyman (ed.), *Metals Handbook*, Vol. I, 8th ed., American Society for Metals, Metals Park, Ohio, 1961.
6. *Sourcebook on Stainless Steel*, American Society for Metals, Metals Park, Ohio, 1976.
7. American National Standards ASTM A 212-65, ASTM A 302-80, ASTM A 508-80A, and ASTM A 533-80, American National Standards Institute, New York.
8. American National Standard ANSI/ANS-6.4-1977, American National Standards Institute, New York.
9. H. E. Hungerford, "Shielding," in *Fast Reactor Technology: Plant Design*, J. C. Yevick and A. Amorosi (eds.), MIT Press, Cambridge, Mass., 1966, Chap. 8.
10. J. C. Ryman, "On the Applications of Discrete Ordinates Methods to Gamma Photon Transport," Ph.D. dissertation, Kansas State University, 1979, p. 133.
11. J. H. Wilson and R. H. Karcher, "Shielding Effectiveness of Soils against Initial Radiations," Report HN-186, Holmes and Narver, Los Angeles, California 1966.
12. *Handbook of Chemistry and Physics*, 45th ed., Chemical Rubber Co., Cleveland, Ohio, 1964, p. F-85.
13. T. O. Ziebold, "Materials and Metallurgy," in *The Technology of Nuclear Reactor Safety*, Vol. 2, T. J. Thompson and J. G. Beckerley (eds.), MIT Press, Cambridge, Mass., 1973, p. 23.
14. M. T. Robinson, "The Theory of Radiation Induced Defect Production," in *Radiation Damage in Metals*, N. L. Peterson and S. D. Harkness (eds.), American Society for Metals, Metals Park, Ohio, 1975, pp. 1–27.
15. T. A. Gabriel, J. D. Amburgey, and N. M. Greene, "Radiation Damage Calculations: Primary Knock-on Atom Spectra, Displacement Rates, and Gas Production Rates," *Nucl. Sci. Eng.* **61**, 21–32 (1976).
16. D. G. Doran, "Neutron Displacement Cross Sections for Stainless Steel and Tantalum Based on a Lindhard Model," *Nucl. Sci. Eng.* **49**, 130–144 (1972).
17. W. F. Sheely, "Correlation of Radiation Damage to Steel with Neutron Spectrum," *Nucl. Sci. Eng.* **29**, 165–175 (1967).
18. C. J. Serpan, Jr., "Engineering Damage Cross Sections for Neutron Embrittlement of A302-B Pressure Vessel Steel," *Nucl. Eng. Des.* **33**, 19–29 (1975).

19. C. J. Serpan, Jr., "Damage Function Analysis of Neutron Induced Embrittlement in A302-B Steel at 500F (288C)," in *Effects of Radiation on Substructure and Mechanical Properties of Metals and Alloys*, STP-529, American Society for Testing and Materials, Philadelphia, 1972.
20. W. N. McElroy and R. E. Dahl, Jr., "Damage Functions and Data Correlation," *Nucl. Appl. Technol.* **7**, 561–571 (1969).
21. G. R. Odette and T. O. Ziebold, "The Yield Stress Radiation Damage Function of Iron," *Nucl. Sci. Eng.* **49**, 72–81 (1972).
22. G. R. Odette, "Damage Function Data Correlation for the Yield Stress of Iron," *Nucl. Eng. Des.* **33**, 37–47 (1975).
23. H. H. Yoshikawa, W. N. McElroy, and R. L. Simons, "The Definition of Damage Functions from Irradiation Test Data," *Nucl. Eng. Des.* **33**, 11–13 (1975).
24. D. R. Olander, "Fundamental Aspects of Nuclear Reactor Fuel Elements," Report TID-26711-P1, U.S. Energy Research and Development Administration, Washington, D.C., 1976.
25. Z. Zudans, T. C. Yen, and W. H. Steigelmann, *Thermal Stress Techniques in the Nuclear Industry*, Elsevier, New York, 1965.
26. J. F. Harvey, *Theory and Design of Modern Pressure Vessels*, 2nd ed., Van Nostrand Reinhold, New York, 1974.
27. J. F. Harvey, *Pressure Component Construction*, Van Nostrand Reinhold, New York, 1980.

appendix 1

constants and conversion factors

A1.1 PHYSICAL CONSTANTS [1]

Constant	Symbol	Values
Atomic mass unit[a]	u	$1.660\,566 \times 10^{-27}$ kg
Speed of light in vacuum	c	$2.997\,925 \times 10^{8}$ m s^{-1}
Elementary charge	e	$1.602\,189 \times 10^{-19}$ C
Electron rest mass	m_e	$9.109\,535 \times 10^{-31}$ kg
		($5.485\,803 \times 10^{-4}$ u)
Proton rest mass	m_p	$1.672\,649 \times 10^{-27}$ kg
		(1.007 276 u)
Neutron rest mass	m_n	$1.674\,954 \times 10^{-27}$ kg
		(1.008 665 u)
Electron radius (classical)	r_e	$2.817\,938 \times 10^{-15}$ m
Planck's constant	h	$6.626\,176 \times 10^{-34}$ J s
Avogadro's constant	N_A	$6.022\,045 \times 10^{23}$ mol^{-1}

[a]Equivalent to 931.502 MeV.

A1.2 RADIOLOGICAL UNITS

Quantity	Unit	Equivalent in Other Units
Absorbed dose	Gy (gray)	1 J kg^{-1}, 100 rad
Activity	Bq (becquerel)	1 s^{-1}, 2.7027 × 10^{-11} Ci (curie)
Cross section	m^2	10^{28} b (barn)
Dose equivalent	Sv (sievert)	100 rem
Energy	MeV	1.6021 × 10^{-6} erg, 1.6021 × 10^{-13} J
Exposure	R (roentgen)	2.58 × 10^{-4} C kg^{-1}
Kerma	Gy (gray)	1 J kg^{-1}, 10^4 erg g^{-1}

A1.3 PREFIXES FOR SI UNITS

Factor	Prefix	Symbol
10^{18}	exa	E
10^{15}	peta	P
10^{12}	tera	T
10^9	giga	G
10^6	mega	M
10^3	kilo	k
10^2	hecto	h
10^1	deca	da
10^{-1}	deci	d
10^{-2}	centi	c
10^{-3}	milli	m
10^{-6}	micro	μ
10^{-9}	nano	n
10^{-12}	pico	p
10^{-15}	femto	f
10^{-18}	atto	a

A1.4 CONVERSION FACTORS [2]

Quantity	Unit	SI Equivalent
Length	in.	2.54×10^{-2} m[a]
	ft	3.048×10^{-1} m[a]
	mile (statute)	$1.609\,344 \times 10^{3}$ m[a]
	mile (nautical)	1.853×10^{3} m
Area	in^2	6.4516×10^{-4} m^2[a]
	ft^2	$9.290\,304 \times 10^{-2}$ m^2[a]
	acre	$4.046\,873 \times 10^{3}$ m^2
	square mile (statute)	$2.589\,988 \times 10^{6}$ m^2
	hectare	1×10^{4} m^2[a]
Volume	oz (U.S. liq.)	$2.957\,353 \times 10^{-5}$ m^3
	in^3	$1.638\,706 \times 10^{-5}$ m^3
	gal (U.S. liq.)	$3.785\,412 \times 10^{-3}$ m^3
	ft^3	$2.831\,685 \times 10^{-2}$ m^3
Mass	oz (avdp.)	$2.834\,952 \times 10^{-2}$ kg
	lb	$4.535\,924 \times 10^{-1}$ kg
	ton (short)	$9.071\,847 \times 10^{2}$ kg
Force	kg_f	9.806 650 Newton (N)[a]
	lb_f	4.448 222 N
	ton	$8.896\,444 \times 10^{3}$ N
Pressure	lb_f/in^2 (psi)	$6.894\,757 \times 10^{3}$ Pascal (Pa) (1 Pa = 1 N/m^2)
	lb_f/ft^2	$4.788\,026 \times 10^{1}$ Pa
	atm (st'd)	$1.013\,250 \times 10^{5}$ Pa[a]
	in. H_2O (4°C)	$2.490\,82 \times 10^{2}$ Pa
	in. Hg (0°C)	$3.386\,39 \times 10^{3}$ Pa
	mm Hg (0°C)	$1.333\,22 \times 10^{2}$ Pa
	bar	$1. \times 10^{5}$ Pa[a]
Energy	eV	$1.602\,19 \times 10^{-19}$ J
	cal[b]	4.184 J[a]
	Btu[b]	$1.054\,350 \times 10^{3}$ J
	kWh	3.6×10^{6} J[a]
	MWd	8.64×10^{10} J[a]

[a]Exact conversion factor.
[b]Thermochemical units.

REFERENCES

1. C. M. Lederer and V. Shirley (eds.), *Table of Isotopes*, 7th ed., Wiley-Interscience, New York, 1978, App. 1.
2. "Standard for Metric Practice," American National Standard ANSI/ASTM E 380-76, American National Standards Institute, New York.

appendix 2

mathematical functions of importance in shielding analysis

A2.1 ELLIPTIC INTEGRALS [1]

Incomplete elliptic integrals of the first and second kinds, respectively, are defined as

$$\begin{aligned} F_e(k, \theta) &\equiv \int_0^{\theta} du\,(1 - k^2 \sin^2 u)^{-1/2} \\ &= \int_0^{\sin\theta} dv\,[(1 - v^2)(1 - k^2 v^2)]^{-1/2}, \end{aligned} \tag{A2.1}$$

$$\begin{aligned} E_e(k, \theta) &\equiv \int_0^{\theta} du\,(1 - k^2 \sin^2 u)^{1/2} \\ &= \int_0^{\sin\theta} dv\,(1 - v^2)^{-1/2}(1 - k^2 v^2)^{1/2}, \end{aligned} \tag{A2.2}$$

where $0 < k^2 < 1$. The integrals are "complete" if $\theta = \pi/2$.

Special properties of the elliptic integrals are listed below. In all cases $m = 0, 1, 2, \ldots$.

For θ of any magnitude, with $k^2 < 1$,

$$F_e(k, m\pi \pm \theta) = 2mF_e\left(k, \frac{\pi}{2}\right) \pm F_e(k, \theta), \tag{A2.3}$$

$$E_e(k, m\pi \pm \theta) = 2mE_e\left(k, \frac{\pi}{2}\right) \pm E_e(k, \theta); \tag{A2.4}$$

or, for $k^2 > 1$,

$$F_e(k, \theta) = k^{-1} F_e(k^{-1}, \sin^{-1}(k \sin \theta)). \tag{A2.5}$$

A2.2 SIEVERT OR SECANT INTEGRAL [2]

The Sievert (or secant) integral is defined as

$$F(\theta, b) \equiv \int_0^\theta dx\, e^{-b\sec x}, \tag{A2.6}$$

where $b \geq 0$ and $0 \leq \theta \leq \pi/2$. Tables and graphs of $F(\theta, b)$ are widely available in the shielding literature and the function is illustrated in Fig. A2.1. Obviously, interpolation is difficult. One aid in interpolation between θ values is, for small values of δ,

$$F(\theta + \delta, b) \simeq F(\theta, b) + \delta e^{-b\sec\theta}. \tag{A2.7}$$

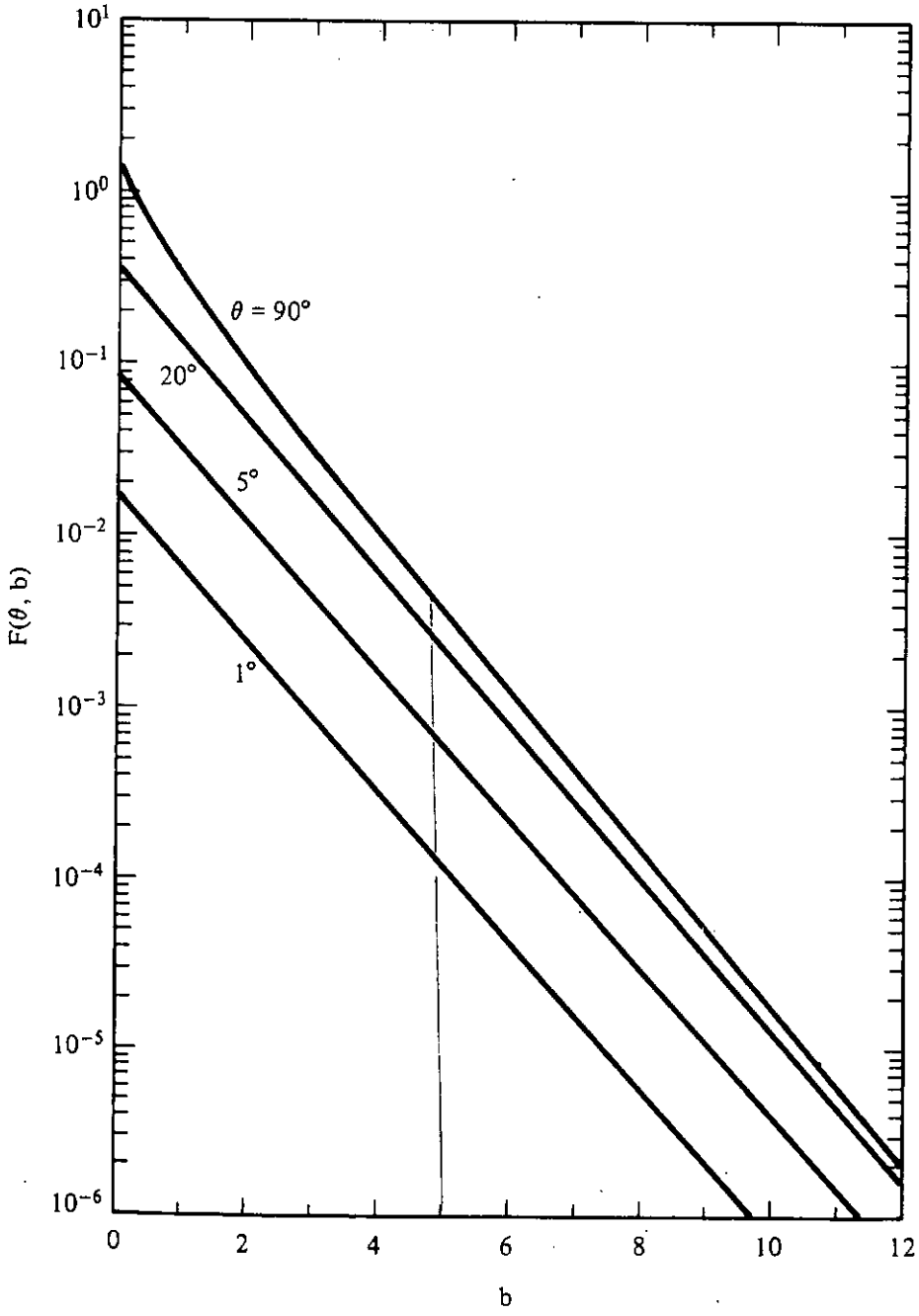

Figure A2.1 Function $F(\theta, b)$ versus b for several values of the parameter θ.

Another aid arises from the fact that the principal functional dependence of $F(\theta, b)$ is as θe^{-b}. Thus, interpolation is greatly facilitated by use of tables of $\bar{F}(\theta, b)$, where

$$F(\theta, b) = \theta e^{-b}\bar{F}(\theta, b). \tag{A2.8}$$

Values of $\bar{F}(\theta, b)$ are provided in Table A2.1.

A2.3 EXPONENTIAL INTEGRAL FUNCTIONS [1]

The exponential integral functions for positive integral n and real $x > 0$ are defined as

$$E_n(x) \equiv x^{n-1}\int_x^\infty du\, u^{-n}e^{-u} = \int_1^\infty dv\, v^{-n}e^{-xv} = \int_0^1 dw\, w^{n-2}e^{-x/w}. \tag{A2.9}$$

A closely related function is $Ei(x)$, defined as the principal value of $-\int_{-x}^{\infty} du\, u^{-1}e^{-u}$. Thus for positive x, $E_1(x) = -Ei(-x)$. The evaluation of these integrals with finite limits is often encountered in many shielding calculations, and can be readily expressed as differences of the exponential functions. For example,

$$\int_{x_1}^{x_2} du\, u^{-1}e^{-u} = \begin{cases} E_1(x_1) - E_1(x_2), & x_1, x_2 > 0; \\ Ei(-x_2) - Ei(-x_1), & x_1, x_2 < 0. \end{cases} \tag{A2.10}$$

Tables and graphs of the exponential functions are widely available in the shielding literature, and from Fig. A2.2 it is seen that these functions vary rapidly with their arguments. For large arguments, the principal functional dependence of $E_n(x)$ is $x^{-1}e^{-x}$ [$x^{-1}e^{x}$ for $Ei(x)$]; and thus, by extracting these asymptotic dependencies from the functions, much more slowly varying functions, suitable for tabular interpolation, result. In Table A2.2 the following slowly varying functions are tabulated: $\bar{Ei}(x) \equiv xe^{-x}Ei(x)$, $\bar{E}_1(x) \equiv xe^{x}E_1(x)$, and $\bar{E}_2(x) \equiv xe^{x}E_2(x)$.

Special values

$$E_0(x) \equiv x^{-1}e^{-x}, \tag{A2.11a}$$

$$E_n(0) = (n-1)^{-1}, \qquad n > 1. \tag{A2.11b}$$

Series representations. For $n > 0$, and especially valuable for $x \gg 1$,

$$E_n(x) = x^{-1}e^{-x}\left[1 + \sum_{i=1}^{\infty}\frac{(-1)^i(n+i-1)!}{x^i(n-1)!}\right]. \tag{A2.12}$$

For $x \ll 1$ and $n > 0$, a useful series representation is

$$E_n(x) = \frac{(-x)^{n-1}}{(n-1)!}(-\ln x - \gamma + A_n) - \sum_{\substack{m=0 \\ m\neq n-1}}^{\infty}\frac{(-x)^m}{(m-n+1)m!}, \tag{A2.13}$$

Table A2.1 Function $\bar{F}(\theta, b)$ for Various Values of the Parameters θ and b

θ (deg)	θ (rad)	b = 0.01	0.05	0.10	0.20	0.40	0.60	0.80	1.00	1.25	1.50	1.75	2.00	2.50	3.00
1.0	0.01745	1.00000	1.00000	0.99999	0.99999	0.99998	0.99997	0.99996	0.99995	0.99994	0.99992	0.99991	0.99990	0.99987	0.99985
2.5	0.04363	1.00000	0.99998	0.99997	0.99994	0.99987	0.99981	0.99975	0.99968	0.99960	0.99952	0.99944	0.99937	0.99921	0.99905
5.0	0.08727	0.99999	0.99994	0.99987	0.99975	0.99949	0.99924	0.99898	0.99873	0.99841	0.99810	0.99778	0.99746	0.99683	0.99620
7.5	0.13090	0.99997	0.99986	0.99971	0.99943	0.99885	0.99828	0.99771	0.99714	0.99643	0.99571	0.99500	0.99429	0.99288	0.99146
10.0	0.17453	0.99995	0.99974	0.99949	0.99898	0.99796	0.99694	0.99592	0.99491	0.99364	0.99238	0.99112	0.98986	0.98736	0.98486
12.5	0.21817	0.99992	0.99960	0.99920	0.99840	0.99680	0.99520	0.99361	0.99203	0.99005	0.98809	0.98613	0.98417	0.98029	0.97643
15.0	0.26180	0.99988	0.99942	0.99884	0.99768	0.99537	0.99307	0.99078	0.98850	0.98566	0.98284	0.98003	0.97724	0.97169	0.96621
20.0	0.34907	0.99979	0.99895	0.99791	0.99583	0.99168	0.98757	0.98349	0.97944	0.97443	0.96946	0.96453	0.95965	0.95003	0.94059
25.0	0.43633	0.99967	0.99834	0.99668	0.99337	0.98683	0.98036	0.97398	0.96766	0.95988	0.95522	0.94466	0.93722	0.92267	0.90855
30.0	0.52360	0.99951	0.99755	0.99511	0.99027	0.98071	0.97133	0.96211	0.95306	0.94196	0.93111	0.92050	0.91012	0.89002	0.87078
35.0	0.61087	0.99931	0.99658	0.99317	0.98643	0.97321	0.96032	0.94775	0.93549	0.92060	0.90616	0.89216	0.87858	0.85263	0.82819
40.0	0.69813	0.99907	0.99538	0.99080	0.98176	0.96416	0.94715	0.93072	0.91484	0.89573	0.87741	0.85983	0.84296	0.81121	0.78189
45.0	0.78540	0.99878	0.99393	0.98792	0.97613	0.95334	0.93159	0.91080	0.89094	0.86733	0.84498	0.82382	0.80376	0.76667	0.73320
50.0	0.87266	0.99842	0.99215	0.98443	0.96933	0.94049	0.91335	0.88778	0.86367	0.83543	0.80912	0.78458	0.76166	0.72015	0.68362
60.0	1.04720	0.99743	0.98729	0.97492	0.95113	0.90713	0.86739	0.83140	0.79870	0.76188	0.72896	0.69940	0.67274	0.62665	0.58826
70.0	1.22173	0.99582	0.97948	0.95991	0.92343	0.85967	0.80601	0.76036	0.72113	0.67927	0.64373	0.61317	0.58657	0.54241	0.50707
80.0	1.39626	0.99263	0.96463	0.93267	0.87723	0.79145	0.72795	0.67867	0.63897	0.59864	0.56560	0.53781	0.51396	0.47484	0.44376
90.0	1.57080	0.97326	0.91365	0.86443	0.79598	0.70774	0.64831	0.60365	0.56810	0.53216	0.50276	0.47805	0.45686	0.42208	0.39445

θ (deg)	θ (rad)	b = 3.50	4.00	5.00	6.00	8.00	10.00	12.00	15.00	20.00	25.00	35.00	50.00	60.00	75.00
1.0	0.01745	0.99982	0.99980	0.99975	0.99970	0.99959	0.99949	0.99939	0.99924	0.99899	0.99873	0.99823	0.99747	0.99696	0.99621
2.5	0.04363	0.99889	0.99873	0.99841	0.99810	0.99747	0.99683	0.99620	0.99526	0.99369	0.99212	0.98900	0.98435	0.98127	0.97669
5.0	0.08727	0.99557	0.99494	0.99368	0.99242	0.98992	0.98743	0.98495	0.98125	0.97514	0.96910	0.95722	0.93990	0.92867	0.91229
7.5	0.13090	0.99005	0.98865	0.98584	0.98306	0.97752	0.97205	0.96663	0.95860	0.94549	0.93570	0.90808	0.87338	0.85163	0.82091
10.0	0.17453	0.98238	0.97991	0.97500	0.97014	0.96054	0.95112	0.94187	0.92830	0.90648	0.88561	0.84652	0.79387	0.76229	0.71951
12.5	0.21817	0.97260	0.96880	0.96127	0.95386	0.93934	0.92522	0.91150	0.89163	0.86029	0.83102	0.77806	0.71047	0.67196	0.62217
15.0	0.26180	0.96078	0.95540	0.94482	0.93446	0.91435	0.89505	0.87651	0.85006	0.80930	0.77230	0.70791	0.63049	0.58871	0.53710
20.0	0.34907	0.93132	0.92223	0.90453	0.88747	0.85516	0.82509	0.79706	0.75849	0.70225	0.65439	0.57796	0.49642	0.45650	0.41048
25.0	0.43633	0.89483	0.88151	0.85600	0.83192	0.78763	0.74797	0.71233	0.66534	0.60091	0.54973	0.47425	0.40084	0.36692	0.32894
30.0	0.52360	0.85234	0.83468	0.80149	0.77092	0.71667	0.67018	0.63008	0.57951	0.51423	0.46538	0.39736	0.33439	0.30588	0.27414
35.0	0.61087	0.80515	0.78342	0.74350	0.70779	0.64683	0.59700	0.55573	0.50581	0.44446	0.40041	0.34085	0.28664	0.26219	0.23498
40.0	0.69813	0.75477	0.72965	0.68466	0.64565	0.58172	0.53181	0.49193	0.44523	0.38965	0.35058	0.29826	0.25081	0.22941	0.20560
45.0	0.78540	0.70289	0.67537	0.62741	0.58715	0.52365	0.47599	0.43890	0.39634	0.34646	0.31164	0.26512	0.22294	0.20392	0.18276
50.0	0.87266	0.65131	0.62259	0.57385	0.53416	0.47351	0.42927	0.39536	0.35679	0.31183	0.28048	0.23861	0.20065	0.18353	0.16448
60.0	1.04720	0.55581	0.52802	0.48282	0.44747	0.39522	0.35789	0.32951	0.29733	0.25986	0.23373	0.19884	0.16721	0.15294	0.13707
70.0	1.22173	0.47796	0.45344	0.41411	0.38363	0.33877	0.30677	0.28244	0.25486	0.22273	0.20034	0.17044	0.14332	0.13109	0.11749
80.0	1.39626	0.41824	0.39677	0.36235	0.33568	0.29642	0.26842	0.24713	0.22300	0.19489	0.17530	0.14913	0.12540	0.11471	0.10280
90.0	1.57080	0.37177	0.35268	0.32209	0.29838	0.26348	0.23860	0.21967	0.19822	0.17324	0.15582	0.13256	0.11147	0.10196	0.09138

Source: *Ref. 2; by permission of the American Nuclear Society.*

TABLE A2.2 Normalized Exponential Integral Functions[a]
$Ei(x)$, $E_1(x)$, and $E_2(x)$

x	$\bar{E}i(x) = xe^{-x}Ei(x)$	$\bar{E}_1(x) = xe^{x}E_1(x)$	$\bar{E}_2(x) = xe^{x}E_2(x)$
0.0	0	0	0
0.01	−0.03978	0.04078	0.00954
0.02	−0.06498	0.06845	0.01863
0.03	−0.08440	0.09148	0.02726
0.04	−0.09997	0.11163	0.03553
0.05	−0.11262	0.12972	0.04351
0.06	−0.12292	0.14622	0.05123
0.08	−0.13787	0.17566	0.06595
0.10	−0.14684	0.20146	0.07985
0.15	−0.15029	0.25522	0.11172
0.20	−0.13456	0.29867	0.14027
0.30	−0.06727	0.36676	0.18997
0.40	0.02809	0.41913	0.23235
0.60	0.25351	0.49676	0.30194
0.80	0.48434	0.55300	0.35760
1.00	0.69717	0.59635	0.40365
1.25	0.92435	0.63879	0.45151
1.50	1.10492	0.67239	0.49142
1.75	1.24186	0.69979	0.52537
2.00	1.34097	0.72266	0.55469
2.50	1.45163	0.75881	0.60296
3.00	1.48373	0.78625	0.64125
3.50	1.47178	0.80787	0.67246
4.00	1.43821	0.82538	0.69847
5.00	1.35383	0.85211	0.73945
6.00	1.27888	0.87161	0.77037
8.00	1.18185	0.89824	0.81410
10.00	1.13147	0.91563	0.84367
12.00	1.10565	0.92791	0.86504
15.00	1.07578	0.94080	0.88794
20.00	1.05596	0.95437	0.91258
25.00	1.04366	0.96287	0.92831
35.00	1.03036	0.97294	0.94726
50.00	1.02085	0.98076	0.96223
75.00	1.01370	0.98701	0.97435
100.00	1.01021	0.99019	0.98058
150.00	1.00676	0.99342	0.98693
200.00	1.00505	0.99505	0.99015
500.00	1.00201	0.99801	0.99602
1000.00	1.00100	0.99900	0.99801
∞	1.00000	1.00000	1.00000

[a]For small arguments, these functions are readily computed from Eqs. (A2.13) to (A2.13b). Specifically, for $x < 0.01$, only the first term under the summation sign is needed.

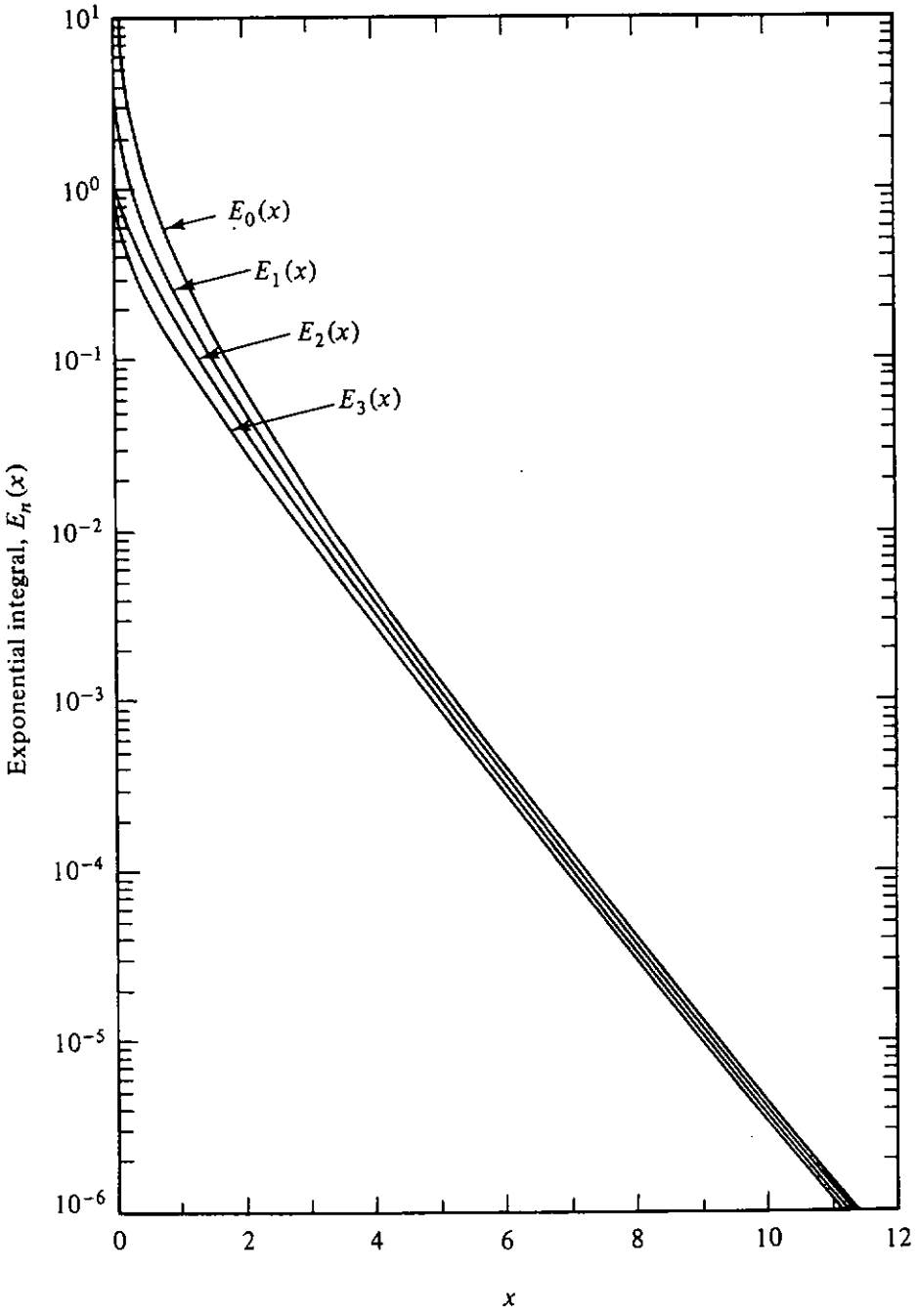

Figure A2.2 First four exponential integral functions $E_n(x)$.

where $\gamma = 0.577216\ldots$, $A_1 = 0$, and, for $n > 1$, $A_n = \sum_{m=1}^{n-1} m^{-1}$. Note that, for $x > 0$,

$$E_1(x) = -\gamma - \ln x - \sum_{n=1}^{\infty} \frac{(-x)^n}{nn!}, \tag{A2.13a}$$

whereas

$$Ei(x) = \gamma + \ln x + \sum_{n=1}^{\infty} \frac{x^n}{nn!}. \tag{A2.13b}$$

Derivatives and simple integrals

$$\frac{d}{dx} E_n(x) = -E_{n-1}(x), \qquad n \geq 1, \tag{A2.14}$$

$$\int du\, E_n(u) = -E_{n+1}(u) + \text{const.}, \qquad n \geq 0, \tag{A2.15}$$

$$\int_x^\infty du\, E_n(u) = E_{n+1}(x), \qquad n \geq 0, \tag{A2.16}$$

where x and u are positive.

Recurrence relationships. Integration of Eq. (A2.9) by parts leads to

$$E_n(x) = (n-1)^{-1}[e^{-x} - xE_{n-1}(x)], \qquad n > 1. \tag{A2.17}$$

Successive integrations by parts leads to

$$E_n(x) = \left[\sum_{i=0}^{n-m-1} \frac{(-x)^i e^{-x}(n-2-i)!}{(n-1)!}\right] + \frac{(-x)^{n-m}(m-1)!}{(n-1)!} E_m(x). \tag{A2.18}$$

where $n > m \geq 1$.

Special integrals. Direct application of Eq. (A2.18) leads to the result that, for ac and ad positive,

$$\begin{aligned}\int_c^d dx\, x^{-m} E_n(ax) = \Bigg[&\frac{(n-m-1)!\,(-a)^{m-1}}{(n-1)!} E_{n-m+1}(ax) \\ &- \sum_{i=0}^{m-1} \frac{(n-2-i)!\,(-a)^i}{(n-1)!\, x^{m-i-1}} E_{m-i}(ax)\Bigg]\Bigg|_c^d, \qquad n > m \geq 1.\end{aligned} \tag{A2.19}$$

Repeated integrations by parts leads to the result that, for $ad > -b$, $ac > -b$, $k/a < 1$, and $a \neq k \neq 0$:

$$\begin{aligned}\int_c^d dx\, e^{kx} E_n(ax+b) = \Bigg[&k^{-1} e^{kx} \sum_{i=0}^{n-1} \left(\frac{a}{k}\right)^i E_{n-i}(ax+b) \\ &- k^{-1}\left(\frac{a}{k}\right)^{n-1} e^{-kb/a} E_1\left(\left[1 - \frac{k}{a}\right][ax+b]\right)\Bigg]\Bigg|_c^d.\end{aligned} \tag{A2.20}$$

For $k/a > 1$, the E_1 function in the last term is replaced by $-Ei((k/a - 1)(ax + b))$. Finally, for $kd > -b$, $kc > -b$, and $k = a \neq 0$:

$$\int_c^d dx\, e^{kx} E_n(kx+b) = \left[k^{-1} e^{kx} \sum_{i=0}^{n-1} E_{n-i}(kx+b) + k^{-1} e^{-b} \ln(kx+b)\right]\Bigg|_c^d. \tag{A2.21}$$

A2.4 LEGENDRE POLYNOMIALS [1]

The Legendre polynomial $u = P_n(x)$, $n = 0, 1, 2, \ldots$, is one set of solutions to the differential equation

$$(1 - x^2)u'' - 2xu' + n(n+1)u = 0. \tag{A2.22}$$

The first few terms are

$$P_0(x) = 1, \qquad P_2(x) = \frac{3x^2 - 1}{2},$$

$$P_1(x) = x, \qquad P_3(x) = \frac{5x^3 - 3x}{2}.$$

The higher-order polynomials may be generated by use of the recursion relationship

$$P_n(x) = (2n - 1)\frac{x}{n}P_{n-1}(x) - n^{-1}(n - 1)P_{n-2}(x) \tag{A2.23}$$

or the series

$$P_n(x) = \sum_{i=0}^{m} \frac{(-1)^i(2n - 2i)!\, x^{n-2i}}{2^n i!\,(n - 1)!\,(n - 2i)!}, \tag{A2.24}$$

where m is $n/2$ or $(n - 1)/2$, whichever is integral. Note that as n is even or odd, $P_n(x)$ contains only even or odd powers of x up to the nth power.

The Legendre polynomials are orthogonal with unit weight function over the interval $(-1, 1)$, such that

$$\int_{-1}^{1} dx\, P_n(x)P_m(x) = \begin{cases} 0, & m \neq n, \\ \dfrac{2}{2n + 1}, & m = n. \end{cases} \tag{A2.25}$$

Equation (A2.24) may be written as

$$P_n(x) = \alpha_n \sum_{m=0}^{n} \gamma_m^n x^m, \tag{A2.26}$$

and its inverse as

$$x^n = \beta_n \sum_{m=0}^{n} \zeta_m^n P_m(x), \tag{A2.27}$$

where α_n, β_n, γ_m^n, and ζ_m^n are constants. As n is even or odd, only even or odd m-indexed values of γ_m^n and ζ_m^n are nonzero. Using Eq. (A2.27) and the orthogonality property, it follows that

$$\int_{-1}^{1} dx\, x^m P_n(x) = 0, \qquad n > m. \tag{A2.28}$$

The Legendre polynomials are complete on the interval $(-1, 1)$, that is, an arbitrary function $f(x)$ can be expanded uniquely as

$$f(x) = \sum_{n=0}^{\infty} \frac{(2n + 1)}{2} f_n P_n(x) \tag{A2.29}$$

and it follows from the orthogonality property, Eq. (A2.25), that the expansion coefficients f_n are given by

$$f_n = \int_{-1}^{1} dx\, f(x)P_n(x). \tag{A2.30}$$

In certain problems in radiation shielding there arise the associated Legendre functions of the first kind, $P_n^m(x)$, which may be generated using

the relationship

$$P_n^m(x) = (-1)^m(1 - x^2)^{m/2}\frac{d^m}{dx^m}P_n(x). \tag{A2.31}$$

These functions are needed, for example, in evaluating $P_n(\cos\theta_s)$, where $\cos\theta_s \equiv \mathbf{\Omega}\cdot\mathbf{\Omega}' = \cos\theta\cos\theta' + \sin\theta\sin\theta'\cos(\psi - \psi')$. In this case

$$P_n(\cos\theta_s) = P_n(\cos\theta)P_n(\cos\theta') + 2\sum_{m=1}^{n}\frac{(n-m)!}{(n+m)!}P_n^m(\cos\theta)P_n^m(\cos\theta')\cos[m(\psi - \psi')]. \tag{A2.32}$$

A2.5 CHANDRASEKHAR *H* FUNCTIONS [3]

The function presented in Table A2.3 is one of a number of specialized functions described by Chandrasekhar in his treatise on radiative transfer. The function

TABLE A2.3 The Function $H(\kappa, \cos\theta)$

$\cos\theta$	$\kappa =$ 0.1	$\kappa =$ 0.2	$\kappa =$ 0.3	$\kappa =$ 0.4	$\kappa =$ 0.5	$\kappa =$ 0.6	$\kappa =$ 0.7
0.00	1.0000	1.0000	1.0000	1.0000	1.0000	1.0000	1.0000
0.10	1.0124	1.0256	1.0399	1.0554	1.0724	1.0913	1.1130
0.20	1.0186	1.0389	1.0611	1.0858	1.1135	1.1452	1.1825
0.30	1.0230	1.0483	1.0764	1.1079	1.1439	1.1858	1.2364
0.40	1.0263	1.0555	1.0881	1.1252	1.1680	1.2186	1.2806
0.50	1.0289	1.0612	1.0976	1.1392	1.1877	1.2458	1.3179
0.60	1.0311	1.0659	1.1054	1.1509	1.2043	1.2689	1.3501
0.70	1.0328	1.0698	1.1120	1.1608	1.2186	1.2889	1.3781
0.80	1.0344	1.0732	1.1176	1.1694	1.2309	1.3063	1.4029
0.90	1.0357	1.0761	1.1225	1.1768	1.2417	1.3217	1.4250
1.00	1.0368	1.0786	1.1268	1.1834	1.2513	1.3354	1.4447
$\cos\theta$	$\kappa =$ 0.8	$\kappa =$ 0.85	$\kappa =$ 0.9	$\kappa =$ 0.925	$\kappa =$ 0.95	$\kappa =$ 0.975	$\kappa =$ 1.0
0.00	1.0000	1.0000	1.0000	1.0000	1.0000	1.0000	1.0000
0.10	1.1388	1.1541	1.1721	1.1828	1.1952	1.2111	1.2474
0.20	1.2286	1.2570	1.2914	1.3123	1.3373	1.3703	1.4503
0.30	1.3006	1.3411	1.3914	1.4225	1.4605	1.5117	1.6425
0.40	1.3611	1.4129	1.4785	1.5198	1.5710	1.6414	1.8293
0.50	1.4133	1.4758	1.5560	1.6073	1.6718	1.7621	2.0128
0.60	1.4590	1.5315	1.6259	1.6870	1.7647	1.8753	2.1941
0.70	1.4995	1.5814	1.6893	1.7601	1.8509	1.9822	2.3740
0.80	1.5358	1.6265	1.7474	1.8274	1.9313	2.0834	2.5527
0.90	1.5685	1.6675	1.8008	1.8899	2.0065	2.1795	2.7306
1.00	1.5982	1.7050	1.8501	1.9480	2.0771	2.2710	2.9078

Source: *Refs. 3 and 4.*

$H(\kappa, \cos\theta)$ is a solution of the nonlinear integral equation

$$\frac{1}{H(\kappa, \cos\theta)} = (1 - \kappa)^{1/2} + \frac{\kappa}{2}\int_0^1 \frac{du\, uH(\kappa, u)}{u + \cos\theta}. \tag{A2.33}$$

It may be evaluated using the equation [5]

$$H(\kappa, \cos\theta) = \frac{1}{(\nu_0 + \cos\theta)(1 + \cos\theta)(1 - \kappa)^{1/2}} \times \exp\left[-\frac{1}{\pi}\int_0^1 \frac{du}{u + \cos\theta} \tan^{-1}\frac{\kappa u\pi/2}{1 - \kappa u \tanh^{-1} u}\right], \tag{A2.34}$$

where ν_0 is the positive root of $1 - \kappa\nu_0 \tanh^{-1}(\nu_0^{-1})$.

A2.6 DIRAC DELTA FUNCTION [6]

One way of representing the Dirac delta function is in terms of the function $g(x)$ illustrated in Fig. A2.3.

$$\delta(x - x_0) \equiv \lim_{\epsilon \to 0} g(x). \tag{A2.35}$$

Alternative representations are

$$\delta(x - x_0) = \pi^{-1} \lim_{\lambda \to \infty} \frac{\sin[\lambda(x - x_0)]}{(x - x_0)}, \tag{A2.36}$$

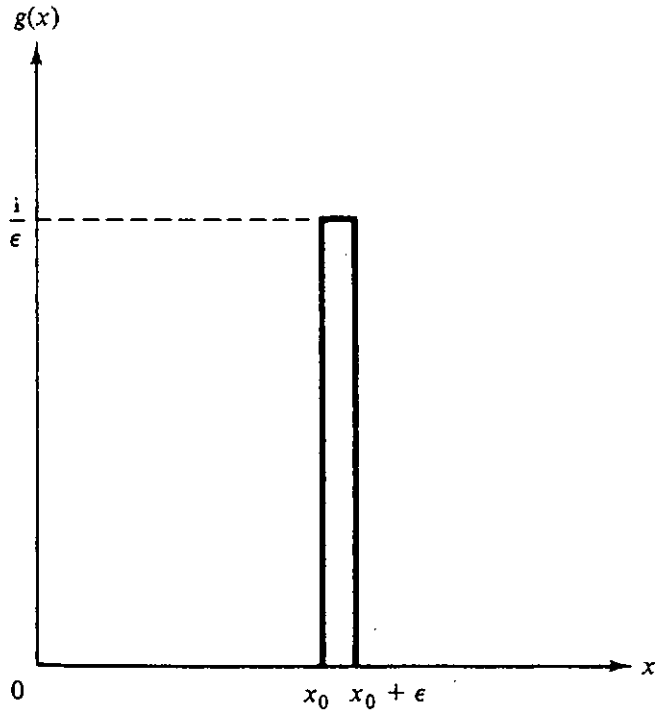

Figure A2.3 Function $g(x)$ which becomes a Dirac delta function as $\epsilon \longrightarrow 0$.

$$\delta(x - x_0) = \pi^{-1} \lim_{\epsilon \to 0^+} \frac{\epsilon}{(x - x_0)^2 + \epsilon^2}. \tag{A2.37}$$

Note that $\delta(x - x_0) = 0$ if $x \neq x_0$, and

$$\int_a^b dx\, \delta(x - x_0) = \begin{cases} 1, & a \leq x_0 \leq b, \\ 0, & \text{otherwise.} \end{cases} \tag{A2.38}$$

In the delta function properties listed below, it is assumed that $f(x)$ is a suitably well-behaved function and that $a \leq x_0 \leq b$.

$$\int_a^b dx\, f(x)\delta(x - x_0) = \int_a^b dx\, f(x)\delta(x_0 - x) = f(x_0), \tag{A2.39}$$

$$\int dy\, f(y) \int_a^b dx\, \delta(y - x)\delta(x - x_0) = \int dy\, f(y)\delta(y - x_0). \tag{A2.40}$$

If a function $g(x)$ is the argument of a delta function, then

$$\begin{aligned} \int_a^b dx\, f(x)\delta(g(x)) &= \int_a^b dx\, f(x) \sum_n \frac{\delta(x - x_n)}{|g'(x_n)|} \\ &= \sum_n \frac{f(x_n)}{|g'(x_n)|}, \end{aligned} \tag{A2.41}$$

where x_n are those roots of $g(x)$ with $a \leq x_n \leq b$, subject to $g'(x_n) \neq 0$. Thus, for example,

$$\int_a^b dx\, f(x)\delta(cx - d) = |c|^{-1} f\left(\frac{d}{c}\right), \tag{A2.42}$$

where c and d are constants, and $a \leq d/c \leq b$.

The concept of the delta function may be generalized to several dimensions. For example, in Cartesian coordinates,

$$\delta(\mathbf{r} - \mathbf{r}_0) = \delta(x - x_0)\delta(y - y_0)\delta(z - z_0). \tag{A2.43}$$

If non-Cartesian coordinates are used to express $\mathbf{r}$, it is proper to include the Jacobian in the definition of $\delta(\mathbf{r} - \mathbf{r}_0)$; thus, if $\mathbf{r} = \mathbf{r}(s, t, u)$,

$$\delta(\mathbf{r} - \mathbf{r}_0) = \frac{\delta(s - s_0)\delta(t - t_0)\delta(u - u_0)}{\partial(x, y, z)/\partial(s, t, u)}. \tag{A2.44}$$

Examples in common non-Cartesian coordinate systems are as follows. For cylindrical coordinates:

$$\delta(\mathbf{r} - \mathbf{r}_0) = \frac{\delta(r - r_0)\delta(\psi - \psi_0)\delta(z - z_0)}{r}. \tag{A2.45}$$

For spherical-polar coordinates with θ as an independent variable:

$$\delta(\mathbf{r} - \mathbf{r}_0) = \frac{\delta(r - r_0)\delta(\psi - \psi_0)\delta(\theta - \theta_0)}{r^2 \sin\theta}, \tag{A2.46}$$

$$\delta(\mathbf{\Omega} - \mathbf{\Omega}_0) = \frac{\delta(\psi - \psi_0)\delta(\theta - \theta_0)}{\sin\theta}. \tag{A2.47}$$

For spherical-polar coordinates with $\cos\theta$ as an independent variable:

$$\delta(\mathbf{r} - \mathbf{r}_0) = \frac{\delta(r - r_0)\delta(\psi - \psi_0)\delta(\cos\theta - \cos\theta_0)}{r^2}, \tag{A2.48}$$

$$\delta(\mathbf{\Omega} - \mathbf{\Omega}_0) = \delta(\psi - \psi_0)\delta(\cos\theta - \cos\theta_0). \tag{A2.49}$$

REFERENCES

1. M. Abramowitz and I. A. Stegun (eds.), *Handbook of Mathematical Functions*, NBS Appl. Math. Series 55, U.S. Government Printing Office, Washington, D.C., 1964.
2. K. Shure and O. J. Wallace, "Compact Tables of Functions for Use in Shielding Calculations," *Nucl. Sci. Eng.* **56**, 84 (1975).
3. S. Chandrasekhar, *Radiative Transfer*, Dover, New York, 1960.
4. Y. Sobouti, *Astrophys. J.*, Suppl. 7, 441 (1963).
5. M. R. Mendelson and G. L. Summerfield, "One-Speed Neutron Transport in Two Adjacent Half Spaces," *J. Math. Phys.* **5**, 668–674 (1964).
6. J. J. Duderstadt and L. J. Hamilton, *Nuclear Reactor Analysis*, Wiley, New York, 1976.

appendix 3

cross sections and related data for photon and neutron interactions

A3.1 PHOTON INTERACTIONS

The photon mass coefficients presented in the following tables are extracted from two sources, and minor discrepancies are to be noted. The discrepancies arise from different interpretations of cross section information and indicate the uncertainties in our knowledge about photon cross sections. To maintain consistency, data from the same source should be used throughout a shielding calculation.

Table A3.1 Mass Coefficients ($cm^2\ g^{-1}$) for Air[a]

E (MeV)	$\frac{\mu_C}{\rho}$	$\frac{\mu_{Ca}}{\rho}$	$\frac{\mu_{pp}}{\rho}$	$\frac{\mu_{ppa}}{\rho}$	$\frac{\mu_{ph}}{\rho}$	$\frac{\mu_{pha}}{\rho}$	$\frac{\mu}{\rho}$	$\frac{\mu_a}{\rho}$	$\frac{\mu_{en}}{\rho}$
0.01	0.132	0.00247			4.59	4.56	4.72	4.59	4.57
0.015	0.147	0.00407			1.25	1.25	1.40	1.26	1.25
0.02	0.156	0.00563			0.497	0.495	0.653	0.503	0.501
0.03	0.163	0.00846			0.131	0.131	0.293	0.140	0.139
0.04	0.163	0.0109			0.0508	0.0507	0.214	0.0624	0.0616
0.05	0.161	0.0130			0.0245	0.0244	0.186	0.0381	0.0374
0.06	0.159	0.0149			0.0135	0.0134	0.172	0.0288	0.0283
0.08	0.152	0.0178			0.00529	0.00528	0.158	0.0235	0.0231
0.1	0.146	0.0201			0.00254	0.00254	0.148	0.0230	0.0227
0.15	0.132	0.0240			0.000694	0.000694	0.133	0.0249	0.0247
0.2	0.121	0.0263			0.000278	0.000278	0.122	0.0267	0.0265
0.3	0.106	0.0286			0.0000762	0.0000762	0.106	0.0287	0.0287
0.4	0.0950	0.0294			0.0000098	0.0000098	0.095	0.0295	0.0294
0.5	0.0868	0.0298			0.0000051	0.0000051	0.0868	0.0296	0.0298
0.6	0.0803	0.0295			0.0000031	0.0000031	0.0803	0.0295	0.0295
0.8	0.0705	0.0287			0.0000015	0.0000015	0.0705	0.0289	0.0287
1	0.0636	0.0278			0.0000009	0.0000009	0.0636	0.0279	0.0278
1.5	0.0515	0.0253	0.0000968	0.0000309	0.0000004	0.0000004	0.0516	0.0256	0.0254
2	0.0438	0.0232	0.000387	0.000189	0.0000003	0.0000003	0.0442	0.0237	0.0234
3	0.0346	0.0197	0.00112	0.000740			0.0357	0.0211	0.0205
4	0.0289	0.0173	0.00187	0.00139			0.0308	0.0194	0.0187
5	0.0250	0.0154	0.00253	0.00202			0.0275	0.0182	0.0174
6	0.0221	0.0139	0.00312	0.00260			0.0252	0.0173	0.0165
8	0.0180	0.0117	0.00414	0.00361			0.0222	0.0162	0.0153
10	0.0154	0.0102	0.00495	0.00445			0.0203	0.0155	0.0146

[a]Coherent scattering is excluded and Compton coefficients are for bound electrons. Compton, photoelectric, and pair-production absorption mass coefficients have been corrected for bremsstrahlung losses. Their total is thus μ_{en}/ρ.

Source: *Ref. 1.*

Table A3.2 Mass Cofficients ($cm^2\ g^{-1}$) for Water[a]

E (MeV)	$\frac{\mu_C}{\rho}$	$\frac{\mu_{Ca}}{\rho}$	$\frac{\mu_{pp}}{\rho}$	$\frac{\mu_{ppa}}{\rho}$	$\frac{\mu_{ph}}{\rho}$	$\frac{\mu_{pha}}{\rho}$	$\frac{\mu}{\rho}$	$\frac{\mu_a}{\rho}$	$\frac{\mu_{en}}{\rho}$
0.01	0.155	0.00291			4.72	4.72	4.87	4.72	4.72
0.015	0.170	0.00470			1.28	1.28	1.45	1.29	1.29
0.02	0.178	0.00642			0.499	0.499	0.676	0.506	0.505
0.03	0.183	0.00952			0.131	0.131	0.314	0.141	0.140
0.04	0.183	0.0122			0.0499	0.0499	0.233	0.0628	0.0620
0.05	0.180	0.0146			0.0238	0.0238	0.204	0.0389	0.0383
0.06	0.177	0.0166			0.0131	0.0131	0.190	0.0302	0.0296
0.08	0.170	0.0199			0.00502	0.00502	0.175	0.0253	0.0249
0.1	0.163	0.0224			0.00240	0.00240	0.165	0.0252	0.0248
0.15	0.147	0.0268			0.000649	0.000649	0.148	0.0276	0.0274
0.2	0.135	0.0292			0.000256	0.000256	0.135	0.0297	0.0295
0.3	0.118	0.0318			0.0000699	0.0000699	0.118	0.0319	0.0319
0.4	0.106	0.0328					0.106	0.0328	0.0328
0.5	0.0966	0.0331					0.0966	0.0330	0.0331
0.6	0.0895	0.0328					0.0895	0.0329	0.0328
0.8	0.0786	0.0319					0.0786	0.0321	0.0319
1	0.0707	0.0310					0.0707	0.0311	0.0310
1.5	0.0573	0.0282	0.0000966	0.0000308			0.0574	0.0285	0.0283
2	0.0489	0.0259	0.000384	0.000188			0.0493	0.0264	0.0260
3	0.0385	0.0220	0.00112	0.000741			0.0396	0.0233	0.0227
4	0.0322	0.0193	0.00188	0.00141			0.0341	0.0214	0.0207
5	0.0278	0.0172	0.00253	0.00202			0.0303	0.0200	0.0192
6	0.0246	0.0155	0.00313	0.00261			0.0277	0.0189	0.0181
8	0.0201	0.0130	0.00416	0.00364			0.0242	0.0176	0.0167
10	0.0171	0.0113	0.00497	0.00445			0.0221	0.0167	0.0158

[a]Coherent scattering is excluded and Compton coefficients are for bound electrons. Compton, photoelectric, and pair-production absorption mass coefficients have been corrected for bremsstrahlung losses. Their total is thus μ_{en}/ρ.

Source: *Ref. 1.*

Table A3.3 Mass Cofficients ($cm^2\ g^{-1}$) for Concrete[a]

E (MeV)	$\frac{\mu_C}{\rho}$	$\frac{\mu_{Ca}}{\rho}$	$\frac{\mu_{pp}}{\rho}$	$\frac{\mu_{ppa}}{\rho}$	$\frac{\mu_{ph}}{\rho}$	$\frac{\mu_{pha}}{\rho}$	$\frac{\mu}{\rho}$	$\frac{\mu_a}{\rho}$	$\frac{\mu_{en}}{\rho}$
0.01	0.119	0.00224			26.0	25.1	26.2	26.0	25.1
0.015	0.137	0.00380			7.84	7.65	7.98	7.85	7.65
0.02	0.147	0.00531			3.27	3.21	3.42	3.28	3.21
0.03	0.156	0.00811			0.923	0.911	1.08	0.932	0.919
0.04	0.158	0.0105			0.373	0.369	0.531	0.384	0.380
0.05	0.157	0.0127			0.184	0.182	0.341	0.198	0.195
0.06	0.155	0.0146			0.103	0.103	0.259	0.119	0.117
0.08	0.150	0.0176			0.0418	0.0415	0.192	0.0600	0.0591
0.1	0.145	0.0200			0.0208	0.0207	0.166	0.0413	0.0407
0.15	0.132	0.0239			0.00583	0.00581	0.138	0.0301	0.0298
0.2	0.121	0.0262			0.00240	0.00239	0.124	0.0289	0.0286
0.3	0.106	0.0286			0.000690	0.000689	0.107	0.0294	0.0293
0.4	0.0952	0.0295			0.000275	0.000275	0.0954	0.0298	0.0298
0.5	0.0869	0.0298			0.000145	0.000145	0.0871	0.0298	0.0299
0.6	0.0805	0.0295			0.0000891	0.0000891	0.0806	0.0297	0.0296
0.8	0.0707	0.0287			0.0000426	0.0000426	0.0707	0.0289	0.0287
1	0.0636	0.0278			0.0000245	0.0000245	0.0636	0.0280	0.0278
1.5	0.0516	0.0254	0.000154	0.0000491	0.0000079	0.0000079	0.0518	0.0257	0.0254
2	0.0441	0.0232	0.000613	0.000298	0.0000048	0.0000048	0.0447	0.0240	0.0236
3	0.0347	0.0197	0.00175	0.00116	0.0000022	0.0000022	0.0364	0.0218	0.0208
4	0.0290	0.0172	0.00292	0.00217	0.0000004	0.0000004	0.0319	0.0205	0.0194
5	0.0250	0.0152	0.00391	0.00309	0.0000003	0.0000003	0.0289	0.0196	0.0183
6	0.0221	0.0138	0.00481	0.00396	0.0000003	0.0000003	0.0269	0.0191	0.0177
8	0.0181	0.0115	0.00630	0.00543	0.0000002	0.0000002	0.0244	0.0184	0.0170
10	0.0154	0.00996	0.00757	0.00665	0.0000001	0.0000001	0.0230	0.0181	0.0166

[a]Coherent scattering is excluded and Compton coefficients are for bound electrons. Compton, photoelectric, and pair-production absorption mass coefficients have been corrected for bremsstrahlung losses. Their total is thus μ_{en}/ρ. Composition by weight fraction: H, 0.0056; O, 0.4983; Na, 0.0171; Mg. 0.0024; Al, 0.0456; Si, 0.3158; S, 0.0012; K, 0.0192; Ca, 0.0826; and Fe, 0.0122.

Source: *Ref. 1.*

Table A3.4 Mass Cofficients ($cm^2\ g^{-1}$) for Iron[a]

E (MeV)	$\frac{\mu_C}{\rho}$	$\frac{\mu_{Ca}}{\rho}$	$\frac{\mu_{pp}}{\rho}$	$\frac{\mu_{ppa}}{\rho}$	$\frac{\mu_{ph}}{\rho}$	$\frac{\mu_{pha}}{\rho}$	$\frac{\mu}{\rho}$	$\frac{\mu_a}{\rho}$	$\frac{\mu_{en}}{\rho}$
0.01	0.0860	0.00162			169.	139.	169.	169.	139.
0.015	0.105	0.00290			54.4	48.0	54.5	54.4	48.0
0.02	0.116	0.00420			24.3	22.1	24.4	24.3	22.1
0.03	0.129	0.00673			7.73	7.27	7.86	7.74	7.28
0.04	0.134	0.00892			3.32	3.17	3.45	3.33	3.18
0.05	0.136	0.0110			1.68	1.62	1.82	1.69	1.63
0.06	0.136	0.0127			0.960	0.931	1.10	0.975	0.944
0.08	0.134	0.0156			0.404	0.396	0.538	0.421	0.411
0.1	0.129	0.0179			0.204	0.201	0.333	0.223	0.219
0.15	0.120	0.0217			0.0591	0.0583	0.179	0.0816	0.0800
0.2	0.111	0.0240			0.0245	0.0243	0.136	0.0490	0.0483
0.3	0.0979	0.0264			0.00722	0.00718	0.105	0.0340	0.0336
0.4	0.0881	0.0272			0.00327	0.00326	0.0913	0.0307	0.0304
0.5	0.0805	0.0275			0.00181	0.00180	0.0824	0.0294	0.0293
0.6	0.0746	0.0274			0.00115	0.00115	0.0758	0.0288	0.0286
0.8	0.0657	0.0266			0.000582	0.000581	0.0662	0.0275	0.0272
1	0.0591	0.0257			0.000354	0.000353	0.0594	0.0264	0.0260
1.5	0.0481	0.0235	0.000345	0.000107	0.000162	0.000162	0.0486	0.0244	0.0237
2	0.0410	0.0213	0.00133	0.000626	0.000100	0.000100	0.0424	0.0232	0.0221
3	0.0322	0.0180	0.00371	0.00235	0.0000539	0.0000539	0.0360	0.0224	0.0204
4	0.0270	0.0155	0.00609	0.00433	0.0000359	0.0000359	0.0331	0.0225	0.0199
5	0.0233	0.0137	0.00815	0.00614	0.0000269	0.0000269	0.0315	0.0229	0.0198
6	0.0206	0.0123	0.00995	0.00778	0.0000216	0.0000216	0.0305	0.0232	0.0201
8	0.0168	0.0102	0.0128	0.0104	0.0000156	0.0000156	0.0296	0.0240	0.0206
10	0.0143	0.00860	0.0154	0.0127	0.0000122	0.0000122	0.0298	0.0252	0.0213

[a]Coherent scattering is excluded and Compton coefficients are for bound electrons. Compton, photoelectric, and pair-production absorption mass coefficients have been corrected for bremsstrahlung losses. Their total is thus μ_{en}/ρ.

Source: *Ref. 1.*

Table A3.5 Mass Cofficients ($cm^2\ g^{-1}$) for Lead[a]

	E (MeV)	$\frac{\mu_C}{\rho}$	$\frac{\mu_{Ca}}{\rho}$	$\frac{\mu_{pp}}{\rho}$	$\frac{\mu_{ppa}}{\rho}$	$\frac{\mu_{ph}}{\rho}$	$\frac{\mu_{pha}}{\rho}$	$\frac{\mu}{\rho}$	$\frac{\mu_a}{\rho}$	$\frac{\mu_{en}}{\rho}$
	0.01	0.0456	0.000855			124.	124.	124.	124.	124.
L_{III}	0.01304	0.0549	0.00133			61.0	61.0	61.0	61.0	61.0
						158.	113.	158.	158.	113.
	0.015	0.0596	0.00165			110.	82.8	110.	110.	82.8
L_{II}	0.015200	0.0602	0.00168			107.	80.8	107.	107.	80.8
						148.	109.	148.	148.	109.
L_I	0.015861	0.0616	0.00179			132.	98.8	132.	132.	98.8
						153.	114.	153.	153.	114.
	0.02	0.0695	0.00251			83.1	66.3	83.1	83.1	66.3
	0.03	0.0828	0.00430			28.5	24.7	28.6	28.5	24.7
	0.04	0.0910	0.00608			13.2	11.9	13.3	13.2	11.9
	0.05	0.0956	0.00770			7.21	6.63	7.30	7.21	6.63
	0.06	0.0983	0.00922			4.39	4.10	4.48	4.39	4.10
	0.08	0.100	0.0117			1.97	1.87	2.07	1.99	1.88
K	0.088004	0.100	0.0126			1.51	1.44	1.61	1.52	1.45
						7.30	2.30	7.38	7.33	2.31
	0.1	0.0997	0.0138			5.23	2.08	5.32	5.26	2.09
	0.15	0.0965	0.0175			1.80	1.08	1.90	1.82	1.10
	0.2	0.0913	0.0197			0.843	0.590	0.933	0.863	0.610
	0.3	0.0814	0.0219			0.289	0.231	0.369	0.311	0.253
	0.4	0.0738	0.0225			0.141	0.119	0.215	0.164	0.142
	0.5	0.0677	0.0228			0.0823	0.0724	0.150	0.106	0.0951
	0.6	0.0631	0.0227			0.0538	0.0483	0.117	0.0773	0.0709
	0.8	0.0555	0.0220			0.0285	0.0263	0.0840	0.0515	0.0483
	1	0.0500	0.0208			0.0180	0.0169	0.0680	0.0401	0.0378
	1.5	0.0407	0.0191	0.00159	0.000480	0.00858	0.00823	0.0509	0.0305	0.0278
	2	0.0349	0.0173	0.00500	0.00229	0.00523	0.00509	0.0451	0.0288	0.0247
	3	0.0274	0.0141	0.0115	0.00692	0.00282	0.00276	0.0416	0.0299	0.0238
	4	0.0229	0.0119	0.0168	0.0112	0.00188	0.00185	0.0416	0.0326	0.0250
	5	0.0198	0.0103	0.0213	0.0148	0.00139	0.00137	0.0424	0.0352	0.0265
	6	0.0175	0.00901	0.0248	0.0176	0.00108	0.00107	0.0433	0.0372	0.0277
	8	0.0143	0.00718	0.0305	0.0217	0.000750	0.000744	0.0456	0.0407	0.0297
	10	0.0122	0.00593	0.0360	0.0254	0.000570	0.000567	0.0488	0.0451	0.0320

[a]Coherent scattering is excluded and Compton coefficients are for bound electrons. Compton, photoelectric, and pair-production absorption mass coefficients have been corrected for bremsstrahlung losses. Their total is thus μ_{en}/ρ.

Source: *Ref. 1.*

TABLE A3.6 Values of the Mass Attenuation Coefficient μ/ρ ($cm^2\ g^{-1}$) Including only Compton Scattering, the Photoelectric Effect, and Pair Production

Photon Energy (MeV)	$_1$H	$_4$Be	$_6$C	$_7$N	$_8$O	$_{11}$Na	$_{12}$Mg	$_{13}$Al
0.01	0.385	0.536	2.16	3.57	5.57	15.1	20.3	25.8
0.015	0.376	0.268	0.721	1.09	1.62	4.37	5.98	7.66
0.02	0.369	0.206	0.387	0.541	0.754	1.88	2.56	3.24
0.03	0.357	0.171	0.230	0.276	0.335	0.638	0.839	1.03
0.04	0.346	0.159	0.193	0.212	0.236	0.355	0.437	0.514
0.05	0.335	0.152	0.179	0.187	0.199	0.254	0.298	0.334
0.06	0.326	0.147	0.170	0.174	0.181	0.209	0.236	0.255
0.08	0.309	0.139	0.158	0.160	0.162	0.170	0.183	0.189
0.10	0.294	0.132	0.149	0.150	0.152	0.152	0.161	0.162
0.15	0.265	0.119	0.134	0.134	0.134	0.131	0.136	0.134
0.2	0.243	0.109	0.122	0.123	0.123	0.118	0.122	0.120
0.3	0.211	0.0945	0.106	0.106	0.107	0.102	0.106	0.103
0.4	0.189	0.0847	0.0953	0.0953	0.0954	0.0914	0.0943	0.0921
0.5	0.173	0.0773	0.0870	0.0870	0.0871	0.0834	0.0861	0.0840
0.6	0.160	0.0715	0.0805	0.0805	0.0805	0.0771	0.0796	0.0777
0.8	0.140	0.0628	0.0707	0.0707	0.0707	0.0677	0.0699	0.0682
1.0	0.126	0.0565	0.0635	0.0636	0.0636	0.0609	0.0628	0.0613
1.5	0.103	0.0459	0.0517	0.0517	0.0518	0.0496	0.0512	0.0500
2	0.0875	0.0393	0.0443	0.0444	0.0445	0.0428	0.0441	0.0431
3	0.0691	0.0313	0.0356	0.0357	0.0359	0.0348	0.0360	0.0353
4	0.0581	0.0267	0.0305	0.0308	0.0310	0.0304	0.0316	0.0311
5	0.0505	0.0235	0.0271	0.0274	0.0278	0.0276	0.0288	0.0284
6	0.0450	0.0212	0.0247	0.0251	0.0255	0.0256	0.0268	0.0266
8	0.0375	0.0182	0.0216	0.0221	0.0226	0.0232	0.0244	0.0244
10	0.0325	0.0163	0.0196	0.0203	0.0209	0.0218	0.0231	0.0232
15	0.0254	0.0136	0.0170	0.0178	0.0187	0.0203	0.0217	0.0220
20	0.0215	0.0123	0.0158	0.0167	0.0177	0.0197	0.0213	0.0217
30	0.0175	0.0110	0.0147	0.0159	0.0170	0.0196	0.0214	0.0220
40	0.0154	0.0104	0.0144	0.0157	0.0170	0.0199	0.0218	0.0225
50	0.0142	0.0102	0.0143	0.0156	0.0170	0.0203	0.0223	0.0231
60	0.0133	0.0100	0.0143	0.0157	0.0172	0.0207	0.0227	0.0236
80	0.0124	0.00993	0.0144	0.0160	0.0176	0.0213	0.0235	0.0244
100	0.0119	0.00993	0.0146	0.0162	0.0179	0.0219	0.0242	0.0251

TABLE A3.6 (Cont.)

Photon Energy (MeV)	$_{14}$Si	$_{15}$P	$_{16}$S	$_{18}$Ar	$_{19}$K	$_{20}$Ca	$_{26}$Fe	$_{29}$Cu
0.01	33.6	40.2	50.3	63.8	80.1	95.6	172.	223.
0.015	9.97	12.0	15.2	19.5	24.6	29.6	55.7	73.3
0.02	4.20	5.10	6.42	8.27	10.5	12.6	25.1	33.0
0.03	1.31	1.55	1.95	2.49	3.14	3.82	7.87	10.6
0.04	0.635	0.731	0.891	1.11	1.39	1.67	3.46	4.71
0.05	0.396	0.444	0.527	0.630	0.777	0.925	1.84	2.50
0.06	0.292	0.318	0.367	0.420	0.512	0.595	1.13	1.52
0.08	0.207	0.215	0.238	0.252	0.296	0.334	0.550	0.718
0.10	0.173	0.175	0.189	0.189	0.216	0.237	0.342	0.427
0.15	0.140	0.138	0.145	0.136	0.150	0.159	0.184	0.208
0.2	0.125	0.122	0.127	0.117	0.127	0.133	0.139	0.148
0.3	0.107	0.104	0.107	0.0979	0.106	0.109	0.107	0.108
0.4	0.0954	0.0928	0.0958	0.0868	0.0938	0.0966	0.0921	0.0919
0.5	0.0870	0.0846	0.0873	0.0789	0.0852	0.0877	0.0829	0.0821
0.6	0.0804	0.0781	0.0806	0.0729	0.0786	0.0809	0.0761	0.0752
0.8	0.0706	0.0685	0.0707	0.0639	0.0689	0.0709	0.0664	0.0654
1.0	0.0634	0.0617	0.0635	0.0574	0.0619	0.0636	0.0596	0.0586
1.5	0.0517	0.0502	0.0517	0.0468	0.0505	0.0519	0.0486	0.0478
2	0.0447	0.0436	0.0448	0.0406	0.0439	0.0452	0.0425	0.0419
3	0.0367	0.0358	0.0371	0.0338	0.0366	0.0377	0.0361	0.0359
4	0.0324	0.0317	0.0329	0.0302	0.0328	0.0340	0.0331	0.0332
5	0.0297	0.0292	0.0304	0.0280	0.0306	0.0317	0.0315	0.0318
6	0.0279	0.0275	0.0287	0.0267	0.0292	0.0304	0.0306	0.0310
8	0.0257	0.0255	0.0268	0.0252	0.0277	0.0289	0.0299	0.0307
10	0.0246	0.0245	0.0259	0.0245	0.0270	0.0284	0.0299	0.0310
15	0.0235	0.0237	0.0252	0.0242	0.0269	0.0284	0.0309	0.0324
20	0.0234	0.0236	0.0253	0.0246	0.0274	0.0291	0.0322	0.0341
30	0.0239	0.0243	0.0262	0.0257	0.0287	0.0308	0.0347	0.0370
40	0.0246	0.0251	0.0271	0.0267	0.0300	0.0321	0.0367	0.0393
50	0.0252	0.0258	0.0279	0.0276	0.0311	0.0333	0.0384	0.0412
60	0.0256	0.0264	0.0286	0.0284	0.0319	0.0343	0.0397	0.0426
80	0.0268	0.0275	0.0299	0.0297	0.0335	0.0359	0.0418	0.0449
100	0.0276	0.0283	0.0308	0.0307	0.0346	0.0371	0.0432	0.0466

TABLE A3.6 (Cont.)

Photon Energy (MeV)	$_{42}$Mo	$_{50}$Sn	$_{53}$I	$_{74}$W	$_{82}$Pb	$_{92}$U	Absorption Edges
0.01	84.0	139.	158.	91.2	132.	173.	
0.015	26.8	44.3	53.4	136.	112.	60.3	L_3 edge
0.02	11.7	20.1	24.7	63.7	83.4	68.5	
0.03	28.3	41.5	7.98	21.5	27.9	39.6	L_2, L_1 edges
0.04	13.0	18.4	22.3	9.86	13.0	18.7	
0.05	6.97	9.94	12.3	5.39	7.17	10.4	
0.06	4.25	6.15	7.55	3.30	4.47	6.45	
0.08	1.92	2.95	3.52	7.66	2.12	3.04	
0.10	1.05	1.64	1.91	4.29	5.62	1.71	K edge
0.15	0.399	0.597	0.673	1.50	1.99	2.47	
0.2	0.228	0.311	0.349	0.738	0.969	1.23	
0.3	0.131	0.155	0.168	0.302	0.385	0.484	
0.4	0.101	0.110	0.116	0.180	0.221	0.273	
0.5	0.0858	0.0911	0.0936	0.129	0.154	0.185	
0.6	0.0766	0.0790	0.0807	0.103	0.120	0.140	
0.8	0.0663	0.0655	0.0660	0.0772	0.0856	0.0963	
1.0	0.0576	0.0571	0.0574	0.0639	0.0689	0.0754	
1.5	0.0467	0.0459	0.0459	0.0487	0.0509	0.0538	
2	0.0414	0.0408	0.0409	0.0433	0.0450	0.0470	
3	0.0365	0.0366	0.0369	0.0401	0.0415	0.0435	
4	0.0348	0.0355	0.0359	0.0398	0.0414	0.0434	
5	0.0343	0.0353	0.0359	0.0406	0.0424	0.0443	
6	0.0343	0.0357	0.0364	0.0416	0.0436	0.0455	
8	0.0351	0.0370	0.0378	0.0440	0.0467	0.0481	
10	0.0363	0.0387	0.0397	0.0466	0.0496	0.0509	
15	0.0396	0.0428	0.0441	0.0527	0.0553	0.0578	
20	0.0425	0.0464	0.0479	0.0581	0.0611	0.0641	
30	0.0473	0.0520	0.0539	0.0663	0.0701	0.0739	
40	0.0507	0.0560	0.0581	0.0720	0.0760	0.0804	
50	0.0534	0.0591	0.0614	0.0764	0.0806	0.0854	
60	0.0555	0.0615	0.0640	0.0798	0.0843	0.0893	
80	0.0587	0.0653	0.0678	0.0848	0.0899	0.0950	
100	0.0611	0.0678	0.0705	0.0881	0.0936	0.0993	

Source: *Ref. 2.*

Table A3.7 Values[a] of the Mass Absorption Coefficient μ_a/ρ, the Mass Energy Transfer Coefficient μ_{tr}/ρ, and the Mass Energy Absorption Coefficient μ_{en}/ρ ($cm^2\ g^{-1}$)

Photon Energy (MeV)	Air			Water			$_1H$			$_6C$			$_7N$		
	μ_a/ρ	μ_{tr}/ρ	μ_{en}/ρ	μ_a/ρ	μ_{tr}/ρ	μ_{en}/ρ	μ_a/ρ	μ_{tr}/ρ	μ_{en}/ρ	μ_a/ρ	μ_{tr}/ρ	μ_{en}/ρ	μ_a/ρ	μ_{tr}/ρ	μ_{en}/ρ
0.01	4.63	4.61	4.61	4.79			0.00986			1.97			3.38		
0.015	1.27	1.27	1.27	1.28			0.0110			0.536			0.908		
0.02	0.512	0.511	0.511	0.512			0.0135			0.208			0.362		
0.03	0.148			0.149			0.0185			0.0594			0.105		
0.04	0.0668			0.0677			0.0231			0.0306			0.0493		
0.05	0.0406			0.0418			0.0271			0.0233			0.0319		
0.06	0.0305			0.0320			0.0306			0.0211			0.0256		
0.08	0.0243			0.0262			0.0362			0.0205			0.0223		
0.10	0.0234			0.0256			0.0406			0.0215			0.0224		
0.15	0.0250			0.0277			0.0481			0.0245			0.0247		
0.2	0.0268			0.0297			0.0525			0.0265			0.0267		
0.3	0.0287			0.0319			0.0569			0.0287			0.0287		
0.4	0.0295			0.0328			0.0586			0.0295			0.0295		
0.5	0.0297		0.0296	0.0330			0.0593			0.0297			0.0297		0.0296
0.6	0.0296		0.0295	0.0329			0.0587			0.0296		0.0295	0.0296		0.0295
0.8	0.0289		0.0289	0.0321			0.0574			0.0289		0.0288	0.0289		0.0289
1	0.0280		0.0278	0.0311		0.0309	0.0555			0.0279		0.0279	0.0280		0.0279
1.5	0.0256		0.0254	0.0284		0.0282	0.0507			0.0256		0.0255	0.0256		0.0255
2	0.0237	0.0236	0.0234	0.0263	0.0262	0.0260	0.0465		0.0464	0.0237	0.0235	0.0234	0.0237	0.0236	0.0234
3	0.0211	0.0207	0.0205	0.0233	0.0229	0.0227	0.0400	0.0399	0.0398	0.0209	0.0206	0.0204	0.0211	0.0207	0.0205
4	0.0195	0.0189	0.0186	0.0214	0.0209	0.0206	0.0355	0.0353	0.0352	0.0191	0.0187	0.0185	0.0194	0.0189	0.0186
5	0.0182	0.0178	0.0174	0.0200	0.0195	0.0191	0.0320	0.0319	0.0317	0.0178	0.0174	0.0171	0.0181	0.0177	0.0173
6	0.0173	0.0168	0.0164	0.0190	0.0185	0.0180	0.0294	0.0292	0.0290	0.0168	0.0164	0.0161	0.0172	0.0167	0.0163
8	0.0163	0.0157	0.0152	0.0176	0.0170	0.0166	0.0255	0.0253	0.0252	0.0155	0.0151	0.0147	0.0161	0.0156	0.0151
10	0.0156	0.0151	0.0145	0.0168	0.0162	0.0157	0.0229	0.0227	0.0225	0.0147	0.0143	0.0138	0.0154	0.0149	0.0143

Table A3.7 (Continued)

Photon Energy (MeV)	$_8$O			$_{11}$Na			$_{12}$Mg			$_{13}$Al			$_{14}$Si		
	μ_a/ρ	μ_{tr}/ρ	μ_{en}/ρ	μ_a/ρ	μ_{tr}/ρ	μ_{en}/ρ	μ_a/ρ	μ_{tr}/ρ	μ_{en}/ρ	μ_a/ρ	μ_{tr}/ρ	μ_{en}/ρ	μ_a/ρ	μ_{tr}/ρ	μ_{en}/ρ
0.01	5.39			14.9			20.1			25.6	25.5	25.5	33.4	33.3	33.3
0.015	1.44			4.20			5.80			7.48	7.47	7.47	9.78	9.75	9.75
0.02	0.575			1.70			2.38			3.06			4.02	4.01	4.01
0.03	0.165			0.475			0.671			0.868			1.14	1.14	1.14
0.04	0.0733			0.199			0.276			0.357			0.473	0.472	0.472
0.05	0.0437			0.106			0.144			0.184			0.241		
0.06	0.[illegible]2			0.0668			0.0888			0.111			0.144		
0.08	0.0249			0.0382			0.0475			0.0562			0.0700		
0.10	0.0237			0.0297			0.0346			0.0386			0.0459		
0.15	0.0251			0.0260			0.0279			0.0285			0.0312		
0.2	0.0268			0.0264			0.0277			0.0276			0.0292		
0.3	0.0288			0.0277			0.0288			0.0282			0.0294		
0.4	0.0295			0.0284			0.0294			0.0287			0.0298		
0.5	0.0297			0.0285			0.0294			0.0287		0.0286	0.0298		
0.6	0.0296			0.0284			0.0293			0.0286		0.0286	0.0296		0.0295
0.8	0.0289			0.0277		0.0275	0.0286		0.0285	0.0279		0.0277	0.0289		0.0288
1	0.0280		0.0278	0.0268		0.0266	0.0276		0.0275	0.0270		0.0269	0.0279		0.0277
1.5	0.0256		0.0254	0.0246	0.0245	0.0243	0.0254	0.0253	0.0251	0.0248	0.0247	0.0245	0.0257	0.0255	0.0253
2	0.0238	0.0236	0.0234	0.0230	0.0227	0.0225	0.0237	0.0234	0.0232	0.0232	0.0229	0.0226	0.0241	0.0237	0.0234
3	0.0212	0.0208	0.0206	0.0208	0.0202	0.0199	0.0216	0.0210	0.0206	0.0212	0.0206	0.0202	0.0221	0.0214	0.0210
4	0.0196	0.0191	0.0188	0.0195	0.0188	0.0184	0.0204	0.0196	0.0191	0.0201	0.0193	0.0188	0.0211	0.0202	0.0196
5	0.0185	0.0179	0.0175	0.0186	0.0179	0.0174	0.0196	0.0187	0.0181	0.0194	0.0185	0.0179	0.0204	0.0194	0.0187
6	0.0177	0.0171	0.0166	0.0181	0.0173	0.0167	0.0190	0.0182	0.0175	0.0190	0.0181	0.0172	0.0200	0.0191	0.0182
8	0.0166	0.0160	0.0155	0.0174	0.0167	0.0159	0.0185	0.0177	0.0168	0.0186	0.0177	0.0168	0.0197	0.0187	0.0177
10	0.0160	0.0154	0.0148	0.0172	0.0164	0.0155	0.0183	0.0176	0.0165	0.0185	0.0176	0.0165	0.0198	0.0188	0.0175

Table A3.7 (Continued)

Photon Energy (MeV)	$_{15}$P			$_{16}$S			$_{18}$Ar			$_{19}$K			$_{20}$Ca		
	μ_a/ρ	μ_{tr}/ρ	μ_{en}/ρ	μ_a/ρ	μ_{tr}/ρ	μ_{en}/ρ	μ_a/ρ	μ_{tr}/ρ	μ_{en}/ρ	μ_a/ρ	μ_{tr}/ρ	μ_{en}/ρ	μ_a/ρ	μ_{tr}/ρ	μ_{en}/ρ
0.01	40.1	39.8	39.8	50.1	49.7	49.7	63.6	62.3	62.3	79.9	77.6	77.6	95.4	91.6	91.6
0.015	11.9	11.8	11.8	15.0	14.9	14.9	19.3	19.1	19.1	24.4	23.9	23.9	29.4	28.6	28.6
0.02	4.93	4.91	4.91	6.24	6.21	6.21	8.10	8.02	8.02	10.3	10.2	10.2	12.4	12.2	12.2
0.03	1.39	1.39	1.39	1.77	1.77	1.77	2.33	2.31	2.31	2.97	2.94	2.94	3.65	3.60	3.60
0.04	0.573	0.572	0.572	0.729	0.727	0.727	0.967	0.962	0.962	1.23	1.23	1.23	1.51	1.50	1.50
0.05	0.293			0.372			0.490	0.488	0.488	0.626	0.623	0.623	0.770	0.764	0.764
0.06	0.173			0.218			0.285	0.284	0.284	0.368	0.366	0.366	0.447	0.444	0.444
0.08	0.0820			0.101			0.128			0.162	0.162	0.162	0.197	0.196	0.196
0.10	0.0511			0.0609			0.0735			0.0915	0.0913	0.0913	0.109		
0.15	0.0322			0.0357			0.0377			0.0442			0.0497		
0.2	0.0293			0.0311			0.0304			0.0343			0.0371		
0.3	0.0288			0.0299			0.0278			0.0304			0.0318		
0.4	0.0291			0.0301			0.0275			0.0298			0.0309		
0.5	0.0291			0.0300			0.0272			0.0294		0.0293	0.0304		
0.6	0.0288			0.0297			0.0269		0.0268	0.0291		0.0290	0.0300		0.0299
0.8	0.0280		0.0278	0.0290		0.0288	0.0262		0.0261	0.0283		0.0282	0.0291		0.0289
1	0.0272		0.0270	0.0280		0.0278	0.0253		0.0251	0.0273		0.0270	0.0281	0.0280	0.0278
1.5	0.0249	0.0248	0.0246	0.0257	0.0256	0.0253	0.0233	0.0232	0.0229	0.0251	0.0250	0.0247	0.0259	0.0257	0.0254
2	0.0236	0.0231	0.0228	0.0242	0.0238	0.0235	0.0220	0.0215	0.0212	0.0238	0.0233	0.0229	0.0245	0.0240	0.0236
3	0.0216	0.0209	0.0204	0.0225	0.0216	0.0211	0.0206	0.0198	0.0192	0.0223	0.0214	0.0208	0.0231	0.0220	0.0214
4	0.0207	0.0198	0.0192	0.0216	0.0205	0.0199	0.0200	0.0189	0.0182	0.0217	0.0206	0.0198	0.0226	0.0213	0.0205
5	0.0201	0.0191	0.0184	0.0211	0.0200	0.0192	0.0197	0.0185	0.0177	0.0215	0.0202	0.0193	0.0225	0.0211	0.0200
6	0.0198	0.0188	0.0179	0.0209	0.0197	0.0188	0.0196	0.0184	0.0174	0.0215	0.0202	0.0190	0.0225	0.0211	0.0198
8	0.0197	0.0187	0.0175	0.0208	0.0197	0.0184	0.0198	0.0186	0.0173	0.0218	0.0205	0.0190	0.0229	0.0215	0.0198
10	0.0198	0.0188	0.0174	0.0210	0.0200	0.0184	0.0201	0.0190	0.0174	0.0223	0.0210	0.0191	0.0235	0.0222	0.0201

Table A3.7 (Continued)

Photon Energy (MeV)	$_{26}$Fe			$_{29}$Cu			$_{50}$Sn			$_{82}$Pb			$_{92}$U		
	μ_a/ρ	μ_{tr}/ρ	μ_{en}/ρ	μ_a/ρ	μ_{tr}/ρ	μ_{en}/ρ	μ_a/ρ	μ_{tr}/ρ	μ_{en}/ρ	μ_a/ρ	μ_{tr}/ρ	μ_{en}/ρ	μ_a/ρ	μ_{tr}/ρ	μ_{en}/ρ
0.01	171.	142.	142.	223.	160.	160.	139.	136.5	136.4	132.	131.	131.	173.	171.	170.
0.015	55.5	49.3	49.3	73.2	59.4	59.4	44.1	43.7	43.6	112.	91.7	91.7	60.2	59.6	59.4
0.02	24.9	22.8	22.8	32.8	28.2	28.2	20.0	19.8	19.8	83.3	69.2	69.1	68.3	55.5	55.5
0.03	7.72	7.28	7.28	10.5	9.50	9.50	41.4	16.2	16.2	27.8	24.6	24.6	39.4	33.0	33.0
0.04	3.31	3.17	3.17	4.56	4.24	4.24	18.3	9.97	9.96	12.9	11.8	11.8	18.6	16.3	16.3
0.05	1.69	1.64	1.64	2.35	2.22	2.22	9.81	6.25	6.24	7.05	6.57	6.54	10.3	9.30	9.25
0.06	0.989	0.961	0.961	1.39	1.32	1.32	6.03	4.20	4.19	4.35	4.11	4.08	6.34	5.82	5.78
0.08	0.422	0.414	0.414	0.593	0.573	0.573	2.84	2.19	2.18	2.01	1.92	1.91	2.94	2.76	2.73
0.10	0.223	0.219	0.219	0.311	0.302	0.302	1.53	1.26	1.25	5.51	2.28	2.28	1.61	1.54	1.52
0.15	0.0820	0.0814	0.0814	0.108	0.106	0.106	0.504	0.446	0.442	1.90	1.16	1.15	2.39	1.12	1.19
0.2	0.0498	0.0495	0.0495	0.0602	0.0597	0.0597	0.230	0.211	0.209	0.893	0.637	0.629	1.15	0.712	0.704
0.3	0.0342	0.0335	0.0335	0.0371	0.0370	0.0370	0.0892	0.0853	0.0843	0.324	0.265	0.259	0.425	0.322	0.315
0.4	0.0308			0.0318			0.0550	0.0536	0.0530	0.169	0.147	0.143	0.222	0.184	0.178
0.5	0.0295			0.0298			0.0428	0.0423	0.0416	0.108	0.0984	0.0951	0.140	0.122	0.118
0.6	0.0287		0.0286	0.0287		0.0286	0.0361	0.0358	0.0353	0.0792	0.0737	0.0710	0.100	0.0902	0.0864
0.8	0.0275		0.0273	0.0273	0.0272	0.0271	0.0302	0.0301	0.0294	0.0525	0.0503	0.0481	0.0640	0.0599	0.0569
1	0.0264		0.0262	0.0261	0.0261	0.0258	0.0271	0.0270	0.0264	0.0407	0.0396	0.0377	0.0479	0.0458	0.0432
1.5	0.0243	0.0241	0.0237	0.0240	0.0237	0.0233	0.0239	0.0233	0.0226	0.0303	0.0288	0.0271	0.0336	0.0317	0.0295
2	0.0233	0.0225	0.0220	0.0230	0.0222	0.0217	0.0234	0.0220	0.0210	0.0286	0.0259	0.0240	0.0310	0.0278	0.0255
3	0.0225	0.0212	0.0204	0.0225	0.0211	0.0202	0.0243	0.0219	0.0205	0.0299	0.0260	0.0234	0.0321	0.0276	0.0246
4	0.0225	0.0209	0.0199	0.0228	0.0211	0.0200	0.0259	0.0232	0.0212	0.0324	0.0281	0.0245	0.0346	0.0298	0.0256
5	0.0228	0.0211	0.0198	0.0233	0.0214	0.0200	0.0275	0.0247	0.0221	0.0350	0.0306	0.0259	0.0371	0.0324	0.0270
6	0.0232	0.0215	0.0199	0.0239	0.0220	0.0202	0.0291	0.0262	0.0230	0.0374	0.0331	0.0272	0.0394	0.0348	0.0281
8	0.0243	0.0226	0.0204	0.0252	0.0234	0.0209	0.0319	0.0292	0.0245	0.0419	0.0378	0.0294	0.0434	0.0392	0.0298
10	0.0254	0.0238	0.0209	0.0265	0.0248	0.0215	0.0345	0.0319	0.0258	0.0457	0.0419	0.0310	0.0471	0.0432	0.0312

[a]Values are given for μ_{tr}/ρ and μ_{en}/ρ only if they are different from μ_a/ρ.

Source: *Ref. 2.*

TABLE A3.8 Thermal Absorption and Scattering Cross Sections for Some Naturally Occurring Elements with 2200 m s^{-1} Neutrons

Atomic Number	Element or Compound	Atomic or Mol. Wt.	Density[a] (g/cm^3)	Nuclei per Unit Volume[a] (10^{+24} cm^{-3})	Microscopic Cross Section (barns)	
					σ_a	σ_s
1	H	1.008	8.9[b]	5.3[b]	0.33	38
	H_2O	18.016	1	0.0335[c]	0.66	103
	D_2O	20.030	1.10	0.0331[c]	0.001	13.6
3	Li	6.940	0.534	0.0463	71	1.4
4	Be	9.013	1.85	0.1236	0.010	7.0
	BeO	25.02	3.025	0.0728[c]	0.010	6.8
5	B	10.82	2.45	0.1364	755	4
6	C	12.011	1.60	0.0803	0.004	4.8
7	N	14.008	0.0013	5.3[b]	1.88	10
8	O	16.000	0.0014	5.3[b]	20[b]	4.2
11	Na	22.991	0.971	0.0254	0.525	4
12	Mg	24.32	1.74	0.0431	0.069	3.6
13	Al	26.98	2.699	0.0602	0.241	1.4
14	Si	28.09	2.42	0.0522	0.16	1.7
15	P	30.975	1.82	0.0354	0.20	5
16	S	32.066	2.07	0.0389	0.52	1.1
19	K	39.100	0.87	0.0134	2.07	1.5
20	Ca	40.08	1.55	0.0233	0.44	3.0
24	Cr	52.01	7.1	0.0822	3.1	3
25	Mn	54.94	7.2	0.0789	13.2	2.3
26	Fe	55.85	7.86	0.0848	2.62	11
27	Co	58.94	8.9	0.0910	38	7
28	Ni	58.71	8.90	0.0913	4.6	17.5
29	Cu	63.54	8.94	0.0848	3.85	7.2
30	Zn	65.38	7.14	0.0658	1.10	3.6
40	Zr	91.22	6.4	0.0423	0.185	8
47	Ag	107.88	10.5	0.0586	63	6
48	Cd	112.41	8.65	0.0464	2450	7
49	In	114.82	7.28	0.0382	191	2.2
50	Sn	118.70	6.5	0.0330	0.625	4
51	Sb	121.76	6.69	0.0331	5.7	4.3
52	Te	127.61	6.24	0.0295	4.7	5
53	I	126.91	4.93	0.0234	7.0	3.6
62	Sm	150.35	7.7	0.0309	5600	5
63	Eu	152	5.22	0.0207	4300	8
74	W	183.86	19.3	0.0632	19.2	5
79	Au	197	19.32	0.0591	98.8	9.3
80	Hg	200.61	13.55	0.0407	380	20
81	Tl	204.39	11.85	0.0349	3.4	14
82	Pb	207.21	11.35	0.0330	0.170	11
83	Bi	209	9.747	0.0281	0.034	9
90	Th	232.05	11.3	0.0293	7.56	12.6
91	Pa	231	15.4	0.0402	200	—
92	U	238.07	18.9	0.0478	7.68	8.3
	UO_2	270.07	10	0.0223[c]	7.6	16.7

[a]Mass and atomic densities are for the pure element at standard temperature and pressure.
[b]Value has been multiplied by 10^5.
[c]Molecules/cm^3.

Source: *Excerpted from Ref. 3.*

Table A3.9 Cross Section and Photon Yields for Thermal Neutron Capture in Various Elements

Z	Element	Capture Cross Section	Photons/100 Captures for Energy Ranges (MeV)										
			0–1	1–2	2–3	3–4	4–5	5–6	6–7	7–8	8–9	9–10	10–11
1	Hydrogen	330 mb	0.00	0.00	100.00	0.00	0.00	0.00	0.00	0.00	0.00	0.00	0.00
3	Lithium	33 mb	12.42	4.91	89.33	0.00	0.00	0.00	1.07	4.02	0.00	0.00	0.00
4	Beryllium	9.5 mb	25.52	0.00	24.15	46.29	0.00	2.01	62.90	0.00	0.00	0.00	0.00
5	Boron	102 mb	0.00	0.00	0.00	0.00	110.14	0.00	39.50	47.85	0.00	0.00	0.00
6	Carbon	3.4 mb	0.00	29.75	0.00	32.40	68.27	0.00	0.00	0.00	0.00	0.00	0.00
7	Nitrogen	75 mb	13.02	0.00	51.68	46.83	22.84	19.69	24.65	0.00	0.00	0.00	0.00
11	Sodium	534 mb	92.67	20.47	72.65	65.36	3.23	6.33	22.44	0.00	0.00	0.00	0.00
12	Magnesium	63 mb	59.63	68.75	64.04	95.83	6.62	10.77	11.57	3.72	4.74	0.75	0.00
13	Aluminum	235 mb	27.51	8.77	31.25	26.02	37.09	8.12	10.29	38.74	0.00	0.00	0.00
14	Silicon	160 mb	11.72	13.28	31.93	82.66	63.78	4.50	13.61	7.04	2.03	0.00	0.00
15	Phosphorus	190 mb	40.66	54.11	52.13	54.48	26.90	12.89	18.09	7.89	0.00	0.00	0.00
16	Sulfur	512 mb	75.55	0.00	77.18	36.42	17.94	63.48	0.00	3.91	2.66	0.00	0.00
17	Chlorine	33.2 b	31.30	73.53	30.15	20.99	13.79	13.46	37.73	20.37	2.99	0.00	0.00
19	Potassium	2.10 b	54.35	46.71	59.27	38.55	26.17	37.36	3.52	6.10	0.00	0.00	0.00
20	Calcium	430 mb	24.01	93.49	51.87	17.11	23.03	12.54	43.84	2.16	0.00	0.00	0.00
22	Titanium	6.09 b	30.97	80.89	6.95	12.49	11.14	2.39	84.95	0.30	0.19	0.00	0.00
24	Chromium	3.10 b	40.51	16.07	20.67	9.22	4.21	11.03	11.89	24.61	37.66	10.97	0.00
25	Manganese	13.3 b	17.50	12.42	24.21	15.42	17.05	31.34	10.76	37.99	0.00	0.00	0.00
26	Iron	2.62 b	27.83	24.76	9.54	11.32	11.22	10.93	10.12	58.86	0.82	4.15	0.11
27	Cobalt	38.0 b	93.74	20.54	15.94	17.84	15.66	33.62	34.67	11.39	0.00	0.00	0.00
28	Nickel	4.6 b	26.16	6.59	6.05	3.65	3.70	7.45	17.04	14.04	58.99	0.00	0.00
29	Copper	3.85 b	81.75	6.02	4.57	4.96	10.10	10.19	16.21	64.87	0.00	0.00	0.00
30	Zinc	1.10 b	16.00	63.86	51.02	28.37	21.16	19.64	18.20	18.70	1.30	1.11	0.00
32	Germanium	2.45 b	110.18	64.17	66.77	38.26	26.62	19.57	18.06	5.08	1.46	0.01	0.00
40	Zirconium	185 mb	80.78	60.86	84.07	47.18	25.07	15.50	22.00	1.20	0.81	0.00	0.00
42	Molybdenum	2.7 b	82.89	83.30	87.29	46.35	27.74	15.64	10.65	2.89	1.04	0.00	0.00
47	Silver	63.0 b	68.31	44.12	78.08	42.41	25.12	19.08	5.93	1.74	0.00	0.00	0.00
48	Cadmium	3620 b	103.99	37.27	98.08	59.40	30.72	24.32	5.58	2.62	0.81	0.29	0.00
49	Indium	198 b	33.57	106.96	100.67	37.58	18.27	7.40	0.93	0.00	0.00	0.00	0.00
50	Tin	625 mb	14.10	61.46	105.42	59.74	32.28	18.01	9.94	6.18	1.10	0.29	0.00
73	Tantalum	19.1 b	45.13	58.41	86.61	40.97	20.39	6.21	0.83	0.00	0.00	0.00	0.00
74	Tungsten	19.1 b	79.87	27.60	68.04	33.96	19.30	13.54	9.68	1.19	0.00	0.00	0.00
80	Mercury	372 b	91.86	46.40	58.11	28.80	36.26	36.82	11.22	0.63	0.00	0.00	0.00
82	Lead	170 mb	0.00	0.00	0.00	0.00	0.00	0.00	5.04	94.06	0.00	0.00	0.00
83	Bismuth	34 mb	0.00	0.00	0.00	0.00	111.70	0.00	0.00	0.00	0.00	0.00	0.00

Source: *Data of Ref. 4.*

Table A3.10 Photon Production Cross Sections for Fast-Neutron Inelastic or Nonelastic Interactions with Several Nuclides and Elements[a]

Element or Isotope	Gamma Energy Group (MeV)	Photon Production Cross Section for Fast Neutrons (mb)									
		Neutron Energy (MeV)									
		0.5	1	1.5	2	3	4	5	7	10	14
$^{6}Li^{b}$	3.5–4.0							7.5	5.4	5.0	5.0
$^{7}Li^{b}$	0.45–0.51		147	200	195	217	284	282	226	138	80
$^{10}B^{c}$	4.0–4.5								3.5	4.0	1.8
	3.0–4.0						1.3	3.3	13.4	14.0	6.3
	2.0–3.0					3.0	11.5	27.3	33.9	27.1	12.1
	1.0–1.66				1.2	15.4	34.4	48.3	46.2	31.2	16.2
	0.7–0.8		0.2	4.7	67.9	48.0	72.9	106	87.8	59.4	28.1
$^{12}C^{d}$	4.0–4.5							28.2	188	346	221
$^{16}O^{c}$	7.0–7.5									44	53
	6.0–7.0								50	150	178
	4.0–5.0										20
	2.0–3.0									10	50
	1.66–2.0									2	10
$^{23}Na^{b}$	6.0–7.0								33	93	26
	5.0–6.0								117	220	40
	4.0–5.0							44	87	53	55
	3.0–4.0						27	97	112	70	68
	2.0–3.0					116	291	237	250	118	118
	1.0–2.0					124	263	260	255	148	204
	0.6–1.0					10	32	30	33	38	60
	0.4–0.45	13.7	479	336	565	642	668	628	628	250	4.5
Si[c]	10.0–12.0										25
	8.0–10.0									17	51
	7.0–8.0									77	51
	6.0–7.0								6	102	112
	5.0–6.0								11	85	99
	4.0–5.0							2	65	69	77
	3.0–4.0						3	8	52	38	73
	2.0–3.0					32	40	79	165	141	169
	1.66–2.0				213	477	543	589	596	469	384
	1.0–1.66			11	20	19	30	39	42	69	82

Table A3.10 (Continued)

Element or Isotope	Gamma Energy Group (MeV)	Photon Production Cross Section for Fast Neutrons (mb)									
		Neutron Energy (MeV)									
		0.5	1	1.5	2	3	4	5	7	10	14
Al[c]	8.0–10.0									27	37
	7.0–8.0									51	48
	6.0–7.0								21	75	66
	5.0–6.0								80	132	96
	4.0–5.0							27	99	122	113
	3.0–4.0						117	139	257	277	265
	2.0–3.0					187	272	308	396	444	366
	1.33–2.0					31	80	77	86	122	116
	1.0–1.33			141	208	233	225	235	230	182	115
	0.7–1.0		2.8	94	94	94	135	128	111	90	61
Fe[b]	8.0–10.0									47	60
	7.0–8.0									68	42
	6.0–7.0								23	129	110
	5.0–6.0								74	168	103
	4.0–5.0							20	105	220	137
	3.0–4.0					2.3	166	333	411	475	248
	2.0–3.0					86	442	502	634	609	313
	1.0–2.0			11	47	291	615	858	1120	1270	879
	0.8–1.0		400	698	865	1030	1210	1280	1320	1240	742
	0.45–0.8					97	233	240	120	168	120
Pb[b]	6.0–7.0								68	22	7
	5.0–6.0							3	172	54	101
	4.0–5.0						14	192	329	115	382
	3.0–4.0						56	160	407	182	505
	2.0–3.0					287	976	1470	1860	465	876
	1.0–2.0			6	79	300	676	1050	1520	1080	1610
	0.7–1.0		105	264	376	575	982	1250	1280	1300	1210
	0.51–0.7		100	154	252	425	1070	1370	1310	1280	1230
	0.4–0.51			6	15	28	89	168	183	178	210
	0.2–0.4			20	31	66	210	310	293	368	320

[a]Cross sections are negligible for omitted gamma energy groups.
[b]Cross sections are for all nonelastic reactions.
[c]Cross sections are for all inelastic scatterings.
[d]Cross sections are for inelastic scattering from the first excited state.

Source: *Data of Ref. 5.*

Table A3.11 Gamma Photon Activity Due to Thermal Neutron Capture

Radioactive Isotope	Half-Life	$E\gamma$ (MeV)	Yield % Per Disintegration	Parent Isotope	Isotopic % or Half-Life	Activation Cross Section (barns)
^{12}B	0.027 s	~4.5	~4	^{11}B	81.2	<50 mb
^{16}N	7.4 s	6.1	55	^{15}N	0.37	24 ± 8 μb
		7.1	20			
^{19}O	29.4 s	1.4	70	^{18}O	0.20	0.21 ± 0.04 mb
^{24}Na	15.1 h	2.76	99.96	^{23}Na	100	0.53 ± 0.02
		1.38	99.96			
		4.14	0.04			
^{28}Al	2.3 m	1.78	100	^{27}Al	100	0.21 ± 0.02
^{31}Si	2.65 h	1.26	0.07	^{30}Si	3.12	0.11 ± 0.01
^{41}A	1.83 h	1.37	99.3	^{40}A	99.6	0.53 ± 0.02
^{42}K	12.46 h	1.53	18	^{41}K	6.91	1.15 ± 0.11
^{47}Ca	4.9 d	1.31	71	^{46}Ca	0.0033	0.25 ± 0.10
		0.82	5			
		0.49	5			
^{49}Ca	8.8 m	3.10	89.78	^{48}Ca	0.185	1.1 ± 0.1
		4.05	9.88			
^{56}Mn	2.58 h	2.98	0.4	^{55}Mn	100	13.4 ± 0.3
		2.13	15			
		2.65	1.8			
		1.81	24			
		0.845	99			
^{59}Fe	45.1 d	0.191	3	^{58}Fe	0.31	0.9 ± 0.2
		1.29	43			
		1.10	57			

^{60m}Co	10.5 m	0.058	99.7	^{59}Co	100	16 ± 3
^{60}Co	5.3 y	1.17	99.9	^{59}Co	100	20 ± 3
		1.33	100	^{60m}Co	10.5 m (99.7%)	
^{95}Zr	63.3 d	0.754	54	^{94}Zr	17.4	0.09 ± 0.03
		0.722	43			
^{97}Zr	17 h	1.15	80	^{96}Zr	2.8	0.10 ± 0.05
		1.72	20			
		0.58	80			
^{116m}In	54.2 m	0.137[a]	3	^{115}In	95.8	145 ± 15
		1.49	21			
		0.40	25			
		1.27	129			
		2.09	25			
^{233}Th	22.1 m	0.662	0.05	^{232}Th	100	7.34 ± 0.15
		0.448	0.10			
		0.350	0.004			
		0.172	0.03			
^{233}Pa	26.95 d	0.417[a]	20	^{233}Th	23.5 m	
		0.104	35			
		0.313	80			
		0.058	111			
		0.028	39			
^{239}U	23.5 m	0.075	100	^{238}U	99.274	2.76 ± 0.09
^{239}Np	2.33 d	0.067[a]	62	^{239}U	23.5 m	
		0.285	87			
		0.105	30			
		0.228	4			

[a]Effective values—multiple gamma photons are grouped and assigned the highest energy in the group.

Source: *Excerpted from Ref. 6.*

Table A3.12 Data for the Neutron Kerma Response Function [7] in a Four-Element Approximation to Tissue[a] [8]

E (MeV)	$\mathfrak{R}_K(E)$ (cGy cm^2)	E (MeV)	$\mathfrak{R}_K(E)$ (cGy cm^2)
0.110(−04)	0.147(−11)	0.900(+00)	0.217(−08)
0.200(−04)	0.122(−11)	0.940(+00)	0.227(−08)
0.360(−04)	0.112(−11)	0.980(+00)	0.245(−08)
0.630(−04)	0.122(−11)	0.105(+01)	0.248(−08)
0.110(−03)	0.156(−11)	0.115(+01)	0.246(−08)
0.200(−03)	0.237(−11)	0.125(+01)	0.256(−08)
0.360(−03)	0.393(−11)	0.135(+01)	0.265(−08)
0.630(−03)	0.662(−11)	0.145(+01)	0.269(−08)
0.110(−02)	0.114(−10)	0.155(+01)	0.277(−08)
0.200(−02)	0.204(−10)	0.165(+01)	0.287(−08)
0.360(−02)	0.362(−10)	0.175(+01)	0.291(−08)
0.630(−02)	0.622(−10)	0.185(+01)	0.303(−08)
0.110(−01)	0.106(−09)	0.195(+01)	0.304(−08)
0.200(−01)	0.183(−09)	0.210(+01)	0.313(−08)
0.360(−01)	0.303(−09)	0.230(+01)	0.318(−08)
0.630(−01)	0.470(−09)	0.250(+01)	0.331(−08)
0.820(−01)	0.567(−09)	0.270(+01)	0.346(−08)
0.860(−01)	0.587(−09)	0.290(+01)	0.360(−08)
0.900(−01)	0.605(−09)	0.310(+01)	0.373(−08)
0.940(−01)	0.624(−09)	0.330(+01)	0.406(−08)
0.980(−01)	0.641(−09)	0.350(+01)	0.415(−08)
0.105(+00)	0.672(−09)	0.370(+01)	0.425(−08)
0.115(+00)	0.713(−09)	0.390(+01)	0.418(−08)
0.125(+00)	0.752(−09)	0.420(+01)	0.431(−08)
0.135(+00)	0.789(−09)	0.460(+01)	0.431(−08)
0.145(+00)	0.825(−09)	0.500(+01)	0.455(−08)
0.155(+00)	0.860(−09)	0.540(+01)	0.444(−08)
0.165(+00)	0.892(−09)	0.580(+01)	0.464(−08)
0.175(+00)	0.924(−09)	0.620(+01)	0.475(−08)
0.185(+00)	0.954(−09)	0.660(+01)	0.489(−08)
0.195(+00)	0.983(−09)	0.700(+01)	0.510(−08)
0.210(+00)	0.103(−08)	0.740(+01)	0.537(−08)
0.230(+00)	0.108(−08)	0.780(+01)	0.529(−08)
0.250(+00)	0.113(−08)	0.820(+01)	0.525(−08)
0.270(+00)	0.118(−08)	0.860(+01)	0.542(−08)
0.290(+00)	0.123(−08)	0.900(+01)	0.551(−08)
0.310(+00)	0.128(−08)	0.940(+01)	0.555(−08)
0.330(+00)	0.132(−08)	0.980(+01)	0.568(−08)
0.350(+00)	0.137(−08)	0.105(+02)	0.582(−08)
0.370(+00)	0.142(−08)	0.115(+02)	0.624(−08)
0.390(+00)	0.148(−08)	0.125(+02)	0.621(−08)
0.420(+00)	0.162(−08)	0.135(+02)	0.645(−08)
0.460(+00)	0.164(−08)	0.145(+02)	0.670(−08)
0.500(+00)	0.160(−08)	0.155(+02)	0.687(−08)
0.540(+00)	0.165(−08)	0.165(+02)	0.695(−08)
0.580(+00)	0.171(−08)	0.175(+02)	0.705(−08)
0.620(+00)	0.177(−08)	0.185(+02)	0.715(−08)
0.660(+00)	0.183(−08)	0.195(+02)	0.727(−08)
0.700(+00)	0.189(−08)	0.210(+02)	0.742(−08)
0.740(+00)	0.194(−08)	0.230(+02)	0.739(−08)
0.780(+00)	0.199(−08)	0.250(+02)	0.734(−08)
0.820(+00)	0.204(−08)	0.270(+02)	0.736(−08)
0.860(+00)	0.210(−08)	0.290(+02)	0.724(−08)

[a]Composition, by mass is 10.1% H, 11.1% C, 2.6% N, and 76.2% O. For $E < 10^{-5}$ MeV, the kerma response function can be calculated approximately as $\mathfrak{R}_K(E) = 3.3 \times 10^{-15} E^{-1/2}$, where $\mathfrak{R}_K$ and E have the same units as in this table [Derived from data of Ref. 9].

Source: *Ref. 7, reproduced by permission of Academic Press, Inc., and the authors.*

REFERENCES

1. E. Storm and H. I. Israel, "Photon Cross Sections from 0.001 to 100 MeV for Elements 1 through 100," Report LA-3753, Los Alamos Scientific Laboratory, Los Alamos, N.Mex. 1967.
2. J. H. Hubbell and M. J. Berger, "Photon Attenuation and Energy Absorption Coefficients. Tabulations and Discussion," 2nd ed., Report 8681, National Bureau of Standards, Washington, D.C., 1966.
3. "Reactor Physics Constants," 2nd ed., Report ANL-5800, Argonne National Laboratory, Argonne, Ill., 1963, p. 30.
4. V. J. Orphan, N. C. Rasmussen, and T. L. Harper, "Line and Continuum Gamma-Ray Yields from Thermal Neutron Capture in 75 Elements," Report GA-10248, Gulf General Atomic, Inc., San Diego, CA, 1970.
5. R. W. Roussin, C. R. Weisbin, J. E. White, N. M. Green, R. Q. Wright, and J. B. Wright, "VITAMIN-C: The CRT Processed Multigroup Cross Section Library for Neutronics Studies," ORNL/RSIC-37 (ENDF-296), Radiation Shielding Information Center, Oak Ridge National Laboratory, Oak Ridge, Tenn., 1980.
6. "Reactor Physics Constants," 2nd. ed., Report ANL-5800, Argonne National Laboratory, Argonne, Ill., 1963, p. 638.
7. R. S. Caswell and J. J. Coyne, "Kerma Factors for Neutron Energies below 30 MeV," *Radiat. Res.* **83**, 217–254 (1980).
8. "Radiation Quantities and Units," Report 33, International Commission on Radiation Units and Measurements, Washington, D.C., 1980, p. 20.
9. "Protection against Neutron Radiation," Report 38, National Council on Radiation Protection and Measurements, Washington, D.C., 1971.

appendix 4

buildup factors for gamma photons

Tables A4.1 to A4.8 in this appendix list buildup factors for monoenergetic point isotropic photon sources in infinite, homogeneous shielding media. Tables A4.9 and A4.10 list parameters for the Berger form of the buildup factor. Tables A4.11 and A4.13 list parameters for the Taylor and related forms of the buildup factor. Table A4.12 lists buildup factors for photons obliquely incident on concrete slabs.

Buildup factors depend not only upon the photon initial energy, E_0, the shielding medium, and the mean-free-path lengths $\mu_0 r$ of penetration, but also upon the type of detector response. The following is a guide to the selection of appropriate data for buildup factors with various combinations of attenuating media and detector responses:

Shielding Medium	Type of Detector Response	
	Kerma in Air	Kerma in Shielding Medium
Air	A4.1	A4.1, A4.9
Water	A4.2, A4.10, A4.13	A4.2, A4.9
Concrete	A4.3, A4.10, A4.11, A4.12	A4.4, A4.9
Iron	A4.5, A4.10	A4.6, A4.9
Lead	A4.7, A4.10	A4.8, A4.9

As indicated in the tables, buildup factors for air-kerma response are essentially the same as those for exposure response.

Table A4.1 Energy Transfer (Kerma) and Exposure Buildup Factors for an Isotropic Point Source in Air[a]

	E_0 (MeV)										
$\mu_0 r$	0.04	0.06	0.08	0.1	0.2	0.5	1	2	5	10	15
0	1.00	1.00	1.00	1.00	1.00	1.00	1.00	1.00	1.00	1.00	1.00
0.5	2.20	2.58	2.52	2.35	1.90	1.60	1.47	1.38	1.29	1.20	1.15
1	3.38	4.76	4.83	4.46	3.28	2.44	2.08	1.83	1.57	1.37	1.28
2	5.85	10.8	12.0	11.4	7.74	4.84	3.60	2.81	2.09	1.68	1.49
3	8.47	18.9	22.9	22.5	15.0	8.21	5.46	3.86	2.60	1.97	1.70
4	11.2	29.1	37.9	38.4	25.6	12.6	7.60	4.96	3.11	2.26	1.90
5	14.1	41.5	57.4	59.9	40.0	17.9	10.0	6.13	3.61	2.54	2.11
6	17.0	56.1	82.0	87.8	58.9	24.2	12.7	7.35	4.12	2.82	2.30
7	20.1	73.2	112	123	82.8	31.6	15.6	8.61	4.62	3.10	2.50
8	23.3	92.7	148	166	112	40.1	18.8	9.92	5.12	3.37	2.70
10	30.0	140	242	282	192	60.6	25.8	12.6	6.13	3.92	3.08
15	49.0	316	636	800	545	134	47.0	20.0	8.63	5.25	4.03
20	71.4	596	1,350	1,810	1,220	241	72.8	27.9	11.1	6.55	4.96
25	97.2	1,010	2,540	3,570	2,360	385	103	36.2	13.6	7.84	5.87
30	126	1,600	4,390	6,430	4,150	567	136	45.0	16.1	9.11	6.75
35	159	2,410	7,140	10,600	6,770	788	173	54.0	18.5	10.4	7.58
40	195	3,480	11,100	15,700	10,500	1,050	212	63.2	21.0	11.6	8.31

[a]The data were obtained from calculations for an energy-transfer (kerma) detector, but are valid for exposure detectors also with errors of less than a few percent.

Source: *Ref. 1; by permission of the American Nuclear Society.*

Table A4.2 Energy Transfer (Kerma) and Exposure Buildup Factors for an Isotropic Point Source in Water[a]

	E_0 (MeV)										
$\mu_0 r$	0.04	0.06	0.08	0.1	0.2	0.5	1	2	5	10	15
0	1.00	1.00	1.00	1.00	1.00	1.00	1.00	1.00	1.00	1.00	1.00
0.5	2.27	2.63	2.54	2.36	1.92	1.61	1.47	1.38	1.29	1.21	1.16
1	3.58	4.94	4.93	4.52	3.42	2.45	2.08	1.83	1.57	1.38	1.29
2	6.41	11.5	12.5	11.7	8.22	4.87	3.62	2.82	2.10	1.70	1.51
3	9.50	20.6	24.3	23.5	15.7	8.29	5.50	3.87	2.62	2.00	1.72
4	12.8	32.4	40.8	40.6	26.4	12.7	7.66	4.99	3.12	2.29	1.93
5	16.3	46.9	62.7	64.0	41.3	18.1	10.1	6.16	3.63	2.57	2.14
6	19.9	64.3	90.6	94.8	61.0	24.6	12.8	7.38	4.14	2.85	2.34
7	23.8	84.8	125	134	86.2	32.2	15.7	8.66	4.64	3.13	2.53
8	27.8	109	167	183	118	40.8	18.9	9.97	5.14	3.40	2.73
10	36.5	167	278	314	202	61.8	26.0	12.7	6.14	3.94	3.11
15	61.6	390	754	917	582	137	47.4	20.1	8.62	5.24	4.04
20	92.1	758	1,650	2,120	1,310	247	73.5	28.0	11.1	6.51	4.93
25	128	1,320	3,160	4,260	2,580	395	104	36.4	13.5	7.75	5.81
30	169	2,140	5,560	7,780	4,640	582	138	45.2	15.9	8.97	6.64
35	216	3,270	9,190	13,100	7,890	809	175	54.3	18.3	10.2	7.42
40	269	4,820	14,500	20,300	12,800	1,080	214	63.6	20.7	11.3	8.09

[a]The data were obtained from calculations for an energy-transfer (kerma) detector, but are valid for exposure detectors also with errors of less than a few percent.

Source: *Ref. 1; by permission of the American Nuclear Society.*

Table A4.3 Exposure (Air Kerma) Buildup Factors for an Isotropic Point Source in Ordinary Concrete

	E_0 (MeV)										
$\mu_0 r$	0.04	0.06	0.08	0.1	0.2	0.5	1	2	5	10	15
0	1.00	1.00	1.00	1.00	1.00	1.00	1.00	1.00	1.00	1.00	1.00
0.5	1.30	1.68	1.84	1.89	1.78	1.57	1.45	1.37	1.27	1.19	1.15
1	1.46	2.15	2.58	2.78	2.72	2.27	1.98	1.77	1.53	1.35	1.26
2	1.69	2.89	3.96	4.63	5.05	4.03	3.24	2.65	2.04	1.64	1.46
3	1.87	3.54	5.31	6.63	8.00	6.26	4.72	3.60	2.53	1.93	1.66
4	2.01	4.17	6.69	8.80	11.6	8.97	6.42	4.61	3.03	2.22	1.86
5	2.14	4.77	8.09	11.1	15.9	12.2	8.33	5.68	3.54	2.51	2.07
6	2.25	5.34	9.52	13.6	20.9	15.9	10.4	6.80	4.05	2.80	2.28
7	2.35	5.90	11.0	16.3	26.7	20.2	12.7	7.97	4.57	3.10	2.50
8	2.45	6.44	12.5	19.2	33.4	25.0	15.2	9.18	5.09	3.40	2.71
10	2.62	7.52	15.7	25.6	49.6	36.4	20.7	11.7	6.15	4.01	3.16
15	2.98	10.2	24.3	44.9	109	75.6	37.2	18.6	8.85	5.57	4.34
20	3.27	12.7	33.8	69.1	201	131	57.1	26.0	11.6	7.19	5.59
25	3.51	15.2	44.3	97.9	331	203	80.1	33.9	14.4	8.86	6.91
30	3.73	18.2	55.4	131	507	292	106	42.2	17.3	10.6	8.27
35	3.91	21.9	66.8	170	734	399	134	50.9	20.5	12.3	9.63
40	4.03	26.5	78.1	214	1,020	523	164	59.8	24.8	14.5	10.9

Source: *Ref. 2; by permission of the American Nuclear Society.*

Table A4.4 Energy Transfer (Kerma) Buildup Factors for an Isotropic Point Source in Ordinary Concrete

	E_0 (MeV)										
$\mu_0 r$	0.04	0.06	0.08	0.1	0.2	0.5	1	2	5	10	15
0	1.00	1.00	1.00	1.00	1.00	1.00	1.00	1.00	1.00	1.00	1.00
0.5	1.31	1.81	2.19	2.39	2.11	1.66	1.49	1.39	1.32	1.18	1.13
1	1.47	2.37	3.27	3.89	3.65	2.55	2.11	1.83	1.57	1.34	1.24
2	1.72	3.25	5.30	7.06	7.69	4.89	3.59	2.80	2.05	1.61	1.42
3	1.90	4.02	7.26	10.4	12.9	7.89	5.35	3.82	2.54	1.88	1.61
4	2.04	4.74	9.21	14.1	19.3	11.6	7.35	4.92	3.04	2.16	1.80
5	2.17	5.43	11.2	17.9	27.0	16.0	9.61	6.07	3.55	2.43	1.99
6	2.28	6.08	13.2	22.1	36.0	21.1	12.1	7.28	4.06	2.71	2.18
7	2.39	6.72	15.3	26.6	46.6	27.0	14.8	8.55	4.58	2.99	2.38
8	2.48	7.35	17.4	31.5	58.8	33.7	17.8	9.86	5.10	3.28	2.58
10	2.66	8.59	21.9	42.1	88.5	49.6	24.3	12.6	6.16	3.85	3.00
15	3.02	11.6	34.1	74.7	199	105	44.0	20.0	8.86	5.33	4.08
20	3.31	14.5	47.6	116	372	183	67.9	28.1	11.6	6.86	5.23
25	3.57	17.4	62.4	165	620	286	95.5	36.7	14.4	8.45	6.45
30	3.79	20.0	78.3	222	958	414	126	45.7	17.3	10.1	7.71
35	3.96	22.3	95.3	286	1,400	567	160	55.0	20.2	11.7	8.97
40	4.08	23.9	113	358	1,940	747	197	64.6	23.9	13.4	10.2

Source: *Ref. 2; by permission of the American Nuclear Society.*

Table A4.5 Exposure (Air Kerma) Buildup Factors for an Isotropic Point Source in Iron

	E_0 (MeV)										
$\mu_0 r$	0.04	0.06	0.08	0.1	0.2	0.5	1	2	5	10	15
0	1.00	1.00	1.00	1.00	1.00	1.00	1.00	1.00	1.00	1.00	1.00
0.5	1.04	1.11	1.19	1.26	1.47	1.48	1.41	1.35	1.27	1.19	1.14
1	1.06	1.15	1.27	1.40	1.86	1.99	1.85	1.71	1.51	1.33	1.24
2	1.08	1.21	1.39	1.61	2.59	3.12	2.85	2.49	1.97	1.59	1.41
3	1.09	1.25	1.49	1.78	3.33	4.44	4.00	3.34	2.46	1.86	1.59
4	1.10	1.29	1.57	1.94	4.08	5.96	5.30	4.25	2.98	2.16	1.80
5	1.11	1.32	1.64	2.07	4.85	7.68	6.74	5.22	3.53	2.50	2.04
6	1.12	1.34	1.70	2.20	5.64	9.58	8.31	6.25	4.11	2.87	2.31
7	1.13	1.37	1.75	2.31	6.44	11.7	10.0	7.33	4.73	3.27	2.61
8	1.13	1.39	1.81	2.41	7.25	14.0	11.8	8.45	5.38	3.71	2.95
10	1.14	1.42	1.90	2.61	8.90	19.1	15.8	10.8	6.75	4.69	3.77
15	1.16	1.49	2.08	3.01	13.2	35.1	27.5	17.4	10.7	7.88	6.80
20	1.17	1.54	2.22	3.33	17.6	55.4	41.3	24.6	15.2	12.3	11.8
25	1.18	1.58	2.34	3.61	22.2	79.9	57.0	32.5	20.3	18.1	20.0
30	1.19	1.62	2.45	3.86	26.9	108	74.5	40.9	25.9	25.7	32.8
35	1.20	1.64	2.53	4.07	31.7	141	93.5	49.8	32.0	35.3	52.6
40	1.21	1.66	2.59	4.23	36.4	177	114	59.1	38.8	47.6	82.8

Source: *Ref. 1; by permission of the American Nuclear Society.*

Table A4.6 Energy Transfer (Kerma) Buildup Factors for an Isotropic Point Source in Iron

	E_0 (MeV)										
$\mu_0 r$	0.04	0.06	0.08	0.1	0.2	0.5	1	2	5	10	15
0	1.00	1.00	1.00	1.00	1.00	1.00	1.00	1.00	1.00	1.00	1.00
0.5	1.04	1.12	1.23	1.38	2.13	1.79	1.53	1.40	1.26	1.15	1.10
1	1.06	1.17	1.34	1.45	2.94	2.66	2.14	1.84	1.49	1.27	1.18
2	1.08	1.23	1.51	1.94	4.34	4.57	3.50	2.76	1.93	1.48	1.31
3	1.09	1.28	1.61	2.13	5.72	6.75	5.04	3.74	2.39	1.69	1.44
4	1.10	1.31	1.70	2.31	7.14	9.25	6.79	4.80	2.86	1.93	1.59
5	1.11	1.34	1.78	2.48	8.58	12.1	8.74	5.93	3.37	2.19	1.76
6	1.12	1.37	1.84	2.63	10.0	15.3	10.9	7.12	3.91	2.47	1.96
7	1.12	1.39	1.91	2.77	11.5	18.8	13.2	8.37	4.47	2.78	2.17
8	1.13	1.41	1.96	2.90	13.1	22.7	15.7	9.67	5.07	3.12	2.42
10	1.14	1.45	2.06	3.13	16.1	31.4	21.1	12.4	6.33	3.87	2.99
15	1.16	1.52	2.26	3.61	24.2	58.8	37.1	20.0	9.92	6.29	5.06
20	1.17	1.57	2.41	4.00	32.5	93.9	56.2	28.5	14.1	9.59	8.44
25	1.18	1.61	2.54	4.34	41.0	136	77.9	37.7	18.7	14.0	13.8
30	1.19	1.65	2.65	4.63	49.8	186	102	47.4	23.7	19.6	22.2
35	1.20	1.67	2.73	4.85	58.8	242	128	57.7	28.9	26.7	35.0
40	1.20	1.68	2.77	4.98	68.1	305	156	68.4	34.0	35.4	54.1

Source: *Ref. 1; by permission of the American Nuclear Society.*

Table A4.7 Exposure (Air Kerma) Buildup for an Isotropic Point Source in Lead[a]

	E_0 (MeV)									
$\mu_0 r$	0.04	0.06	0.08	0.1	0.2	0.5	1	2	5	10
0	1.00	1.00	1.00	1.00	1.00	1.00	1.00	1.00	1.00	1.00
0.5	1.01	1.02	1.04	1.77	1.10	1.16	1.23	1.26	1.21	1.12
1	1.01	1.03	1.06	2.35	1.22	1.24	1.38	1.44	1.32	1.18
2	1.02	1.04	1.08	3.68	1.27	1.38	1.66	1.80	1.56	1.31
3	1.02	1.05	1.09	5.96	1.27	1.50	1.93	2.17	1.85	1.48
4	1.02	1.06	1.11	9.84	1.29	1.61	2.18	2.55	2.19	1.68
5	1.03	1.06	1.12	16.2	1.31	1.70	2.42	2.93	2.58	1.93
6	1.03	1.07	1.12	26.4	1.32	1.79	2.65	3.32	3.01	2.24
7	1.03	1.07	1.13	43.2	1.34	1.87	2.86	3.71	3.50	2.63
8	1.03	1.07	1.14	71.1	1.35	1.94	3.07	4.11	4.05	3.11
10	1.03	1.08	1.15	198	1.37	2.07	3.47	4.93	5.36	4.43
15	1.04	1.09	1.17	2,810	1.40	2.34	4.37	7.04	10.1	11.8
20	1.04	1.10	1.19	40,700	1.43	2.55	5.19	9.26	17.9	33.0
25	1.04	1.10	1.20	60(+4)	1.45	2.74	5.95	11.6	30.2	93.4
30	1.04	1.11	1.21	94(+5)	1.47	2.90	6.66	13.9	48.8	262
35	1.04	1.11	1.22	16(+7)	1.48	3.04	7.34	16.4	76.4	722
40	1.05	1.11	1.23	29(+8)	1.47	3.14	8.01	19.0	117	1,960

[a]A number such as 60(+4) means 60×10^4.

Source: *Unpublished data of G. L. Simmons and C. M. Eisenhauer.*

Table A4.8 Energy Transfer (Kerma) Buildup Factors for an Isotropic Point Source in Lead[a]

	E_0 (MeV)									
$\mu_0 r$	0.04	0.06	0.08	0.1	0.2	0.5	1	2	5	10
0	1.00	1.00	1.00	1.00	1.00	1.00	1.00	1.00	1.00	1.00
0.5	1.01	1.03	1.05	2.05	1.81	1.84	1.93	1.78	1.20	1.12
1	1.01	1.03	1.07	2.78	1.83	1.72	1.95	1.96	1.33	1.17
2	1.02	1.04	1.09	4.70	1.85	1.90	2.28	2.29	1.63	1.29
3	1.02	1.05	1.11	8.24	1.87	2.11	2.74	2.80	1.89	1.40
4	1.02	1.06	1.12	14.2	1.89	2.28	3.14	3.34	2.18	1.54
5	1.02	1.06	1.13	23.6	1.91	2.42	3.51	3.88	2.53	1.70
6	1.03	1.07	1.14	38.7	1.92	2.55	3.86	4.42	2.91	1.91
7	1.03	1.07	1.15	63.4	1.94	2.67	4.20	4.95	3.35	2.16
8	1.03	1.08	1.15	104	1.96	2.78	4.53	5.50	3.83	2.46
10	1.03	1.08	1.17	292	1.98	2.97	5.14	6.63	4.98	3.28
15	1.03	1.09	1.19	4,150	2.04	3.37	6.53	9.55	9.15	7.65
20	1.04	1.10	1.20	59,500	2.08	3.69	7.78	12.6	15.9	19.9
25	1.04	1.11	1.22	87(+4)	2.11	3.96	8.93	15.8	26.5	54.1
30	1.04	1.11	1.23	13(+6)	2.13	4.20	10.0	19.2	42.5	148
35	1.04	1.11	1.23	22(+7)	2.16	4.40	11.1	22.5	66.1	404
40	1.04	1.11	1.24	38(+8)	2.17	4.54	12.1	25.6	100	1,080

[a]A number such as 87(+4) means 87×10^4.

Source: *Unpublished data of G. L. Simmons and C. M. Eisenhauer.*

Table A4.9 Parameters for the Berger Form of the Material Kerma Buildup Factor for an Isotropic Point Source in Five Materials[a]

Energy (MeV)	Air			Water			Concrete			Iron			Lead		
	a	*b*	Max. % Dev.	*a*	*b*	Max. % Dev.	*a*	*b*	Max. % Dev.	*a*	*b*	Max. % Dev.	*a*	*b*	Max. % Dev.
0.015	0.08	−0.034	8.0	0.10	−0.040	7.9	0.01	−0.029	2.1	0.00		1.0			
0.02	0.23	−0.032	11.6	0.27	−0.032	12.0	0.03	−0.041	3.6	0.00		2.9			
0.03	0.93	−0.009	11.8	1.08	−0.008	9.8	0.11	−0.041	8.7	0.01	−0.039	1.6	0.00		2.0
0.04	2.40	0.018	2.2	2.69	0.024	4.8	0.27	−0.035	12.6	0.02	−0.032	3.9	0.01	−0.074	1.9
0.05	4.05	0.050	14.2	4.48	0.057	16.4	0.57	−0.027	13.8	0.04	−0.034	5.7	0.01	−0.049	1.4
0.06	5.27	0.075	22.6	5.67	0.082	25.1	0.99	−0.016	10.2	0.08	−0.043	7.2	0.01	−0.028	2.3
0.08	6.11	0.102	33.3	6.41	0.108	35.4	2.01	0.008	4.3	0.18	−0.039	11.7	0.03	−0.045	3.7
0.1	5.93	0.113	39.3	5.71	0.121	42.5	2.90	0.030	8.0	0.36	−0.037	14.1	0.32	0.474	43.6
0.15	4.70	0.121	41.0	4.71	0.125	42.7	3.87	0.057	16.8	0.94	−0.017	12.5	0.46	−0.068	30.7
0.2	3.94	0.113	40.8	4.11	0.117	38.6	3.65	0.069	22.0	1.56	0.001	4.9	0.26	−0.065	21.3
0.3	3.10	0.094	37.0	3.13	0.096	37.4	2.99	0.071	24.9	2.10	0.022	6.9	0.22	−0.051	16.3
0.4	2.61	0.079	32.5	2.63	0.080	33.1	2.53	0.065	24.2	2.06	0.034	10.8	0.27	−0.044	15.6
0.5	2.29	0.067	29.2	2.30	0.068	29.4	2.23	0.058	23.0	1.93	0.037	12.8	0.33	−0.037	15.1
0.6	2.05	0.058	25.7	2.07	0.058	26.4	1.99	0.052	21.3	1.78	0.037	13.6	0.40	−0.033	13.3
0.8	1.71	0.045	20.8	1.73	0.045	20.9	1.69	0.041	18.5	1.55	0.033	13.6	0.49	−0.026	11.9
1	1.50	0.035	17.2	1.51	0.035	17.1	1.45	0.034	15.4	1.32	0.030	13.6	0.55	−0.020	10.0
1.5	1.16	0.021	10.7	1.17	0.021	10.6	1.14	0.021	9.8	1.10	0.020	8.6	0.55	−0.004	11.7
2	0.97	0.013	6.6	0.98	0.013	6.8	0.96	0.014	6.2	0.94	0.016	6.6	0.59	0.000	4.8
3	0.75	0.005	2.6	0.76	0.004	2.5	0.75	0.006	3.2	0.72	0.013	4.7	0.41	0.027	10.1
4	0.61	0.001	1.2	0.62	0.000	1.3	0.61	0.003	1.7	0.57	0.013	4.1	0.33	0.036	3.7
5	0.53	−0.002	2.0	0.53	−0.002	2.1	0.50	0.003	2.1	0.45	0.016	5.0	0.24	0.057	5.6
6	0.47	−0.004	1.9	0.46	−0.003	3.3	0.45	0.000	2.2	0.38	0.019	4.4	0.18	0.074	7.9
8	0.37	−0.004	3.7	0.38	−0.005	4.6	0.35	0.001	2.7	0.27	0.027	3.7	0.09	0.116	10.4
10	0.31	−0.004	3.9	0.32	−0.006	4.0	0.29	0.001	2.4	0.21	0.035	3.5	0.05	0.154	14.4
15	0.23	−0.006	3.1	0.23	−0.006	3.7	0.19	0.005	2.5	0.11	0.063	4.6			

[a]Data are valid, within the absolute deviations noted, over the range 0 to 40 mean-free-path lengths.

Source: *Refs. 1 and 3; by permission of the American Nuclear Society. Values for lead were obtained from unpublished buildup factor data by Eisenhauer and Simmons.*

Table A4.10 Parameters for the Berger Form of the Air Kerma Buildup Factor for a Point Isotropic Source in Four Materials[a]

Energy (MeV)	Water			Concrete			Iron			Lead		
	a	*b*	Max. % Dev.	*a*	*b*	Max. % Dev.	*a*	*b*	Max. Dev. %	*a*	*b*	Max. % Dev.
0.015	0.09	−0.036	8.1	0.01	−0.029	2.1	0.00		1.0			
0.02	0.26	−0.032	10.9	0.03	−0.041	3.6	0.02	−0.032	3.9			
0.03	1.01	−0.006	10.0	0.10	−0.036	8.8	0.01	−0.036	2.1	0.00		2.0
0.04	2.58	0.024	4.6	0.26	−0.035	12.1	0.02	−0.032	3.9	0.01	−0.066	2.1
0.05	4.36	0.057	16.5	0.52	−0.026	12.8	0.04	−0.034	5.7	0.01	−0.046	1.5
0.06	5.59	0.082	25.4	0.78	−0.008	12.5	0.07	−0.039	6.7	0.01	−0.028	2.3
0.08	6.47	0.108	35.5	1.42	0.007	4.1	0.14	−0.034	9.2	0.02	−0.029	3.9
0.1	6.11	0.120	40.8	1.83	0.028	5.8	0.24	−0.030	9.8	0.20	0.479	44.5
0.15	4.88	0.125	42.7	2.19	0.054	15.0	0.52	−0.015	7.1	0.21	−0.075	18.9
0.2	4.13	0.118	39.3	2.20	0.065	19.2	0.77	0.004	2.0	0.08	−0.054	10.0
0.3	3.18	0.096	38.2	2.03	0.067	21.3	1.06	0.022	7.2	0.08	−0.040	7.0
0.4	2.67	0.080	33.7	1.87	0.061	21.7	1.15	0.033	10.8	0.11	−0.033	6.6
0.5	2.32	0.068	29.9	1.73	0.055	20.7	1.16	0.036	12.2	0.15	−0.028	7.0
0.6	2.07	0.059	26.7	1.60	0.049	19.7	1.14	0.036	12.8	0.19	−0.024	7.1
0.8	1.74	0.045	21.4	1.41	0.040	16.9	1.09	0.032	12.7	0.25	−0.019	6.5
1	1.50	0.036	17.0	1.27	0.032	14.6	1.03	0.028	11.6	0.30	−0.015	5.3
1.5	1.16	0.021	10.6	1.02	0.021	9.7	0.88	0.020	8.6	0.36	−0.007	3.7
2	0.97	0.013	7.1	0.89	0.014	6.8	0.76	0.018	8.4	0.38	0.004	1.9
3	0.74	0.005	2.5	0.71	0.007	3.1	0.66	0.014	4.8	0.37	0.019	3.9
4	0.62	0.000	0.9	0.59	0.004	1.0	0.56	0.015	4.1	0.31	0.038	4.1
5	0.52	−0.002	2.1	0.49	0.004	3.2	0.49	0.017	4.0	0.24	0.062	3.2
6	0.47	−0.005	2.0	0.45	0.002	1.6	0.42	0.021	2.9	0.19	0.082	3.0
8	0.38	−0.006	3.7	0.36	0.001	2.2	0.33	0.028	3.2	0.11	0.125	7.7
10	0.31	−0.005	3.9	0.30	0.003	2.9	0.25	0.039	3.2	0.07	0.161	10.5
15	0.23	−0.008	2.9	0.21	0.004	2.5	0.15	0.066	4.8			

[a]These air kerma parameters may be used as a good approximation for evaluating the exposure buildup factor except at high energies in lead. Data are valid, within the absolute deviations noted, over the range 0 to 40 mean-free-path lengths.

Source: *Refs. 1 and 3; by permission of the American Nuclear Society. Values for lead are based on unpublished buildup factor data by Eisenhauer and Simmons.*

Table A4.11 Parameters for the Taylor Form of the Exposure Buildup Factor for Gamma Photons from a Point Isotropic Source in Ordinary Concrete, to 40 Mean-Free-Path Lengths

Source Energy (MeV)	Parameter			Maximum Percent Deviation
	A	α	β	
0.04	2.33	−0.0147	0.317	4.5
0.06	5.29	−0.0414	0.210	5.3
0.08	18.3	−0.0382	0.0469	4.7
0.10	73.8	−0.0394	−0.0145	6.0
0.20	144	−0.0741	−0.0598	20.2
0.50	62.0	−0.0688	−0.0424	22.2
1.00	97.0	−0.0396	−0.0271	15.2
2.00	38.7	−0.0250	−0.00227	7.0
5.00	10.42	−0.0244	0.0269	1.5
10.00	5.10	−0.0269	0.0450	2.3
15.00	4.04	−0.0267	0.0393	2.7

Source: *Ref. 4; by permission of the American Nuclear Society.*

Table A4.12 Exposure Buildup Factors for Gamma Photons Obliquely Incident on Slabs of Ordinary Concrete

	0.661 MeV			
mfp	$\cos\theta_0 = 1.0$	0.75	0.50	0.25
1.0	1.94 ± 0.06[a]	1.90 ± 0.05	2.37 ± 0.05	4.55 ± 0.12
2.0	2.79 ± 0.07	3.10 ± 0.10	5.21 ± 0.15	61.0 ± 2.2
4.0	5.05 ± 0.15	7.26 ± 0.28	31.6 ± 1.2	$1.96 \times 10^4 \pm 8.0 \times 10^2$
6.0	7.69 ± 0.21	16.1 ± 0.65	215.0 ± 9.0	$6.88 \times 10^6 \pm 3.3 \times 10^5$
8.0	11.1 ± 0.3	33.7 ± 1.5	$1.52 \times 10^3 \pm 7.0 \times 10^1$	—
10.0	14.7 ± 0.4	66.7 ± 3.1	—	—

	1.25 MeV			
mfp	$\cos\theta_0 = 1.0$	0.75	0.50	0.25
1.0	1.75 ± 0.05	1.87 ± 0.05	2.12 ± 0.04	4.14 ± 0.11
2.0	2.51 ± 0.07	2.94 ± 0.09	4.42 ± 0.12	43.3 ± 1.5
4.0	4.39 ± 0.13	5.78 ± 0.20	19.6 ± 0.7	$9.35 \times 10^3 \pm 4.4 \times 10^2$
6.0	6.24 ± 0.18	11.3 ± 0.4	101.0 ± 4.0	$2.24 \times 10^6 \pm 1.1 \times 10^5$
8.0	8.09 ± 0.22	20.6 ± 0.8	541.0 ± 24.0	—
10.0	10.2 ± 0.3	37.2 ± 1.4	—	—

	2.50 MeV			
mfp	$\cos\theta_0 = 1.0$	0.75	0.50	0.25
1.0	1.66 ± 0.04	1.92 ± 0.06	1.93 ± 0.04	3.24 ± 0.09
2.0	2.14 ± 0.06	2.71 ± 0.09	3.55 ± 0.10	23.9 ± 0.9
4.0	3.30 ± 0.09	5.16 ± 0.19	11.8 ± 0.4	$2.80 \times 10^3 \pm 1.4 \times 10^2$
6.0	4.59 ± 0.13	9.13 ± 0.36	40.6 ± 1.6	$4.10 \times 10^5 \pm 2.4 \times 10^4$
8.0	5.89 ± 0.17	14.5 ± 0.6	161.0 ± 7.9	—
10.0	7.09 ± 0.19	23.8 ± 1.1	—	—

	6.13 MeV			
mfp	$\cos\theta_0 = 1.0$	0.75	0.50	0.25
1.0	1.42 ± 0.04	1.68 ± 0.06	1.75 ± 0.03	2.55 ± 0.08
2.0	1.91 ± 0.06	2.38 ± 0.08	2.63 ± 0.06	10.1 ± 0.5
4.0	2.56 ± 0.07	4.05 ± 0.16	5.99 ± 0.17	544.0 ± 37.0
6.0	3.26 ± 0.10	6.40 ± 0.33	15.9 ± 0.7	$4.02 \times 10^4 \pm 3.3 \times 10^3$
8.0	4.08 ± 0.12	9.47 ± 0.56	47.3 ± 3.3	—
10.0	4.80 ± 0.14	14.2 ± 1.0	—	—

[a]All uncertainties listed represent the estimated standard error of the sample mean.

Source: *Ref. 5; reproduced by permission of the American Nuclear Society.*

Table A4.13 Three-Exponential Parameters for the Exposure Buildup Factors for a Point Isotropic Source in Infinite Water, to 40 Mean-Free-Path Lengths[a]

E (MeV)	A_1	A_2	α_1	α_2	α_3
15.000	6.661(+0)[b]	−1.496(+0)	−5.032(−2)	1.018(−1)	−5.774(−2)
10.000	8.889(+0)	−2.360(+0)	−4.839(−2)	9.146(−2)	−5.524(−2)
8.000	1.011(+1)	−3.046(+0)	−4.734(−2)	8.321(−2)	−5.452(−2)
6.000	1.047(+1)	−3.919(+0)	−5.176(−2)	7.394(−2)	−6.205(−2)
5.000	1.251(+1)	−6.071(+0)	−4.129(−2)	5.030(−2)	−5.231(−2)
4.000	1.928(+1)	−1.417(+1)	−2.575(−2)	2.054(−2)	−4.182(−2)
3.000	1.162(+2)	−6.740(+1)	−2.395(−2)	−7.309(−3)	−3.262(−2)
2.000	4.159(+2)	−2.687(+2)	−3.784(−2)	−2.974(−2)	−4.663(−2)
1.500	2.941(+2)	−2.179(+2)	−4.964(−2)	−3.988(−2)	−6.392(−2)
1.000	1.128(+3)	−1.174(+3)	−1.031(−2)	−5.925(−3)	7.813(−2)
0.800	1.102(+3)	−1.308(+3)	−1.141(−2)	−2.141(−3)	4.240(−2)
0.600	4.316(+3)	−4.588(+3)	−1.751(−2)	−1.406(−2)	3.682(−2)
0.500	1.232(+3)	−1.664(+3)	−2.843(−2)	−1.351(−2)	2.686(−2)
0.400	1.182(+3)	−2.019(+3)	−3.850(−2)	−1.678(−2)	1.292(−2)
0.300	1.251(+3)	−1.756(+3)	−5.541(−2)	−3.475(−2)	1.528(−2)
0.200	1.206(+3)	−2.149(+3)	−7.780(−2)	−4.773(−2)	−9.998(−3)
0.150	1.242(+3)	−2.317(+3)	−8.536(−2)	−5.025(−2)	−9.997(−3)
0.100	1.503(+3)	−2.736(+3)	−8.190(−2)	−4.753(−2)	−6.323(−3)
0.080	1.477(+3)	−2.543(+3)	−7.303(−2)	−4.109(−2)	1.458(−3)
0.060	1.641(+3)	−2.712(+3)	−4.888(−2)	−2.589(−2)	6.546(−3)
0.050	5.106(+2)	−6.189(+2)	−4.231(−2)	−1.852(−2)	6.537(−2)
0.040	1.183(+2)	−1.462(+2)	−2.852(−2)	6.613(−3)	6.739(−2)
0.030	1.039(+1)	−6.924(−1)	−3.174(−2)	9.030(−1)	6.484(−2)
0.020	4.960(+0)	−6.395(−1)	−1.058(−3)	5.505(−1)	3.524(−2)
0.015	1.258(+1)	−3.984(−1)	−2.509(−2)	3.955(−1)	−2.659(−2)

[a]These data may also be used for air, to a good approximation.

[b]Read as $6.661 \times 10^{+0}$.

Source: *Ref. 6; reproduced by permission of the American Nuclear Society.*

REFERENCES

1. A. B. Chilton, C. M. Eisenhauer, and G. L. Simmons, "Photon Point Source Buildup Factors for Air, Water, and Iron," *Nucl. Sci. Eng.* **73**, 97–107 (1980).
2. C. M. Eisenhauer and G. L. Simmons, "Point Isotropic Buildup Factors in Concrete," *Nucl. Sci. Eng.* **56**, 263–270 (1975).
3. A. B. Chilton, "Tschebycheff-Fitted Berger Coefficients for Eisenhauer–Simmons Gamma-Ray Buildup Factors in Ordinary Concrete," *Nucl. Sci. Eng.* **69**, 436–438 (1979).
4. A. B. Chilton, "Optimized Taylor Parameters for Concrete Buildup Factor Data," *Nucl. Sci. Eng.* **64**, 799–800 (1977).

5. E. M. Fournie and A. B. Chilton, "Gamma-Ray Buildup Factors for Concrete Slab Shields under Slant Incidence Conditions," *Nucl. Sci. Eng.* **76**, 66–69 (1980).
6. A. Foderaro and R. J. Hall, "Application of Three-Exponential Representation of Photon Buildup Factors to Water," *Nucl. Sci. Eng.* **78**, 74–78 (1981).

appendix 5

decay characteristics of selected radionuclides

This appendix lists, by nuclide, the half-life in years (y), days (d), hours (h), minutes (m), or seconds (s). The column labeled "Total β, e (MeV/dis.)" is the average of the sum per disintegration of the kinetic energies of all charged particles released, including conversion and Auger electrons. Gamma and x photons are listed for energies greater than 5 keV and frequencies greater than 0.1 % (i.e., probabilities of release greater than 0.001 per disintegration).

Knowledge of decay characteristics improves continuously, as new research findings are incorporated into the data base. Readers may wish to supplement the information given here with that appearing in the current literature. Unless otherwise indicated, data are from L. T. Dillman, and F. C. Von der Lage, "Radionuclide Decay Schemes and Nuclear Parameters for Use in Radiation-Dose Estimation," Pamphlet No. 10, Medical Internal Radiation Dose Committee, Society of Nuclear Medicine, New York, 1975. Data for nuclides identified by an asterisk are from M. J. Martin, and P. H. Blichert-Toft, "Radioactive Atoms. Auger-Electron, α-, β-, γ-, and X-Ray Data," *Nuclear Data Tables*, Section A, Vol. 8, 1970. Data for nuclides identified by a dagger are from M. J. Martin, "Nuclear Decay Data for Selected Radionuclides," Report ORNL-5114, Oak Ridge National Laboratory, Oak Ridge, Tenn., 1976. (Another useful and comprehensive compilation of data is "Radioactive Decay Data Tables," by David C. Kocher, published as Report DOE/TIC-11026, National Technical Information Service, Springfield, Virginia, 1981.)

In certain instances data are given for decay of a nuclide in equilibrium with a radioactive daughter [e.g., ^{95}Zr and ^{95m}Nb(eq)]. Energies and frequencies, in these instances, are per disintegration of the parent.

Table A5.1

Nuclide	Half-Life	Total β, e (MeV/dis.)	Gamma and X Photons		
			Frequency (%)	MeV	Ref.
3 H	12.3 y	0.0057	—	—	
14 C	5730. y	0.0493	—	—	
16 N	7.12 s	2.695	69.0	6.129	†
			5.0	7.117	
			0.76	2.741	
			0.13	1.753	
24 Na	15.0 h	0.5547	99.99	1.3685	
			99.91	2.7539	
32 P	14.3 d	0.6948	—	—	
35 S	87.0 d	0.0488	—	—	
38 Cl	37.3 m	1.527	44.0	2.1675	*
			32.8	1.6424	
40 K	1.27×10^9 y	0.4974	10.32	1.4609	
45 Ca	163. d	0.0772	—	—	
51 Cr	27.7 d	0.0037	19.48	0.0049	
			10.18	0.3200	
			2.24	0.0054	
54 Mn	312. d	0.0040	99.97	0.8348	
			21.41	0.0054	
			2.39	0.0059	
55 Fe	2.70 y	0.0041	23.39	0.0058	
			2.57	0.0064	
59 Fe	45.0 d	0.1178	55.48	1.0990	
			44.11	1.2920	
			2.92	0.1922	
			0.96	0.1420	
			0.23	0.3347	
57 Co	270. d	0.0185	85.90	0.1220	
			30.83	0.0064	
			15.54	0.0063	
			10.40	0.1364	
			9.54	0.0144	
			4.99	0.0070	
			0.15	0.6921	
58 Co	71.3 d	0.0351	99.46	0.8106	
			31.00	0.5110	
			14.41	0.0064	
			7.26	0.0063	
			2.33	0.0070	
			0.59	0.8636	
			0.50	1.6748	
60 Co	5.26 y	0.0949	99.98	1.3324	
			99.78	1.1732	
63 Ni	92. y	0.0171	—	—	*

Table A5.1 (Continued)

Nuclide	Half-Life		Total β, e (MeV/dis.)	Gama and X Photons		
				Frequency (%)	MeV	Ref.
65 Zn	243.	d	0.0069	50.59	1.1154	
				31.91	0.0080	
				3.70	0.0089	
				3.00	0.5110	
85m Kr	4.36	h	0.2511	76.06	0.1512	
				13.56	0.3050	
				2.21	0.0126	
				1.77	0.0133	
				1.10	0.0125	
				0.46	0.0141	
85 Kr	10.7	y	0.2451	0.42	0.5140	
84 Rb	33.0	d	0.1303	75.24	0.8815	
				42.40	0.5110	
				25.41	0.0126	
				12.68	0.0125	
				5.38	0.0141	
				0.82	1.8970	
				0.53	0.0143	
				0.45	1.0160	
86 Rb	18.6	d	0.6675	8.75	1.0766	
87m Sr	2.80	h	0.0626	83.19	0.3884	
				5.54	0.0141	
				2.77	0.0140	
				1.22	0.0158	
89 Sr	50.5	d	0.573	0.015	0.9091	*
90 Sr	28.1	y	0.1961	—	—	
90 Y	64.0	h	0.9314	—	—	
91 Y	58.9	d	0.606	0.22	1.21	*
[95 Zr and	65.5	d[a]	0.1230	54.3	0.7569	*
95m Nb(eq.)]	3.61	d		43.5	0.7242	
				0.9	0.0169	
				0.46	0.2354	
				0.09	0.0022	
95 Nb	35.1	d	0.0450	99.80	0.7658	*
				0.13	0.0178	
[99 Mo and	66.2	h[b]	0.411	89.6	0.1405	*
99m Tc(eq.)]	6.02	h		13.8	0.7397	
				11.6	0.0187	
				6.7	0.1811	
				4.8	0.7782	
				1.46	0.3664	
				1.3	0.0406	
				1.2	0.0024	
				0.14	0.8231	
				0.11	0.9610	

Table A5.1 (Continued)

Nuclide	Half-Life		Total β, e (MeV/dis.)	Gamma and X Photons		
				Frequency (%)	MeV	Ref.
[103 Ru and 103m Rh(eq.)]	39.6	d	0.102	89.	0.4969	*
	57.	m		8.3	0.0206	
				7.05	0.0027	
				5.4	0.6102	
				0.8	0.5569	
				0.36	0.4438	
				0.34	0.0531	
				0.21	0.2949	
[106 Ru and 106 Rh(eq.)]	369.	d	1.439	20.6	0.5118	*
	30.4	s		9.94	0.6221	
				1.48	1.0501	
				0.71	0.6162	
				0.41	0.8735	
				0.39	1.1275	
				0.15	1.5620	
				0.11	0.0216	
109m Ag	40.0	s	0.0762	19.55	0.0221	
				9.89	0.0219	
				8.25	0.0029	
				4.95	0.0249	
				3.76	0.0880	
				0.96	0.0255	
110m Ag	252.2	d	0.0670	94.7	0.6575	†
				72.9	0.8847	
				34.3	0.9347	
				24.35	1.3843	
				22.36	0.7639	
				16.74	0.7067	
				13.11	1.5050	
				10.72	0.6776	
				7.32	0.8180	
				6.49	0.6870	
				4.66	0.7443	
				3.99	1.4758	
				3.66	0.4468	
				2.78	0.6203	
				1.18	1.5623	
				0.37	0.0222	
				0.28	0.7081	
				0.24	0.6262	
				0.20	0.0220	
				0.14	0.6766	
				0.13	1.3343	
				0.13	0.9972	
				0.12	0.0249	
				0.11	0.3654	

Table A5.1 (Continued)

Nuclide	Half-Life	Total β, e (MeV/dis.)	Gamma and X Photons		
			Frequency (%)	MeV	Ref.
110 Ag	24.6 s	1.1815	4.50	0.6577	†
109 Cd	453. d	0.0056	37.04	0.0221	
			18.74	0.0219	
			9.39	0.0249	
			9.07	0.0029	
			1.83	0.0255	
115m In	4.50 h	0.1911	39.25	0.3356	
			20.30	0.0242	
			10.32	0.0240	
			5.36	0.0032	
			5.29	0.0272	
			1.06	0.0279	
125 I	60.2 d	0.0195	76.15	0.0274	
			39.06	0.0272	
			22.26	0.0037	
			20.56	0.0309	
			6.66	0.0354	
			4.26	0.0318	
131 I	8.06 d	0.1919	82.01	0.3644	
			6.53	0.6367	
			5.78	0.2843	
			2.58	0.0801	
			2.49	0.0297	
			1.73	0.7228	
			1.28	0.0294	
			0.68	0.0336	
			0.36	0.3257	
			0.29	0.1772	
			0.29	0.5029	
			0.14	0.6430	
			0.14	0.0345	
			0.10	0.3180	
133 I	20.8 h	0.4121	86.27	0.5295	
			3.57	0.8753	
			1.93	1.2989	
			1.60	1.2375	
			1.59	0.7074	
			1.48	0.5104	
			1.02	0.8561	
			0.74	0.6808	
			0.50	0.8753	
			0.41	0.7691	
			0.37	0.2634	
			0.37	0.9105	
			0.35	0.0297	

[continued]

Table A5.1 (Continued)

Nuclide	Half-Life		Total β, e (MeV/dis.)	Gamma and X Photons		
				Frequency (%)	MeV	Ref.
133 I [continued]				0.32	0.6180	
				0.22	0.4229	
				0.22	0.3440	
				0.18	0.0294	
				0.14	0.4172	
				0.14	1.0528	
				0.13	1.3516	
				0.13	0.8209	
				0.12	0.2663	
133m Xe	2.19	d	0.1976	29.35	0.0297	
				15.14	0.0294	
				10.92	0.0041	
				8.10	0.0336	
				8.03	0.2335	
				1.70	0.0345	
133 Xe	5.31	d	0.1372	36.03	0.0809	
				25.52	0.0309	
				13.21	0.0306	
				8.23	0.0043	
				7.12	0.0349	
				1.50	0.0359	
				0.61	0.0796	
135m Xe	15.29	m	0.0950	81.2	0.5266	†
				7.13	0.0298	
				3.84	0.0295	
				2.54	0.0336	
				1.7	0.0041	
135 Xe	9.09	h	0.3161	90.13	0.2498	†
				2.90	0.6082	
				2.66	0.0310	
				1.43	0.0306	
				0.95	0.0035	
				0.63	0.0043	
				0.36	0.4080	
				0.29	0.1582	
				0.22	0.3584	
134 Cs	2.05	y	0.1702	96.93	0.6048	
				86.74	0.7960	
				13.17	0.5693	
				8.53	0.5630	
				7.87	0.8019	
				3.49	1.3654	
				1.99	1.1684	
				1.58	0.4755	

[continued]

Table A5.1 (Continued)

Nuclide	Half-Life	Total β, e (MeV/dis.)	Gamma and X Photons		
			Frequency (%)	MeV	Ref.
134 Cs [continued]			0.99	1.0381	
			0.42	0.0321	
			0.21	0.0318	
[137 Cs and	30.0 y	0.2496	84.96	0.6616	
137m Ba(eq.)]	2.55 m		3.70	0.0321	
			1.92	0.0318	
			1.26	0.0044	
			1.04	0.0363	
			0.22	0.0374	
140 Ba	12.8 d	0.315	23.8	0.5374	*
			18.0	0.0047	
			14.0	0.0300	
			6.2	0.1629	
			4.5	0.3048	
			3.2	0.4237	
			2.1	0.4376	
			1.29	0.0139	
			1.24	0.0342	
			0.7	0.661	
			0.6	0.602	
			0.4	0.498	
			0.3	0.637	
			0.26	0.512	
			0.21	0.466	
			0.19	0.177	
			0.17	0.1327	
140 La	40.27 h	0.541	95.6	1.5966	*
			45.	0.4870	
			23.1	0.8158	
			21.	0.3288	
			6.9	0.9252	
			5.5	0.8678	
			4.4	0.7518	
			3.3	0.4326	
			3.3	2.5220	
			2.5	0.9196	
			1.51	0.0355	
			0.86	2.3484	
			0.8	0.1311	
			0.7	0.2666	
			0.64	0.9505	
			0.6	0.2420	
			0.27	0.0048	
			0.23	0.1094	

[continued]

Table A5.1 (Continued)

Nuclide	Half-Life		Total β, e (MeV/dis.)	Gamma and X photons		
				Frequence (%)	MeV	Ref.
140 La [continued]				0.14	0.1735	
				0.11	2.5479	
141 Ce	32.38	d	0.1706	49.0	0.1455	*
				16.6	0.0367	
				3.2	0.0050	
[144 Ce and	284.	d	1.318	10.8	0.1335	*
144 Pr(eq.)]	17.28	m		9.0	0.0367	
				2.10	0.0050	
				1.54	0.0801	
				1.51	0.6965	
				0.74	2.1857	
				0.39	0.0409	
				0.29	1.4891	
				0.22	0.0336	
				0.14	0.0534	
147 Pm	2.623	y	0.0621	—	—	*
169 Yb	32.0	d	0.1913	77.50	0.0507	
				45.16	0.0631	
				41.54	0.0497	
				40.27	0.0075	
				26.16	0.1979	
				24.72	0.0575	
				17.31	0.1771	
				11.42	0.1305	
				11.04	0.3076	
				5.69	0.0593	
				3.82	0.1097	
				1.90	0.1181	
				1.74	0.2610	
				0.78	0.0936	
				0.21	0.0207	
				0.12	0.2404	
198 Au	2.69	d	0.3280	95.55	0.4117	
				1.39	0.0708	
				1.07	0.6758	
				0.76	0.0688	
				0.60	0.0099	
				0.56	0.0118	
				0.48	0.0802	
				0.22	1.0876	
				0.13	0.0831	

[continued]

Table A5.1 (Continued)

Nuclide	Half-Life	Total β, e (MeV/dis.)	Gamma and X Photons		
			Frequence (%)	MeV	Ref.
203 Hg	46.5 d	0.0985	81.73	0.2792	
			6.38	0.0728	
			3.52	0.0708	
			2.75	0.0102	
			2.58	0.0122	
			2.24	0.0825	
			0.63	0.0855	
			0.34	0.0142	
210 Po	138.4 d	5.3048(α)	—	—	*
[210 Pb and	21.3 y	0.4289	23.4	0.0108	*
210 Bi(eq.)]	5.012 d		4.05	0.0465	
222 Rn	3.824 d	5.486(α)	—	—	*
226 Ra	1600. y	0.0033	3.3	0.1860	*
		4.771(α)	0.85	0.0117	
			0.73	0.0858	
[226 Ra and	1600. y	0.987	[c]	1.748	*
222 Rn and	3.824 d	23.945(α)			
218 Po and	3.05 m				
214 Pb and	26.8 m				
214 Bi and	19.8 m				
214 Po(eq.)]	162. $\times 10^{-6}$ s				

[a]95 Zr decays to 95m Nb in 1.8% of its disintegrations, to 95 Nb in 98.2%.

[b]99 Mo decays to 99m Tc in 86.3% of its disintegrations, to 99 Tc in 13.7%.

[c]In the equilibrium mixture, the average total energy of all photons released per disintegration of ^{226}Ra is 1.748 MeV.

appendix 6

parameters for use in calculating fission-product photon source strengths

In Tables A6.1 through A6.6, values of α_{ij} and λ_{ij} are given for use in calculating gamma-photon emission rates following thermal-neutron-induced fission of ^{235}U and ^{239}Pu. The parameters, which are valid for use over the time range 10^{-4} to 10^{+9} s, are given for all fission products, for gaseous fission products, and for total energy release through either gamma photons or beta particles. Data are used as follows: If $F_j(t)$ is the mean rate of energy release (MeV s^{-1}) through gamma photons with energies in group j at time t (s) after a single fission event, then

$$F_j(t) = \sum_{i=1}^{N_j} \alpha_{ij} e^{-\lambda_{ij} t}, \qquad j = 1 \text{ to } 6.$$

If Γ_j (MeV per fission) is the rate of energy release in group j at time t_s (s) following operation at a constant fission rate (s^{-1}) for time t_0 (s), normalized to unit fission rate, then

$$\Gamma_j(t_0, t_s) = \sum_{i=1}^{N_j} \frac{\alpha_{ij}}{\lambda_{ij}} e^{-\lambda_{ij} t_s} (1 - e^{-\lambda_{ij} t_0}).$$

Use of the α_{ij} and λ_{ij} parameters for calculation of source strengths following extended periods of reactor operation at high power does not account for absorption of neutrons by fission products. For long-term operation at high thermal-neutron flux densities, corrections for absorption may be significant [1]. The photon energy release rates do not include bremsstrahlung resulting from fission-product beta particles.

Table A6.1 Gamma-Ray Spectra Constants for All Fission Products Resulting from the Thermal-Neutron-Induced Fission of ^{235}U

Group 1 5–7.5 MeV		Group 2 4–5 MeV		Group 3 3–4 MeV	
Alpha	Lambda	Alpha	Lambda	Alpha	Lambda
1.222(−13)[a]	6.125(−07)	5.629(−20)	2.787(−13)	2.753(−18)	6.788(−14)
5.409(−12)	1.036(−06)	7.981(−20)	6.023(−08)	2.665(−18)	3.951(−08)
6.711(−08)	8.330(−04)	9.578(−14)	5.236(−07)	6.126(−16)	3.800(−07)
1.606(−05)	3.562(−03)	4.786(−11)	1.060(−06)	1.825(−11)	5.905(−07)
4.867(−05)	6.743(−03)	2.069(−08)	7.083(−05)	7.970(−11)	9.240(−07)
1.514(−04)	2.279(−02)	3.461(−08)	1.894(−04)	2.066(−07)	7.721(−05)
2.159(−03)	1.337(−01)	1.045(−06)	7.889(−04)	2.481(−06)	1.396(−04)
3.220(−03)	5.023(−01)	2.742(−04)	4.142(−03)	1.192(−05)	6.358(−04)
4.559(−03)	2.539(+00)	6.462(−04)	1.226(−02)	2.584(−04)	3.452(−03)
		1.341(−03)	4.521(−02)	1.376(−03)	1.188(−02)
		2.204(−03)	1.962(−01)	2.320(−03)	4.160(−02)
		2.572(−03)	7.021(−01)	2.799(−03)	1.999(−01)
		2.750(−03)	2.953(+00)	3.506(−03)	6.763(−01)
				3.559(−03)	2.940(+00)

Group 4 2–3 MeV		Group 5 1–2 MeV		Group 6 0–1 MeV	
Alpha	Lambda	Alpha	Lambda	Alpha	Lambda
2.719(−17)	8.227(−11)	7.708(−17)	2.364(−10)	2.817(−11)	7.350(−10)
2.632(−11)	2.772(−08)	9.292(−12)	2.524(−08)	4.535(−11)	2.139(−08)
5.115(−09)	6.458(−07)	7.734(−12)	9.229(−08)	1.574(−08)	1.157(−07)
5.519(−09)	2.515(−06)	7.168(−08)	6.247(−07)	1.794(−07)	1.396(−06)
3.111(−06)	6.159(−05)	2.206(−08)	1.768(−06)	1.056(−06)	6.652(−06)
1.758(−05)	1.356(−04)	3.466(−06)	2.719(−05)	3.168(−06)	2.344(−05)
7.848(−05)	5.446(−04)	1.457(−05)	8.664(−05)	7.944(−05)	1.844(−04)
1.872(−04)	2.839(−03)	1.033(−04)	3.403(−04)	2.230(−04)	7.375(−04)
2.816(−03)	1.199(−02)	2.339(−04)	1.119(−03)	7.722(−04)	3.390(−03)
5.830(−03)	4.591(−02)	3.038(−03)	7.746(−03)	4.001(−03)	1.452(−02)
9.529(−03)	1.998(−01)	1.112(−02)	2.754(−02)	2.313(−02)	6.692(−02)
1.234(−02)	7.130(−01)	2.343(−02)	1.156(−01)	9.434(−02)	2.918(−01)
1.240(−02)	3.003(+00)	4.586(−02)	5.380(−01)	2.007(−01)	1.064(+00)
		5.000(−02)	2.754(+00)	1.722(−01)	3.665(+00)

[a]Read as 1.222×10^{-13}, etc.

Source: *Ref. 1.*

Table A6.2 Gamma-Ray Constants for Gaseous Fission Products Resulting from the Thermal-Neutron-Induced Fission of ^{235}U

Group 1 5–7.5 MeV		Group 2 4–5 MeV		Group 3 3–4 MeV	
Alpha	Lambda	Alpha	Lambda	Alpha	Lambda
3.881(−13)[a]	1.304(−03)	1.497(−14)	1.550(−05)	1.775(−15)	5.408(−06)
6.668(−06)	1.029(−02)	2.266(−11)	7.579(−05)	1.722(−13)	1.553(−05)
6.756(−05)	1.346(−02)	4.864(−08)	3.688(−04)	3.278(−09)	8.677(−05)
3.320(−04)	1.565(−01)	8.485(−06)	3.871(−03)	1.144(−06)	2.835(−04)
9.110(−04)	5.523(−01)	1.647(−04)	1.502(−02)	1.323(−06)	5.487(−04)
3.679(−04)	3.502(+00)	4.094(−04)	5.545(−02)	6.721(−05)	3.799(−03)
		6.971(−04)	3.263(−01)	1.043(−03)	4.057(−02)
		4.188(−04)	8.814(−01)	1.456(−03)	5.327(−01)
		1.538(−04)	4.390(+00)	2.246(−04)	4.286(+00)
				−2.909(−04)	4.348(−02)

Group 4 2–3 MeV		Group 5 1–2 MeV		Group 6 0–1 MeV	
Alpha	Lambda	Alpha	Lambda	Alpha	Lambda
6.639(−09)	2.452(−06)	3.207(−08)	2.452(−06)	1.240(−14)	2.047(−09)
6.160(−10)	2.340(−06)	3.056(−09)	2.352(−06)	1.898(−18)	3.349(−09)
6.039(−11)	4.950(−06)	1.141(−07)	1.117(−05)	3.111(−09)	8.555(−07)
3.099(−06)	6.345(−05)	2.786(−06)	3.253(−05)	4.583(−08)	1.370(−06)
3.490(−06)	1.323(−04)	1.438(−05)	1.719(−04)	2.254(−07)	3.034(−06)
2.667(−05)	7.990(−04)	1.671(−04)	3.291(−03)	8.757(−07)	1.411(−05)
9.846(−05)	4.164(−03)	2.692(−03)	1.404(−02)	1.903(−05)	1.310(−04)
7.477(−04)	1.328(−02)	3.945(−03)	5.476(−02)	8.518(−06)	1.227(−04)
1.982(−03)	5.980(−02)	1.105(−02)	3.054(−01)	3.138(−04)	5.802(−03)
3.316(−03)	2.866(−01)	6.945(−03)	8.506(−01)	2.488(−03)	2.840(−02)
2.204(−03)	8.184(−01)	2.536(−03)	4.365(+00)	9.115(−03)	1.293(−01)
7.020(−04)	4.437(+00)			3.004(−02)	5.482(−01)
				2.034(−02)	2.682(+00)

[a]Read as 3.881×10^{-13}, etc.

Source: *Ref. 1.*

Table A6.3 Gamma- and Beta-Decay Constants for Fission Products Resulting from the Thermal-Neutron-Induced Fission of ^{235}U

Beta—All Fission Product		Gamma—All Fission Product		Beta—Gaseous Fission Product		Gamma—Gaseous Fission Product	
Alpha	Lambda	Alpha	Lambda	Alpha	Lambda	Alpha	Lambda
6.169(−11)[a]	7.953(−10)	2.808(−11)	7.332(−10)	1.380(−12)	2.028(−09)	1.240(−14)	2.047(−09)
2.249(−09)	2.758(−08)	6.038(−10)	4.335(−08)	2.620(−13)	2.099(−07)	3.484(−18)	1.320(−08)
2.365(−08)	2.082(−07)	3.227(−08)	1.932(−07)	7.574(−09)	1.031(−06)	1.220(−08)	9.928(−07)
2.194(−07)	1.846(−06)	4.055(−07)	1.658(−06)	7.796(−08)	2.398(−06)	2.832(−07)	2.513(−06)
1.140(−05)	2.404(−05)	8.439(−06)	2.147(−05)	1.216(−06)	1.646(−05)	3.726(−06)	2.319(−05)
1.549(−04)	2.337(−04)	2.421(−04)	2.128(−04)	1.877(−05)	1.519(−04)	4.578(−05)	1.293(−04)
1.991(−03)	1.897(−03)	1.792(−03)	1.915(−03)	6.329(−04)	2.908(−03)	4.305(−04)	2.942(−03)
3.256(−02)	1.926(−02)	2.810(−02)	1.769(−02)	8.696(−03)	2.006(−02)	8.058(−03)	1.905(−02)
2.227(−01)	1.573(−01)	1.516(−01)	1.652(−01)	4.500(−02)	1.657(−01)	3.405(−02)	1.725(−01)
5.381(−01)	1.264(+00)	4.162(−01)	1.266(+00)	6.016(−02)	9.246(−01)	5.284(−02)	9.698(−01)
1.282(−01)	5.196(+00)	1.053(−01)	5.222(+00)	9.890(−03)	5.155(+00)	9.123(−03)	5.458(+00)

[a]Read as 6.169×10^{-11}, etc.

Source: *Ref. 1.*

Table A6.4 Gamma-Ray Spectra Constants for All Fission Products Resulting from the Thermal-Neutron-Induced Fission of ^{239}Pu

Group 1 5–7.5 MeV		Group 2 4–5 MeV		Group 3 3–4 MeV	
Alpha	Lambda	Alpha	Lambda	Alpha	Lambda
3.551(−12)[a]	6.432(−07)	2.772(−19)	3.156(−10)	1.379(−17)	3.270(−10)
1.534(−11)	1.078(−06)	3.503(−19)	7.321(−09)	1.750(−17)	7.358(−09)
9.105(−08)	8.915(−04)	5.478(−11)	8.850(−07)	5.700(−11)	6.865(−07)
1.216(−05)	3.906(−03)	9.182(−11)	1.241(−06)	2.102(−10)	1.159(−06)
1.383(−04)	1.886(−02)	2.100(−08)	9.023(−05)	7.128(−07)	1.015(−04)
1.740(−03)	1.633(−01)	7.495(−06)	1.224(−03)	3.335(−06)	2.363(−04)
2.578(−03)	1.103(+00)	4.127(−04)	7.188(−03)	1.029(−04)	2.457(−03)
9.624(−04)	4.416(+00)	1.417(−03)	4.254(−02)	1.747(−03)	1.636(−02)
		2.061(−03)	3.343(−01)	2.650(−03)	1.137(−01)
		1.755(−03)	2.387(+00)	2.667(−03)	9.134(−01)
		−3.568(−19)	3.649(−09)	1.057(−03)	3.986(+00)
				−1.784(−17)	3.622(−09)

Group 4 2–3 MeV		Group 5 1–2 MeV		Group 6 0–1 MeV	
Alpha	Lambda	Alpha	Lambda	Alpha	Lambda
1.825(−16)	7.500(−10)	7.722(−16)	1.303(−09)	3.089(−11)	7.540(−10)
2.106(−11)	2.738(−08)	3.254(−11)	2.274(−08)	3.958(−10)	2.915(−08)
4.709(−09)	6.376(−07)	6.484(−08)	6.241(−07)	1.942(−08)	1.540(−07)
7.790(−09)	2.294(−06)	2.711(−08)	1.715(−06)	4.232(−07)	2.159(−06)
1.366(−06)	5.700(−05)	3.841(−06)	2.962(−05)	3.663(−06)	1.672(−05)
3.158(−05)	2.188(−04)	7.917(−05)	2.550(−04)	1.145(−04)	2.332(−04)
1.592(−04)	1.689(−03)	4.005(−04)	1.645(−03)	6.005(−04)	1.633(−03)
3.620(−03)	1.629(−02)	8.113(−03)	1.663(−02)	5.969(−03)	1.784(−02)
8.160(−03)	1.265(−01)	2.347(−02)	1.305(−01)	6.108(−02)	1.766(−01)
1.026(−02)	1.106(+00)	3.093(−02)	1.013(+00)	1.678(−01)	1.245(+00)
2.448(−03)	5.581(+00)	1.241(−02)	4.115(+00)	3.897(−02)	5.803(+00)

[a]Read as 3.551×10^{-12}, etc.

Source: *Ref. 1.*

Table A6.5 Gamma-Ray Spectra Constants for Gaseous Fission Products Resulting from the Thermal-Neutron-Induced Fission of ^{239}Pu

Group 1 5–7.5 MeV		Group 2 4–5 MeV		Group 3 3–4 MeV	
Alpha	Lambda	Alpha	Lambda	Alpha	Lambda
1.867(−16)[a]	2.646(−04)	3.746(−13)	1.551(−05)	1.086(−14)	3.767(−06)
7.847(−11)	1.799(−03)	1.690(−11)	8.283(−05)	5.064(−12)	1.431(−05)
2.332(−05)	1.287(−02)	2.011(−08)	3.646(−04)	1.246(−07)	1.717(−04)
5.407(−05)	7.512(−02)	3.071(−06)	4.032(−03)	1.476(−06)	5.364(−04)
2.131(−04)	3.736(−01)	1.319(−04)	2.218(−02)	3.387(−05)	5.157(−03)
9.512(−05)	2.275(+00)	2.159(−04)	1.219(−01)	3.933(−04)	4.566(−02)
		1.606(−04)	8.296(−01)	3.374(−04)	4.092(−01)
		1.930(−05)	4.867(+00)	6.828(−05)	3.064(+00)
Group 4 2–3 MeV		Group 5 1–2 MeV		Group 6 0–1 MeV	
Alpha	Lambda	Alpha	Lambda	Alpha	Lambda
8.365(−09)	2.456(−06)	4.024(−08)	2.456(−06)	5.703(−15)	2.046(−09)
4.819(−10)	2.760(−06)	5.327(−09)	3.154(−06)	2.692(−18)	4.900(−09)
1.014(−06)	5.871(−05)	2.446(−06)	2.846(−05)	1.594(−08)	9.912(−07)
3.541(−06)	2.015(−04)	9.731(−06)	1.617(−04)	2.830(−07)	2.501(−06)
3.897(−05)	1.528(−03)	6.733(−05)	2.322(−03)	9.359(−07)	1.395(−05)
6.004(−04)	1.561(−02)	1.790(−03)	1.635(−02)	2.550(−05)	1.523(−04)
1.149(−03)	1.205(−01)	2.975(−03)	1.387(−01)	8.799(−05)	3.690(−03)
7.649(−04)	8.295(−01)	2.518(−03)	8.389(−01)	1.083(−03)	2.219(−02)
8.963(−05)	4.917(+00)	3.125(−04)	4.866(+00)	4.705(−03)	1.706(−01)
				7.543(−03)	1.158(+00)
				1.482(−03)	4.931(+00)

[a]Read as 1.867×10^{-16}, etc.

Source: *Ref. 1.*

Table A6.6 Gamma- and Beta-Decay Constants for Fission Products Resulting from the Thermal-Neutron-Induced Fission of ^{239}Pu

Beta—All Fission Product		Gamma—All Fission Product		Beta—Gaseous Fission Product		Gamma—Gaseous Fission Product	
Alpha	Lambda	Alpha	Lambda	Alpha	Lambda	Alpha	Lambda
2.835(−11)[a]	8.016(−10)	3.062(−11)	7.441(−10)	6.411(−13)	2.047(−09)	5.703(−15)	2.046(−09)
2.776(−09)	2.425(−08)	4.761(−10)	2.856(−08)	4.791(−18)	5.532(−09)	2.692(−18)	4.900(−09)
1.811(−08)	2.399(−07)	3.390(−08)	2.052(−07)	9.763(−09)	1.027(−06)	1.601(−08)	9.916(−07)
2.485(−07)	1.959(−06)	4.775(−07)	1.772(−06)	9.019(−08)	2.384(−06)	3.369(−07)	2.501(−06)
7.942(−06)	2.208(−05)	7.251(−06)	2.071(−05)	1.183(−06)	1.585(−05)	3.263(−06)	2.158(−05)
1.512(−04)	2.548(−04)	2.278(−04)	2.323(−04)	1.375(−05)	1.703(−04)	4.000(−05)	1.539(−04)
1.869(−03)	1.833(−03)	1.336(−03)	1.727(−03)	4.336(−04)	2.761(−03)	1.796(−04)	2.280(−03)
2.543(−02)	1.786(−02)	2.076(−02)	1.699(−02)	3.841(−03)	1.776(−02)	3.772(−03)	1.764(−02)
1.434(−01)	1.530(−01)	9.920(−02)	1.566(−01)	1.059(−02)	1.439(−01)	9.534(−03)	1.464(−01)
2.938(−01)	1.206(+00)	2.223(−01)	1.213(+00)	8.181(−03)	7.672(−01)	1.144(−02)	1.021(+00)
6.142(−02)	5.098(+00)	4.919(−02)	5.126(+00)	7.977(−04)	5.105(+00)	2.034(−03)	4.890(+00)

[a]Read as 2.835×10^{-11}, etc.

Source: *Ref. 1.*

Use of the parameters in calculating $\Gamma_j(t_0, t_s)$ values leads to results in good agreement with those of the CINDER code [2] but to significantly greater energy release rates for the 4- to 5- and 5- to 7.5-MeV energy groups than are given by ORIGEN code [3, 4] calculations (see Section 4.2.2) or ADENA code [5] calculations. Comparisons are shown in Figs. A6.1 and A6.2. The

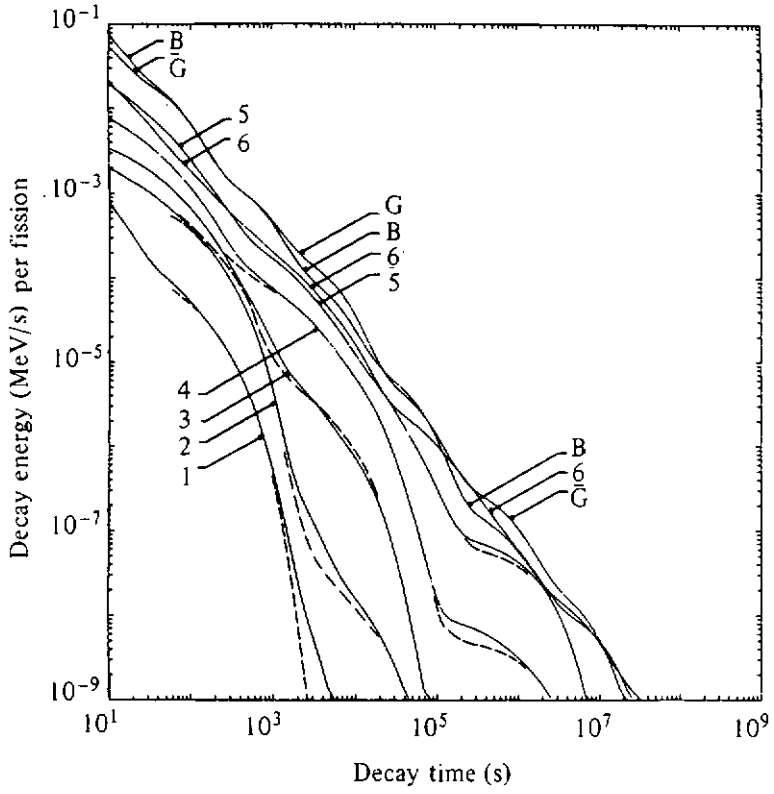

Figure A6.1 Total gamma (G)- and beta (B)-energy emission rates as a function of time after the thermal-neutron-induced fission of ^{235}U. The curves identified by the numbers 1 to 6 are the energy emission rates for fission-product gamma photons with energies in the ranges (5–7.5), (4–5), (3–4), (2–3), (1–2), and (0–1) MeV, respectively. The solid lines are results of calculations performed using the α_{ij} and λ_{ij} parameters [1]. The dashed lines are results from calculations using the ORIGEN code [3, 4].

differences in energy release rates may be attributed to differences in data bases [6]. The α_{ij} and λ_{ij} parameters and the CINDER code are based on version IV of the Evaluated Nuclear Data Files (ENDF/B-IV). Data for the ORIGEN code calculations are based, in part, on version V of the Evaluated Nuclear Data Files and, in part, on Evaluated Nuclear Structure Data Tables. Data for the ADENA calculations are based on ENDF/B-V, adjusted by comparison with experiment.

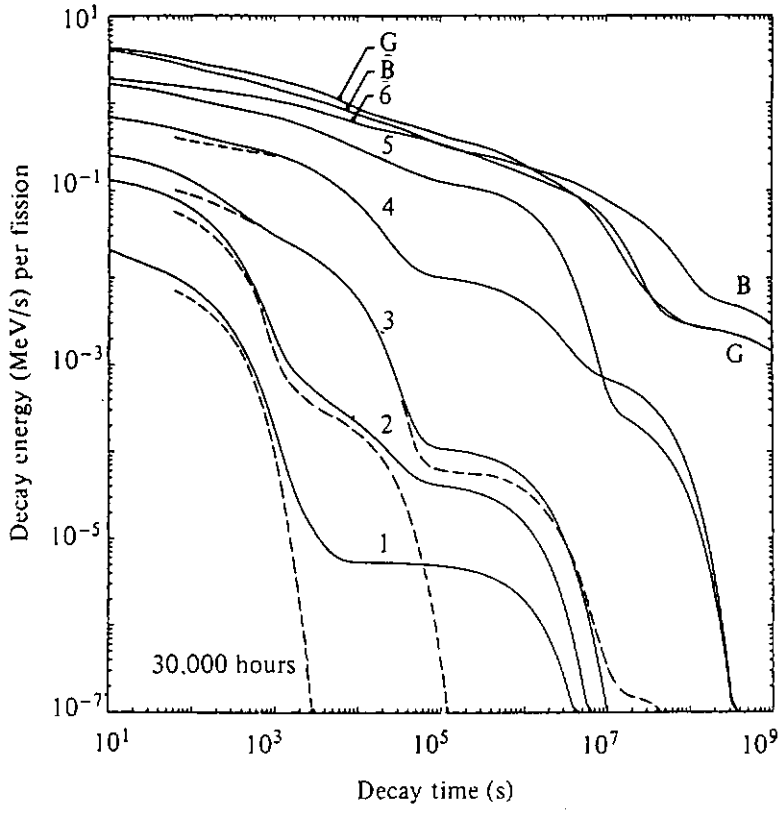

Figure A6.2 Total beta- and gamma-energy emission rates as a function of time after operation of a fission system for 30,000 h at a constant fission rate of one per second. The energy-group structure is the same as in Fig. A6.1. The solid lines are results of calculations performed using the α_{ij} and λ_{ij} parameters [1]. The dashed lines are results of calculations using the ORIGEN code [3, 4].

REFERENCES

1. R. J. LaBauve, T. R. England, D. C. George, and C. W. Maynard, "Fission Product Analytic Impulse Source Functions," *Nucl. Technol.* **56**, 332–339 (1982). The parameters have also been published in "Delayed Photon Sources for Shielding Applications," Report LA-UR 80-3305, Los Alamos Scientific Laboratory, Los Alamos, N.M., 1980.
2. T. R. England, R. Wilczynski, and N. L. Whittemore, "CINDER-7: An Interim Report for Users," Report LA-5885-MS, Los Alamos Scientific Laboratory, Los Alamos, N.M., 1976. See also Report LA-6472-PR, 1976, p. 60; and Report LA-6266-PR, 1976, p. 13.
3. O. W. Hermann and R. M. Westfall, "ORIGEN-S: SCALE System Module to Calculate Fuel Depletion, Actinide Transmutation, Fission Product Buildup and Decay, and Associated Radiation Source Terms," Sec. F7 of *SCALE: A Modular Code System for Performing Standardized Computer Analyses for Licensing Evaluation*, Report NUREG/CR-0200, Vol. 2, Oak Ridge National Laboratory, Oak Ridge, Tenn., October, 1982.

4. J. C. Ryman, "ORIGEN-S Data Libraries," Sec. M6 of *SCALE: A Modular Code System for Performing Standardized Computer Analyses for Licensing Evaluation*, Report NUREG/CR-0200, Vol. 3, (ORNL/NUREG/CSD-2/V3/R1) Oak Ridge National Laboratory, Oak Ridge, Tenn., 1983.
5. D. C. George, R. J. LaBauve, and T. R. England, "Application of Adjusted Data in Calculating Fission Product Decay Energies and Spectra," Report LA-9362-MS, Los Alamos Scientific Laboratory, Los Alamos, N.M., 1982.
6. R. J. LaBauve, T. R. England, and D. C. George, "Integral Data Testing of ENDF/B Fission Product Data and Comparisons of ENDF/B with Other Fission Product Data Files," Report LA-9090-MS, Los Alamos Scientific Laboratory, Los Alamos, N.M., 1981.

index